https://icbem-icebi-eit-2022.org/

International Conference on Bioelectromagnetism, Electrical Bioimpedance, and Electrical Impedance Tomography

ICBEM-ICEBI-EIT 2022

June 29 – July 1, 2022
Virtual / Kyung Hee University

Hosted by **ICBEM** Bioelectromagnetism **ICEBI** Electrical Bioimpedance **EIT** Electrical Impedance Tomography

Supported by **IFMBE**

Organized by **KYUNG HEE UNIVERSITY** **Impedance Imaging Research Center**

Sponsored by BiLab sciospec Dräger IKES Ikju Electronics KOREA TOURISM ORGANIZATION

Welcome Message

Dear Colleagues,

On behalf of the Organizing Committee, it is my great pleasure to welcome you to the ICBEM-ICEBI-EIT 2022, which is the first joint conference of three closely-related fields of bioelectromagnetism, electrical bioimpedance and electrical impedance tomography. In these ever-fascinating fields of science, engineering and medicine, I have been working with you and senior members for many years and thought that it would be great to have a joint conference covering many partially-overlapping topics from basics to engineering and clinical applications. I would like to deeply thank the leadership teams of the ISBEM, ISEBI and EIT for their support, collaboration and companionship to make it happen.

Until last year, I thought that we could have a face-to-face meeting. However, early this year, the Organizing Committee had to make a difficult decision to run the conference in a cyber space. Although we wanted to meet all of you face-to-face, we had no choice but to accept this unavoidable situation. While we were preparing for an online meeting, however, we realized that we should think out of the box since a cyber space could offer numerous new opportunities as well as conveniences and cost-effectiveness. I would like to thank the Local Organizing Committee for their many months of devoted and diligent efforts to make it happen. I also would like to thank the industry sponsors for their generous financial supports and understanding about the change in the conference format.

The Conference starts on June 29th with 3 plenary talks, 7 invited talks, 13 oral sessions, 3 mini-symposia, 2 special sessions, 2 workshops and poster sessions. Although there will be no traditional social events, we offer numerous cyber meeting opportunities. During the Conference, society meetings will be also held in the cyber space. Just before the plenary talk on June 29th, there will be a short ceremony to announce the Herman P. Schwan Awardee of the year 2022. I heartfully congratulate the Awardee for her seminal work on bioimpedance measurements and lifetime achievements. While the scientific program promises to be an outstanding experience, I hope that you will also have some time to meet colleagues in the cyber space and exchange ideas and share experiences for future collaborations.

At the closing ceremony on July 1st, finalized plans for the next meetings will be announced. After all of those unprecedented challenges we faced over the last 3 years and with still-existing uncertainties, I cannot predict whether the next ones will be face-to-face meetings or not. Nevertheless, I am sure we can keep on finding better ways of collaborations, especially since we are seeing great opportunities to find new applications of bioelectromagnetism, electrical bioimpedance and electrical impedance imaging from many talks presented in this joint conference.

Finally, I would like to take this opportunity to thank all the authors, all the reviewers, and all the volunteers for their efforts and valuable support to make this joint conference a reality.

Eung Je Woo, Ph.D.
Conference Chair, ICBEM-ICEBI-EIT 2022

Organizing Committee			
Conference Chair	Eung Je Woo	Kyung Hee University	Korea
Program Chair	Tong In Oh	Kyung Hee University	Korea
Program Co-chair	Hyung Joong Kim	Kyung Hee University	Korea
Program Co-chair	EunAh Lee	Kyung Hee University	Korea
ICBEM	Jaakko Malmivuo	Tampere University of Technology	Finland
ICBEM	Uwe Pliquett	Institut für Bioprozessund Analysenmesstechnik	Germany
ICEBI	Pedro Bertemes Filho	Universidade do Estado de Santa Catarina	Brazil
ICEBI	Orjan Grottem Martinsen	University of Oslo	Norway
ICEBI	Pere Riu	Universitat Politècnica de Catalunya	Spain
EIT	Ryan Halter	Dartmouth College	USA
EIT	Rosalind J. Sadleir	Arizona State University	USA
EIT	Zhanqi Zhao	Hochschule Furtwangen University	Germany

Scientific Program Committee		
Tong In Oh	Kyung Hee University	Korea
Hyung Joong Kim	Kyung Hee University	Korea
EunAh Lee	Kyung Hee University	Korea
Kirill Aristovich	University College London	UK
Pedro Bertemes Filho	State University of Santa Catarina	Brazil
Alistair Boyle	Kite Medical Ltd.	Ireland
Martin Bulst	Sciospec Scientific Instruments	Germany
Sungbo Cho	Gachon University	Korea
Chi Ryang Chung	Samsung Medical Center	Korea
Ryan Halter	Dartmouth College	USA
Huaiwu He	Union Medical Hospital	China
Geon-Ho Jahng	Kyung Hee University	Korea
Sunkook Kim	Sungkyunkwan University	Korea
Jin Woong Kim	Chosun University	Korea
Hyeuknam Kwon	Yonsei University	Korea
Jaakko Malmivuo	Tampere University of Technology	Finland
Satoru Nebuya	Shimane University	Japan
Uwe Pliquett	Institut für Bioprozessund Analysenmesstechnik	Germany
Vincent Senez	University of Lille	France
Igor Serša	Jožef Stefan Institute	Slovenia
Khin Khin Tha	Hokkaido University	Japan
Christian Tronstad	Oslo University Hospital	Norway
Tae Hoon Kim	Wonkwang University	Korea

Program at a Glance

<table>
<tr><th>Time (KST)</th><th colspan="2">6/29 (Wed)</th><th colspan="2">6/30 (Thu)</th><th colspan="2">7/1 (Fri)</th></tr>
<tr><td>05:25~05:30</td><td colspan="2">Opening & Introduction</td><td colspan="2"></td><td colspan="2"></td></tr>
<tr><td>05:30~06:00</td><td colspan="2">Invited Talk 01</td><td colspan="2">Invited Talk 03</td><td colspan="2">Invited Talk 05</td></tr>
<tr><td>06:00~07:30</td><td colspan="2">Oral Session 01</td><td colspan="2">Mini Symposium 01</td><td colspan="2">Special Session 02</td></tr>
<tr><td>07:30~12:30</td><td colspan="2" rowspan="2">Intermission</td><td colspan="2">Intermission</td><td colspan="2" rowspan="2">Intermission</td></tr>
<tr><td>12:30~13:00</td><td colspan="2" rowspan="2">Oral Session 06</td></tr>
<tr><td>13:00~13:45</td><td colspan="2" rowspan="3">Oral Session 02</td><td colspan="2" rowspan="3">Oral Session 09</td></tr>
<tr><td>13:45~14:00</td><td colspan="2">Break</td></tr>
<tr><td>14:00~14:15</td><td colspan="2" rowspan="2">Invited Talk 04</td></tr>
<tr><td>14:15~14:30</td><td colspan="2">Break</td><td colspan="2">Break</td></tr>
<tr><td>14:30~15:00</td><td colspan="2">Invited Talk 02</td><td colspan="2" rowspan="2">Mini Symposium 02</td><td colspan="2">Invited Talk 06</td></tr>
<tr><td>15:00~16:00</td><td colspan="2">Special Session 01</td><td colspan="2">Oral Session 10</td></tr>
<tr><td>16:00~16:15</td><td colspan="6">Break</td></tr>
<tr><td>16:15~16:30</td><td colspan="2">Break</td><td colspan="2" rowspan="2">Oral Session 07</td><td colspan="2" rowspan="2">Oral Session 11</td></tr>
<tr><td>16:30~17:30</td><td colspan="2">Oral Session 03</td></tr>
<tr><td>17:30~17:45</td><td colspan="6">Break</td></tr>
<tr><td>17:45~18:00</td><td colspan="2" rowspan="2">Oral Session 04</td><td colspan="2" rowspan="2">Oral Session 08</td><td colspan="2" rowspan="2">Oral Session 12</td></tr>
<tr><td>18:00~19:00</td></tr>
<tr><td>19:00~19:30</td><td>Break</td><td>Poster QnA in Metaverse (P01~P05)</td><td>Break</td><td>Poster QnA in Metaverse (P06~P10)</td><td>Break</td><td>Poster QnA in Metaverse (P11~P15)</td></tr>
<tr><td>19:30-20:30</td><td colspan="2">Plenary Talk 01
ISEBI Herman Schwan Award Ceremony & Award Lecture</td><td colspan="2">Plenary Talk 02</td><td colspan="2">Plenary Talk 03</td></tr>
<tr><td>20:30-21:00</td><td rowspan="3">Oral Session 05</td><td></td><td rowspan="3">Mini Symposium 03</td><td></td><td colspan="2" rowspan="2">Oral Session 13</td></tr>
<tr><td>21:00-21:30</td><td rowspan="2">EIT 2022 Steering Committee Meeting</td><td rowspan="2">ISBEM General Assembly</td></tr>
<tr><td>21:30-22:00</td><td colspan="2">Invited Talk 07</td></tr>
<tr><td>22:00-22:10</td><td colspan="4">Break</td><td colspan="2">Closing Ceremony</td></tr>
<tr><td>22:10-22:40</td><td colspan="2" rowspan="4">Workshop 01</td><td rowspan="3">Workshop 02</td><td>ICPRBI Meeting</td><td colspan="2" rowspan="4"></td></tr>
<tr><td>22:40-23:10</td><td>ISEBI General Assembly</td></tr>
<tr><td>23:10-23:30</td><td rowspan="2"></td></tr>
<tr><td>23:30-24:00</td><td></td></tr>
</table>

Program in Detail

DAY 1 **Wednesday, June 29**

Time	Duration	Session & Lecture Title	Chair / Organizer / Speaker
05:25-05:30	5′	Opening & Introduction	Eung Je Woo (Kyung Hee University)
05:30-06:00	30′	Invited Talk 01	Chair : Eung Je Woo (Kyung Hee University)
05:30-05:50	20′	MEG–MRI and Multi-locus TMS	Risto J. Ilmoniemi (Aalto University School of Science)
05:50-06:00	10′	Discussion	
06:00-07:30	90′	Oral Session 01 Electrical Impedance Tomography	Chair : **Steffen Leonhardt** (RWTH Aachen University) **Kirill Aristovich** (University College London)
06:00-06:15	15′	3D Mechanical Ventilation Control System Based on Electrical Impedance Tomography	Zhixi Zhang (The University of Edinburgh)
06:15-06:30	15′	Potential for Stroke Monitoring using Electrical Impedance Tomography with Scalp-Mounted Electrodes	Taweechai Ouypornkochagorn (Srinakharinwirot University)
06:30-06:45	15′	Feasibility Study of Peripheral Nerve Repair Monitoring with Electrical Impedance Tomography	Zhe Liu (The University of Edinburgh)
06:45-07:00	15′	High resolution EIT based heart rate detection using Synchrosqueezing	Henryk Richter (University of Rostock)
07:00-07:15	15′	Vesicoureteral Reflux Imaged in an Animal Model Using EIT	Alistair Boyle (Kite Medical)
07:15-07:30	15′	Simulation Phantoms for Evaluating an Automated Whole Breast Ultrasound/EIT system	Ethan K. Murphy (Dartmouth College)
07:30-13:00		Intermission	
13:00-14:15	75′	Oral Session 02 Tissue Property Imaging by MRI I	Chair : **Geon-Ho Jahng** (Kyung Hee University) **Hyung Joong Kim** (Kyung Hee University)
13:00-13:15	15′	Measurements of Electrical Properties in humans in vivo using Magnetic Resonance Imaging	Rosalind J. Sadleir (Arizona State University)
13:15-13:30	15′	Comparison of Diffusion Tensor MREIT and Conductivity Tensor Imaging in human subjects	S. Z. K. Sajib (Arizona State University)

Program in Detail

DAY 1 Wednesday, June 29

Time	Duration	Session & Lecture Title	Chair / Organizer / Speaker
13:30-13:45	15′	Detection of Electrical Conductivity Increases caused by Increased Neural Activity in vitro using Functional Magnetic Resonance Electrical Impedance Tomography	C. Barnett (Arizona State University)
13:45-14:00	15′	Low-frequency Conductivity Tensor Images of Rat Brain Tumor Using a 9.4T MRI	Nitish Katoch (Kyung Hee University Hospital)
14:00-14:15	15′	Assessment of electroporation in different complex structures by means of MREIT	Marko Stručić (University of Ljubljana)
14:15-14:30	15′	Break	
14:30-15:00	30′	**Invited Talk 02**	**Chair : EunAh Lee** (Kyung Hee University)
14:30-14:40	10′	Introduction for special session	EunAh Lee (Kyung Hee University)
14:40-15:00	20′	Recent advances in cell reprogramming and gene editing technology as the novel therapeutics for Neurological diseases	Jongpil Kim (Dongguk University)
15:00-16:00	60′	**Special Session 01** Effect of Galvano-Transduction in Tissue Regeneration	**Organizer : EunAh Lee** (Kyung Hee University)
15:00-15:20	20′	Biomimetic Surface Modification of Bioelectrodes for Improved Biocompatibility and Bioperformance	Jae Young Lee (Gwangju Institute of Science and Technology)
15:20-15:40	20′	Electrical and optical record of drug response on hiPSC Cardiomyocytes using Indium Tin Oxide electrode	Sungbo Cho (Gachon University)
15:40-16:00	20′	Panel Discussion	All Speakers and Moderator
16:00-16:30	30′	Break	
16:30-17:30	60′	**Oral Session 03** Electrical Impedance Imaging Algorithm I	**Chair : Hyeuknam Kwon** (Yonsei University)
16:30-16:45	15′	A Top-to-Bottom Generator of EIT and CT Bolus Signals	Diogo Filipe Silva (RWTH Aachen University)
16:45-17:00	15′	Light-weight CNNs with Dynamic Convolution for Lung EIT	Hao Yu (The University of Edinburgh)

Program in Detail

DAY 1 Wednesday, June 29

Time	Duration	Session & Lecture Title	Chair / Organizer / Speaker
17:00-17:15	15′	A Learning-Based 3D EIT Image Reconstruction Method	Zhaoguang Yi (The University of Edinburgh)
17:15-17:30	15′	Unsupervised Clustering of Lung Perfusion Features	Diogo Filipe Silva (RWTH Aachen University)
17:30-17:45	15′	Break	
17:45-19:00	75′	**Oral Session 04** Bio-impedance Measurement I	**Chair : Uwe Pliquett** (Institut für Bioprozessund Analysenmesstechnik) **Christian Tronstad** (Oslo University Hospital)
17:45-18:00	15′	Numerical and experimental studies on underwater fish monitoring with electrical impedance measurements	Lukasz J. Nowak (Wageningen University and Research)
18:00-18:15	15′	Dielectric relaxation spectroscopy mearsurements on amino acids	Jie Hou (Oslo University Hospital)
18:15-18:30	15′	Blood viscosity on glucose level using electrical impedance spectroscopy	Pedro Bertemes Filho (State Univertisy of Santa Catarina)
18:30-18:45	15′	Impact of Aortic Wall Stiffness on the Morphology of Impedance Cardiography Signal	Vahid Badeli (Graz University of Technology)
18:45-19:00	15′	Changes in Electrical Impedance of Pork Meat during Salt Diffusion by Wet-curing with Sodium-chloride	Philipp York Zimmermann (Hungarian University of Agriculture and Life Sciences)
19:00-19:30	30′	Break & Poster QnA in Metaverse	
19:30-20:30	60′	**Plenary Talk 01** ISEBI Herman Schwan Award Ceremony & Award Lecture	**Chair : Eung Je Woo** (Kyung Hee University) **Pere J Riu** (Universitat Politècnica de Catalunya)
19:30-20:30	60′	Bioimpedance – A Century of Research	Camelia Gabriel (MCL Technology)

Program in Detail

DAY 1 **Wednesday, June 29**

Time	Duration	Session & Lecture Title	Chair / Organizer / Speaker
20:30-22:00	90'	**Oral Session 05** Bioelectromagnetism	**Chair : Seward B. Rutkove** (Beth Israel Deaconess Medical Center) **Martin Bulst** (Sciospec Scientific Instruments)
20:30-20:45	15'	Cole model in time domain	Uwe Pliquett (Institut für Bioprozessund Analysenmesstechnik)
20:45-21:00	15'	Effect of Geometric Complexity of the Heart Model on the Inverse Problem of Electrocardiography	R. Martin Arthur (Washington University in St. Louis)
21:00-21:15	15'	Validation of non-empirical fat-free mass estimation model for a wrist-worn device	Aleksandr Polokhin (AURA Devices, Inc.)
21:15-21:30	15'	Robot Assisted Electrical Impedance Scanning (RAEIS) : concept, and current status of development	Zhuoqi Cheng (University of Southern Denmark)
21:30-21:45	15'	Cole bioimpedance parameters influence on strawberry ripening binary classification using decision trees	Pietro Ibba (Free University of Bolzano-Bozen)
21:45-22:00	15'	Impedivity of various human breast tissues	Wei Wang (Micro Image Biotech Ltd)
22:00-22:10	10'	Break	
22:10-24:00	110'	**Workshop 01**	**Sciospec Scientific Instruments**
22:10-24:00	110'	Impedance measurements - instruments, sensors & beyond. An introduction on how to choose, design and successfully use setups for electrical impedance spectroscopy	Sebastian Wegner (Sciospec Scientific Instruments) Martin Bulst (Sciospec Scientific Instruments) Sophie Müller (Sciospec Scientific Instruments)

Program in Detail

DAY 2 Thursday, June 30

Time	Duration	Session & Lecture Title	Chair / Organizer / Speaker
05:30-06:00	30'	Invited Talk 03	Chair : Tong In Oh (Kyung Hee University)
05:30-05:50	20'	Opportunities for clinical translation of impedance sensing and imaging devices	Ryan Halter (Dartmouth College)
05:50-06:00	10'	Discussion	
06:00-07:30	90'	Mini Symposium 01 Measuring Bioimpedance by Biosensors	Organizer : César A Gonzalez (Instituto Politécnico Nacional)
06:00-06:10	10'	Introduction for mini-symposium	Organizer
06:10-06:30	20'	Instrumentalization impacts when using biosensors	Pedro Bertemes Filho (State University of Santa Catarina)
06:30-06:50	20'	Dielectrophoretic electro-manipulation of biological cells and their characterization based on electrical impedance	Marius Andrei Olariu (Technical University of Iasi)
06:50-07:10	20'	Sensing accumulation of nanoparticles in tissue by electrical impedance	Svetlana Kashina (University of Guanajuato)
07:10-07:30	20'	Panel Discussion	All Speakers
07:30-12:30		Intermission	
12:30-13:45	75'	Oral Session 06 Tissue Property Imaging by MRI II	Chair : Rosalind J. Sadleir (Arizona State University) Matej Kranjc (University of Ljubljana)
12:30-12:45	15'	Single measurement of liver surface nodularity allows differentiation of liver fibrosis stage	Tae-Hoon Kim (Wonkwang University)
12:45-13:00	15'	Cerebral gray matter volume changes in postmenopausal estrogen replacement therapy	Tae-Hoon Kim (Wonkwang University)
13:00-13:15	15'	Evaluation of Low-frequency Conductivity Tensor Imaging Methods	Nitish Katoch (Kyung Hee University Hospital)
13:15-13:30	15'	Evaluation of Ionizing Radiation Induced Brain Tissue Response by MR-based Electrical Conductivity Imaging	Bup Kyung Choi (Kyung Hee University Hospital)

Program in Detail

DAY 2 Thursday, June 30

Time	Duration	Session & Lecture Title	Chair / Organizer / Speaker
13:30-13:45	15'	Characteristics of High and Low Frequency Conductivities in Patients with Alzheimer's Disease	Geon-Ho Jahng (Kyung Hee University Hospital at Gangdong)
13:45-14:00	15'	Break	
14:00-14:30	30'	**Invited Talk 04**	**Chair : Hyung Joong Kim** (Kyung Hee University)
14:00-14:20	20'	Noninvasive Assessment of Tissue Electrical Conductivity : Potential Clinical Value	Khin Khin Tha (Hokkaido University)
14:20-14:30	10'	Discussion	
14:30-16:00	90'	**Mini Symposium 02** Imaging Electrical Properties by MRI	**Organizer : Khin Khin Tha** (Hokkaido University) **Moderator : Nico van den Berg** (University Medical Centre Utrecht)
14:30-14:32	2'	Introduction for mini-symposium	Organizer
14:32-14:52	20'	Imaging Electrical Properties by MRI: Principles and Technical Aspects	Ulrich Katscher (Philips Research Laboratories)
14:52-15:12	20'	Tissue Electrical Properties : Findings of Animal Experiment on Tissue Response to Ionizing Radiation	Jin Woong Kim (Chosun University Hospital)
15:12-15:32	20'	Measurements of Electrical Properties in humans in vivo using Magnetic Resonance Imaging	Rosalind J. Sadleir (Arizona State University)
15:32-15:52	20'	Are we ready for the clinics?	Stefano Mandija (University Medical Center Utrecht)
15:52-16:00	8'	Panel Discussion	All Speakers
16:00-16:15	15'	Break	
16:15-17:30	75'	**Oral Session 07** Bio-impedance Measurement II	**Chair : Vincent Senez** (University of Lille)
16:15-16:30	15'	Wearable Device for Blood Glucose Level Analysis Using Electrical Bioimpedance and Near-infrared : Preliminary Results	Pedro Bertemes Filho (State University of Santa Catarina)
16:30-16:45	15'	Total body water in Colombian older adults through bioelectrical impedance analysis	Villada-Gómez Johan Sebastian (Universidad de Caldas)

Program in Detail

DAY 2 Thursday, June 30

Time	Duration	Session & Lecture Title	Chair / Organizer / Speaker
16:45-17:00	15′	Skin impedance in a sensor-sock for diabetic foot assessment	Christian Tronstad (Oslo University Hospital)
17:00-17:15	15′	The influence of isometric and isotonic muscle contraction on measured resistance and reactance during seated leg curls	Alfred Hülkenberg (RWTH Aachen University)
17:15-17:30	15′	Neural Noise Module: Automated Error Modeling using Adversarial Neural Networks	Benjamin Schindler (Universität Leipzig)
17:30-17:45	15′	Break	
17:45-19:00	75′	**Oral Session 08** Bioelectromagnetic Instrumentation	**Chair : Orjan Grottem Martinsen** (University of Oslo) **Ryan Halter** (Dartmouth College)
17:45-18:00	15′	A Hybrid FE-EFG Method for 2D MIT Forward Problem Computation	Hassan Yazdanian (K. N. Toosi University of Technology)
18:00-18:15	15′	Contactless magnitude induction phase shift measurement for assessment of cerebrovascular autoregulation on cerebral ischemic rabbits	Xu Jia (Army Medical University)
18:15-18:30	15′	Reduced effective sensitivity of Acoustoelectric Tomography	Ben Keeshan (Carleton University)
18:30-18:45	15′	A Modified Howland Current Source Design for Simultaneous EIT/ECG Data Acquisition	Ahmed Abdelwahab (State University of New York)
18:45-19:00	15′	EIT-based Surgical Margin Probe Development	Shannon Kossmann, Sophie Lloyd (Dartmouth College)
19:00-19:30	30′	Break & Poster QnA in Metaverse	
19:30-20:30	60′	**Plenary Talk 02**	**Chair : Eung Je Woo** (Kyung Hee University) **Pedro Bertemes Filho** (State University of Santa Catarina)
19:30-20:15	45′	Harvesting electrical energy from twisted carbon nanotube yarns and biomedical applications	Seon Jeong Kim (Hanyang University)

Program in Detail

DAY 2 Thursday, June 30

Time	Duration	Session & Lecture Title	Chair / Organizer / Speaker
20:15-20:30	15′	Discussion	
20:30-22:00	90′	**Mini Symposium 03** Stroke Volume and Lung Perfusion Measurements using Electrical Impedance Tomography : State of the Art	**Organizer : Zhanqi Zhao** (Fourth Military Medical University) **Yun Long** (Peking Union Medical College Hospital)
20:30-20:35	5′	Introduction for mini-symposium	Organizer
20:35-20:50	15′	Electrical Impedance Tomography Use for the Assessment of Regional Lung Perfusion	Inéz Frerichs (University Medical Centre Schleswig-Holstein)
20:50-21:05	15′	Estimation of Stroke Volume using Lead forming for Continuous Monitoring without image reconstruction	Kyounghun Lee (Kyung Hee University Hospital)
21:05-21:20	15′	Saline bolus-based EIT method of lung perfusion in the diagnosis of pulmonary embolism	Siyi Yuan (Peking Union Medical College Hospital)
21:20-21:35	15′	Lung perfusion by EIT in COVID-19	Tommaso Mauri (University of Milan)
21:35-21:50	15′	Regional Ventilation/Perfusion match by Electrical Impedance Tomography: where are we now?	João Batista Borges (Charles University)
21:50-22:00	10′	Panel Discussion	All Speakers
22:00-22:10	10′	Break	
22:10-23:30	80′	**Workshop 02**	**Draeger Korea**
22:10-23:30	80′	Image-Guided Lung Protection – Introducing the concept and clinical application examples	Eckhard Teschner (Draegerwerk AG & Co. KGaA)

Program in Detail

DAY 3 Friday, July 1

Time	Duration	Session & Lecture Title	Chair / Organizer / Speaker
05:30-06:00	30'	**Invited Talk 05**	**Chair : Eung Je Woo** (Kyung Hee University)
05:30-05:50	20'	The EIT Experience at MedIT Aachen – history and perspectives	Steffen Leonhardt (RWTH Aachen University)
05:50-06:00	10'	Discussion	
06:00-07:30	90'	**Special Session 02** Food Quality Control and Assessment by Impedance Spectroscopy	**Organizer : Pedro Bertemes Filho** (State University of Santa Catarina)
06:00-06:10	10'	Introduction for special session	Organizer
06:10-06:30	20'	Bioimpedance spectroscopy as tool for bovine milk rastreability	Pedro Bertemes Filho (State University of Santa Catarina)
06:30-06:45	15'	Measuring perishable seafood using bioimpedance spectroscopy	Keith Cox (Certified Quality Foods)
06:45-07:00	15'	Electrical impedance for fast and simple assessment of sugar beet quality	Chris Gansauge (Institut für Bioprozessund Analysenmesstechnik)
07:00-07:20	20'	Detection of PSE-like meat quality : How does subjective quality ranking compare with bioimpedance testing?	Sisay Mebre Abie (Norwegian University of Life Sciences)
07:20-07:30	10'	Panel Discussion	All Speakers
07:30-13:00		Intermission	
13:00-14:15	75'	**Oral Session 09** Electrical Impedance Imaging Algorithm II	**Chair : Kiwan Jeon** (National Institute for Mathematical Sciences)
13:00-13:15	15'	The Degree of Lung Collapse Estimation Method Using Convolutional Autoencoder and Neural Regression in Electrical Impedance Tomography	Won-Doo Seo (Yonsei University Graduate School)
13:15-13:30	15'	The calculation of Flow Index by electrical impedance tomography	Pu Wang (Fourth Military Medical University)

Program in Detail

DAY 3 Friday, July 1

Time	Duration	Session & Lecture Title	Chair / Organizer / Speaker
13:30-13:45	15′	Predicting outcomes of high flow nasal cannula based on EIT indexes using machine learning	Zhe Li (Renji Hospital, Shanghai Jiao Tong University)
13:45-14:00	15′	A Physical Model of the Rat Thorax for EIT Measurements	Silke Borgmann (University of Freiburg)
14:00-14:15	15′	Detection of a False Prior in Discrete Cosine Transformation based EIT Algorithm	Rongqing Chen (University of Freiburg)
14:15-14:30	15′	Break	
14:30-15:00	30′	**Invited Talk 06**	**Chair : Tong In Oh** (Kyung Hee University)
14:30-14:50	20′	Electrical Impedance Tomography to Aid Implantable Neural Interfaces	Kirill Aristovich (University College London)
14:50-15:00	10′	Discussion	
15:00-16:00	60′	**Oral Session 10** Fast Neural Electrical Impedance Tomography	**Chair : Zhanqi Zhao** (Fourth Military Medical University)
15:00-15:15	15′	Geometrical Optimisation of Depth Arrays for Fast Neural EIT	Adam Fitchett (University College London)
15:15-15:30	15′	EIT imaging of rhythmic neural activity in the vagus nerve	Enrico Ravagli (University College London)
15:30-15:45	15′	Characterising and imaging slow impedance responses to evoked somatosensory activity in the rat brain using EIT	Karolina Kozeniauskaite (University College London)
15:45-16:00	15′	Imaging Conductvitiy Changes in a Saline Tank with Magnetic Detection Electrical Impedance Tomography with Optically Pumped Magnetometers	Kai Mason (University College London)
16:00-16:15	15′	Break	
16:15-17:30	75′	**Oral Session 11** Clinical Application of Bio-impedance I	**Chair : Igor Serša** (Jožef Stefan Institute) **Benjamin Sanchez** (University of Utah)
16:15-16:30	15′	Screening of Cervical Intraepithelial Neoplasia based on Multiple Features Extraction of Bioimpedance Spectroscopy	Tingting Zhang (Kyung Hee University Hospital)

Program in Detail

DAY 3 Friday, July 1

Time	Duration	Session & Lecture Title	Chair / Organizer / Speaker
16:30-16:45	15′	Bioelectrical impedance method to determine postoperative swelling of the knee joint	Lucas Lindeboom (Stichting IMEC Nederland/Holst Centre)
16:45-17:00	15′	Estimation of skeletal muscle specific force in diseased muscle using needle electrical impedance myography	Benjamin Sanchez (University of Utah)
17:00-17:15	15′	Assessment of the Diagnostic Value of Body Impedance in Pre-eclampsia Screening	Svetlana Pavlovna Shchelykalina (Pirogov Russian National Research Medical University)
17:15-17:30	15′	Electrical Impedance Spectroscopy of Ex-Vivo Human Lung Tissue	Harshavardhan Devaraj (Dartmouth College)
17:30-17:45	15′	Break	
17:45-19:00	75′	**Oral Session 12** Clinical Application of Bio-impedance II	**Chair : Richard Bayford** (Middlesex University) **Satoru Nebuya** (Shimane University)
17:45-18:00	15′	Initial Results in a hdEEG/EIT Clinical Study on Strokes	Haley Richards (Dartmouth College)
18:00-18:15	15′	Non-invasive Hemodynamic Monitoring during Hemodialysis using Electrical Impedance Images	Jinwon Mok (Kyung Hee University)
18:15-18:30	15′	Neural Network-Based Cardiac-Related Image Denoising for Chest Electrical Impedance Tomography	Ke Zhang (Tsinghua University)
18:30-18:45	15′	Quantitative Analysis of Severity in Obstructive Sleep Apnea Patients based on Tidal Volume Reduction and Event Duration for Sleep-related Breathing Disorders	Taewook Chang (Kyung Hee University Hospital)
18:45-19:00	15′	Assessment of low back pain in helicopter pilots using electrical bio-impedance technique	Hang Wang (Fourth Military Medical University)
19:00-19:30	30′	Break & Poster QnA in Metaverse	
19:30-20:30	60′	**Plenary Talk 03**	**Chair : Eung Je Woo** (Kyung Hee University)
19:30-20:15	45′	Electrical Impedance Tomography for advanced respiratory monitoring – perspectives beyond the Covid-19 pandemic	Tobias Becher (University Medical Center Schleswig-Holstein)

Program in Detail

DAY 3 Friday, July 1

Time	Duration	Session & Lecture Title	Chair / Organizer / Speaker
20:15-20:30	15'	Discussion	
20:30-21:30	60'	**Oral Session 13** Clinical Application of Bio-impedance III	**Chair : Inez Frerichs** (University Medical Centre Schleswig-Holstein)
20:30-20:45	15'	Using EIT to guide chest physiotherapy in patients with pneumonia	Qing Li (Beijing Rehabilitation Hospital, Capital Medical University)
20:45-21:00	15'	Ventilation Volume of Mechanically Ventilated Patients from EIT Data on a Novel Electrode Solution : A Case Study	Nilton Barbosa da Rosa Junior (Colorado State University)
21:00-21:15	15'	Impact of Patient Position on Neonatal Chest EIT	Nima Seifnaraghi (Middlesex University)
21:15-21:30	15'	Electrical Impedance Tomography to Assess Pulmonary Function in Amyotrophic Lateral Sclerosis Patients	Allaire Doussan (Dartmouth College)
21:30-22:00	30'	**Invited Talk 07**	**Chair : Kyounghun Lee** (Kyung Hee University Hospital)
21:30-21:50	20'	Patterns of regional ventilation, perfusion and V/Q match images by EIT in acute respiratory failure	Huaiwu He (Peking Union Medical College Hospital)
21:50-22:00	10'	Discussion	
22:00-22:10	10'	**Closing Ceremony**	**Eung Je Woo** (Kyung Hee University)

Contents

Day 1. Wednesday, June 29

Day 2. Thursday, June 30

Day 3. Friday, July 1

DAY 1

Wednesday, June 29, 2022

Invited Talk 01

Speaker Risto Ilmoniemi (Aalto University School of Science)

“MEG–MRI and Multi-locus TMS”

Proceedings of the International Conference of Bioelectromagnetism, Electrical Bioimpedance,
and Electrical Impedance Tomography June 29 – July 1, 2022 / Kyung Hee University, Seoul, Korea

MEG–MRI and Multi-locus TMS

Risto J. Ilmoniemi
Department of Neuroscience and Biomedical Engineering, Aalto University School of Science, Finland

Correspondence : risto.ilmoniemi@aalto.fi

Abstract–Noninvasive neurophysiological methods include electroencephalography (Berger, 1929), magnetoencephalography (Cohen, 1972), transcranial magnetic stimulation (Barker et al., 1985), and transcranial electrical stimulation (Nitsche and Paulus 2000). I will describe two novel neurophysiological technologies under development in my research group. We are building a system where superconducting quantum interference devices measure both magnetoencephalographic and magnetic resonance imaging signals; this combination will offer unprecedented accuracy of positional data, new kinds of ultra-low-field magnetic resonance information and improved workflow. Furthermore, we are developing novel multi-locus transcranial magnetic stimulation technology, consisting of multiple coils that allow millisecond-scale control of the cortical target location and a closed-loop operation, with feedback from concurrent electroencephalography.

Acknowledgments

These projects have received funding from the European Research Council (ERC Synergy) under the European Union's Horizon 2020 research and innovation programme (ConnectToBrain, grant agreement No 810377), from the European Union's Horizon 2020 research and innovation programme under grant agreement No 686865 (BREAKBEN), from the Academy of Finland, and from the Jane and Aatos Erkko Foundation. The author would like to express his gratitude to his research group members and collaborators.

References

Barker AT, Jalinous R and Freeston IL 1985 Non-invasive magnetic stimulation of human motor cortex The Lancet 325 1106–7

Berger H 1929 Über das Elektroenkephalogramm des Menschen Archiv für Psychiatrie und Nervenkrankheiten 87 527–70

Cohen D 1972 Magnetoencephalography: detection of the brain's electrical activity with a superconducting magnetometer Science 175 664–6

Nitsche MA and Paulus W 2000 Excitability changes induced in the human motor cortex by weak transcranial direct current stimulation *Journal of Physiology* **527** 633–9

DAY 1

Wednesday, June 29, 2022

Oral Session 01

Electrical Impedance Tomography

Chair Steffen Leonhardt (RWTH Aachen University)
Kirill Aristovich (University College London)

O 01-01 **3D Mechanical Ventilation Control System Based on Electrical Impedance Tomography**
Zhixi Zhang (The University of Edinburgh)

O 01-02 **Potential for Stroke Monitoring using Electrical Impedance Tomography with Scalp-Mounted Electrodes**
Taweechai Ouypornkochagorn (Srinakharinwirot University)

O 01-03 **Feasibility Study of Peripheral Nerve Repair Monitoring with Electrical Impedance Tomography**
Zhe Liu (The University of Edinburgh)

O 01-04 **High resolution EIT based heart rate detection using Synchrosqueezing**
Henryk Richter (University of Rostock)

O 01-05 **Vesicoureteral Reflux Imaged in an Animal Model Using EIT**
Alistair Boyle (Kite Medical)

O 01-06 **Simulation Phantoms for Evaluating an Automated Whole Breast Ultrasound/EIT system**
Ethan K. Murphy (Dartmouth College)

Proceedings of the International Conference of Bioelectromagnetism, Electrical Bioimpedance,
and Electrical Impedance Tomography June 29 – July 1, 2022 / Kyung Hee University, Seoul, Korea

3D Mechanical Ventilation Control System Based on Electrical Impedance Tomography

Zhixi Zhang[1], Hao Yu[1] and Jiabin Jia[1]
[1] Agile Tomography Group, Institute for Digital Communications, School of Engineering,
The University of Edinburgh, Edinburgh, U.K.

Correspondence : Jiabin Jia, e-mail : jiabin.jia@ed.ac.uk

Abstract–The number of patients with lung disease is increasing year by year worldwide, therefore, some effective diagnosis, monitoring and treatment techniques are more and more demanding. Electrical Impedance Tomography (EIT) is gradually used in the medical field due to its low cost, no radiation and real-time monitoring. Most of the traditional ventilators can only provide one-dimensional information such as pressure. Such information cannot analyze the local lung injury. The combination of EIT and ventilator can realize real-time bedside monitoring, expand the dimension of effective information and clearly see the volume change of the lung, which could help doctors better analyze the quality of lung function. In this study, three-dimensional lung imaging was realized through single-layer electrodes, and tidal volume information is extracted from 3D reconstruction images as feedback input for the control system to achieve a closed control loop. An active disturbance rejection control (ADRC) method with excellent anti-disturbance ability is designed in the work to inprove the stability the system. The simulation results show that the mechanical ventilation system proposed can not only effectively follow the breathing rhythm, but also observe the three-dimensional state of the lungs in real-time.

Keywords: Electrical impedance tomography; mechanical ventilation; lung image; control system.

1. Introduction

As an essential medical device, mechanical ventilation can improve respiratory function and reduce breathing consumption for patients who are physically unable to breathe (Bellani *et al* 2016), such as acute respiratory distress syndrome (ARDS) (Rodríguez-Olivares *et al* 2021). However, conventional ventilator could cause the ventilator induced lung injury (VILI), which was expounded in Smith's work (Smith *at al* 2013). Due to the unique imaging modality, EIT can provide medical information with no side effects on the human body. Therefore, using the medical information provided by EIT to guide the mechanical ventilation systems can effectively reduce VILI. Similar concept was proposed by Tregidgo (Tregidgo *et al* 2018). However, EIT is mainly used as a monitoring instrument to measure the change of lung volume in time, rather than providing automatic guidance for the air flow control of the ventilator in practice.

In order to improve the intelligence of the ventilator and utilize the advantages of EIT as much as possible, mechanical ventilation guided by EIT is studied in this work. The paper uses the reconstructed image of EIT as a feedback loop input to realize a closed-loop ventilator control. Furthermore, 3D EIT images can provide more valuable information, such as localized lung dilation or atelectasis. The structure of this paper is organized as follow. Section 2 describes the detail of the method and Section 3 introduces the setting of parameters. Section 4 demonstrates the 3D reconstruction imaging results and the simulation results of control system. Section 5 discusses the results and conclusion is drawn in Section 6.

2. Method

This section introduces how to realize a closed-loop mechanical ventilation system, which consists of three parts, namely the 3D EIT image reconstruction process, the ADRC control strategy and the mathematical model of the respiratory system. The respiratory tidal volume is obtained by calculating the number of pixels in the EIT lung images. The difference between the reference and reconstructed tidal volume is used as a input control signal.

2.1 3D imaging reconstruction

The reconstructed 3D image can observe the degree of expansion and contraction of the patient's lung tissue due to inhomogeneity. In addition, the local position of VILI can be identified as early as possible regardless of whether the patient is lying on his back or on his side.

Figure 1 shows the 3D thoracic and lung models in COMSOL. Taking Z = 0 as the datum plane, the heights of intercepted planes are -11cm, -13cm, -14cm, -15cm, -16cm, -17cm and -19cm, and the model is divided into eight parts from top to bottom. Sixteen electrodes were evenly placed in the middle layer (Z = -15cm) , around the thoracic cavity. Applying the excitation current and measuring the excitation voltage is achieved through a layer of electrodes. Injection of the excitation current and measurement of the excitation voltage is achieved through a layer of electrodes. Cross sectional images in the other layers are reconstructed using measurement voltage and sensitive matrix in each layer.

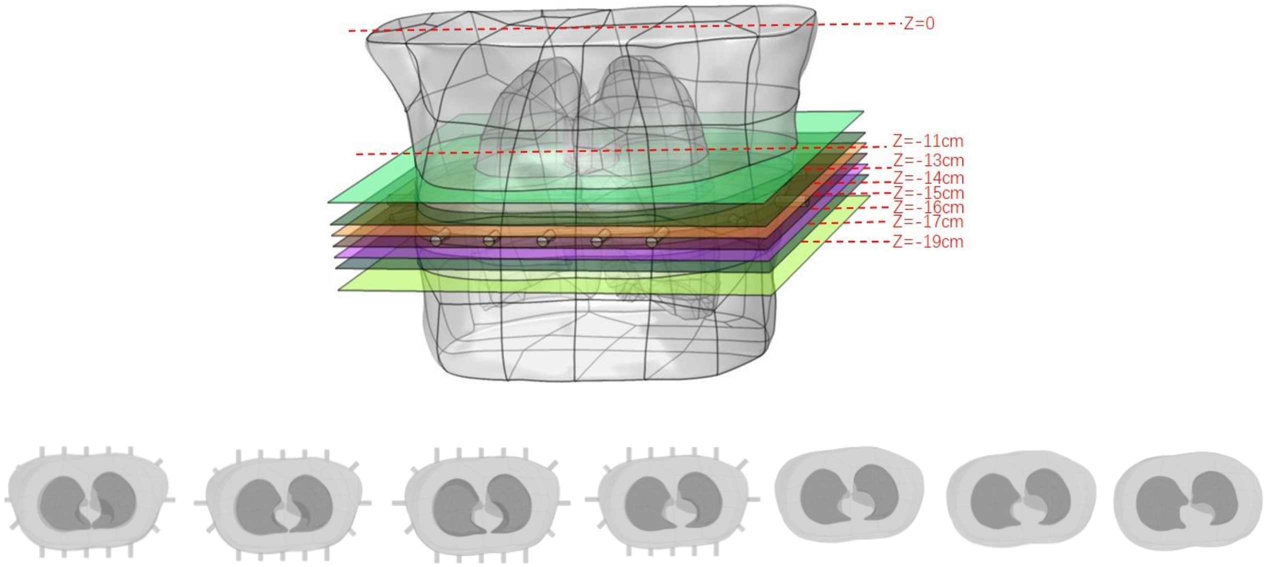

Z = -11cm Z = -13cm Z = -14cm Z = -15cm Z = -16cm Z = -17cm Z = -19cm

Figure 1. 3D lung model in COMSOL and sections of different heights.

2.2 ADRC control strategy

Linear ADRC was proposed by Gao (Gao 2006) to make the application of the control strategy more convenient. To address the disturbance problem of the ventilation system, a single closed-loop linear ADRC is designed. The block diagram of linear ADRC is shown in Figure 2.

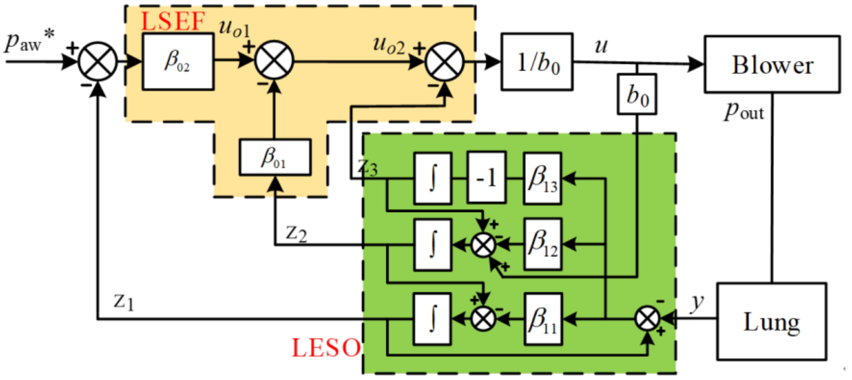

Figure 2. Block diagram of the linear ADRC control strategy.

2.3 Respiratory System

The basic respiratory system contains a blower, connection hose and lung. The lung volume is controlled by controlling the airway pressure. To simplify the mathematical model of the lung, a linear one-compartment model is adopted in the paper (Jaber *et al* 2020). The relationship between air flow rate and pressure can be found in the below formulas

$$Q(t) = \frac{dV(t)}{dt} \tag{1}$$

where $Q(t)$ = inspiratory flow [L/s]
$V(t)$ = the lung volume [L]

$$Q(t) = \frac{P_{mou}(t) - P_{lung}(t)}{R_{lung}} \tag{2}$$

where $P_{mou}(t)$ = the pressure at the mouth [CmH_2O]
$P_{lung}(t)$ = lung airway pressure [CmH_2O]
R_{lung} = lung resistance [CmH_2O s/L].

$$\dot{P}_{lung} = \frac{P_{mou} - P_{lung}}{C_{lung} R_{lung}} \tag{3}$$

where C_{lung} = the compliance of lung [L/ CmH_2O].

3. Parameters setup

3.1 Parameters of reconstruction

In the COMSOL modelling process, the electrical conductivity of the thorax and the lung in the end-expiratory state is set to 0.48 S/m and 0.12 S/m respectively. The amplitude of excitation current is set as $0.01A$. In addition, the end-expiratory state is taken as the reference.

3.2 Parameters of respiratory system

According to the real situation of a human body, the breathing pattern is simplified to sinusoidal waveform, the breathing cycle is 4s, and the tidal volume is 0.5L. In the simulation, it is assumed that the ventilator provides all the air volume required by the human body to make it stable at normal breathing levels.

In the lung mathematical model, the two most important parameters are the compliance of the lung and the airway resistance of the lung. To simplify the model, the value of lung compliance varies linearly. Initially, lung compliance is 0.2 [L/ CmH2O] and airway resistance is 0.1[CmH2O s/L].

4. Results

4.1 3D imaging reconstruction results of EIT

First of all, Figure 3 shows the sensitive fields of different heights. In addition, the more important result is the reconstructed image of seven layers of lungs at different heights including the middle excitation layer in half a respiratory cycle, accompanied by 50dB Gaussian noise.

The conductivity change along the air volume in the lungs from the end of inspiration to the end of expiration can be clearly seen in the Figure 3. The darker the colour of the lungs, the more air there is in the lungs. During exhalation, the lungs gradually decrease in volume and become lighter in colour. When approaching the end-expiratory state, the imaging quality is relatively low, and the effect of noise is relatively large. Although the shape of the lungs is not clearly reconstructed, the two lungs can be clearly seen with relatively clear boundaries.

In order to achieve better imaging results, the number of iterations for each layer of images is different. The inhalation process is the mirror image of the exhalation process and is not shown in this paper.

4.2 The simulation results of control system

The two respiration curves are shown in Figure 4. The solid black line represents the reference signal, which is the expected tidal volume curve for normal human breathing. The red line represents the output curve of the control system, which is affected by the EIT reconstructed image information. From the curves, it can be seen that the output curve lags slightly with the reference curve. And the peak-to-peak value is slightly lower than the reference curve.

At the 4th second, a small disturbance signal is added to the system. The output signal has a slight fluctuation but is quickly adjusted back to track the reference signal.

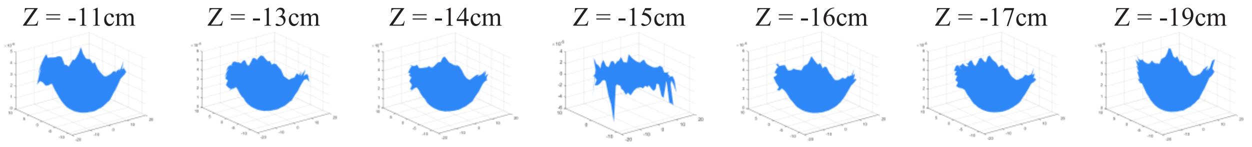
Z = -11cm Z = -13cm Z = -14cm Z = -15cm Z = -16cm Z = -17cm Z = -19cm

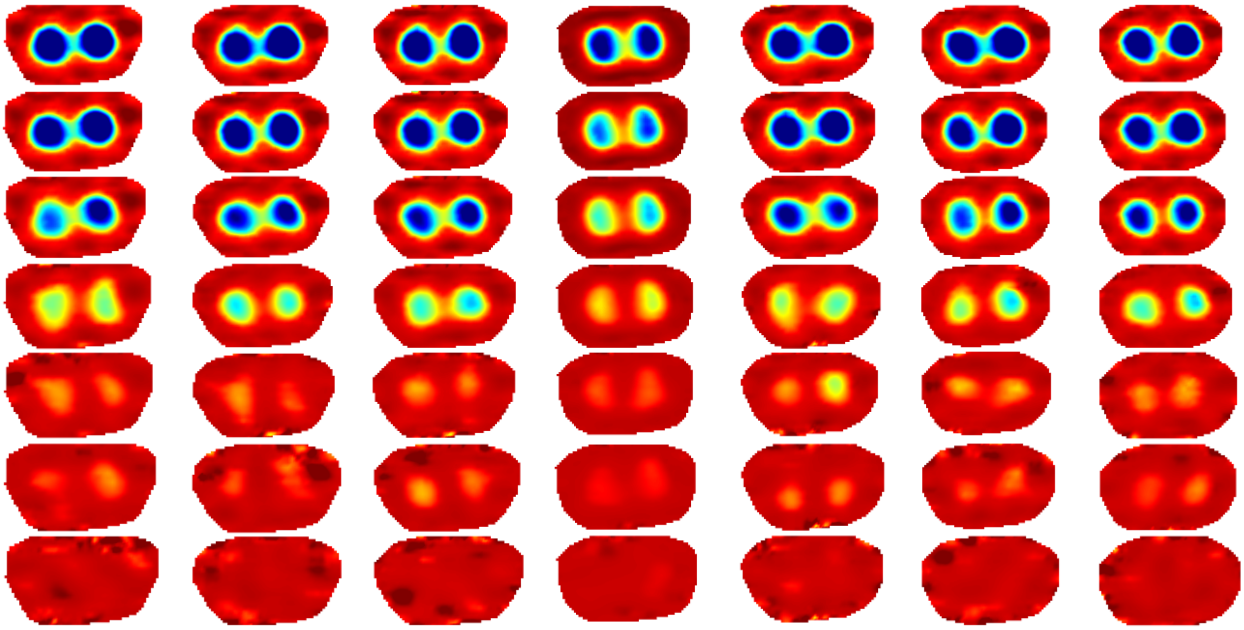

Figure 3. Lung image reconstruction results of half breathing cycle with 50dB noise.

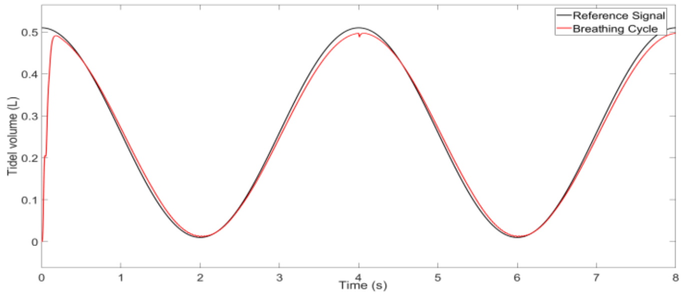

Figure 4. The breathing cycle results of mechanical ventilation.

5. Discussion

Introducing the EIT image information into the control system can increase multiple controllable variables. The joint regulation of multiple variables can make the system control more precise. It can also provide more effective medical information. However, in the process of realizing 3D image reconstruction, in order to improve the imaging speed, the imaging quality is sacrificed. In the follow-up work, machine learning methods could be applied to maintain high imaging speed and quality.

6. Conclusions

The work introduced in this paper mainly has two aspects. On the one hand, it reconstructs 3D images by means of 2D image reconstruction. On the other hand, real-time lung volume is extracted from 3D EIT reconstruction images to achieve a closed-loop control. Achieving closed-loop control is an important part of advancing mechanical ventilation into intelligent control.

References

Bellani G, Laffey JG, Pham T, et al. 2016 Epidemiology, Patterns of Care, and Mortality for Patients With Acute Respiratory Distress Syndrome in Intensive Care Units in 50 Countries, *JAMA*. **315** 788–800.

Gao Z. 2006 Scaling and bandwidth-parameterization based controller tuning, *Proceedings of the American control conference*. **6** 4989–4996.

Jaber M, Hamawy L., Hajj-Hassan M, Ali A. M. and Kassem A., 2020 MATLAB/Simulink Mathematical Model for Lung and Ventilator, *2020 32nd International Conference on Microelectronics (ICM)*. **2020** 1-5.

Rodríguez-Olivares N. A., Nava-Balanzar L. and Barriga-Rodríguez L. 2021 Differential Pressure Spirometry for Mechanical Ventilation Using Dichotomic Search *IEEE Transactions on Instrumentation and Measurement*. **70** 1-10.

Smith J. B. and Bates H. T. J. 2013 Assessing the Progression of Ventilator-Induced Lung Injury in Mice, *IEEE Transactions on Biomedical Engineering*. **60** 3449-3457.

Tregidgo F. J. H, Crabb G. M., Hazel L. A. and Lionheart R. B. W. 2018 On the Feasibility of Automated Mechanical Ventilation Control Through EIT, *IEEE Transactions on Biomedical Engineering*. **65** 2459-2470.

O 01-02

Proceedings of the International Conference of Bioelectromagnetism, Electrical Bioimpedance,
and Electrical Impedance Tomography June 29 – July 1, 2022 / Kyung Hee University, Seoul, Korea

Potential for Stroke Monitoring using Electrical Impedance Tomography with Scalp-Mounted Electrodes

Taweechai Ouypornkochagorn[1], Nataša Terzija[2], Paul Wright[3], John L. Davidson[3],
Nick Polydorides[4] and Hugh McCann[4]
[1]Department of Biomedical Engineering, Srinakharinwirot University, Thailand
[2]Arriver Software GmbH, Unterschleißheim, Germany
[3]Department of Electrical and Electronic Engineering, The University of Manchester, Manchester, UK
[4]School of Engineering, The University of Edinburgh, Edinburgh, UK.

Correspondence : Taweechai Ouypornkochagorn, e-mail : taweechai@g.swu.ac.th

Abstract–Electrical Impedance Tomography of the human head using scalp-mounted electrodes may be of value for stroke diagnosis and/or monitoring. To image the relevant cerebral hemodynamics, there is a complex interplay between measurement sensitivity, frame rate, number of measurements per frame, and the chosen image reconstruction method, including both the data inversion maths and the head model. Analysis of the performance of a novel non-linear data inversion method is presented here, and it is applied to human data recorded by a measurement system operating at two different sensitivity levels, with near-diametric 10 kHz current injection yielding 509 nearest-neighbour measurements per frame. Image reconstruction of simulated data from 20mm-diameter "blood" spheres placed at different locations in the brain indicates excellent localisation at both sensitivity levels. Analysis of real data obtained with the more sensitive measurement system, using the novel image reconstruction method, enables 50 frames per second imaging of the sub-second cerebral hemodynamics underlying the rheoencephalographic waveform that is synchronised with the cardiac cycle. Robust imaging during transient hemodynamic response tests requires careful account to be taken of the rheoencephalographic waveform, and shows excellent consistency with the expected cerebral hemodynamic phenomena. The methodology discussed here is promising for further stroke studies.

Keywords: Cerebral; hemodynamic; transient hyperemic response; THR.

1. Introduction

We have demonstrated previously a methodology for Electrical Impedance Tomography (EIT) using scalp-mounted electrodes that is sensitive to cerebral hemodynamics (Ouypornkochagorn, et al., 2022). A major challenge for its application to stroke diagnosis and/or monitoring is its capability to localise a bleed without having had prior access to the patient, to respond to changes in its status, and to present the resulting images to a clinician, all of which we address in this paper. Other authors have considered the application of EIT to stroke monitoring, e.g. (Goren, et al., 2018). However, we have used a measurement system that has a unique combination of high frame rate and low noise, with image reconstruction using a novel non-linear method.

2. Methods

2.1 EIT Hardware

We have used the EIT sub-system of the fEITER instrument, initially reported in (McCann, et al., 2011) and described in detail in (Ouypornkochagorn, et al., 2022). Briefly, it is a 32-electrode system, illustrated in Figure 1, with 10 kHz excitation current in 20 programmable near-diametric current patterns, acquiring data (509 nearest-neighbour voltage measurements) at 100 frames per second (fps). As described in (Ouypornkochagorn, et al., 2022), the initial version (Mk. I) achieved a signal-to-noise-ratio (SNR) in the range 77 - 86 dB in human trials, and the improved version (Mk. II) achieved 86 – 95 dB, both providing common-mode rejection ratio >90 dB at 10 kHz. The excitation current amplitude of the Mk. I system is 0.353 mA_{rms}, and that of the Mk. II system is 0.707 mA_{rms}.

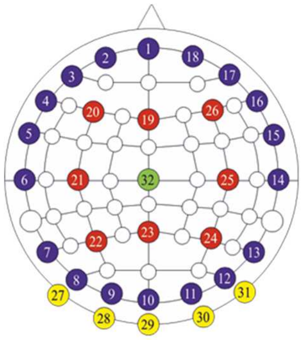

Figure 1. Electrode configuration.

2.2 Inverse Model

A generic model was used containing 208k elements (built upon on the 53k model generously supplied by Prof. D. Holder's UCL group (Gilad, et al., 2007)). Electrode array geometry was included. Five tissues were contained in the model with different conductivities: scalp (0.584 S/m), skull (0.0084 S/m), CSF (1.802 S/m), grey matter (0.2849 S/m), and white matter (0.2556 S/m) (Ouypornkochagorn, et al., 2014). The generic model was extensively validated in two stages, as described in (Ouypornkochagorn, et al., 2022): predicted scalp voltages were compared quantitatively with human measurement data, showing an excellent match; the match was only minimally improved when a subject-specific model was created from MRI scans of the measured human subject. To be able to use a generic model is of critical logistical importance when applying the methodology described in this paper to stroke patients in the clinical environment.

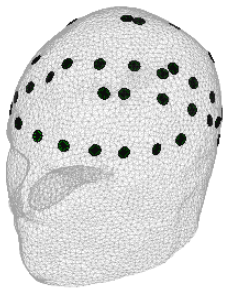

Figure 2. Electrode configuration and the used model 3D forward model of the head, showing the scalp electrodes

2.3 Image Reconstruction

The reconstruction algorithm is an improved version of the Gauss-Newton method as described in detail in (Ouypornkochagorn, et al., 2022). The estimation is based on nominal conductivity σ_N which is instead used as the conductivity at the time frame i. $\tilde{\sigma}_{(i+1,i)}$ is the estimated conductivity at time frame $i+1$ where the measurement voltage V_{i+1} is replaced with $\tilde{V}_{(i+1,i)}$ as shown in (1) and (2). $\delta\tilde{\sigma}_{(i+1,i)}$ is the difference image between frames $i+1$ and i in accordance with the model U. Note that the conductivity of the skull region was set to be unchanged in the data inversion process.

$$\tilde{\sigma}_{(i+1,i)} = \arg\min_{\tilde{\sigma}} \left\{ \left\| \tilde{V}_{(i+1,i)}(\sigma_N) - U(\tilde{\sigma}) \right\|^2 \right\} \tag{1}$$

$$\tilde{V}_{(i+1,i)}(\sigma_N) = U(\sigma_N) + V_{i+1} - V_i \tag{2}$$

$$\delta\hat{\sigma}_{(i+1,i)} = \tilde{\sigma}_{(i+1,i)} - \sigma_N \tag{3}$$

The new method is non-linear and is much more robust against modelling error than previous methods (Ouypornkochagorn, et al., 2015). Computation of the 3D reconstructed images is rendered practical on non-specialist desktop systems by using the Regularised Newton-Krylov GMRes method, with 200 Krylov subspaces. Nevertheless, the computation process takes about 40 minutes for each image (Ouypornkochagorn, et al., 2022).

3. Results

3.1 Steady-state simulations

To validate the performance of the reconstruction algorithm, many simulations of conductivity change were performed with conductivity inclusions in different locations, and with different measurement noise levels, illustrated by the two examples presented here. A 20mm-diameter sphere-shaped inclusion with the conductivity of 0.65 S/m (i.e. equivalent to blood) was simulated at the front and then the left of the head in the region of the grey and the white matter. The boundary voltage was generated from a forward model, where the geometry is the same as the inverse model, having 274k elements. The conductivity of the CSF, the grey, and the white matter was set to 0.2556 S/m. The excitation current was set to 1 mA_{rms}.

Figure 3 shows the voltage changes in response to the two different inclusions: they are typically around 10 μV_{rms} or less, and the maximum voltage change is 32 μV_{rms}. Such small voltage responses indicate the importance of measurement noise, and a high SNR EIT system is necessary. The differences between the voltages predicted for the two simulated cases are very small, less than 10 μV_{rms} in most cases, further emphasising the importance of low-noise measurement. Moreover, in real human EIT measurements, repetitive cardiosynchronous voltage changes of similar magnitude, resulting from the rheoencephalography phenomenon (see section 3.2), must be taken into account.

The reconstructed images of the two example inclusions are shown in Figure 4. Each inclusion is clearly seen in the reconstructed images, and is well localised. Even though the shape of the inclusion is not a perfect sphere, the localisation error is small, expressed as the distance between the centre of the inclusion and the centre of gravity of the reconstructed image (Yasin, et al., 2011), *viz.* 16 mm for the front case and 23 mm for the left case. When measurement noise at the 70 dB SNR level is included in (many) repeats of the simulations, the mean reconstruction errors are changed by less than 1 mm. Clearly, the modelling shows that the methodology is sensitive to such stroke phenomena, and permits good localisation. In due course, it will be important to refine the presentation of the results in visual terms for clinical staff. The images in Figure 4 suggest that it may be desirable to present a sphere, perhaps of variable radius, positioned at the centroid of the reconstructed 3D solution.

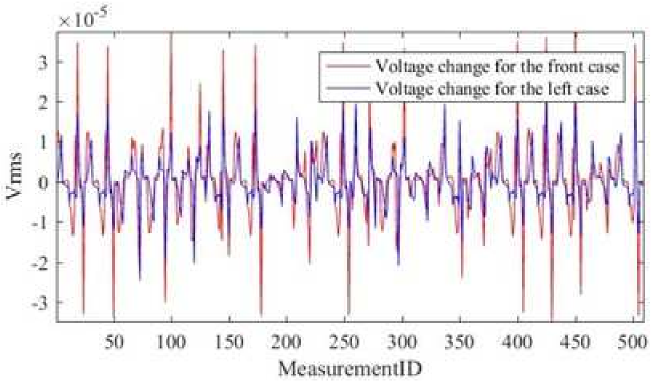

Figure 3. Voltage change due to the presence of the inclusion at the front and the left side of the head. The negative values arise from the use of a fixed order of calculation for the nearest-neighbour voltage differences.

(a) (b)

Figure 4. Reconstructed images of the inclusions situated at the front (a) and the left side (b). The dash red circle represents the exact position of each inclusion. Note that the change in the scalp region is not shown here.

3.2 Human trials

To date, no trials have been carried out on stroke patients. However, our trials summarised in (Ouypornkochagorn, et al., 2022) are highly relevant. Firstly, for monitoring on a medium-term timescale of a few seconds, it is necessary to account for the effects of the REG phenomenon that was described in (Ouypornkochagorn, et al., 2022), *viz.* the effects of perfusion of the brain by the cardiac process, as illustrated by the two example images shown below. These repeated changes in brain perfusion generate cardiosynchronous EIT voltage changes with typical magnitudes around 5 - 15 μV_{rms} and some are as high as 50 μV_{rms}, necessitating careful isolation of voltage changes due to any other perfusion or ischaemia processes.

(a) (b)

Figure 5. Reconstructed images of REG showing brain perfusion due to the cardiac process : (a) at 300 ms and (b) at 500 ms after the beginning of a ~1-second period cardiac cycle. The measurements were made with fEITER Mk. II.

The Transient Hyperemic Response (THR) trials described in (Ouypornkochagorn, et al., 2022) may serve as a first trial of sensitivity to gross changes in brain perfusion. A brief occlusion was applied to the left or right middle cerebral artery (MCA) and then the occlusion was released. Blood flow velocity was expected to be increased during the occlusion at the non-occlusion side due to the predictable fall in blood flow to the brain on the occluded side (Giller, 1991) (Smielewski, et al., 1996). To take account of the REG phenomenon, we averaged the EIT measurements over a complete cardiac cycle prior to carrying out the image reconstruction process, as described in (Ouypornkochagorn, et al., 2022). Examples of reconstructed images are shown in Figure 6, where the expected hemodynamic changes can clearly be seen: In each case, the decrease of conductivity is obvious on the occluded side, as well as the increase of conductivity on the non-occluded side. The amplitude of the peak local conductivity changes in the 3D images was ~20 times larger than those observed in the REG images.

(a) (b)

Figure 6. Reconstructed images during (a) left occlusion and (b) right occlusion of THR trials. The measurements were made with fEITER Mk. I.

4. Conclusions

Imaging cerebral hemodynamics, using scalp-mounted EIT with a generic head model has been demonstrated successfully. Promising localisation performance was found by simulation. The impedance changing behaviour of REG due to the normal perfusion of the brain by the cardiac process is repetitively observable. Successful imaging of the changing cerebral hemodynamics during THR indicates the potential of the method for application to stroke monitoring. The high SNR and high temporal resolution rate of the EIT system and the use of the novel reconstruction algorithm are essential features of the methodology.

References

Gilad O, Horesh L, and Holder D S 2007 Design of electrodes and current limits for low frequency electrical impedance tomography of the brain *Med. Bio. Eng. Comput.* **45**, 621-633

Giller C A 1991 A bedside test for cerebral autoregulation using Transcranial Doppler ultrasound *Acta Neurochirurgica*, **108**, 7-14

Goren N, Avery J, Dowrick T, Mackle E, Witkowska-Wrobel A, Werring D, and Holder D 2018 Multi-frequency electrical impedance tomography and neuroimaging data in stroke patients *Scientific Data*, **5**(180112)

McCann H, Ahsan S T, Davidson J L, Robinson R L, Wright P, and Pomfrett C J 2011 A portable instrument for high-speed brain function imaging: fEITER *33rd Ann. Int. Conf. IEEE Eng. Med. Biol. (EMBC)*, 7029-7032

Ouypornkochagorn T, Polydorides N, and McCann H 2014 In vivo estimation of the scalp and skull conductivity *Proc. 15th Int. Conf. Biomedical Applications of Electrical Impedance Tomography*.

Ouypornkochagorn T, Polydorides N, and McCann H 2015 Tackling Modelling Error in the Application of Electrical Impedance Tomography to the Head. *37th Ann. Int. Conf. IEEE Eng. Med. Biol. (EMBC)*, 622-625

Ouypornkochagorn T, Terzija N, Wright P, Davidson J L, Polydorides N and McCann H 2022 Scalp-Mounted Electrical Impedance Tomography of Cerebral Hemodynamics *IEEE Sensors Journal*, **22**(5), 4569-4580, doi:10.1109/JSEN.2022.3145587

Smielewski P, Czosnyka M, Kirkpatrick P, McEroy H, Rutkowska H, and Pickard J D 1996 Assessment of cerebral autoregulation using carotid artery compression *Stroke*, **27**, 2197-2203

Yasin M, Böhm S, Adler A, and Gaggero P O 2011 Evaluation of EIT system performance *Physiol. Meas.* , **32**, 851-865

Proceedings of the International Conference of Bioelectromagnetism, Electrical Bioimpedance,
and Electrical Impedance Tomography June 29 – July 1, 2022 / Kyung Hee University, Seoul, Korea

Feasibility Study of Peripheral Nerve Repair Monitoring with Electrical Impedance Tomography

Zhe Liu[1], Yunjie Yang[1]
[1]Institute for Digital Communications, School of Engineering, The University of Edinburgh, Edinburgh, UK

Correspondence : Yunjie Yang, e-mail : y.yang@ed.ac.uk

Abstract–In regenerative medicine, Engineered Nerve Guidance Conduits (ENGC) are increasingly attracting attention for peripheral nerve repair because they can overcome some drawbacks, e.g., the potential formation of the neuroma, of the 'gold method' - autograft techniques. However, there are as yet no methods to monitor the status of the treated nerve. This paper presents a feasibility study of EIT on monitoring the process of peripheral nerve repair using a miniature EIT sensor. The 16-electrode sensor and nerve repair process are modeled, and the time-varying EIT images indicating the nerve repair process are reconstructed using the Tikhonov regularization algorithm. These numerical results demonstrate the potential and the feasibility of EIT in peripheral nerve repair monitoring.

Keywords: Peripheral nerve repair; engineered nerve guidance conduits; Electrical Impedance Tomography; image reconstruction.

1. Introduction

Peripheral nerve injuries could be caused by tumour extirpation or other diseases, significantly influencing patients' daily life. Therefore, repairing the injured nerve is of significant importance. Autograft techniques are conventionally considered as the gold method for nerve repair. However, these methods might result in surgical complications, such as losing sensitivity or forming neuroma (Fadia N B *et al* 2020). Therefore, methods based on Engineered Nerve Guidance Conduit (ENGC) are proposed as an alternative for nerve repair. In this method, the conductive conduit and external applied electrical potential are usually combined to promote the nerve regeneration because it is reported that external electrical fields can help move cells toward the electrodes (anode or cathode) (Zhao Y *et al* 2020). Nevertheless, there is still no effective method to monitor the process of nerve repair. Thus, a new imaging technique to undertake such a task is desired and worth exploring.

Electrical Impedance Tomography (EIT) is a tomographic imaging technique to estimate the conductivity distribution of the sensing region through the voltage data measured at the sensing region's boundary (Bayford R H 2006, Metherall P *et al.* 1996). It is widely adopted in some fields, such as industrial processes monitoring (Seppänen A *et al.* 2009, Dang C *et al.* 2021). Especially, EIT is a promising technique in biomedical engineering due to its advantages of non-invasion, non-radiation, and high temporal resolution. In clinical applications, EIT has been used to monitor lung functions (Frerichs I *et al.* 2002). In the laboratory research, EIT is investigated in stoke screening (Dowrick T *et al.* 2016), breast cancer imaging (Cherepenin V *et al.* 2001), and nerve imaging (Aristovich K *et al.* 2018). In EIT applications on nerve imaging, Ravagli *et al*. proposed an optimized electrode driven pattern and improved EIT's performance on imaging fascicular Compound Action Potentials (CAP) in peripheral nerves (Ravagli E *et al.* 2019). The same group also reported a systematic EIT-based method to image CAP, and they proved that EIT could successively differentiate individual fascicles, i.e., peroneal, sural, and tibial, when different stimulations were applied (Ravagli E *et al* 2020). The previous research provides a strong foundation for nerve imaging. The basic principle of applying EIT to monitor nerve repair is more straightforward than CAP imaging, i.e. the occupied volume of the neurons determines the impedance of the sensing region. Therefore, this paper proposes to use EIT to monitor the nerve repair process, which is explored and verified by numerical simulation. The results indicate the feasibility of EIT in nerve repair monitoring and, meanwhile, reveal the potential of the proposed technique to be applied in real scenarios.

This paper is organized as follows: Section II states the principle of the EIT image reconstruction, and the modelling of the EIT sensor and nerve repair process. Section III illustrates the results and discussion. Section IV draws conclusions and discusses future work.

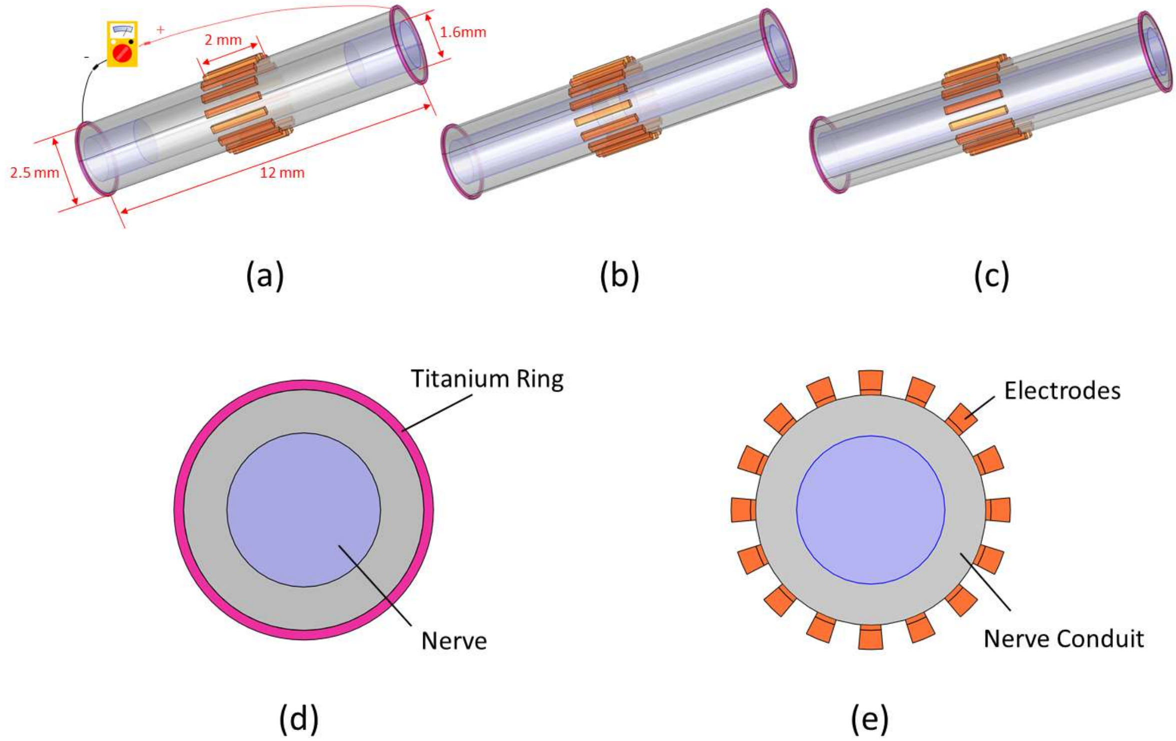

Figure 1. Modelling of the neural EIT sensor and three stages of repairing peripheral nerve: (a) the beginning of repairing, (b) nerve entering the EIT sensor, and (c) the repaired nerve. The (d) and (e) are cross-sections of the models. The purple domains represent the injured nerve, the pink domains denote the Titanium rings applying stimulation voltages, the orange domains stand for the EIT sensor and the gray tube represents the nerve guidance conduit.

2. Methodology

2.1 Principle of EIT Image Reconstruction

Image reconstruction of EIT aims to estimate the conductivity distribution within the imaging region $\Omega \in R^d, d = 2 \text{ or } 3$, through boundary current injection. In EIT, the boundary voltage measurements $V \in R^m$ are related to the discrete conductivity distribution $\sigma \in R^n$ by the following non-linear equation:

$$V = F(\sigma) + \Psi, \tag{1}$$

where $\Psi \in R^m$ is the measurement noise. The j^{th} element of σ denotes the conductivity value of the j^{th} subregion of Ω. As (1) is hard to solve, in practical implementation, the linearized EIT forward model is usually adopted, which is formulated as (Lionheart W R 2004):

$$\Delta V = J\Delta\sigma + \psi, \tag{2}$$

where $\Delta V \in R^m$ and $\Delta\sigma \in R^m$ are the variations of the voltage measurements and the conductivity between two distinct time points. $\psi \in R^m$ represents the measurement noise eliminating common components of the two time points. $J \in R^{m\times n}$ denotes the sensitivity matrix, which is defined by:

$$J_{\alpha\beta}(i,j) = \frac{\partial V}{\partial \sigma}(i,j) = -\int_{\Omega_i} \nabla u^{\alpha} \nabla u^{\beta} d\omega, \tag{3}$$

where $J_{\alpha\beta}(i,j)$ represents the sensitivity in the j^{th} subregion of Ω at the i^{th} measurement, where u^{α} and u^{β} stand for the electrical potential distribution when the currents are injected into the electrode pair $(e_{\alpha}, e_{\alpha+1})$ and $(e_{\beta}, e_{\beta+1})$, respectively. In this study, (2) is solved by the Tikhonov regularization method and the solution is expressed as (Vauhkonen M *et al* 2008):

$$\Delta\hat{\sigma} = (J^T J + \mu I)^{-1} J^T \Delta V, \tag{4}$$

where, $I \in R^{n\times n}$ is an identity matrix and μ accounts for the regularization parameter.

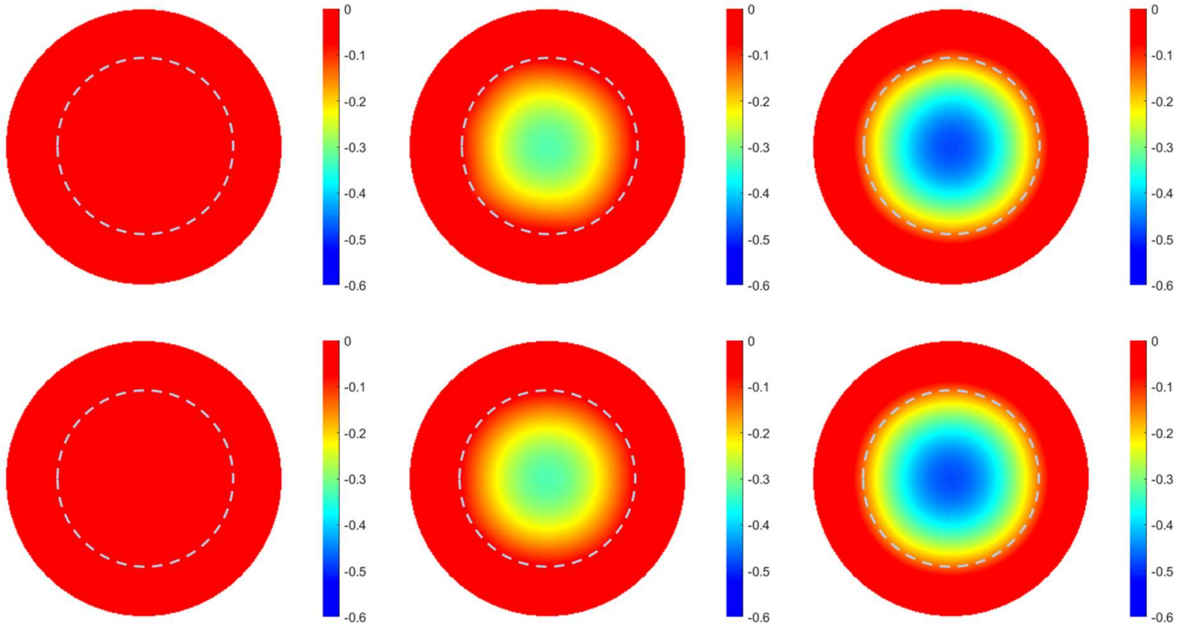

Figure 2. Image reconstruction of three stages of the nerve repair process. Images from leftist column to rightist column correspond to stage 1 to stage 3 accordingly. The top row is the results when applying stimulation voltages and the bottom row is the results when not applying stimulation voltages. The dashed curve represents the hollow region of the nerve conduit. For all images, the range of colorbar is fixed from -0.6 to 0 for displaying purpose.

2.2 Modelling of EIT Sensor and Nerve Repair Process

In ENGC–based nerve repair, the conductive nerve guidance conduit warps the impaired peripheral nerve. Additional electrical potentials are applied to the two Titanium rings attached to the ends of the conduit to stimulate neurons growing towards the breakage. In COMSOL Multiphysics, we modelled the growing nerve at three distinct stages (see Figure 1), i.e., the beginning of repairing (labeled as stage 1), nerve entering the EIT sensor region (labeled as stage 2), and the repaired nerve (labeled as stage 3). The outer diameter of the conduit is set as 2.5 mm and its inner diameter is set as 1.6 mm which is the same as the diameter of the damaged nerve. Sixteen electrodes made of Titanium are attached to the surface of the conduit, and the length is set as 2 mm. The Phosphate Buffered Saline (PBS), with a conductivity of 2 S/m, fills the region between two broken nerves. The conductivity of the nerve and the conduit wall is set as 0.8 S/m and 12 S/m, respectively. As the stimulation voltage is applied intermittently, we consider two situations for the measurement. The first one is that the measurement is conducted when the stimulation voltage is applied, and it is set as 0.5 V. The second one is that the measurement is conducted when the stimulation voltage is not applied. Ultimately, we obtained two sets of measurement data.

3. Results and Discussion

Image reconstruction results based on the Tikhonov regularization (4) are illustrated in Figure 2. The first row is the results based on the measurement while applying stimulation voltages, and the second row is the results based on the measurement when no stimulation voltages are applied. Both methods demonstrate similar reconstructed EIT images, which indicates that the reconstruction is not sensitive to external DC electrical stimulation. Images from left to right correspond to the three stages of nerve repairing. At the stage of repairing beginning, the growing nerve does not enter the region covered by the EIT sensor. Thus, there is no inclusion appearing in the image. Comparing the rest two stages, the conductivity values of the image corresponding to stage 2 are lower than those of the image corresponding to stage 3, and the size of the area of the negative conductivity change corresponding to stage 2 is smaller than that corresponding to stage 1. These two aspects reveal how much the portion of the nerve grows into the region covered by the EIT sensor. In summary, different stages of nerve repairing can be differentiated by EIT imaging, which suggests that EIT has the potential to be used to monitor the nerve repair process.

4. Conclusions

This paper conducted a proof-of-concept study of EIT imaging on nerve repair. Three significant stages of repairing the nerve are simulated, and the conductivity image is reconstructed by Tikhonov regularization. The results prove EIT is feasible in monitoring the nerve repair process. In future work, the EIT sensor exclusive to nerve imaging will be manufactured, and the effectiveness of EIT on nerve repair will be further verified by real-world experiments.

References

Fadia N B, Bliley J M, DiBernardo G A, Crammond D J, Schilling B K, Sivak W N, Spiess A M, Washington K M, Waldner M and Liao H-T 2020 Long-gap peripheral nerve repair through sustained release of a neurotrophic factor in nonhuman primates Science Translational Medicine 12 eaav7753

Zhao Y, Liang Y, Ding S, Zhang K, Mao H-q and Yang Y 2020 Application of conductive PPy/SF composite scaffold and electrical stimulation for neural tissue engineering Biomaterials 255 120164

Bayford R H 2006 Bioimpedance tomography (electrical impedance tomography) Annu. Rev. Biomed. Eng. 8 63-91

Metherall P, Barber D C, Smallwood R H and Brown B H 1996 Three-dimensional electrical impedance tomography Nature 380 509-12

Seppänen A, Voutilainen A and Kaipio J 2009 State estimation in process tomography—reconstruction of velocity fields using EIT Inverse Problems 25 085009

Dang C, Darnajou M, Bellis C, Ricciardi G, Mylvaganam S and Bourennane S 2021 Improving EIT-based visualizations of two-phase flows using an eigenvalue correlation method IEEE Transactions on Instrumentation and Measurement 70 1-9

Frerichs I, Hinz J, Herrmann P, Weisser G, Hahn G, Quintel M and Hellige G 2002 Regional lung perfusion as determined by electrical impedance tomography in comparison with electron beam CT imaging IEEE transactions on medical imaging 21 646-52

Dowrick T, Blochet C and Holder D 2016 In vivo bioimpedance changes during haemorrhagic and ischaemic stroke in rats: towards 3D stroke imaging using electrical impedance tomography Physiological Measurement 37 765

Cherepenin V, Karpov A, Korjenevsky A, Kornienko V, Mazaletskaya A, Mazourov D and Meister D 2001 A 3D electrical impedance tomography (EIT) system for breast cancer detection Physiological measurement 22 9

Aristovich K, Donegá M, Blochet C, Avery J, Hannan S, Chew D J and Holder D 2018 Imaging fast neural traffic at fascicular level with electrical impedance tomography: proof of principle in rat sciatic nerve Journal of neural engineering 15 056025

Ravagli E, Mastitskaya S, Thompson N, Aristovich K and Holder D 2019 Optimization of the electrode drive pattern for imaging fascicular compound action potentials in peripheral nerve with fast neural electrical impedance tomography Physiological measurement 40 115007

Ravagli E, Mastitskaya S, Thompson N, Iacoviello F, Shearing P R, Perkins J, Gourine A V, Aristovich K and Holder D 2020 Imaging fascicular organization of rat sciatic nerves with fast neural electrical impedance tomography Nature communications 11 1-10

Lionheart W R 2004 EIT reconstruction algorithms: pitfalls, challenges and recent developments Physiological measurement 25 125

Vauhkonen M, Vadász D, Karjalainen P A, Somersalo E and Kaipio J P 1998 Tikhonov regularization and prior information in electrical impedance tomography IEEE transactions on medical imaging 17 285-93

O 01-04

ICBEM Bioelectromagnetism ICEBI Electrical Bioimpedance EIT Electrical Impedance Tomography

Proceedings of the International Conference of Bioelectromagnetism, Electrical Bioimpedance,
and Electrical Impedance Tomography June 29 – July 1, 2022 / Kyung Hee University, Seoul, Korea

High resolution EIT based heart rate detection using Synchrosqueezing

Henryk Richter[1], Lisa Krukewitt[2], Fabian Müller-Graf[2], Amelie Zitzmann[2], Jonas Merz[2], Stephan Böhm[2], Volker Kühn[1]
[1]Institute of Communications Engineering, University of Rostock, Germany
[2]Department of Anesthesiology and Intensive Care Medicine, University Medical Center Rostock, Rostock, Germany

Correspondence : Henryk Richter, e-mail : henryk.richter@uni-rostock.de

Abstract: A major challenge in EIT based monitoring of cardiovascular activity is the relatively low signal-to-noise ratio of perfusion related signals. This work is aiming at high resolution instantaneous heart rate estimation in frequency domain to aid in de-noising and beat-by-beat analysis. Our approach is based on the Fourier domain Synchrosqueezing transform. We evaluate the performance of our algorithm by synchronous in vivo measurements of EIT and ECG.

Keywords: EIT; Synchrosqueezing; HR detection

1 Introduction

EIT has been studied extensively for medical applications in the area of ventilation monitoring and, more recently, monitoring of the perfusion process. One major challenge for perfusion monitoring is the dominance of the ventilation signal in EIT. Several algorithms have been proposed to separate ventilation and perfusion signal parts (Deibele et al. 2008; Jang et al. 2020; Richter et al. 2021) which also have the benefit of relaxing the heart rate estimation task. Typically, perfusion related signals are measured with significantly lower amplitude in comparison to the ventilatory signal, such that the noise influence becomes a major concern. A common approach in noise reduction of cardiac signals is the averaging over multiple cardiac cycles using the R-Peaks of a parallel measured ECG as a trigger (Vonk Noordegraaf et al. 2000). From the signal processing perspective, the cardiac signal is an instationary process where the heart rate varies on a beat by beat basis. The variational property of the heart rate along with significant measurement noise poses a challenge to accurate estimates of the instantaneous heart rate by classic methods like STFT or parametric approaches like MUSIC. The Synchrosqueezing transform (SST) (Daubechies and Maes 1996; Thakur and Wu 2011; Daubechies et al. 2011) is a post-processing method to time-scale (Wavelets) or time-frequency (Fourier) signal transforms. Synchrosqueezing reassigns coefficients in scale or frequency in order to reduce their uncertainty at discrete points in time.

2 Materials and Methods

2.1 Animal Model and Anaesthesia

The study was approved by the governmental ethical board for animal research (Landesamt für Landwirtschaft, Lebensmittelsicherheit und Fischerei, Mecklenburg-Vorpommern, Germany; No: 7221.3-1-037/19, 29 August 2019) and was carried out in accordance with the EU-directive 2010/63/EU and the Animal Research: Reporting of In Vivo Experiments guidelines 2.0 (ARRIVE 2.0) (Müller-Graf et al. 2021). Six healthy German Landrace pigs (24.4–48.3 kg, 12–15 weeks old) were cared for and premedicated according to internal standards of the Institute for Experimental Surgery at Rostock University Medical Centre. Animals were given free access to standard laboratory chow and water. The initial state (animals anesthetized, prior to intervention) served as control; therefore, no randomisation was needed. The investigators were not blinded. For premedication animals received an intramuscular injection of 8 mg/kg body weight azaperone and 20 mg/kg body weight ketamine. Two peripheral venous catheters were placed in the veins of both ears.

After preoxygenation, anaesthesia was induced using 0.2 mg fentanyl, 100 mg propofol , 4 mg pancuronium and maintained by continuous intravenous infusion of 4–8 mg kg^{-1}h^{-1} propofol, 5–10 μg kg^{-1}h^{-1} fentanyl, 6.4 mg h^{-1} pancuronium and 0.1 mg kg^{-1}h^{-1} midazolam The pigs were intubated endotracheally (ID 7.0 mm) and mechanically ventilated in a pressure-controlled mode using a Dräger Primus ventilator with tidal volumes of 6 mL kg^{-1} and a PEEP of 5 mbar. Respiratory rate was adjusted to maintain end-tidal partial pressure of CO2 at 5 ± 0.4 kPa.

2.2 Data acquisition

The EIT data was acquired with the EIT Pioneer Set (Sentec AG, Landquart, Switzerland) using 32 electrodes, at a frame rate of 47.68 Hz. The other data series were acquired at 1 kHz using bridge transducer amplifiers in combination with dedicated hard- and software (PowerLab 16/35, and LabChart 8, both ADInstruments, Dunedin, New Zealand). Stored data was exported from LabChart into a MATLAB-compatible formatand synchronized in time with the EIT frames.

2.3 Signal processing

The spectral analysis of the EIT signal can be either carried out on the raw data in electrode space or in image space after reconstruction, respectively. In this work, the Fourier-based Synchrosqueezing transform (Oberlin et al. 2014) is applied. We consider a time signal $x(t)$ out of the EIT measurement series, either obtained from the heart region of subsequent reconstructed images or the time series from one of the insertion/measurement electrode pairs in electrode space. The Fourier transform of that signal $x(t)$ is given by

$$X(f) = \int_{-\infty}^{\infty} x(t)\mathrm{e}^{-j2\pi f t}\mathrm{d}t \tag{1}$$

Adding a sliding window $g(t)$ to the formulation leads to the local spectra of short-time Fourier transform (STFT):

$$X_f(f,t) = \int_{-\infty}^{\infty} x(\tau)g(\tau - t)\mathrm{e}^{-j2\pi f(\tau-t)}\, d\tau \tag{2}$$

The resulting spectrogram $|X_f(f,t)|$ spans the time-frequency (TF) plane defined by observations within the time intervals $g(\tau - t)$ with respect to frequencies f in order to follow instationary processes.

The Synchrosqueezing transform models the input signal $x(t)$ as a multicomponent signal of the type

$$x(t) = \sum_{k=1}^{K} x_k(t) = \sum_{k=1}^{K} A_k(t)\mathrm{e}^{-j2\pi\phi_k(t)}, \tag{3}$$

where $A_k(t)$ and $\phi'_k(t)$ are the instantaneous amplitudes and frequencies, respectively. Under the assumption of slow variation of these parameters, an approximation of $\tilde{x}(t)$ can be formulated that is based on a sum of pure waves:

$$\tilde{x}(t) = \sum_{k=1}^{K} A_k \mathrm{e}^{-j2\pi\left[\phi(t)-\phi'_k(\tau-t)\,t\right]}, \tag{4}$$

The corresponding STFT $X_f(f,t)$ becomes:

$$\tilde{X}_f(f,t) = \sum_{k=1}^{K} x_k(t)\hat{g}(f - \phi'_k(t)). \tag{5}$$

A multicomponent signal $x_k(t)$ is concentrated in TF plane around dominant frequencies (called ridges), defined by $f(t) = \phi'_k(t)$. With frequencies $\phi'_k(t)$ separated well beyond the support of the frequency neighborhood $\hat{g}(f)$, each mode occupies a distinct domain of the TF plane, allowing their detection, separation and reconstruction (Oberlin et al. 2014).

Given $\tilde{X}_f$, the SST moves coefficients in $\tilde{X}_f(f,t)$ according to the map $(f,t) \mapsto (\hat{\eta}_f(f,t),t)$, where $\hat{\eta}_f$ is the local instantaneous frequency at time t and filtered at frequency f, defined as

$$\hat{\eta}_f(f,t) = \frac{1}{2\pi}\frac{\partial \arg \tilde{X}_f(f,t)}{\partial t}. \tag{6}$$

This expression is a local approximation of the instantaneous frequencies $\phi'_k(t)$. In closed form, the Synchroqueezed TF plane $T_f(\eta,t)$ is mapped from $\tilde{X}_f(f,t)$ by:

$$T_f(\eta,t) = \frac{1}{g(0)}\int_{-\infty}^{\infty} \tilde{X}_f(f,t)\delta\left(\eta - \hat{\eta}_f(f,t)\right)\, df \tag{7}$$

Given that the sliding window $g(\tau - t)$ for the STFTs was parameterized with a step size Δt of one sample, then both $\tilde{X}_f(f,t)$ and the remapped result $T_f(\eta,t)$ are available at a temporal resolution matching the EIT frame sampling rate. For the spectral resolution in f, η is an application-specific parameter which is no longer strictly tied to the conventional tradeoff in time-frequency resolution.

Following the Synchrosqueezing mapping, the relevant signals or their frequencies may be extracted. In case of EIT heart rate detection, we employ an initial estimate and apply a local search algorithm across the frequency range for each time step. Some frequency coefficients below the threshold of the Synchrosqueezing remapping algorithm and windowing effects in presence of abrupt rate changes may lead to mis-detection of the true local maximum.

These potential issues can be mitigated by a lowpass filter $g_l(\eta)$ on the frequency coefficients, whose support follows the same constraint on separated frequencies $\phi'_k(t)$ that applies to $\hat{g}$.

$$D_f(\eta,t) = |T_f(\eta,t)| * g_l(\eta) \tag{8}$$

From the resulting spectrogram $D_f(\eta,t)$, the instantaneous frequency corresponding to the heart rate can be extracted iteratively across time within the local neighborhood L with the previous estimate $\hat{R}_H(t - \Delta t)$ as center point.

$$\hat{R}_H(t) = \underset{\eta_1\in[-L,L]}{\arg\max}\ D_f\big(\eta_1 + \hat{R}_H(t-\Delta t),t\big) \tag{9}$$

3 Results

Fig. 1a shows the initial STFT over 3812 EIT frames. A single insertion/measurement electrode pair from the dorsal region of the subject was selected. The sliding window was set to a length of 701 samples or 14 seconds. The observed sequence begins with 20 cycles/minute ventilated breathing, followed by 40 seconds apnea. Afterwards, ventilation was resumed. The subject's heart rate is visible around the 1 Hz mark. Due to varying heart rate and an STFT window stretching over several heart beats, the instantaneous heart rate cannot readily be determined from this initial spectrogram.

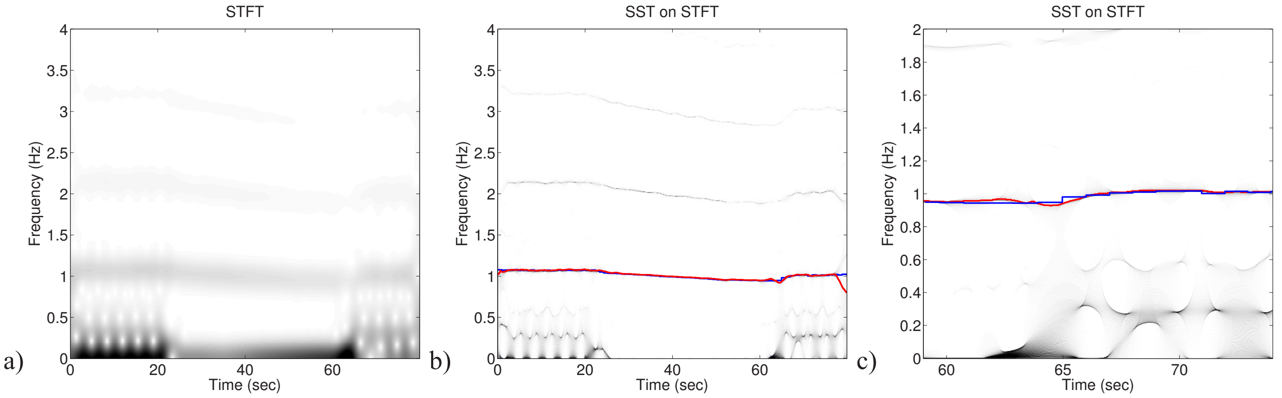

Figure 1: a) STFT with a 701 point Hermitian sliding window over 80 seconds, b) Synchrosqueezing result after post-processing the STFT. Overlayed instantaneous heart rate from ECG (blue) and EIT Synchrosqueezing (red), c) Closer zoom into the plot from b)

After post-processing the spectrogram with the Synchrosqueezing process, the instantaneous rates of ventilation and perfusion cycles are concentrated into distinct maxima of fundamental frequencies and their harmonics (fig. 1b). The synchronously captured ECG based heart rate (blue) closely matches the estimate from the SST output spectrogram (red), with a mean square difference (MSD) of 0.02 BPM or 0.0003 Hz.

In contrast to the ECG based approach whose estimated heart rate only changes at each new detected heartbeat, the Synchrosqueezed EIT based approach is able to follow changes of the heart rate closely and exhibits a smooth curve (fig. 1c). The average MSD across multiple 60 sec. EIT measurements was found at 0.03 BPM in our evaluation.

The previous experiments were conducted on EIT sequences with active ventilation. The significantly higher amplitudes of the ventilation signal in comparison to the perfusion signal also extend over the harmonics. The same challenges applying to signal separation by filtering are also of relevance for the SST.

Therefore, the following experiments were conducted with EIT data after suppression of the ventilation component by using the method outlined in (Richter et al. 2021). A case of abruptly changing heart rate is depicted in fig. 2, where a saline Bolus injection was applied at 20 seconds into the measurement in a subject of already elevated heart rate and irregular ECG.

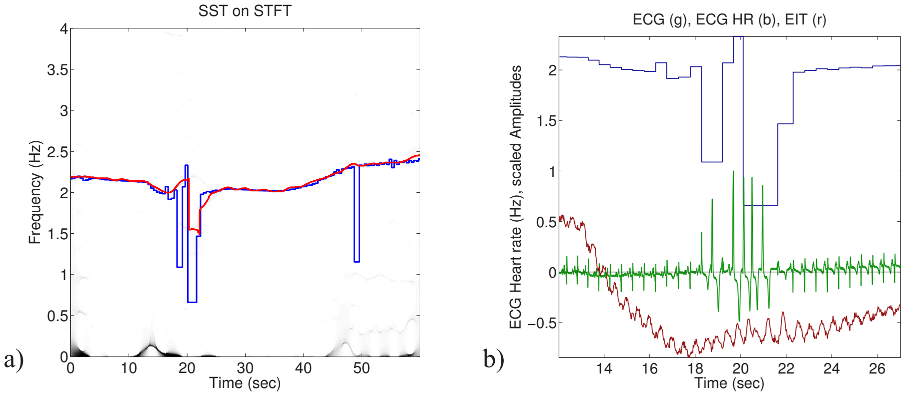

Figure 2: a) Synchrosqueezing result of EIT sequence with suppressed ventilation and a saline Bolus injection around the 20s mark. Overlayed instantaneous heart rate from ECG (blue) and EIT Synchrosqueezing (red), b) corresponding time signals of EIT (red), ECG (green) and ECG derived heart rate (blue)

In this case, disturbances during the saline Bolus injection led to difficulties for the ADInstruments software towards ECG based heart rate estimation, while the EIT Synchrosqueezing based approach returned plausible results in such corner cases.

Another example of a healthy subject is shown in fig. 3a, where the heart rate increases during Bolus injection. Corresponding ECG and EIT time signals are depicted in fig. 3b.

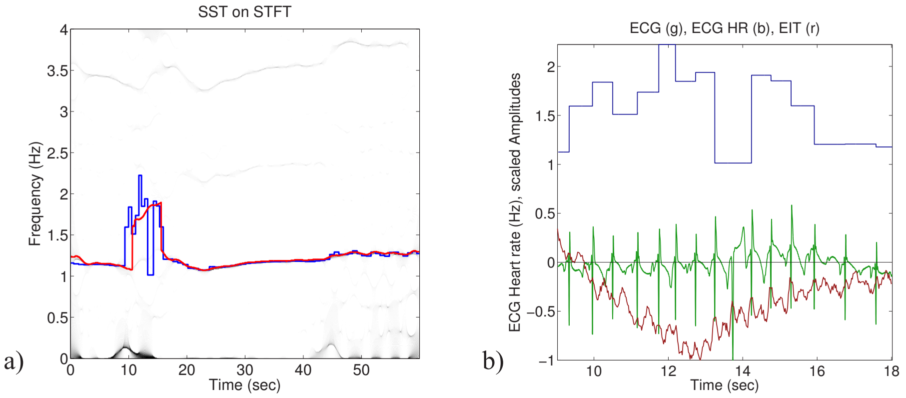

Figure 3: a) Synchrosqueezing result of EIT sequence with suppressed ventilation and a saline Bolus injection around the 10s mark. Overlayed instantaneous heart rate from ECG (blue) and EIT Synchrosqueezing (red), b) corresponding time signals of EIT (red), ECG (green) and ECG derived heart rate (blue)

4 Discussion

The experimental results suggest that Synchrosqueezing appears to be a viable alternative to classic heart rate estimation methods. Since the SST is invertible, the option of consecutive time and frequency domain signal processing is retained. Candidate operations in this area include signal separation of ventilation and perfusion or noise suppression. The instantaneous frequencies may also be used as steering vectors for ensemble averaging in time domain.

Potential challenges towards SST based frequency estimation are present at the beginning and near the end of the observation interval. This is depicted in fig. 1b, where the frequency localization is challenged especially at the end of that sequence. The underlying reason is the sliding window which contains less samples from the input signal towards the corners of the observation interval. As a consequence, the estimator is not consistent and will exhibit higher variance in those parts of the spectrogram.

As outlined in eq. 5, the success of the SST depends on the separation of signal components. Frequency localization is challenged in cases where the harmonics of the ventilation signal are near to the fundamental of the perfusion signal in the time-frequency plane. An example for that constraint can be seen in fig. 1c, near the 65 second time mark.

5 Conclusions

In this paper, we proposed a method to estimate a subject’s heart rate directly from EIT frames by using the Fourier domain Synchrosqueezing transform. A prominent benefit of this approach is the sample-by-sample temporal resolution of the Synchrosqueezed output spectrum whose frequency resolution is a parameter that can also be adjusted to meet the application requirements. This flexibility is a significant bonus over the classic STFT and also parametric spectral estimation methods like MUSIC or ESPRIT.

Experimental results suggest that this method of heart rate detection is fairly robust in presence of noisy source signals. Potential applications include signal separation, noise reduction and triggering for ensemble averaging.

References

Daubechies, I. and Maes, S. A nonlinear squeezing of the continuous wavelet transform based on auditory nerve models. In *In Wavelets in medicine and biology (eds A Aldroubi, M Unser)*, pages 527–546. CRC Press, Boca Raton, FL, 1996. doi: 10.1201/9780203734032.

Daubechies, I., Lu, J., and Wu, H.-T. Synchrosqueezed wavelet transforms: An empirical mode decomposition-like tool. *Applied and Computational Harmonic Analysis*, 30(2):243–261, 2011. ISSN 1063-5203. doi: https://doi.org/10.1016/j.acha.2010.08.002.

Deibele, J. M., Luepschen, H., and Leonhardt, S. Dynamic separation of pulmonary and cardiac changes in electrical impedance tomography. *Physiological Measurement*, 29(6):S1–S14, jun 2008. doi: 10.1088/0967-3334/29/6/s01.

Jang, G. Y., Jeong, Y. J., Zhang, T., Oh, T. I., Ko, R.-E., Chung, C. R., Suh, G. Y., and Woo, E. J. Noninvasive, simultaneous, and continuous measurements of stroke volume and tidal volume using EIT: feasibility study of animal experiments. *Scientific Reports*, 10(1), July 2020. doi: 10.1038/s41598-020-68139-3.

Müller-Graf, F., Merz, J., Bandorf, T., Albus, C. F., Henkel, M., Krukewitt, L., Kühn, V., Reuter, D., Vollmar, A., Pulletz, S., Böhm, S. H., Reuter, D. A., and Zitzmann, A. Correlation of Pulse Wave Transit Time and Pulmonary Artery Pressure in a Porcine Model of Pulmonary Hypertension. *Biomedicines 2021*, 9(9):1–14, 2021. doi: 10.3390/biomedicines9091212.

Oberlin, T., Meignen, S., and Perrier, V. The fourier-based synchrosqueezing transform. In *2014 IEEE International Conference on Acoustics, Speech and Signal Processing (ICASSP)*, pages 315–319, 2014. doi: 10.1109/ICASSP.2014.6853609.

Richter, H., Krukewitt, L., Müller-Graf, F., Merz, J., Zitzmann, A., and Kühn, V. Signal separation in raw eit measurements. In *Proceedings of the 21st International Conference on Biomedical Applications of Electrical Impedance Tomography*, page 38. jun 2021.

Thakur, G. and Wu, H.-T. Synchrosqueezing-based recovery of instantaneous frequency from nonuniform samples. *SIAM Journal on Mathematical Analysis*, 43(5):2078–2095, Jan 2011. ISSN 1095-7154. doi: 10.1137/100798818.

Vonk Noordegraaf, A., Janse, A., Marcus, J. T., Bronzwaer, J. G. F., Postmus, P. E., Faes, T. J. C., and de Vries, P. M. J. M. Determination of stroke volume by means of electrical impedance tomography. *Physiological Measurement*, 21(2):285–293, may 2000. doi: 10.1088/0967-3334/21/2/308.

Proceedings of the International Conference of Bioelectromagnetism, Electrical Bioimpedance,
and Electrical Impedance Tomography June 29 – July 1, 2022 / Kyung Hee University, Seoul, Korea

Vesicoureteral Reflux Imaged in an Animal Model Using EIT

Alistair Boyle[1,2], Hari Om Aggrawal[1] and Sarah Loughney[1]
[1] Kite Medical, Galway, Ireland
[2] Systems and Computer Engineering, Carleton University, Ottawa, Canada

Correspondence: Alistair Boyle, e-mail : alistair.boyle@kitemedical.ie

Abstract - A preclinical study was conducted in July 2021 to detect Vesicoureteral Reflux (VUR) non-invasively using Electrical Impedance Tomography (EIT). VUR involves the backflow of urine from the bladder to the ureters or kidneys and diagnosed predominantly in the paediatric population from birth to 5 years of age. To recreate VUR in three healthy pigs, stents were positioned at the junction between the bladder and ureters – the Ureterovesical Junctions (UVJ). A Foley catheter was introduced into the bladder via the urethra and used to inject solution mimicking the properties of urine. The stents opened the UVJ to allow urine to more freely travel from the bladder into the ureters and the kidneys during bladder infusion. The simulated VUR was confirmed using fluoroscopic imaging. VUR is a long-term condition, whereas this stenting procedure resulted in acute kidney reflux. VUR achieved using this method was approximately Grade II-III (2-3). The refluxed solution was detectable through regional conductivity changes reconstructed from EIT measurements and localised to the correct kidney. Conductivity changes were observable in 73% of cycles without motion (8 of 11) and 44% of cycles with motion (4 of 9).

Keywords: Vesicoureteral Reflux (VUR); animal model; kidney; bladder.

1. Introduction

Vesicoureteral Reflux (VUR) is an anatomical and/or functional disorder causing backflow of urine from the bladder to the kidneys (Figure 1). With a prevalence of 1.8% in the paediatric population, the condition occurs in 30-40% of children who present with Urinary Tract Infections (UTIs) (Sargent 2000, Hoberman *et al.* 2003). It is the most common urinary tract abnormality in babies and children up to five years of age (Snow *et al.* 2010). VUR has potentially serious consequences such as renal scarring and renal parenchymal damage secondary to increased risk of recurrent febrile urinary tract infections (UTIs). VUR associated nephropathy can lead to hypertension and end stage renal disease (Mattoo 2002). There are five grades of VUR ranked based on the severity of urine backflow and dilation of the ureters and kidneys. VUR often resolves over time, but in certain cases requires surgical intervention.

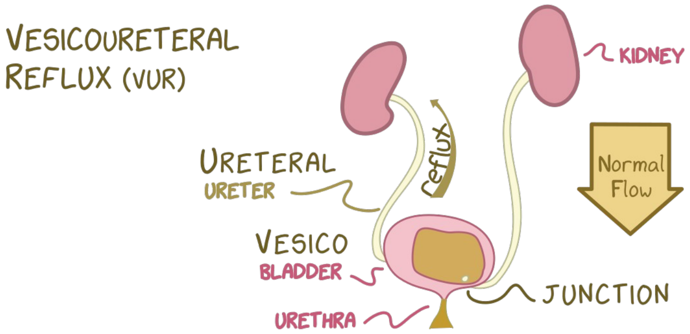

Figure 1. The kidneys are protected by the lower ribs, near the spine, at the back of the abdominal wall. The kidneys are in the retroperitoneal space, separated from the visceral organs (stomach, liver, intestines, and colon) by a thin layer of the peritoneum. The right kidney is typically lower than the left due to the placement of the liver. Normally, urine flows from the kidneys to the bladder through the ureters (3-4 mm dia. and 9-21 cm long in children 1-7 years of age), assisted by smooth muscle peristalsis along the lower third of the ureters. The ureters enter on the underside of the bladder.

The gold standard method used to detect VUR is the Voiding Cystourethrogram (VCUG) and involves radiation exposure, catheterisation and observed voiding. Guidelines recommend that ultrasound be performed on patients with signs of VUR, and if the ultrasound shows concerning features such as uretral dilation or hydronephrosis, a VCUG is recommended. However, ultrasound is not sufficiently sensitive to detect VUR (sensitivity is 0.44 with a 95% CI of 0.34 to 0.54) (Shaikh et al. 2016). More recently, contrast-enhanced Voiding Urosonography (ceVUS) has started to gain popularity in place of the VCUG procedure in the USA (ceVUS has been widely used in Europe for some time). A ceVUS will avoid radiation exposure but still requires catheterisation. A VCUG uses fluoroscopy to observe the introduction of radiocontrast into the bladder through a catheter (Figure 2). VUR is detected when the contrast agent moves from the bladder into the ureters or kidneys. In the most severe VUR (Grade V), the contrast agent fills and dilates the ureters and the kidneys.

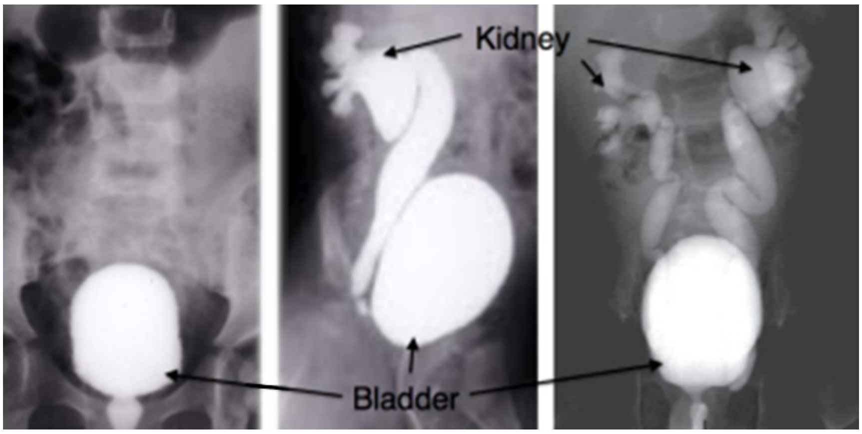

Figure 2. X-ray images of contrast agent in a patient (*left*) with no VUR (full bladder), and (*middle and right*) with severe Grade V VUR (side and front views, respectively; bladder, ureters and kidneys filled).

The VCUG procedure is traumatising and painful for the child, and it is stressful for parents, medical imaging staff and physicians. Specific risks associated with the VCUG are catheter associated UTIs, bladder spasm, painful urination post-procedure, and contrast agent allergic reaction. Behaviours consistent with post-traumatic stress disorder have been observed in young children after a VCUG, such as repetitive play, difficulty communicating, sudden changes in behaviour, and a newfound fear of health care settings (Stashinko *et al.* 1998). There is a clinical need for a non-invasive VUR detection method without radiation exposure and trauma.

A pre-clinical trial using a 32-electrode EIT system and inertial measurement units (IMU) was conducted in July 2021 on three pigs. Ethics approval for the animal study was granted by the Government of Cantabria, Spain (GAN/55/2013, reference PI-06-21, NIF: 72034697P). The key features distinguishing this data from previous pre-clinical VUR experiments by Kite Medical (Dunne *et al.* 2019) are:

- Stenting of the ureters, rather than severing them, thereby including bladder filling effects in the data. A stent was positioned between the ureters and bladder, where previously a catheter directly infused solution into the ureters.
- Intentional movement of the animal during data collection. Six IMUs (accelerometer, gyroscope, magnetometer) were used to directly measure the movement and to quantify the amount of movement at the skin surface around the kidney where electrodes were most densely placed.
- New EIT hardware and software.
- Electrode positions optimised to detect VUR and to isolate nuisance conductivity parameters (Aggrawal *et al.* 2021) in a 3D arrangement where previously a 2D ring of electrodes was used.

This paper reports briefly on this new animal model of VUR, the analysis of these results, and addresses the primary question “Does it work?”, concluding with the overall outcome and next steps.

2. Method

For three pigs, the following procedure was completed:

1. The animal was anaesthetised and ventilated. Either one or both UVJs were stented. Placement of the stent was confirmed with CT or fluoroscopy.
2. Sensors were applied and calibrated.
3. Up to 32 cycles of catheterised filling and draining the bladder were completed while capturing measurements. For the first and last cycles, x-ray contrast agent and fluoroscopy were used to confirm VUR. Otherwise, saline was used with conductivity values that similar to urine. On alternating cycles, movement was modelled by manipulating the pig’s left leg. Each stage of a cycle (empty, filling, filled, draining, back to empty again) was 30 to 90 seconds. Data was recorded continuously throughout the experiment.

The experiment was conducted in July 2021 at Hospital virtual Valdecilla (HvV) in Santander, Spain. In these experiments, up to 32 cycles per pig were possible. To accelerate the experiment, the data was collected continuously across all cycles for each pig.

Movement results in noise in the signal that can be challenging to overcome. The intention was to produce a steady movement artefact. Initial movement was a gentle circular rotation of the leg: foot approximately circling a 15 cm diameter region at 3 Hz with movement largely restricted to the area around the left thigh. By halfway through the first pig, the movement had transitioned to using the pig's lower leg (fibula and tibia) to lever the hip (still at approximately 2 Hz) causing the hip to lift off the table and the whole surface of the pig to shake at higher harmonics of the movement frequency.

Data was analysed by constructing models of the initial shape for each pig using photogrammetry. The stimulus and measurement sequences were designed specifically for our 3D electrode arrangement to localise conductivity changes in both kidneys, (Aggrawal *et al.* 2021). The model was meshed; then simulations of current density were used to iteratively refine the mesh density based on the element-wise sensitivity computed from the Jacobian (Figure 3).

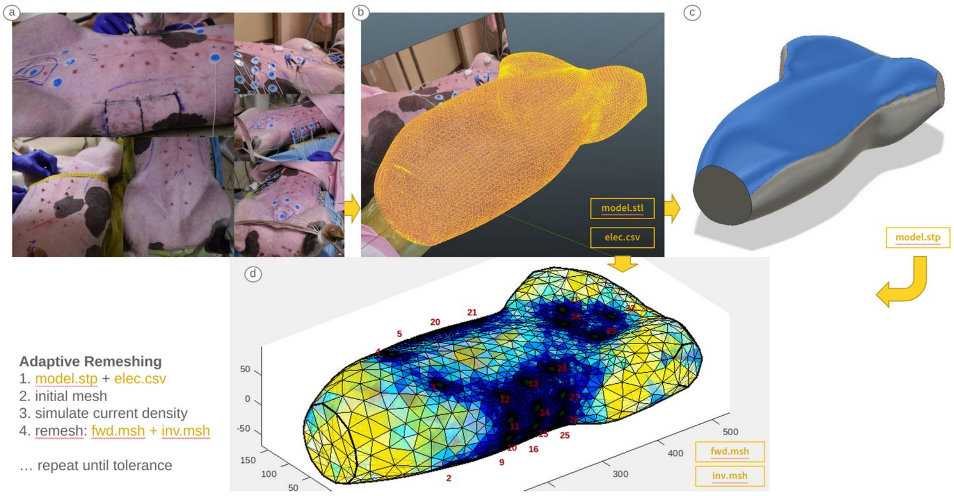

Figure 3. (a) Photos were acquired from many angles, (b) a model was constructed from the photos using 3D modelling software, (c) the 3D model was converted to a set of smooth surfaces so that the model vertices did not define the mesh density, (d) the smooth 3D model was meshed with electrodes. The electrode coordinates were acquired from the photos and mapped to the 3D model-space.

The EIT data was used to reconstruct conductivity change in 3D. Blocks of data were filtered over time to compare empty to full bladder states. The dynamics of a transition from empty to full and back to the empty state were observed, both with and without movement. The IMU data was used to (a) corroborate when movement was happening and to quantify the movement of the leg and around the electrodes, and (b) to confirm the breathing signal in the EIT data.

3. Results

The bilateral and unilateral stent cases presented distinct patterns in the conductivity reconstructions. The unilateral case was clearly identifiable with increases in conductivity (red region) on the left side of the pig, matching the location of the stent. The region of conductivity change is clearly associated with the location of the kidney. For the bilateral case, the conductivity increase is shared between right and left side. The situation is identifiable with or without motion (Figure 4, Figure 5).

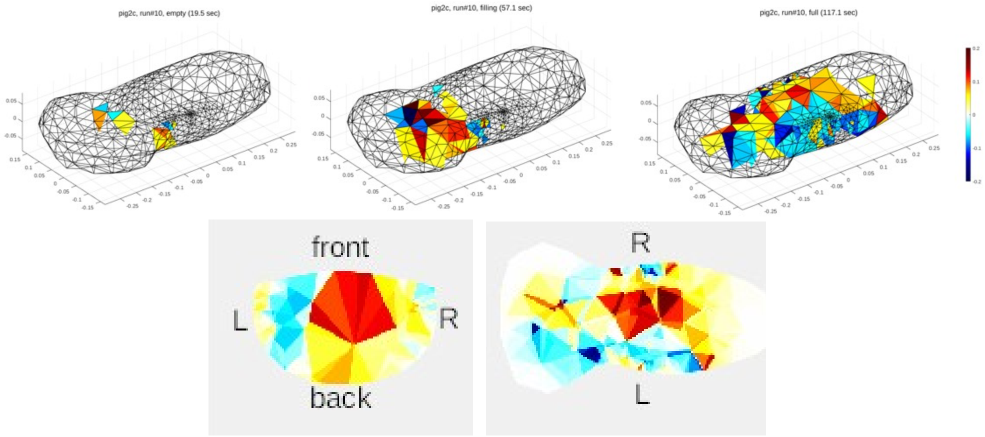

Figure 4. (*above*) Bilateral filling (pig A) from empty, filling (bladder changes), to full state (kidney changes); no motion; (*below*) A cross-sectional view in x, y, and z-axes in the full state, illustrating bilateral changes in conductivity near the kidneys.

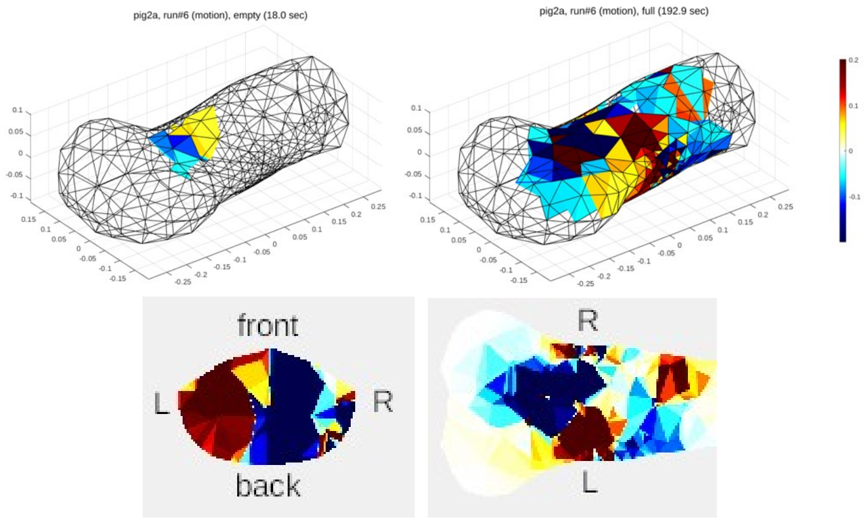

Figure 5. (*above*) Unilateral filling (pig B, left-side stent) from empty to full state bladder state (left-kidney changes); with motion; (*below*) A cross-sectional view (x- and z-axes; full state), clearly illustrates unilateral changes in conductivity for the left kidney.

4. Discussion

In the study, we recreated approximately Grade II to III VUR. The acute VUR condition induced by a stent means that stretching of the ureters into a tortuous expanded tube, associated with chronic Grade IV or V VUR, was not possible. A porcine model was the most appropriate animal model to simulate VUR because physiological characteristics and the dielectric properties of the porcine kidney are similar to that of humans (Paltiel *et al.* 2000).

Multiple photographs were acquired to build a 3D model of each pig. Use of a camera or video in a human clinical trial is problematic from a privacy perspective. Developing high quality initial models is important for 3D EIT reconstructions. CT and MRI data for developing Statistical Shape Models of the lower abdomen in both pigs and humans is under-represented in the available data sets we have examined. CT/MRI data are expensive to acquire. Many of the promising data sets did not include the exterior of the body: most renal and bladder CT/MRI use a narrow field of view to focus on specific organs. Therefore, fast methods for acquiring patient-specific models are important.

Improved 3D EIT reconstructions using IMU data to track movement is a promising avenue for further work.

5. Conclusions

The available evidence suggests that VUR is detectable, independent of breathing, and in many cases independent of aggressive, repetitive movement of the lower limbs. Changes in induced unilateral and bilateral VUR were correctly localised. This data provides further evidence of the potential for EIT to identify VUR in a non-invasive and radiation-free manner.

In the cases where conductivity changes were not detected, the key issues were measurement noise due to either movement (typical bioimpedance/electrode movement effects) or intermittent instrument noise. Instrument noise must be addressed going forward. Further algorithm development will help to mitigate residual movement effects.

Acknowledgments

Thanks to the hardworking team at Kite Medical and HvV for making these experiments possible.

References

Aggrawal H O and Boyle A. 2021 Region of Interest Guided Stimulation Pattern Selection Strategy for Electrical Impedance Tomography, *Proceedings of the 21st International Conference on Biomedical Applications of Electrical Impedance Tomography (EIT 2021)*, Galway, Ireland; **2021** p19.

Dunne E, O'Halloran M, Craven D, Puri P, Frehill P, Loughney S *et al.* 2019 Detection of Vesicoureteral Reflux using Electrical Impedance Tomography. *IEEE Trans Biomed Eng.* **66**(8):2279-2286.

Hoberman A, Charron M, Hickey R W, Baskin M, Kearney D H, Wald E R. 2003 Imaging studies after a first febrile urinary tract infection in young children. *N Engl J Med*. **348**(3):195-202.

Mattoo T K. 2011 Vesicoureteral reflux and reflux nephropathy. *Adv Chronic Kidney Dis*. **18**(5):348-54.

Paltiel H J, Mulkern R V, Perez-Atayde A, Connolly L P, Zurakowski D Z, Treves S T *et al.* 2000 Effect of chronic, low-pressure, sterile vesicoureteral reflux on renal growth and function in a porcine model: a radiologic and pathologic study. *Radiology*. **217**(2):507-15.

Sargent M A. 2000 What is the normal prevalence of vesicoureteral reflux? *Pediatr Radiol*. **30**(9):587-93.

Shaikh N, Spingarn RB, Hum SW. 2016 Dimercaptosuccinic acid scan or ultrasound in screening for vesicoureteral reflux among children with urinary tract infections. *Cochrane Database Syst Rev*. **7**:CD010657.

Snow B W, Taylor M B. 2010 Non-invasive vesicoureteral reflux imaging *J Pediatr Urol.* **6**(6):543-9.

Stashinko E E, Goldberger J. 1998 Test or trauma? The voiding cystourethrogram experience of young children. *Issues Compr Pediatr Nurs*. **21**(2):85-96.

Proceedings of the International Conference of Bioelectromagnetism, Electrical Bioimpedance,
and Electrical Impedance Tomography June 29 – July 1, 2022 / Kyung Hee University, Seoul, Korea

Simulation Phantoms for Evaluating an Automated Whole Breast Ultrasound/EIT system

Ethan K. Murphy[1], Harshavardhan Devaraj[1], and Ryan J. Halter[1,2]
[1]Thayer School of Engineering, Hanover, NH, 03755, USA
[2]Geisel School of Medicine, Dartmouth College, Hanover, NH 03755, USA

Correspondence: Ethan K. Murphy, e-mail : ethan.k.murphy@dartmouth.edu

Abstract– A combined automated whole breast ultrasound (ABUS) and electrical impedance tomography (EIT) system and a simulation study emulating the ABUS/EIT scenario are described. The simulation study revealed important sensitivity limitations of the system. Specifically, it was found that under ideal conditions tumors $\geq$2.0 cm in diameter could always be accurately reconstructed, 1.5 cm in diameter are accurate for depths < ~2.5 cm, 1.0 cm in diameter are accurate for depth < ~2 cm, and tumours of <0.5 cm in diameter could not accurately be detected. Additionally, it was revealed that our current soft-prior EIT algorithm is highly sensitive to inaccurate boundary information, indicating the need for modifications to the current algorithm.

Keywords: Electrical impedance tomography, soft-prior EIT, breast cancer, data fusion.

1. Introduction

Breast cancer is the 2nd most common cancer among American women; roughly 1 in 8 women will develop breast cancer, and ultimately about 1 in 39 women will die of the disease. Mammographic screening is a vital tool in detecting cancer early and reducing mortality due to breast cancer; unfortunately for women with dense breasts it has higher rates of false negatives and false positives. Ultrasound (US) is a supplemental screening technique that has good sensitivity in dense breasts (and is otherwise comparable to mammography) (Berg, 2004), is inexpensive, and is widely available. Unfortunately, US has high rates of false positives (higher than mammography, partially due to fibroadenomas and complicated cysts). Overall, there is a significant need for improved imaging on women with dense breasts.

Here we consider a combination of automated-whole-breast ultrasound (ABUS) with electrical impedance tomography (EIT) in order to improve the discriminating ability of US or ABUS alone. EIT appears promising for this application based on a number of ex vivo electrical impedance studies, which have reported strong contrast between cancer and both adipose and mammary gland tissues (Chauveau, 1999), as well as fibroadenomas (Jossinet, 1998) and fibrocystic tissues (Halter 2009), and prior in vivo imaging results, e.g. (Poplack, 2007). Following our phantom work (Murphy, 2017), we installed 31 electrodes into the rotating plate of a commercial ABUS system (SOFIA, https://ivuimaging.com/) (Fig. 1A-B). Initial gelatine-based phantom experiments appeared to be very sensitive to modelling errors. To further explore the impact of these modelling errors, we explored via simulation the sensitivity to various inclusions (sizes and contrasts) assuming ideal and noisy segmentation data.

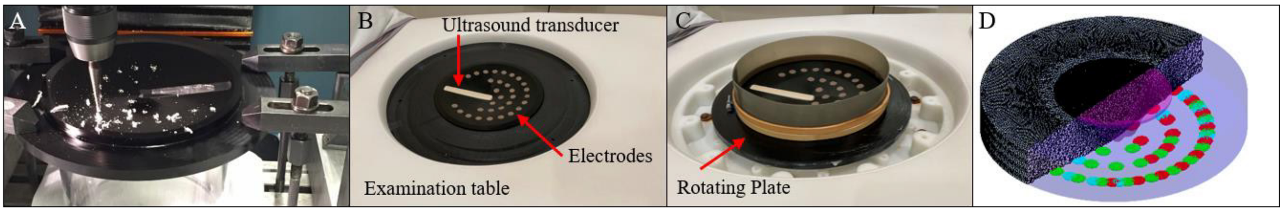

Figure 1. A. Drilling electrodes for a combined ABUS/EIT system, B. Installed electrodes within the commercial ABUS system which includes a custom examination table, C. a simple modification for enabling phantom studies, and D. a corresponding simulated scenario showing the FEM mesh, encoded mammary gland, and 3 states (rotations at red, green, and cyan angular locations) chosen to maximize electrode covereage of the bottom of the tank. Note the inner plate (best seen in C) rotates to form the full 3D ABUS scan.

2. Methods

This section summarizes the ABUS system and processing, the fused ABUS/EIT approach, and the parameters of the simulation study.

2.1 ABUS system and processing

During standard patient ABUS data collection, the rotating plate (best seen in Fig. 1C) collects 788 ultrasound images in one 360-degree rotation in ~60 seconds using a Hitachi Hi Vision Preirus ultrasound system. The pixels are then transformed into 3D space and are interpolates onto a rectilinear voxel-based image where standard image processing techniques can be performed. Specifically, we use Mimics (a 3D Medical Image Processing from Materialise) to segment the mammary gland or lesion/inclusions in subjects or phantom studies. Surface triangulations of the important structures are output, and then incorporated into the soft-prior EIT algorithm. A simple, exhaustive search on 3 states (rotations) to maximize electrode area on the bottom surface was performed resulting in rotation values of 0^o, 84^o and 198^o, (see Fig. 1D). Thus, following ABUS image acquisition, the rotating plate is actuated to these 3 angular locations and EIT data recorded.

2.2 Soft-prior EIT

The EIT algorithm investigated here was previously described in (Murphy, 2017) and utilized for 3D prostate phantom imaging (Murphy, 2020). Briefly, we rely on an accurate finite element method (FEM)-based forward model using tetrahedral elements constructed using gmsh (https://gmsh.info/). The h-values of the mesh (mesh density) was tuned to ensure the forward solver was accurate. Absolute reconstructions are performed using an iterative Gauss Newton solver. The segmentation information is incorporated into the inverse problem via the regularization matrix; specifically, within individual tissue types, non-smooth solution are penalized but there is no penalty across different tissue – *allowing natural jumps of electrical properties across different tissues*.

2.3 Simulation Study Parameters

A mammary gland surface was simulated (see magenta surface in Fig. 1D), and each test set had a simulated spherical tumour with diameters ranging from 0.5 to 2.5 cm with contrasts relative to the mammary gland of 0.63x, 1.2x, and 1.5x. Each tumour was located within the mammary gland, along the positive x- or y-axes with centres separated by 0.5 cm. This resulted in 615 tumour tests. The forward mesh had the mammary gland encoded within it. Two inverse mesh assumptions were taken: 1) the inverse mesh had ideal mammary gland information (although using different mesh densities from the forward mesh), and 2) the inverse mesh had inaccurate mammary gland information specified by a root mean square (RMS) error of 0.125, 0.25, 0.5, 1.0, and 2.0 mm from the ideal mammary gland. Absolute reconstructions were performed on all 615 tumours for both the ideal and inaccurate mammary gland scenarios. The metric of interest was the average conductivity of the inclusion.

3. Results

The results of our simulation study for ideal and inaccurate mammary gland information are given in Figs 2 & 3, respectively, where only tumour contrasts of 0.63x and 1.2x are presented – results for 1.5x were found to be similar. For the ideal mammary gland information, one can see that inclusions of 2.0-2.5 cm in size are always accurately reconstructed, 1.5 cm in size are accurate when its depth is $< \sim 2.5$ cm, 1.0 cm in size are accurate when its depth is $< \sim 2$ cm, and 0.5 cm in size cannot be accurately reconstructed. These results have no added noise to them, beyond using separate forward and inverse meshes, and thus appear to essentially represent the best possible results for soft-prior EIT – *i.e. the inaccuracy is due to the physics-based sensitivity limits of EIT*. The inaccurate mammary gland reconstructions (Fig. 3) show the tumour reconstruction and the average adipose and mammary gland values as well. These results indicate that the knowledge of the mammary gland has to be extremely accurate (~0.125 mm RMS) using our current soft-prior absolute EIT approach to achieve accurate reconstructions.

4. Discussion

This small simulation study represents important steps in the development of this ABUS/EIT technology. First, it was important to characterize the best-case sensitivity of the system, i.e. essentially asking what is the smallest tumour that can accurately be reconstructed with no noise present. Second, while having perfect knowledge of the mammary gland geometry is impossible, this study showed us *how* accurate that information needs to be with our current method. Because segmenting the mammary gland surface to within an RMS of 0.125 mm is likely unachievable, a reasonable path forward would be to adjust the method to be less sensitive to inaccurate boundary information. Approaches that may be explored include 1) simultaneous optimization of the encoded boundaries and conductivities, 2) exploration of different subsets of impedance patterns that could be less sensitivity to inaccurate knowledge of the mammary gland, and 3) alternative soft-prior implementations. Boundary reconstruction algorithms in EIT appear promising (Ren, 2018), but most of their work has been in 2D or in simulation and has relied on knowing the conductivity of the background and inclusions. Another soft-prior approach (Steiner, 2008), which we had previously explored (Murphy, 2017), may be promising here as it imposes the boundary information in a weaker/less hard manner, than the approach used here.

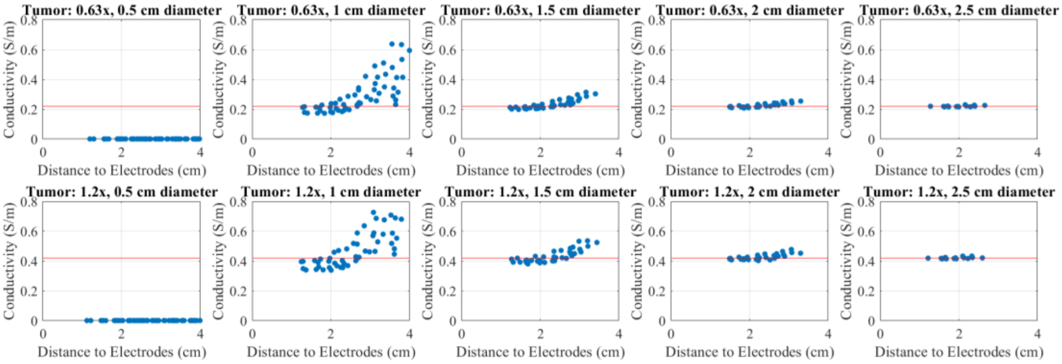

Figure 2. Absolute EIT reconstructions of simulated inclusions of various sizes (across columns) and two contrasts (across rows) as a function of the inclusion distance to the electrodes assuming *ideal* knowledge of the mammary gland and inclusion shape, size, and location. The results provide an estimate for the minimum size location that a can be reconstructed and its depth into the tissue.

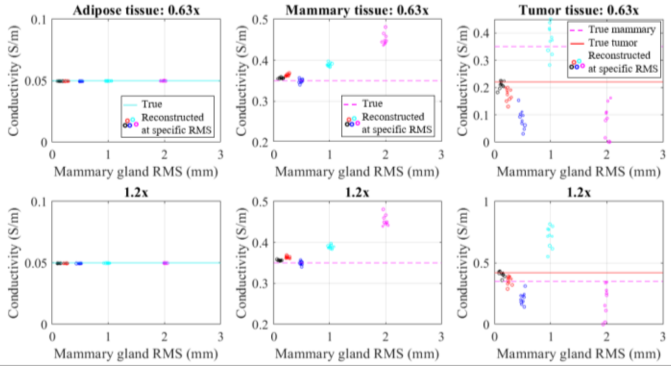

Figure 3. Absolute EIT reconstructions of adipose, mammary, and tumor tissue from simulated tests with inclusions (2.5 cm diameter) with one of two contrasts (across rows) as a function of the inclusion distance to the electrodes assuming the knowledge of the mammary gland is a certain RMS of the ideal mammary gland surface. The results provide an estimate for the apparent accuracy of mammary gland knowledge needed

5. Conclusions

The simulation study of an ABUS/EIT system underdevelopment revealed important sensitivity limitations (tumour accuracy based on size and depth) and revealed high sensitivity to inaccurate boundary information that indicates modifications to the current soft-prior EIT algorithm are needed.

Acknowledgments

This work was supported in part by the US National Institutes of Health (NIH) under grant 5R03EB027224-02. We would also like to thank Mark Stribling, President & CEO of iVu imaging for use and permission to modify their ABUS system.

References

Berg, W. a. et al. Diagnostic Accuracy of Mammography, Clinical Examination, US, and MR Imaging in Preoperative Assessment of Breast Cancer. Radiology 233, 830–849 (2004).

Chauveau, N. *et al.* Ex Vivo Discrimination between Normal and Pathological Tissues in Human Breast Surgical Biopsies Using Bioimpedance Spectroscopy. *Ann. N. Y. Acad. Sci.* **873**, 42–50 (1999).

Jossinet, J. & Lavandier, B. The discrimination of excised cancerous breast tissue samples using impedance spectroscopy. *Bioelectrochemistry Bioenerg.* **45**, 161–167 (1998).

Halter, R. J. *et al.* The correlation of in vivo and ex vivo tissue dielectric properties to validate electromagnetic breast imaging: initial clinical experience. *Physiol. Meas.* **30**, S121–S136 (2009).

Murphy, E.K., Mahara, A., Wu, X. and Halter, R.J., 2017. Phantom experiments using soft-prior regularization EIT for breast cancer imaging. *Physiological measurement*, *38*(6), p.1262.

Murphy, E.K., Wu, X., Everitt, A.C. and Halter, R.J., 2020. Phantom studies of fused-data TREIT using only biopsy-probe electrodes. *IEEE transactions on medical imaging*, *39*(11), pp.3367-3378.

Poplack, S.P., Tosteson, T.D., Wells, W.A., Pogue, B.W., Meaney, P.M., Hartov, A., Kogel, C.A., Soho, S.K., Gibson, J.J. and Paulsen, K.D., 2007. Electromagnetic breast imaging: results of a pilot study in women with abnormal mammograms. Radiology, 243(2), pp.350-359.

Ren, S., Soleimani, M., Xu, Y. and Dong, F., 2018. Inclusion boundary reconstruction and sensitivity analysis in electrical impedance tomography. *Inverse Problems in Science and Engineering*, *26*(7), pp.1037-1061.

Steiner, G., Soleimani, M. and Watzenig, D., 2008. A bio-electromechanical imaging technique with combined electrical impedance and ultrasound tomography. *Physiological measurement*, *29*(6), p.S63.

DAY 1

Wednesday, June 29, 2022

Oral Session 02

Tissue Property Imaging by MRI I

Chair Geon-Ho Jahng (Kyung Hee University)
Hyung Joong Kim (Kyung Hee University)

O 02-01 **Measurements of Electrical Properties in humans in vivo using Magnetic Resonance Imaging**
Rosalind J. Sadleir (Arizona State University)

O 02-02 **Comparison of Diffusion Tensor MREIT and Conductivity Tensor Imaging in human subjects**
S. Z. K. Sajib (Arizona State University)

O 02-03 **Detection of Electrical Conductivity Increases caused by Increased Neural Activity in vitro using Functional Magnetic Resonance Electrical Impedance Tomography**
C. Barnett (Arizona State University)

O 02-04 **Low-frequency Conductivity Tensor Images of Rat Brain Tumor Using a 9.4T MRI**
Nitish Katoch (Kyung Hee University Hospital)

O 02-05 **Assessment of electroporation in different complex structures by means of MREIT**
Marko Stručić (University of Ljubljana)

Proceedings of the International Conference of Bioelectromagnetism, Electrical Bioimpedance,
and Electrical Impedance Tomography June 29 – July 1, 2022 / Kyung Hee University, Seoul, Korea

Measurements of Electrical Properties in humans in vivo using Magnetic Resonance Imaging

R. Sadleir[1], S. Z. K. Sajib[1,2], E. Boakye[1], S. Sahu[1], and M. Chauhan[1,3]
[1]School of Biological and Health Systems Engineering, Arizona State University, Tempe, AZ, USA
[2]Canon Medical Research, Cleveland, OH, USA
[3]University of Kansas Medical Center, Kansas City, KS, USA

Correspondence : Rosalind J. Sadleir, e-mail : rsadleir@asu.edu

Abstract–Measurement of conductivity distributions at high (Larmor frequency) and low (<1 MHz) frequencies can be obtained using MRI image data obtained using Electric Properties Tomography (Voigt et al., 2011) (EPT), Magnetic Resonance Electrical Impedance Tomography (Seo et al., 2003) (MREIT), or Conductivity Tensor Imaging (Katoch et al., 2019) (CTI) strategies. In addition, electromagnetic fields in the brain resulting from transcranial or intracranial neuromodulation such as tDCS deep brain stimulation can be measured and used to inform electrode location methods or mechanism hypotheses. In the practical sense, measurement of these data on human subjects is relatively straightforward in CTI or EPT methods, where electrodes are not required, but more complex when the safety and artefactual implications of electrode and electrode wire locations and materials must be considered when using MREIT to measure field distributions. Subjects may also be affected by administration of MREIT currents. We will first review previous strategies to measure conductivity and field distributions in human subjects. We will then focus on methods for obtaining high quality and accurate images of the human brain using MREIT during neuromodulation (Chauhan et al., 2018), including practical details for ensuring that electrodes are applied safely, stable electrode contact is ensured, and wire tracks can be determined. Finally, because typical neuromodulation electrode locations may involve significant current flow out of the transverse plane, we will also demonstrate approaches that can improve reconstruction of full conductivity and electromagnetic field data in these cases.

Acknowledgments

The authors would like to thank Sharmeen Maze, Wendy Johnson and Chris Blais for their support in scanning and coordinating subjects imaged during our studies.

References

CHAUHAN, M., INDAHLASTARI, A., KASINADHUNI, A. K., SCHÄR, M., MARECI, T. H. & SADLEIR, R. J. 2018. Low-Frequency Conductivity Tensor Imaging of the Human Head in vivo using DT-MREIT: First Study. *IEEE Transactions on Medical Imaging,* 37**,** 966-976.

KATOCH, N., CHOI, B. K., SAJIB, S. Z. K., LEE, E., KIM, H. J., KWON, O. I. & WOO, E. J. 2019. Conductivity tensor imaging of in vivo human brain and experimental validation using giant vesicle suspension. *IEEE Transactions on Medical Imaging,* 38**,** 1569-1577.

SEO, J. K., YOON, J. R., WOO, E. J. & KWON, O. 2003. Reconstruction of conductivity and current density images using only one component of magnetic field measurements. *IEEE Transactions on Biomedical Engineering,* 50**,** 1121-1124.

VOIGT, T., KATSCHER, U. & DOESSEL, O. 2011. Quantative conductivity and permittivity imaging of the human brain using electric properties tomography. *Magnetic Resonance in Medicine,* 66**,** 456-466.

ICBEM Bioelectromagnetism ICEBI Electrical Bioimpedance EIT Electrical Impedance Tomography

Proceedings of the International Conference of Bioelectromagnetism, Electrical Bioimpedance,
and Electrical Impedance Tomography June 29 – July 1, 2022 / Kyung Hee University, Seoul, Korea

Comparison of Diffusion Tensor MREIT and Conductivity Tensor Imaging in human subjects

S. Z. K. Sajib[1,2], E. Boakye[1], S. Sahu[1], M. Chauhan[1,3] and R. Sadleir[1]
[1]School of Biological and Health Systems Engineering, Arizona State University, Tempe, AZ, USA
[2]Canon Medical Research, Cleveland, OH, USA
[3]University of Kansas Medical Center, Kansas City, KS, USA

Correspondence : Rosalind J. Sadleir, e-mail : rsadleir@asu.edu

Abstract–: Diffusion tensor magnetic resonance electrical impedance tomography (Kwon et al., 2014) (DT-MREIT) and electrodeless conductivity tensor imaging (CTI) are alternate modalities for quantifying low-frequency tissue anisotropic conductivity tensor properties by considering the relationship between ion mobility and water diffusion. However, DT-MREIT requires external current application, which may involve risk of injury or peripheral neural stimulation, while electrodeless CTI can provide both isotropic and anisotropic conductivity distributions (Lee et al., 2020) by decomposing high-frequency conductivity σ_H measured using MR Electrical Properties Tomography (Gurler and Ider, 2016) (MREPT) into its extra- and intra-cellular parts and incorporating the tissue microstructure parameters estimated from multi-b-value diffusion-weighted images. Both methods have potential application to estimating neuromodulation fields or formulating forward models used for electrical source imaging. However, a direct comparison of these two modalities has not yet been performed. Therefore, the aim of this study was to test the equivalence of these two modalities in both phantoms and human subjects. We imaged phantoms and human subjects using both DT-MREIT and CTI procedures and found generally good agreement between the two modalities within assumptions made in reconstructions using each technique such as boundary conductivity and the ratio of intra and extracellular conductivities. We present points of difference and suggestions for future validation work.

References

GURLER, N. & IDER, Y. Z. 2016. Gradient-based electrical conductivity imaging using MR phase. *Magnetic Resonance in Medicine,* 77**,** 137-150.

KWON, O., JEONG, W. C., SAJIB, S. Z. K., KIM, H. J. & WOO, E. J. 2014. Anisotropic conductivity tensor imaging in MREIT using directional diffusion rate of water molecules. *Physics in medicine and biology,* 59**,** 2955-2974.

LEE, M. B., JAHNG, G.-H., KIM, H. J., WOO, E. J. & KWON, O. I. 2020. Extracellular electrical conductivity property imaging by decomposition of high-frequency conductivity at Larmor-frequency using mult-b-value diffusion-weighted imaging. *PLoS ONE,* 15**,** e0230903.

Proceedings of the International Conference of Bioelectromagnetism, Electrical Bioimpedance,
and Electrical Impedance Tomography June 29 – July 1, 2022 / Kyung Hee University, Seoul, Korea

Detection of Electrical Conductivity Increases caused by Increased Neural Activity in vitro using Functional Magnetic Resonance Electrical Impedance Tomography

C. Barnett[1], G. K. Fuller[1], A. Turcheck[1], M. Afrifa[1], M. Boggess[2] and R. J. Sadleir[1]
[1]School of Biological and Health Systems Engineering, Arizona State University, Tempe, AZ, USA
[2]Cornell Statistical Consulting Unit, Ithaca, NY, USA

Correspondence : Rosalind J. Sadleir, e-mail : rsadleir@asu.edu

Abstract– The aim of this study was to further process previously analyzed data (Sadleir et al., 2017) to confirm that fMREIT can directly observe neural conductivity changes as a result of activity changes in vitro. The data were obtained from experiments on Aplysia abdominal ganglia performed using 100 µA or 1mA imaging currents. We found significant variability changes in 1-mA-current data, but not 100 µA data in (Sadleir et al., 2017), and conductivity contrasts were anticipated to be more pronounced in 1 mA than 100 µA data following modeling findings. We then reconstructed and compared conductivity changes in regions within active tissue or in an inactive background region using the Harmonic B_z (Seo et al., 2003) or transversal J-substitution (Nam et al., 2007) MREIT reconstructions in experiments where tissues that were treated with a neuroirritant solution to increase activity, or that had a control solution administered. Using the Harmonic B_z algorithm we found a significant increase in conductivity ($p<0.05$) within treated tissues compared to the control condition. No significant changes in background media or control experiments were found. Findings for transversal J-substitution reconstructions were positively correlated with Harmonic B_z results.

Acknowledgments

The authors thank C. Falgas, S. Holland, S. C. Grant and E. J. Woo for contributions to this data set.

References

NAM, H. S., I., L. B., CHOI, J., PARK, C. & KWON, O. 2007. Conductivity imaging with low level current injection using transversal J-substitution algorithm in MREIT. *Physics in medicine and biology,* 52**,** 6717-6730.

SADLEIR, R. J., FU, F., FALGAS, C., HOLLAND, S. K., BOGGESS, M., GRANT, S. C. & WOO, E. J. 2017. Direct Detection Of Neural Activity In Vitro Using Magnetic Resonance Electrical Impedance Tomography (MREIT). *NeuroImage,* 161**,** 104-119.

SEO, J. K., YOON, J. R., WOO, E. J. & KWON, O. 2003. Reconstruction of conductivity and current density images using only one component of magnetic field measurements. *IEEE Transactions on Biomedical Engineering,* 50**,** 1121-1124.

ICBEM Bioelectromagnetism ICEBI Electrical Bioimpedance EIT Electrical Impedance Tomography

Proceedings of the International Conference of Bioelectromagnetism, Electrical Bioimpedance,
and Electrical Impedance Tomography June 29 – July 1, 2022 / Kyung Hee University, Seoul, Korea

Low-frequency Conductivity Tensor Images of Rat Brain Tumor Using a 9.4T MRI

Nitish Katoch[1], Bup Kyung Choi[1], Min Jung Kim[2], Young Hoe Hur[2], Eun JunYoon[3],
Jin Woong Kim[3], Hyung Joong Kim[1] and Eung Je Woo[1]

[1]Medical Science Research Institute, Kyung Hee University Hospital, Seoul, Korea
[2]Department of Hepato-Biliary-Pancreas Surgery, Chonnam National University Medical School, Gwangju, Korea
[3]Department of Radiology, Chosun University Hospital and Chosun University College of Medicine, Gwangju, Korea

Correspondence : Hyung Joong Kim, e-mail : bmekim@khu.ac.kr

Abstract– Cell proliferation, invasion, and ionic aggregation are critical features of cancer cells. The electrical conductivity of biological tissues at low frequencies is determined by cellularity, ionic concentration, and their mobility. Anisotropic conductivity imaging of tumors has the potential to give useful information in terms of heterogeneity and invasive nature. This study reports tumor development in relation to changes in the ionic environment using a low-frequency Conductivity Tensor Imaging (CTI) technique. B1 mapping for electrical conductivity distribution at Larmor frequency and multi-b-value diffusion imaging to differentiate extracellular and intracellular tissue compartments and their diffusion coefficients have been used to develop conductivity tensor imaging. Applying to a F98 cerebral tumor-bearing rat, a longitudinally following tumor cell inoculation on days 8, 11, and 14 was performed. Changes in the concentration of ions and cellular states of tumor growth are reflected in both high and low-frequency. Anisotropic conductivities of tumoral tissues were significantly lower ($p<0.01$) than the normal regions of the brain and progressive with growth ($p<0.01$). In conclusion, we demonstrate a novel contrast mechanism based on ionic concentration and mobility, which may aid in providing useful information about tumor heterogeneity in probing the microenvironment of brain tumors for devising better treatment therapy.

Keywords: MRI; conductivity tensor imaging; brain tumors; anisotropy; diffusion tensor imaging.

1. Introduction

On both the macroscopic and microscopic scales, tumors have structural heterogeneity. The tumor origin affects cell shape, density, and cytoarchitecture, which is influenced by local oxygen gradients, nutritional and growth factors, metabolites, genetically divergent clones, and interactions with neighboring tissues (Marusyk & Polyak, 2010). To investigate this link we test the hypothesis that ionic variance, caused by microscopic anisotropy and isotropic heterogeneity, is associated with ionic aggregation and cell density in brain tumors (Gupta et al., 2000; Lesbats et al., 2021). Glioblastomas (GBMs) are the most common type of malignant brain tumors, comprising approximately half of all the primary malignant tumors in the brain. The electrical properties of brain tumors at low-frequency are unknown. Electrical conductivity of biological tissues is determined by the cellular structure and density, extracellular volume fraction, composition and amount of extracellular matrix materials, membrane characteristics, and the concentrations and mobility of major ions in the extracellular and intracellular fluids (Choi et al., 2020; Katoch et al., 2018). The inherent qualities of the particle, such as size and shape, and the ambient variables of the fluid, such as temperature, hydration, and viscosity, affect the mobility of a charge carrier. Mobility is also influenced by the structural qualities of cells, such as size, shape, density, layout, extracellular matrix components, and intracellular organelles (Grimnes & Martinsen, 2011).

Ions in the extracellular space cannot permeate cellular membranes at low frequencies, thus, they must circulate about the cells. When the cellular structure has a directional feature, the low-frequency conductivity has the same anisotropy or directional property. The movements of the ions inside the cells are confined, whilst an externally generated electric field hampers the motions of the ions outside the cells. The anisotropic conductivity of biological tissue with a complicated cellular structure may have many directional components. In this paper, we express the anisotropic conductivity of biological tissue as a conductivity tensor of 3×3 matrix. Though the expression of an anisotropic conductivity as a tensor with three directional components could be an over-simplification for a real tissue with a complicated cellular structure, it provides a practically useful and mathematically manageable way of handling the tissue anisotropy.

To map anisotropic conductivity distribution, *Sajib* et al. recently developed a novel low-frequency conductivity tensor imaging (CTI) method (Sajib, Kwon, Kim, & Woo, 2018). In CTI, a pixel-dependent scale factor is calculated to produce subject-specific conductivity tensor information. CTI combines two MR techniques where ion concentration is modulated from high-frequency conductivity from MREPT technique, and tissue microstructure parameters are reconstructed from diffusion-weighted imaging (DWI) (Katoch et al., 2018; Sajib et al., 2018). In this preclinical feasibility study, a new electrodeless low-frequency conductivity tensor imaging (CTI) method is utilized to characterize an intracranial model of rat gliomas at ultra-high magnetic fields of 9.4T with a spatial resolution of 0.3×0.3×0.3 mm^3. The measured conductivity values from tumoral tissue are compared with normal tissue.

2. Method

2.1 Animal model

Animal care, treatment, and experiments were carried out according to the regulations of the UK Home Office Animals (Scientific Procedures) Act 1986 and with the local animal welfare committee's ethical approval. F98 cells (ATCC CRL-2937TM) were transcranially injected into the right cortex to generate intracranial tumors. To explore the potential of CTI for low-frequency conductivity mapping, brain tumors were induced by transcranial injection of F98 cells in the right cortex. An F344 female (100-120 g) rat was injected with 50,000 F98 cells suspended in a 5 µL PBS solution.

2.2 Conductivity tensor image reconstruction

The CTI method derives a low-frequency conductivity tensor **C** by using a high-frequency isotropic conductivity (σ_H) obtained using the MREPT technique and the information about water diffusion obtained by the *multi-b* diffusion-weighted imaging method. Since the details of its basic theory and algorithm are available in, we simply introduce the following CTI formula in this paper (Sajib et al., 2018):
Here, the low-frequency conductivity tensor is expressed as:

$$\mathbf{C} = \alpha \bar{c}_e \, \mathbf{D}_e^w \tag{1}$$

Using the reference value of β=0.41, the apparent effective extracellular ion concentrations of (1) can be estimated

$$\bar{c}_e = \frac{\sigma_H}{\alpha d_e^w + (1-\alpha) d_i^w \beta} \tag{2}$$

Using $\bar{c}_e$ from (2) in (1) , the conductivity tensor image was reconstructed using the CTI formula can be expressed as:

$$\mathbf{C} = \alpha \bar{c}_e \mathbf{D}_e^w = \frac{\alpha \sigma_H}{\alpha d_e^w + (1-\alpha) d_i^w \beta} \mathbf{D}_e^w = \eta \mathbf{D}_e^w \tag{3}$$

where, σ_H is the high-frequency conductivity at the Larmor frequency, α is the extracellular volume fraction, $\bar{c}_e$ is apparent extracellular ion-concentrations, β is the ion concentration ratio of intracellular and extracellular spaces, d_e^w and d_i^w are the extracellular and intracellular water diffusion coefficients, respectively, and $\mathbf{D}_e^w$ is the extracellular water diffusion tensor. The computed scale factor (η) was multiplied at every pixel by the extracellular diffusion tensor $(\mathbf{D}_e^w)$ to calculate the absolute conductivity tensor (Katoch et al., 2018; Sajib et al., 2018).

2.3 MRI acquisition protocols

All animals were scanned using a 9.4T biospec MRI scanner (Bruker Biospin, Inc. Germany) equipped with an 86 mm transmission birdcage coil in transmitting mode and a 4-channel array surface coil in receiving mode. The imaging parameters were as follows: TR/TE = 4341/8 ms, number of echoes = 10, NEX = 2, slice thickness = 0.3 mm, number of slices = 38, matrix size = 128×64, and FOV = 40×20 mm^2 (Lesbats et al., 2021). *Multi-b-value* diffusion-weighted imaging (DWI) data sets were obtained using the single-shot spin-echo echo-planar-imaging pulse sequence to calculate α, d_e^w, d_i^w, and $\mathbf{D}_e^w$. The number of directions of the diffusion-weighting gradients was 20 with b-values of 50, 150, 300, 500, 700, 1000, 1400, 1800, 2200, 2600 and 3000 s/mm^2. TR/TE = 2500/23 ms, slice thickness = 0.3 mm, flip angle = 90°, number of excitations = 5, number of slices = 38 and acquisition matrix = 128×64 (Katoch et al., 2018). An additional conventional T2 weighted scan of 5 minutes was also acquired for anatomical reference.

For image analysis, two VOIs were created, including the tumor reflecting the invasive areas of the tumor and the contralateral normal brain cortex. The electrical conductivity values at high and low-frequency at time points are shown in Table 1. Representative ROIs are depicted in Figure. 1 on a slice with the maximum size of tumor for representative rats.

3. Results

Figure 1 shows the CTI images with the widest extent of tumor from a rat brain using eq. (3), respectively. The images cover the tumor from a representative rat showing the variation of the intermediate variable of CTI and low-frequency conductivity from top to bottom row for 8th, 11th and 14th day after tumor cell implantations. We plotted longitudinal and transversal components defined as $\sigma_{\parallel}$ and $\sigma_{\perp}$ for tensor. The images of the scale factor (η) between tensors were also plotted for the conductivity tensor. The mean values of the reconstructed conductivity values were also measured from tumor and normal tissues and displayed in Table 1. The segmented VOIs are overlayed and displayed on T2-weighted images in figure 1.

The conductivity images in both low- and high-frequency conductivity show a differentiated contrast compared to normal regions of rat brain. The extracellular volume fraction (α) shows a higher contrast at boundary regions of tumor. This could have stemmed from the accumulation of fluids forming an edematic region. The ventricles appear enlarged in figure 1 due to excessive fluid accumulation due to restriction in CSF flow (hydrocephalus) caused by the tumor. The conductivity of tumor region was significantly different compared to the contralateral cortex on each of 8th, 11th and 14th days after injecting tumor cells. Focusing only on the tumor region, the conductivity of tumor was progressively and significantly increasing with respect to volume change in tumor. High-frequency conductivity tends to be a weighted sum of intra- and extracellular spaces. It is observed that the $\boldsymbol{\sigma}_H$ was higher in tumorous region, however we observed a decrease in extracellular ionic mobility in proportional to lower extracellular water diffusivity. The σ_H at day 8 was 0.68 and reached 1.19 S/m on 14th day after implantation. The average increase of 42% was observed in σ_H images. These results were similar to those from the findings of *Clementine* et al (Lesbats et al., 2021). There is a significant increase in conductivity values of the tumor compared to the normal brain, which is also reported in Na-MRI of brain tumors, indicating an imbalance in the Na+/K+ pumps (Nagy, Lustyik, Nagy, Zarandi, & Bertoni-Freddari, 1981). The σ_H in contralateral regions remain the same in all three-time points, as shown in Table 1.

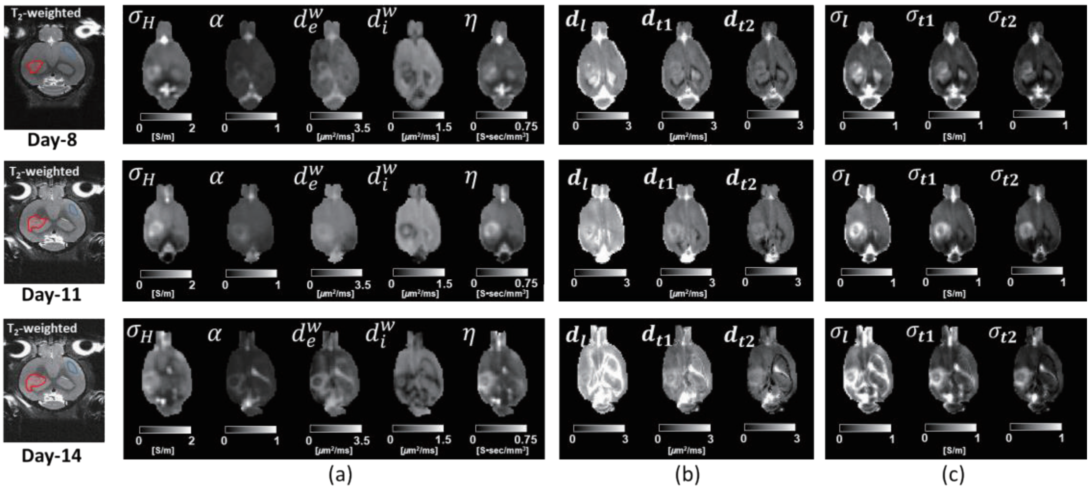

Figure 1. In-vivo reconstructed conductivity tensor images of rat brain tumor for day 8, 11 and 14. T2-weighted images, (**a**) high-frequency conductivity (σ_H), extracellular volume fraction (α), extracellular water diffusion coefficient (d_e^w), intracellular water diffusion coefficient (d_i^w) and scale factor (η), respectively. (**b**) Water-diffusion tensor ($\mathbf{D}_e^w$), and (**c**) conductivity tensor images (**C**).

Table 1 shows the measured extracellular water-diffusion tensor measured from tumor and normal brain regions. The parallel ($\boldsymbol{d}_\parallel$) and perpendicular diffusivity ($\boldsymbol{d}_\perp$) of extracellular spaces significantly decreases (P<0.1) with the increase in tumor volume (P<0.1). These changes in extracellular diffusivity in both parallel and perpendicular components could be co-related with a decrease in extracellular space measured in α (Zamecnik, 2005). The α tends to reduce as tumor grow and could be seen as an aggregation of cancer cells with tumor growth. Figure 1 also shows the isotropic $d_i^w$and d_e^w, the values of d_e^w reduces with growth in tumor and d_i^w remains same, respectively. The understanding of the decrease in d_e^wcould be from squeezing extracellular space, and diffusion tends to be more hindered in tumorous region. At low-frequencies, electrical conductivity exhibits the property of anisotropy that can be observed in CTI images. The measured conductivity values in normal regions was ranged from 0.35 to 0.38 S/m, with an anisotropic ratio (AR) of 2.01. The low-frequency conductivity values in the tumor region were smaller than the normal regions and ranged from 0.18 to 0.29 S/mm. The conductivity values between the normal region and tumor were significantly different (P<0.1).

Table 1. Average values of high-frequency (σ_H) and water-diffusion tensor ($\mathbf{D}_e^w$), and conductivity tensor (**C**) from segmented VOIs overlayed on T2-weighted images in figure 1. $\boldsymbol{\sigma}_\parallel = \boldsymbol{\sigma}_l$ is a parallel conductivity and $\boldsymbol{\sigma}_\perp = (\boldsymbol{\sigma}_{t1} + \boldsymbol{\sigma}_{t2})/\mathbf{2}$ is a perpendicular component of conductivity tensor. The number of voxels are similar in both the regions.

Day	ROI	σ_H [S/m]	Water diffusion tensor [μm²/ms]		Conductivity tensor [S/m]	
			$\boldsymbol{d}_\parallel$	$\boldsymbol{d}_\perp$	$\boldsymbol{\sigma}_\parallel$	$\boldsymbol{\sigma}_\perp$
Day-8	**Normal**	0.68±0.08	1.34±0.07	1.03±0.06	0.35±0.02	0.24±0.02
	Tumor	0.86±0.13	1.47±0.07	1.14±0.03	0.29±0.02	0.23±0.01
Day-11	**Normal**	0.72±0.05	1.39±0.12	1.09±0.06	0.38±0.04	0.24±0.03
	Tumor	0.97±0.11	1.25±0.04	1.11±0.03	0.22±0.03	0.18±0.02
Day-11	**Normal**	0.72±0.06	1.38±0.03	1.01±0.05	0.36±0.05	0.26±0.03
	Tumor	1.19±0.08	0.98±0.05	1.02±0.03	0.18±0.02	0.15±0.01

4. Discussion

Electrical conductivity is primarily determined by the product of ion concentration and mobility (Grimnes & Martinsen, 2011). While the effect of the ionic concentration is independent of frequency, mobility depends on the frequency, especially for those ions in the extracellular fluid since their movements at low frequency are hindered by the cell membranes. This frequency dependence in ionic mobility originates from anisotropy at low frequency. Considering that numerous molecules surround ions, their mobility should generally change with frequency. CTI method can provide electrical conductivity in both high- and low-frequency ranges, thus implying both cell density effect and the anisotropic behavior of the tumors (Katoch et al., 2018; Lesbats et al., 2021).

The conductivity of tumor at high-frequency increases with tumor growth, whereas interestingly, the low-frequency reduces as an increase in the cell density with change in tumor volume. Due to the missing membrane effect, the conductivity at high-frequency reflects the change in ionic concentration, especially from aggregated cancer cells. It is well known that the intracellular metabolite concentration is higher in cancer cells, indicating an imbalance in the Na+/K+ pumps (Nagy et al., 1981). The decreased $\sigma_{\parallel}$ and $\sigma_{\perp}$ is possibly due to lower extracellular space and lower mobility in those spaces. The visualization of low-frequency conductivity added the information of cell size, density, and swelling. The conductivity values are almost similar in edema for low and high frequency due to the absence of tumor cells or fluid accumulation. The lower contrast and conductivity values in $\mathbf{C}$ at the center of the tumor can be seen as the increase in tumor cell density, which appears high in high-frequency conductivity. It provides contrast information from both intra- and extracellular spaces. The distinct contrast information of high- and low-frequency conductivity can be helpful in the early detection of tumor and treatment planning. We believe that the measurement of anisotropic conductivity from a CTI method, as used in the current study, provides a novel contrast for the characterization of brain tumors. This information may be complementary to other contrast mechanisms, including mean diffusivity, and may aid in a better understanding of the biology of brain tumors. Conductivity imaging, in general, add more valuable diagnostic information in non-invasive preclinical and clinical practice.

5. Conclusions

CTI can probe the structural heterogeneity of tumor tissue in terms of the variance of apparent conductivity within a voxel. This study established the understanding of tumor electrical properties within its microenvironment. The conductivity at a low-frequency in tumor reduces in negative correlation to cellularity, whereas conductivity at a frequency of 300 MHz increase with tumor growth. The percentage increase could be as high as 42% in $\boldsymbol{\sigma}_H$ and reduces up to 60% in $\boldsymbol{\sigma}_L$. In conclusion, CTI allows non-invasive mapping of parameters that reflect variable cell eccentricity and density with ionic behavior. These results constitute convincing evidence that a link exists between cellular state and heterogeneity of tumor and parameters from CTI. Decomposing effects of anisotropic low- and isotropic high-frequency conductivity facilitates an improved interpretation of tumor progressions.

Acknowledgments

This research was funded by the National Research Foundation of Korea (NRF) grants funded by the Korea government (No. 2019R1A2C2088573, 2020R1A2C200790611, 2021R1A2C2004299).

References

Choi, B. K., Katoch, N., Kim, H. J., Park, J., Ko, I. O., Kwon, O. I., & Woo, E. J. (2020). Validation of conductivity tensor imaging using giant vesicle suspensions with different ion mobilities. *BioMedical Engineering OnLine, 19*(1), 1-17.

Grimnes, S., & Martinsen, O. G. (2011). *Bioimpedance and bioelectricity basics*: Academic press.

Gupta, R. K., Cloughesy, T. F., Sinha, U., Garakian, J., Lazareff, J., Rubino, G., . . . Alger, J. R. (2000). Relationships between choline magnetic resonance spectroscopy, apparent diffusion coefficient and quantitative histopathology in human glioma. *Journal of neuro-oncology, 50*(3), 215-226.

Katoch, N., Choi, B. K., Sajib, S. Z., Lee, E., Kim, H. J., Kwon, O. I., & Woo, E. J. (2018). Conductivity tensor imaging of in vivo human brain and experimental validation using giant vesicle suspension. *IEEE transactions on medical imaging, 38*(7), 1569-1577.

Lesbats, C., Katoch, N., Minhas, A. S., Taylor, A., Kim, H. J., Woo, E. J., & Poptani, H. (2021). High-frequency electrical properties tomography at 9.4 T as a novel contrast mechanism for brain tumors. *Magnetic resonance in medicine, 86*(1), 382-392.

Marusyk, A., & Polyak, K. (2010). Tumor heterogeneity: causes and consequences. *Biochimica et Biophysica Acta (BBA)-Reviews on Cancer, 1805*(1), 105-117.

Nagy, I. Z.-., Lustyik, G., Nagy, V. Z.-., Zarandi, B., & Bertoni-Freddari, C. (1981). Intracellular Na+: K+ ratios in human cancer cells as revealed by energy dispersive x-ray microanalysis. *The Journal of cell biology, 90*(3), 769-777.

Sajib, S. Z., Kwon, O. I., Kim, H. J., & Woo, E. J. (2018). Electrodeless conductivity tensor imaging (CTI) using MRI: basic theory and animal experiments. *Biomedical engineering letters, 8*(3), 273-282.

Zamecnik, J. (2005). The extracellular space and matrix of gliomas. *Acta neuropathologica, 110*(5), 435-442.

Proceedings of the International Conference of Bioelectromagnetism, Electrical Bioimpedance,
and Electrical Impedance Tomography June 29 – July 1, 2022 / Kyung Hee University, Seoul, Korea

Assessment of electroporation in different complex structures by means of MREIT

Marko Stručić[1], Jessica Genovese[2], Vitalij Novickij[3], Samo Mahnič-Kalamiza[1], Igor Serša[4],
Damijan Miklavčič[1] and Matej Kranjc[1]
[1] University of Ljubljana, Faculty of Electrical Engineering, Tržaška c. 25, 1000 Ljubljana, Slovenia
[2] University of Bologna, Department of Agricultural and Food Sciences, P. Goidanich 60, Cesena, Italy
[3] Institute of High Magnetic Fields, Vilnius Gediminas Technical University, Naugarduko g. 41, 03227 Vilnius, Lithuania
[4] Institut "Jožef Stefan", Jamova cesta 39, 1000 Ljubljana, Slovenia

Correspondence : Matej Kranjc, e-mail : matej.kranjc@fe.uni-lj.si

Abstract- The aim of our study was to investigate the degree of membrane permeabilisation by applying Pulsed Electric Field (PEF) treatment to plant and animal food matrices (potato, apple, chicken) using magnetic resonance electrical impedance tomography and T_2 mapping. The effect of electroporation treatment on T_2 relaxation times was evaluated by comparing the electric field distribution obtained by magnetic resonance electrical impedance tomography with the induced decrease of T_2 values. The research results provided useful insights into the evaluation of electroporation and suggest that magnetic resonance electrical impedance tomography could be used as an efficient tool to improve the efficacy of electroporation treatments.

Keywords: electroporation, PEF treatment, electric field, magnetic resonance imaging, magnetic resonance electrical impedance tomography.

1. Introduction

Electroporation or Pulsed Electric Field (PEF) treatment of food is an emerging industrial processing technology with a potential to replace conventional thermal food processes widely used to improve food stability and guarantee its microbiological safety [1]. This technology uses application of short electric pulses with high amplitude affecting cell membrane permeability or in extreme cases even destroying the cell membrane. PEF treatment requires moderate energy consumption, is fast, allows for better retention of flavour and colour, and preserves nutritional properties of foods [2]. Despite the numerous benefits of PEF treatment, there is still debate about the appropriate assessment of its effects. In this respect, several research papers reported on the analysis of the electric current signals during the application of the high-voltage pulse, demonstrating that the dynamics of electric current can be used as a key characterization feature of tissue electroporation [3,4]. However, there are limits in obtaining detailed information regarding the detection and quantification of electroporation effects in highly inhomogeneous multicellular systems, with a clear drawback of these results being affected by additional phenomena, which can be superimposed or altered in other ways. Magnetic resonance electric impedance tomography (MREIT) is a method capable of reconstructing the electric field distribution during pulse delivery indirectly through use of magnetic resonance imaging (MRI) and numerical algorithms, thus making it an attractive tool for monitoring and evaluation of electroporation treatment of tissues.

The goal of our investigation was to explore the level of membrane permeabilization in plant and animal tissues as an underlying mechanism of PEF treatment from subjecting these tissues to PEF treatment, whereby we employed different MRI assessment methods (current density imaging, MREIT, and transversal relaxation time T_2 mapping). Experiments were performed in apple fruit and potato tuber tissue, since these vegetable matrices are increasing in complexity and of substantial interest in industrial PEF applications. Additionally, chicken broiler *Pectroalis major* muscle was selected as a reference skeletal muscle due to its high homogeneity, as it is almost completely composed of IIB (fast twitch glycolytic) type fibres [5].

2. Materials and Methods

2.1 Plant and Animal Tissues

The apples (*Malus domestica*, cv 'Golden Delicious') and potatoes (*Solanum tuberosum*, cv 'Liberta') used for this study were purchased at the local market (Ljubljana, Slovenia). Boneless and skinless *Pectoralis major* muscles were obtained from the same flock of broiler chickens (Ross 308 hybrid, slaughter age 46 days, average weight 2.9 kg) farmed and processed under commercial conditions and, before trials, stored at 1 °C. Each fillet was sampled using the cranial portion of the breast and cut along the direction of muscle fibres. From each sample, disks 26 mm in diameter and 30 mm in thickness were manually cut using a sharp stainless steel cork-borer.

2.2 Pulsed Electric Field Treatment

Electroporation treatment of the cylindrical-shape plant samples was performed using an electric pulse generator lab prototype (Novickij et al., 2016) connected to a pair of custom-built needle electrodes inserted into the sample tissue. The electrodes, made of platinum/iridium alloy (Pt/Ir: 90/10 %), had a diameter of 1 mm and were placed at a centre-to-centre distance of 10.4 mm. PEF protocol consisted of two sequences of 4 pulses with a duration of 100 µs per pulse and with a repetition rate of 5000 s^{-1}. For every tissue studied, the voltage amplitude was adjusted to obtain a sufficient signal-to-noise ratio of the electric field in the sample (i.e. apple 1180 V; potato 750 V; chicken 860 V). The trigger input of the generator was connected to the MRI spectrometer and synchronized with the Current Density Imaging (CDI) pulse sequence. The delivery of the electric pulses was monitored with an oscilloscope (WavePro 7300A, LeCroy, NY, USA) and a current probe (AP015, LeCroy, NY, USA).

2.3 Current Density Imaging and Magnetic Resonance Electrical Impedance Tomography

Magnetic Resonance Imaging (MRI) was performed on tissues while applying PEF treatment, following the method described in [6]. The MRI scanner consisted of a 2.35 T horizontal bore superconducting magnet (100 MHz proton MR frequency) (Oxford Instruments, Abingdon, UK) connected to an Apollo spectrometer (Tecmag, Houston TX, USA) and equipped with microimaging accessories with maximum gradients of 250 mT/m (Bruker, Ettlinger, Germany). The samples were scanned during the application of the electrical pulses using the Current Density Imaging (CDI) method to obtain a map of the current-induced magnetic field change in the sample, as determined by MRI phase shift registration [7]. The map was then processed using the J-substitution algorithm of the magnetic resonance electrical impedance tomography (MREIT), which is based on the iterative solution of the Laplace's equation [8]. The CDI data, together with the known sample geometry and the potentials at the electrodes, were used as inputs to the MREIT algorithm to calculate the map of distribution of the electric field in the plant tissue. In this study, the CDI pulse sequence (Fig. 1) was performed with two acquisitions of relaxation enhancement (RARE) imaging sequence [9] using the following parameters: field of view 30 mm, imaging matrix 64 x 64, inter-echo delay 2.64 ms, and slice thickness of 8 mm. In the sequence, electric pulses were delivered between the excitation RF pulse and the first refocusing RF pulse. The MREIT algorithm was solved using the finite element method with the MATLAB 2021b numerical computing environment (MathWorks, Natick, MA, USA) on a desktop PC.

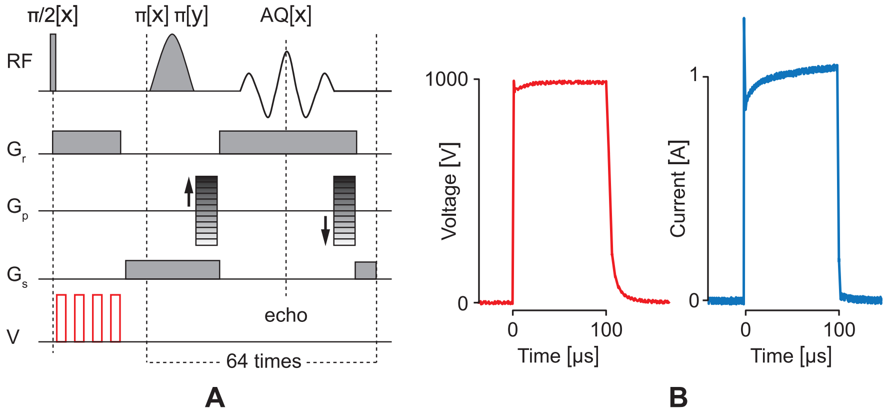

Figure 1. (A) Two-shot RARE CDI sequence that was used to create a map of current-induced magnetic field changes. The first part of the sequence is a current encoding part with four (100 µs long) high-voltage electric pulses (red line) delivered immediately after the nonselective 90° radiofrequency (RF) excitation pulse. (B) Measurements of the voltage (red line) and electric current (blue line) of one of the representative electric pulses.

2.4 T_2-weighted imaging

Plant tissues were dynamically monitored with a multiparametric MRI consisting of T_2-weighted imaging. A multi-spin-echo (MSE) imaging sequence based on the Carr-Purcell-Meiboom-Gill (CPMG) multi-echo train (Carr and Purcell, 1954) was chosen to acquire T_2-weighted MR images before and immediately after PEF treatment (i.e. a total of 18 min after pulsation). The T_2 pulse sequence was performed with the following imaging parameters: field of view 30 mm;

imaging matrix 128 x 128; inter-echo delay 70 ms, slice thickness of 5.1 mm. T_2 maps were calculated using the MRI Analysis Calculator plug-in of ImageJ image processing software (NIH, US), fitting raw MSME data to variable TE (n = 8 echoes) ($R^2 > 0.9$). Additional analysis and quantitative assessment of the T_2-weighted images was performed using MATLAB 2021b (MathWorks, Natick, MA, USA) on a desktop PC.

3. Results

In our study, we obtained the distributions of electric fields in apple, potato and chicken samples subjected to PEF treatment. In addition to the MREIT, T_2 mapping was also performed in the same samples to determine the changes in tissue water content that would occur due to electroporation. The effect of electroporation treatment on T_2 relaxation times was evaluated by measuring T_2 times before and after treatment. In addition, the changes in T_2 relaxation rates were related to the distribution of the electric field, which was determined using MREIT. Fig. 2A shows an example of subtracted T_2-weighted images obtained as (T_2 map after PEF treatment) - (T_2 map before PEF treatment) of apple, potato, and chicken. The T_2 changes and electric field distribution were evaluated considering a region crossing the centre of the sample. Fig. 2C shows a general decrease in T_2 relaxation times after PEF treatment in both potato and apple tissues, while no significant changes were observed in chicken skeletal muscle exposed to the high voltage pulses.

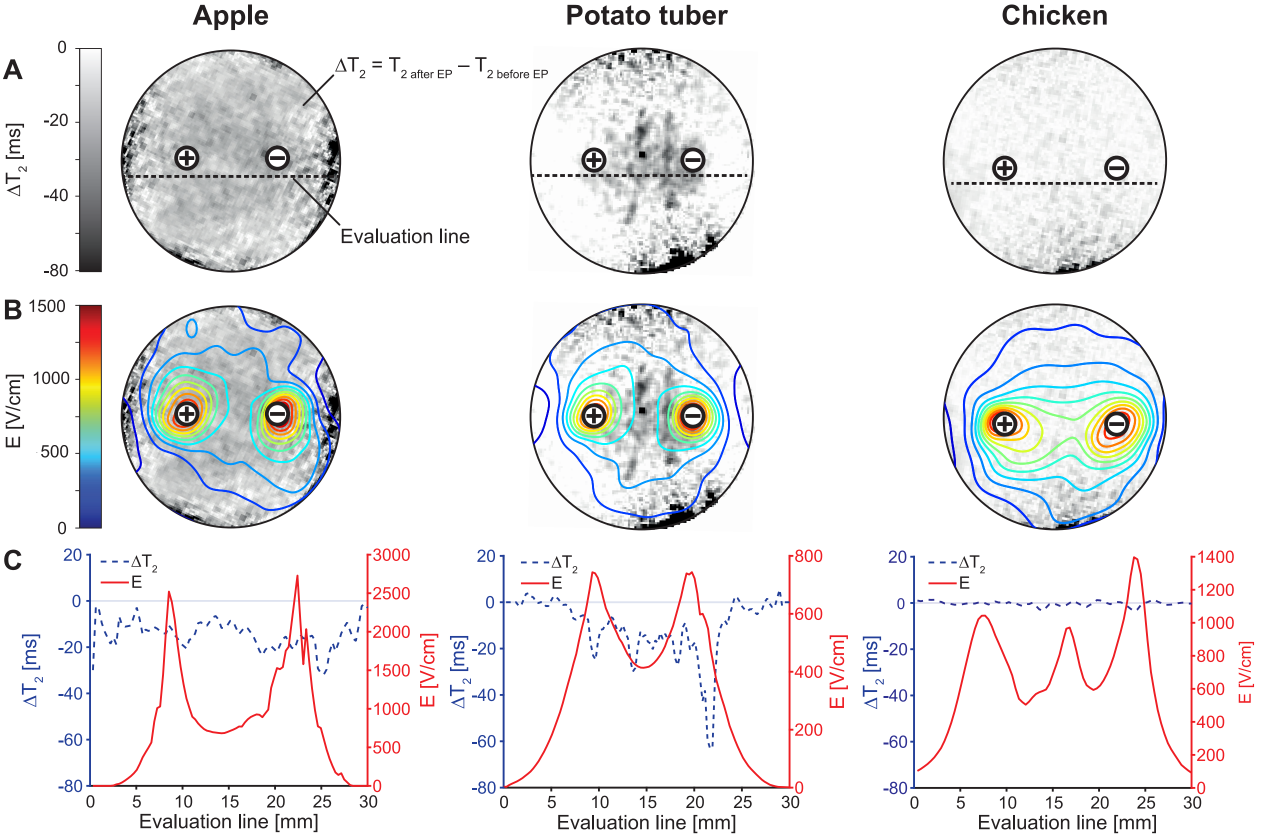

Figure 2. (A) Subtraction of T_2-weighted images acquired before and after electroporation treatment (i.e. total imaging time 18 min after the PEF treatment) in apple tissue, potato tuber and chicken breast. Location of electrodes are marked with + and – sign, while an evaluation line is depicted as black dotted line. (B) The distribution of electric field obtained with MREIT during the electroporation treatment superimposed on the T_2 differences. (C) T_2 differences (blue dotted line) and electric field (solid red line) along the evaluation line.

4. Discussion

Magnetic resonance imaging has been used to monitor spatially-dependent electroporation achieved by PEF treatment in plant tissues [6,10]. Current density imaging (CDI) and magnetic resonance electrical impedance tomography (MREIT) have already been proposed as efficient methods to monitor the electric field distribution in the tissue during the electroporation treatment of plants [6], and for medical applications of electroporation *in vivo*, such as monitoring of the electric field distribution during electroporation of mouse tumours for prediction of reversible [11] and irreversible electroporated areas [12]. In this study, we compared the distribution of the electric field with the transverse relaxation time T_2, which was used as an indicator of the redistribution of water and solutes in the tissues after PEF treatment [13]. In fact, the T_2 relaxation value correlates with the proton exchange between water and solutes, as well as with the diffusion of water protons through internally generated magnetic field gradients, leading to differences in the magnetic susceptibility of the tissue exposed to the magnetic field, e.g. at the interfaces between air and fluid-filled pores. Therefore, the T_2 values are to some extent associated with the structure of the sample based on its water content. The overall decrease in T_2 in plant tissues due to electroporation could be attributed to the loss of compartmentalisation and diffusion of intracellular water and leakage of ions through the tonoplast and plasma membrane, leading to changes in internal morphology (e.g. shrinkage of total volume) and different water-solution interactions. The ability of MREIT to monitor local changes due to electroporation is most evident in potato tissue, where T_2 changes are only visible in areas exceeding the threshold for electroporation (≈ 250 V/cm for potato). In contrast, no changes in water mobility were detected in chicken breast muscles using MR imaging. Since poultry muscles are composed mainly of fast-twitch fibres associated with anaerobic glycolysis, *rigour mortis* sets in very fast [14]. As rigour progresses, the space in which water can be held in the myofibrils decreases and fluid can be forced into the extra myofibrillar spaces where it is more easily lost as a drip. The absence of T_2 changes in this case study therefore reinforces the premise that the structural layers of the skeletal muscle studied were already severely degraded approximately 48 hours *post mortem,* and therefore no release of intracellular water could be detected by MRI.

5. Conclusions

The monitoring of the electric field distribution during the application of electric pulses using magnetic resonance and electrical impedance tomography is described and experimentally investigated on various complex structures. The research findings provided useful insights into the evaluation of electroporation and suggest that magnetic resonance electrical impedance tomography could be used as an efficient tool to improve the effectiveness of PEF treatment. Since monitoring is performed during pulse delivery, the determined electric field distribution considers all heterogeneities and changes that occur in the treated tissue. This near-real-time information can also be used for fine adjustments of PEF treatment parameters, such as the amplitude of electric pulses, or changing their number during the PEF treatment. Additional research is warranted to cover the full spectrum of possibilities offered by the MREIT in the field of electroporation.

Acknowledgments

This work was supported by the Slovenian Research Agency (research core funding No. P2-0249, funding for Junior Researcher to MS and project No. J2-1733 to MK).

References

[1] Mahnič-Kalamiza S, Vorobiev E and Miklavčič D 2014 Electroporation in Food Processing and Biorefinery *J. Membr. Biol.* **247** 1279–304

[2] Barba F J, Parniakov O, Pereira S A, Wiktor A, Grimi N, Boussetta N, Saraiva J A, Raso J, Martin-Belloso O, Witrowa-Rajchert D, Lebovka N and Vorobiev E 2015 Current applications and new opportunities for the use of pulsed electric fields in food science and industry *Food Res. Int.* **77** 773–98

[3] Langus J, Kranjc M, Kos B, Šuštar T and Miklavčič D 2016 Dynamic finite-element model for efficient modelling of electric currents in electroporated tissue *Sci. Rep.* **6** 26409

[4] Genovese J, Kranjc M, Serša I, Petracci M, Rocculi P, Miklavčič D and Mahnič-Kalamiza S 2021 PEF-treated plant and animal tissues: Insights by approaching with different electroporation assessment methods *Innov. Food Sci. Emerg. Technol.* **74** 102872

[5] Verdiglione R and Cassandro M 2013 Characterization of muscle fiber type in the pectoralis major muscle of slow-growing local and commercial chicken strains *Poult. Sci.* **92** 2433–7

[6] Kranjc M, Bajd F, Serša I, de Boevere M and Miklavčič D 2016 Electric field distribution in relation to cell membrane electroporation in potato tuber tissue studied by magnetic resonance techniques *Innov. Food Sci. Emerg. Technol.* **37** 384–90

[7] Joy M, Scott G and Henkelman M 1989 In vivo Detection of Applied Electric Currents by Magnetic-Resonance Imaging *Magn. Reson. Imaging* **7** 89–94

[8] Khang H S, Lee B Il, Oh S H, Woo E J, Lee S Y, Cho M H, Kwon O, Yoon J R and Seo J K 2002 J-substitution algorithm in magnetic resonance electrical impedance tomography (MREIT): phantom experiments for static resistivity images. *IEEE Trans. Med. Imaging* **21** 695–702

[9] Sersa I 2008 Auxiliary phase encoding in multi spin-echo sequences: application to rapid current density imaging. *J. Magn. Reson.* **190** 86–94

[10] Dellarosa N, Ragni L, Laghi L, Tylewicz U, Rocculi P and Dalla Rosa M 2016 Time domain nuclear magnetic resonance to monitor mass transfer mechanisms in apple tissue promoted by osmotic dehydration combined with pulsed electric fields *Innov. Food Sci. Emerg. Technol.* **37** 345–51

[11] Kranjc M, Markelc B, Bajd F, Čemažar M, Serša I, Blagus T and Miklavčič D 2015 In Situ Monitoring of Electric Field Distribution in Mouse Tumor during Electroporation. *Radiology* **274** 115–23

[12] Kranjc M, Kranjc S, Bajd F, Serša G, Serša I and Miklavčič D 2017 Predicting irreversible electroporation-induced tissue damage by means of magnetic resonance electrical impedance tomography. *Sci. Rep.* **7** 10323

[13] Hjouj M and Rubinsky B 2010 Magnetic resonance imaging characteristics of nonthermal irreversible electroporation in vegetable tissue. *J. Membr. Biol.* **236** 137–46

[14] Schreurs F J G 2000 Post-mortem changes in chicken muscle *Worlds. Poult. Sci. J.* **56** 319–46

DAY 1

Wednesday, June 29, 2022

Invited Talk 02

Speaker Jongpil Kim (Dongguk University)

“Recent advances in cell reprogramming and gene editing technology as the novel therapeutics for Neurological diseases”

Proceedings of the International Conference of Bioelectromagnetism, Electrical Bioimpedance,
and Electrical Impedance Tomography June 29 – July 1, 2022 / Kyung Hee University, Seoul, Korea

Recent advances in cell reprogramming and gene editing technology as the novel therapeutics for Neurological diseases

Jongpil Kim[1]
[1] Dept. of Chemistry & Biomedical Engineering, Dongguk University Seoul, 04620, Korea,

Correspondence: Jongpil Kim, jpkim153@dongguk.edu

Abstract– Recent advances in cellular and genetic engineering technology have garnered considerable interest for human disease modelling and cell replacement strategies. We are interested in exploiting new advances in cell reprogramming and gene editing technology to develop a deeper understanding for the basis of neurodegenerative diseases, and ultimately to develop new therapies for these diseases. Recently, our group have developed a novel nanobiotechnology approach to control cell fate of the somatic cells in in vivo brain. This study provides a proof of principle for in vivo reprogramming as a potentially viable and safe therapeutic strategy for the treatment of Parkinson disease (Nature Nanotechnology, 2017). Moreover, our group developed CRISPR/Cas9 system for efficient in vivo gene editing in the brain. In this study, I will discuss the recent updates on the in vivo therapeutic editing using CRISPR/Cas9 as a novel therapeutic agent for Alzheimer's disease (Nature Neuroscience 2019).

Acknowledgments

References

Park H 2019 In vivo neuronal gene editing via CRISPR-Cas9 amphiphilic nanocomplexes alleviates deficits in mouse model of Alzheimer's disease. *Nature Neuroscience*, 2019,**22**,524-528

Kim H 2019 Modeling G2019S-LRRK2 Sporadic Parkinson's Disease in 3D Midbrain Organoids. Stem Cell Reports. 2019 Mar 5;**12**(3):518-531

Yoo J 2017 Electromagnetized gold nanoparticles mediated direct lineage reprogramming into induced dopamine neurons in vivo for Parkinson's disease therapy. *Nature Nanotechnology,* 2017 Oct;**12**(10):1006-1014.

DAY 1

Wednesday, June 29, 2022

Special Session 01

Effect of Galvano-Transduction in Tissue Regeneration

Organizer EunAh Lee (Kyung Hee University)

S 01-01 **Biomimetic Surface Modification of Bioelectrodes for Improved Biocompatibility and Bioperformance**
Jae Young Lee (Gwangju Institute of Science and Technology)

S 01-02 **Electrical and optical record of drug response on hiPSC Cardiomyocytes using Indium Tin Oxide electrode**
Sungbo Cho (Gachon University)

Proceedings of the International Conference of Bioelectromagnetism, Electrical Bioimpedance,
and Electrical Impedance Tomography June 29 – July 1, 2022 / Kyung Hee University, Seoul, Korea

Biomimetic Surface Modification of Bioelectrodes for Improved Biocompatibility and Bioperformance

Jondarm Yi[1], Sanghun Lee[1], Semin Kim[1], Jin-Oh Jeong[1] and Jae Young Lee[1]
[1]School of Materials Science and Engineering, Gwangju Institute of Science and Technology (GIST), Gwangju, Korea

Correspondence : Jae Young Lee, e-mail : jaeyounglee@gist.ac.kr

Abstract– Implantable bioelectrodes enable precise recording or stimulation of electrical signals with living tissues in close contact. However, their performance is frequently compromised owing to adverse tissue reactions, including biofouling and inflammation [1]. To address these issues, we elaborate to modify polpypyrrole (PPy) electrodes by engineering chemical compositions and nanostructures. First, to mitigate biofouling, surface modification of bioelectrodes using various biomaterials has been attempted [2,3]. We electrochemically introduced hyaluronic acid, zwitter ionic polymers, and chemical compounds. We could obtain electrodes resistant to non-specific protein and cell adhesion while preventing alteration in electrical/electrochemical properties of PPy electrodes. Next, we aimed to fabricate biocompatible and functional implantable conductive polymer bioelectrodes with optimal topography for the modulation of macrophage responses because macrophages play key roles in foreign body reactions by either inducing or resolving inflammatory tissue reactions. We produced heparin-doped polypyrrole (PPy/Hep) electrodes of different surface roughness, with Ra values from 5.5 nm to 17.6 nm, by varying the charge densities during electrochemical synthesis. In particular, PPy/Hep-900 (Ra = 14 nm) was optimal with respect to electrochemical properties and the suppression of inflammatory M1 polarization. In vivo implantation indicated that PPy/Hep-900 significantly reduced macrophage recruitment, suppressed inflammatory polarization, and mitigated fibrotic tissue formation. In addition, the implanted PPy/Hep-900 electrodes could successfully record electrocardiographic signals for up to 10 days without substantial decreases in sensitivity, while other electrodes substantially lost their signal sensitivity during implantation. Altogether, we demonstrate that modulating the surface properties of PPy bioelectctrodes can benefit the design and applications of high-performance and high-biocompatibility bioelectrodes.

Acknowledgments

This work was supported by a grant from the National Research Foundation of Korea (NRF) funded by the Ministry of Science, ICT, and Future Planning (NRF-2021R1A4A3025206 and NRF-2019R1A2C2002515).

References

[1] Newbold C, Mergen S, Richardson R, Seligman P, Millard R, Cowan R and Shepherd R Impedance Changes in Chronically Implanted and Stimulated Cochlear Implant Electrodes. *Cochlear Implants Int.* 2014, **15 (4)**, 191–199.

[2] Kim S, Jang Y, Jang L K, Sungwoo S H, Kim T, Cho S-W, Lee J Y Electrochemical deposition of dopamine-hyaluronic acid conjugate for anti-fouling bioelectrodes *J. Mater. Chem. B* **2017**, 4507-4513.

[3] Jeong J-O, Kim S, Park J, Lee S, Park P-S, Lim Y-M and Lee J Y Biomimetic nonbiofouling electrodes grafted with zwitterionic polymer using gamma ray *J. Mater. Chem. B* , 8 (2020), 7225-7232.

[4] Lee S, Pakr J, Kim S, Ok J, Yoo J I, Kim Y S, Ahn Y, Kim T, Ko H C and Lee J Y High-performance implantable bioelectrodes with immunocompatible topography for modulation of macrophage responses *ACS Nano* in press.

ICBEM Bioelectromagnetism ICEBI Electrical Bioimpedance EIT Electrical Impedance Tomography

Proceedings of the International Conference of Bioelectromagnetism, Electrical Bioimpedance,
and Electrical Impedance Tomography June 29 – July 1, 2022 / Kyung Hee University, Seoul, Korea

Electrical and optical record of drug response on hiPSC Cardiomyocytes using Indium Tin Oxide electrode

Daesoo Kim[1], Yujin Park[2,3], Sun-Woong Kang[3] and Sungbo Cho[1,4]
[1] Department of Electronic Engineering, Gachon University, Seongnam 13120, Korea
[2] Department of Polymer Science and Engineering, Chungnam National University, Daejeon 34134, Korea
[3] Research Group for Biomimetic Advanced Technology, Korea Institute of Toxicology, Daejeon 34114, Korea
[4] Department of Health Sciences and Technology, GAIHST, Gachon University, Incheon 21999, Korea.

Correspondence : Sungbo Cho, e-mail : sbcho@gachon.ac.kr

Abstract– Label-free and real-time monitoring of cells is increasingly required for better drug development and toxicology of materials since it can record the cellular responses without the interference of the fluorescent markers binding to cellular proteins or DNA. Comprehensive in vitro Proarrhythmia Assay provides a nonclinical assessment of the proarrhythmic potential of drug candidates by analyzing the cellular cardiac electrophysiologic activity. Since the human induced pluripotent stem cell-derived Cardiomyocytes (hiPSC-CM) expresses main ion channel activities of human's hearts, cardiotoxicity assessment using hiPSC-CM is proposed to investigate the translating preclinical cardiovascular safety data to humans.

This study reported the feasibility of the transparent Indium Tin Oxide (ITO) for the electrical and optical recording of drug (isoproterenol and nifedipine) response on hiPSC-CM by microscopic image analysis, electrical cell-substrate impedance sensing (ECIS), and local field potential (LFP) measurement. The experimental results demonstrated that the hiPSC-CM were well adhered and spread on the surface of transparent ITO electrode, and showed a stable beating after 7 days of cultivation from the inoculation onto the electrode. The cellular adhesion and spreading on the electrode were confirmed by ECIS during cell cultivation or the drug application. From the monitoring of LPF, it was shown that the drug application increased the beating frequency of the cells and decreased the field potential duration. Therefore, it was concluded that the ITO electrode is feasible for the electrical and optical monitoring of the hiPSC-CM.

Acknowledgments

This work was supported by National Research Foundation of Korea (NRF-2019R1A2C1088680, 2020M3A9E4104385).

References

Wells, S., Waddell, H., Sim, C., Lim, S., Bernasochi, G., Pavlovic, D., Kirchhof, P., Porrello, E., Delbridge, L., & Bell, J. 2019 Cardiomyocyte functional screening: Interrogating comparative electrophysiology of high-throughput model cell systems *American Journal of Physiology-Cell Physiology* **317** 1256-1267

Park, I., Nguyen, T., Park, J., Yoo, A. Y., Park, J. K., & Cho, S. 2018 Impedance characterization of chitosan cytotoxicity to MCF-7 breast cancer cells using a Multidisc indium tin oxide microelectrode array *Journal of The Electrochemical Society* **165** 55–59

Fassina, L., Assenza, M. R., Miragoli, M., Isidori, A. M., Naro, F., & Barbagallo, F. 2022 Cell shortening and calcium homeostasis analysis in adult cardiomyocytes via a new software tool *Biomedicines* **10** 640

Zwartsen, A., Korte T.d., Nacken, P., Lange, D.W.d., Westerink, Remco H.S., Hondebrink, L. 2019 Cardiotoxicity screening of illicit drugs and new psychoactive substances (NPS) in human iPSC-derived cardiomyocytes using microelectrode array (MEA) recordings *Journal of Molecular and Cellular Cardiology* **136** 102-112

DAY 1

Wednesday, June 29, 2022

Oral Session 03

Electrical Impedance Imaging Algorithm I

Chair Hyeuknam Kwon (Yonsei University)

O 03-01 **A Top-to-Bottom Generator of EIT and CT Bolus Signals**
Diogo Filipe Silva (RWTH Aachen University)

O 03-02 **Light-weight CNNs with Dynamic Convolution for Lung EIT**
Hao Yu (The University of Edinburgh)

O 03-03 **A Learning-Based 3D EIT Image Reconstruction Method**
Zhaoguang Yi (The University of Edinburgh)

O 03-04 **Unsupervised Clustering of Lung Perfusion Features**
Diogo Filipe Silva (RWTH Aachen University)

Proceedings of the International Conference of Bioelectromagnetism, Electrical Bioimpedance,
and Electrical Impedance Tomography June 29 – July 1, 2022 / Kyung Hee University, Seoul, Korea

A Top-to-Bottom Generator of EIT and CT Bolus Signals

Diogo Filipe Silva, Steffen Leonhardt, Chuong Ngo
Chair of Medical Information Technology, RWTH Aachen University, Aachen, Germany

Correspondence : Diogo Filipe Silva, e-mail : silva@hia.rwth-aachen.de

Abstract The existence of an underlying bolus shape from which all other bolus curves from a subject can be derived is an interesting finding from the field of tracer kinetics. Based on this principle, we designed a bolus curve synthesizer which primarily builds a governing modality-agnostic bolus curve. Next, by addressing the effects of different tracers and imaging systems, it morphs the curve into its corresponding measured shapes in electrical impedance tomography, and computerized tomography with preserved perfusion parameters. Noise and artifacts were also implemented, resulting in realistic waveforms for different physiological scenarios and anatomical locations. This contribution is particularly interesting for building large datasets to develop, train, and validate perfusion estimation algorithms.

Keywords: *Tracer Kinetics; Dynamic Computerized Tomography; Enhanced Electrical Impedance Tomography; Signal Generator; Datasets*

1. Introduction

Tracer kinetics research on dynamic computerized tomography (CT) indicates that, underlying a subject's bolus curves, lies an invariant gamma-variate-shaped (Glenny *et al* 1991) density function of transit times (Zierler 2000). In fact, despite originating distinct density functions, both diffusible and non-diffusible tracers can be mapped into the aforementioned invariant shape (Goresky 1963).

In this work, we loosely classify the differences between the CT and electrical impedance tomography (EIT) bolus signals as tracer-specific and modality-specific distinctions. In EIT, the most commonly used contrast agent, a sodium chloride solution, is a much more diffusible than those most used in CT, e.g., iodine-based materials. This tracer-specific distinction is noticeable from, e.g., the more pronounced baseline increase in EIT relative to CT partly due to the higher retention of particles in static interstitial distribution volume. Modality-dependent factors include the much higher partial volume effect in EIT, the distinct measurement units, and the different sampling frequencies.

While tracer kinetics methods for perfusion estimation have been researched for decades in the field of CT, they have been lightly tackled in the field of EIT in comparison. Nonetheless, the rationale can be adapted from the former to the latter, given the common roots of the bolus signal from both modalities. Bridging this gap is now of particular interest considering recent efforts to validate EIT bolus-derived perfusion metrics, often with CT as gold standard (Kircher *et al* 2021). Bearing in mind the frequent absence of quality ground truth, validation of perfusion estimation methods is often performed against artificially generated or morphed data (Patil and Johnson 2011).

With this contribution, we aim at describing a generator framework for CT and EIT time-intensity bolus curves built from a single underlying source curve with the desired perfusion parameters.

2. Materials & Methods

2.1 Materials

To later serve as a realistic template signal to integrate in the model, a single 30 seconds EIT recording was obtained from a mechanically ventilated pig weighing 60 kg during a breath hold with a PEEP of 12 cmH$_2$O – we will designate this signal as pulsatile signal. The recording was obtained with a Dräger Pulmovista® 500 with a 16-electrode belt, at an operating frequency of 80 kHz. The voltage channels were processed so as to attained normalized-difference impedance values. Images were then obtained with the GREIT (Adler *et al* 2009) algorithm, with a noise figure of 0.5.

2.2 Underlying Model

First Pass

In Hentze et al. 2021, a variation of the original gamma-variate function y_{base} is described, which is especially useful since the abstract curve parameters α and β are unfolded into interpretable perfusion parameters, as Equation (1) shows.

$$y_{base}(t) = K \cdot \left(\frac{1}{1-RD}\frac{t-T_{peak}}{MTT}\right)^{\frac{1}{RD}-1} e^{-\frac{1}{RD}\frac{t-T_{peak}}{MTT}} \tag{1}$$

The model's arguments are, therefore, time to peak (T_{peak}), mean transit time (MTT), relative dispersion (RD), and a scalar K, explained in Section 2.4.

2.3 Addressing Tracer-Specific Distinctions

The source curve described in Chapter 1 was obtained by firstly removing any recirculation components. In this Section, we describe the re-inclusion of the recirculation effects due to tracer diffusion and secondary passes in order to start differentiating the underlying model into EIT and CT bolus curves.

Inclusion of Tracer Diffusion

The tracer-kinetics rationale behind the inclusion of this effect is that, as the first-pass traverses the target volume compartment, some of the tracer material diffuses out of the blood or plasma volumes into, at least, interstitial volumes, originating a progressive build-up of static intensity in the region. While the diffusion rate is not accessible through this model extension, the amount of tracer that diffuses can be modelled as a fraction, retention factor (RF), of the total incoming tracer quantity. The resulting model y_{diff} becomes

$$y_{diff}(t) = (1-RF) \cdot y_{base}(t) + RF \cdot \int_0^t y_{base}(\tau) \cdot d\tau. \tag{2}$$

Since obtaining an analytical expression for the underlying model's integral is a non-trivial task, we coded its term as the empirical cumulative function of the underlying model instead. The empirical cumulative function tends to the analytical integral as the number of samples increases, so we first sampled the signals at 1 kHz for increased precision.

Inclusion of Secondary Passes

This effect simply adds $N-1$ secondary, identically structured pulses with their own set of parameters – the same described so far by Equations (1) and (2). The resulting signal y_{total} after this extension, is simply the superposition of the N separately modelled pulses as N bolus passes. Here, dependencies between the parameters of the first, second and further passes can be established according to physiological principles (e.g., relatively later, lower and flatter second pass pulses) covering a variety of scenarios. The superposition principle then yields

$$y_{total}(t) = \sum_{i=1}^{N} y_{diff,i}\left(t \middle| K_i, RD_i, T_{peak,i}, MTT_i, RD_i\right). \tag{3}$$

2.4 Addressing Modality-Specific Distinctions

In this Section, we provide the option to scale the model into a particular modality's scale and sampling rate, to further differentiate the signals into their respective modality specifications.

Amplitude

Until now, the model's amplitude has been kept inside $[0, 1]$, providing enough liberty to now define a modality-specific scaling. Since scaling depends on a number of factors, e.g., pixel or voxel location, even in the same modality, a simple and flexible scalar K was added to the initial baseline model in Equation (1).

Sampling Rate

Finally, it is now necessary to downsample the original curves sampled at 1 kHz to each modality's sampling frequency. In this contribution, we assume that the desired CT curves are sampled at 1 Hz, and the EIT curves at 50 Hz (framerate). This step is particularly important for the CT modality, since the very low sampling rate often does not allow the true shape of the curve to be visually understandable due to aliasing.

2.5 Inclusion of Artifacts and Noise

We now describe including noise and artifacts in the simulated signals to test algorithm robustness.

EIT Noise

One of the common sources of residual noise in the EIT bolus curves results from imperfect low-pass filtering of the raw EIT signal. Although the residual frequency components are not usually exacerbated, they may differ depending on the heart-rate variability of the subject. We thus imagined the corresponding worst-case scenario, where the relevant spectrum of the pulsatile signal remains unfiltered and superimposes the simulated bolus signal. We also considered that this contaminating signal's shape and amplitude depends on pixel location. Accordingly, four pixels from different regions were selected, and the frequency spectra of their 30 second pulsatile signal, shown in Figure 1, was analysed. Each was subjected to an FIR low-pass filter with a passband frequency of 15 Hz and stopband frequency of 20 Hz to ensure only the most prominent harmonics remained. The result could then be scaled by $K_{eit,noise}$ and added to the bolus signal.

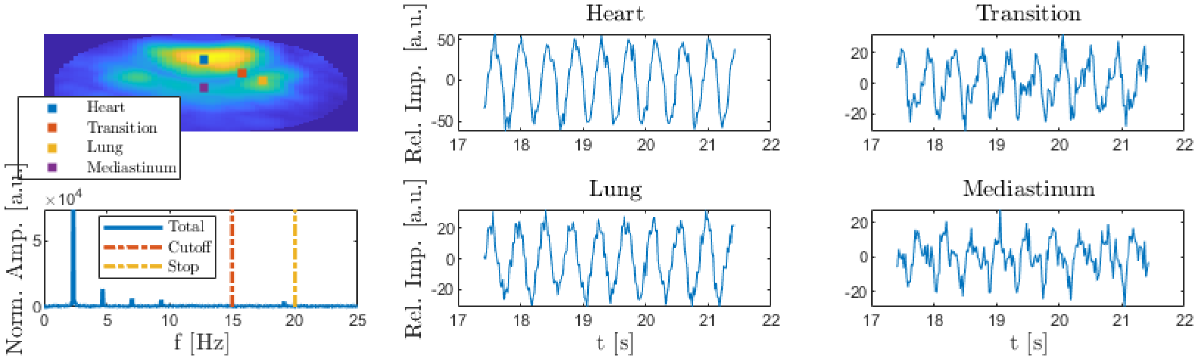

Figure 1. Top left: pixels for region-specific contamination of the EIT bolus signals; bottom left: total frequency spectrum of the noise signals; Remaining temporal plots: template noise signals extracted at the selected pixels from a real pulsatile recording.

CT Artifacts

Motion artifacts are a common finding in CT bolus curves, especially in interface regions between multiple tissue types with noticeably different voxel intensities. This is the case, for example, of vessel voxels near the vessel wall. Such voxels will alternate between enclosing vessel and lung parenchyma tissue at the frequency of the residual movement in that region. Although CT scans are usually performed with ECG-gating and under apnoea, slight residual cardiac or ventilatory movements might persist. In this work, we assume both types of movement are present, and thus superimposed two oscillators with a assumed frequencies of 60 beats-per-minute, as the heart rate (HR), and 12 breaths-per-minute, as the respiratory rate (RR). Additionally, the amplitude of the resulting coupled oscillator y_{osc} was modelled by the difference between a simulated vessel and tissue bolus curves. A scalar $K_{ct,noise} \in [0,1]$ was added to allow simulating different artifact intensities (e.g., although less intensely, a voxel closer to the vessel lumen might still experience motion artifacts),

$$\begin{aligned} y_{osc}(t) &= F_{card} \cdot \sin(2\pi \cdot f_{HR} \cdot t) + F_{resp} \cdot \sin(2\pi \cdot f_{RR} \cdot t), \\ y_{ct,noise}(t) &= K_{ct,noise}(y_{total.vessel} - y_{total.tissue}) \cdot y_{osc}(t). \end{aligned} \tag{4}$$

3. Results

We now showcase the basic capabilities of the model by manually inputting illustrative perfusion parameters. Firstly, source curves are modelled and then downsampled to their respective curves in EIT and CT domain - shown in Figure 2.

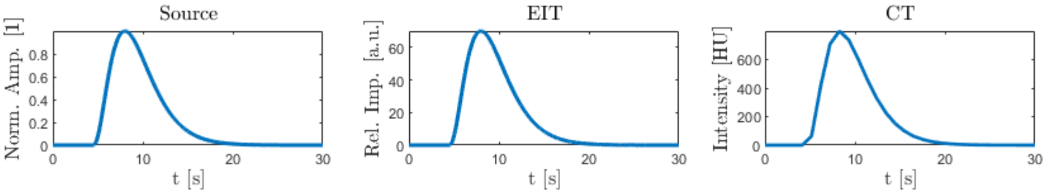

Figure 2. From left to right: idealized underlying gamma-variate-shaped curve (1 kHz); underlying curve as measured with EIT (50 Hz); underlying curve as measured in CT (1 Hz). $T_{peak} = 8$ s, $MTT = 8$ s, $RD = 0.3$.

After addressing tracer- and modality-specific distinctions for EIT, and including pulsatile noise the images in Figure 3 were obtained. Given the amount of parameters involved in the simulation of both passes, parameters are not denoted.

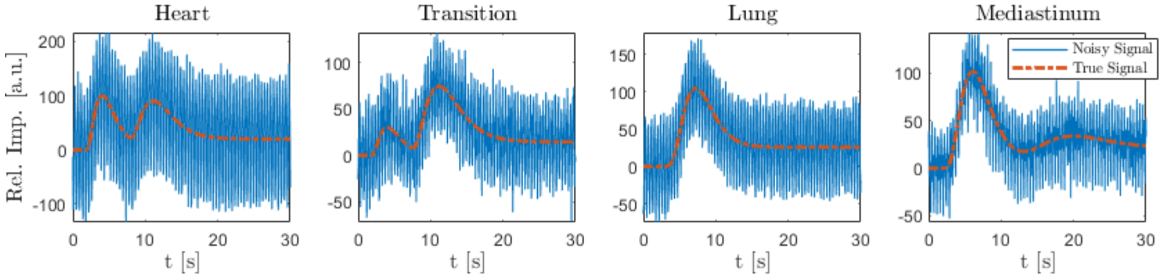

Figure 3. Simulated EIT Bolus curves after inclusion of tracer diffusion and secondary passes (in dashed red), with additive pulsatile contamination (in full blue), for elected regions.

After addressing tracer- and modality-specific distinctions for CT, and including pulsatile noise the images in Figure 4 were obtained. Given the amount of parameters involved in the simulation of both passes, parameters are not denoted.

4. Discussion

In Figure 1, we observe the importance of the sampling rate of both modalities in preserving the underlying perfusion features. With a sampling frequency an order of magnitude lower, the CT bolus curve presents a heavily deformed shape, which might mislead algorithms in estimating, among others, its peak amplitude. The model provides enough flexibility to model the characteristic bolus signals from multiple anatomical regions in both modalities. In EIT, the superposition of both left and right heart flows can be convincingly simulated for the heart region. This interaction can be reproduced at a lower degree on the transition region. Supremacy of the first-pass can also be synthesized with variable influence of a second-pass, leading to distinct curves for the lung and mediastinum regions. In CT, realistic simulation of different types of tissue are possible, demonstrated by the taller, sharper and earlier peaks of the vessel voxel in comparison to the tissue. Finally, addition of noise and artifacts also looks plausible. In EIT, the expectedly different amplitudes and shapes of the region-specific noises are appreciable. In CT, while the 1 kHz representations are idealizations of the underlying movement, its 1 Hz counterpart presents shapes typically found in experimental data, which can easily mislead estimation.

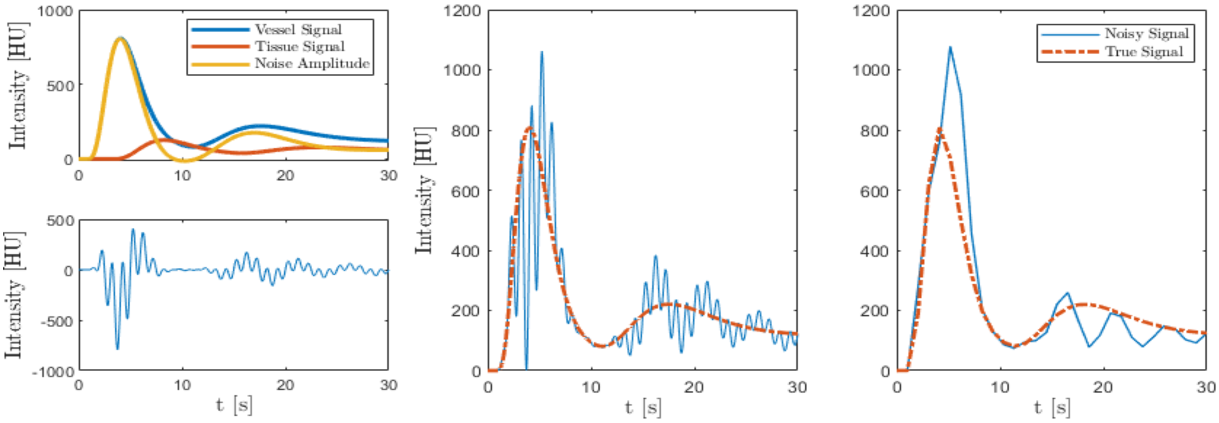

Figure 4. Top left: amplitude modulation of the motion artifacts from the difference between simulated vessel and tissue bolus curves; bottom left: resulting motion artifact oscillating signal; centre: clean and contaminated CT bolus curve at 1 kHz; right: clean and contaminated CT bolus curve at 1 Hz, which should be observable in the dynamic CT volumes.

5. Conclusions

This contribution describes a bolus curve synthesizer for both EIT and CT imaging modalities from a common source curve designed from pre-defined perfusion parameters. While the current choice of noise and artefact inclusions is limited, the modular structure of the framework easily allows for integration of new contamination types in the future. A particularly interesting one would be partial volume effects. Ultimately, this framework can swiftly yield a large dataset for developing, training and validating algorithms for extraction of perfusion metrics against reliable ground truth by simply performing a parameter sweep over the types of scenarios on which one wishes to experiment. This ability becomes particularly important with the increasing interest of validating EIT-derived perfusion metrics with dynamic CT as gold standard, as well as the rise of Machine Learning algorithms in need of quantity and quality of training data.

References

Adler A, Arnold J H, Bayford R, Borsic A, Brown B, Dixon P, Faes T J C, Frerichs I, Gagnon H, Gärber Y, Grychtol B, Hahn G, Lionheart W R B, Malik A, Patterson R P, Stocks J, Tizzard A, Weiler N and Wolf G K 2009 GREIT: a unified approach to 2D linear EIT reconstruction of lung images *Physiol. Meas.* **30** S35–55 Online: https://iopscience.iop.org/article/10.1088/0967-3334/30/6/S03

Glenny R W, Robertson H T, Yamashiro S and Bassingthwaighte J B 1991 Applications of fractal analysis to physiology *J. Appl. Physiol.* **70** 2351–67 Online: https://www.physiology.org/doi/10.1152/jappl.1991.70.6.2351

Goresky C A 1963 A linear method for determining liver sinusoidal and extravascular volumes *Am. J. Physiol. Content* **204** 626–40 Online: https://www.physiology.org/doi/10.1152/ajplegacy.1963.204.4.626

Hentze B, Muders T, Hoog Antink C, Putensen C, Larsson A, Hedenstierna G, Walter M and Leonhardt S 2021 A model-based source separation algorithm for lung perfusion imaging using electrical impedance tomography *Physiol. Meas.* **42** 084001 Online: https://iopscience.iop.org/article/10.1088/1361-6579/ac0e84

Kircher M, Elke G, Stender B, Hernandez Mesa M, Schuderer F, Dossel O, Fuld M K, Halaweish A F, Hoffman E A, Weiler N and Frerichs I 2021 Regional Lung Perfusion Analysis in Experimental ARDS by Electrical Impedance and Computed Tomography *IEEE Trans. Med. Imaging* **40** 251–61 Online: https://ieeexplore.ieee.org/document/9201018/

Patil V and Johnson G 2011 An improved model for describing the contrast bolus in perfusion MRI *Med. Phys.* **38** 6380–3 Online: http://doi.wiley.com/10.1118/1.3658570

Zierler K 2000 Indicator Dilution Methods for Measuring Blood Flow, Volume, and Other Properties of Biological Systems: A Brief History and Memoir *Ann. Biomed. Eng.* **28** 836–48 Online: http://link.springer.com/10.1114/1.1308496

Proceedings of the International Conference of Bioelectromagnetism, Electrical Bioimpedance,
and Electrical Impedance Tomography June 29 – July 1, 2022 / Kyung Hee University, Seoul, Korea

Light-weight CNNs with Dynamic Convolution for Lung EIT

Hao Yu[1], Zhixi Zhang[1] and Jiabin Jia[1]
[1] Institute for Digital Communications, The University of Edinburgh, Edinburgh, U.K.

Correspondence : Jiabin Jia, e-mail : jiabin.jia@ed.ac.uk

Abstract–Electrical Impedance Tomography (EIT) as a merging medical modality is wildly used in the clinical field, particularly for lung imaging due to the advantages of real-time, non-invasive and low cost. Deep learning as a nonlinear method recently has attracted great attention from researchers since it is efficient to solve the highly ill-posed inverse problem in EIT. Although the deep architecture design can enhance the regression prediction ability of the network, it consumes more computational resources and increases the hardware burden. To balance the prediction performance and the computational resources, in the paper, dynamic convolutions, which can improve the conductivity distribution reconstruction performance without increasing the depth of the network are applied in the light-weight Convolutional Neural Networks (CNNs). A lung EIT data set was established based on computed tomography (CT) images and the performance of the proposed method is evaluated in simulation. The work shows the potential of the light-weight network for lung EIT, which can improve network performance while maintaining a certain network depth.

Keywords: Electrical Impedance Tomography; light-weight CNNs; dynamic convolution; thoracic image.

1. Introduction

Due to the difference in electrical conductivity distribution in the lung lesion area, EIT as a promising technology can be used to real-time diagnose lung disease (Zhang *et al* 2020). As the performance of computing hardware increases, the use of deep learning methods to solve the EIT inverse problem is receiving increasing attention from academics. Chen proposed a Fully Connected-Unet network to reconstruct cell imaging (Chen et al 2020). Ren proposed a two-stage network, consisting of a pre-reconstruction block to get initial conductivity and a CNN post-process block, to improve the robustness of the reconstruction results (Ren et al 2020). Indeed, the effectiveness of proposed networks has been demonstrated in simulation and experiments. However, as the network depth and model complexity increase, the number of network parameters and the computational complexity will also increase substantially, which brings an obstacle to the implementation of the network on limited hardware.

Inspired by Chen's work (Chen *et al* 2020), light-weight CNNs with dynamic convolution is designed to balance performance degradation and complex deep network design, our paper proves the effectiveness of dynamic convolution in light-weight network for detecting lung diseases through simulation. The remainder of the paper is organized as follows. The method is introduced in Section 2. Section 3 gives the process of lung EIT data generation and details the training setup. Section 4 qualitatively and qualitatively analyses the reconstruction results of the test set. Discussion is made in Section 5 and Section 6 concludes the paper.

2. Method

In the work, instead of the traditional static convolution kernel, the dynamic kernel is used in the light-weight network to achieve the reconstruction of lung conductivity distribution, so as to diagnose lung diseases.

2.1 Dynamic convolution

The definition of the dynamic convolution is as follows,

$$\begin{gathered} \boldsymbol{y} = g\left(\widetilde{\boldsymbol{W}}^T(\boldsymbol{x})\boldsymbol{x} + \widetilde{\boldsymbol{b}}(\boldsymbol{x})\right) \\ \widetilde{\boldsymbol{W}}(\boldsymbol{x}) = \sum_{k=1}^{K} \pi_k(\boldsymbol{x})\, \widetilde{\boldsymbol{W}}_k, \widetilde{\boldsymbol{b}}(\boldsymbol{x}) = \sum_{k=1}^{K} \pi_k(\boldsymbol{x})\, \widetilde{\boldsymbol{b}}_k \\ \text{s.t. } 0 \leq \pi_k(\boldsymbol{x}) \leq 1, \sum_{k=1}^{K} \pi_k(\boldsymbol{x}) = 1 \end{gathered} \tag{1}$$

where g is an activation function, $\widetilde{\boldsymbol{W}}$ and $\widetilde{\boldsymbol{b}}$ are the aggregated weight and bias respectively. π_k is the attention weight varying for the input $\boldsymbol{x}$, resulting in dynamic convolution having a stronger feature representation than static convolution. $\boldsymbol{y}$ is the output of the dynamic convolution layer. K is the aggregating multiple, which is 4 in the paper. The structure of dynamic convolution layer is shown in Figure 1. By changing the traditional fixed convolution kernel into a convolution kernel that can adaptively adjust the attention according to the input, the performance of the light-weight model could be improved. More detailed theoretical analysis can be found in (Chen *et al* 2020).

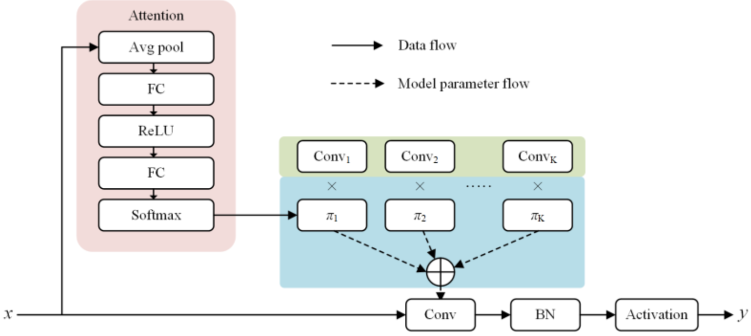

Figure 1. The structure of dynamic convolution layer.

2.2 Light-weight CNNs

In the paper, light-weight CNNs ─ LeNet (Tan *et al* 2019) and VGG-type (Alippi, Disabato and Roveri 2018) network are designed to reconstruct conductivity distribution and the architecture of the networks with measurement voltages as input is shown in Figure 2. N denotes the number of convolution layers. For LeNet, the number of convolutional layers N is 2, and 3, 5 for VGG-3 and VGG-5 networks, respectively. Each convolutional layer consists of a 3×3 convolution kernel, followed by a batch normalization layer, a ReLU activation function and a max-pool layer.

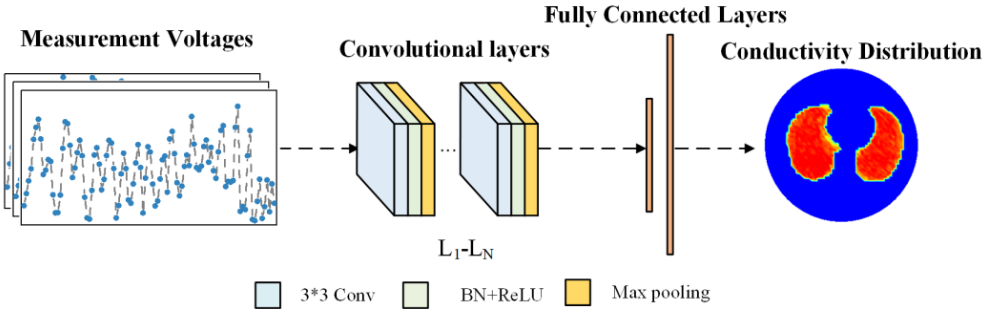

Figure 2. Achrtechture of the neworks.

3. Training setup

3.1 EIT data generation

CT images of 17 patients are selected and the lung contours are obtained by global thresholding image segmentation algorithm. After getting the lung contours, COMSOL Multiphysics$^{@}$ is used to simulate different lung conditions, so as to measure boundary voltages of EIT. In the paper, adjacent excitation and measurement modes are used. Besides, to increase the robustness of the model, white Gaussian noise with 50 dB and 40 dB Signal-to-Noise Ratio (SNR) is added into the voltages. After augmentation, the size of the training set and test set is 67497 and 5088 respectively. The generation process schematic is shown in Figure 3.

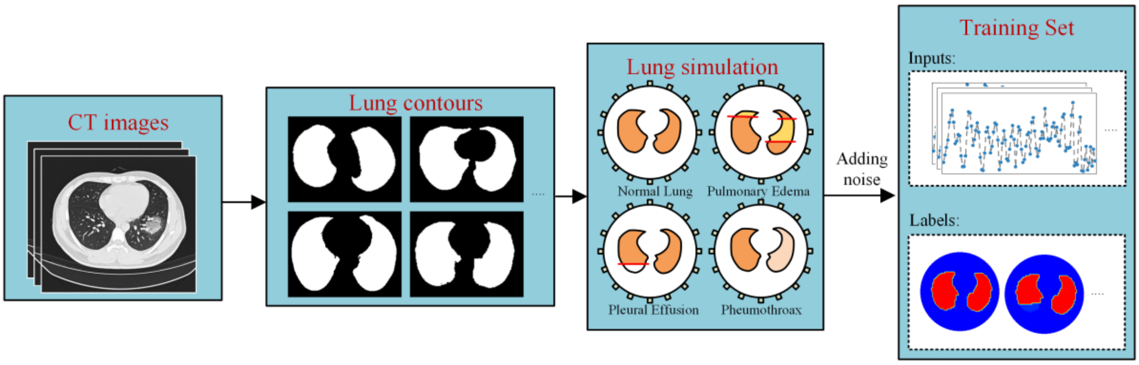

Figure 3. Generation of Lung EIT data.

3.2 Normalization

Data need to be normalized firstly to improve the network generalization, and the expression is given by:

$$\begin{aligned} \Delta V &= \frac{V_{mea} - V_{ref}}{V_{ref}} \\ \Delta\sigma &= -\frac{\sigma_{gt} - \sigma_{ref}}{\sigma_{ref}} \end{aligned} \tag{2}$$

where ΔV = relative voltage
$\Delta\sigma$ = relative reconstruction conductivity distribution
V_{mea}, V_{ref} = measurement and reference voltages [V]
$\sigma_{gt}, \sigma_{ref}$ = ground truth and reference conductivity distribution [S/m].

3.3 Setup

Due to the similar network architecture, all networks are trained with the same hyperparameters. The batch size is set to100, and the learning rate with 0.001 initial value will decay 0.1 every 20 epochs with 60 maximum iterations. Adam optimizer (Bock and Weiß 2019) is applied in the networks to dynamically adjust network learning parameters. To overcome the overfitting problem, L2 regularization is adopted and the parameter is set to 10^{-5}. Besides, all the networks are implemented in the Pytorch environment on the computer with NVidia GeForce RTX 2070 GPU and i7 9700K CPU.

4. Results

To evaluate the regression performance under different methods, three evaluation metrics are introduced: Relative Error (RE), Correlation Coefficient (CC) and Structural Similarity Index (SSIM). The lung conductivity distribution results in four cases by different networks and different kernel types are shown in Figure 4. From the figure we can qualitatively analyse that all the networks can reconstruct contours of the normal lung and diagnose pneumothorax, but for LeNet and Dynamic Convolution VGG-3 (DY-VGG-3) models, the reconstruction results of tissue sections with high electrical conductivity are not accurate enough. For case 2 and case 3, VGG-type networks could reflect pulmonary edema and pleural effusion, but LeNet type networks fail to extract multiscale information from measurement voltages to reconstruct lung images due to shallow network. Broadly speaking, in these four cases, the use of deep networks and dynamic convolutions allow the reconstruction results to more closely resemble the ground truth. It should be mentioned that all the conductivity shown in the figure is relative conductivity.

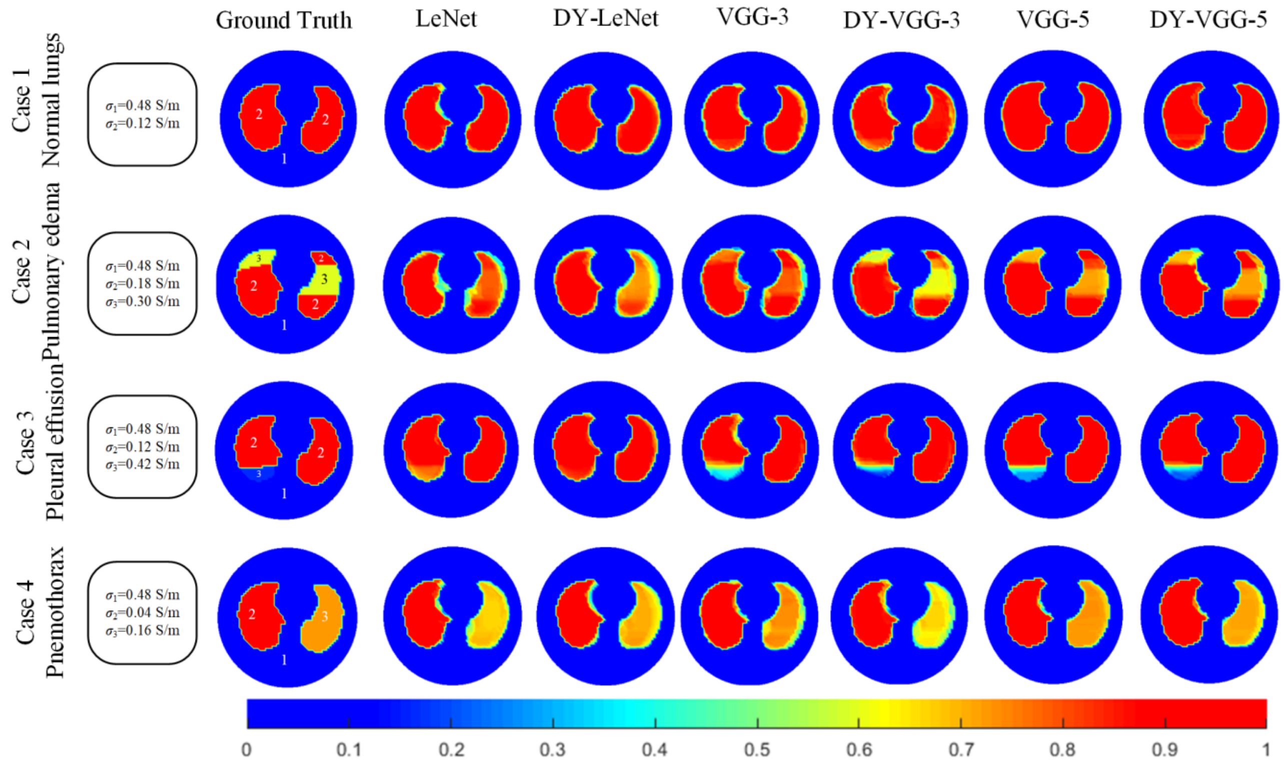

Figure 4. Lung image reconstruction results by different networks and convolution kernels.

The results of quantitative analysis of the test set are shown in Figure 5. It can be clearly seen that within a certain number of network layers, the performances of conductivity reconstruction results become increasingly better in terms of CC, RE and SSIM metrics as the network depth increases. The average evaluation metrics of the VGG-5 network could achieve 27.39% RE, 0.9267 CC and 0.9158 SSIM.

In addition, models using dynamic convolution kernels have better performance in metrics than those using static convolution kernels within the same network depth. The average evaluation metrics of the DY-VGG-5 network could achieve 26.96% RE, 0.9354 CC and 0.9225 SSIM.

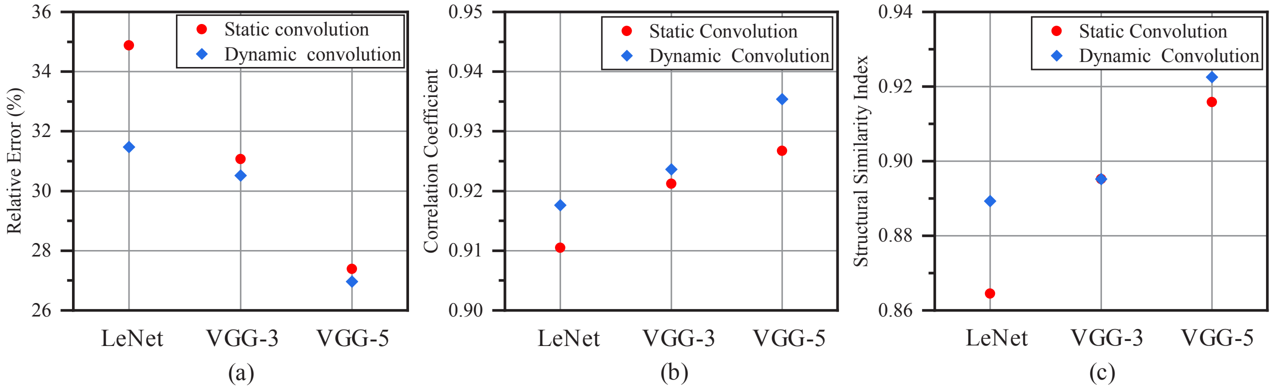

Figure 5. Average evaluation metrics of the test set by different networks. (a) RE. (b) CC. (c) SSIM.

5. Discussion

In this paper, dynamic convolution is used in light-weight networks to improve the reconstruction performance. However, according to the authors' attempts, when the depth and the structure of network are deep and complex enough, the prediction performance of the network with dynamic convolution may not be increased, even decreased as the multi-scale information extracted from measurement voltages has been fully utilised or the existence of overfitting problem. Therefore, the use of this method requires careful adjustments and optimization of the network structure to improve the performance of the model. Besides, to improve prediction performance and enhance the robustness of network for detecting lung diseases, one could also design a more complex network or multimodal fusion technology could be used, but in these ways, the parameters and calculations will increase significantly.

6. Conclusions

In the work, EIT lung data set is established and light-weight network with dynamic convolution is proposed to reconstruct conductivity to diagnose lung diseases. The applied dynamic convolution would not increase the depth of networks. The qualitative and quantitative analysis of the test set show that dynamic convolution can be used to obtain more accurate predicted conductivity in light-weight networks, thus optimizing the evaluation metrics RE, CC and SSIM metrics. The work has a positive effect on the light-weight EIT models and implementation of models with limited hardware resources, which accelerates the combination of deep learning methods with real-time EIT.

References

Alippi C, Disabato S and Roveri M 2018 Moving convolutional neural networks to embedded systems: the alexnet and VGG-16 case. In *2018 17th ACM/IEEE International Conference on Information Processing in Sensor Networks* **2018** 212-223

Bock S and Weiß M 2019 A proof of local convergence for the Adam optimizer. *In 2019 International Joint Conference on Neural Networks (IJCNN)* **2019** 1-8

Chen Y, Dai X, Liu M, Chen D, Yuan L and Liu, Z 2020 Dynamic convolution: Attention over convolution kernels. In *Proceedings of the IEEE/CVF Conference on Computer Vision and Pattern Recognition* **2020** 11030-11039

Chen Z, Yang Y, Jia J and Bagnaninchi 2020 Deep learning based cell imaging with electrical impedance tomography. In *2020 IEEE International Instrumentation and Measurement Technology Conference* **2020** 1-6

Ren S, Sun K, Tan C and Dong F 2019 A two-stage deep learning method for robust shape reconstruction with electrical impedance tomography. *IEEE Trans. on Instru. and Meas.* **69** 4887-4897

Tan C, Lv S, Dong F and Takei M 2019 Image Reconstruction Based on Convolutional Neural Network for Electrical Resistance Tomography. *IEEE Sens. J., vol.* **19** 196-204

Zhang K, Guo R, Li M, Yang F, Xu S and Abubakar A 2020 Supervised descent learning for thoracic electrical impedance tomography. *IEEE Trans. on Biomed. Eng.* **68** 1360-1369

Proceedings of the International Conference of Bioelectromagnetism, Electrical Bioimpedance,
and Electrical Impedance Tomography June 29 – July 1, 2022 / Kyung Hee University, Seoul, Korea

A Learning-Based 3D EIT Image Reconstruction Method

Zhaoguang Yi[1], Zhou Chen[1], and Yunjie Yang[1]
[1]Institute for Digital Communications, School of Engineering, the University of Edinburgh, UK

Correspondence : Zhaoguang Yi, e-mail : yizhaoguang@outlook.com

Abstract– Deep learning has been widely employed to solve the Electrical Impedance Tomography (EIT) image reconstruction problem. Most existing physical model-based and learning-based approaches focus on 2D EIT image reconstruction. However, when they are directly extended to the 3D domain, the reconstruction performance in terms of image quality and noise robustness is hardly guaranteed mainly due to the significant increase in dimensionality. This paper presents a learning-based approach for 3D EIT image reconstruction, which is named Transposed convolution with Neurons Network (TN-Net). Simulation and experimental results show the superior performance and generalization ability of TN-Net compared with prevailing 3D EIT image reconstruction algorithms.

Keywords: Deep learning, Electrical Impedance Tomography (EIT), 3D image reconstruction

1. Introduction

Electrical Impedance Tomography (EIT) has subscribed to the belief that it is a non-intrusive and non-radiative imaginging modality in clinical and industrial sectors. In EIT, the conductivity distribution within the region of interest can be reconstructed using boundary voltage measurements induced by current injections. The EIT-image-reconstruction problem is a long-standing challenge in the field due to its ill-posed and ill-conditioned nature (Yang, 2018). Recently, researchers have made noteworthy progress on both physical model-based, and learning-based 2D EIT image reconstruction algorithms (Yang *et al* 2014, Chen *et al* 2020). However, the EIT image reconstruction problem especially in 3D remains to be thoroughly investigated. Directly transferring from 2D to 3D based on the developed approaches usually requires extensive computational resources. Additionally, further improvements with respect to image quality and noise reduction performance are required.

This paper proposes a Transposed convolution with Neurons Network (TN-Net) for the EIT-image-reconstruction in 3D. The proposed network structure is inspired by the 3D Generative Adversarial Network (3D-GAN) (Wu *et al* 2016). Before the transposed convolution layers, a decoder is introduced, which can decode the normalized EIT measurement data to a more representative version in probability domain. The decoder is constructed by a stack of fully connected layers, which add a portion of buffering to the transposed convolutional layer compared to passing the measurement data directly, making the network perform better. After mapping the measurement domain to a low-dimensional probability domain based on the decoder, the subsequent 3D transposed convolution layers complete the interpretation from the low-dimensional probabilistic space to the high dimensional space representing 3D reconstructed results (Wu *et al* 2016).

Three main contributions of this work are:

1. A network architecture TN-Net for 3D EIT image reconstruction is proposed. The decoder conducts structural learning which tackles the nonlinearity of the inverse problem. The following transposed convolutional layers further enhances the image quality of 3D reconstructions. Using the same computing resources, the TN-Net enables higher-quality 3D EIT image reconstruction compared with non-structural learning..
2. A 3D EIT dataset is constructed, which comprises 21,135 randomly generated multi-object, multi-conductivity level phantoms.
3. The TN-Net is verified using simulation and experimental data, demonstrating its superior performance in terms of computational efficiency, noise robustness, and generalization ability over the exisiting reconstruction algorithms.

2. Methodology

2.1 Electrical Impedance Tomography

The forward problem of EIT is to reconstruct the conductivity distribution from induced boundary voltage measurements. The commonly used Complete Electrode Model (CEM) (Holder, 2004) for EIT is described by:

$$\nabla \cdot (\sigma(x,y)\nabla \mu(\mathrm{x},\mathrm{y})) = 0, (\mathrm{x},\mathrm{y}) \in \Omega \tag{1}$$

$$\mathrm{u} + \mathrm{Z}_l \sigma \frac{\partial u}{\partial n} = U_l, \mathrm{l} = [1, \mathrm{N}] \tag{2}$$

$$\int_{e_l} \sigma \frac{\partial u}{\partial n} dS = I_l, \mathrm{l} = [1, \mathrm{N}] \tag{3}$$

$$\sigma \frac{\partial u}{\partial n} = 0 \tag{4}$$

where N is the number of electrodes, σ is the conductivity distribution, $\partial\Omega$ is the the boundary, e_l is the lth electrode, and u is the potential on the boundary, which is excited by the injected current I. The complete electrode model can be solely solved by using the conservation of charges and the arbitrary choice of reference potentials, i.e. $\sum_{l=1}^{\mathrm{N}} \mathrm{I}_l = 0$, $\sum_{l=1}^{\mathrm{N}} \mathrm{u}_l = 0$.

The inverse problem of EIT is to estimate an unknown image σ from given voltage measurements V. In this work, without requiring any a priori knowledge, the nonlinear relationship between the perturbation of conductivity distribution $\Delta\sigma$ and the induced voltage measurement changes ΔV is learned via a deep network.

2.2 Network Structure

TN-Net is developed to reconstruct 3D EIT images from boundary voltage measurements. The network structure is shown in Figure 1. TN-Net consists of two parts: decoding and reconstructing parts.

Our trials show that the expressive power of transposed convolutional layers was insufficient to solve the inverse problem of 3D EIT. We propose to add a decoding part using three fully connected layers, with feature sizes of 256,512, and 1024, respectively. Each fully connected layer is followed by a dropout layers. During training, before feeding the input data into the network, we introduce an independent noise addition module to add noise of 35dB SNR to the input data, which drives the model to learn eternal patterns from all kinds of noise-contaminated data, thus increasing its generalizability.

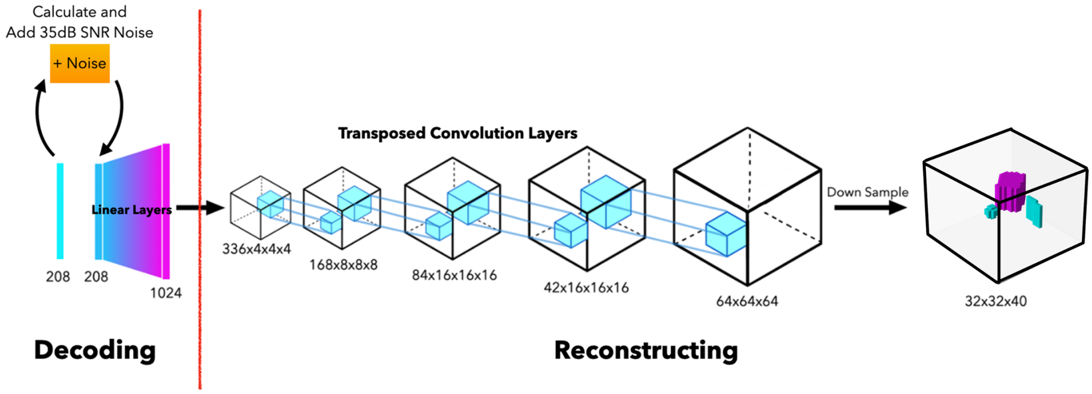

Figure 1. The architecture of TN-Net.

The reconstructing part is inspired by the 3D-GAN (Wu *et al* 2016), which contains 4 transposed convolution layers with convolution kernels of (4,4,4) and stride of (2,2,2). Each transposed convolution layer is paired with a batch normalization layer and a Leaky ReLU layer. Finally, the resulting reconstructed conductivity distribution with a high-resolution of 64*64*64 is downsampled to 32*32*40. The source code of TN-Net is available from: https://github.com/Josh-Yi/TN-Net.

3. Experimental Setup

3.1 3D EIT Dataset

The 3D EIT dataset is generated using COMSOL Multiphysics by solving the forward problem of 3D EIT using the Finite Element Method (FEM). As shown in Fig. 2, the COMOSOL model was built based on the experimental equipment, consisting of two 16-electrode layers. We adopt the adjacent measurement strategy (Yang *et al* 2017), and the completed non-redundant measurement cycle consists of 208 voltage measurements. The targeted 3D image to be reconstructed is a 32*32*40 conductivity distribution. The measurement-image pairs are calibrated and normalized to eliminate common errors caused by systematic defects. Four types of phantoms (see Fig. 3) are generated with randomly selected shape, size, rotation angle, conductivity, and number of objects for the dataset according to the generation rules listed in Table 1.

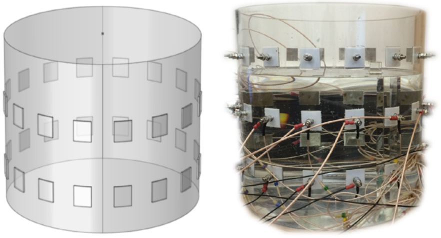

Figure 2. The 3D model of the 32 electrode EIT sensor and the real-world sensor.

Table 1. *3D EIT* Dataset Generation Rules.

Total	2 Objects -	2 Objects ±	3 Objects -	3 Objects ±
21,135	4,352	4,520	7,201	5,062

- indicates that the normalized conductivity change is negative, while ± means the phantoms have both negative and positive conductivity changes.

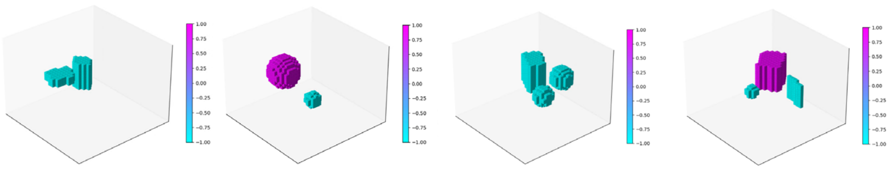

2 Objects - 2 Objects ± 3 Objects - 3 Objects ±

Figure 3. Four representative examples in the 3D EIT dataset.

3.2 Network Training

As mention in Section 2.2, an additive noise of 35dB SNR is added to the EIT measurement in the training process in a way that the model continuously sees different noise-contaminated samples during each epoch. Dynamically adding the noise can increase the model's robustness and prevent overfitting. The optimizer is the Adam (Loshchilov, 2019) with a learning rate of 0.002, a weight decay of 0.01, and betas of (0.9, 0.999). The model is trained 300 epochs with a batch size of 442. The model at 260-th epoch achieved the minimal validation loss and was selected as the final model.

4. Results

We compare the proposed TN-Net with two 3D EIT reconstruction algorithms, i.e., one-step Gauss-Newton solver with Laplace Regularization (One-Step) (Yang *et al* 2014) and the original generator of 3D-GAN (Wu *et al* 2016).

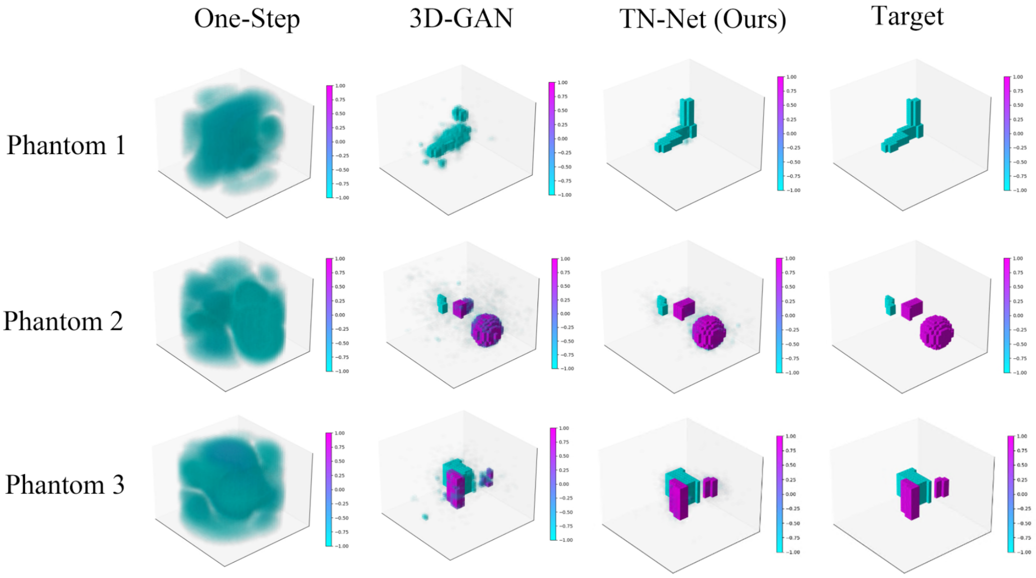

Figure 4. 3D EIT reconstruction results of unseen simulation data.

The test data are added with 30 dB noise worse than the training process. Some representative results from the testing set are shown in Fig. 4. Obviously, our TN-Net stands out compared with the other two methods. It has the best noise resistance performance by reconstruting the best positions and shapes of all inclusions. Furthermore, TN-Net is capable of better distinguishing phantoms with both positive and negative conductivity changes, outperforming the other methods.

Table 3 reports quantitative comparisons of all methods over the testing data based on the statistic average of Root Means Square Error (RMSE), 3D Structural Similarity Index (SSIM), Peak Signal to Noise Ratio (PSNR), and inference time. Apart from the best RMSE, SSIM, and PSNR, the TN-Net has higher imaging speed than the traditional one-step method and is slightly slower than 3D-GAN due to the deeper architecture of TN-Net with an additional decoder. Nevertheless, the execution time of TN-Net (below 40 ms) is sufficiently good for implementing real-time 3D EIT imaging.

Table 2. Result evaluation on the whole test dataset.

	RMSE	SSIM	PSNR	Inference Time
Ours	**7.616e-5**	**0.9657**	**30.709dB**	0.0311s
One-Step	0.1267	0.6193	21.847dB	0.0478s
3D-GAN	9.176e-5	0.9485	29.082dB	**0.0306s**

The average inference time is tested on an Intel i9-12900k. The best results are highlighted in bold.

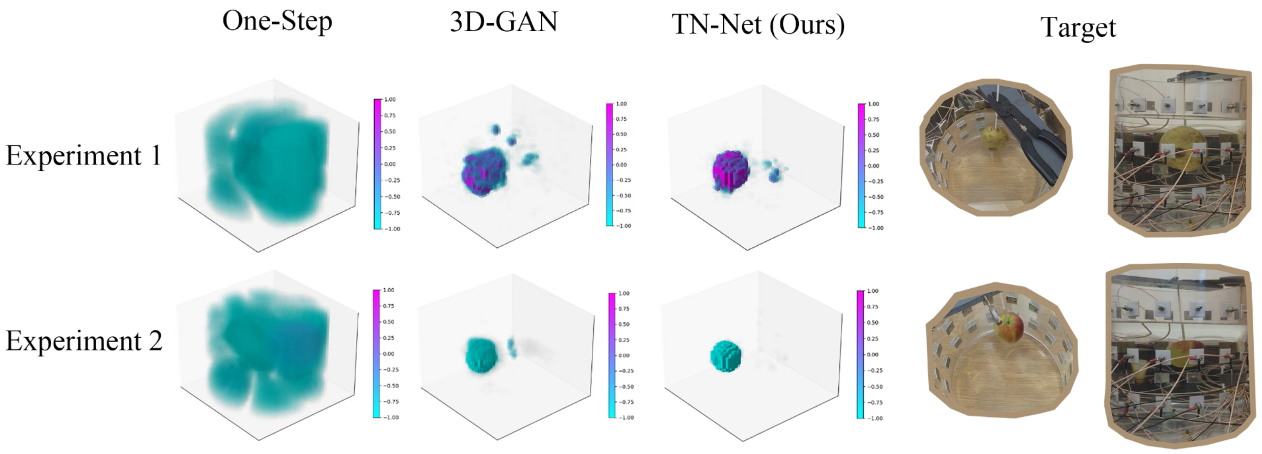

Figure 5. 3D EIT reconstruction results using experimental data.

We also validate the proposed method using real-world data (see Fig. 5). Two phantoms are reconstructed with current injection of 25 kHz and a 3D EIT sensor with 16*2 electrodes. The potato in Experiment 1 is a tuber with higher ionic and water content than Experiment 2 with an apple, which is successfully recognized by 3D-GAN and TN-Net. The experimental results further verified the generalization ability and superior performance of the TN-Net over the other methods.

5. Conclusion

This paper proposes a novel learning-based 3D-EIT reconstruction method named TN-Net. TN-Net has demonstrated its robustness and superior performance on both simulation and real-world 3D EIT data. TN-Net is around 40% faster and 60% more accurate in terms of SSIM than the comparing algorithms. Future work will investigate the application of the proposed TN-Net in 3D tissue imaging.

References

Yang Y 2018 Advanced digital electrical impedance tomography system for biomedical imaging

Chen Z, Xiang Z, Bagnaninchi P -O and Yang Y **2020** MMV-Net: A Multiple Measurement Vector Network for Multifrequency Electrical Impedance Tomography *IEEE Trans Neural Networks and Learning Systems*

Wu J, C Zhang, Xue T, Freeman W, Tenenbaum J. 2016 Learning a probabilistic latent space of object shapes via 3d generative-adversarial modeling *Advances in Neural Information Processing Systems* **2016** 82–90

Holder D, Electrical Impedance Tomography: Methods, History and Applications, Institute of Physics, **2004**

Loshchilov I, Hutter, F 2019 *Decoupled Weight Decay Regularization.*

Yang Y, Jia J, Polydorides N, & Mccann H 2014 Effect of structured packing on EIT image reconstruction 2014 *IEEE Imaging Systems and Techniques (IST)* **2014** 53-58

Yang Y, Jia J 2017 A multi-frequency electrical impedance tomography system for real-time 2D and 3D imaging *Rev Sci Instrum* **2017**

O 03-04

Proceedings of the International Conference of Bioelectromagnetism, Electrical Bioimpedance,
and Electrical Impedance Tomography June 29 – July 1, 2022 / Kyung Hee University, Seoul, Korea

Unsupervised Clustering of Lung Perfusion Features

Diogo Filipe Silva, Clara Wemmer, Maria-Lenka Wolter, Steffen Leonhardt, Chuong Ngo
Chair of Medical Information Technology, RWTH Aachen University, Aachen, Germany

Correspondence : Diogo Filipe Silva, e-mail : silva@hia.rwth-aachen.de

Abstract Although it is currently possible to derive a number of perfusion metrics from the famous EIT bolus signal, and recent studies hinting at a high potential for clinical implementation of such methods, the amount of produced data could benefit from a knowledge systematization process capable of producing concise, accurate and relevant information about the regional perfusion status. As a textbook scenario for the employment of machine learning techniques, but not enough ground truth for supervised algorithms, we investigated the optimization of an unsupervised clustering workflow to summarize the regional perfusion information into physiologically meaningful anatomical regions. To this end, we performed feature selection, algorithm selection and tuning, and implemented appropriate pre-processing. We then tested the optimized workflow against real animal trial data. It was found that a combination of K-Means with principal component analysis using mean transit time, time-of-peak, and relative dispersion as cluster features produced the best results in healthy data, and had potential to perform just as well in pathology scenarios.

Keywords: *Machine Learning; Enhanced Electrical Impedance Tomography; Clustering; Pulmonary Perfusion*

1. Introduction

In recent years, electrical impedance tomography (EIT) research has placed a strong emphasis in understanding cardiac-related signals, its components, and its clinical potential. One of the major questions associated with this research vector, is the viability of estimating perfusion parameters from bolus curves observed after the injection of a saline solution (Borges *et al* 2012). As such, many algorithms were recently introduced, capable of deriving a number of perfusion metrics from these signals (Hentze *et al* 2021). Although highly necessary, metric maps obtained from such methods may be excessive information in a clinical scenario, lacking the ability to deliver accurate, relevant and summarized information about the different regions of the thoracic cross-section under examination.

In this work, we optimize an unsupervised clustering workflow to identify physiologically meaningful anatomical regions from derived perfusion metrics. A balanced ratio of accuracy and stability across subjects was favoured. Effectively, this provides an interesting way to summarize the current perfusion state of macro regions-of-interest with potential for future development along the lines of automatic classification of healthy and pathological regions.

2. Materials

2.1 Data

For this work, EIT data was recorded from 2 mechanically ventilated pigs under apnea during 1-minute long breath hold maneuvers, in which an 10 mL NaCl 0.9% injection was administered after 20 seconds. A Dräger Pulmovista® 500 with a 16-electrode belt was used at an operating frequency of 80 kHz. Each animal yielded 4 recordings, one of them after positioning a balloon catheter in wedge position on the left pulmonary artery. From each of these recordings, 9 perfusion features were extracted using the model-based source separation method described in (Hentze *et al* 2021): peak amplitude (Y_{peak}), time-of-peak (T_{peak}), time-to-peak (TTP), mean transit time (MTT), relative dispersion (RD) (Bassingthwaighte 1977), normalized residual of the fit (RESNORM), time-of-arrival (TOA), α and β (shape parameters of the gamma-variate curve), maximum slope (SLOPE), and area-under-curve (AUC). Additionally, the X and Y coordinates of each pixel were also included in the feature pool. A visual summary of some of these features is found in Figure 1.

An important note to the reader is that, instead of following the conventional LPS DICOM orientation, images in this contribution follow an orientation of posterior to anterior on the Y-axis, and right to left on the X-axis.

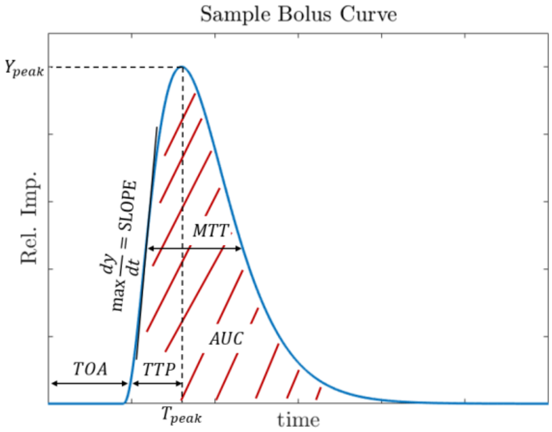

Figure 1. Visual summary of the extracted perfusion features later used to optimize the clustering workflow. RD, $RESNORM$, α and β are not here depicted since they cannot be easily understood from the time-intensity curve.

2.2 Software

For efficient testing of different feature combinations, clustering methods and pre-processing, we used the unsupervised learning toolbox of the open source software Orange Data Mining. This visual programming framework enables rapid prototyping, analysis and visualization of basic machine learning algorithms.

3. Methods

3.1 Feature selection

Selecting and generating useful features from the original ones is crucial for the effectiveness of clustering applications. Therefore, we tested the possible combinations from groups of one until a maximum of four features, and compared them with regard to their stability and ability to recognise meaningful clusters. Their performance was evaluated based on their integration on a K-Means algorithm set to identify 5 clusters. Moreover, X and Y were always included besides the feature groups, since anatomical location plays a central role in the physiologically expected clusters.

3.2 Algorithm selection

DBSCAN is a density-based approach, which forms clusters based on the minimum number of data points located in a certain neighbourhood. The advantages are that not all data points are assigned to a cluster and it is capable of handling outliers and noise autonomously. Therefore, the number of clusters is automatically adapted to the perfusion situation. As a downside, DBSCAN requires finer subject-specific parameter tuning. Hence, other approaches were implemented with the determined feature combination, including Louvain Clustering and Hierarchical Clustering. However, we decided to focus on K-Means as an alternative to DBSCAN, as it preliminarily showed a reasonable stability/simplicity ratio.

3.3 Algorithm tuning

We need a minimum of 4 clusters to be able to segregate the right and left regions of the heart, and the right and left lungs. Since K-means does not autonomously deal with outliers and noise, the number of clusters to be fit was set to at least 5, so as to cluster these impurities into isolated, distinguishable clusters in post-processing. Each feature was normalised to equalize their weights during training. The seed initialization method K-Means++ was implemented. The number of epochs was set to 30, each with a maximum of 400 iterations. For the DBSCAN algorithm, we compared the use of Euclidean and Cosine neighbourhood distance with each other.

3.4 Influence of Pre-Processing

Approaches of dimensionality reduction are common pre-processing strategies to boost clustering efficacy. Principal component analysis (PCA) is an algorithm that reduces the dimension of the input data by projecting the original features onto the N orthogonal vectors pointing in the direction of highest variance in the data. It thus compresses a large feature space and generates a predetermined number N of principal components (PCs). As the data provided contain a large set of relevant features, including PCA pre-processing could be an option to obtain new, more fruitful features through a weighted linear combination of the existing ones. It could also help dealing with outliers beforehand, as features that contribute the least for the variance in data will have a lighter weight in the combination.

4. Results

4.1 Feature selection

It was found that SLOPE and AUC behaved very differently across subjects. Since RESNORM is more deeply related to the quality of the fitting process than to the underlying physiological phenomena, it was simply used for a threshold-based outlier removal during pre-processing. Ultimately, MTT, T_{peak} and RD composed the best performing group out of the remaining possibilities. Colormaps of these selected features can be found in Figure 2.

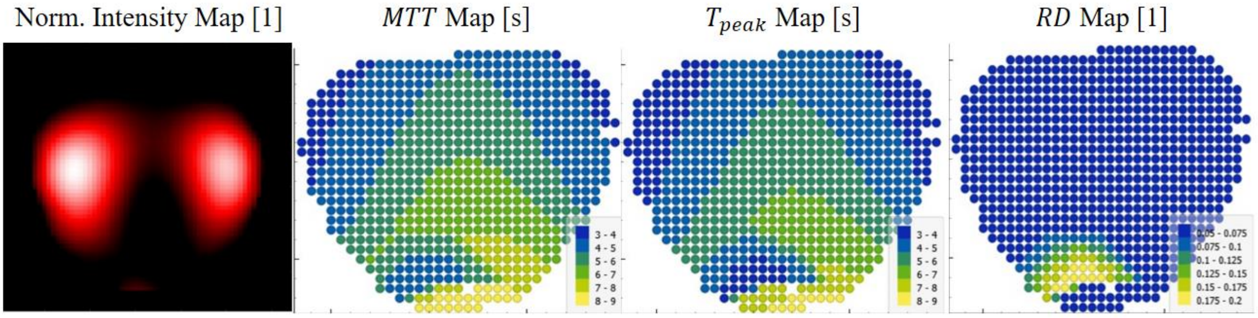

Figure 2. From left to right: the bolus intensity mask due to lung effects; colormap of the MTT, in seconds; colormap of the T_{peak}, in seconds; colormap of the RD, in [0,1]. Changes in RD in the lung region are hardly perceptible due to the resolution of Orange's colormap.

4.2 Algorithm selection

By applying k-Means to the selected feature space, we obtained stable clusters of the right heart, left heart, right lung and left lung in space and time for all healthy recordings of the animal trials Figure 3. Compared to DBSCAN, the K-Means algorithm is very sensitive to outliers, as all data points are forced into a cluster. We, therefore, chose the classical K-Means since the outlier handling could be addressed in pre- or post-processing with tailored approaches. A total number of 5 to 6 clusters were found to work best for all datasets.

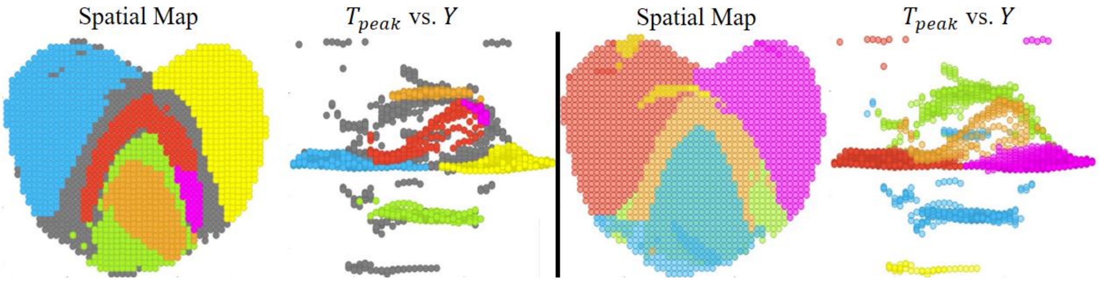

Figure 3. To the left: the clusters resulting from DBSCAN; to the right: the clusters resulting from K-Means. T_{peak} vs. Y maps provide a visualization of each pixel's T_{peak} as a function of its Y coordinate. Cluster colors are not coherent between right and left plots.

4.3 Pre-processing

Including PCA pre-processing into our clustering strategy, we observed a slightly smoother repartition of the four main clusters. In Figure 4, it can be observed that the orange outlier cluster, assigned without PCA, was appropriately assigned as one of the main clusters after its implementation. In this case, we obtained a smoother repartition of the data points to the left and right compartment of each heart and lung by applying PCA. This was also verified for the remaining recordings, as more spatially coherent structures were achieved.

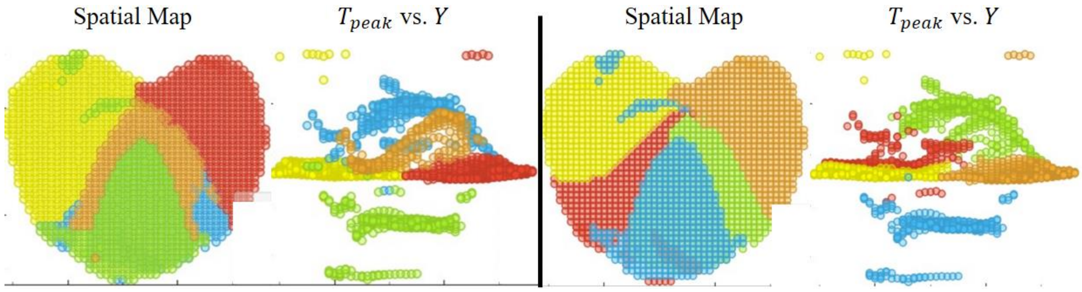

Figure 4. To the left: the clusters resulting from K-Means without PCA; to the right: the result of including PCA as pre-processing. The orange cluster to the left was further separated into a transition zone between the heart and lung divided into right and left halves. Cluster colors are not coherent between right and left plots.

4.4 Pathological Data

Figure 5 depicts the results for data from the same subject with and without a perfusion defect on the left lung. A delay of T_{peak} for the compartment of the left lung (yellow cluster in the bottom plots) and, as a result, to the compartment of the left heart (red cluster in the bottom plots) can be observed. The spatial separation under this pathological scenario seems to have slightly worsened, and that $SLOPE$ could be a useful feature to include.

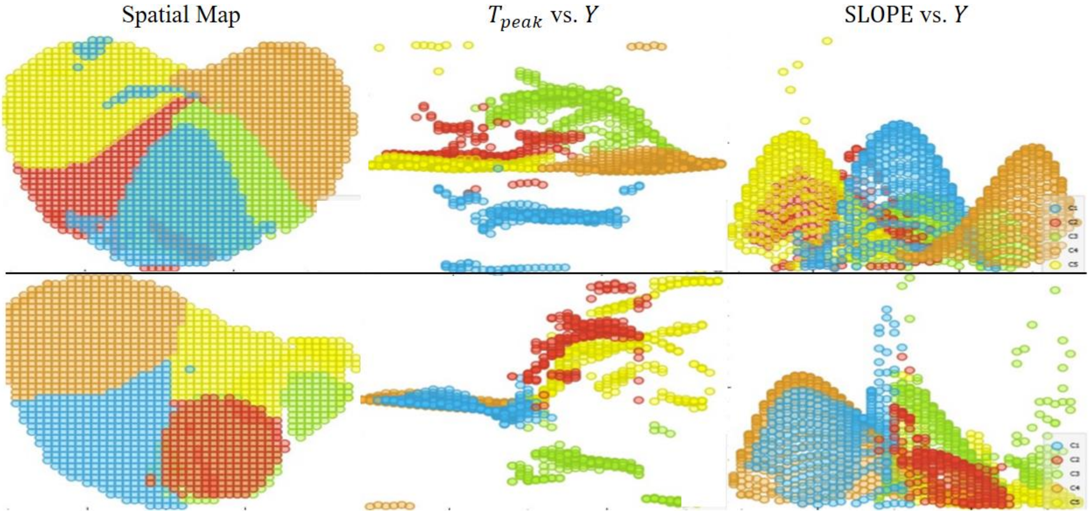

Figure 5. Top row: K-Means and PCA approach on recording under healthy state; bottom row: K-Means and PCA approach on recording of the same subject with a left lung perfusion defect. The last column depicts $SLOPE$ colormaps, which hint at the feature's usefulness to clustering in such pathology scenarios. Cluster colors are not coherent between top and bottom plots.

5. Discussion

Some redundancy between time-related features might have played a role in the rejection of TTP and TOA. Along with X and Y, encoding spatial knowledge, MTT, and T_{peak} carry temporal knowledge, and RD bolus shape information. The ensemble, as seen in Figure 2, constitutes, therefore, a theoretically balanced feature space. The addition of PCA also allowed stable partition of main clusters into sub-clusters, providing higher resolution information. Although it reduces the susceptibility of K-Means to outliers, post-processing methods to exclude outlier-like clusters should be implemented in the future. This would allow, e.g., choosing a higher number of target clusters, from which the outlier ones could be removed. Such an approach would have improved the results in the pathology scenario of Figure 5, by further partitioning the blue cluster, and classifying the green cluster as defect or outlier. Considering $SLOPE$ for analysing perfusion defects would make sense, since this feature equates to the calculation of relative blood flow according to the Fick principle (Fritts and Cournand 1958).

6. Conclusions

We arrived at a methodology that identifies physiologically significant clusters (and subclusters) of heart and lung with potential to pinpoint regions with pathology. Developing look-up tables for cluster identification based on each cluster's centre of mass here could provide an interesting conclusion. However, the sensitivity to outliers should be addressed. The selected feature space MTT, T_{peak}, RD and axial coordinates confirms the parameter selection of (Hentze *et al* 2021).

References

Bassingthwaighte J B 1977 Relative Dispersion: A Characterizing Feature of Specific Vascular Beds. *Anesth. Analg.* **56** 72–7

Borges J B, Suarez-Sipmann F, Bohm S H, Tusman G, Melo A, Maripuu E, Sandström M, Park M, Costa E L V., Hedenstierna G and Amato M 2012 Regional lung perfusion estimated by electrical impedance tomography in a piglet model of lung collapse *J. Appl. Physiol.* **112** 225–36

Fritts H W and Cournand A 1958 The Application of the Fick Principle to the Measurement of Pulmonary Blood Flow *Proc. Natl. Acad. Sci.* **44** 1079–87

Hentze B, Muders T, Hoog Antink C, Putensen C, Larsson A, Hedenstierna G, Walter M and Leonhardt S 2021 A model-based source separation algorithm for lung perfusion imaging using electrical impedance tomography *Physiol. Meas.* **42** 084001

DAY 1

Wednesday, June 29, 2022

Oral Session 04

Bio-impedance Measurement I

Chair Uwe Pliquett (Institut für Bioprozessund Analysenmesstechnik)
Christian Tronstad (Oslo University Hospital)

O 04-01 **Numerical and experimental studies on underwater fish monitoring with electrical impedance measurements**
Lukasz J. Nowak (Wageningen University and Research)

O 04-02 **Dielectric relaxation spectroscopy mearsurements on amino acids**
Jie Hou (Oslo University Hospital)

O 04-03 **Blood viscosity on glucose level using electrical impedance spectroscopy**
Pedro Bertemes Filho (State Univertisy of Santa Catarina)

O 04-04 **Impact of Aortic Wall Stiffness on the Morphology of Impedance Cardiography Signal**
Vahid Badeli (Graz University of Technology)

O 04-05 **Changes in Electrical Impedance of Pork Meat during Salt Diffusion by Wet-curing with Sodium-chloride**
Philipp York Zimmermann (Hungarian University of Agriculture and Life Sciences)

ICBEM Bioelectromagnetism ICEBI Electrical Bioimpedance EIT Electrical Impedance Tomography

Proceedings of the International Conference of Bioelectromagnetism, Electrical Bioimpedance,
and Electrical Impedance Tomography June 29 – July 1, 2022 / Kyung Hee University, Seoul, Korea

Numerical and experimental studies on underwater fish monitoring with electrical impedance measurements

Lukasz J. Nowak[1] and Martin J. Lankheet[1]
[1]Experimental Zoology Group, Wageningen University and Research, the Netherlands

Correspondence : Lukasz J. Nowak, e-mail : lukasz.nowak@wur.nl

Abstract–Underwater fish monitoring plays an important role in natural resources management. Sonars and echosounders are typical solutions used for this purpose, working especially well in open water reservoirs. They fail, however, to detect fish in shallow, turbid waters or in the seabed, due to complex acoustic reflection patterns. Feasibility of alternative video monitoring means is strongly restricted by limited visibility underwater. In the present study we investigate the possibilities of using electrical impedance measurements for close-range fish detection. This technique could potentially bridge the gap in the applicability range of exisiting monitoring means. We developed two independent numerical models for determining impedance values in a water tank with a fish using four-electrode measurement setup. We compared the results of simulations to the results of experimental measurements conducted in laboratory conditions. The experiments were carried out using an impedance analzer and a pair of CCD cameras for simultaneous recording of fish position relative to the electrodes. The comparison of data demonstrates fair agreement between the numerical predictions and the experimental measurements. Both examined models yielded a similar pattern of results, but with a slightly different bias. Fish presence in the direct vicinity of electrodes is indicated by clear decays in both resistance and reactance values.

Keywords: electrical impedance; fish detection; numerical simulations; underwater monitoring

1. Introduction

Underwater fish monitoring plays an important role in natural resources management and implementing new strategies and technologies for sustainable fisheries. Detection means are most often based on ultrasound systems and exploit phenomena related to reflection of acoustics waves on interfaces between propagation media with different mechanical properties. Gas-filled swim bladders constitute strong acoustic reflectors, and thus fish equipped with such organs are relatively easy to detect in open water reservoirs (MacLennan and Simmonds, 1992). Mechanisms based on echolocation fail however, in shallow, turbid waters, with multiple air bubbles present. Similarly, acoustical detection of flatfish without a swim bladder that are buried in a seabed encounter also significant difficulties. Alternative fish monitoring techniques are also not without flaws: manual fish counting can be applied only in specific sites, such as fish passes, and engages significant human resources (Bieluch et al., 2017); automated video monitoring systems suffer from limited visibility underwater; and satelite data are useful for relatively large-scale monitoring and low depths (Knudby et al., 2010).

Here, we propose a new approach based on electrical impedance measurements. We exploit the fact that fish tissues have electrical properties that are significantly different from those of the surrounding water (Niu and Lee, 2000; Zhao et al., 2017). In fresh water presence of a fish in the vicinity of measurement electrodes should manifest itself by decays in the determined resistance and reactance values. A detection system based on electrical impedance analysis utilizes simple and cheap sensors, and its operation can be fully automated. It therefore has the potential to bridge the gap in the applicability range of exisiting monitoring means.

The aim of the present study is to determine – both numerically and experimentally – the detection capabilities and performance of a fish detection system utilizing electrical impedance measurements. A numerical model of the considered phenomena – if capable of accurate predictions – can constitute an useful tool for optimization of the hardware setup, saving time and resources otherwise required for experimental tuning of parameters. For this reason we compare two different simulation approaches against the results of experimental measurements, to test their validity in the considered application.

2. Methods

2.1 Experimental setup

The measurements were conducted in a tank with dimensions 400 mm x 240 mm x 295 mm, filled with tap water to a depth of approximately 214 mm. During experiments, a single gold fish was swimming freely inside the tank. An MFIA impedance analyzer (Zurich Instruments, Switzerland) was used to determine resistance and reactance values continuously at a data rate of approximately 104 samples per second. The signal frequency was set to 10 kHz. A four-electrode setup was used in order to mitigate the effects of double layer formation at the current carrying electrodes. Each electrode pair was built from a single piece of standard printed circuit board substrate, with dimensions 30 mm x 30 mm. The electrode pairs were located 166 mm apart, next to one of the walls of the tank.

During measurements the three-dimensional fish position was recorded using two CCD cameras (Basler, Germany) mounted in front of the tank. The recorded footage was analysed on-the-fly to extract fish contour and position using in-house developed Python scripts. The extracted localization data were merged with the impedance data based on time stamp values.

2.2 Numerical simulations

Numerical models used to determine impedance values utilized the Finite Element Method, and were implemented in COMSOL Multiphysics. The model geometry reflected the dimensions and arrangement of the experimental setup, and included the tank and electrodes with mounting systems. The water resistivity was set to $21\,\Omega \cdot m$. The fish was represented by an ellipsoid with dimensions 50 mm x 20 mm x 30 mm, with resistivity $2\,\Omega \cdot m$.

Two different approaches to impedance calculations were applied. In the first case we used the reciprocal relation to determine volume impedance density values of all the considered domains, and then integrated the results over the whole volume of interest (Grimnes and Martinsen, 2014; Høgetveit, 2011):

$$Z^V = \iiint \rho \frac{\overrightarrow{J_{CC}} \cdot \overrightarrow{J_{PU}}}{I^2} dV \qquad (1)$$

where ρ = resistivity of a voxel dV $[\Omega \cdot m]$

$\overrightarrow{J_{CC}} \cdot \overrightarrow{J_{PU}}$ = scalar product of current density vectors related to electric current flow between current carrying (CC) and voltage pickup (PU) electrodes $[\frac{A}{m^2}]$

I = electric current density; here, set to 1 A.

In the second approach we calculated the impedance Z^{meas} directly as a ratio of the voltage difference value obtained by surface integration over the PU electrodes to the electric current intensity between the CC electrodes, set to 1 A. The geometry of the considered problem with determined current intensity distribution between the electrodes is illustrated in Figure 1.

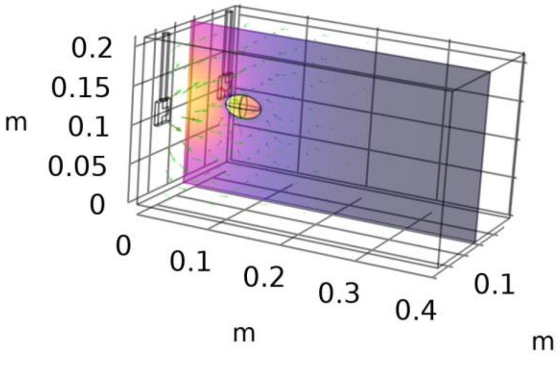

Figure 1. Geometry of the developed numerical model with calculated current intensity distribution between the electrodes.

3. Results

Impedance values Z^V and Z^{meas} determined numerically as functions of fish locations along the electrode axis (i.e., along axis perpendicular to the line connecting middle points of electrodes and just in front of their surfaces) and along the central axis (i.e., along axis perpendicular to the electrode plane, centrally between them) are illustrated in Figures 2 and 3. Results obtained using both numerical approaches are similar, predicting decays in the real and imaginary impedance parts due to presence of the fish in the vicinity of the measurement electrodes. The character and size of the changes are consistent, however the absolute calculated resistance values differ by approximately 25 Ω.

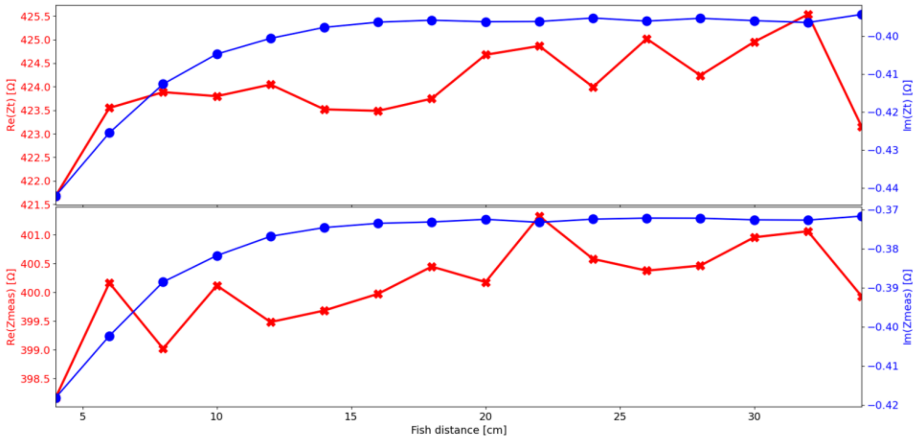

Figure 2. Z^V (top plot) and Z^{meas} (bottom plot) values determined numerically as functions of fish locations along the central axis (i.e., along axis perpendicular to the electrode plane, centrally between them).

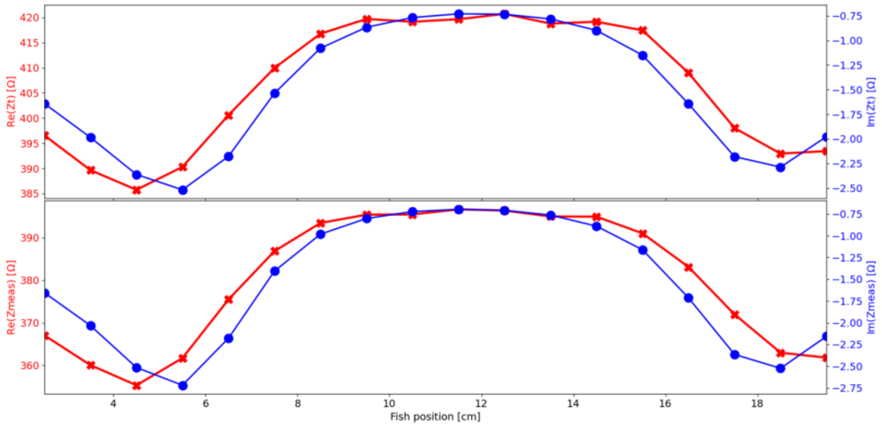

Figure 3. Z^V (top plot) and Z^{meas} (bottom plot) values determined numerically as functions of fish locations along electrode axis (i.e., along axis perpendicular to the line connecting middle points of electrodes and just in front of their surfaces).

The impedance values determined experimentally are illustrated in Figure 4 as functions of fish coordinates along all three cartesian axes. Significant decays are observed only for locations close to the measurement electrodes and the character of the observed changes is similar for both real and imaginary parts. In the z direction we see the double peaks as shown in Figure 3, whereas the pattern in the x direction nicely corresponds to the predictions in Figure 2.

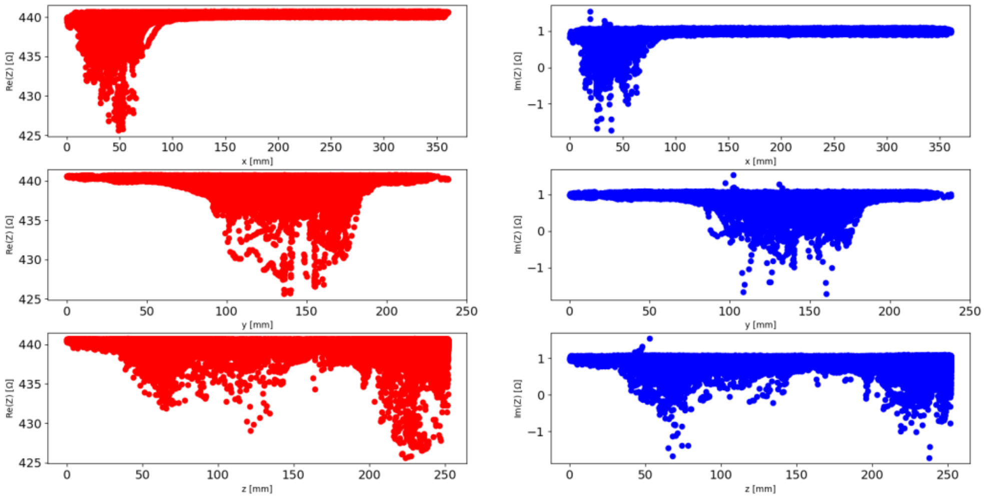

Figure 4. Resistance (left) and reactance (right) values determined experimentally as functions of fish coordinates inside the tank along all three cartesian axes. Top plots: x axis (length, perpendicular to the electrode plane); middle plots: y axis (depth); bottom plots: z axis (perpendicular to the axis connecting electrode middle points).

4. Discussion

Fish presence in the vicinity of electrodes clearly manifests itself by decays in the measured resistance and reactance values. The described system is thus capable of detecting fish based on the introduced operation principle. The detection range of the considered system is limited to aproximately 10 cm (for a fish length of about 5 cm), as illustrated by both experimental results and numerical simulations. Highest changes in the measured values are observed when fish is close to one of the electrode pairs, which creates sensitivity hotspots. Such a relatively low detection range can be advantageous for the described applications of interests, as it could help to mitigate the influence of potential noise originating outside the region where fish are expected.

Comparison of results obtained numerically and experimentally shows that the described numerical models can constitute useful tools for design and development of hardware configurations optimized for specific environmental conditions. Both approaches give similar predictions, however shifted in absolute resistance values. Differences between the experimental setup and modelled setup, e.g. related to fish properties, do not allow us to prefer one modelling approach above the other. Due to the slight bias in predictions, the two modelling apporaches cannot be used interchangeably or directly compared. Once the calculation method is chosen it should be consistently applied. Using simulations for tuning system parameters can potentially help to save time and resources otherwise required for iterative experimental validation.

Electrical impedance measurements utilize simple, low-cost sensors (electrodes) which can be shaped and arranged in countless possible ways. Further research could focus on exploiting this fact combined with the demonstrated usefulness of numerical simulations in predicting detection performance. System capabilities could be further expanded by adding multiple measurement channels. Another possible investigation direction is extracting more useful information from the signal by frequency sweeping and analysis of both real and imaginary impedance parts on this background.

5. Conclusions

We investigated the possibilities of underwater fish monitoring using electrical impedance measurements. The study included both numerical simulations and experimental measurements. Obtained results were consistent and demonstrated that the adopted approach allows for fish detection in the range up to approximately 10 cm from the electrode plane. Calculations of impedance values based on integration of volume impedance density over all domains and using only voltage surface integrals over pickup electrodes yield in similar results, with some constant bias in the resistance component. The numerical models can constitute a useful tool in predicting detection performance and optimizing hardware setup for specific environmental conditions.

Acknowledgments

The study was conducted within framework of the research project “Optimizing electrical pulse fishing for minimal ecological impact” funded by the Dutch Research Council (NWO), grant no. 18527

References

Bieluch, K.H., Willis, T., Smith, J., Wilson, K.A., 2017. The Complexities of Counting Fish: Engaging Citizen Scientists in Fish Monitoring. Maine policy review 26.

Grimnes, S., Martinsen, O.G., 2014. Bioimpedance and Bioelectricity Basics. Academic Press.

Høgetveit, J.O., 2011. From 3D tissue data to impedance using Simpleware ScanFE+IP and COMSOL Multiphysics – a tutorial. Journal of Electrical Bioimpedance 2, 13–32. https://doi.org/10.5617/jeb.173

Knudby, A., LeDrew, E., Brenning, A., 2010. Predictive mapping of reef fish species richness, diversity and biomass in Zanzibar using IKONOS imagery and machine-learning techniques. Remote Sensing of Environment 114, 1230–1241. https://doi.org/10.1016/j.rse.2010.01.007

MacLennan, D.N., Simmonds, E.J., 1992. Fisheries Acoustics, Fish & Fisheries Series. Springer Netherlands, Dordrecht.

Niu, J., Lee, J.Y., 2000. A New Approach for the Determination of Fish Freshness by Electrochemical Impedance Spectroscopy. Journal of Food Science 65, 780–785. https://doi.org/10.1111/j.1365-2621.2000.tb13586.x

Zhao, X., Zhuang, H., Yoon, S.-C., Dong, Y., Wang, W., Zhao, W., 2017. Electrical Impedance Spectroscopy for Quality Assessment of Meat and Fish: A Review on Basic Principles, Measurement Methods, and Recent Advances. Journal of Food Quality 2017, e6370739. https://doi.org/10.1155/2017/6370739

Proceedings of the International Conference of Bioelectromagnetism, Electrical Bioimpedance,
and Electrical Impedance Tomography June 29 – July 1, 2022 / Kyung Hee University, Seoul, Korea

Dielectric relaxation spectroscopy mearsurements on amino acids

Jie Hou[1,2], Runar Strand-Amundsen[1], Ørjan Grøttem Martinsen[1,2]
[1] Department of Clinical and Biomedical Engineering, Oslo University Hospital, 0424 Oslo, Norway
[2]Department of Physics, University of Oslo, Sem Sælands vei 24, 0316 Oslo, Norway.

Correspondence : Jie Hou, Runar Strand-Amundsen, Ørjan Grøttem Martinsen
e-mail : jieho@fys.uio.no, runar@sensocure.no, o.g.martinsen@fys.uio.no

Abstract - Neurodegenerative diseases are related to the function of neurotransmitters, where low concentration or deformed conformation can hinder successful binding to the respective receptors. Therefore, methods to study and monitor the concentration change of the neurotransmitters are of interest. In this study, we performed microwave frequency dielectric measurement on three amino acids dessolved in water to study the dielectric properties of the molecules.

Keywords: Dielectric relaxation spectroscopy, Microwave frequency, GABA(γ-aminobutyric acid), Dopamine, Proline

1. Introduction

Dielectric relaxation spectroscopy (DRS) is a subcategory of impedance spectroscopy, used to measure the dielectric properties of materials as a function of frequency. Dielectric measurements at microwave frequencies can be used on solids, liquids, or semi-solid materials such as biological tissue. We have previously used this technique to measure the dielectric properties of various solutions in the 200 MHz to 14 GHz region. The dielectric properties in this frequency region are dominated by the orientation mechanisms of dipolar molecules. In addition, DRS measurements can be used to calculate the geometric properties of the involved molecules, given that the type and concentration of molecules are known. Molecular geometry is of interest for several fields of research, ranging from physics to chemistry and medicine. With respect to neurodegenerative diseases, molecular geometry is of interest as it to a certain degree can determine the ability of a molecule to bind to its receptors. In this paper, we focus on mixture solutions with three different amino acids. These amino acids consist of large polarizable molecules that can affect the dielectric properties of the solution.

2. Methods

When an electric field is applied to a material, the dipole molecules within the material will respond to the alternating electric field. At low frequencies, the dipole molecules will be able to rotate and follow the direction of the applied oscillating field. The time that a molecule needs to rotate with a field, depends on the properties of the solvent and the solute molecule. A large molecule needs more time to rotate than a small molecule. With increasing field frequency, the molecules (dependent on the dipole moment) will not be able to rotate completely and become fully polarized and will instead start to vibrate. This vibrational movement leads to a loss of energy in the form of heat.

Dielectric properties are often expressed with permittivity:

$$\varepsilon^* = \varepsilon' - j\varepsilon''$$

where the real part ε' is the dielectric constant, which represents the energy storage and the imaginary part ε'' is the dielectric loss, which represents the energy dissipation.

Permittivity was measured with a vector network analyser (VNA) and an open-ended coaxial probe. A VNA measures the transmission and reflection of an applied signal. An open-ended coaxial probe is a coaxial line that is a cut-off section of a transmission line. Measurements with an open-ended coaxial probe rely on analysis of the reflection of the electric field from the boundary between the probe and the material under test. The electric wave propagates along the coaxial line towards the material under test, and when there is an impedance mismatch between the probe and the sample, a reflection will occur. The reflected signal is returned to the VNA to be converted into complex permittivity values. Figure 1 shows the current density from a COMSOL simulation of the probe in contact with water.

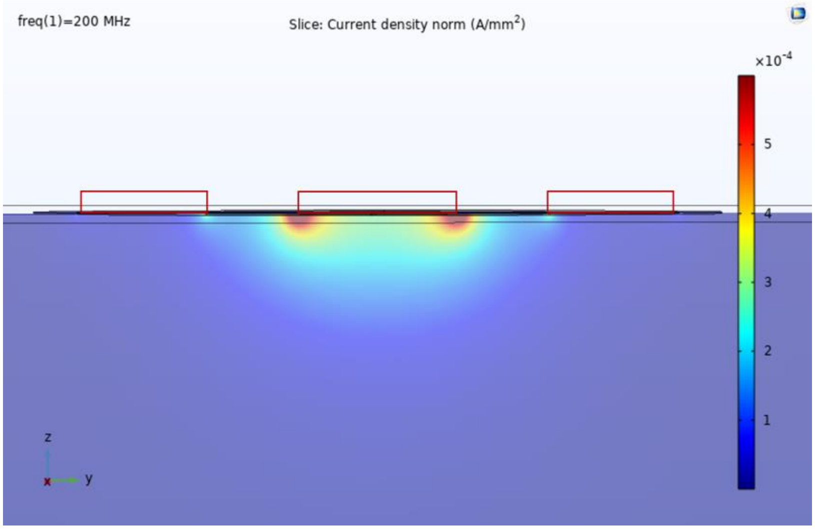

Figure 1. Current density plot of coaxial probe electrodes in contact with water

The distribution of the current density plot in figure 1, indicates the area of sensitivity around the probe electrodes in a liquid environment. The DAK 3.5 probe (inner and outer conductor dimensions are a = 0,93 mm and b = 3,5 mm, respectively.) from Schmid & Partner Engineering AG, Switzerland, which measures in the frequency range 200 MHz - 20 GHz and the R140 VNA from Copper Mountain Technologies, which measures from 200 MHz to 20 GHz were used to study the dielectric properties of three molecules; GABA (γ-aminobutyric acid), dopamine and proline. Combining the frequency limitations of the probe and the VNA, the frequency range for our experimental setup was 200 MHz - 14 GHz.

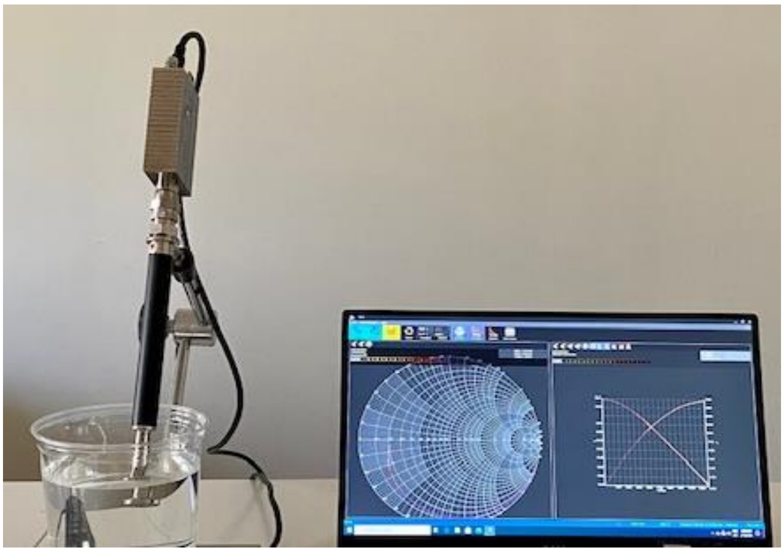

Figure 2. Instrumental setup.

3. Results

The three amino acids each gave a distinct contribution to the dielectric properties of mixture solution under measurement.

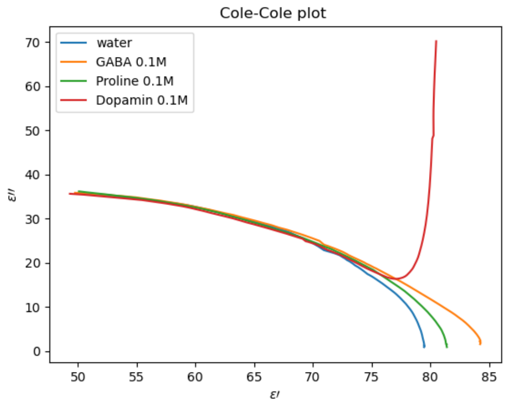

Figure 3. Cole-Cole plot of GABA, dopamine and proline solution of the same concentration. Measurement frequency range was 200 MHz - 14 GHz.

Figure 3 shows a Cole-Cole plot of three molecules with concentration 0.1 M at 22 °C together with pure water for comparison. The three molecules respond differently due to their electrical properties and geometries resulting in diffences in the measured permittivity. Dopamine showed an oppsite behavior in the low frequency region compared to the other two molecules. GABA had a higher dielectric loss in the low frequency region compared to proline, possibly caused by different molecular conformation and thus dipole moment.

4. Discussion

Dielectric relaxation spectroscopy can be used to study neurotransmitters, where the conformation of molecules can be investigated under different temperature conditions. Knowledge of specific molecular conformation is important as it to a certain degree determines whether the neurotransmitters can successfully bind to their respective receptors and therefore have an inhibitory/excitatory effect on the signaling in the brain.

Our group has previously studied the dielectric properties of the neurotransmitter GABA (γ-aminobutyric acid), which is an inhibitory neurotransmitter primarily located in the animal brain [1]. We used a two-pole Cole-Cole equation (one accounts for the GABA molecules and the other one accounts for the water molecules) to model the measured permittivity data. We investigated the effective dipole moment of the GABA molecule and the interaction strength between neighboring molecules under different temperatures and concentrations. Interestingly, we observed a resonance behavior with high concentrations of GABA at physiological temperature, where the dielectric properties suddenly changed at certain temperatures [1].

It is important to study the dielectric properties of dopamine as it is a vital neurotransmitter in the brain, it sends messages between the nerve cells, and correct conformation and concentration are essential for successful signal transfer and thus regulation of the brain activity. Proline is a metabolic precursor of GABA and as it shares similar structures with the GABA molecule, with one additional carbon atom for proline. Thus, it is important to compare the dielectric properties of these two molecules. First to investigate whether dielectric relaxation spectroscopy can detect the small difference between similar molecules, second, to study how these molecules respond differently to the electric field and thus be able to differentiate them.

Knowledge about the dielectric properties of amino acids is lacking, and future investigations on the concentration and temperature dependence of these molecules can be carried out by dielectric relaxation spectroscopy non-invasively to better understand the mechanism of the neurodegenerative diseases.

5. Conclusions

Dielectric relaxation spectroscopy is a powerful tool to study the geometric and dielectric properties of molecules. Based on the permittivity measurements on neurotransmitters, we gain knowledge about their response to electric fields, which in turn gives information about their respective molecular conformation. In addition, this technique can be used to measure the unknown concentrations of neurotransmitters, which enables us to monitor the concentration change in patients with neurodegenerative diseases that are related to lack of neurotransmitters. This can potentially be implemented through a miniaturized implantable device.

References

1. Hou, J., Abie, S.M., Strand-Amundsen, R. et al. Temperature dependence of the microwave dielectric properties of γ-aminobutyric acid. Sci Rep 11, 18082 (2021). https://doi-org.ezproxy.uio.no/10.1038/s41598-021-97178-7

Proceedings of the International Conference of Bioelectromagnetism, Electrical Bioimpedance,
and Electrical Impedance Tomography June 29 – July 1, 2022 / Kyung Hee University, Seoul, Korea

Blood viscosity on glucose level using electrical impedance spectroscopy

Bruna Gabriela Pedro[1,2], Pedro Bertemes Filho[1,2]
[1] State Univertisy of Santa Catarina , Joinville, Brazil
[2]Department of Electrical Engineering

Correspondence : Bruna Gabriela Pedro, e-mail : bruna.pedro@edu.udesc.br

Abstract− Human blood is primarily composed of plasma and hematocrit, and the complications of diabetes change all these parameters by generating severe chronic complications. For patients with longterm disease, the study of blood rheology points out effects of hardening of red blood cells and changes in blood viscosity. These changes are generated by oxidative stress, which turns into a vicious cycle and worsens the disease condition. Bioelectrical impedance analysis (BIA) has been used to develop non-invasive glucose measurement devices for continuous monitoring. This work presents a mathematical modeling of the electrical impedance as a function of glucose concentration. It is obtained by interpolating the Drude, Krieger and Bruna mod- els. The plasma viscosity is related to blood conductivity whereas the equation parameters to the electrical impedance modulus. The proposed model predicted the glucose level closer to the gold standard one.

Keywords : Bioimpedance; Blood glucose; Mathematical modeling; Plasma viscosity

1. Introduction

The chronic complications of diabetes are particularly serious. They reach a large number of diabetic patients a few years after the beginning of the syndrome. They determine morbidity and mortality and can be divided into vascular and non-vascular complications. The etiopathogenesis of the chronic complications of the disease is characterized by diabetic microangiopathy, diabetic retinopathy, nephropathy andblood viscosity (da Silva Azevedo 1986).

It is evident that poor management of the disease triggers poor quality of life (Somer and Meiselman 1993)(Baynes 1991)(da Silva Azevedo 1986) and high costs to the health system (Bertemes-Filho 2016). Therefore, research on non-invasive glucose measurement devices has been developed with the aim of pro- viding continuous monitoring and without protrusions on the patient's fingers. Bioelectrical impedance spectroscopy is one of the techniques used and that seeks to improve data processing such as artificial neural networks (ANNs) (Bertemes-Filho 2016) and analytical models (Pedro at al 2020a).

ANNs are statistical tools that use a group of sample data to find patterns (Alves 2007). However, it has some disadvantages in relation to the analytical model, for example: having a mar- gin of error that grows as the measurement moves away from the samples and not providing a correlation between other parameters of the system. Whereas, an analytical model has only propagated errors and the explicit relationship of the parameters (Pedro et al 2020b).

A mathematical model is a scientific model that uses mathematical formulas to express relationships, predictions, variables, parameters, entities and relationships between variables (Friedenthal et al 2015). Therefore, the understanding of the determining parameters and changes of a system must be analyzed and subsequently connected to the resulting effects. In the case of an analytical model for blood glucose detection using electrical impedance spectroscopy, a deeper understanding of bloodrheology is relevant.

Blood is a suspension composed of two phases, a continuous aqueous phase represented by plasma that contains salts, sugars, proteins and another discrete phase that includes leukocytes, platelets and erythrocytes, which constitute more than 99.5% of the particulates. Plasma is a Newtonian fluid, but blood has a non-Newtonian behavior, mainly due to the presence of red blood cells (Pereira et al 2015). It features characteristics of Bingham fluids, pseudoplastics and concentrated emulsions. The main rheological property of the blood studied is the ap- parent viscosity of the blood, scaled by the viscosity of the plasma (de Carvalho and de Oliveira 2006).

Some of the determinants of blood viscosity are erythrocyte mass, their deformability and aggregation, and also the concentration of plasma proteins. Decreased erythrocyte de- formability has several causes: alteration of hemoglobin (glycosylation, autoxidation, abnormal hemoglobins, etc.), alteration of membrane lipids (altered phospholipid/cholesterol ratio and formation of lipoperoxides), accumulation of sorbitol and glycosylation of membrane proteins (mainly spec- trin, makes the globule more rigid and less deformable) (da Silva Azevedo 1986).

In advanced stages of diabetes complications, whether due to ignorance or indiscipline, erythrocytes undergo deformations such as anisocytosis and poikilocytosis due to the stiffening of the red blood cell wall, leading to crenation (Somer and Meiselman 1993). Stiffening of red blood cells occurs because blood glucose eigenvalue leads to electrolyte imbalance in cell membrane and also to oxidative stress which is one of the main causes of cell damage (Baynes 1991)(da Silva Azevedo 1986). Consequently, cells aggregate more easily and cannot bend to pass through narrower pathways such as capillaries (Somer and Meiselman 1993).

Another problem is the decrease in plasma proteins that cease to exert osmotic functions due to glycosylation[2], phenomena such as fructosamine and solvation are part of the vicious cycle that is oxidative stress leading to dehydration, kidney overload, increased blood pressure and ketoacidosis.

These changes in blood viscosity of blood in diabetic patients are discussed in numerous works, among them (Somer and Meiselman 1993) shows in Figure 1 that there is a linear behavior of viscosity for measuring only plasma and plasma containing rigid cells, showing that the viscosity of the solution with the granulated bodies has higher viscosity. It also shows the non-linear behavior of the viscosity of plasma containing normal cells and plasma containing normal cells and fibrinogen, the difference of which resulted in lower levels of aggregation of red blood cells. If the behavior of the curve with rigid cells is analyzed in relation to normal cells and fibrinogen, it is evident that there is a change in viscosity from diabetic to normal blood, justified by changes in the rigidity of red blood cells and the imbalance of plasma proteins.

Another article that corroborates is (Desouky 2009) for studies of the rheological and electrical properties of blood states that the viscosity is higher in diabetics, resulting in greater aggregation and less deformity of red blood cells, the dielectric con-stant and conductivity are also higher for patients with the disease, as reported in (Abdalla et al 2010).

In the literature review, it was found that hematocrit, fibrinogen and temperature were influential factors in blood viscosity (Oliveira 2009)(Hund et al 2017). However, factors such as glucose and albumin identified in (Pedro and Bertemes-Filho 2021) are not mentioned.

In this article, an interpolation of the Krieger model adapted for blood (Hund et al 2017) with the model for water viscosity as a function of glucose given by (Ferreira 2018) in addition to the introduction of the albumin and glucose factor in the plasma viscosity is made. It also investigates the influence of glucose variation on plasma viscosity in the Bruna model proposed in (Pedro et al 2020a).

2. Mathematical Models

2.1 Bruna model

The interpretation of the relaxation time presented in Bruna model (Pedro et al 2020a) represents the time response due to the applied electric field into the sample under study. This might be explained by the orientation of the particles inside the sample in order to have the minimum resistance of the dielectrophoretic force (Abdalla 2010) The model considers the red blood cells as spheres surrounded by an insulating layer, which, when subjected to the action of an external electric field, present polarization. The blood sample may also contain proteins and glucose molecules as non-conducting spheres. The red blood cell and protein spheres rotate in response to the electric field and are opposed by frictional interaction with the surrounding viscous fluid. The relaxation time in response to this orientation is given by:

$$\tau = \frac{4\pi R^3}{\kappa T}\eta \tag{1}$$

where τ is the relaxation time, R is the radius of the sphere, κ is Boltzmann's constant, T is the absolute temperature and η is the viscosity of the composite matrix.

2.2 Drude model

Drude's theory is an application of the Kinetic Theory of gases to electrons in a metal and based on Newton's Laws. According to Drude, the electronic charge transport is due to the random movement of free and independent electrons, which are scattered by the immobile ions during collisions (Rocha et al 2015). The free electron model describes the process of electrical conduction in metals and provides an estimate of the value of conductivity in terms of intrinsic properties of metals (Cardona and Peter 2005), then:

$$\sigma = \frac{ne^2\tau}{m_e} \tag{2}$$

where n the number of electrons, e is the electron charge, m_e is electron mass and τ scattering time.

The model is adapted for red blood cells and glucose atoms immersed in the plasma of the blood. The free particles are the ions and electrons released in the process of glucose hydrolysis. Therefore:

$$\sigma = \frac{nq^2\tau}{m_q} \tag{3}$$

where n is the number of free particles carrying charge in the solution (ions and electrons), q the particle charge, m_q particle mass and τ the scattering time.

2.3 Adapted Krieger model for blood viscosity

According to (Hund et al 2017), the blood viscosity can be described as:

$$\eta = \eta_{pl}\left(1 - \frac{Hct}{Hct*}\right) \tag{4}$$

where η_{pl} is the plasma viscosity, $\frac{Hct}{Hct*}$ is the volumetric fraction of red blood cells.

The parameter n_{pl} is given by:

$$\eta_{pl} = \overline{\eta_{pl}}\left(1 + \left(\alpha[LM] - \overline{[LM]}\right)\right)\left(\frac{T}{\bar{T}}\right)^b \tag{5}$$

where the slashed terms are reference values for a normal (healthy) case, α is the proportionality values, $[LM]$ represent large molecules, b is a constant and T is the absolute temperature.

2.4 Viscosity as a function of glucose concentration

The models for blood viscosity listed in the literature do not include albumin or glucose concentration. However, (Ferreira 2018) presents results of the change in viscosity of the solution composed of water (solvent) and glucose (solute) and indicated that it has the following behavior:

$$\ln \eta = D + \frac{B}{T} + Cw_1 \tag{6}$$

where η is the viscosity, T is the temperature and w_1 is the mass fraction of solute (same meaning of k' in the Bruna model). D, B and C are adjustable parameters.

3. Proposed analytical model

The improvement of the Bruna model considers the impedance modulus as a function of glucose concentration.

3.1 Plasma viscosity

The viscosity of blood plasma can be given as a linear relationship of the viscosity of water (Oliveira 2019).

Taking into account other blood proteins, such as albumin, equation 5 can be rewritten by:

$$\eta_{pl} = e^{\left(D + \frac{B}{T} + Ck'\right)}\sum\left(1 + \left(\alpha[LM] - \overline{[LM]}\right)\right)\left(\frac{T}{\bar{T}}\right)^b \tag{7}$$

Considering both temperature and amount of proteins constant, then the viscosity can be described by:

$$\eta_{pl} = Ae^{Ck\prime} \tag{8}$$

Where

$$A = e^{\left(D + \frac{B}{T}\right)}\sum\left(1 + \left(\alpha[LM] - \overline{[LM]}\right)\right)\left(\frac{T}{\bar{T}}\right)^b \tag{9}$$

3.2 Plasma conductivity

Replacing equation 8 into 1, then:

$$\tau = \frac{4\pi R^3}{\kappa T} A e^{Ck'} \tag{10}$$

Replacing τ in equation 3, the plasma conductivity (σ_h) is given by:

$$\sigma = \frac{nq^2}{m_q}\frac{4\pi R^3}{\kappa T} A e^{Ck'} \tag{11}$$

If the different parameters of glucose are constant, then:

$$\sigma = B e^{Ck'} \tag{12}$$

where

$$B = \frac{nq^2}{m_q}\frac{4\pi R^3}{\kappa T} \tag{13}$$

3.3 Blood´s electrical conductivity effect at Bruna model

According to (Pedro at al 2020a), the electrical conductivity of blood is:

$$\sigma_m = (1 - k + k')^{\frac{3}{2}}\ \sigma_h \tag{14}$$

where σ_m is the blood conductivity, σ_h is the plasma conductivity, k is the volumetric fraction of red blood cells and k' is the volumetric fraction of glucose.

The parameter $(1 - k + k')$ decreases as increasing red blood cells which, in turns, increase due to glucose level. However, when considering the influence of glucose on plasma viscosity, it is necessary to substitute, σ_h from equation 12 into 14, then:

$$\sigma_m = (1 - k + k')^{\frac{3}{2}}\ B e^{Ck'} \tag{15}$$

3.4 Electrical impedance versus glucose concentration

In order to correlate the modulus of the electrical impedance ($|Z|$) with the electrical conductivity, then σ_m of equation 15 and τ of equation 10 are used, so that:

$$|Z| = a\sqrt{1 + \frac{(f^2+b)^2}{f^2(cf^2+d)^2}} \tag{16}$$

where

$$a = \frac{L}{AB^4}\frac{1}{e^{4Ck'}(1-k+k')^6} \tag{17}$$

$$b = \frac{2R^3A^2}{\kappa T}\ e^{2Ck'} \tag{18}$$

$$c = \frac{2\pi(\varepsilon_\infty - \Delta\varepsilon)}{Be^{Ck'}(1-k+k')^{\frac{3}{2}}} \tag{19}$$

$$d = \frac{\varepsilon_\infty 2R^2 m_p A}{nq^2\kappa T}\frac{e^{Ck'}}{e^{4Ck'}(1-k+k')^6} \tag{20}$$

In order to assess the relative variation of $|Z|$ in terms of glucose concentration k' and frequency f, equation 16 was normalized and rewritten in terms of $e^{Ck'}$, $(1 - k + k')$ and f, so that:

$$|Z| = a'\frac{1}{e^{4Ck'}(1-k+k\prime)^6}\sqrt{1+\frac{\left(f^2+b\prime e^{2Ck'}\right)^2}{f^2\left(\frac{c\prime}{e^{Ck'}(1-k+k\prime)^{\frac{3}{2}}}f^2+d\prime\frac{e^{Ck'}}{e^{4Ck'}(1-k+k\prime)^6}\right)^2}} \tag{21}$$

where

$$a' = \frac{L}{AB^4} \tag{22}$$

$$b' = \frac{2R^3A^2}{\kappa T} \tag{23}$$

$$c' = \frac{2\pi(\varepsilon_\infty - \Delta\varepsilon)}{Be^{Ck'}} \tag{24}$$

$$d' = \frac{\varepsilon_\infty 2R^2 m_p A}{nq^2\kappa T} \tag{25}$$

Equation 21 was plotted considering parameters a', b', c' and d'equal to unit. The value of the volumetric fraction of red blood cells was set to 45% (Somer and Meiselman 1993), then $k = 0.45.$ A frequency has its values between 0.5 and 1.0, this facilitates the visualization of glucose changes, as values of higher orders of magnitude can be considered as incorporated into the system constants. Figure 1 shows the impedance spectra for a glucose concentration (k') range of 4.0 to 6.8 mmol/L. It can be observed that the impedance modulus decreases as glucose concentration increases whereas frequency increases, which was also observed by (Pedro et al 2020b) and (Kamat 2014).

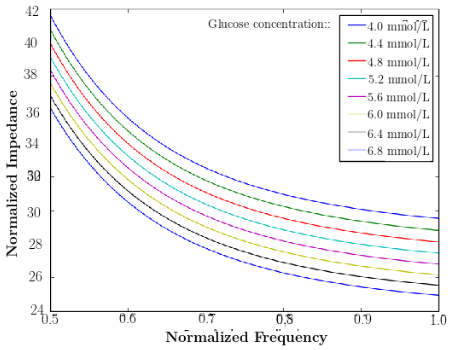

Figure 1. Normalized electrical impedance as a function of normalized frequency and glucose concentration.

4. Discussions

It should bear in mind that blood were considered particles suspended in a conducting fluid and it contains different types of particles with different masses. Micro-masses form electric dipoles under an electric field. Then, heavy cells form freely rotated dipoles which have a more significant rotational motion in comparison to lighter particles and lesser linear motion. In contrast, lighter cells have higher drift speed in a linear motion and less significant rotational motion. In other words, larger particles such as hemoglobin and glucose are responsible for changing blood viscosity, while ions are responsible for electrical conductivity. These findings were observed in the proposed model.

According to the proposed model, it can be shown that the plasma conductivity depends only on charged molecules. If we write σ_h as a summation for each individual particle, then:

$$\sigma_{h_i} = \textstyle\sum_i^n \sigma_{h_i} \tag{26}$$

where

$$\sigma_{h_i} = \frac{n_i {q_i}^2 \tau_i}{m_{q_i}} \tag{27}$$

Large particles (e.g., hemoglobin and glucose) have zero charge, then resulting in a null respective σ_{h_i}. This implies that all charge transport is done by the charged particles of the solution. Therefore, the contribution of insulating particles is much more affected by the free path of the conducting particles, as predicted by the Drude model. This effect can be represented in figure 2, which shows that the increase of fixed particles increases the travelling path along the solution. As a result, the changes in conductivity cannot be observed due to the increase in the scattering/relaxation time. On the other hand, there is an increase in the amount of conducting particles in the solution, since chemical phenomena due to glucose reaction releases electrons (Pedro and Bertemes-Filho 2021)(Baynes 1991)(Somer and Meiselman 1993).

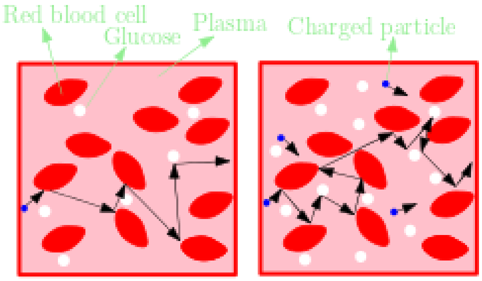

Figure 2. Representative impacts of the non-conducting particles in the solution conductivity due to glucose hydrolysis.

The glucose concentrations of previous models (Pedro and Bertemes-Filho 2021)(Pedro et al 2020a)(Pedro et al 2020b) are described in mmol/L. However, the influence of glucose due to red blood cells and frequency were not analyzed. Therefore, a fair comparison between these models to the proposed one here should be considered.Then, the mathematical models are written as follows:

$$|Z_{norm}| = \sqrt{\frac{a}{(1-k+k\prime)^3} + \frac{(b+cf^2)^2}{f^2(g+df^2)^2}} \tag{28}$$

where $|Z|$ is the impedance described by model in \cite{eu}, parameters a, b, c, d and g are equal to unit, $k = 0.45$ e $f = [0.5{:}\ 1.0]$according to figure 3.

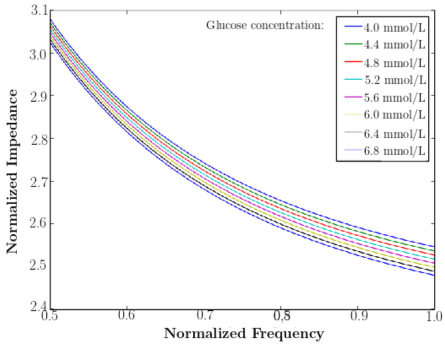

Figure 3. Normalized electrical impedance as a function of normalized frequency and glucose concentration, according to equation 28.

It can be observed that the impedance values are greater than the ones predicted by equation $|Z_{norm}|$. This allows a better identification between the spectrum of $|Z(k', f)|$ and $|Z(k' + \Delta k', f)|$, where $\Delta k'$ is the change in glucose concentration. For example, a change in glucose from 4.0 to 4.4 mmol/L gives a $\Delta k' = 0.000172$, which results in $\Delta|Z(f = 0.5)| = 0.00783$ (equation 21) and 0.8211 (equation 28). It can be observed that the real impedance change is about 105 times higher than it was predicted by (Pedro et al 2020).

It can also be observed that the impedance decreases more rapidly as increasing frequencies for all glucose concentration, in contrast to what it was found in (Pedro et al 2020). It should be emphasized that other types of parameters, such as temperature, mass, charge, particle radius and plasma proteins, need to be taken into account for a more complete and accurate model, as mentioned in (Ferreira 2018).

4.1 Conclusions

It was showed that both impedance modulus and conductivity of blood takes into account hematocrit concentration, temperature, plasma proteins, permittivity, charge, mass, and particle radius, frequency and glucose concentration. By adding glucose and albumin into blood, it was also found that the plasma viscosity may change the conductivity or impedance of the solution. These findings might be useful for non-invasive glucose measurement devices.

References

Abdalla, S., Al-Ameer, S., e Al-Magaishi, S. (2010). *Propriedades elétricas com relaxamento através de humanos sangue*. Biomicrofluídica 4, 034101.

Alves, D.M. (2007). *Quantificação da glicemia através da análise de imagens da íris humana usando redes neurais* (Tese de Doutorado, Universidade do Estado de Santa Catarina).

Ashcroft, N.W., & Mermin, N.D. (1976). *Física do estado sólido*.

Baynes, J.W. (1991). *Papel do estresse oxidativo no desenvolvimento de complicações no diabetes.* Diabetes, 40(4), 405-412.

Razera, T. M., Korbes, G. D. F., Bertemes Filho, P., Paterno, A. S., Sommacal, L. F., Pogere, A., & Dias, D. D. C. (2016). *Reconhecimento de padrões para classificação da impedância elétrica do tecido cervical*. J. informe de saúde, 829-838.

Cardona, M., & Peter, Y.Y. (2005). *Fundamentos de semicondutores* (Vol. 619). Springer-Verlag Berlim Heidelberg.

de Carvalho, J. A. A., & de Oliveira, T. T. (2006). *Mecânica dos fluidos aplicada a escoamento do sangue na microcirculação*.

Desouky, O.S. (2009). *Comportamento reológico e elétrico dos eritrócitos em pacientes com diabetes mellitus*. Rom J Biophys, 19(4), 239-250.

Ferreira, A.F.B. (2018). *Determinação de propriedades volumétricas e de transporte de diferentes tipos de carboidratos em meio aquoso.*

Friedenthal, S., Moore, A., & Steiner, R. (2015). *Integrando sysml em um ambiente de desenvolvimento de sistemas*. Um Guia Prático para SysML (Terceira Edição), terceira edição, Morgan Kaufmann, 507-541.

Hund, S.J., Kameneva, M.V., & Antaki, J.F. (2017). *Uma representação matemática quase mecanicista para a viscosidade do sangue.* Fluidos, 2(1), 10.

Kamat, D.K., Bagul, D., & Patil, P.M. (2014). *Medição da glicemia pela técnica de bioimpedância*. Avanços em Eletrônica, 2014.

Oliveira, P. (2009). Viscosidade do sangue. UBI, 034101

Pedro, B. G., Marcôndes, D. W. C., & Bertemes-Filho, P. (2020a). *Analytical model for blood glucose detection using electrical impedance spectroscopy*. Sensors, 20(23), 6928.

Pedro, B. G. Marcôndes, D. W. C., and Bertemes-Filho, P. *Modelo analítico para o cálculo do nível de glicose no sangue usando espectroscopia de impedância elétrica*. In: Congresso Brasileiro de Engenharia Biomédica, 2020b, Vitória. Anais do XXVII Congresso Brasileiro de Engenharia Biomédica 1, 1–4

Pedro, B. G., & Bertemes-Filho, P. (2021, August). *Glucose detection of ringer-lactate solution using electrical bioimpedance: preliminary results*. In Journal of Physics: Conference Series (Vol. 2008, No. 1, p. 012003). IOP Publishing.

Pereira, M., Malagoni, R., & Finzer, J. (2015). *Reologia do escoamento do sangue em sangue.* Blucher Chemical Engineering Proceedings, 1(3), 2135-2140.

Pérez, C.A.S. (2000). *O modelo do elétron livre de Drude completa 100 anos*. Caderno Brasileiro de Ensino de Física, 17(3), 348-359.

Rocha, R.P. (2015). *Tempo de relaxamento em sistemas moleculares desordenados*.

Somer, T., & Meiselman, H.J. (1993). *Distúrbios da viscosidade do sangue*. Annals of Medicine, 25(1), 31-39.

Proceedings of the International Conference of Bioelectromagnetism, Electrical Bioimpedance,
and Electrical Impedance Tomography June 29 – July 1, 2022 / Kyung Hee University, Seoul, Korea

Impact of Aortic Wall Stiffness on the Morphology of Impedance Cardiography Signal

Vahid Badeli[1], Eniz Museljic[1], Alice Reinbacher-Köstinger[1], Manfred Kaltenbacher[1]
[1]Institute of Fundamentals and Theory in Electrical Engineering, Graz University of Technology, Graz, Austria

Correspondence : Vahid Badeli, e-mail : vahid.badeli@tugraz.at

Abstract–Aortic wall stiffness plays a significant role in accelerating the risk of cardiovascular diseases and causes hemodynamic changes in the aorta. The aorta significantly contributes to the thoracic impedance measurements with impedance cardiography. In this study, a 3D finite element simulation model has been set up to investigate the impact of aortic wall stiffness on the morphology of the impedance cardiography signal. The results agree with experimental studies and show a possible reason for the inaccuracy of hemodynamic monitoring in older patients with impedance cardiography.

Keywords: Aortic wall stiffness; bioimpedance; impedance cardiography; numerical simulation.

1. Introduction

Aortic stiffness occurs when the aorta's wall thickens and loses elasticity over time, increasing the pulse wave velocity (PWV) [Sun Z 2015]. This condition is a hallmark of aging, and classic cardiovascular risk factors play a role in accelerating this process. Aortic stiffness has been linked to an increased risk of atherosclerotic heart disease, myocardial infarction, heart failure, and stroke [Sethi et al. 2014]. Model-based studies estimate that 1.56 billion people worldwide may be affected by systemic arterial hypertension by 2025 [Zimmermann et al. 2021]. The necessity of preventive care has led to a growing interest in the non-invasive evaluation of aortic stiffness. Therefore, monitoring aortic wall stiffness has become increasingly important and could guide treatment strategies and the prevention of systemic arterial hypertension [Sethi et al. 2014]. Impedance cardiography (ICG) is a non-invasive, convenient, and cheap method to diagnose several cardiac diseases by measuring the human thorax impedance changes, see Figure 1. These impedance changes partially originate from the blood flow pulsation into the aorta because of the higher electrical conductivity of the blood-filled aorta compared to that of the surrounding tissue types [Badeli et al. 2020]. However, the morphology of the signal is still not accurately known [Tronstad et al., 2019]. The experimental study of Tronstad et al. has shown the age-related differences in the morphology of the ICG signals. Tronstad et al. indicated a measurable difference in ICG morphology between young and older persons. The measurable difference is most probably a result of the physiological changes in the vascular system due to stiffening arteries [Tronstad et al., 2019]. Thus, hemodynamic measurements of the older patients by ICG might result in wrong evaluations due to aortic wall stiffness. In this work, a 3D simulation model of the human thorax with ICG measurement has been set up to investigate the impact of aortic wall stiffness on the morphology of the ICG signal.

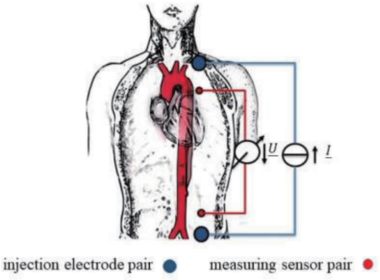

Figure1. Tetrapolar spot electrode configuration of ICG.

2. Methods

2.1 Sources of the ICG signal

The thoracic impedance changes originate from several sources such as heart contraction, blood perfusion into the lungs, blood flow-induced conductivity change, deformation and movement of organs, and volumetric changes of the aorta and arteries leading to expansion and contraction [Sitter et al. 2016]. Furthermore, various electrode configurations provide the impedance changes of different regions of the human thorax with different sensitivities even though the impedance waveform may look similar [Sitter et al. 2016]. Thus, as suggested in [Sitter et al. 2016], the spot electrode configuration is more suitable for measuring cardio-synchronous impedance changes while the oscillating respiratory component can be filtered out due to a different frequency than the cardiac cycle. In addition, the simulation study in [Badeli 2020] showed that for such a setup, the blood flow-induced conductivity changes and the volumetric changes of the aorta are the main factors in defining the significant features of the ICG signal. Thus, since the discrepancy between compliant and stiff aorta matters in this work, only these two factors will be considered sources of the thoracic impedance changes. Static thoracic base impedance $\left|\underline{\boldsymbol{Z}}_{\mathbf{0}}\right|$ is the measured electrical impedance without respiratory or cardiac activity that varies among individuals and depends on the frequency of the applied current and the electrode configuration. When the time-dependent-pulsatile impedance change $\Delta\left|\underline{\boldsymbol{Z}}(\boldsymbol{t})\right|$ is superimposed on $\left|\underline{\boldsymbol{Z}}_{\mathbf{0}}\right|$, the time-varying total transthoracic impedance $\left|\underline{\boldsymbol{Z}}(\boldsymbol{t})\right|$ is registered.

2.1.1 Blood-flow induced conductivity changes

The electrical conductivity of blood alters with hemodynamic changes in the aorta. The red blood cells (RBCs) can be considered non-conductive in frequencies up to 1 MHz [Hoetink et al. 2004]. In the stationary condition, the random orientation of RBCs induces isotropic behavior in the blood. When the heart pumps the blood into the aorta (systolic phase), the RBCs get aligned in the flow direction and deformed due to higher shear stress, particularly in the aorta's wall proximity, see Figure 2. On the one hand, this phenomenon increases the blood conductivity in the flow direction. On the other hand, the blood conductivity decreases perpendicular to the flow direction, leading to an anisotropic behavior of the flowing blood. The blood flow-induced conductivity variations can be calculated using the Maxwell-Fricke equation:

$$\frac{\sigma_c}{\sigma_p} = \frac{1 - \mathrm{H}}{1 + (\mathrm{C} - 1)\mathrm{H}}, \qquad (1)$$

where σ_c and σ_p are the conductivity values of the control volume and the plasma, respectively. H is the hematocrit value, the volume fraction of RBCs in the blood. C is the shape factor that incorporates the deformation and orientation of the RBC in a control volume and depends on the shear stress magnitude τ and the shear rate magnitude $\dot{\gamma}$ [Hoetink et al. 2004]. Shape factor C can be evaluated either considering the electrical field in the flow direction or perpendicular to it, as shown in Figure 2, reflecting blood's anisotropic behavior.

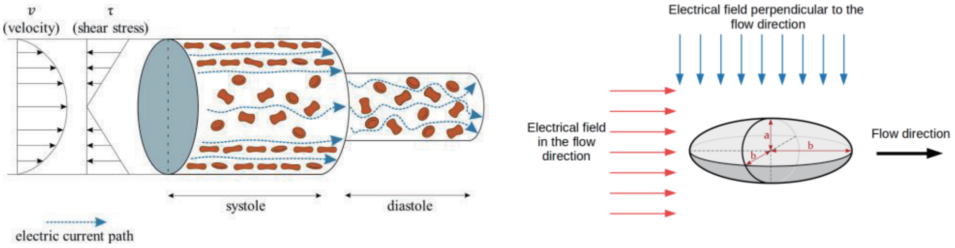

Figure 2. Left: RBCs' orientation and deformation in a blood vessel during the systole and diastole [Badeli et al., 2020]. Right: A RBC at high shear rate and complete alignment to the direction of the flow. Two electric field directions are depicted, with blue perpendicular and red parallel to the flow direction.

The method developed by [Hoetink et al. 2004] has been used to calculate the shape factor C in this work. The aorta geometry to be used in the simulation model is shown in Figure 3, divided into three segments: the inlet, the arch, and the descending aorta. Mean velocity values of the blood passing through each segment are taken from [Zimmermann et al. 2021]. They measured the flow field quantities using a patient-specific 3D printed aorta with two wall stiffness degrees, one compliant and one nearly rigid wall. The blood flow-induced conductivity changes have been evaluated for each segment using these data. Please note that only in the aortic arch, since the electric field is assumed perpendicular to the flow, the electrical conductivity perpendicular to the flow has been calculated. This argument is also suggested in [Wroteck et al., 2005]. These conductivity values will be added to the simulation model as material properties, i.e., electrical conductivity, of the respective part in the blood-filled aorta domain.

2.2 3D finite element simulation model

A 3D finite element (FEM) simulation model of the human thorax has been set up in openCFS [openCFS] to solve the time-harmonic current flow problem. Since the duration of a cardiac cycle is much higher than the period of the injection current, the simulation can be performed in the frequency domain. In the model, the aorta geometry is a simplified form of the geometry used in [Zimmermann et al., 2021]. Hypothetical sizes of lungs, spine, and heart are also considered to model the human torso. The geometrical model has been implemented and meshed in corform Cubit software [corform Cubit]. In the simulation, only geometrical changes of the aorta have been taken into account. To model the geometrical changes of the blood-filled aorta, in cases of a compliant and a stiff aorta, the mean relative radius changes of three segments of the aorta, given in [Zimmermann et al. 2021], shown in Figure 3, have been assigned to the geometrical definition of the FEM model. To each tissue in the simulation model, a respective electrical conductivity σ and permittivity ε have been allocated; see Table 1.

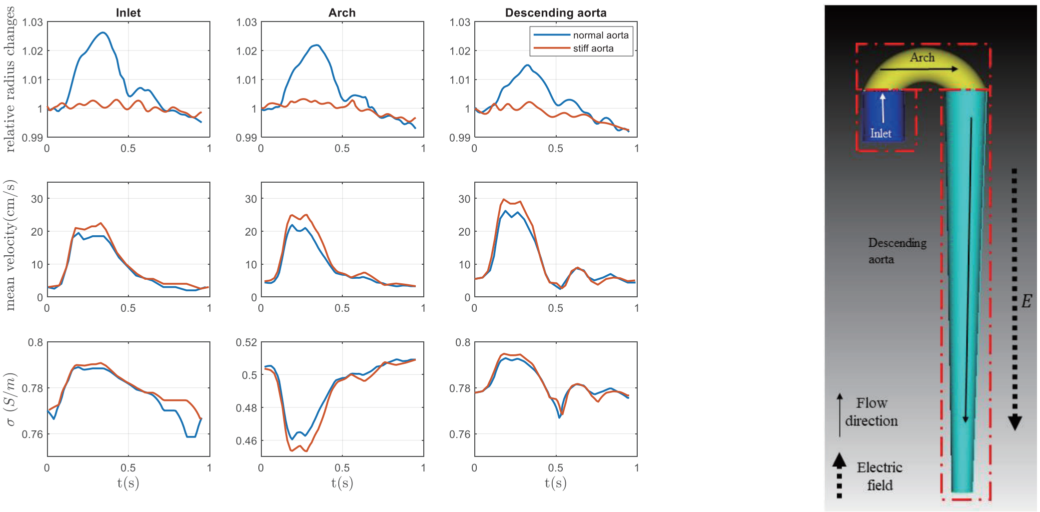

Figure 3. Right: Aorta geometry with assumed blood flow and electric field directions for evaluating the blood flow-induced conductivity changes. Left-Top: relative changes of the aortic radius. Left-Middle: mean velocity changes. Left-Bottom: electrical conductivity changes of blood during a cardiac cycle at three different aorta segments.

The calculated blood-flow-dependent conductivity, shown in Figure 3, has been assigned to the blood-filled aorta's material property, i.e., electrical conductivity. One pair of injection electrodes, and one pair of sensors between them, have been positioned on the chest. For the rest of the tissues that have not been considered, such as ribs, fat, muscles, etc., a mean value of conductivity and permittivity has been assigned to the thorax domain to reach a realistic value of the base impedance. Finally, solving Laplace's equation for electric potential V allows the evaluation of potential differences between the sensors

$$\nabla.([\sigma + j\omega\varepsilon]\,\nabla V) = 0, \qquad (2)$$

where ω is the angular frequency, σ is the electric conductivity, and ε is the electric permittivity. The boundary conditions are:

- $\int_S [\sigma + j\omega\varepsilon]\nabla V \cdot \mathbf{n}\, dS = I_0$, on the top source electrode;
- $V = 0$, on the bottom source electrode;
- $\mathbf{n}.[\sigma + j\omega\varepsilon]\nabla V = 0$, on the thorax surface

where $\mathbf{n}$ is the normal unit vector. Finally, the impedance can be calculated using Ohm's law:

$$\underline{Z} = \frac{\underline{V}_{top} - \underline{V}_{bottom}}{\underline{I}_0}. \qquad (3)$$

The injected current has a magnitude of $I_0 = 5$ mA and a frequency of 100 kHz. The negative of the first derivative of the impedance signal $-d|\underline{Z}|/dt$ is known as the ICG signal and is usually used for extracting hemodynamic parameters from the ICG measurements.

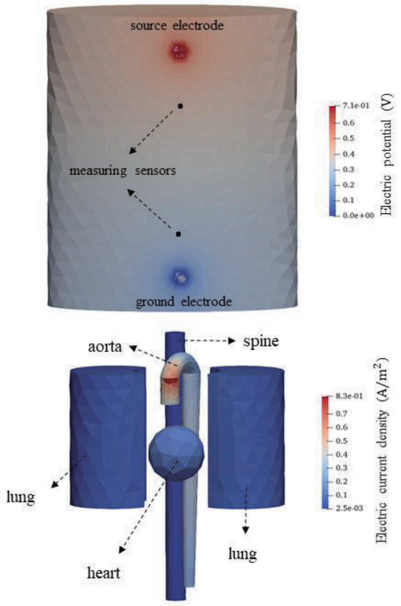

Figure 4. 3D FEM simulation model of the human thorax. Top: Thorax domain and the electric potential distribution. Bottom: Tissues inside the thorax and electric current density distribution.

Table 1. Electrical conductivity and relative permittivity of thoracic tissues [Badeli et al., 2020].

Tissue type	$\sigma\ [S.m^{-1}]$	ε_r
Lung (inflated)	0.110	2581
Bone	0.020	228
Heart Muscle	0.216	9561
Blood	$\sigma_{blood}(v(t))$	5200

3. Results and Discussion

Figure 4-Top shows the ICG electrode/sensor positions and the electric potential distribution on the thorax domain. Figure 4-Bottom shows the tissues and the electric current density distribution inside the thorax. It is evident in Figure 4-Bottom that the higher conductivity of the blood-filled aorta affects the electric conductivity distribution significantly. Figure 5-Top depicts the cardio-synchronous changes of the impedance signal for two case studies, i.e., a case with a normal (compliant) and one with a stiff aorta. It is evident from the figure that in the case of aortic stiffness due to very shallow movements of the wall, the impact of the volumetric changes of the aorta is decreased significantly. Also, the PWV increases and, therefore, mean velocity and blood conductivity at the peak systole are higher in a stiff aorta than in a normal (compliant) aorta. However, the impact of the higher blood conductivity on the ICG signal is suppressed by less wall elasticity. Figure 5-Bottom shows a comparison of the ICG signals of each case. This figure is even more informative of the former in terms of the dynamics of the aorta. The change in the morphology

of the ICG signal is noticeable and agrees with the experimental results in [Tronstad et al., 2019] that pointed out age-related differences in the morphology of the ICG signal, which is in close relationship with the aortic stiffness index. What is crucial in comparing these two signals is that in the aortic stiffness case, the signal's peak is reduced and shifted towards the left. The reason is that the signal is highly dependent on the blood-flow conductivity variations in the case of aortic stiffness. Thus, the ICG signals' peak occurs when the velocity and, consequently, the blood conductivity is the highest, while in the normal (compliant) aorta, the signals' peak happens when the aortic radius is the highest and, therefore, the most volume of the very conductive blood-filled aorta exists in the measurements domain. Based on the simulation results, the discussion above highlights the necessity of considering an aging index and aortic stiffness index when evaluating the hemodynamic parameters by ICG. By looking closer at the obtained results from this study, one can say that the dependency of the ICG signal on the blood flow is very high for the older group if we agree upon the explicit dependence of aging and aortic stiffness. From one point of view, this could be a drawback in evaluating the hemodynamic parameters by ICG. However, it allows the detection of many different aortic diseases in older groups that impact the blood flow in the aorta, such as aortic stenosis, aortic aneurysm, and aortic dissection. This argument is not only limited to the aortic stiffness and ICG but also can be extended to the application of impedance plethysmography for different arteries. Authors believe that proper simulation models, together with clinical verification, can reveal unexplained morphological aspects of the bioimpedance signals, e.g., unknown third wave seen in the plethysmography signals of the peripheral arteries in [Wiegerinck et al., 2021].

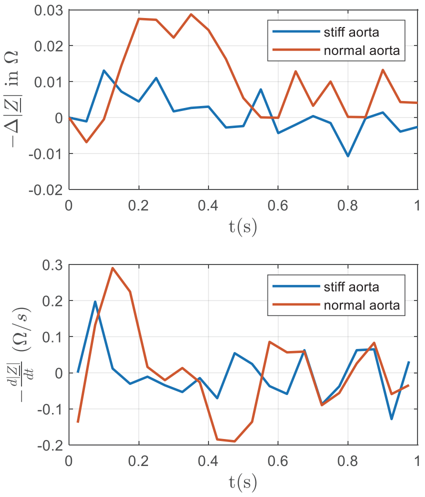

Figure 5. Top: cardio-synchronous changes of the impedance signal. Bottom: the ICG signals for two cases.

4. Conclusions

A 3D simulation model of the human thorax with ICG has been set up in this work to investigate the impact of aortic stiffness on the ICG signal. The results show a significant effect of the wall stiffness on the morphology of the ICG signal. For future work, a verification of the current findings will be done by designing clinical measurements. Also, a coupled computational fluid mechanics and finite element model will be implemented to accurately model the blood flow and the electrical conductivity of blood for simulating the ICG signal.

Acknowledgments

This work is supported by the LEAD Project "Mechanics, Modelling and Simulation of Aortic Dissection," funded by Graz University of Technology.

References

Aria S, Elfarri Y, Elvegård M, Gottfridsson A, and Grønaas HS 2019 Measuring Blood Pulse Wave Velocity with Bioimpedance in Different Age Groups Sensors, 19,4, 850.

Badeli V, Melito G. M, Reinbacher-Köstinger A, Bíró O, and Ellermann K 2020 Electrode positioning to investigate the changes of the thoracic bioimpedance caused by aortic dissection – a simulation study J Electr Bioimp, vol. 11, pp. 38-48.

Hoetink AE, Faes TJ, Visser KR, and Heethaar RM 2004 On the flow dependency of the electrical conductivity of blood IEEE Trans Biomed Eng Jul;51(7):1251-61.

https://www.opencfs.org/.

https://www.coreform.com/.

Sun Z 2015 Aging, Arterial Stiffness and Hypertension Hypertension. 65, 2, 252–256.

Sethi S, Rivera O, Oliveros R, and Chilton R 2014 Aortic stiffness: pathophysiology, clinical implications, and approach to treatment Integrated blood pressure control, 7, 29–34.

Sitter A. D, Verdaasdonk R. M, and Faes T. J. C 2016 Do mathematical model studies settle the controversy on the origin of cardiac synchronous trans-thoracic electrical impedance variations? A systematic review Journal of Physiological Measurement, 37. R88–R108.

Tronstad C, Høgetveit J. O, Elvebakk O, and Kalvøy H 2019 Age-related differences in the morphology of the impedance cardiography signal Electr Bioimp, vol. 10, pp. 139-145.

Wtorek and Polinski A 2005 The Contribution of Blood-Flow- Induced Conductivity Changes to Measured Impedance IEEE Transaction on Biomedical Engineering, VOL. 52, NO. 1.

Wiegerinck A. I. P, Thomsen A, Hisdal J, Kalvøy H and Tronstad C 2021 Electrical impedance plethysmography versus tonometry to measure the pulse wave velocity in peripheral arteries in young health volunteers: a pilot study J Electr Bioimp, vol. 12, pp. 169-172

Zimmermann J, Loecher M, Kolawole F O, Bäumler K, Gifford K, Dual S A, Levenston M, Marsden A L and Ennis D B 2021 On the impact of vessel wall stiffness on quantitative flow dynamics in a synthetic model of the thoracic aorta Sci Rep 11, 6703.

ICBEM Bioelectromagnetism ICEBI Electrical Bioimpedance EIT Electrical Impedance Tomography

Proceedings of the International Conference of Bioelectromagnetism, Electrical Bioimpedance,
and Electrical Impedance Tomography June 29 – July 1, 2022 / Kyung Hee University, Seoul, Korea

Changes in Electrical Impedance of Pork Meat during Salt Diffusion by Wet-curing with Sodium-chloride

Philipp York Zimmermann, Flóra Vitális and Eszter Vozáry
Department of Food Industrial Measurements and Process Control,
Hungarian University of Agriculture and Life Sciences, Budapest, Hungary

Correspondence : Philipp York Zimmermann, e-mail : pz@zimmermanns.hu

Abstract– During traditional curing of meat, it is important to measure the salt content of the meat so that no more salt penetrates after reaching the optimal salt concentration. The value of the electrical impedance parameters of the meat depends on the salinity. Electrical impedance spectrum inside pork loin cubes of 3,5 cm x 3,5 cm x 3,5 cm was measured between two home-made pin electrodes with precision LCR meters HP 4284A and HP 4285A in frequency range from 10 Hz to 1 MHz and from 75 kHz to 30 MHz, respectively. The impedance magnitude and phase angle was measured during curing process in 15 minute intervals for 90 minutes. The spectra after open-short correction were approached with serial connection of a resistance and a distributed element with the Solver function of Excel. The parameters of electrical model circuit were determined. The resistances, the relaxation time and exponent decreased as the salt concentration increased causing higher ion content, higher viscosity and more disorderly. A slower decrease in resistance relative to the decrease in resistance of the distributed element may indicate that the salt first penetrates into the extracellular part and only then into the cells.

Keywords: Electrical impedance spektrum, distribeted model element, salt content, meat, curing

1. Introduction

Pork salting has a long tradition and is one of the most common preservation methods in the food industry. The salt is used during pickling to preserve and improve the taste of the product (Keenan 2016). Preserving meat combines physical and chemical methods to ensure safe consumption of the product. Salting can be dry and wet. During wet curing, the meat is immersed in saline, which causes the meat to osmotically dry out (Curcic *et al* 2013; Lawrie and Ledward 2006). The two main mass transfers during the salting process are salt uptake and moisture change (Zhao *et al* 2020).

According to the healthy nutrition accepted today, it is not good to consume too much salt. Therefore, in the case of conventional salting processes, it is advisable to monitor the change in salinity and, if a microbiologically safe salt concentration level has been reached in the meat, the salting process should be stopped. The changes of electrical impedance parameters of meat can be used for the determination of salt concentration inside meat piece during curing process. Research is focused on developing new, non-destructive analytical methods that yield rapid results. In the meat industry, post-slaughter meat quality has been examined using electrical impedance spectroscopy (EIS), with various defects occurring such as pale soft exudative (PSE) meat and dark hard dry (DFD) meat (Pliquett *et al* 2003).

Several methods and tools have been developed to determine the salt concentration inside meat during conventional pickling (Garcia-Breijo *et al* 2008; Masot *et al* 2010) . From the change in the electrical impedance spectrum of the meat, the salt concentration can be determined (Kaltenecker *et al* 2013). These tests did not follow the pickling processes in time.

The aim of the present work was to determine the change in the parameters of the electrical impedance spectra measured in pork meat during wet curing as a function of the curing time and to find the relationship between the change in the parameters and the diffusion of salt.

2. Material and Methods

For the experiments, a boneless pork loin (longissimus dorsi) was purchased from the local butcher and delivered to the laboratory in a refrigerated bag with ice batteries (~ 4 ° C). Measurements were taken about 1 hour after purchase. The size of the meat sample was a 3 cm x 3 cm cube cut from the middle of the pork longissimus dorsi and weighed about 70 g.

Wet pickling was used in the experiment. To prepare the saline solution, the household salt was dissolved in distilled water (16 g NaCl / 100 g distilled water), and the solution was stored at room temperature (22 ° C) until the start of the measurement. First, the impedance of an open and a short circuit between the electrodes was measured. These measurements were later used to open-short-circuit correction the impedance spectra measured on the sample. The sample was placed in a 200 ml vessel on a wire rack. Electrodes were inserted into the freshly cut pork cube and the electrical impedance of the meat was measured without saline. This was the control measurement. The saline solution was then poured into the container and the electrical impedance spectrum of the meat was measured at 15-minute intervals for 90 minutes.

The magnitude (Z) and the phase angle (φ) of electrical impedance were measured with a Hewlett Packard (HP) 4284A and a Hewlett Packard (HP) 4285A precision LCR meters in the frequency range from 20 Hz to 1 MHz and from 75 kHz to 30 MHz, respectively. Measurements were performed in a logarithmic sequence at 99 frequencies. The measuring voltage was 1 V. The connection between the LCR meters and the computer was provided by a GPIB-USB interface. Measurements were performed using LabView software. All measured spectra were corrected for stray inductance and capacitance by a calculation recommended by HP (open and short correction).

Two stainless steel 0.4 mm thick needles were used as electrodes (Figure 1), the surface of which, except for the last 4 mm, was coated with an electrically insulating shrink tube. The two stainless steel needles were attached to a terminal block and a 50-ohm BNC coaxial cable was connected to each electrode. Each impedance spectrum was measured with two electrodes. The electrode was inserted perpendicular to the meat fibers into the meat. The distance between the two electrodes was 1 cm.

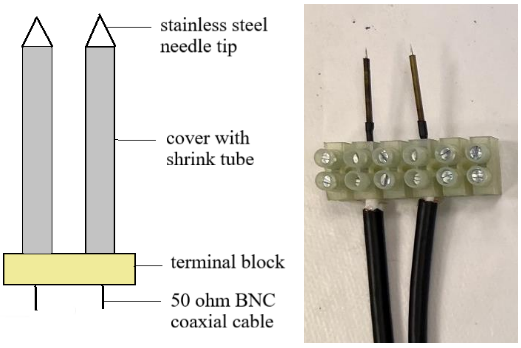

Figure 1. The structure of electrodes.

The measured and corrected spectra were approached with model circuit

$$Z = R_1 + \frac{R}{1+(i\omega\tau)^{\psi}}, \tag{1}$$

where Z is the complex impedance, R_1 and R are resistances, $\omega = 2\pi f$ is the circular frequency, f is the measuring frequency, τ is the relaxation time and ψ is the power exponent. The second member of the model circuit is the complex impedance of a non-ideal parallel RC member. The capacity is given by the expression $C = \tau/R$. Approaching calculations were performed using the Solver function of the Excel program.

The measurements were repeated four times, always with freshly purchased meat.

3. Results

At 63 Hz frequency the impedance values of each meat slice were 3395 ohms, 3685 ohms, 3553 ohms and 2665 ohms, and the phase angle values at this frequency were 27.5 °, 27.6 °, 26.1 ° and 27.5 °, respectively. In all four measurements, the magnitude of the impedance decreased with increasing salting time and the minimum value of the impedance phase angle has shifted towards higher frequencies. The value of phase angle at minimum are decreased. The spectral changes of meat electrical impedance during the salting process are illustrated by the change in the magnitude (Figure 2A) and phase angle (Figure 2B) spectra of one of the slices. The impedance spectrum of the zero-time salted meat in the saline solution showed a very small decrease in the magnitude of the impedance compared to the control, and it gave a very small shift in the phase angle. After the fourth measurement (45 min), the rate of decrease in impedance magnitude decreased. The phase angle also shifted less at the end of salting than at the beginning of the salting.

The parameters of the model (Equation (1)) fitted to the measured impedance curves, the values of the resistances R_1, R, the τ relaxation time and the ψ parameter decreased with increasing pickling time (Table 1).

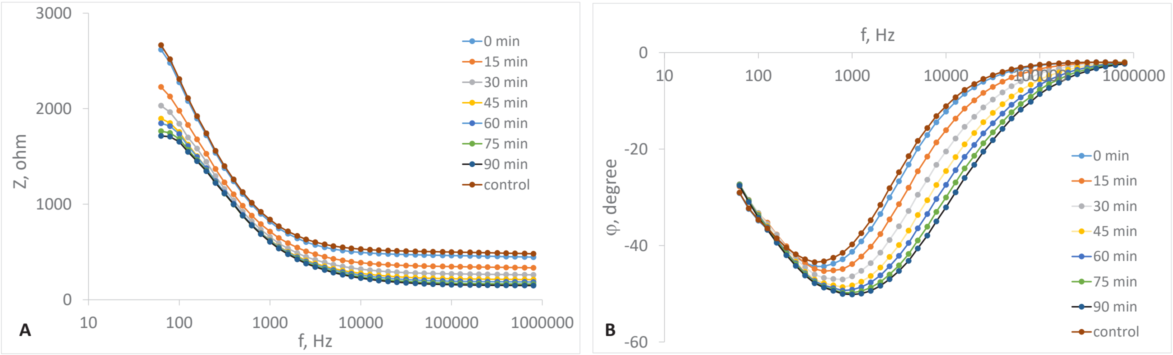

Figure 2. Impedance magnitude (A) and phase angle (B) of pork loin (Longissimus Dorsi) as a function of frequency at various curing time

The parameters R and τ reached an equilibrium value after 45-60 minutes, after a relatively short time (Figure 3 B and C). The decrease of the parameter R_1 was slower, it did not approach the equilibrium value in the examined time range (Figure 3 A).

Table 1. Parameters of fitted curves

Curing time, min	R_1, ohm	R, ohm	τ, s	ψ	C, μF	R/R_1
0 (control)	459,6	4037,8	0,002553	0,7596	63,2	8,8
0	422,6	4006,4	0,002522	0,7558	62,9	9,5
15	311,9	3341,7	0,002174	0,7409	65,0	10,7
30	238,1	3103,0	0,002030	0,7307	65,4	13,0
45	187,8	2992,7	0,001997	0,7208	66,7	15,9
60	161,8	3000,6	0,001988	0,7109	66,2	18,5
75	138,3	2957,7	0,001993	0,7007	67,4	21,4
90	125,8	3003,6	0,001988	0,6857	66,2	23,9

The equations shown in the graphs of the curves in Figure 3 give a mathematical description of the fitted curves. The time in the denominator of the fraction in the exponent is the relaxation time of each process, i.e., the time during which the initial value decreases to one-e-th. e is the Euler number. For parameters R and τ this relaxation time is very similar (~ 14 minutes), while for parameter R_1 it is much larger (35 minutes).

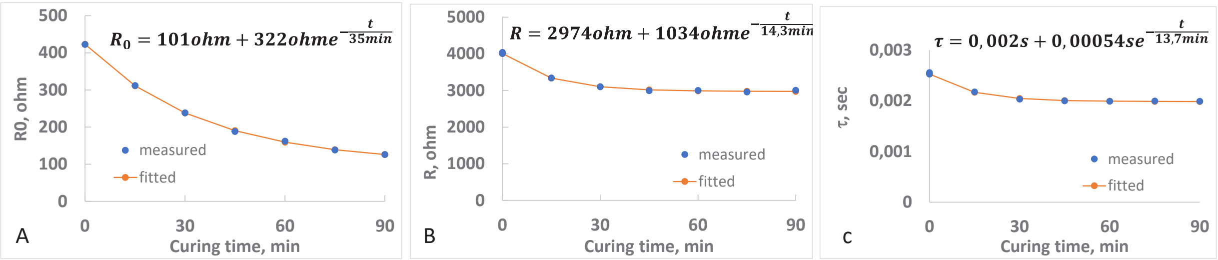

Figure 3. Changes of parameters R_1 (A), R (B) and τ (C) as a function of pickling time

4. Discussion

A decrease in the magnitude of the impedance (Figure 2A) with increasing curing time may indicate that the electrical resistance of the meat has decreased with the penetration of salt ions. The shift of the phase angle (Figure 2B) towards higher frequencies resulted in less relaxation time in Equation (1), which may indicate an increase in the polarizability of the meat tissue with increasing salt concentration. The value of parameter ψ (column 5 of Table 1) also decreased during diffusion. This indicated that after the penetration of the salt, the structure of the meat changed, became more disordered. An increase in parameter C (column 6 of Table 1) may indicate that the polarization properties of the meat have changed, and the polarizability has increased.

The circuit model (Equation (1)) we fitted to the measured impedance spectra is often used to describe the impedance of meat (Pliquett 2003). If the measuring frequency is low, the impedance is essentially equal to the sum of $R_1 + R$, which corresponds to the resistance of the intercellular part of meat tissue. If, on the other hand, the frequency is high, the impedance is essentially equal to R_1, which corresponds to the resistance of the intracellular part of meat tissue (Grimness and Martinsen 2008). Based on Figures 3 A and B, a slower decrease in R1 and a faster decrease in R may indicate that the salt enters to the intracellular part more slowly than to the intercellular part of meat tissue

An increase in the R / R_1 ratio may indicate that although the change between cells occurs more rapidly during salt diffusion, the decrease in resistance is smaller than within cells. This may be since the viscosity within the cells is lower than between the cells and the penetration of relatively little salt already can cause a significant decrease in resistance.

5. Conclusions

Electrical impedance spectroscopy was suitable for the analysis of salt diffusion in the pork meat. Based on the decrease in impedance magnitude and the impedance phase angle shift, low-frequency electrical impedance measurements can be used to monitor salt diffusion in meat tissue. The model used for the experiment also explained that the salt penetrates more rapidly between cells than within cells.

For accurate measurements, additional studies may be performed, such as comparison of chemically determined salt concentration and impedance parameters during diffusion. It is also important to know how the salt concentration and impedance parameters change as the meat size changes.

Acknowledgments

This research was supported by the European Union and cofinanced by the European Social Fund (grant agreement no. EFOP-3.6.3-VEKOP-16-2017-00005). The manuscript may include acknowledgments.

References

Curcic B Lj, Lato L, P, Levića Lj B, Kneževića V M, Nicetin M R, Filipovic V S and Kuljanin T A 2013 Osmotic dehydration of pork meat cubes: Response surface method analysis *Acta Periodica Technologica* **44** 11–19

García-Breijo E, Lato L P, Levića Lj B, Kneževića V M, Nicetin M R, Filipovic V S and Kuljanin T A 2008 Development of a puncture electronic device for electrical conductivity measurements throughout meat salting *Sensors and Actuators A: Physical* **148** 63–67

Grimnes S and Martinsen O G 2008 *Bioimpedance and bioelectricity basics* Amsterdam, New York, London: Elsevier

Kaltenecker P, Szöllősi D, Friedriech L and Vozáry E 2013 Determination of salt content in various depth of pork chop by electrical impedance spectroscopy *J. Phys.: Conf. Ser.* **434** 012094

Keenan D F 2016 Pork meat quality, production and processing on *Encyclopedia of Food and Health* Elsevier 419-431

Labrador R.H, Masot R, Alcaniz M, Baigts D, Soto J, Martinez-Manez R, Garcia-Breijo E, Gil L and Barat J M 2010. Prediction of NACL, nitrate and nitrite contents in minced meat by using a voltammetric electronic tongue and an impedimetric sensor. *Food Chemistry* **122** 864–870

Lawrie R A and Ledward D A 2006 *Lawrie's meat science* 7th ed.. Woodhead Publishing, Cambridge ISBN 10: 1-84569-161-X (e-book)

Masot R, Alcaniz M, Fuentes A, Schmidt F C, Barat J M, Gil L, Baigts D, Martinez-Manez R.and Soto J 2010 Design of a low-cost non-destructive system for punctual measurements of salt levels in food products using impedance spectroscopy *Sensors and actuators A: Physical* **158** 217-223

Pliquett U, Altmann M and Schöberlein L 2003 Py—a parameter for meat quality *Meat Science* **65** 1429–1437

Zhao X, Sun Y and Zhou Y 2020. Modeling the NACL diffusion in beef during brining process *Journal of Food Science* **85** 2852–2856

DAY 1

Wednesday, June 29, 2022

Plenary Talk 01

ISEBI Herman Schwan Award Ceremony & Award Lecture

Proceedings of the International Conference of Bioelectromagnetism, Electrical Bioimpedance,
and Electrical Impedance Tomography June 29 – July 1, 2022 / Kyung Hee University, Seoul, Korea

Bioimpedance – A Century of Research

Camelia Gabriel

As a field of study, bioimpedance is a true interdisciplinary science with a very long history and rather humble beginnings. The pioneers who helped establish this science achieved major leaps in knowledge from scant impedance measurements. They postulated and detected the presence of a resistive cell membrane as well as obtained its physical characteristics. This very early success should be remembered and acknowledged as a landmark in the history of bioimpedance research.

This opened the scope to the development of the concept of polar and polarizable molecules, and the ensuing theory of polarization. Applied to biological molecules it provided information on their dipole moment, molecular structure, shape and size. Applied to biological tissue it implied several interactions mechanisms occurring at the cellular and molecular levels. These were later confirmed and interpreted by dielectric spectroscopy. That was a landmark.

The biological consequences of the interactions of electromagnetic fields with biological systems, including people, became the focus of research worldwide. With the increase exposure of people to RF and microwave sources it became necessary to define metrics of exposure and determine safe levels. This opened the floodgates to research into bioeffects, dielectric properties and dosimetry. Another landmark was achieved.

Looking back, although progress in bioimpedance research has been continuous throughout the years, it was propelled at certain stages by landmark findings, theoretical and technical advancement and the penetration of emfs in everyday life. Today, this field of study is in the midst another paradigm step. This one belongs to the fast-developing tomographic techniques and the subject matter of this conference. Dielectric spectroscopy remains a necessary adjunct technology with some yet unresolved issues. These will be discussed and illustrated.

DAY 1

Wednesday, June 29, 2022

Oral Session 05

Bioelectromagnetism

Chair Seward B. Rutkove (Beth Israel Deaconess Medical Center)
Martin Bulst (Sciospec Scientific Instruments)

O 05-01 **Cole model in time domain**
Uwe Pliquett (Institut für Bioprozessund Analysenmesstechnik)

O 05-02 **Effect of Geometric Complexity of the Heart Model on the Inverse Problem of Electrocardiography**
R. Martin Arthur (Washington University in St. Louis)

O 05-03 **Validation of non-empirical fat-free mass estimation model for a wrist-worn device**
Aleksandr Polokhin (AURA Devices, Inc.)

O 05-04 **Robot Assisted Electrical Impedance Scanning (RAEIS): concept, and current status of development**
Zhuoqi Cheng (Mærsk Mc-Kinney Møller Institute, University of Southern Denmark)

O 05-05 **Cole bioimpedance parameters influence on strawberry ripening binary classification using decision trees**
Pietro Ibba (Free University of Bolzano-Bozen)

O 05-06 **Impedivity of various human breast tissues**
Wei Wang (Micro Image Biotech Ltd)

Proceedings of the International Conference of Bioelectromagnetism, Electrical Bioimpedance,
and Electrical Impedance Tomography June 29 – July 1, 2022 / Kyung Hee University, Seoul, Korea

Cole model in time domain

Uwe Pliquett, Danny Echtermeyer, Chris Gansauge
Institut für Bioprozessund Analsenmesstechnik e.V., 37308 Heilbad Heiligenstadt, Germany

Correspondence : Uwe Pliquett, e-mail : uwe.pliquett@iba-heiligenstadt.de

Abstract– Really measured impedance spectra can often only with difficulties and considerable effort adapted to models with ideal elements only (RLC). Models like the Cole model use fractal exponents, which allows for a high quality of fit in the frequency domain. With the help of this model, distributed properties arising for instance form individual time constants in cell suspensions or tissues, can be described. Evaluating the relaxation behavior in the time domain according to the Cole model yields either a distribution of relaxation times (DRT) or the Mittag-Leffler function (MLF), which describes a relaxation behavior between an exponential and a quadratic function. While the MLF represents generally an exact solution, this is only true for DRT in case of infinitely many relaxation times. In practice, however, it turns out that the adaptation to a DRT is considerably less computationally intensive and more robust than the adaptation to the MLF. Here it is shown that both models are theoretically equivalent, but the distributed time constants are easier to use.

Keywords: relaxation, impedance, Muttag-Leffler-function, distribution of time constants

1. Impedance of cell based material

The impedance of biological materials summarizes the electrical properties of all elements in the measurement volume. Cell-based materials have inter-individual properties such as cell size, metabolic status, and the structure of intracellular membrane systems. Each cell shows a characteristic frequency and contributes a certain amount to the total impedance. The resistance of the extracellular electrolytes, what determines the impedance at low frequencies, is mainly determined by the electrolytic conductivity but also by the volume fraction enclosed by intact cell membranes. The cytosolic electrolytes determine mostly the extent of the dispersion region (R_0-R_∞) (Foster and Schwan, 1989) (Fig.1). At low frequencies, the current through the insulating cell membranes is blocked so that the imaginary part vanishes. This applies at very high frequencies as well, at which the current flows unhindered through the cells because of the capacitively short-circuited cell membranes. The frequency at which the influence of the cell membranes leads to a minimum in the imaginary part is the characteristic frequency f_0 (Fig.1B).

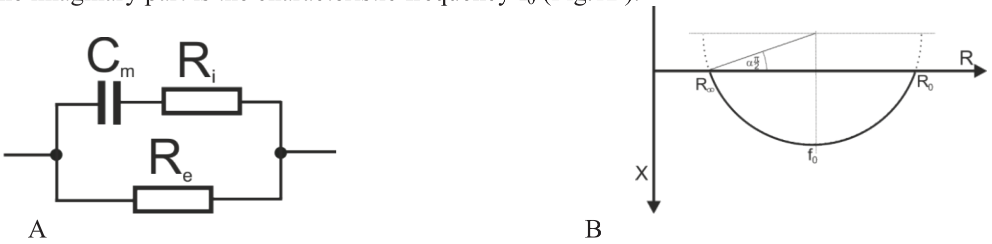

Fig. 1 (A) 2R1C-model for cell based material. C_m lumps the membrane capacity, R_i is closely connected to the intracellular resistance (cytolsol) and R_e mimics the electrolyte surrounding the cells. (B) Nyquist diagram for real objects with shifted half circle

If all individual cells had identical properties, the total impedance could be represented by ideal capacitances and resistances, as in the case of the 2R1C model (Fig.1A). This arrangement has the impedance of

$$Z = \frac{R_e + sC_m R_e R_i}{1 + sC_m(R_e + R_i)} = R_\infty + \frac{R_0 - R_\infty}{1 + s\tau_0} \qquad (1)$$

which yields an ideal semicircle as a locus diagram. It should be noted that the first term in Eq.1 corresponds to the general representation using the elements of the equivalent circuit, while the second term uses the characteristic features of the Nyquist diagram. τ is the relaxation time.

$$\tau_0 = \frac{1}{2\pi f_0} \tag{2}$$

Because of the distribution of individual cell properties (Fig.2), the semicircle for such materials is shifted along the imaginary axis (depressed semicircle). (Fig.1B).

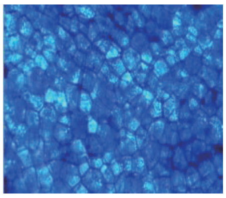

Fig. 2 Cellular structure of the potato showing different behavior of individual cells with respect to size and morphology.

R.H.Cole and K.S.Cole were the first to interpret this phenomenon in the permittivity plane and introduced a distribution of relaxation times (DRT) based on the imaginary part of the spectrum. Also known as the Cole-Cole distribution (Cole and Cole, 1941), this mathematical model uses an exponent a for the differential operator d/dt = s = σ + jω, as the distribution parameter. K.S.Cole later adapted this to the impedance plane (Cole model). This cannot be represented with an equivalent circuit made of real elements (Fig.1.A). By introducing a fractional exponent α, 0<α<1 (usually between 0.65 and 0.95), for sτ, the semicircle shifts along the imaginary axis, resulting in an excellent fit for most cell-based materials in the ß-dispersion region but also in general for many materials with distributed behavior.

$$Z = R_\infty + \frac{R_0 - R_\infty}{1 + (s\tau)^\alpha} \tag{3}$$

It is advantageous use a symmetrically logarithmic function g(τ) for the distribution of the relaxation times (DRT) caused by the individual cell properties. This corresponds to the contribution to the total impedance for a single relaxation time or, in practice, for an arbitrarily small interval of relaxation times. The impedance for a relaxation time is according to Eq.1, second term:

$$Z(\tau) = \frac{g(\tau)}{1 + s\tau} \tag{4}$$

The exact solution is for g(τ) is

$$g(\tau) = \frac{R}{2\pi} \frac{\sin((1-\alpha)\pi)}{\cosh(\alpha \ln({}^{\tau}/_{\tau_0}) - \cos((1-\alpha)\pi))} \tag{5}$$

R = R_0-R_∞, α and τ_0 are the constants from eq.3. The total impedance is the integral over the individual impedances plus the resistance at very high frequencies R_∞.

$$Z = R_\infty + \int_0^\infty \frac{g(\tau)}{1 + s\tau} d\tau \tag{6}$$

In the simplest case, this construct corresponds to an infinite chain of parallel RC combinations. However, in practice, the calculation is limited to discrete, predetermined relaxation times. The same information that can be obtained from the impedance spectrum is also found in the electrical response to a transient stimulus such as a step function.

As an example, the response of fresh potato tissue to a current jump initially shows a sudden rise in voltage, which, according to the equivalent circuit (Fig.1A), corresponds to the voltage drop across the parallel circuit of $R_e||R_i$ or R_∞. The further course of the curve corresponds to the charging of the membrane structures.

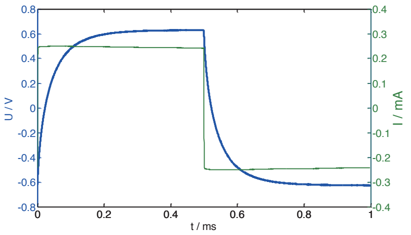

Fig. 3 Voltage response of a potato to a square wave current function without dc-offset. The potato was contacted by a pair of stainless steel rods (Ø = 3 mm) with 2 cm length and a distance of 2 cm.

The Laplace inverse transformation of the impedance multiplied by a current step yields the voltage trace across the test object. In case of ideal behavior such as in Fig.1, this is a simple exponential function:

$$U(t) = I_0 R_0 - \frac{I_0 R_0^2}{R_0 + R_\infty} e^{-\frac{t}{\tau_0}} \quad ; \quad \tau = C_m(R_0 + R_\infty) \tag{7}$$

which unfortunately departs in for most cell based materials considerably from real behavior. The transformation of impedances with fractional exponents (Eq.3) of s is not trivial. It yields in special cases simple functions, such as a $1/t^2$-function with $\alpha = 0.5$. Between a = 0.5 and 1 the transformation gives something between the quadratic and the exponential function, which is described by the Mittag-Leffler function (MLF) (Haubold et al., 2011).

$$\mathfrak{E}_{\alpha,\beta}(z) = \sum_{k=0}^{\infty} \frac{z^k}{\Gamma(\alpha k + \beta)} \tag{8}$$

G is the gamma-function and α is the distribution parameter. Here, ß is generally 1. According to the correspondence table (Monje et al., 2010) and after some simple manipulation, the voltage as function of time based on the inverse Laplacian transform of the impedance in eq.3 is:

$$u(t) = i_0\left[R_s + R_b - R_b \mathfrak{E}_\alpha\left(-\frac{t^\alpha}{\tau_{\text{ß}}}\right)\right] \tag{9}$$

It should be noted, that time constant in eq.3 is related to $t_{\text{ß}}$ by $t_{\text{ß}} = t^{1/a}$. While exponential functions, including sums of exponential functions, can be fitted relatively easily, the Mittag-Leffler-function poses a challenge because, especially with small a (a<0.9), it converges only slowly and thus generates a high computational effort. This is particularly critical if the precision (termination condition) is restricted in the interest of a fast calculation.

Here we show first that both transformations (DRT, MLF) represent an exact solution within the computational accuracy. For this purpose, typical values were assumed for the relaxation strength which is the voltage difference across the object between infinite engagement and the time when the current step occurs (U_∞-U_0), the apparent relaxation time τ, which corresponds to the characteristic frequency in the frequency domain, and the distribution paramter α. As reference, the expected (exact) impedance was calculated from the relaxation functions in time domain using Fast Fourier Transformation. Finally, the deviation from the expected impedance (eq.3) was recorded.

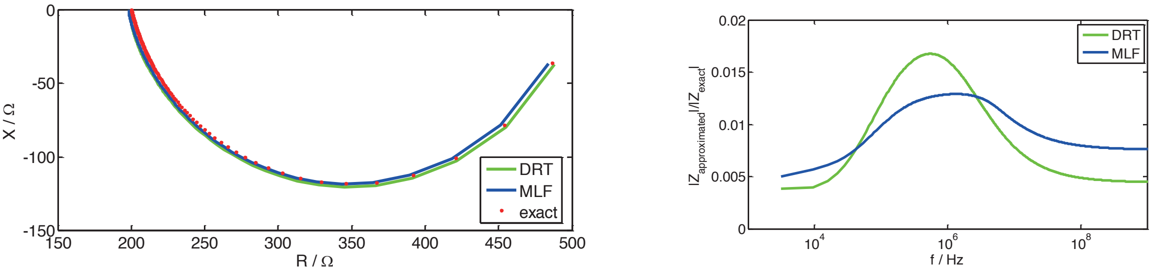

Fig. 4 4 (A) Nyquist diagram for an impedance according to Eq.3 (U_0 = 0.2V ($U_{t=0}$), U_∞ = 0.5V ($U_{t\to\infty}$) , I_0 = 1 mA (current amplitude of the square wave function), t = 30 µs, a = 0.85). The resistors are calculated as $R_0 = U_\infty / I_0$ and $R_\infty = (U_\infty - U_0) / I_0$. (B) relative error of the impedance magnitude for both transformation with respect to the exactly calculated impedance.

2. Processing the step response of potato tissue

First, it should be shown on the basis of the data in fig. 1 that the fit to a distribution of relaxation times is equivalent to that to the Mittag-Leffler function. In order to reduce the computational effort, the voltage curve was reduced to a few points by averaging using logarithmic spacing (Fig. 5, red circles).

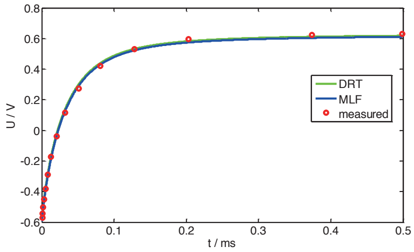

Fig. 5 Fit of the voltage response (Fig.2) to a distribution of relaxation times (DRT) and the Mittag-Leffler-function (MLF).

In both cases, the transformation into the frequency domain is simple, since both models yield directly the parameters of the Cole model. For comparison, the impedance calculated using the Fourier transformation of the current and voltage curves was superimposed (Fig.5 red circles).

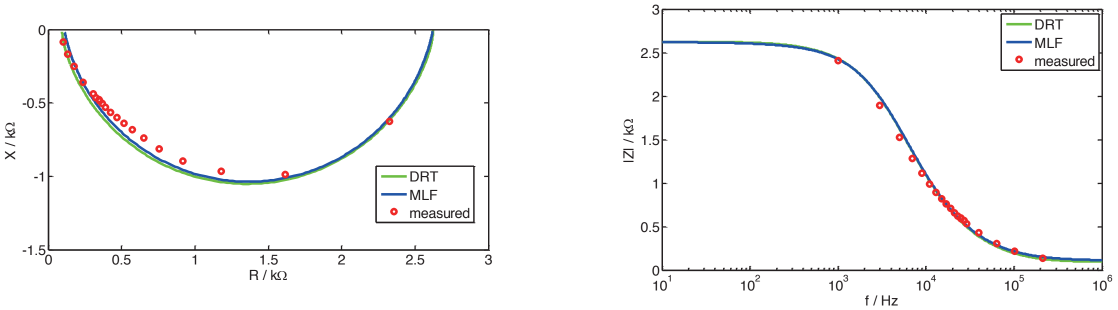

Fig. 6 Nyquist diagram for the impedance calculated by Fourier transformation from the time-functions shown in fig.3, the transformation using the Mittag-Leffler function (MLF) as well as the distributed relaxation times (DRT).

3. Discussion

In principle, both mathematical methods are suitable for approximating the Cole model from the relaxation behavior in the time domain. In practice, however, there are significant differences. While the fit procedure (Marquardt-Levenberg algorithm) works well with both methods for distribution coefficients above $\alpha=0.9$, even with noisy data, the calculation times for the MLF at $\alpha<0.9$ are considerably longer. The precision of the procedure for calculating the MLF implemented in Matlab (Podlubny and Kacenak, 2006) can be set. Especially with low precision ($< 10^{-8}$) there are significant jumps in the calculated values, which either makes a fit more difficult or impossible. When using a higher precision, the computing time increases significantly, especially with data that is difficult to fit, or the fitting routine is aborted without a usable result. The distribution of relaxation times appears to be considerably more robust, but has the disadvantage that the relaxation times (fig. 6) are arbitrary and it is therefore basically not an analytical method.

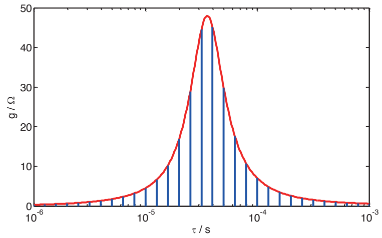

Fig. 7 Distribution of relaxation times for the data presented here (Fig.4). Even if it is not explicitly required, the logarithmic distribution is advantageous, both with regard to the computational effort and the accuracy of the data fitting.

Nevertheless, the method is very robust with about 10 - 30 discrete, logarithmically arranged relaxation times and allows the calculation of a relaxation curve with, for example, 30 time instants within less than 1 µs using a normal PC and Matlab. In general, it should be noted that not all data can be fully fitted with a simple Cole model, which may require adding more elements, which is behind the scope of this paper.

4. Conclusion

The direct transformation of models with fractal exponents in frequency domain like the Cole model yields the Mittag-Leffler function. However, this function poses problems during fit procedures. The distribution of relaxation times is equivalent but requires less computation and is more robust which makes it a good choice for processing relaxation data.

References

COLE, K. S. & COLE, R. H. 1941. Dispersion and absorption in dielectrics I. Alternating current characteristics. *The Journal of chemical physics,* 9, 341-351.

FOSTER, K. R. & SCHWAN, H. P. 1989. Dielectric properties of tissues and biological materials : A critical review. *CRC Crit.Rev.Biomed.Eng.,* 17, 25-104.

HAUBOLD, H. J., MATHAI, A. M. & SAXENA, R. K. 2011. Mittag-Leffler functions and their applications. *Journal of Applied Mathematics,* 2011.

MONJE, C. A., CHEN, Y., VINAGRE, B. M., XUE, D. & FELIU, V. 2010. *Fractional-order Systems and Controls,* London, Springer.

PODLUBNY, I. & KACENAK, M. 2006. Mittag-Leffler function, The MATLAB routine.

ICBEM Bioelectromagnetism ICEBI Electrical Bioimpedance EIT Electrical Impedance Tomography

Proceedings of the International Conference of Bioelectromagnetism, Electrical Bioimpedance,
and Electrical Impedance Tomography June 29 – July 1, 2022 / Kyung Hee University, Seoul, Korea

Effect of Geometric Complexity of the Heart Model on the Inverse Problem of Electrocardiography

R. Martin Arthur and Yujing Lin
Electrical & Systems Engineering, Washington University in St. Louis
St. Louis, Missouri, USA

Correspondence : R. Martin Arthur, e-mail : rma@ese.wustl.edu

Abstract–The electrocardiographic (ECG) inverse problem offers more sophisticated approaches for assessing the electrical condition of the heart than the standard 12-lead ECG. Because of the ill-posted nature of the ECG inverse problem, regularization must be used to obtain clinically meaningful estimates of heart-surface potentials. We compared optimal inverse solutions using L_1 regularization with those found using zero-order Tikhonov (ZOT) regularization in two heart-torso models with known heart-surface potentials, but different spatial detail. In the model based on the Visible Human Male with an epicardial-shell heart-model, there was no difference in relative error (RE) and correlation coefficient (CC) during activation and recovery of the ventricles (QT interval) between L_1 and ZOT inferred heart-surface potentials. In the heart-torso model based on the ECGSIM package with a ventricular heart model there were significant differences in RE and CC throughout the QT interval. At the peak of the R wave, RE was reduced from 0.841 (ZOT) to 0.358 (L_1). L_1 regularization reduced RE compared to ZOT except during the downstroke of the R wave. These results suggest that improvement with L_1 regularization is dependent on heart model complexity, not its sampling density.

Keywords: Inverse problem; zero-order Tikhonov regularization; L_1 regularization; spatial detail, heart models

1. Introduction

Electrophysiological changes in the heart, along with alterations in both cardiac and torso geometry, affect body-surface electrocardiograms (ECGs). Although the standard 12-lead ECG offers valuable beside information on cardiac electrical function, it is limited by a) sampling only 9 body-surface points and b) not incorporating individualized volume- conductor information. As a result, the standard ECG has limited utility in the assessment of subtle electrical features, [Arthur, 2012].

More sophisticated approaches for assessing the electrical condition of the heart than the standard 12-lead set have been studied for decades [Gulrajani 1998]. With detailed electrocardiographic body-surface maps and individualized volume-conductor torso models, cardiac sources can be accurately inferred [Ghosh *et al* 2009].

Because of the ill-posed (unstable with respect to measurement errors) nature of the ECG inverse problem, regularization methods are used to obtain meaningful solutions. The most commonly used method is zero-order Tikhonov (ZOT) regularization [Beetner *et al* 2004]. ZOT regularization is based on minimizing the L_2-norm of heart-surface potentials. Although L_2-based algorithms constrain inverse solutions so that they are clinically useful, L_1-norm techniques, which penalize the gradients of heart-surface potentials, may be superior to higher order norms in that they yield less-smoothed solutions with more localized detail.

Our objective was to determine whether or not L_1 regularization improved estimates of known heart-surface potentials compared to ZOT regularization. We found relative errors (REs) and correlation coefficients (CCs) for optimal L_1- and ZOT-regularized inverse solutions at each instant during the QT.

2. Simulated Body-Surface Potentials

To compare inverse ECG solutions found using L_1 and ZOT regularization, heart-surface potentials were estimated from from *known* heart-surface potentials in models taken from 1) images of the Visible Human Male (VHM) [Spitzer 1996] and 2) the ECGSIM package [Van Oosterom 2004]. Because we knew the actual heart-surface potentials, we found optimal inverse solutions.

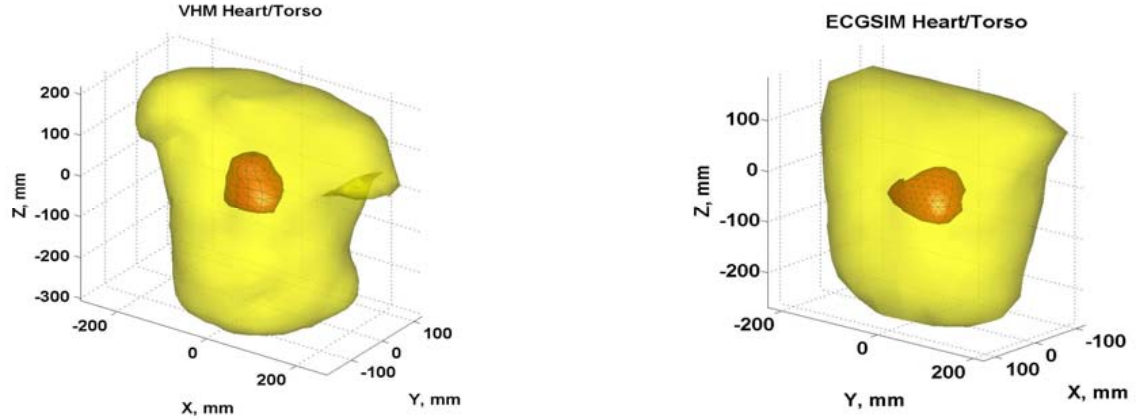

Figure 1. Body-surface potentials from known heart-surface potentials. Left) VHM model with a 93-node heart in an 802-node torso. Right) ECGSIM model with a 257-node ventricular heart in a 300-node torso.

The main sections may be further divided into subsections with subheadings. If subheadings are used, the first subheading shall be immediately after the main heading.

2.1 Visible Human Male Model with Body-Surface Potentials Calculated from Measured Ventricular Potentials

To form the 802-node VHM torso model in Fig. 1, we segmented color images of the Visible Human Male 8 in 1-cm steps from the neck to the pelvis and used the resulting point cloud to form a radial-basis-function torso model 4. The heart of the Visible Human Male, was segmented at 1-cm intervals to form a 93-node heart surface model from adjacent contours. To study effects of sampling density, the 93-node heart was upsampled by factors of 4 and 16, i.e., to 366 and 1458 nodes.

Known heart-surface potentials were determined from measurements made with a 90-electrode sock in an adult male with a myocardial infarct during normal sinus rhythm using intraoperative mapping techniques described previously 11. Measured heart-surface potentials were matched on a least-squares-error basis with a fourth-degree spherical harmonic, which was then used to calculate the potentials Φ_H at the nodes of the heart model.

Body-surface potentials ΦB were found at each node of the torso model from ΦH using

$$\mathbf{\Phi}_B = \mathbf{Z}_{BH}\mathbf{\Phi}_H \ , \tag{1}$$

where Z_{BH} is a transfer-coefficient matrix, found using the method of Barr and co-workers [Barr 1977].

2.2 ECGSIM Model with Heart- and Body-Surface Potentials from Heart-Surface Action Potentials

The ECGSIM package provided ventricle and torso geometry (see Fig. 1), along with the timing of depolarization and repolarization of heart-surface action potentials (APs) in a normal male 9. We used our bi-domain forward-problem platform to calculate known heart-surface potentials Φ_H at each of the 257 nodes of the ECGSIM heart model from APs or trans-membrane potentials Φm found using logistic-curve templates for depolarization and repolarization positioned in the QT interval, using the ECGSIM values for depolarization and repolarization times at each heart node 1.

$$\mathbf{\Phi_H = A\Phi m} \quad , \tag{2}$$

where **A** is our bidomain forward-problem solution for the heart surface.

Body-surface potentials ΦB were calculated at each of the 300 nodes of the ECGSIM torso model from our bidomain ΦH values (Eq. 2) using Eq. 1, the same expression used for our VHM model 12. Note that direct calculation of body-surface potentials using our bidomain model agreed with ΦB using Eq. 1. The correlation coefficient was 0.9985 over the QT interval.

2.3 Inverse Algorithms

ECG inverse problem solutions were found in two heart-torso models for which we had known heart-surface potentials. One heart model was a conventional epicardial shell (VHM). The other was a ventricular model (ESGSIM). These differences allowed us to assess the impact of sampling density and complexity of the heart model on inverse-solution accuracy.

$$\hat{\mathbf{\Phi}}_H = (\mathbf{Z}_{BH}^T\mathbf{Z}_{BH} + \tau\mathbf{R}^T\mathbf{R})^{-1}\mathbf{Z}_{BH}^T(\mathbf{\Phi}_B + \mathbf{\Phi}_N) \quad . \tag{3}$$

$\mathbf{\Phi}_N$ is additive noise. $\mathbf{R = I}$, zero-order Tikhonov regularization [Ramanathan, 2001], [Beetner, 2004].

Because the cost function takes the absolute value of the normal derivative of the heart-surface potentials, heart-surface potentials were solved iteratively. Details in [Ghosh Rudy, 2009]. Superscript (k) indicates the kth iteration

$$\hat{\Phi}_H^{(k)} = \left(Z_{BH}^T Z_{BH} + \tau D^T W_\beta^{(k)}(\Phi_H^{(k-1)})D\right)^{-1} Z_{BH}^T(\Phi_B + \Phi_N) \ . \tag{4}$$

Results

The heart model for the VHM was an epicardial shell over the atria and ventricles (See Fig. 1). The relative error (RE) and correlation coefficient (CC) values for both the L1 and ZOT optimal inverse solutions for the VHM model are shown in Fig. 2. For this model, RE and CC are almost identical throughout the QT interval for the L1 and ZOT regularization regimes for both the 93-node and 366-node heart models. Increase in the number of heart nodes by another factor of 4 (1458 nodes) produced no significant change in either RE or CC throughout the QT interval.

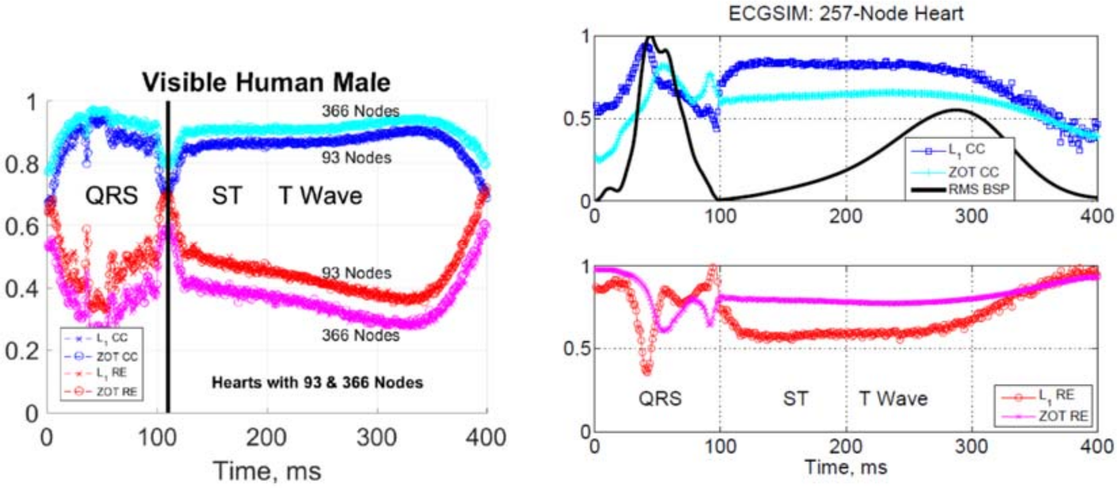

Figure 2. Comparison of REs and CCs using L1 and ZOT regularization for inverse solutions over the QT interval in our Visible-Human-Male model 9. RE was reduced and CC increased when the number of nodes in the heart model was increased from 93 to 366. The vertical line separates the QRS complex from the ST segment and the T wave.

The ECGSIM heart model is not a whole-heart epicardial shell like the VHM model. It is a ventricular model with left and right ventricular cavities 9 (See Fig. 1.). The relative error (RE) and correlation coefficient (CC) values for both the L1 and ZOT optimal inverse solutions for the ECGSIM model are shown in Fig. 3. Unlike the VHM model results, RE and CC are significantly different throughout most of the QT interval for the L1 and ZOT regularization regimes. L1 regularization had lower RE and higher CC than ZOT regularization except during parts of the downstroke of the R wave. At the peak of the R wave RE was reduced from 0.841 (ZOT) to 0.358 (L1), a factor of 2.4.

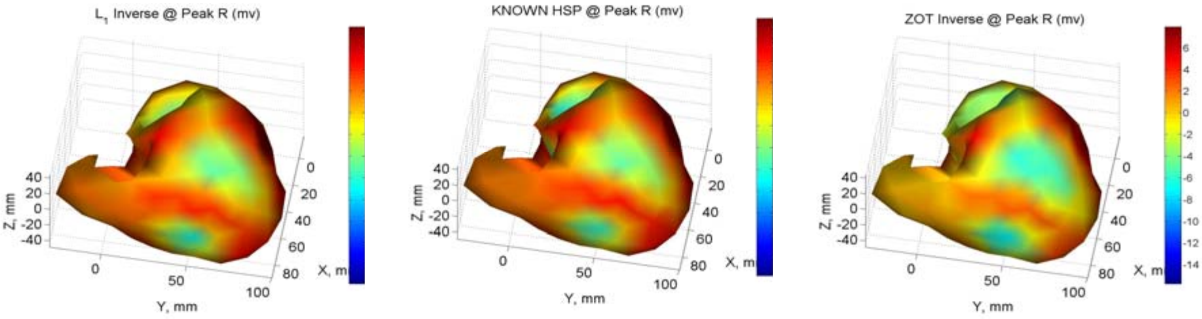

Figure 3. Body-surface potentials from known heart-surface potentials. Left) VHM model with a 93-node heart in an 802-node torso. Right) ECGSIM model with a 257-node ventricular heart in a 300-node torso.

3. Discussion

To test the possible benefits of L_1 regularization compared to conventional zero-order Tikhonov (ZOT) regularization for imaging heart-surface potentials, we found optimal estimates for inferred heart-surface potentials during the QT interval on two heart models in simulations with different geometries and different spatial sampling densities.

L_1 and ZOT regularization results were virtually identically throughout the QT interval using the heart-torso anatomy from the Visible Human Male. Increasing the number of nodes in the VHM heart model from 93 to 366 resulted in an improvement in both RE and CC, although L_1 and ZOT regularization still performed almost identically (See Fig. 2.).

These results contrast with those published by Ghosh and coworkers, who reported that L_1 regularization improved spatial resolution, that is, presumably reduced RE and increased CC in inferred heart-surface potentials []7. In our study, however, L_1 and ZOT regularization yielded identical RE and CC values on the VHM epicardial-shell heart model. Methodological differences between Ghosh's work and ours include the construction of the heart model and the use of data with known heart-surface potentials in our case, as opposed to data in human subjects without known potentials. Further work is needed to delineate the reasons underlying these apparently disparate results. In contrast to the VHM heart-model results, L_1 regularization performance was markedly better than ZOT in the ECGSIM heart-torso model (Fig. 3), presumably because i It provided a more challenging geometry for the inverse problem than the VHM model.

Although L_1 improvement was better on average over the QT interval (reduced RE and improved CC) for the ECGSIM model, that improvement was dependent on the specific instant in the QT interval (Fig. ??). In particular, RE reduction was greatest during the upstroke of the R wave and consistently better during the T wave. Improvement with L1 regularization in these time intervals suggests that it will yield more reliable activation and recovery times than ZOT regularization for a ventricular heart model.

4. Conclusions

L_1 regularization had the same relative error in estimates of heart-surface potentials as zero-order Tikhonov regularization on a conventional epicardial heart model. In a ventricular heart-model, however, L_1 regularization is likely to provide heart-surface potential maps with lower relative error than ZOT regularization. In addition, it may yield better estimates for assessing event timing during the QT interval than ZOT regularization..

Acknowledgments

This work was supported in part by NIH grant R01-HL50295 and by the Wilkinson Trust at Washington University.

References

Arthur, R. (1983). Signal quality of resting electrocardiograms. J of Electrocardiology, 16(3), 235–244.

Arthur, R., Beetner, D., Ambos, H., und Cain, M. (1998). Improved estimation of pericardial potentials from body-surface maps using individualized torso models. J of Electrocardiology, 31 (supplement), 106–113.

Arthur, R., Lin, Y., Wang, S., and Trobaugh, J. (2012). Effects of Changes in Action Potential Duration on the Electrocardiogram in Type II Diabetes. International Journal of Bioelectromagnetism, 14(3), 141–153.

Arthur, R. und Trobaugh, J. (2012). Electrocardiographic Textbooks Based on Template Hearts Warped Using Ultrasonic Images. IEEE Trans on Biomed Engr, 59(9), 2531–2537.

Barr, R., Ramsey, III, M., and Spach, M. (1977). Relating epicardial to body surface potential distributions by means of transfer coefficients based on geometry measurements. IEEE Trans on Biomed Engr, BME-24, 1–11.

Beetner, D. and Arthur, R. (2004). Estimation of heart-surface potentials using regularized multipole sources. IEEE Trans on Biomed Engr, 51, 1366–1373.

Ghosh, S. und Rudy, Y. (2009). Application of L1-Norm Regularization to Epicardial Potential Solution of the Inverse Electrocardiography Problem. Ann Biomed Engr, 37(5), 902–912.

Gulrajani, R. (1998). The forward and inverse problems of electrocardiography: Gaining a better qualitative and quantitative understanding of the heart's electrical activity. IEEE Engr in Med and Biol Magazine, 17(5), 84–102.

Hood, M., Pogwitzd, S., Peirick, J., and Cain, M. (1992). Contribution of myocardium responsible for ventricular tachycardia to abnormalities detected by analysis of signal-averaged ECGs. Circulation, 86, 1888–1901.

Ramanathan, C. and Rudy, Y. (2001). Electrocardiographic Imaging: II Effect of Torso Inhomogeneities on Noninvasive Reconstruction of Epicardial Potentials, Electrograms, and Isochrones. J Cardiovasc Electrophysiol, 12(2), 241–252.

Shou, G., Xia, L., Liu, F., Jiang, M., and Crozier, S. (2011). On Epicardial Potential Reconstruction Using Regularization Schemes with the L1-norm Data Term. Phys Med Biol, 56(1), 57–72.

Spitzer, V., Ackerman, M., Scherzinger, A., and Whitlock, D. (1996). The visible human male: A technical report. J Am Med Inform Assoc, 3, 118–130.

van Oosterom, A. and Oostendorp, T. (2004). ECGSIM: an interactive tool for studying the genesis of QRST waveforms. Heart, 90, 165–168.

van Oosterom, A. (2012). The inverse problem of bioelectricity: an evaluation. Med Biol Eng Comput, 50(9), 891–902.

Proceedings of the International Conference of Bioelectromagnetism, Electrical Bioimpedance,
and Electrical Impedance Tomography June 29 – July 1, 2022 / Kyung Hee University, Seoul, Korea

Validation of non-empirical fat-free mass estimation model for a wrist-worn device

Aleksandr Polokhin[1,2], Anna Pronina[1,3], Andrey Boev[1] and Stas Gorbunov[1]
[1]AURA Devices, Inc., Wilmington, DE, USA
[2]Institute of Biomedical Systems, National Research University of Electronic Technology MIET, Moscow, Russia
[3]Department of Human and Animal Physiology, Moscow State University, Moscow, Russia

Correspondence : Aleksandr Polokhin, e-mail : a.polokhin@auraband.io

Abstract– Fat-free mass (FFM) estimation has dramatic importance for body composition evaluation, often providing a basis for treatment of obesity and muscle dystrophy. However, current methods of FFM estimation have several drawbacks, usually related to either cost-effectiveness and equipment size (dual-energy X-ray absorptiometry (DEXA) scan) or model limitations. In this study, we present and validate a new FFM estimation model, based on hand-to-hand bioimpedance analysis (BIA) and arm volume. Forty-two participants underwent the full body DEXA scan, a series of anthropometric measurements, and upper body BIA measurements with the custom designed wearable wrist-worn impedance meter. A new two truncated cones (TTC) model was trained on DEXA data and achieved the best performance metrics of 0.886 ± 0.051 r^2, 0.052 ± 0.009 % mean average error, and 6.884 ± 1.283 kg maximal residual error in FFM estimation. The model further demonstrated its effectiveness in Bland-Altman comparisons with skinfold thickness-based FFM estimation method, achieving the least mean bias (0.007 kg). Thus, the novel TTC model can provide an alternative to full-body BIA measurements, demonstrating an accurate FFM estimation independently of population variables.

Keywords: bioelectrical impedance analysis; fat free mass; upper-body measurement; multiple linear regression; predictive modeling.

1. Introduction

Obesity, one of the most crucial problems in healthcare, has risen dramatically in the past few decades. Among the present methods of body composition evaluation, bioelectrical impedance analysis (also known as bioimpedance analysis or BIA), is one of the most widely used, as it provides a quick and efficient way to estimate and control body fat level. Fat-free mass (FFM), i.e. the difference between fat mass (FM) and total body mass (TBM), is commonly employed by researchers and specialists studying body composition. In general, FFM, as well as FM, can be used as a basis for creating a personal diet plan in order to prevent obesity or muscle dystrophy. Purely anthropometric FFM estimation methods, such as equations derived by Duerenberg (Deurenberg *et al* 1991), Peterson (Peterson *et al* 2003), and the Navy Seal formula (Shaheen *et al* 2019), have limitations, mostly arising from their strong dependency on the traits of the original experimental sample: ethnicity, sex (gender), age, and general health.

Thus, BIA can be a way to overcome the challenges of DEXA and anthropometric FFM estimation, since the current production level of the electronics manufacturing industry makes it possible to use it widely. The method utilizes variations in human body electric conductivity, altered by the impinged frequencies and body composition (Sizoo *et al* 2021). Usually, BIA models are formed by training multiple linear regressions, where DEXA results are used as training data (even though DEXA as an FFM estimation method does have its own bias (Patterson *et al* 1989). An example of this approach is the single cylinder-based BIA model, in which FFM is determined by the value of height^2/R (known as bioimpedance index, BI), where R denotes the real part of bioimpedance (resistance) between voltage (sensing) electrodes.

In this study, we modified the five-cylinder model into a new model, which includes two upper limbs, for a custom designed bioelectrical impedance meter. With this modification, we expect to keep the advantages of the five-cylinder model, i.e., minimize the empirical estimation of body parts and take additional sex and age variables out of consideration, while employing the hand-to-hand measurement scheme.

Our main aim for the present study was to build a novel non-empirical FFM estimation model based on anthropometric parameters and BIA values, measured with a wearable wrist-worn impedance meter. Finally, we compared the non-empirical model effectiveness against the population-based model.

2. Subjects and methods

2.1 The Participants

Forty-two healthy adults (21 male, median age: 21.5, age range: 18-56) of Caucasian ethnicity participated in the study. Participants self-reported no recent history of hospitalization, alcohol or diuretic drug consumption. Initial exclusion criteria also included chronic and acute conditions like diabetes mellitus, cancer, renal failure, hepatitis-related diseases, pregnancy, and presence of pacemakers or other electrical implants. Participants were recruited via advertisement on social media and were offered a compensation. They were informed of the experimental purpose, methods, procedures, and safety-related information and signed the informed consent before participation. The study was conducted in accordance with the Declaration of Helsinki.

2.2 Experimental Procedure

Before the experiment, all participants were asked to fill out a questionnaire assessing their age, gender, physical training, habitual levels of smoking and alcohol consumption, recent intake of water and caffeine-containing products, normal sleep routine, medication, and menstrual cycle. After filling out the questionnaire, they were asked to take off any metal attachments such as jewelry and piercings and change into cotton medical gowns.

At the first step of the experiment, a Lunar iDXA (GE Healthcare, USA) whole body scan was taken. After that, TBM and height was assessed with scales (VEM-150, MAS-SA-K, Russia) and a stadiometer (RM-1, Diakoms MED, Russia). Then anthropometric measurements were taken, which included hips, waist, and arm, shoulder and wrist circumferences on both sides. Skinfold thickness was assessed with a caliper at 4 sites (triceps, subscapular, suprailiac and mid-thigh) as described in (Peterson *et al* 2003). Finally, segmental body impedance measurements were performed with InBody 230 (Biospace Co., Ltd., Republic of Korea).

2.3 Bioimpedance Measurements

In order to analyze upper-body impedance a wearable wrist-worn impedance meter (WIM) was designed as a modification of AURA Strap, a wrist-wearable Apple Watch accessory (AURA Devices, Inc., USA). WIM is based on CS1259 (analog front-end with 24-bit ADC designed for Body impedance analysis, Chipsea Technologies Shenzhen Corp Ltd, China) and uses a tetra-polar BIA measurement scheme. During the experiment, WIM prototype was placed on the left wrist 2 cm down from the lunate bone. The upper current and voltage electrodes of WIM contacted the central zone of the volar wrist of the left arm and the thenar of the right hand. Hand-to-hand bioimpedance was measured in a standing posture using current frequency of 50 kHz. During the measurement, the elbows were flexed to 90 degrees while the hands were at the level of the solar plexus. Every measurement was replicated five times.

2.4 Upper body Bioelectrical Impedance model Measurements

The truncated cones model is shown in Figure 1, where hand-to-hand bioelectrical impedance consists of two serial impedances of right and left arm, $|Z|_{RA}$ and $|Z|_{LA}$, and torso impedance $|Z|_{TORSO}$. Although the torso accounts for around ½ of total body mass, its impedance could be not considered due to its low value resulting from high cross-sectional area (Patterson *et al* 1989). The volume of the arms can be represented by the sum of the volumes of two truncated cones, where the shoulder circumference is the length of the base circle and the wrist circumference is the length of the top surface circle. As a result, the new hand-to-hand impedance model for FFM estimation, the two truncated cones (TTC) model, includes the following variables: arm volume, TBM, BI and body mass index (BMI).

2.5 Statistical Analysis

Linear regression equations for the FFM estimation were built via the least squares method using the Scikit-learn library for Python. In the single cylinder (SC) model, height, age, TBM, sex, and BI were the independent variables, while fat-free body mass, obtained by DEXA scan (FFM_{DXA}) was the dependent variable. In the new TTC model, arm volume, BMI, and BI were the independent variables with the same dependent variable. Due to the moderate amount of original observations (N = 42), the bootstrap resampling method with 1,000,000 samples was used to derive regression coefficients (mean training sample size n_{train} = 26.75, mean testing sample n_{test} = 15.25). Coefficient of determination (r^2), mean absolute percentage error (MAPE) and maximal residual error were the metrics of choice to evaluate both models' performance.

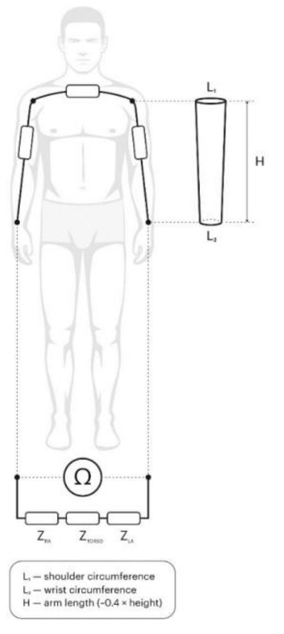

Figure 1. The hand-to-hand bioelectrical impedance scheme of the TTC model

In order to investigate the agreement between FFM estimates provided by the SC and TTC models with DEXA reference, Bland–Altman plot was created. Mean biases with 95 % confidence intervals were calculated as the main measures of agreement between the results, and ± 1.96 standard deviations were set as the limits of agreement (LOA).

3. Results

3.1 Anthropometry and Bioelectrical Impedance

The results of anthropometric measurements and calculations, DEXA scan, and WIM BIA measurements can be seen in Table 1. The physical condition of the participants was rather broad, from athletic to moderate obesity: BMI and body fat percentages of males were (23.69 ± 2.29) kg/m2 and (20.35 ± 7.55) % respectively, while BMI and body fat percentages of females were (23.51 ± 5.13) kg/m2 and (33.18 ± 5.9) % respectively.

Table 1. Anthropometric, body composition and bioelectrical impedance data

	All (N=42: n_{male} =21, n_{female} =21)	
	Mean ± STD	**Range**
Age, years	27.02 ± 10.2	18 - 56
TBM, kg	69.56 ± 11.29	45.83 - 100.95
Height, cm	171.89 ± 8.86	156.0 - 196.0
BMI, kg/m^2	23.6 ± 3.97	18.17 - 38.87
Total arms volume, cm^3	6109.06 ± 1505.04	3480.64 - 10970.02
FFM$_{DEXA}$, kg	50.99 ± 10.94	34.51 - 86.59
FM$_{DEXA}$, %	26.77 ± 9.34	8.32 - 48.39
Re(Z), Ohm	562.21 ± 138.21	304.83 - 831.84

3.2 Upper body bioimpedance approximation with arm volume

Arm volume multiplied by TBM/FFM ratio can be used to approximate the sum of the arms' impedance determined by the five-cylinder human body model used in InBody 230 (Kushner *et al* 1992) (Figure 2a). The coefficient of determination r^2 was 0.782 and 0.788 for the sum of left and right arm impedance ($|Z|_{LA} + |Z|_{RA}$) measured at 20 kHz and 100 kHz, respectively. Thus, changes in bioimpedance imply changes in geometry of measured limbs. High value of r^2 (0.792) in the case of WIM Re(Z) approximation can be interpreted as arm impedance making the main contribution to the value of the real part of bioimpedance. These results provided additional grounding to the TTC model, as total arm volume was used as an independent variable in FFM estimation.

3.3 FFM estimation regression

Two linear regressions were built in this study: one for the SC model and one for the TTC model. As can be seen in Figure 2c, the two models' distribution of maximal residual error demonstrated drastically different shapes. The TTC model error followed close to normal distribution, while the SC model error had a more complex multimodal distribution. The appearance of several peaks was likely caused by different multilinear regression independent variables or their interaction.

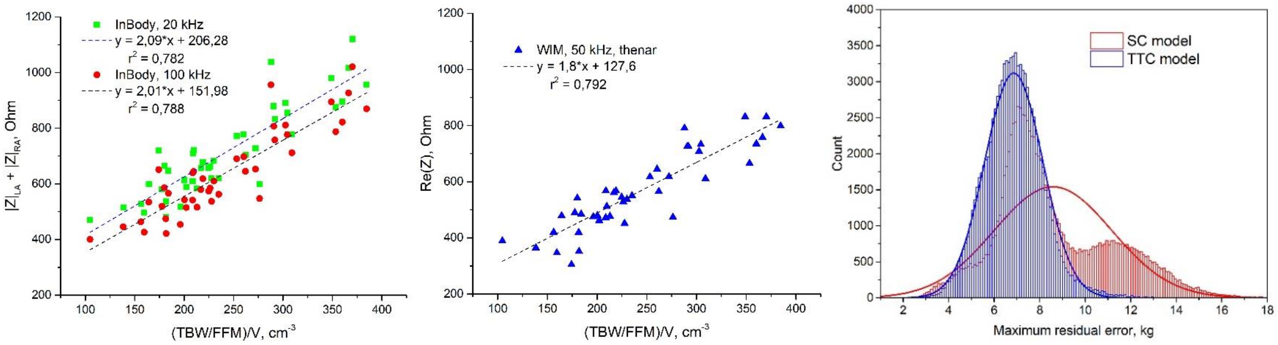

a b c

Figure 2. Arm volume multiplied by TBM/FFM ratio approximates bioimpedance: InBody 230 arm impedance (a) and approximation of real part of bioimpedance measured with WIM (b). Maximal residual error (distribution shapes were obtained during 100,000-sample bootstrap procedure) (c).

3.4 Bland-Altman plots

The Bland-Altman plots in Figure 3a demonstrate the agreement between the SC and TTC model FFM estimation and reference method (DEXA). As can be seen, the mean bias between estimates was only -0.007 kg, while the limits of agreement were (-5.517; 5.517) kg, which indicated good accordance. Bland-Altman plot was also built for FFM estimates provided by equation based on skinfold thickness measurements (Peterson *et al* 2003) (Figure 3b). Although skinfold-based method calculations reached the fine agreement with reference values (-0.381 kg mean bias); its LOA (-9.087; 8.325) kg were much broader.

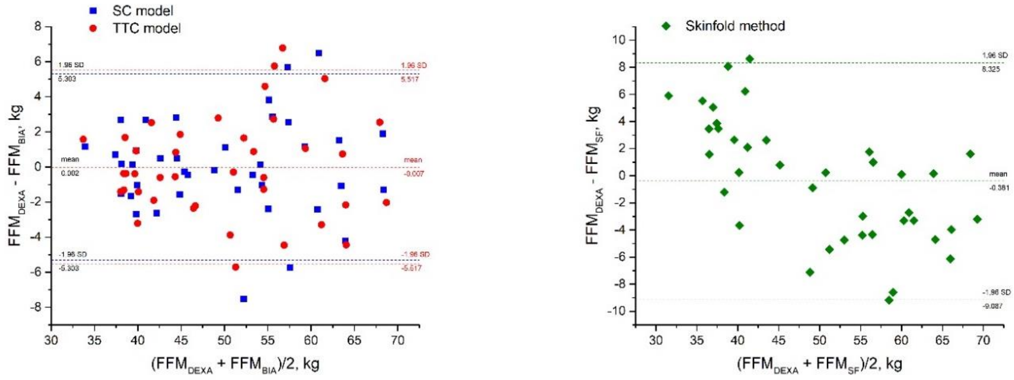

a

b

Figure 3. Bland-Altman plots for WIM FFM estimates validation: SC model: confidence intervals for the mean bias: (-0.874, 0.879) kg, for upper LOA: (4.380, 6.937) kg, for lower LOA: (-6.932, -4.375) kg; TTC model: for mean bias: (-0.920, 0.905) kg, for upper LOA: (4.547, 7.208) kg, for lower LOA: (-7.223, -4.562) kg (a). Skinfold thickness calculations: confidence intervals for the mean bias: (-1.792, 0.955) kg, for upper LOA: (6.653, 10.651) kg, for lower LOA: (-11.488, -7.4918) kg (b).

4. Discussion

We derived both empirical and non-empirical regression equations based on the single cylinder and TTC models. One of the main advantages of the TTC model turned out to be the uniformity of distribution of maximal residual error. In practical use, it can lead to a significant FFM prediction error. The TTC model, on the other hand, did not have this disadvantage. Comparison of the SC and TTC models' performance with the results obtained by DEXA scan demonstrated the high accuracy of both models, with mean bias between the methods being not significantly different from zero. These results demonstrating the new TTC (as well as SC) model for the WIM suggest that it can provide an accurate and effective method to assess body fat-free mass.

In the future, the TTC model can be enhanced by employing bioimpedance spectroscopy (also known as multifrequency BIA), since the use of several frequencies makes it possible to differentiate total body water into extracellular and intracellular spaces and avoid the effect of body hydration status on FFM prediction (Vermeiren *et al* 2021). Last but not least, the geometrical shape of the arms can be more closely approximated: instead of a truncated cone, each arm can be represented as a more realistic complex geometrical object consisting of several truncated cones.

5. Conclusions

In this study, we developed the novel TTC model of FFM estimation based on hand-to-hand BIA measurements of the wrist-worn impedance meter. We also demonstrated the agreement between the model and reference DEXA estimates of fat-free mass. The advantages of TTC model predictive performance were determined.

Acknowledgments

The research was supported by AURA Devices, Inc. The authors express gratitude to AURA Devices researchers Jahan Gani-zade and Egor Brysyakin, who made valuable contributions to the investigation and analysis of experimental data.

References

Deurenberg P., Weststrate J., Seidell J. 1991 Body mass index as a measure of body fatness: Age- and sex-specific prediction formulas *Br. J. Nutr.*, **65 (2)**, 105-114

Kushner R.F. 1992 Bioelectrical impedance analysis: a review of principles and applications *Journal of the American Nutrition Association*, **11 (2)**, 199-209

Patterson R. 1989 Body fluid determinations using multiple impedance measurements *IEEE Eng. Med. Biol. Mag.,* **8 (1)**, 16-18.

Peterson M., Czerwinski S., Siervogel R. 2003 Development and validation of skinfold-thickness prediction equations with a 4-compartment model *Am. J. Clin. Nutr.*, **77 (5)**, 1186–1191

Shaheen A., Javed N., Azam F., Khan M., Mahboob A.S., Mumtaz S. 2019 Comparison of Bioelectrical Impedance and Navy Seal Formula to Measure Body Composition in Medical Students *Cureus*, **11 (5)**, e4723

Sizoo D., de Heide L.J.M., Emous M., van Zutphen T., Navis G., van Beek A.P. 2021 Measuring Muscle Mass and Strength in Obesity: a Review of Various Methods Obesity *Surgery*, **31**, 384–393 18

Vermeiren E., Ysebaert M., van Hoorenbeeck K., Bruyndonckx L., van Dessel K., van Helvoirt M., *et al*. 2021 Comparison of bioimpedance spectroscopy and dual energy X-ray absorptiometry for assessing body composition changes in obese children during weight loss *Eur. J. Clin. Nutr.*, **75**, 73–84

Proceedings of the International Conference of Bioelectromagnetism, Electrical Bioimpedance,
and Electrical Impedance Tomography June 29 – July 1, 2022 / Kyung Hee University, Seoul, Korea

Robot Assisted Electrical Impedance Scanning (RAEIS): concept, and current status of development

Zhuoqi Cheng[1], and Thiusius Rajeeth Savarimuthu[1]
[1]Mærsk Mc-Kinney Møller Institute, University of Southern Denmark, Odense, Denmark

Correspondence : Zhuoqi Cheng, e-mail : zch@mmmi.sdu.dk

Abstract–Robot assisted Minimally Invasive Surgery (RMIS) is widely used for a variety of medical treatments nowadays. In RMIS, tissue recognition is a critical step but few technology is available for assistance. To address this challenge, we develop the Robot Assisted Electrical Impedance Scanning (RAEIS) system. The RAEIS system can be directly implemented on most existing RMIS robotic system without introducing external instruments to the surgical site. In this paper, we present the concept of the RAEIS system and the achievements in three research directions by early 2022.

Keywords: Electrical Bioimpedance; Electrical Impedance Tomography; Robot Assisted Minimally Invasive Surgery; Robot Assisted Electrical Impedance Scanning.

1. Introduction

Robotic assisted Minimally Invasive Surgery (RMIS) is regularly deployed and well integrated in modern medical treatments. During a RMIS, tissue recognition is critical but remains challenging for surgeons. This is frequently required for decision making in a surgical process and for detecting critical or subsurface tissues such as early-stage cancer, lymph nodes and blood vessels. However, the current existing RMIS systems can provide very limited perception information to the surgeon. Surgeon still heavily relies on the endoscopic vision for the above tasks. In our previous study, we present a tissue identification system based on sensing the Electrical Bio-Impedance (EBI) property of soft tissue, which can be implemented directly on a bipolar robotic forceps (Cheng *et al* 2019). The two jaws of the bipolar forceps are used to config a bipolar sensing and is controlled to contact the target tissue surface by the robot. The integrated system is proven to provide real-time and on-site tissue identification. However, the limitation of a bipolar sensing is that the measured impedance is very sensitive to the pressing depth of the forceps, which is hard to control when interacting with soft tissues.

The improvement of the previous system leads to the new version based on a tripolar configuration, named Robot Assisted Electrical Impedance Scanning (RAEIS). The proposed system can be easily implemented on most existing robotic systems for RMIS with little modification of the existing RMIS system and without introducing external instruments to the surgical site. An experimental platform is developed as shown in Fig. 1(C). In addition to two robotic forceps, the system involves an impedance spectroscope (ELIKO Quadra) for current excitation and voltage measurement. This paper presents the concept of the RAEIS system and summarizes the preliminary achievements during its development. Specifically, we demonstrate that the RAEIS system is capable of performing flexible & autonomous scanning, image tissue subsection, different tissue identification and subsurface critical tissue detection.

2. Methods

The proposed system can be implemented by two independent robotic forceps which are used for electrosurgery in RMIS, namely one tool is used as the current source electrode (CSE) and the other is the voltage measurement electrode (VME). A big ground electrode (GND) is required to be attached on the patient body and placed relatively far from the measurement site. In practice, the GND can also be reused as the current return pad for electrosurgery. As shown in Fig. 1(A), excitation current I is injected into the tissue via point A. We assume that the tissue under measurement is homogeneous, and the tissue surface is flat. The injected current disperses from the source radially into the tissue. Given the tissue conductivity σ, the electric potential at position M on the tissue surface can be calculated as

$$V_M = \frac{I}{2\pi\sigma}\left(\frac{1}{d} - \frac{1}{r_0}\right) \tag{1}$$

where d is the distance between M and A [mm], and r_0 is the equivalent radius of CSE [mm].

Considering that r_0 is difficult to be measured, we use differential voltage for sensing. Specifically, the VME measures the electric potential at 2 different positions M and N. By this means, the conductivity of tissue can be calculated as

$$\sigma = \frac{I}{2\pi V_{MN}}\left(\frac{1}{d} - \frac{1}{d+\Delta d}\right) \tag{2}$$

Normally, the excitation can be alternative current. The image part of the measured voltage can also be used to calculate the permittivity of the material. The sensing accuracy of the proposed method is evaluated using standard saline solutions (0.1%, 0.2% and 0.3%). The measured resistivity are 6.2Ωm, 3.2Ωm and 2.2Ωm given the reference values of 5.9Ωm, 3.0Ωm, and 2.0Ωm respectively (Cheng *et al* 2021c).

During the sensing phase, alternative current in different frequencies are used for excitation, and the measured voltages generally present a dependence of the excitation frequency. The phenomenon that the conductivity and permittivity of biological tissue is generally a function of the applied frequency has been well studied previously (Gabriel *et al* 1996). Using different frequencies in excitation source can perform better in tissue recognition generally. As a preliminary study, the RAEIS system is tested on different ex-vivo animal tissues including porcine muscle, bovine muscle, chicken muscle and porcine liver in a wide spectrum from 1kHz to 349kHz (Cheng *et al* 2022a). The measured conductivity values are shown in Fig. 2, which are coherent to the values reported in previous literature (Andreuccetti *et al* 2012).

A special case where a subsurface object of conductivity σ_2 presents is shown in Fig. 1(B). In this case, a part of the injected current reflects from the interface of 2 materials, and detected by the VME. Thus, the voltage difference between point M and N can be calculated as follows according to (Kearey *et al* 2002).

$$V^*_{MN} = \frac{I}{2\pi\sigma_1}\left[\frac{\Delta d}{d\cdot\Delta d} + 2\sum_{n=1}^{\infty}\left(\frac{k^n}{\sqrt{d^2+(2nh)^2}} - \frac{k^n}{\sqrt{(d+\Delta d)^2+(2nh)^2}}\right)\right] \tag{3}$$

where h = thickness of the top layer [mm]
k = reflection coefficient $(\sigma_1 - \sigma_2)/(\sigma_1 + \sigma_2)$

By substituting VMN in Eq. (2) with Eq. (3), the calculated conductivity is a function of d and can indicate the present of subsurface nonhomogeneous region. Considering the complexity in real surgical environment, a machine learning method is developed for subsurface lymph nodes detection based on the input of σ (Årsvold *et al* 2021).

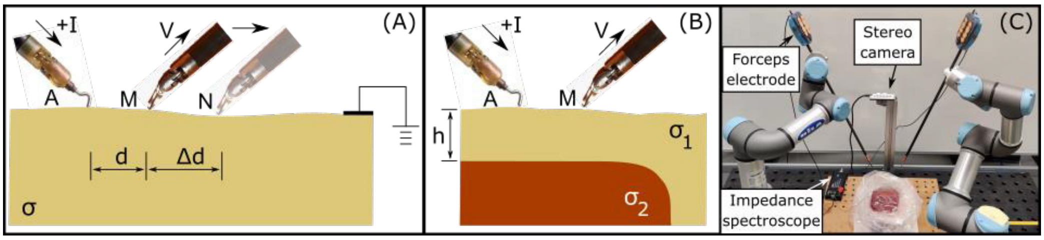

Figure 1. (A) Illustration of the sensing procedure using RAEIS; (B) Modeling the sensing on tissue containing a supeficial layer σ1 and a subsurface layer σ2; (C) Setup of the RAEIS system for experimental studies.

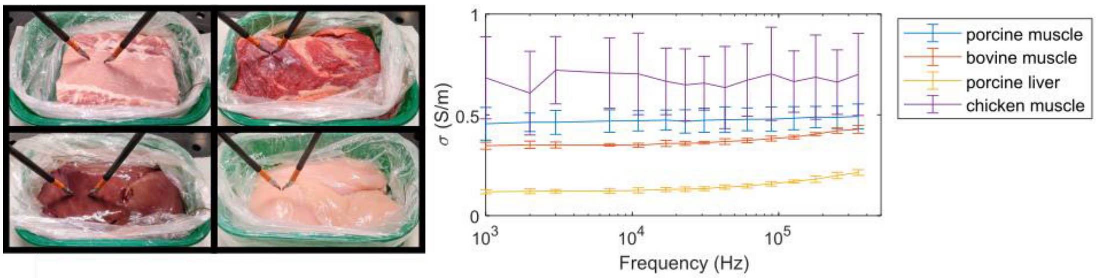

Figure 2. (A) Illustration of the sensing procedure using RAEIS; (B) Modeling the sensing on tissue containing a supeficial layer σ1 and a subsurface layer σ2; (C) Setup of the RAEIS system for experimental studies.

The development of RAEIS system is mainly devoting on three research topics, which are presented as follows.

2.1 Grid scanning v.s. active search

For each measurement, the proposed RAEIS system senses the electrical property of a small region around the CSE and VME. Therefore, a scanning strategy is needed for inspecting an area. The tissue surface is approximated as a 2D space, and 2 scanning methods are proposed. The first method is a grid based scanning. An evenly distributed grid is generated over the target area and the sensing is performed on each node of the grid. For the second method, a strategy called Active Search (AS) is proposed. AS is an efficient area searching approach with higher sampling priority in where the target tissue is more likely to present or where sensing information is lacking. It integrates a Gaussian processes for estimating the distribution of conductivity. According to the estimated distribution, Bayesian optimization is used for determining the subsequent sensing position. These two steps run iteratively until the area searching is accomplished.

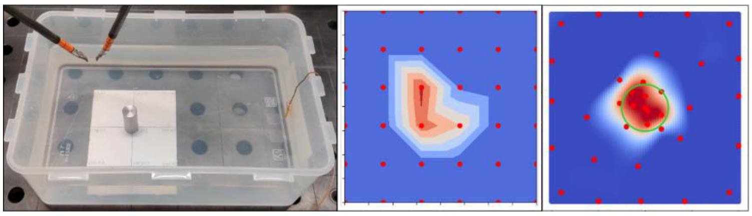

Figure 3. (Left) The water tank setup (a metal cylinder submerged inside water); (Middle) Results of conductivity distribution using grid scanning; (Right) Results of conductivity distribution based on the AS method.

Evaluation study was conducted based on water tank as shown in Fig. 3(left). Tap water was used and a metal cylinder (Ø=10mm) was submerged with a 5mm distance from the cylinder top surface to the water surface. We carried out a comparative study using both the grid scanning and active search method. The sensed conductivity distribution using a 6*6 grid is shown in Fig. 3(middle) and the result of 36 points active search is shown in Fig. 3(right). The results indicate that the active search method can be more efficient and effective for sensing the non-homogeneous region than the grid method. To achieve a similar accuracy, the active search method uses 12 sampling points while the grid scanning method requires 49 points (Cheng *et al* 2022b).

2.2 Robot Assisted Electrical Impedance Tomography (RAEIT)

Electrical impedance tomography (EIT) is a different sensing and reconstruction method compared to the above point based sensing. The target area is considered as a whole during the reconstruction. The contribution of the RAEIT system is to robotize the EIT sensing procedure and implement this method in RMIS based on two forceps electrodes. Each forceps is used as an electrode and controlled to multiple predefined positions for either injecting excitation current or measuring electric potentials. Given the geometric model, the EIDORS library is used to reconstruct the electrical conductivity distribution through solving a forward problem and an inverse problem iteratively (Vauhkonen *et al* 2001).

In our research, we demonstrate that the RAEIT can operate on a line of nodes (Cheng *et al* 2021a) as shown in Fig. 4(B). Two example applications based on ex vivo pig liver and muscle phantom were conducted, namely subsurface tissue detection (Fig. 4(A)) and margin detection (Fig. 4(B)). The reconstructed image of scenario Fig. 4(A) is shown in the upper subfigure of Fig. 4(C), and the result of scenario Fig. 4(B) is shown in the lower subfigure. The red region indicates higher conductivity, corresponding to the location of muscle.

In addition, we demonstrate to use the RAEIT system in a planar 2D scanning and reconstruction. A similar water tank setup as shown in Fig. 3(left) was used and the EIT measurement was performed on a 4*4 grid. The EIT scanning area is 90*90mm, covering a part of the water tank with the metal cylinder in the center. The reconstructed image of the whole water tank is shown in Fig. 4(D). In addition, the RAEIT system was evaluated on a subsurface lymph node detection task and an average of 74.3% sensitivity was reported (Cheng *et al* 2021b).

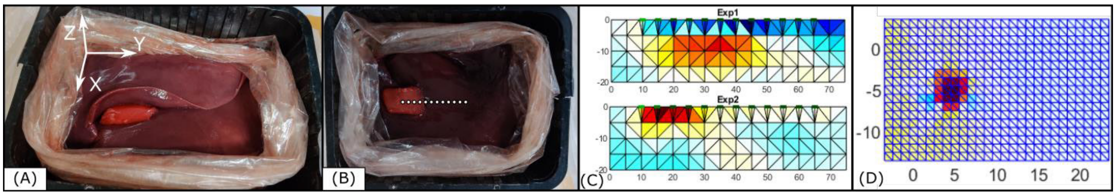

Figure 4. (A) Ex vivo tissue phantom simulating a subsurface liver cancer scenrio where a piece of muscle simulating the tumor (top liver layer is flipped over); (B) Ex vivo tissue phantom simulating a surgical margin; (C) The reconstructed images of (A) and (B) using RAEIT line sensing; (D) The reconstructed images of the water tank setup based on a RAEIT 2D grid sensing (unit: cm).

2.3 Model based sensing

The establishment of Eq. (1) is under the assumption that the tissue surface is relatively flat. This method may suffer a relatively low sensing accuracy when sensing on very curved tissue surface. To address this issue, we propose a 3D model-based sensing method as shown in Fig. 5(A). This method requires to construct a 3D finite element model of the sensing region using a 3D camera. The positions of CSE and VME in practice (Fig. 5(B)) are recorded and used to retrieve the electrical potentials in the 3D model (Fig. 5(C)), which is obtained through solving the forward problem using EIDORS. By comparing the measured differential voltage in practice ($\Delta\Phi^r$) and the values given by the FE model ($\Delta\Phi^m$), the tissue conductivity σ^r is proportional to the reference value in simulation σ^m.

$$\frac{\sigma^r}{\sigma^m} = \frac{\Delta\Phi^r}{\Delta\Phi^m} \tag{4}$$

The system was evaluated on ex vivo tissue phantom including porcine liver and muscle. The measured conductivity using the proposed method are found to be coherent to the data reported in literature. For more details, please kindly refer to (Piccinelli *et al* 2022).

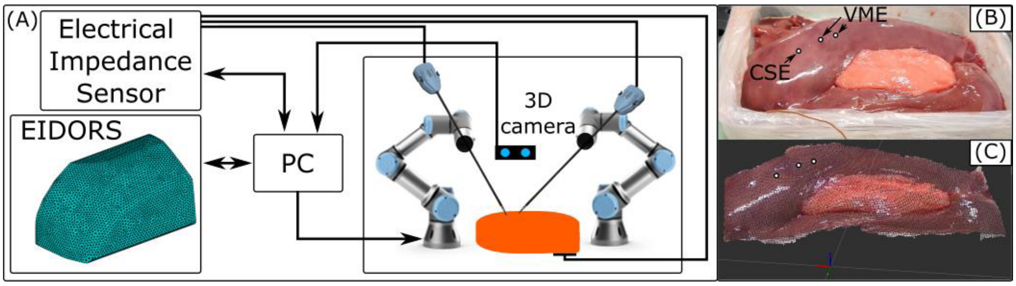

Figure 5. (A) System achitec of the model based sensing method; (B) Example of the CSE and VME location on cureved tissue surface; (C) Retrieving voltages in corresponding electrode locations in reconstructed model simulation.

3. Discussion and conclusions

This paper presents a novel concept of robotizing electrodes for electrical impedance sensing during a RMIS. The proposed system has been evaluated using different experimental setups such as water tank and ex vivo tissue phantoms. The experimental results demonstrate the strong capability of the system in accurate sensing, subsurface tissue detection and tissue subsection imaging. Thanks to the involvement of robot, the sensing can be performed on different locations flexibly and the scanning can be managed in different scales. The future direction will focus on the electrodes position optimization in order to generate a focused sensitivity in the target region.

References

Andreuccetti, D., Fossi, R. & Petrucci C. 2012. An Internet resource for the calculation of the dielectric properties of body tissues in the frequency range 10 Hz-100 GHz. *http://niremf. ifac. cnr. it/tissprop/.*

Årsvold, A.T., Zeltner, A.S., Cheng, Z. , Schwaner, K.L., Jensen, P.T. & Savarimuthu, T. R. 2021. Lymph Node Detection Using Robot Assisted Electrical Impedance Scanning and an Artificial Neural Network. *International Symposium on Medical Robotics (ISMR)*. **2021** 1-6.

Cheng, Z. , Dall'Alba, D. , Caldwell, D. G. , Fiorini, P. , & Mattos, L. S. 2020. Design and Integration of Electrical Bio-Impedance Sensing in a Bipolar Forceps for Soft Tissue Identification: A Feasibility Study. *17th International Conference on Electrical Bioimpedance*. **2020** 3-10.

Cheng, Z., Dall'Alba, D., Fiorini, P., & Savarimuthu, T. R. 2021a. Robot-Assisted Electrical Impedance Scanning system for 2D Electrical Impedance Tomography tissue inspection. *43rd Annual International Conference of the IEEE Engineering in Medicine and Biology Society* **2021** 3729-3733.

Cheng, Z., Dall'Alba, D., Fiorini, P., & Savarimuthu, T. R. 2021b. Robot Assisted Electrical Impedance Tomography System for Minimally Invasive Surgery. *20th IEEE International Conference on Advanced Robotics*. **2021** 234-240.

Cheng, Z., Schwaner, K. L., Dall'Alba, D., Fiorini, P., & Savarimuthu, T. R. 2021c. An electrical bioimpedance scanning system for subsurface tissue detection in Robot Assisted Minimally Invasive Surgery. *IEEE Trans. Biomed Eng*. **69** 209–219.

Cheng, Z., Dall'Alba, D., Schwaner, K. L., Fiorini, P., & Savarimuthu, T. R. 2022a. Robot assisted electrical impedance scanning for tissue bioimpedance spectroscopy measurement. *Measurement*. **195** 111112.

Cheng, Z., Zeltner, A.S., Årsvold, A.T., Schwaner, K.L., Jensen, P.T. and Savarimuthu, T.R., 2022b. Active Search of Subsurface Lymph Nodes Using Robot-Assisted Electrical Impedance Scanning. *IEEE Trans. on Instrumentation and Measurement* **71** 1-11.

Gabriel, S., Lau, R.W. and Gabriel, C., 1996. The dielectric properties of biological tissues: III. Parametric models for the dielectric spectrum of tissues. *Physics in medicine & biology,* **41(11)**, p.2271.

Kearey, P., Brooks, M. and Hill, I., 2002. An introduction to geophysical exploration (Vol. 4). *John Wiley & Sons.*

Piccinelli, M., Cheng, Z., Dall'Alba, D., Schmidt, M. K., Savarimuthu, T. R., & Fiorini, P. 2022 3D Vision Based Robot Assisted Electrical Impedance Scanning for Soft Tissue Conductivity Sensing. *IEEE Robotics and Automation Letters.* **7** 4055–4062

Vauhkonen, M. , Lionheart, W. , Heikkinen, L. M. , Vauhkonen, P. J. , & Kaipio, J. P. 2001 A matlab package for the eidors project to reconstruct two-dimensional eit images. *Physiological Measurement* **22** 107.

ICBEM Bioelectromagnetism ICEBI Electrical Bioimpedance EIT Electrical Impedance Tomography

Proceedings of the International Conference of Bioelectromagnetism, Electrical Bioimpedance,
and Electrical Impedance Tomography June 29 – July 1, 2022 / Kyung Hee University, Seoul, Korea

Cole bioimpedance parameters influence on strawberry ripening binary classification using decision trees

Pietro Ibba[1], Paolo Lugli[1] and Luisa Petti[1,2]
[1]Faculty of Science and Technology, Free University of Bolzano-Bozen, 39100, Bolzano-Bozen, Italy
[2]Competence Centre of Plant Health, Free University of Bolzano-Bozen, Piazza Universitá 1, 39100, Bolzano-Bozen, Italy

Correspondence : Pietro Ibba, e-mail : Pietro.Ibba@unibz.it

Abstract

Strawberry is one of the most popular fruits in the market. To constantly meet the demanding consumer and market quality standards, a rapid, accurate, and non-destructive evaluation of its quality is strongly needed. In this work, bio-impedance data of 234 strawberries were acquired, directly on-plant and at different ripening stages, and were then fitted with the Cole equivalent circuit model, extracting the four variables of the circuit (R_s, R_p, CPE-T and CPE-P). Afterwards, the influence of the circuit components on the fruit ripening discrimination task was evaluated by means of statistical analysis, selecting only the relevant features. The decision tree method was selected to develop the model for the classification of strawberries into ripe and unripe groups, yielding good overall performance, in terms of F_1, $F_{0.5}$ and F_2 score, of respectively 0.84, 0.78 and 0.92.

Keywords: Bio-impedance, Cole model fitting, Strawberry, fruit ripening, decision trees.

1. Introduction

Strawberry is a widely popular and highly valued non-climacteric fruit cultivated in many areas worldwide (Oo et al. 2018). Indeed, such success relates to the capacity of the producer to consistently meet both market and consumer quality standards. To achieve its maximum quality, such fruit must be harvested at its optimal ripeness stage, commonly when > 80% of the fruit surface shows a deep red color (Rahman et al. 2016). Strawberries are typically harvested following a manually and visually grading by farm-labors, a method which, being subjective, is inherently unreliable. For this reason, producers have been recently increasing the demand for quality monitoring techniques able to precisely and non-destructively classify such fruit maturity stage, allowing thus to reduce waste and increase market value. In this context, bioimpedance has showed a good potential, due to its simplicity, non-invasiveness, and cost-effectiveness. Such technique is based on the physico-chemical response, dependent on several intrinsic and extrinsic factors (e.g., sample geometry and chemical composition), of a sample to the application of an AC voltage in a specific frequency range (Grimnes and Martinsen 2011). Bioimpedance has been widely used for quality characterization of a wide variety of fruit (Grossi and Riccó 2017). Specifically, the strawberries bioimpedance-related works focused on their ripeness evaluation (González-Araiza et. Al., 2017), the detection of fungal diseases (Alejnikov et al. 2020), and the characterization of their post-harvest aging evolution (Al-Ali et al. 2018). Nevertheless, in all of the above works and in general in the fruit-related bioimpedance literature, a clear and well-established data analysis method is lacking. This is mainly related to the intrinsic nature of the bioimpedance data, commonly presenting a high level of autocorrelation and a non-linear relationship with the underlying biological behavior of the sample. For this reason, the reduction of the bioimpedance dataset to a smaller set of features, accounting for most of the information in the measurements, becomes especially important. This is particularly true for supervised machine learning methods, whose quality in the prediction and classification is greatly affected by the amount and relevance of input features. A popular solution is represented by fitting the bioimpedance data to equivalent circuit models, among which the most widely used is the single dispersion Cole electrical model (Cole 1940). This method reduces the spectra into few uncorrelated parameters, explaining the frequency dependent flow of current in a biological tissue, and being at the same time easier to handle statistically and usable as input features for supervised classification methods. Within this framework, the most popular and effective discrimination techniques applied in food are represented by logistic regression, artificial neural networks, support vector machine, naïve bayes, k-nearest neighbors and decision trees (Rivola et al. 2021). In particular, the latter is based on the creation of a model that predicts the class of a target variable by learning simple decision rules inferred from the data features (Wilkinson 2004).

In this work, this method was employed for strawberry ripening classification, to allow a straightforward evaluation of the role of the Cole circuit components on the discrimination task. Furthermore, a fuzzy c-means clustering (fcm) method was employed to divide the fruit in quality classes, starting from strawberry quality measurements, to strengthen and make objective this preliminary task.

2. Materials and methods

2.1 Experimental setup

A total of 20 strawberry frigo-plants (Fragaria×ananassa cv. Elsanta) was planted using a commercially available soil substrate in individual pots and then cultivated in a growth chamber under controlled conditions (24 °C, 70 % relative humidity). Here, a total of 234 strawberries was harvested at different ripening conditions (i.e., both fully ripe, ripening, and unripe). The harvested strawberry quality was characterized by acquiring each fruit size, skin color, relative sugar content, and bioimpedance data. The size was acquired by means of a caliper by measuring the fruit maximum diameter. Strawberry skin color was evaluated determining the color parameters in the CIELab color space using a portable tristimulus colorimeter (Chroma Meter CR-400, Konica Minolta Corp., Osaka, Japan) and the sugar content in terms of total soluble solid content, expressed in degrees Brix (°Bx), was determined using a digital refractometer (Atago, Tokyo, Japan) on fresh extracted fruit juice. Finally, the strawberry bioimpedance data were acquired using an E4990A bench-top impedance analyzer (Keysight Technologies, Santa Rosa, CA, USA) in the 20 Hz – 300 kHz frequency range, over 400 logarithmically spaced frequency points, in a two-electrodes configuration. The electrical contact with the fruit was established, as described in a previous work (Ibba et al., 2021) by means of custom-made screen-printed Ag/AgCl electrodes together with contact gel (FIAB G005 high conductivity ECG/EEG/EMG gel).

2.2 Dataset preparation

The strawberry fruits were split in two classes, namely ripe and unripe, based on their ripening-related quality attributes. Specifically, the fuzzy c-means clustering (fcm) tool, whose functioning principle is described in section 2.3, using the color coordinate a*, already employed in other works as a clustering criterion (González-Araiza et. Al., 2017 and Ibba et al., 2021), plus the fruit size (in cm), and the total soluble solids content (in °Brix), typically correlated to fruit ripening (Montero et al., 1996). Fig. 1 shows the outcome of the clusterization, where the total of 234 sampled strawberries was divided in the two ripening classes, to be used as labels in the binary classification procedure, composed of 152 ripe and 82 unripe samples. To reduce the predictor dataset and simplify the interpretation of the results, the bioimpedance data were fitted with the single dispersion Cole electrical model (Cole 1940) using the real and imaginary components of the bio-impedance spectra as input data. The fitting procedure was carried out by iterating different combinations of initial values of the equivalent circuit components and selecting the ones giving the best fit for each fruit spectrum. Here, the best fit was found by the Matlab Zfit script iterating the fitting until the best possible fit for the given impedance curve was achieved, and by finally extracting the best circuit parameters combination (i.e., the R_p, R_s and CPE values). The quality of the fitting procedure was evaluated in terms of Root Mean Square Error (RMSE).

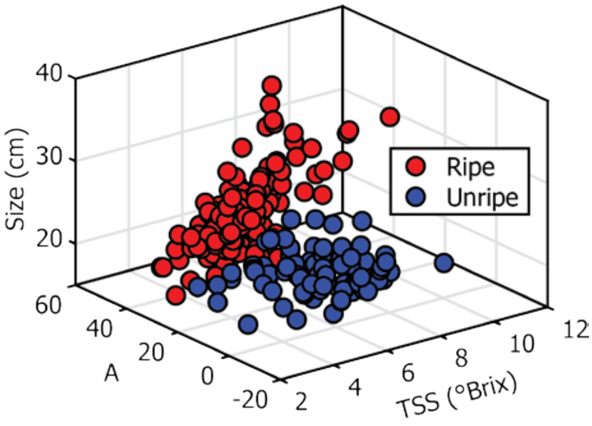

Figure 1. Fcm-based clustering results in ripe and unripe fruit, based on strawberry quality parameters.

2.3 Software and Data Analysis

The data was post-processed and analyzed using Matlab R2020b (The MathWorks Inc., Natick, MA, United States). The data were divided in classes using a fuzzy c-means (fcm) clustering iterative method. Initially, the fcm function generated a random fuzzy partition matrix, indicating the degree of membership of each data point in each cluster. Then, in each clustering iteration, it calculated the cluster centers and updated the fuzzy partition matrix, using the calculated center locations until reaching a minimum improvement threshold (Bezdek 1981). The impedance data were fitted with the equivalent circuit using Matlab Zfit script (by Jean-Luc Dellis, version 1.2.0.0, retrieved February 2018). One-way analysis of variance (ANOVA) was performed to evaluate statistical differences among each circuit parameter for class discrimination. The Tukey's honestly significant difference (HSD) method was performed, and the differences were calculated for an appropriate level of interaction ($p \leq 0.05$) (Montgomery 2001). Results were reported as the mean and standard deviation (SD) of the mean. The decision tree method was selected for data classification. The model was optimized with a grid search of combination of hyperparameters, validating the results with a fixed tenfold cross-validation, and by finally selecting a maximum number of six splits with the split criterion of Gini's diversity index as optimal parameters. The performance of the developed decision tree model was evaluated in terms of F_β-scores with β values of 1, 0.5 and 2, to obtain and select the best models for a balanced, precision-oriented, and recall-oriented classification, respectively (Chinchor 1992, Sasaki 2007).

Results and discussion

2.4 Cole model fitting and parameters selection

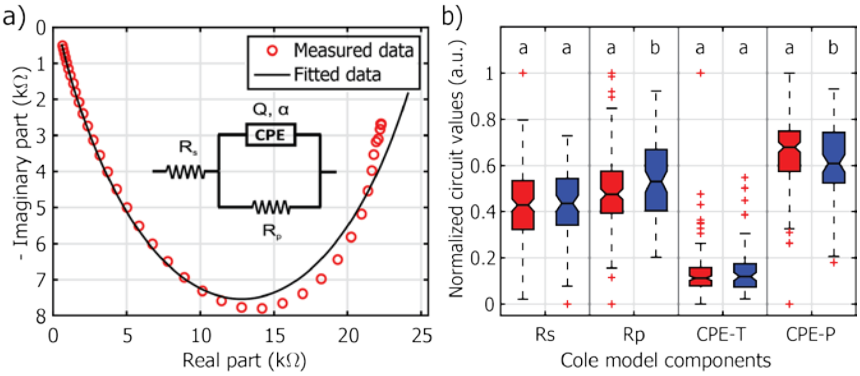

Figure 2 - (a) Equivalent circuit model fitting for the fruit with highest RMSE. The circles represent the experimental results, while the line depicts the fitted curve. (b) Boxplot comparison of the Cole model parameters relevance in the class discrimination, red and blue stand for ripe and unripe fruit, respectively. Different letters represent statistically significant differences among the groups according to ANOVA.

The equivalent circuit model fitting resulted in an average % RMSE, obtained by averaging the values of all the considered 234 fruit samples of 1.35%, corresponding to an average error, in terms of impedance magnitude, of 229.5Ω. Fig. 2a depicts the model fitting for the strawberry with highest RMSE, corresponding to an error of 652.1Ω (3.82%). Given the low error of the fitting results, it is possible to state that Cole model is a good approximation of the impedance of strawberries, and that is thus possible to employ its resulting extracted parameters in the discrimination of the strawberry ripening stage. Afterwards, the relevance of extracted parameters for the discrimination of strawberry ripening was evaluated, to estimate whether a possible reduction of the input features for the decision tree discrimination was possible. Statistical analysis was performed by means of the analysis of variance (ANOVA), to search for statistically significant differences in the parameter values among the two considered classes. Fig.2b gives an overview of the average Cole model electrical parameter values for the two strawberry classes, along with the results of the ANOVA. In the figure, mean values with no common letters are statistically different, according to HSD ($p \leq 0.05$). The statistical analysis clarified that, while R_s and CPE-T (high frequency resistive component and CPE pseudo-capacitance, respectively) presented no statistically relevant differences, the low frequency resistive component (R_p) and the CPE time constant (CPE-P) could have a relevant contribution in the ripening discrimination carried out afterwards. Such results are also validated by studies on other kind of fruit, where a high variability was found in the low frequency impedance magnitude at the varying of banana and apple ageing stages (Ibba et al. 2020) and where CPE-P had a relevant contribution in the discrimination of apples (Ibba et al. 2019).

2.5 Classification of strawberry ripeness

Such extracted features, originated by the strawberries bioimpedance data fitting followed by a further selection of the most relevant circuit parameters, were employed in the strawberry ripening classification by means of a binary decision tree method. The weight in the classification of the selected Cole model variables, is depicted in the schematic of the fine tree classification model shown in Fig. 3a. Results indicate that the CPE-P parameter, representing the time constant α and related to tissue homogeneity, was useful to perform a first separation into fruit with high and low relative R_p values, which were then employed for discriminating the ripe and unripe fruit.

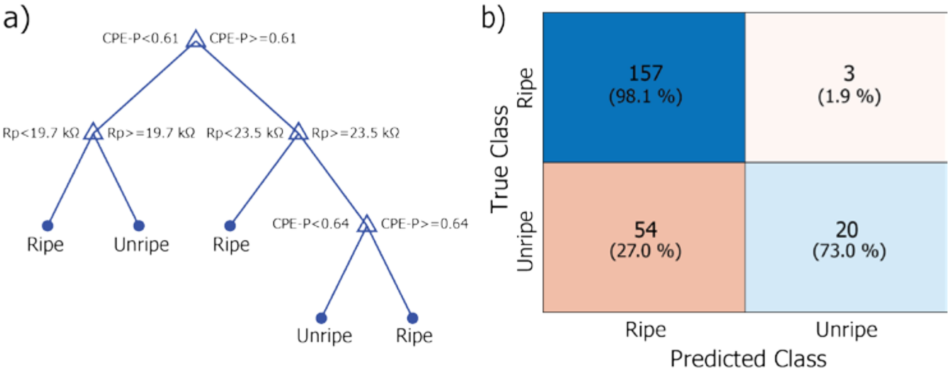

Figure 3 - (a) Schematic of the developed fine tree classification model for determination of strawberry ripeness and (b) confusion matrix showing the number and the relative percentage, of correctly and incorrectly classified fruit.

The resulting strawberry quality classification performance was of 0.84, 0.78 and 0.92, in terms of F_1, $F_{0.5}$ and F_2 scores, respectively. In particular, the developed fine tree model, whose performance is also described using the confusion matrix in Fig. 3b, appeared to classify ripe fruits better than the unripe samples. The classification model correctly predicted 98.1% of the ripe strawberries, while misclassifying only a 1.9% of them as unripe samples. On the other hand, opposite performance was obtained for the second class, where 73.0% and 27.0% of unripe fruit were classified as unripe and ripe, respectively. Such results can be due to the use of a tenfold CV which, recursively predicting from the same dataset, could have caused an overfitting of the model, which was also not tested on unseen data. Such preliminary results, which cannot be considered completely satisfactory, highlight the limits of the employed method, but can also be considered as a promising starting point for future analysis. In fact, despite achieving a poor accuracy on the unripe class, the model appeared strong in the discrimination of the class of interest (i.e., the ripe one). For this reason, it can be considered for an employment in a supervised harvesting context, where a human operator validates its decision in a situation of doubt with the aid of portable impedance analyzers (ref) with on-board discrimination models.

3. Conclusions

In this work, bio-impedance data of strawberries at different ripening stages were fitted with the Cole equivalent circuit model, extracting the four variables of the circuit (R_s, R_p, CPE-T and CPE-P) and evaluating them in terms of their impact on the fruit ripening discrimination. The decision tree method was selected to develop the model for the classification of strawberries into ripe and unripe groups, yielding good overall performance, in terms of F_1, $F_{0.5}$ and F_2 score, of respectively 0.84, 0.78 and 0.92. The results demonstrated how, using few impedance parameters and a reasonable classification criterion, even simple models can achieve good classification performances, also clarifying the role of the employed features in the process and thus, in the explanation of the underlying biological phenomenon. Ideally, the continuous and precise development of such predictive models for fruit quality will pave the way for a more efficient evaluation of fruit quality, allowing to avoid wastes and enhancing the fruit market value.

Acknowledgments

This work has been partially supported by the Italian Institute of Technology (IIT) and by the UNIBZ ID Project BIOFRUIT.

References

Al-Ali A. A., Elwakil A. S. and Maundy B. J. 2018 Bio-impedance measurements with phase extraction using the kramers-kronig transform: Application to strawberry aging *2018 IEEE 61st International Midwest Symposium on Circuits and Systems (MWSCAS)* 468–471.

Alejnikov A. F., Cheshkova A. F. and Mineev V. V. 2020 Choice of impedance parameter of strawberry tissue for detection of fungal diseases *IOP Conf. Ser. Earth Environ. Sci.* 548, 032005.

Bezdek, J. C. 1981 Pattern Recognition with Fuzzy Objective Function Algorithms. Springer US.

Chinchor, N. 1992 MUC-4 evaluation metrics *Proceedings of the 4th conference on Message understanding - MUC4 '92* Association for Computational Linguistics.

Cole K S 1940 Permeability and impermeability of cell membranes for ions *Cold Spring Harbor symposia on quantitative biology*. Vol. 8. Cold Spring Harbor Laboratory Press, 1940

González-Araiza, J. R., Ortiz-Sánchez, M. C., Vargas-Luna, F. M. And Cabrera-Sixto, J. M. 2017 Application of electrical bio-impedance for the evaluation of strawberry ripeness. *International Journal of Food Properties*, 20(5), 1044–1050.

Grimnes S. and Martinsen O. G. 2011 Bioimpedance and bioelectricity basics *Academic press*.

Grossi M. and Riccò B. 2017 Electrical impedance spectroscopy (EIS) for biological analysis and food characterization: A review *Journal of Sensors and Sensor Systems*, vol. 6, no. 2, pp. 303-325.

Ibba P., Falco A., Rivadeneyra A. and Lugli P. 2018 Low-cost bio-impedance analysis system for the evaluation of fruit ripeness *IEEE SENSORS Proceedings*, IEEE Sensors 2018, New Dehli, India, pp. 1–4.

Ibba, P., Cantarella, G., Abera, B.D., Petti, L., Falco, A., Lugli, P. 2020 Selection of Cole Model Bio-Impedance Parameters for the Estimation of the Ageing Evolution of Apples 1*7th International Conference on Electrical Bioimpedance ICEBI 2019*. IFMBE Proceedings, vol 72. Springer, Singapore.

Ibba P, Tronstad C, Moscetti R, Mimmo T, Cantarella G, Petti L, Martinsen Ø, Cesco S and Lugli P 2021 Supervised binary classification methods for strawberry ripeness discrimination from bioimpedance data *Scientific Reports* 11.

Ibba P., Crepaldi M., Cantarella G., Zini G., Barcellona A., Rivola M., Petrelli M., Petti L. and Lugli P. 2021 Design and Validation of a Portable AD5933–Based Impedance Analyzer for Smart Agriculture *IEEE Access*, vol. 9, pp. 63656-63675

Montero, T. M., Mollá, E. M., Esteban, R. M., & López-Andréu, F. J. 1996 Quality attributes of strawberry during ripening. *Scientia Horticulturae*, 65(4), 239-250.

Montgomery, D.C. 2001 Design and Analysis of Experiments. Wiley, New York.

Oo, L. M. and Aung, N. Z. 2018 A simple and efficient method for automatic strawberry shape and size estimation and classification *Biosystems engineering*, 170, 96-107.

Rahman M. M., Moniruzzaman M., Ahmad M. R., Sarker B. C. and Khurshid-Alam M. 2016 Maturity stages affect the postharvest quality and shelf-life of fruits of strawberry genotypes growing in subtropical regions *Journal of the Saudi Society of Agricultural Sciences*, Volume 15, Issue 1, 2016, Pages 28-37.

Rivola M., Ibba P., Lugli P. and Petti L. 2021 Bioimpedance Data Statistical Modelling for Food Quality Classification and Prediction *2021 IEEE International Symposium on Circuits and Systems (ISCAS)*.

Sasaki, Y. 2007 The truth of the f-measure. *Teach Tutor mater*, Vol. 1–5.

Wilkinson L. 2004 Classification and regression trees *Systat*, 11, 35-56.

Proceedings of the International Conference of Bioelectromagnetism, Electrical Bioimpedance,
and Electrical Impedance Tomography June 29 – July 1, 2022 / Kyung Hee University, Seoul, Korea

Impedivity of various human breast tissues

Gerald Sze[1], Zhao Song[1,3], Huijuan Zhang[2], Jie Wang[2], Qi He[2], Rui Guo[1],
Barry Bueles[3] and Wei Wang[1,3,4]
[1]Micro Image Biotech Ltd, Ningbo, China
[2]Shanghai International Peace Maternity and Child Health Hospital of China Welfare Institute, China
[3]Micro Image Biotech International Ltd, Cambridge, UK
[4]Weilian Biotech Ltd, Ningbo, China

Correspondence : Wei Wang, e-mail : w97wang@yahoo.co.uk

Abstract–A series of Electrical Impedance Spectroscopy (EIS) experiment have been carried out to extract unique characteristics of benign and malignant human breast tissue in-vitro in a joint clinical study with the Pathology Department. Digital images of pathology slides for each paraffin-sectioned breast tissues have been taken, so that the effects of unwanted tissue types mixing with the targeted tissues types can be studied. By recognizing mixed tissues in digital pathology slide images, the unwanted mixed tissues can be removed from the EIS data, and the impedance patterns of the target tissue ocused on such as cancer cells. The impedance patterns of the following four types of tissue are initially extracted: adipose tissue, connective tissue, inductal carcinoma (IDC), fibroadenoma. The information within this data will help to achieve the goal of being able to predict the likely different diagnostic results according to each patient's different measureable life parameters such as BMI and age.

Keywords: human breast tissues; impedivity; electrical impedance spectroscopy; EIS; breast cancer.

1. Introduction

Different types of breast tissue were isolated in-vitro from surgically excised pathology from breast tissue and the EIS data for each tissue type was digitally recorded before the tissue was paraffin-sectioned as pathology slides. Based on the characteristics of the impedance patterns of human tissue published by Cole and Cole (1941), and the human breast tissue published by Jossinet (1998) and Wang (2001) as the reference for guidance, the impedance pattern characteristics of several tissue types within human breast tissue were determined using the EIS data.

One of the challenges of EIS studies of in-vitro breast tissues is the mixing of different tissue types in the same biopsy or excised pathology sample which causes great variances in the measured overall impedance. The approach adopted was to analyse the digital pathology slide images to determine the different tissue types present in the sample breast specimen. The direction of the electric current inside the specimen during the EIS measurement was also analysed. The Cole-Cole impedance parameters for the different pure tissue types were used to determine the different tissue types present within the same test pathology specimen. The EIS data sets of the different pure tissue types present in the overall tissue were then extracted from the cleaned pure tissue specimen data sets being examined at a cellular level.

2. Data collection

2.1 Sampling size

68 EIS data sets have been taken from the hospital, of which 31 sets were valid for analysis. 11 sets (35% out of 31) were taken from patients diagnosed with a benign tumour, and 21 sets (68% out of 31) were taken from patients diagnosed with a malignant tumour. Note that some cases had both benign and malignant tissues diagnosed.

2.2 Quality control of EIS specimen

All the sets of data ("set of data" means all EIS measurements from all tissues taken from one patient in a surgical operating room to the pathology laboratory) must satisfy with following criteria to ensure that their quality is sufficient to be "valid". There are two types of data comparison: One compares the different types of tissues taken from the same patient; Another compares the same types of tissues taken from different patients

Timing after surgery

The EIS data must be collected within 15 minutes of surgery with the tissue stored in a in a temperature controlled box (6^oC). The electrical impedance properties in human cells deteriorate rapidly after this period.

Background saline reference data set

The EIS background saline reference data set (filling the testing chamber with 1000µS/cm saline water) must be collected before the human tissue EIS measurement. The saline EIS data set is used as a reference to calibrate the EIS testing unit's internal impedance difference.

Size of tissue according to volume of testing chamber

Tissues are cut to fit the exact size of the cylindrical testing chamber (diameter 5mm and length 8mm). Saline is injected to ensure good contact between the tissue and the electrodes that are located at the two ends of the chamber. The size of tissue sample must not less than the volume of the chamber to avoid the current by-passing the tissue sample through the saline. The saline must not fill more than 10% of the chamber's volume. Otherwise the impedance patterns of the test tissues will be distorted invalidating the impedance measurements of the sample.

Data comparison

There are two types of data comparison: One compares different type of tissues taken from the same patient, another compares same type of tissues taken from different patients.

2.3 Digital pathology slide images

The illustrations below outline the procedures used to capture the digital pathology slide images of breast tissues with different fields of views (FOV):

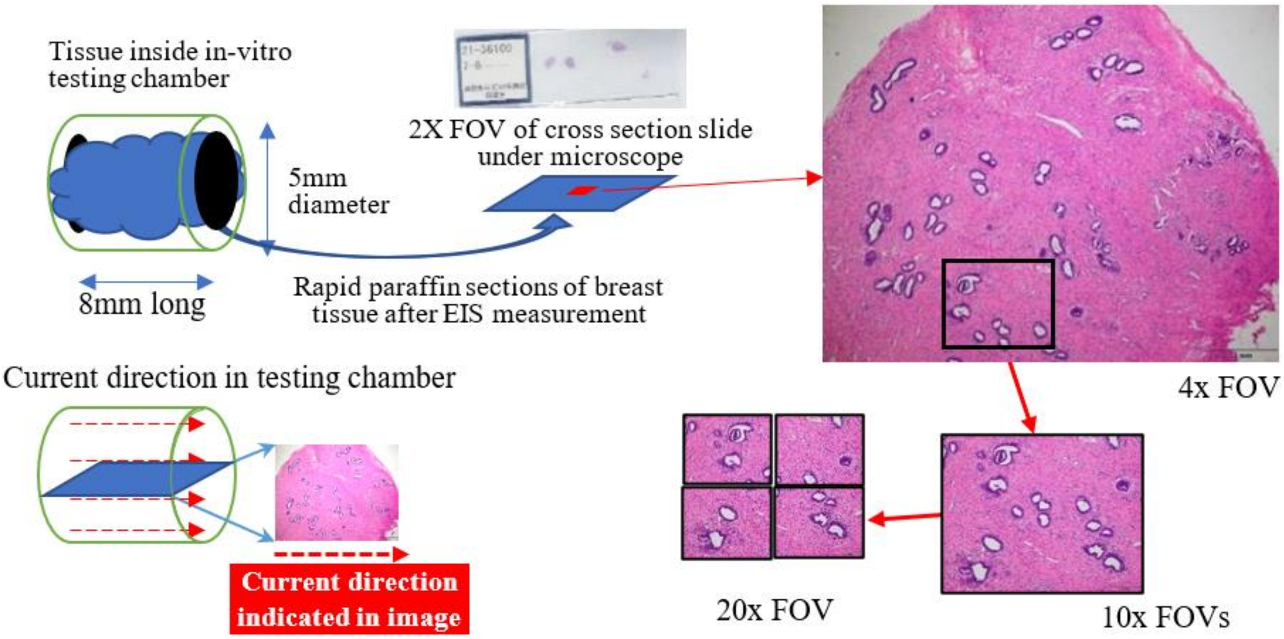

Figure 1. Procedures to capture digital pathology slide images.

2.4 Age and BMI distribution

The 31 valid data sets are collected from 31 patients accordingly: aged below 40 = 7, aged between 40 and 60 = 14, aged above 60 = 10; BMI below 23 = 12, BMI between 23 and 25 = 10, BMI above 25 = 9. 21 patient has been diagnosed with IDC tumour, 11 patients has been diagnosed with fibroadenoma tumour.

3. Methods

3.1 Procedures

There are three steps in verifying pure tissue impedance: i. Categorize tissues into "pure" and "mixed" groups according to the pathology slide images (example of mixed and pure tissues shown in figure 2); ii. From "pure" tissues, determine the impedance data and extract the Cole-Cole parameters as described in section 3.2; iii. Using the patented cascaded model (Wang's US patent).

3.2 Equations

The Cole-Cole equation (Cole 1940, Cole and Cole 1941, McAdams and Jossinet 1995) displays the change in impedance at different frequencies:

$$Z = R_\infty + (R_0 + R_\infty)/(1 + (\mathrm{j}f/F_r))^\propto \tag{1}$$

where R_∞ and R_0 = resistance at infinite or zero frequency
F_r = relaxation frequency
α = relaxation time.

When we assuming the measuring object as a simplified cell suspension model with three element (R, S, C) electrical equivalent circuit (Fricke and Morse 1925), the following equation can be used:

$$Z = \mathrm{RS}/(R + S) + (R - RS/(R + S))/(1 + (\mathrm{j}f/F_r))^\propto \tag{1}$$

where R = extra-cellular resistance, equals to R_0 in (1)
S = intra-cellular resistance
R_∞ = paralleling R and S.

Four Cole-Cole parameters: R, S, F_r, α are calculated from the EIS bio-impedivity curves using these two equations.

4. Results

4.1 Digital pathology slide images of mixed and pure tissues

Below pathology slide images show connective tissues that are affected by different compositions of adipose tissues:

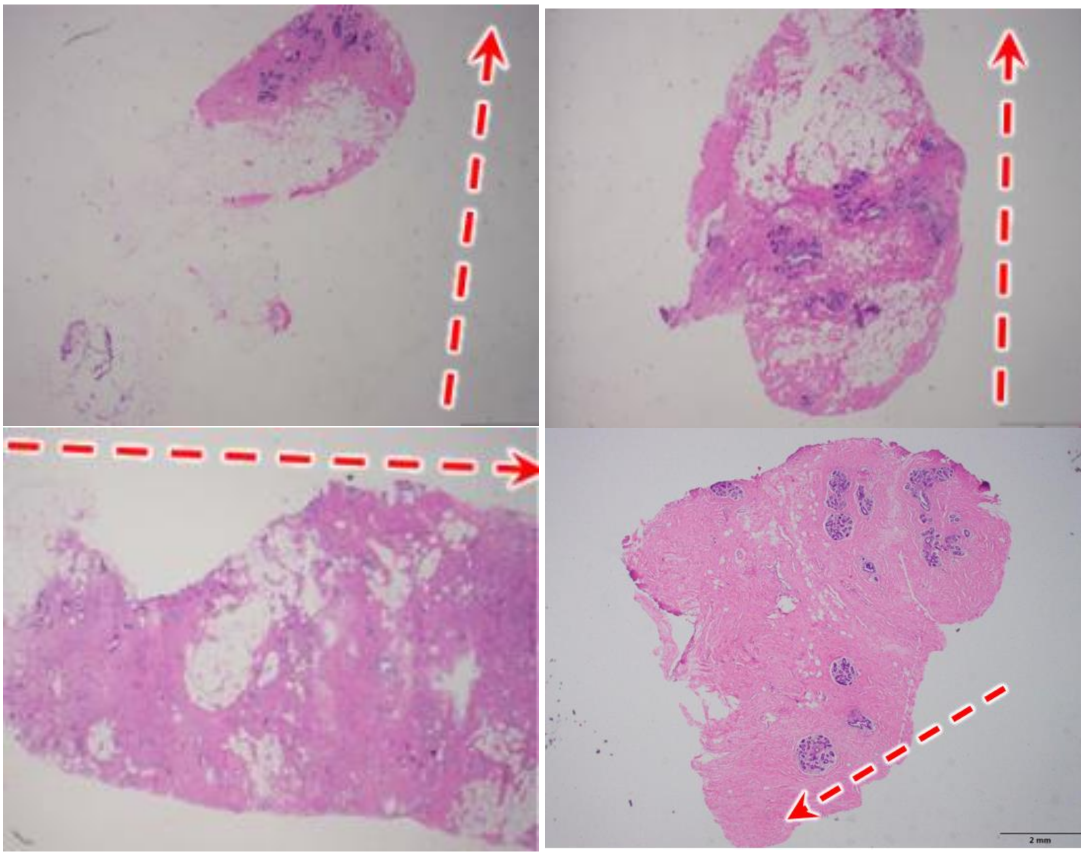

Figure 2. Connective tissues with different composition of adipose tissue (top-left: heavy; top-right: medium; bottom-left: mild; bottom-right: none).

4.2 Calculated Cole-Cole parameters of pure tissues

After selecting pure tissues specimen, the Cole-Cole parameters are calculated from the respective EIS data sets as below:

Table 1. Calculated Cole-Cole parameters for the four types of pure tissues

	R in Ω cm	*S in Ω cm*	*Fr in kHz*	*α*
Connective tissue	*2.97*	*3.22*	*4515*	*0.14*
Adipose tissue	*16.51*	*38.93*	*13379*	*0.48*
IDC	*5.40*	*2.19*	*641*	*0.47*
Fibroadnoma	*3.57*	*3.45*	*6308*	*0.31*

Table 2 lists the Cole-Cole parameters published in Jossinet's paper about the impedance of freshly excised human breast tissue.

Table 2. Calculated Cole-Cole parameters for the four types of pure tissues

	R in Ω cm	*S in Ω cm*	*Fr in kHz*	*α*
Connective tissue	*12.63*	*28.80*	*448*	*0.51*
Adipose tissue	*23.90*	*67.79*	216	*0.57*
IDC	*3.89*	*0.991*	*477*	*0.46*
Fibroadnoma	*2.54*	*10.11*	*497*	*0.59*

5. Discussion

The R and S calculated from the Shanghai data set of connective tissue drops from above 20 Ω·m from Jossinet data sets to below 4 Ω·m. This may be caused by the existence of adipose tissue within the measured connective tissues.

The relaxation frequencies of connective, adipose and fibroadenoma tissues from the Shanghai data sets are much higher than the Jossinet data sets. At this point we need more data to verify these new findings. However, IDC is the tissue type that has the most similar Cole-Cole parameters extracted from the EIS data sets.

6. Conclusions

The work presented is essential before the Electrical Impedance Mammography (EIM) images could be diagnosed because each pixel in 3D EIM images are mixed with surrounding tissues, and the impedance characteristics of mixed tissues must be identified with solid evidence, which could be by using pathology slide images and EIS data on the same tissue.

Acknowledgments

We acknowledge Shanghai International Peace Maternity and Child Health Hospital of China Welfare Institute who provided all data and the opportunities to run the clinical trial during the hard time during COVID pandemic.

References

Cole K 1940 Permeability and impermeability of cell membranes for ions *Cold Spring Harbor Symp., Quant. Biol.* **8** 110–22

Cole K and Cole R 1941 Dispersion and absorption in dielectrics *J. of Chem. Phys.* **5** 341–350

Jossinet J 1998 The impedivity of freshly excised human breast tissue *Physiol. Meas.* **19** 61-75

McAdams E and Jossinet J 1995 Tissue impedance: a historical overview *Physiol. Meas.* **16** (suppl) A1–A13

Wang W, *et al* 2001 Preliminary results from an EIT breast imaging simulation system *Physiol. Meas* **22**(1) 39-48

Wang W, 2005.02 Apparatus and method for detecting abnormalities in bodily matter *US6856842(B1)*

DAY 1

Wednesday, June 29, 2022

Workshop 01

Sciospec Scientific Instruments

W 01 **Impedance measurements - instruments, sensors & beyond. An introduction on how to choose, design and successfully use setups for electrical impedance spectroscopy**
Sebastian Wegner (Sciospec Scientific Instruments)
Martin Bulst (Sciospec Scientific Instruments)
Sophie Müller (Sciospec Scientific Instruments)

ICBEM Bioelectromagnetism ICEBI Electrical Bioimpedance EIT Electrical Impedance Tomography

Proceedings of the International Conference of Bioelectromagnetism, Electrical Bioimpedance,
and Electrical Impedance Tomography June 29 – July 1, 2022 / Kyung Hee University, Seoul, Korea

Impedance measurements - instruments, sensors & beyond An introduction on how to choose, design and successfully use setups for electrical impedance spectroscopy

Martin Bulst, Sophie Müller, Sebastian Wegner
Sciospec Scientific Instruments GmbH, Germany

Correspondence : Martin Bulst, e-mail : m.bulst@sciospec.de

Abstract– Accurately performing electrical impedance spectroscopy can be a challenging task. Choosing equipment, sensors and configurations for impedance measurements involves making many choices building on a deep understanding of specifications, parameters, and general options that even for experienced engineers and scientists can be tricky. Complex cross-dependencies of the components, practical limitations and all too often, unprecise not generally applicable assumptions are just a few of the obstacles to navigate.

This tutorial discusses the most important aspects of measurement setups for electrical impedance spectroscopy and illustrates those on many real-life reference cases both from academic research and industrial application. Some of the topics covered include

- Brief review of basics of impedance spectroscopy
- A tour of common and some not so common impedance applications
- Measuring impedance – overview of available instrument classes and their individual strengths
- Deep dive into the most important specifications and what they practically mean
- Multichannel options
- Parasitic influences
- Electrodes and sensors

All topics are illustrated with practical examples for better understanding of their implications. The goal is to deliver a good understanding of the most important things to watch out for when performing impedance measurements, give practical advice on choices and options and shed some light on a few things that all too often are dominated by over-simplifications or commonly found false assumptions.

Acknowledgments

The authors would like to express their gratitude to the organizing committee for the chance to hold this tutorial and all our partners and customers who helped us collect and understand the presented reference cases and conclusions.

For more information please visit: www.sciospec.com

DAY 2

Thursday, June 30, 2022

Invited Talk 03

Speaker Ryan Halter (Dartmouth College)

“Opportunities for clinical translation of impedance sensing and imaging devices”

Proceedings of the International Conference of Bioelectromagnetism, Electrical Bioimpedance,
and Electrical Impedance Tomography June 29 – July 1, 2022 / Kyung Hee University, Seoul, Korea

Opportunities for clinical translation of impedance sensing and imaging devices

Ryan Halter[1,2]
[1]Thayer School of Engineering, Dartmouth College, Hanover, NH, USA
[2]Geisel School of Medicine, Dartmouth College, Lebanon, NH, USA

Correspondence : Ryan Halter, e-mail : ryan.halter@dartmouth.edu

Abstract– ***Introduction:*** Electrical impedance sensing and imaging has been widely explored for the last three decades primarily in academic settings with multiple publications suggesting the promise of this technology[1]. However, with the exception of ventilation monitoring, limited clinical translation has actually been realized. ***Purpose:*** This talk will explore some multi-modal approaches that couple impedance sensing and imaging with standard-of-care clinical devices as a potential streamlined pathway to translation and ultimately clinical utility. ***Methods:*** Example clinical applications that will be presented include EIT-coupled ultrasound for prostate, breast, and muscle imaging, EIS-coupled biopsy needles for tissue pathology assessment, an endoscopic-like probe for surgical margin assessment and an EIS-coupled surgical drill for bone and soft tissue sensing. ***Findings:*** Coupling impedance sensing and imaging systems to existing medical devices provides two significant benefits: 1) the coupled systems represents a familiar platform to clinicians helping to overcome the “new technology” burden to clinical acceptance and 2) the coupled systems can synergistically improve upon impedance sensing and imaging alone. For example, coupled and synchronously acquired ultrasound images can be used to help guide the EIT reconstruction and produce more accurate and resolved impedance images. ***Conclusion:*** Integrating impedance sensing and imaging into clinically accepted devices presents an opportunity to streamline the clinical acceptance of impedance technologies and impact clinical management of patients.

Acknowledgments

The authors would like to express their gratitude to the National Institutes of Health (1R01CA237654-01A1, 1R41AR076912-01, 1R41CA235994-01, 1R42DE028209-01) and the DoD’s Congressionally Directed Medical Research Program (W81XWH-15-1-0572) for their generous funding of the work presented here.

References

1. Adler, A. and Holder, D. eds., 2021. *Electrical impedance tomography: methods, history and applications*. CRC Press.

DAY 2

Thursday, June 30, 2022

Mini Symposium 01

Measuring Bioimpedance by Biosensors

Organizer César A Gonzalez (Instituto Politécnico Nacional)

M 01-01 **Instrumentalization impacts when using biosensors**
Pedro Bertemes Filho (State University of Santa Catarina)

M 01-02 **Dielectrophoretic electro-manipulation of biological cells and their characterization based on electrical impedance**
Marius Andrei Olariu (Technical University of Iasi)

M 01-03 **Sensing accumulation of nanoparticles in tissue by electrical impedance**
Svetlana Kashina (University of Guanajuato)

Proceedings of the International Conference of Bioelectromagnetism, Electrical Bioimpedance,
and Electrical Impedance Tomography June 29 – July 1, 2022 / Kyung Hee University, Seoul, Korea

Instrumentalization impacts when using biosensors

Pedro Bertemes-Filho[1], Kaue F. Morcelles[1], Sergio H. Pezzin[2], John A. Gomez-Sanchez[1]
[1]State University of Santa Catarina, Dept. Electrical Engineering, Joinville, Brazil
[2]State University of Santa Catarina, Deptment of Chemistry, Joinville, Brazil

Correspondence : Pedro Bertemes-Filho, e-mail : pedro.bertemes@udesc.br

Abstract - As modern medicine becomes more and more integrated, intelligent, and personalized, the demand for novel and specialized biosensors increases. Biosensors are in the center of the current major technological advances in health care and diagnosis, drug delivery, and water and food quality/environmental monitoring. Biosensors are receptor-transducer devices (or probes), which can convert a biological response, from a physiological change caused by enzymes or antibodies, for example, into a measurable electrical signal. At the current state-of-the-art, even low concentrations of specific pathogens, or toxic chemicals, can be measured [1]. Today, the main challenges involved in the development of biosensors are related to the transduction of biosensing signals into electrical (or electrochemical, optical, acoustic etc.) signals, the increase on sensitivity and reproducibility, the decrease of the response time and detection limits, and the miniaturization using micro/nano-fabrication technologies. Recently, several researchers reported significant enhancements in the biosensing technology by using nanomaterials, such as carbon nanotubes, graphene [2] and metal or metal oxide nanoparticles, which present high surface-to-volume ratios, good electrical and thermal conductivities, and mechanical performance [3]. However, one aspect of the design that is often overlooked is electronic instrumentation, which is composed by a low-noise front-end, an amplification unit, a filtering stage, and an analog-to-digital unit. This is a non-ideally process where the circuits introduce inaccuracy, precision degrading, and unreliability for practical biosensors. The most important stage is the low-noise front-end (LNFE) which is connected directly to the biosensor. The topology of the LNFE depends on the nature of the sensor: (i) if the biosensor outputs a voltage, the LNFE is an instrumentation amplifier (INA); (ii) if the biosensor outputs a current, the LNFE can be either a transimpedance amplifier (TIA) or a shunt resistor followed by an INA; (iii) if the biosensor outputs a variation in impedance, the LNFE can be implemented using a bridge circuit, a combination of a current excitation module and an INA, or a combination of a voltage excitation module and a TIA. In case (i), the INA should provide high input impedance, high common-mode rejection ratio, and low input-referred noise for best performance. Furthermore, the INA gain should be designed to reduce the overall noise while maintaining enough dynamic range for the biosensor signal. In case (ii), TIAs are often a better option than shunt resistors, as they provide a lower impedance path to the current. The input impedance of the TIA should be kept small, while still providing enough transimpedance gain and bandwidth for the biosensor current. Moreover, current leakages from parasitic capacitances at the input should be minimized, to improve accuracy and stability. In case (iii), Wheatstone-Bridge circuits are desirable in applications dealing with very small impedance variations in the biosensor. In these cases, the circuit topology should be designed to provide the best sensitivity to the biosensor operation point, as well as to eliminate cable influence and any type of parasitic effect. When excitation circuits are necessary, current sources are typically the best choice, and must be designed with high output impedance, current stability, and voltage compliance [4]. Biosensors based on impedance measurements have an advantage on enzymatic and non-enzymatic electrochemical measurements due to simplicity, sensitivity, selectivity, low detection limit, low cost, and possible miniaturization. However, in some cases, estimation with impedance measurements requires a mathematical model to reduce possible uncertainty values. Measurement using a combination of a biosensor with electrical impedance spectroscopy (EIE) is a better alternative compared to currently used methodologies, with advantages as a non-invasive and non-destructive method [5].

Acknowledgments

Supported by UDESC and CNPq (Nr. 408732/2021-0)

References

[1] Naresh, V.; Lee, N. A., 2021: Review on Biosensors and Recent Development of Nanostructured Materials-Enabled Biosensors. Sensors 21, 1109.
[2] Gomez-Sanchez, J. A.; Hack, R.; Pezzin, S. H.; Bertemes-Filho, P. Biosensor Based on Carbon Nanocomposites for Detecting Glucose Concentration in Water. In: Pedro Bertemes Filho. (Org.). IFMBE Proceedings. 1ed.Singapura: Springer Singapore, 2020, v. 72, p. 33-37
[3] Galvez, A.Z.; Narvaez, E.M.; Martinez, C.C.M.; Merkoci, A., 2017: Nanomaterials connected to antibodies and molecularly imprinted polymers as bio/receptors for bio/sensor applications. Appl. Mater. Today 9, 387–401.
[4] Bertemes-Filho, P. Designing a current source. In: Paul Annus; Mart Min. (Org.). Bioimpedance and Spectroscopy. 1ed.Singapura: Elsevier, 2021, v. 1, p. 79-98.
[5] Tran A. K.; Sapkota, A. Wen, J.; Li, J.; Takei, M. (2018) Linear relationship between cytoplasm resistance and hemoglobin in red blood cell hemolysis by electrical impedance spectroscopy & eight-parameter equivalent circuit. Biosensors and Bioelectronics, 119: 103-109.

ICBEM Bioelectromagnetism ICEBI Electrical Bioimpedance EIT Electrical Impedance Tomography

Proceedings of the International Conference of Bioelectromagnetism, Electrical Bioimpedance,
and Electrical Impedance Tomography June 29 – July 1, 2022 / Kyung Hee University, Seoul, Korea

Dielectrophoretic electro-manipulation of biological cells and their characterization based on electrical impedance

Marius Andrei OLARIU[1]

[1] Department of Electrical Measurements and Materials, Faculty of Electrical Engineering, Technical University of Iasi, Romania

Correspondence : Marius Andrei Olariu, e-mail : molariu@tuiasi.ro

Abstract – Development of new tools for evaluation of metastasis evolution based on separation of circulating tumour cells (CTCs) it is not a new approach and a plethora of studies were reported previously. However, differentiation and confirmation of CTCs from normal cells based on different methods than the immuno-staining ones represents a new goal critical in practical experimentations. Thus, identifying the correlation between the morphology of the CTCs and their electrical properties demonstrated to be a viable alternative solution. Moreover, the experiments performed to date demonstrated that characterization of cancer cells based on their electrical properties obtained with broadband dielectric spectroscopy (BDS) is significantly influenced by the properties of the suspending media. Under these circumstances, within the herein scientific work, based on a series of viability studies at the level of THP-1 cell line (human monocytic cell line derived from an acute monocytic leukemia patient), three sucrose based suspending solutions were analyzed from the viewpoint of electromanipulation (DEP) efficiency and dielectric response obtained through dielectric relaxation spectroscopy (DRS). The practical experiments highlighted how the suspending medium (buffered/ unbuffered) and its conductivity are influencing cells behaviour in the presence of electrical fields. The results confirmed that LCBs (low conductivity buffers) are the most convenient solutions for running these type of experiments as of their minimal influence on cancer cell viability as well as basically experimental operability (e.g. parasitic contribution of electrode polarization on Maxwell-Wagner/interfacial polarization). Correlation of cells' dielectric characteristics obtained via electrical impedance spectroscopy with cells' allowed evident differentiation of various type of cell. The differentiations were assigned to so-called "dielectric phenotype" based on crossover frequencies.

References

P.R.C. Gascoyne, S. Shim, Isolation of circulating tumor cells by dielectrophoresis, Cancers (Basel) 6, 545–579, 2014;

I. Turcan, M.A. Olariu, Dielectrophoretic Manipulation of Cancer Cells and Their Electrical Characterization, ACS Comb. Sci. 22, 554–578, 2020.

I Turcan, I Caras, TG Schreiner, C Tucureanu, A Salageanu, V Vasile, M. Avram, B. Tincu, M.A. Olariu, Dielectrophoretic and Electrical Impedance Differentiation of Cancerous Cells Based on Biophysical Phenotype, Biosensors 11 (10), 401

M 01-03

ICBEM Bioelectromagnetism ICEBI Electrical Bioimpedance EIT Electrical Impedance Tomography

Proceedings of the International Conference of Bioelectromagnetism, Electrical Bioimpedance,
and Electrical Impedance Tomography June 29 – July 1, 2022 / Kyung Hee University, Seoul, Korea

Sensing accumulation of nanoparticles in tissue by electrical impedance

Svetlana Kashina, Andrea Monserrat Cervantes-Guerrero,
Francisco Miguel Vargas-Luna and José Marco Balleza-Ordaz
Department of Physical Engineering, Science and Engineering Division, University of Guanajuato, León, México.

Correspondence : Svetlana Kashina, e-mail : k.svetlana@ugto.mx

Abstract– Synthesis and application of different nanomaterials are the fast-growing fields of research due to nanoparticles' unique properties. Nanoparticles-based materials are used in different fields, such as silver nanoparticles as antiseptics and titanium oxide as photocatalyst. Some drugs based on metallic nanoparticles, such as colloidal iron, are already approved by FDA. However, there is a growing concern about the environmental safety of the materials and that their possible accumulation within living organisms, including humans, may cause negative effects. Nanoparticles' toxicity is widely investigated, but it is still difficult to assess their accumulation in tissue non-invasively. Our research group is studying different applications of electrical bioimpedance, mainly in the biomedical field, so the purpose of this work was to assess the possibility of sensing the accumulation of different nanoparticles by electrical bioimpedance. We used different types of tissues (heart, muscle, liver, and kidney) as *ex vivo* models. Nanoparticles (mainly metallic) were dissolved in medical-grade saline and injected separately into tissue samples. Electrical bioimpedance before and after nanoparticles injection was recorded with potentiostat SP-150 (BioLogic Science Instrument). Meanwhile, no common pattern was observed, it was seen that almost all nanomaterials changed one or both electrical bioimpedance parameters (module and phase). Likewise, different types of tissues respond differently to the nanoparticles: muscle tissue was the least responsive and heart tissue presented the most notorious changes. As a conclusion, we have seen that nanoparticles accumulation can be assessed by electrical bioimpedance in *ex vivo* model, so, in vivo experiments must be conducted.

Acknowledgments

The authors would like to express their gratitude to CONACyT for S. Kashina's postdoctoral scholarship and UG-DAIP for financial support.

References

Anselmo, A. C. and Mitragotri, S. (2019). Nanoparticles in the clinic: An update. Bioengineering & translational medicine, 4(3), e10143.

SOLIS-ROJAS, Michelle, MORENO GONZÁLEZ-TERAN, Gustavo, GÓMEZ-SOLIS, Christian, GALINDO-GONZÁLEZ, Rosario and BALLEZA-ORDAZ, José Marco. Magentite particles change electrical properties of a porcine heart tissue. Journal of Research and Development. 2019, 5-15: 38-40.

MORENO GONZÁLEZ-TERAN, Gustavo, CEJA-FERNANDEZ, Andrea, GALINDO-GONZÁLEZ, Rosario and BALLEZA-ORDAZ, José Marco. Use of metallic nanoparticles for characterization of muscle tissue by electrical impedance spectroscopy (EIS). ECORFAN Journal-Democratic Republic of Congo. 2019, 5-9: 1-3.

DAY 2

Thursday, June 30, 2022

Oral Session 06

Tissue Property Imaging by MRI II

Chair Rosalind J. Sadleir (Arizona State University)
Matej Kranjc (University of Ljubljana)

O 06-01 **Single measurement of liver surface nodularity allows differentiation of liver fibrosis stage**
Tae-Hoon Kim (Wonkwang University)

O 06-02 **Cerebral gray matter volume changes in postmenopausal estrogen replacement therapy**
Tae-Hoon Kim (Wonkwang University)

O 06-03 **Evaluation of Low-frequency Conductivity Tensor Imaging Methods**
Nitish Katoch (Kyung Hee University Hospital)

O 06-04 **Evaluation of Ionizing Radiation Induced Brain Tissue Response by MR-based Electrical Conductivity Imaging**
Bup Kyung Choi (Kyung Hee University Hospital)

O 06-05 **Characteristics of High and Low Frequency Conductivities in Patients with Alzheimer's Disease**
Geon-Ho Jahng (Kyung Hee University Hospital at Gangdong)

ICBEM Bioelectromagnetism ICEBI Electrical Bioimpedance EIT Electrical Impedance Tomography

Proceedings of the International Conference of Bioelectromagnetism, Electrical Bioimpedance,
and Electrical Impedance Tomography June 29 – July 1, 2022 / Kyung Hee University, Seoul, Korea

Single measurement of liver surface nodularity allows differentiation of liver fibrosis stage

Tae-Hoon Kim[1], Chang-Won Jeong[1], Ji Eon Kim[1], Chungsub Lee[1], SiHyeong Noh[1],
Youe Ree Kim[2] and Young Hwan Lee[2]
[1] Medical Convergence Research Center, Wonkwang University, Iksan, Korea
[2]Department of Radiology, Wonkwang University Hospital, Iksan, Korea

Correspondence : Tae-Hoon Kim, e-mail : tae_hoonkim@hanmail.net

Abstract– A simplified method to estimate liver surface nodularity (LSN) score may be useful in the clinic. This study evaluated the regional analysis of LSN in a single liver MRI for staging liver fibrosis. 210 subjects were divided into five fibrosis groups (F_0=29; F_1=20; F_2=32; F_3=50; F_4=79) based on the METAVIR fibrosis score. The mean LSN and regional LSN measurements are compared. The regional LSN scores in five regions-of-interests (ROI_{1-5}) were analyzed in a single axial MRI. Regional variations in LSN scores were compared using ANOVA with Tukey test. The diagnostic performance of mean and regional LSN scores according to fibrosis stage was evaluated with the AUROC. A p-value <0.05 was considered statistically significant. Mean LSN scores and all 5 regional LSN scores showed significant differences between fibrosis groups. Among regional LSN scores, ROI_5 showed the highest AUROC (0.889 at cut-off 1.13) for discriminating F_{0-2} vs. F_{3-4}. Regional ROI_5 LSN score might be useful for clinical decision making and for distinguishing the difference between early fibrosis (F_{0-2}) and advanced fibrosis (F_{3-4}) in the liver.

Keywords: single measurement, regional analysis, liver surface nodularity (LSN), liver fibrosis, METAVIR

1. Introduction

Noninvasive evaluation of liver fibrosis is still challenging in clinical practice. To diagnose fibrosis and cirrhosis of the liver, the importance of assessing liver surface nodularity (LSN) is emerging in the clinical setting. The imaging techniques such as MRI and CT are promising methods to estimate LSN scores. The LSN can be measured from routine liver CT and MR images using post-processing software to generate an LSN score. In clinical practice, a quantitative LSN score is used to diagnose and stage various liver diseases including chronic liver disease (CLD) and non-alcoholic fatty liver disease (NAFLD). Smith *et al.* and Pickhardt *et al.* reported that the quantitative LSN score in CT images progressively increases with higher clinical stages of CLD and/or cirrhosis (end-stage), and is predictive of cirrhosis decompensation and death. Recently, Kim *et al.*, who developed a Matlab-based LSN quantification software using multipolynomial curve-fitting analysis reported that the use of quantitative LSN software can differentiate to stage liver fibrosis in NAFLD (fibrosis grade F_{0-1} vs. F_{2-3} based on pathologic NAFLD activity score), and in CLD (among F_1-F_3 based on serum fibrosis-4 index). The LSN score provides a high reproducibility on both CT and MRI to stage liver fibrosis and cirrhosis (F_4). However, these studies for evaluating liver fibrosis was not clearly distinguished among each fibrosis stage except cirrhosis; and it has restricted widespread use in clinical practice because it requires specific customized software for quantification and the LSN assessment of the whole liver is a time-consuming procedure. Therefore, the assessment of LSN scores using a simplified method, such as the measurement of a single image, may provide a more efficient way than LSN score derived from whole liver images. To our knowledge, no investigations are focusing on a single measurement to assess LSN score from a single MRI image.

The purpose of this study was to compare the regional variation of LSN for assessing liver fibrosis on a single axial liver MR image and to evaluate the diagnostic performance of LSN score in hepatic fibrosis.

2. Materials and Methods

2.1 Subject Population

A total of 210 patients who had undergone liver MRI within 6 months before or after histopathologic investigation, were enrolled from Wonkwang Univ. Hospital (n=85), Chonbuk Natl' Univ. Hospital (n=82), Asan Medical Center (n=14), and Chonnam Natl' Univ. Hospital (n=29). All histological data were analyzed by the Meta-analysis of Histological Data in Viral Hepatitis (METAVIR) fibrosis scoring system. The final cohort was divided into five groups

(F_0-F_4) according to hepatic fibrosis stages as follows: F_0 (n=29), F_1 (n=20), F_2 (n=32), F_3 (n=50) and F_4 (cirrhosis, n=79). This study excluded the patients who had undergone hepatectomy or had a pathologic condition including a large bulging mass that could interrupt measurement of LSN on the anterior or anterolateral surfaces of the liver.

2.2 Magnetic Resonance Imaging

All imaging studies were performed on MR scanners with body matrix coils. T1 weighted images (T1WI) in axial plane were acquired with following parameters: TR/TE= 4.2/1.97 ms, field of view= 38×38×14 cm^3, matrix size= 512×512, number of excitation= 2, slice thickness= 0.74×0.74×2.0 mm^3, number of slices= 70, and scan time was about 14 sec.

A total of four 3.0 T MRI scanners were used. Two MR scanners (Achieva [n=40]; Ingenia CX, [n=45], Philips Healthcare) were used at the Wonkwang University Hospital. At the Chonbuk National University Hospital, three MR scanners (Verio [n=46]; Skyra [n=13], Siemens healthineers) (Achieva, Philips Healthcare [n=23]) were used. At the Asan Medical Center, two MR scanners (Skyra, Siemens [n=13]; Ingenia CX, Philips [n=1]) were used. At the Chonnam National University Hospital, a scanner (Skyra, Siemens [n=29]) scanner was used.

2.3 Post-processing and LSN Analysis in Clinical Patients

The LSN quantification software was developed by the Matlab program (R2016, MathWorks, Natick, Massachusetts). The Wonkwang Abdomen and Liver Total Solution (WALTS) is a customized post-processing program that operates on the Windows platform (Microsoft, Redmond, WA). The main algorithm for assessing the LSN was as follows: bias correction of images via the level set method, liver boundary detection, liver segmentation; and LSN measurements with multipolynomial curve fitting analysis.

All MR images reviewed standard PACS stations and software with standard window settings. LSN analysis using customized WALTS software was independently performed by two experienced radiologists blinded to the radiologic reports of MR datasets. All selected MR images were analyzed using both mean and regional LSN measurements. Following pre-processing of MR image data, liver parenchyma within the liver surface line was used for the deterministic curve-fitting analysis. Regions-of-interests (ROIs) were selected along the boundary of the liver (Fig. 1). The user defines the ROI range across the datapoints of the liver surface line and a smooth curve-fitting line (4th-order line shape) was generated on the selected ROI dataset. Finally, the difference between the liver surface line and the new curve-fitting line was measured on a pixel-by-pixel basis. The difference value was squared, and the mean value, variation, and standard deviation (SD) were calculated. The overall LSN scores in individual subjects were calculated as the arithmetic mean and regional scores of the measurements.

2.4 Statistical Analysis

The LSN scores among fibrosis stages and different ROIs were compared using SPSS program (Chicago, IL, USA). The variation of LSN scores among fibrosis stages (F_0-F_4) and regional LSN variation in ROIs were analyzed using one-way analysis of variance (ANOVA) with Tukey's post-hoc test. The coefficient of variance (CV) in each group was calculated for the variability of measurements. To evaluate the diagnostic performance of mean and regional LSN scores according to fibrosis stages, receiver operating characteristics (ROC) curve analysis was performed to calculate the area under the ROC curve (AUROC), sensitivity, specificity, and diagnostic accuracy (DA). Two-sided p-values less than .05 were considered to indicate statistical significance.

3. Results

3.1 Patient Characteristics

The etiology and serum biochemistry of the enrolled 210 patients (148 men, 62 women; mean age, 56.4±13.2 years) are shown in Table 1. These patients had various liver diseases, including chronic hepatitis B (n=110), chronic hepatitis C (n=9), coinfection (n=4), alcoholic liver disease (n=18), NAFLD/steatohepatitis (NASH) (n=18), and autoimmune hepatitis (n=13). Forty patients had liver disease of unknown cause. The results of blood chemistry showed significant differences among fibrosis stages. There were significant differences between fibrosis stages in the albumin (p=.002), alanine aminotransferase (ALT, p=.011), aspartate aminotransferase (AST, p=.036), and platelet count (p<.001).

Table 1. Etiology of study population and clinical data of serum biochemistry in METAVIR fibrosis stages (F)

	Total (n=210)	F_0 (n=29)	F_1 (n=20)	F_2 (n=32)	F_3 (n=50)	F_4 (n=79)	*p*-value
Age (year)	56.2±13.2	46.8±20.9	54.4±16.9	57.5±10.9	59.7±10.5	57.4±9.0	<0.001 ^{bcd}
Male : Female	148 : 62	21 : 8	13 : 7	21 : 11	35 : 15	58 : 21	0.904
Albumin (g/dL, mean±SEM)	4.14±0.03	4.35±0.05	4.12±0.08	4.05±0.06	4.27±0.05	3.98±0.07	0.003 ^{dj}
ALT (IU/L)	34.6±1.8	20.6±1.6	47.9±12.5	35.7±3.3	34.8±3.2	36.9±2.3	0.011 ^{a}
AST (IU/L)	41.5±2.7	24.3±1.7	57.1±21.3	45.0±7.7	37.3±2.2	47.6±2.8	0.036 ^{a}
Platelet count ($10^3/\mu\ell$)	170.9±4.7	221.3±17.7	175.6±14.4	165.0±8.4	173.9±6.9	143.7±7.1	<0.001 ^{bcd}

ALP: alkaline phosphatase; ALT: alanine aminotransferase; AST: aspartate aminotransferase. The difference among three fibrosis groups was analyzed by ANOVA with Tukey test as follows: $^aF_0$ vs F_1, $^bF_0$ vs F_2, $^cF_0$ vs F_3, $^dF_0$ vs F_4, $^eF_1$ vs F_2, $^fF_1$ vs F_3, $^gF_1$ vs F_4, $^hF_2$ vs F_3, $^iF_2$ vs F_4, and $^jF_3$ vs F_4.

3.2 LSN Measurements in Different ROIs

Figure 1 shows the representative post-processing procedures (A-E), and MR images (F-J). Mean and regional LSN scores in ROIs were significantly different in fibrosis stages (Table 2; ANOVA, p<.001). In multiple comparisons, the mean LSN scores in each fibrosis stage were significantly different.

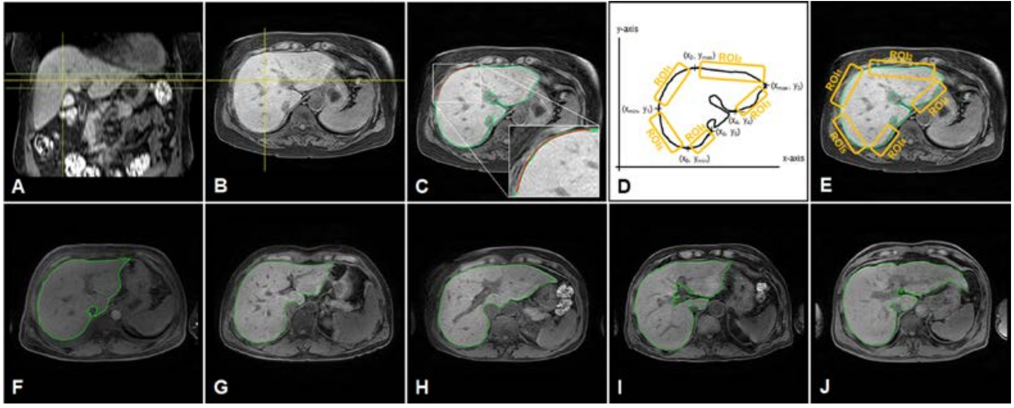

Figure 1. Schematic drawing for selection of ROIs and MRI in each fibrosis stage : (F) F_0, (G) F_1, (H) F_2, (I) F_3 and (J) F_4.

Table 2. Comparison of LSN scores in different region of interests according to fibrosis stages

	ROI_1 LSN	ROI_2 LSN	ROI_3 LSN	ROI_4 LSN	ROI_5 LSN	Mean LSN
F_0	0.93 ± 0.14	0.49 ± 0.12	0.73 ± 0.16	0.78 ± 0.14	0.80 ± 0.08	0.75 ± 0.04
F_1	1.04 ± 0.12	0.61 ± 0.08	0.79 ± 0.09	0.80 ± 0.10	0.89 ± 0.11	0.82 ± 0.05
F_2	1.26 ± 0.17	0.82 ± 0.13	1.09 ± 0.16	1.08 ± 0.19	1.14 ± 0.18	1.08 ± 0.06
F_3	1.35 ± 0.27	0.90 ± 0.19	1.21 ± 0.27	1.14 ± 0.22	1.26 ± 0.18	1.17 ± 0.10
F_4	1.44 ± 0.22	0.99 ± 0.15	1.30 ± 0.27	1.23 ± 0.22	1.33 ± 0.18	1.26 ± 0.09
p-value*	<0.001	<0.001	<0.001	<0.001	<0.001	<0.001
F_0 vs. F_1	0.364	0.050	0.906	0.998	0.348	0.005
F_0 vs. F_2, F_3, F_4	<0.001	<0.001	<0.001	<0.001	<0.001	<0.001
F_1 vs. F_2	0.003	<0.001	<0.001	<0.001	<0.001	<0.001
F_1 vs. F_3, F_4	<0.001	<0.001	<0.001	<0.001	<0.001	<0.001
F_2 vs. F_3	0.388	0.167	0.122	0.618	0.012	<0.001
F_2 vs. F_4	0.001	<0.001	<0.001	0.003	<0.001	<0.001
F_3 vs. F_4	0.148	0.004	0.299	0.095	0.195	<0.001

Abbreviations.–LSN: liver surface nodularity; ROI: region of interest. Data presented mean ± SD.

* The difference among fibrosis groups within each ROI was analyzed by the one-way ANOVA with Tukey test.

3.3 ROC Analysis for Differential Diagnosis According to Fibrosis Stages

The AUROC of LSN scores for the differentiation of fibrosis stages and their DA are summarized in Table 3. Among them, ROI_5 LSN score showed the highest diagnostic performance to differentiate F_0–F_2 from F_3–F_4.

Table 3. Receiver operator curve (ROC) analysis for diagnosing fibrosis stage using regional LSN scores

Comparison	Threshold	Sensitivity (%)	Specificity (%)	PPV (%)	NPV (%)	DA (%)	AUROC	*p*-value
Mean LSN score								
$F_{0–1}$(n=49) vs. $F_{2–4}$(n=161)	0.93	98.8 (159/161)	98.0 (48/49)	99.4 (159/160)	96.0 (48/50)	98.6 (207/210)	0.999	<0.001
$F_{0–2}$(n=81) vs. $F_{3–4}$(n=129)	1.12	89.1 (115/129)	88.9 (72/81)	92.7 (115/124)	83.7 (72/86)	89.0 (187/210)	0.967	<0.001
$F_{0–3}$(n=131) vs. F_4(n=79)	1.18	83.5 (66/79)	80.2 (105/131)	71.7 (66/92)	89.0 (105/118)	81.4 (171/210)	0.900	<0.001
ROI_1 LSN score								
$F_{0–1}$(n=49) vs. $F_{2–4}$(n=161)	1.13	84.5 (136/161)	85.7 (42/49)	95.1 (136/143)	62.7 (42/67)	84.8 (178/210)	0.942	<0.001
$F_{0–2}$(n=81) vs. $F_{3–4}$(n=129)	1.24	72.1 (93/129)	72.8 (59/81)	80.9 (93/115)	62.1 (59/95)	72.4 (152/210)	0.837	<0.001
$F_{0–3}$(n=131) vs. F_4(n=79)	1.31	69.6 (55/79)	68.7 (90/131)	57.3 (55/96)	78.9 (90/114)	69.0 (145/210)	0.774	<0.001
ROI_2 LSN score								
$F_{0–1}$(n=49) vs. $F_{2–4}$(n=161)	0.67	90.7 (146/161)	89.8 (44/49)	96.7 (146/151)	74.6 (44/59)	90.5 (190/210)	0.970	<0.001
$F_{0–2}$(n=81) vs. $F_{3–4}$(n=129)	0.83	78.3 (101/129)	79.0 (64/81)	85.6 (101/118)	69.6 (64/92)	78.6 (165/210)	0.883	<0.001
$F_{0–3}$(n=131) vs. F_4(n=79)	0.92	75.9 (60/79)	77.9 (102/131)	67.4 (60/89)	84.3 (102/121)	77.1 (162/210)	0.822	<0.001
ROI_3 LSN score								
$F_{0–1}$(n=49) vs. $F_{2–4}$(n=161)	0.94	93.8 (151/161)	93.9 (46/49)	98.1 (151/154)	82.1 (46/56)	93.8 (197/210)	0.978	<0.001
$F_{0–2}$(n=81) vs. $F_{3–4}$(n=129)	1.09	82.9 (107/129)	82.7 (67/81)	88.4 (94/116)	75.3 (67/89)	82.9 (174/210)	0.886	<0.001
$F_{0–3}$(n=131) vs. F_4(n=79)	1.16	69.6 (55/79)	68.7 (90/131)	57.3 (55/96)	78.9 (90/114)	69.0 (145/210)	0.792	<0.001

ROI_4 LSN score								
F_{0-1}(n=49) vs. F_{2-4}(n=161)	0.93	86.3 (139/161)	85.7 (42/49)	95.2 (139/146)	65.6 (42/64)	86.2 (181/210)	0.935	<0.001
F_{0-2}(n=81) vs. F_{3-4}(n=129)	1.06	72.9 (94/129)	74.1 (60/81)	81.7 (94/115)	63.2 (60/95)	73.3 (154/210)	0.834	<0.001
F_{0-3}(n=131) vs. F_4(n=79)	1.13	69.6 (55/79)	70.2 (92/131)	58.5 (55/94)	79.3 (92/116)	70.0 (147/210)	0.763	<0.001
ROI_5 LSN score								
F_{0-1}(n=49) vs. F_{2-4}(n=161)	1.01	94.4 (152/161)	93.9 (46/49)	98.1 (152/155)	83.6 (46/55)	94.3 (198/210)	0.977	<0.001
F_{0-2}(n=81) vs. F_{3-4}(n=129)	1.13	82.2 (106/129)	81.5 (66/81)	87.6 (106/121)	74.2 (66/89)	81.9 (172/210)	0.889	<0.001
F_{0-3}(n=131) vs. F_4(n=79)	1.24	73.4 (58/79)	72.5 (95/131)	61.7 (58/94)	81.9 (95/116)	72.9 (153/210)	0.791	<0.001

4. Discussion

This study demonstrated mean LSN score according to the METAVIR fibrosis stages and regional LSN variations with weighting index values on a single axial MR image. In the mean LSN measurement method, LSN scores showed excellent diagnostic performance in the quantification of LSN on routine liver MR scans as a part of a morphologic assessment. In prior studies, Smith et al. and Pickhardt et al. reported the excellent DA of mean LSN score using MRI and CT images in predicting fibrosis or cirrhosis (AUROC of 0.910 and 0.959, respectively). Our findings from mean LSN scores are well-matched with previous studies. Moreover, the regional ROI_5 LSN score demonstrated the best correlation and DA in the differentiation between non-advanced and advanced fibrosis. This result implies mean and regional LSN score from a single MRI image has the potential as a diagnostic tool for staging hepatic fibrosis.

The reproducibility, repeatability and DA are important in evaluating the performance of quantitative analysis. This study investigated the possible variability in LSN measurements (CV values). The quantitative LSN scores revealed the reliable measurements (CV≤20%) as the variation in the mean LSN measurements <10% and single ROIn LSN measurement <20%. Although the variability in the single regional measurement method was approximately doubled as contrasted with the mean measurement method, the processing time for a single ROI measurement method was reduced. In previous studies, this variability in the LSN measurements is reproducible For evaluating hepatic fibrosis, the imaging-based quantification methods have the advantage that they are available in routine MRI and CT imaging in clinical practice. Therefore, it might be an option that the WALTS software-based LSN measurement can provide a reproducible way to quantify fibrosis using routine MR images in clinical practice.

The interesting feature of this result is that the regional LSN scores are significantly different among fibrosis stages with METAVIR scores. In detailed multiple comparisons between fibrosis stages, regional LSN measurements were not significantly different in the contrasts of F_0 vs. F_1 (all ROI_{1-5}), F_2 vs. F_3 (except ROI_5), and F_3 vs. F_4 (except ROI_2). The LSN score was increased with the increasing severity of hepatic fibrosis. Among the ROIs, a ROI_5 LSN score showed the highest diagnostic accuracy. Especially, the advanced fibrosis group (F_3–F_4) had substantially higher LSN scores than the non-advanced fibrosis group (F_0–F_2). Several studies suggest that early-stage liver fibrosis may be reversible. Thus, an accurate and easy-implemented non-invasive diagnosis method to differentiate non-advanced and advanced liver fibrosis is crucial for therapeutic strategies. In this study, a single ROI_5 LSN measurement in clinical practice is useful for rapidly monitoring the discrimination between non-advanced (F_0-F_2) and advanced fibrosis groups (F_3-F_4).

5. Conclusions

A single ROI measurement to evaluate the LSN score is an efficient way of saving processing time in clinical decision making. Moreover, the LSN score in the posterior region of the right lobe (ROI_5) might be a simple LSN measurement region that will help to differentiate fibrosis stages rapidly in clinical practice.

Acknowledgments

This study was supported by the grants of the NRF of Korea (2021R1A5A8029876, 2020R1I1A1A01073871) and the Korea Health Technology R&D Project through the KHIDI, funded by the Ministry of Health & Welfare (HI18C1216).

References

Gheorghe G, Bungău S, Ceobanu G, et al. 2021 The non-invasive assessment of hepatic fibrosis. *J. Formos. Med. Assoc.* **120**(2) 794–803.

Kim TH, Kim JE, Ryu JH, Jeong CW. 2019 Development of liver surface nodularity quantification program and its clinical application in nonalcoholic fatty liver disease. *Sci. Rep.* **9**(1) 9994.

Smith AD, Zand KA, Florez E, et al. 2017 Liver Surface Nodularity Score Allows Prediction of Cirrhosis Decompensation and Death. *Radiology* **283**(3) 711–22.

Kim TH, Jeong CW, Kim JE, et al. 2021 Assessment of Liver Fibrosis Stage Using Integrative Analysis of Hepatic Heterogeneity and Nodularity in Routine MRI with FIB-4 Index as Reference Standard. *J. Clin. Med.* **10**(8) 1697.

Bedossa P, Patel K, Castera L. 2015 Histologic and noninvasive estimates of liver fibrosis. *Clin. Liver Dis.* **6**(1) 5–8.

Goodman ZD. 2007 Grading and staging systems for inflammation and fibrosis in chronic liver diseases. *J. Hepatol.* 47(4): 598–607.

Proceedings of the International Conference of Bioelectromagnetism, Electrical Bioimpedance,
and Electrical Impedance Tomography June 29 – July 1, 2022 / Kyung Hee University, Seoul, Korea

Cerebral gray matter volume changes in postmenopausal estrogen replacement therapy

Tae-Hoon Kim[1], ByoungRyun Kim[2], Youe Ree Kim[3], Chang-Won Jeong[1],
Chungsub Lee[1], and Young Hwan Lee[3]
[1]Medical Convergence Research Center, Wonkwang University, Iksan, Korea
[2]Department of Obstetrics and Gynecology, Wonkwang University Hospital, Iksan, Korea
[3]Department of Radiology, Wonkwang University Hospital, Iksan, Korea

Correspondence: Tae-Hoon Kim, PhD., e-mail: tae_hoonkim@hanmail.net

Abstract– Several structural and volumetric researches reported that localized morphologic changes associated with estrogen meditation. However, it is still unclear how to minimize menopausal symptoms and to protect a woman's brain from decline. This study investigated the potential effects of hormone replacement therapy on sex hormone level and whole brain morphology using a voxel-based morphometry (VBM) method. VBM method was used to evaluate changes in gray matter volume between the two groups by using SPM12 with DARTEL. The variation of brain volume between noERT and ERT groups was analyzed by independent two sample t-test. ERT-treated women group was greater GM volumes in the body and head of caudate nucleus, middle frontal gyrus, superior frontal gyrus, inferior parietal gyrus, amygdala, vermis, angular gyrus, and orbitofrontal gyrus. However, there was no greater GM volume in the noERT group. ERT-treated women might slow down the GM volume reductions compared to menopausal women without ERT.

Keywords: estrogen replacement therapy (ERT), menopause, voxel-based morphometry (VBM), cerebral volume

1. Introduction

Estrogen replacement therapy (ERT) in menopausal women can reduce troublesome menopause symptoms such as night sweats, chills, mood changes, sleep & sexual problems, and hot flushes. Also, a number of studies reported that Hormone replacement therapy can reduce the incidence of Alzheimer's disease (AD) by 64% and even more and prevent age-related cognitive decline, provided that it has been used in the past or for a sufficient period of time. Goto *et al.* reported accelerated volume reduction in the hippocampus (closely related memory function) for postmenopausal women using voxel based morphometry (VBM) and atlas-based methods. Lord *et al.* reported larger hippocampal volumes in estrogen therapy users in a VBM study. Thus, the effect of estrogen therapy might be closely associated with cognitive function. Other findings have been reported, including a positive association between estrogen therapy use and gray matter (GM) density in the inferior parietal lobules and the precuneus. However, it is still unclear how to minimize menopausal symptoms and to protect a woman's brain from decline.

The purpose of this study was to investigate the gray matter difference associated with ERT on sex hormone level and whole brain morphology using a VBM method.

2. Materials and Methods

2.1 Subject Population

Forty menopausal women including of 20 women without ERT (noERT group) and age-matched 20 women with ERT (ERT group) were enrolled in the department of obstetrics and gynecology. Both groups have no history of neurological illness. All participants underwent blood testing for comparing the sex hormone levels. The measured sex hormones included anti-mullerian hormone (AMH), estradiol, testosterone (TS), progesterone, follicle-stimulating hormone (FSH), and luteinizing hormone (LH).

2.2 Magnetic Resonance Imaging

All MRI examinations were obtained using a 3T MRI scanner (Achieva; Philips) with standard 8-channel adult head coil. Brain images were acquired using the 3-dimensional T1-weighted acquisition and the scan parameters were as follows: TR/TE = 8.1/4.6 ms, FOV = 256 × 256 × 180 mm^2, flip angle = 8°, slices = 180, voxel size = 1×1×1 mm^3, acquisition time = 4 minutes 32 seconds.

2.3 Post-processing and Statistical Analysis

Voxel-based morphometry (VBM) was used to evaluate changes in gray matter volume between the two groups by using statistical parametric mappging (SPM12) with Diffeomorphic Anatomical Registration Through Exponentiated Lie Algebra (DARTEL) procedure: gray matter segmentation; multiplication with the non-linear components derived from the normalization matrix (modulation); followed by smooth with a Gaussian kernel of 6 mm FWHM. The variation of brain volume between noERT and ERT groups was analyzed by independent two sample t-test. Significant brain areas were quantified using customized expert system for quantification of brain activation (QUBA) software (Chonnam National University, Gwangju, Korea) (Fig. 1).

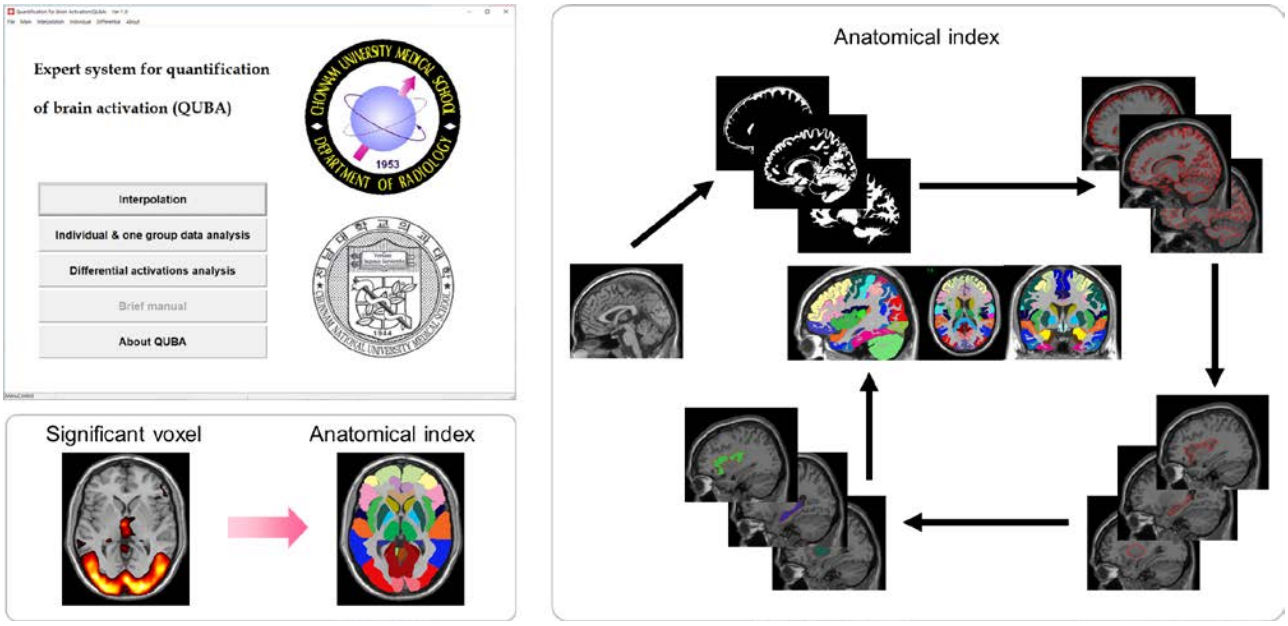

Figure 1. Schematic diagram for quantification of significant brain regions using an expert system for quantification of brain activation (QUBA) program.

3. Results

Table 1 compares the mean sex hormonal levels and hormone therapeutic information in two groups. In ERT group, the duration of ERT (Premina, Angeliq and Livial) is 5.4 ± 5.9 years, the estradiol level showed higher than that of noERT group, whereas the FSH level is lower. These sex hormonal levels were significantly different between both groups ($p<0.05$).

Figure 2 shows the significantly increased GM volumes in ERT group (summarized in Table 2). Voxel-based morphometry indicated that ERT was associated with greater GM volumes in the treated women group, which included the body and head of caudate nucleus, middle frontal gyrus, superior frontal gyrus, inferior parietal gyrus, amygdala, vermis, angular gyrus, and orbitofrontal gyrus. However, there was no greater GM volume in the noERT group.

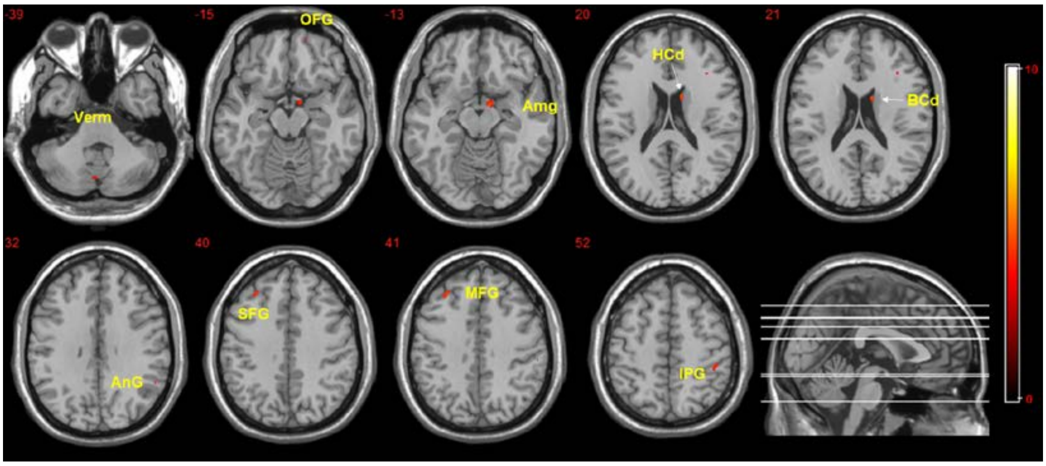

Figure 2. Increased gray matter volumes in estrogen replacement therapy (ERT) group, which analyzed with independent two sample t-test ($p<0.001$; cluster size 5). There was no decreased gray matter volume in ERT group.

Table 1. Patient characteristics and sex hormone levels in the noERT and ERT groups

Hormone levels		noERT (n=20)	ERT (n=20)	*p*-value*
Age (year)		55.9±5.4	57.5±4.4	0.388
BMI (Kg/m^2)		22.9±3.9	22.8±1.7	0.541
ERT duration (year)	(drug, n)	-	5.4±5.9 (Premina 4, Angeliq 3, Livial 3)	-
Anti-mullerian hormone	[ng/mL]	0.02±0.01	0.01±0.00	0.237
Estradiol	[pg/mL]	16.02±9.30	24.76±8.53	0.020
Testosterone	[ng/mL]	0.11±0.05	0.19±0.05	0.547
Progesterone	[ng/mL]	0.08±0.03	0.06±0.01	0.378
FSH	[mIU/L]	73.65±10.95	44.35±4.75	0.010
LH	[mIU/L]	36.26±3.81	34.20±3.85	0.530

Data presented mean ± SEM. ERT stands for estrogen replacement therapy. follicle-stimulating hormone: FSH; and luteinizing hormone: LH.

* The difference between noERT and ERT groups was analyzed by independent two sample t-test.

Table 2. Volume increased areas in cerebral gray matter of ERT group (p<0.001; threshold t-value 3.79)

Anatomical area	Abbr.	*t*-value	MNI			Laterality index* (%)	No. of Pixels		
			x	y	z		Both	Rt-side	Lt-side
Body of caudate nucleus	BCd	5.23	14	5	21	-100.0	21	21	-
Head of caudate nucleus	HCd	5.14	14	6	20	-100.0	165	165	-
Middle frontal gyrus	MFG	4.83	-28	35	41	80.3	71	7	64
Superior frontal gyrus	SFG	4.68	-28	36	40	42.9	21	6	15
Inferior parietal gyrus	IPG	4.44	47	-33	52	-100.0	37	37	-
Amygdala	Amg	4.14	15	-2	-13	-100.0	5	5	-
Vermis	Verm	4.12	-1	-72	-39	47.4	19	5	14
Angular gyrus	AnG	4.07	56	-50	32	-100.0	18	18	-
Orbitofrontal gyrus	OFG	4.06	18	60	-15	-100.0	8	8	-

* Laterality index (%) calculated as a percentage = (No. of Lt-side pixels – Rt-side pixels) / total pixels x 100.

4. Conclusions

ERT-treated women might slow down the GM volume reductions compared to noERT menopausal women. The anatomical structures that showed greater volume in association with ERT included the deep brain areas (caudate and amygdala), cerebellar vermis, and frontal & parietal gyrus.

Acknowledgments

This study was supported by the grants of the NRF (2020R1I1A1A01073871) and KHIDI, funded by the Ministry of Health &Welfare (HI18C1216).

References

Hickey M, Elliott J, Davisonet SL. 2012 Hormone replacement therapy. *BMJ* **344** e763.

Song YJ, Li SR, Li XW, et al. 2020 The Effect of Estrogen Replacement Therapy on Alzheimer's Disease and Parkinson's Disease in Postmenopausal Women: A Meta-Analysis. *Front. Neurosci.* **14** 157.

Ibrahim AW, Sodipo OA, Mshelia IA, Machina BK. 2018 Hormone replacement therapy and Alzheimer's disease in older women: A systematic review of literature. *J. Neurosci. Behav. Health.* **10**(1) 1–8.

Goto M, Abe O, Miyati T, et al. 2011 3 Tesla MRI detects accelerated hippocampal volume reduction in postmenopausal women. *J. Magn. Reson. Imaging* **33**(1) 48–53.

Lord C, Buss C, Lupien SJ, Pruessner JC. 2008 Hippocampal volumes are larger in postmenopausal women using estrogen therapy compared to past users, never users and men: a possible window of opportunity effect. *Neurobiol. Aging* **29**(1) 95–101.

Lord C, Engert V, Lupien SJ, Pruessner JC. 2010 Effect of sex and estrogen therapy on the aging brain: a voxel-based morphometry study. *Menopause* 17(4) 846–51.

Proceedings of the International Conference of Bioelectromagnetism, Electrical Bioimpedance,
and Electrical Impedance Tomography June 29 – July 1, 2022 / Kyung Hee University, Seoul, Korea

Evaluation of Low-frequency Conductivity Tensor Imaging Methods

Nitish Katoch[1], Bup Kyung Choi[1], In Ok Ko[2], Ji Ae Park[2], Hyung Joong Kim[1] and Eung Je Woo[1]
[1]Medical Science Research Institute, Kyung Hee University Hospital, Seoul, Korea
[2]Division of Applied RI, Korea Institute of Radiological and Medical Science, Seoul, Korea

Correspondence : Eung Je Woo, e-mail : ejwoo@khu.ac.kr

Abstract– Cross-sectional imaging of a low-frequency conductivity tensor distribution inside the human body has been obtained through water diffusion tensor for numerous clinical applications. In this study, a recently proposed conductivity tensor imaging method was compared with the existing DTI-based conductivity tensor models. Using a 9.4T MR scanner, two known conductivity phantoms were designed to evaluate the accuracy of these models. An anisotropic tissue phantom was also designed to evaluate the anisotropic distribution of conductivity tensor. Compared to the values measured using an impedance analyzer, the conductivity image of the phantoms by the CTI method showed relative errors between 1.10% and 5.26%. The images by the three models using DTI could not measure the effects of different ion concentrations due to *prior* information of the mean conductivity values. The conductivity tensor imaging of anisotropic phantom shows a similar anisotropy ratio across all phantoms. However, the conductivity errors in transversal and longitudinal components range from 5 % to 9 %. The CTI approach has the lowest inaccuracy in anisotropic conductivity. We conclude that the conductivity tensor model is appropriate for low-frequency conductivity mapping. It can be directly obtained from ion concentration and mobility in extracellular regions, making it acceptable for clinical applications.

Keywords: MRI; conductivity tensor imaging; electrical conductivity; biological tissues; anisotropy.

1. Introduction

Biological tissues consist of extracellular fluid, cells, and extracellular matrix materials. Electrical conductivity is determined by the cellular structure and density, extracellular volume fraction, composition and amount of extracellular matrix materials, membrane characteristics, and the concentrations and mobility of major ions in the extracellular and intracellular fluids. Dominant charge carriers in extracellular and intracellular fluids are sodium, potassium, chloride, and calcium ions (Grimnes & Martinsen, 2011). The conductivity of such a composite material and dominant charge carriers can be expressed as a weighted sum of the conductivity values of its components (Kerner, 1956). The extracellular and intracellular fluids are a conductor of which conductivity is determined by the concentrations and mobility of ions and other mobile charge carriers. The mobility of a charge carrier is determined by the inherent properties of the particle itself, such as its size and shape, as well as the environmental properties such as temperature, hydration, and viscosity of the fluid. In addition, the structural properties such as size, shape, density, and layout of cells, extracellular matrix materials, and intracellular organelles also affect mobility. Cells with thin insulating membranes behave as insulators and lossy dielectrics at low and high frequencies. The electrical conductivity, therefore, exhibits a frequency dependency. Among these, the structural properties may give rise to anisotropic mobility (Grimnes & Martinsen, 2011).

To map anisotropic conductivity distribution, diffusion tensor imaging is broadly used in numerous studies. Using the cross-property relationship, water molecules' diffusion is proportional to ions underlying a similar microstructural environment. *Sen* et al. argued that the two phenomena have identical statistical microstructure characteristics (Sen & Torquato, 1989), whereas *Tuch* et al. demonstrated that the eigenvectors of the water and ions diffusion tensors in extracellular space are similar. Adopting the physical relation between **C** and **D** have the same eigenvector, *Tuch* et al. derived an analytical scale factor (η), which enabled the transformation of a diffusion tensor image into a conductivity tensor image (Tuch, Wedeen, Dale, George, & Belliveau, 2001). Based on the cross-property, three more conductivity tensor models and image reconstruction methods using DTI were developed (Miranda, Pajevic, Pierpoali, Hallett, & Basser, 2001; Sekino, Yamaguchi, Iriguchi, & Ueno, 2003; Wang et al., 2008). Due to the global scale factor (η) assumption, DTI-based methods lack structural heterogeneity. *Sajib* et al. developed a novel low-frequency conductivity tensor imaging (CTI) method to overcome these limitations (Sajib, Kwon, Kim, & Woo, 2018). In CTI, a pixel-dependent scale factor is calculated to produce subject-specific conductivity tensor information. CTI combines two MR techniques where ion concentration is modulated from high-frequency conductivity from MREPT technique, and tissue microstructure parameters are reconstructed from diffusion-weighted imaging (DWI) (Katoch et al., 2018). Combining both, the scale factor (η) between C and D is determined for every pixel using the following: (1) a physical relationship between the water diffusivity and ion mobility and (2) a model-based relation between σ_L and σ_H. This study compared the accuracy of five conductivity tensor models in 2 known conductivity phantom using a 9.4T MRI scanner. An anisotropic tissues phantom was also used to measure the anisotropic conductivity distribution among models and compared with results from the impedance analyzer.

2. Method

2.1 Five conductivity tensor models

To compare different conductivity tensor models, we used the model proposed by *Tuch* et al. called as Linear eigenvalue model (LEM) (Tuch et al., 2001). In LEM, a linear physical model was adopted as $\mathbf{C} = \eta\mathbf{D}$, where $\mathbf{C}$ is the conductivity tensor, D is the water diffusion tensor, and η is the scale factor analytically calculated as 0.844 $S.s/mm^2$. Using the similar relations, a force equilibrium model (FEM) from *Sekino* et al., the volume constraint model (VCM) from *Miranda* et al., and the volume fraction model (VFM) from Wang et al. The fundamentals of these models depend upon calculations of scale factor (η). The details of these models are available at (Miranda et al., 2001; Sekino et al., 2003; Wang et al., 2008). These four methods were compared with the CTI method. The conductivity tensor image was then reconstructed using the CTI formula (Katoch et al., 2018; Sajib et al., 2018):

$$\mathbf{C} = \frac{\alpha\sigma_H}{\alpha d_e^w + (1-\alpha) d_i^w \beta}\mathbf{D}_e^w = \eta\mathbf{D}_e^w \tag{1}$$

where, σ_H is the high-frequency conductivity at the Larmor frequency, α is the extracellular volume fraction, β is the ion concentration ratio of intracellular and extracellular spaces, d_e^w and d_i^w are the extracellular and intracellular water diffusion coefficients, respectively, and $\mathbf{D}_e^w$ is the extracellular water diffusion tensor. The computed scale factor η was multiplied at every pixel by the extracellular diffusion tensor ($\mathbf{D}_e^w$) to calculate the absolute conductivity tensor. For quantification of anisotropic ratio among reconstructed conductivity tensors. The overall anisotropy of muscle tissues was analyzed by introducing the anisotropy ratio (AR), which was defined as follows:

$$\mathbf{AR} = 2\boldsymbol{\sigma}_T/(\boldsymbol{\sigma}_{t1} + \boldsymbol{\sigma}_{t2}) \tag{2}$$

where $\boldsymbol{\sigma}_T$ is the largest eigenvalue of $\mathbf{C}$ along the longitudinal direction, $\boldsymbol{\sigma}_{t1}$ and $\boldsymbol{\sigma}_{t2}$ are the other two eigenvalues in the transversal directions (Katoch et al., 2018; Sajib et al., 2018). The AR value of muscle tissue indicates the degree of anisotropy in principle direction regardless of its location on the image.

2.2 Imaging phantom

A total of three phantoms were built to compare the accuracy and contrast generation of conductivity tensor models. Phantom #1 and #2 comprise a central compartment of giant vesicles. Giant vesicles are cell-alike materials with a thin insulating membrane (Choi et al., 2020). The imaging phantom #1 and #2 consist of three compartments, as shown in figure 1(a).

Phantom #3 is a biological tissue phantom. Phantom #3 consisted of an acrylic cylinder with a diameter of 50 mm and a height of 90 mm. Two resected bovine muscle blocks with a volume of 10×10×10 mm^3, respectively, were positioned in the center of the phantom, and the direction of the muscle fibers was perpendicular to each other (Fig. 1(e)). The phantom was filled with conductive material (agarose gel with 0.3 S/m conductivity) to support the position of the muscle blocks. The electrical conductivity of all the electrolytes and muscles used in the study was measured using an impedance analyzer (SI1260A, AMETEK Inc., UK).

2.3 MRI acquisition protocols

A 9.4 T research MRI scanner was used with a single-channel mouse body coil. The high-frequency conductivity images were acquired using the multi-echo spin-echo sequence with an isotropic voxel resolution of 0.5 mm. The imaging parameters were as follows: TR/TE = 2200/22 ms, NEX = 5, FOV = 65 × 65 mm^2, slice thickness = 0.5 mm, FA = 90°, and image matrix size = 128×128. A single-shot spin-echo echo-planar-imaging pulse sequence was separately used for a *multi-b* diffusion-weighted image which can extract the structural information about the cellular environment. The imaging parameters were as follows: TR/TE = 2000/70 ms, number of signal acquisitions = 2, other parameters were as same as the multi-echo spin-echo sequence across all three phantoms. The number of directions of the diffusion-weighting gradients was 30 with 15 b-values (Choi et al., 2020; Katoch et al., 2018).

3. Results

Figure 1. shows the reconstructed conductivity tensor and diffusion tensor images of phantoms #1 to #3. For all phantoms, we plotted their longitudinal and two transversal components defined as σ_t and $\sigma_{t1,2}$. The images of the scale factor (η) between tensors were also plotted for four conductivity tensor models. The mean values of the reconstructed conductivity values were compared with independently measured conductivity values from the impedance analyzer.

For phantom #1 shown in figure 1(a) and (c), the electrolytes EL_1 and EL_2 had different NaCl concentrations. The LEM and FEM methods failed to distinguish the difference in electrolyte conductivity. The VCM and CTI methods could differentiate both electrolytes (EL_1 and EL_2). Since the reconstruction of η requires *prior* isotropic conductivity values, the accuracy in VCM could have been influenced by the use of conductivity values from an impedance analyzer. For phantom #2 shown in Figures 1(b) and (c), the outer two compartments have the same NaCl concentration but different mobility controlled by changing the viscosity of the electrolyte. Since this change in mobility altered the diffusion coefficient, all four methods were able to distinguish the difference between EL$_3$ and EL$_4$ in phantom #2. The conductivity values measured using FEM were highly underestimated, and the error ranges from 66 to 86%, whereas despite using isotropic literature values in FEM model, the error amounts to 28 to 67% in EL$_1$ and EL$_2$ for both phantoms.

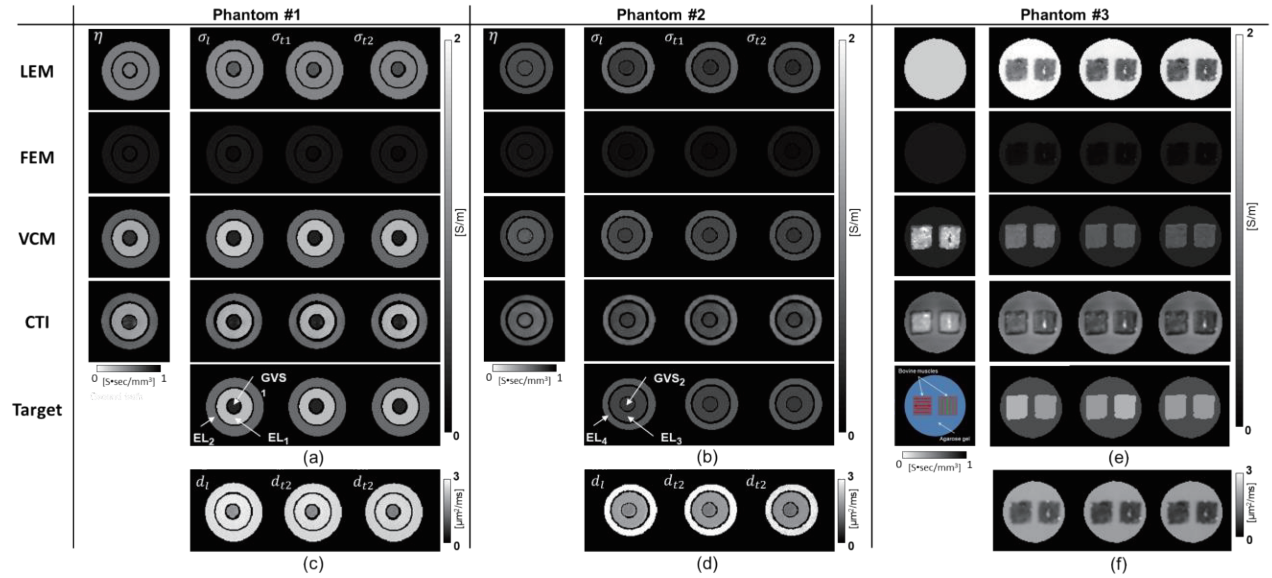

Figure 1. Reconstructed conductivity tensor of phantom #1 to #3. Target images are the true conductivity tensor images generated using the conductivity values measured by the impedance analyzer. (**c**, **d**, and **f**) are the diffusion tensor images of phantoms, respectively.

For phantom #1 and #2, the centremost compartment is filled with giant vesicles. For giant vesicle suspension GVS$_1$ and GVS$_2$, the conductivity values from the impedance analyzer were 0.29 and 0.45 in phantom #1 and #2. For LEM and FEM, the error in giant vesicles ranges from 29 % to 131%, whereas from VCM model 2 to 3%. The CTI method could recover the conductivity values with an error of 1.10% to 5.26% in all the regions of the electrolytes and giant vesicle suspensions. Figures 1(e) and (f) show the muscle tissue phantom conductivity tensors. Three ROIs were used for phantom #3, including two regions from the bovine muscle region and one representing the background agarose gel. The electrical conductivity had a higher value along the fiber direction, that is, longitudinal direction across all models. The anisotropic ratio was also measured across all models and compared with the ratio calculated from values using an impedance analyzer. Figure 1 summarizes the conductivity tensor images from three phantom and four conductivity tensor reconstruction models. Figure 1(c, d, and f) are extracellular diffusion tensor ($\mathbf{D}_e^w$) images. Table 1 shows the errors in the reconstructed conductivity values to the reference values measured by the impedance analyzer (SI1260A, AMETEK Inc., Berwyn, PA, USA).

Table 1. Errors in the reconstructed conductivity values $\sigma_L = (\boldsymbol{\sigma}_T + \boldsymbol{\sigma}_{t1} + \boldsymbol{\sigma}_{t2})/3$ to the reference value measured by the impedance analyzer at 10 Hz. Note that the reference values were themselves used in the VCM method for the compartments of EL$_1$ to EL$_4$.

ROI	LEM (%)	FEM (%)	VCM (%)	CTI (%)
EL$_1$	29.6	86.24	0	1.10
EL$_2$	28.14	75.54	0	4.42
GVS$_1$	131.17	54.83	3.45	1.74
EL$_3$	32.97	73.27	0	3.39
EL$_4$	67.82	66.27	0	5.26
GVS$_2$	28.16	66.27	2.02	2.13
Bovine A	10.52	62.85	23.52	5.26
Bovine B	13.91	67.14	28.91	9.04
Agar	90	26.66	10	30

4. Discussion

In this paper, we compared the four conductivity tensor models and image reconstruction methods using two known conductivities and an anisotropic phantom. The data from the phantom experiments were used to evaluate the accuracy of the reconstructed conductivity images and anisotropic property against the measured conductivity values obtained using the impedance analyzer. In phantom #1 and #2, the LEM and FEM method could not differentiate the electrolytes of different concentrations. The errors in the reconstructed conductivity images using the LEM and FEM were relatively large >28% in different electrolyte concentrations. The error of the VCM method was the smallest compared to the impedance analyzer and could have stemmed from the isotropic known conductivity values used in the reconstruction process. Due to global known conductivity values in VCM and global scale factor (η) in LEM and FEM, these methods do not quantify the heterogenic property in biological tissues. Thus, a single global conductivity value for the entire tissue type may not be sufficient. Without relying on *prior* information of mean isotropic conductivity values, the CTI method recovered conductivity values with an error ranging from 1.10% to 5.26% for all six different compartments in the two phantoms having different ion concentrations and mobilities. Furthermore, the CTI method could adequately handle the effects of different cell densities in two giant vesicle suspensions with different extracellular volume fractions.

Muscle is highly anisotropic tissue because the applied currents flow more easily along muscle fibers than across the fibers. Several studies have reported on the anisotropy of brain tissues using conductivity tensor imaging, but reports on muscle are relatively few, especially in comparison to the *in-vitro* measurements. The average conductivity of bovine muscles A and B using an impedance analyzer was 0.35 and 0.46 S/m. The low-frequency conductivity provides information about the extracellular space, including tissue anisotropy. To analyze the directional property, the anisotropy of the bovine phantom was measured as 1.15 and 1.21, calculated from the measured ratio of conductivity in parallel and perpendicular directions using four-channel electrode methods. The anisotropy ratio (AR) of bovine A and B measured using LEM are 1.25 and 1.24, whereas for agar across all phantoms, close to 1. For all four methods, the values of AR were similar since the structural property primarily determined the anisotropy. In all reconstruction methods, the property of anisotropy attributed to water diffusion tensor thus remains similar. In the CTI method, the magnitudes of error in bovine muscles were the smallest among all models, and error values ranged from 5 to 13%.

5. Conclusions

The accuracy of the four conductivity tensor model was investigated using two phantoms with four electrolytes and two giant vesicles suspensions with known internal conductivity values. To analyze the directional property in conductivity, muscle tissue phantom was utilized. From the experimental results using two phantoms with known internal conductivity values, we found that the VCM and CTI methods' accuracy was better than those of the LEM and FEM methods. Unlike the four methods using DTI, the CTI method did not use *prior* information about mean isotropic conductivity values and produced conductivity images with 1.1% to 5.26% errors. As a result of the muscle tissue phantom, the reconstructed conductivity values of bovine A and B using the CTI method were comparable to measured conductivity values from the impedance analyser with 5.26% to 9.04% errors. Since the four methods using DTI rely on prior information about mean isotropic conductivity values, the results using these three methods could have been different depending on chosen parameter values. The experimental results show that the CTI method could handle the effects of ion concentrations, mobility, and extracellular volume fractions. Therefore, could be more useful in future research of clinical utility.

Acknowledgments

This research was funded by the National Research Foundation of Korea (NRF) grants funded by the Korea government (No. 2019R1A2C2088573, 2020R1A2C200790611, 2021R1A2C2004299).

References

Choi, B. K., Katoch, N., Kim, H. J., Park, J., Ko, I. O., Kwon, O. I., & Woo, E. J. (2020). Validation of conductivity tensor imaging using giant vesicle suspensions with different ion mobilities. *BioMedical Engineering OnLine, 19*(1), 1-17.

Grimnes, S., & Martinsen, O. G. (2011). *Bioimpedance and bioelectricity basics*: Academic press.

Katoch, N., Choi, B. K., Sajib, S. Z., Lee, E. A., Kim, H. J., Kwon, O. I., & Woo, E. J. (2018). Conductivity Tensor Imaging of In Vivo Human Brain and Experimental Validation using Giant Vesicle Suspension. *IEEE transactions on medical imaging*.

Kerner, E. (1956). The electrical conductivity of composite media. *Proceedings of the Physical Society. Section B, 69*(8), 802.

Miranda, P. C., Pajevic, S., Pierpoali, C., Hallett, M., & Basser, P. (2001). *The distribution of currents induced in the brain by magnetic stimulation: a finite element analysis incorporating DT-MRI-derived conductivity data.* Paper presented at the Proceedings of the International Society for Magnetic Resonance in Medicine.

Sajib, S. Z., Kwon, O. I., Kim, H. J., & Woo, E. J. (2018). Electrodeless conductivity tensor imaging (CTI) using MRI: basic theory and animal experiments. *Biomedical engineering letters, 8*(3), 273-282.

Sekino, M., Yamaguchi, K., Iriguchi, N., & Ueno, S. (2003). Conductivity tensor imaging of the brain using diffusion-weighted magnetic resonance imaging. *Journal of applied physics, 93*(10), 6730-6732.

Sen, A. K., & Torquato, S. (1989). Effective conductivity of anisotropic two-phase composite media. *Physical Review B, 39*(7), 4504.

Tuch, D. S., Wedeen, V. J., Dale, A. M., George, J. S., & Belliveau, J. W. (2001). Conductivity tensor mapping of the human brain using diffusion tensor MRI. *Proceedings of the National Academy of Sciences, 98*(20), 11697-11701.

Wang, K., Zhu, S., Mueller, B. A., Lim, K. O., Liu, Z., & He, B. (2008). A new method to derive white matter conductivity from diffusion tensor MRI. *IEEE Transactions on biomedical engineering, 55*(10), 2481-2486.

Proceedings of the International Conference of Bioelectromagnetism, Electrical Bioimpedance,
and Electrical Impedance Tomography June 29 – July 1, 2022 / Kyung Hee University, Seoul, Korea

Evaluation of Ionizing Radiation Induced Brain Tissue Response by MR-based Electrical Conductivity Imaging

Bup Kyung Choi[1], In Ok Ko[2], Nitish Katoch[1], Kyeung Jun Kang[2], Ji-ung Yang[2], Tae Hoon Kim[3],
Eun Ju Yoon[4], Ji Ae Park[2], Jin Woong Kim[4] and Hyung Joong Kim[1]
[1]Medical Science Research Institute, Kyung Hee University Hospital, Seoul, Korea
[2]Division of Applied RI, Korea Institute of Radiological and Medical Science, Seoul, Korea
[3]Medical Convergence Research Center, Wonkwang University Hospital, Iksan, Korea
[4]Department of Radiology, Chosun University Hospital and Chosun University College of Medicine, Gwangju, Korea

Correspondence : Hyung Joong Kim, e-mail : bmekim@khu.ac.kr

Abstract–Non-invasive quantification of radiation-induced damage is an important factor in radiation therapy to maximize radiation dose to cancer cells while minimizing damage to surrounding healthy surrounding tissue. The development of imaging biomarkers to accurately assess post-radiation therapy effects at an early stage is essential for better prognosis and to individualize the examination of brain tumors. MR-based electrical conductivity imaging provides novel contrast information based on the concentration and mobility of ions constituting tissue. It can exhibit high sensitivity in quantifying the therapeutic effect of ionizing radiation in cancer treatment. In this preclinical study, we analyzed the change in conductivity at different doses and quantified the response of the rat brain tissue to irradiation. The variation in conductivity with the elapsed time shows potential as a tool to monitor the therapeutic effect of radiation. The potential of MR-based conductivity imaging in future clinical studies might be beneficial.

Keywords: radiation therapy; electrical conductivity; ionizing radiation; tissue response; magnetic resonance imaging

1. Introduction

Radiation therapy (RT) is a typical non-invasive method of cancer therapy that uses ionizing radiation delivered by a linear accelerator (Voges J *et al.* 1996). Ionizing radiation has sufficient energy to produce ions inside the human body at the molecular level, killing cancer cells by directly damaging the DNA of cancer cells or by creating charged particles that can damage the DNA within the cell (Baskar R *et al.* 2014). Although the effects of irradiation that result in cell death are well established, *in-vivo* quantification of radiation-induced injury is a critical challenge in RT to maximize irradiation doses to cancer cells while minimizing damage to surrounding healthy tissue. In the past, routine monitoring of brain tumors after RT was performed by evaluating the volume changes of viable tumor tissues, which appear several months after RT on contrast-enhanced MRI. However, conventional contrast enhancement MRI is helpful but cannot differentiate viable tumor tissue with various degrees of contrast enhancement. A recent study by Park *et al.* reported the potential of magnetic resonance (MR)-based electrical conductivity imaging as a sensitive tool to measure tissue response after irradiation (Park J A *et al.* 2019). The study reported that the sensitivity of the conductivity was significantly higher than that of conventional MR imaging methods such as T2 and ADC mapping from in vivo animal imaging experiments. Meanwhile, a change in conductivity due to irradiation was reported. However, the relation of magnitude of radiation dose to conductivity changes was yet to be explored.

This preclinical study aims to show the experimental evaluation of MR-based electrical conductivity as an imaging biomarker to assess early tissue damage in RT. From *in-vivo* mouse brain imaging, the absolute conductivity was measured to evaluate the irradiation effects through the changes at different doses and the time elapsed after irradiation. Finally, relative conductivity changes were calculated to quantify the extent of tissue response to irradiation.

2. Materials and methods

2.1 Animal preparation for validation

A total of nine female 6-week-old BALB/c nude mice (weighing 20~23 g) were used for in vivo imaging experiments. The mice were divided into the following three groups: 1 Gy, 5 Gy, and 10 Gy irradiation dose. Each group consisted of three mice, and all mice were subjected to imaging experiments before and 0, 1, 2, 3, and 10 days after irradiation. We injected them with 0.1 mg/kg of atropine sulfate to prevent their dribbling during the imaging experiments. Ten minutes later, we anesthetized each mouse with an intra-muscular injection of 0.2 mL/kg of Zolazepam (Zoletil 50, Virbac, France). For in vivo brain imaging, mice were irradiated with a dose of 1 Gy, 5 Gy, and 10 Gy, respectively, using a small animal image-guided irradiation system X-RAD SmART (Precision X-ray Inc., North Branford, CT, USA) (Seo Y S *et al* 2019).

2.2 Imaging experiment and analysis

The animals were placed inside the bore of an MRI scanner. T2-weighted imaging (T2WI) and electrical conductivity imaging were performed using 9.4T MRI scanner with a birdcage volume RF coil. For T2WI, a fast spin-echo multi-slice (FSE-MS) MR sequence was applied, and the imaging parameters were as follows: repetition time (TR), 2200 ms; echo time (TE), 22 ms; echo train length (ETL), 6; number of averaging, 2; slice thickness, 1 mm; number of slices, 5; matrix size, 128 × 128; field-of-view (FOV), 50 × 50 mm^2. In vivo mouse brain imaging was performed before and after irradiation using a 9.4T MRI. Details of conductivity reconstruction follow the work of Katoch et al. (Katoch N *et al* 2019).

3. Results

3.1 *In vivo* mouse brain imaging with different doses and elapsed times

Figure 1(a) shows the T2WI and electrical conductivity image of in vivo mouse brains according to different irradiation doses. All images were acquired 1 day after irradiation. Compared to before irradiation, morphological differences were not observed in T2WI by the irradiation dose. However, the conductivity images showed different contrasts by the irradiation dose. Specifically, the conductivity image of the 10 Gy dose showed increased contrast throughout the brain region. The contrast was partially increased at 5 Gy. However, no clear contrast was observed in the 1 Gy dose.

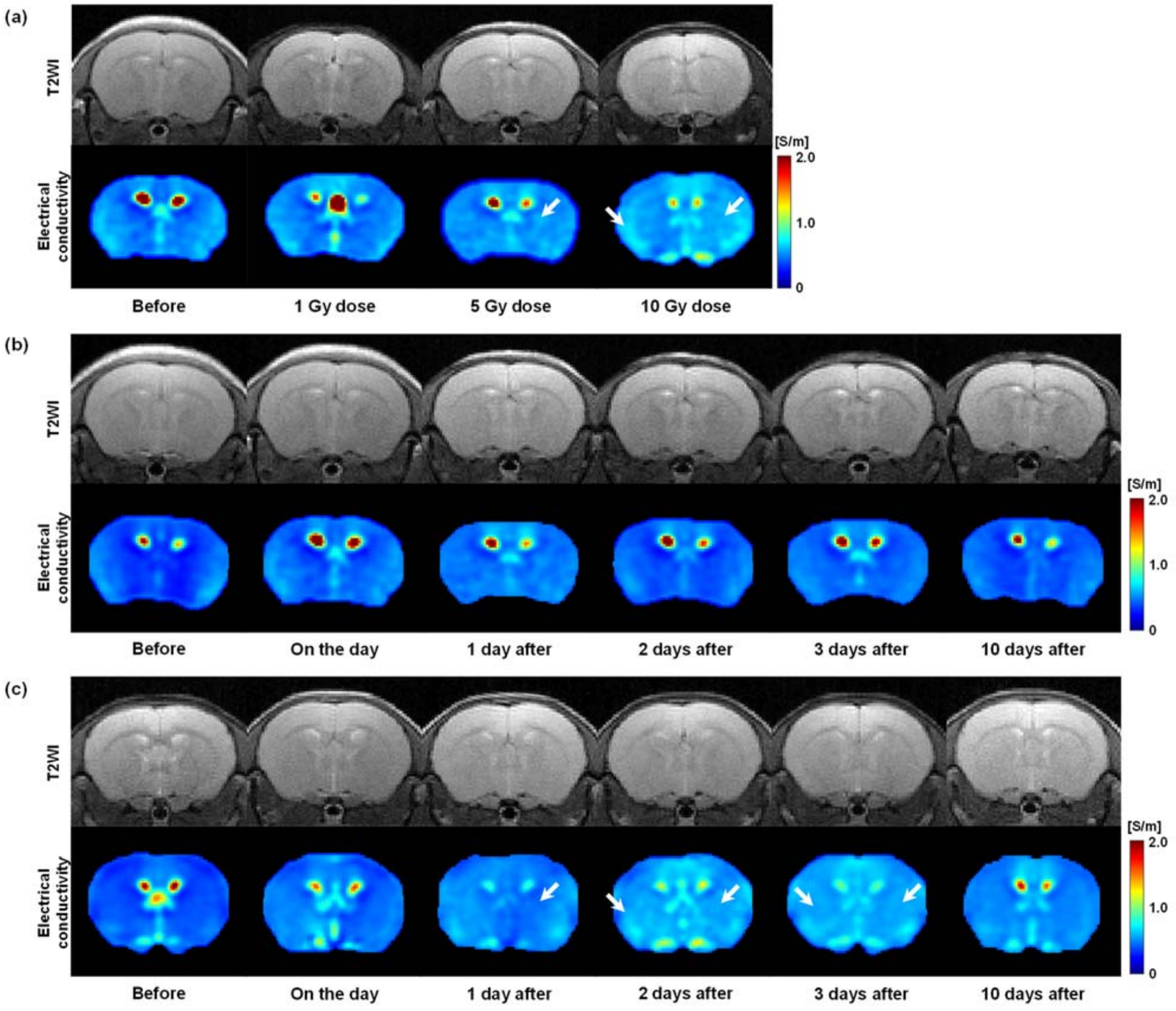

Figure 1. T2-weighted and electrical conductivity (a) images of in vivo mouse brains with respect to tissue response by different irradiation doses at 1 day after irradiation. Time-course variations in T2-weighted and electrical conductivity images of in vivo mouse brains in response to 5 Gy (b) and 10 Gy (c) irradiation doses. White arrows indicate an increase in conductivity contrast.

Figure 1(b) and (c) show a full time-course image of T2WI and electrical conductivity of the in vivo mouse brains after irradiation. All images were obtained at 5 Gy (Figure 1(b)) and 10 Gy (Figure 1(c)) irradiation doses. The morphological changes were not clearly observed in T2WI at both irradiation doses compared to before irradiation. However, the conductivity images showed different contrast variations depending on the irradiation doses and time.

Figure 2(b) and (c) show the conductivity of in vivo brain tissues measured from a full time-course dataset at 5 Gy and 10 Gy irradiation doses. ROIs were placed to cover all brain tissues of both hemispheres, excluding cerebrospinal fluid (CSF) (Figure 2(a)). The conductivity of the 5 Gy dose increased slightly up to 1 day afterward and decreased to 10 days (Figure 2(b)). The conductivity of the 10 Gy dose showed an increased contrast up to 2 days afterward and gradually decreased to 10 days (Figure 2(c)). There was no clear difference between the ROIs at two irradiation doses.

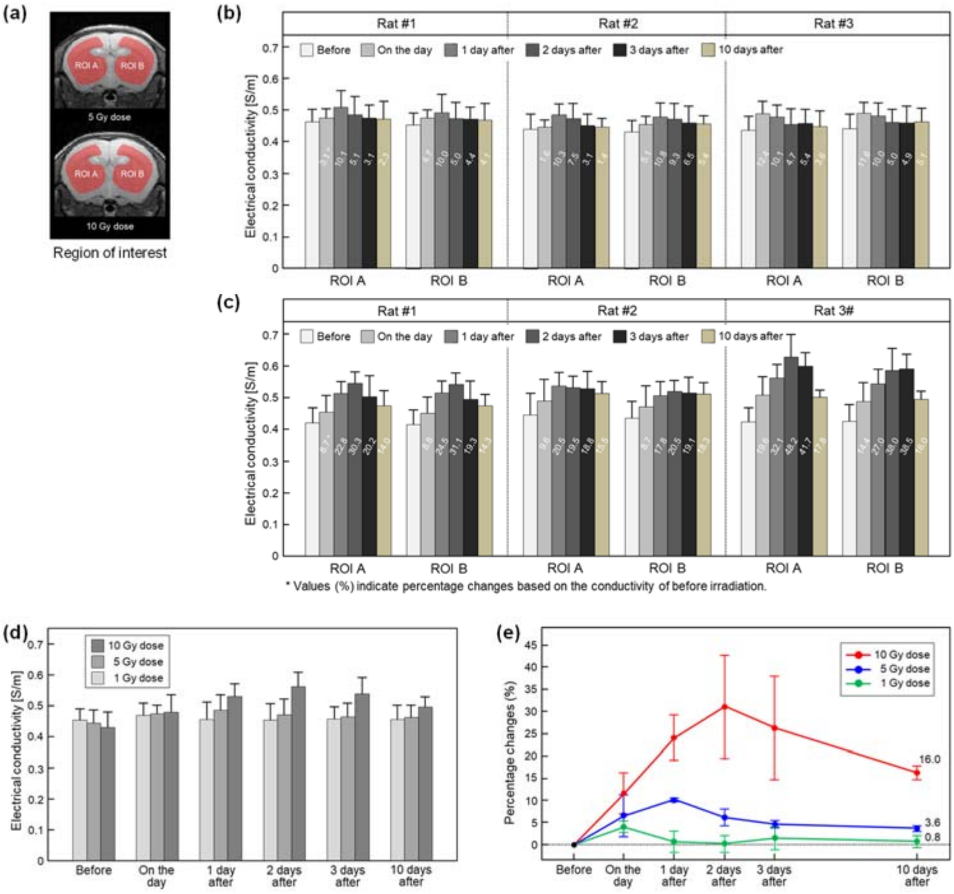

Figure 2. Measurement of absolute conductivity in brain tissues at full time points. ROIs were located in both hemispheres (a), and the conductivity was measured at 5 Gy (b) and 10 Gy (c) irradiation doses. The values inside the bar graph indicate relative conductivity changes. Analysis of in vivo brain conductivity images according to different doses and elapsed time after irradiation. Absolute conductivity (d) and relative conductivity changes (e) were acquired from doses of 1, 5, and 10 Gy with full time points.

Figure 2(d) and (e) show the measurement of absolute conductivity from in vivo mouse brains having a full time-course image by three irradiation doses. Conductivity was measured in all brain tissues except the CSF region. The conductivity changes at the 10 Gy dose was the largest at all measurement times (Figure 2(d)). There was a slight change at the 5 Gy dose and almost no evident change at the 1 Gy dose (Figure 2(d)). The relative conductivity change represents the sensitivity of the irradiation effects on brain tissues based on the values found before irradiation (Figure 2(e)). The sensitivity of the 10 Gy dose increased by 30% up to 2 days after irradiation and then decreased. The 5 Gy dose increased by 10% up to 1 day after irradiation and then decreased. There was no clear change in the 1 Gy dose. When comparing the relative conductivity change 10 days after irradiation, there was a 16% difference in 10 Gy, 3.6% in 5 Gy, and 0.6% in the dose of 1 Gy (Figure 2(e)).

4. Discussion

From the in vivo mouse brain imaging results, the morphological differences were not clearly observed at different doses and elapsed times after irradiation. This can be inferred from the previous report that the changes in T2 relaxation time were within 10% despite the neutron-beam irradiation (Katoch N *et al* 2019). On the contrary, electrical conductivity clearly showed contrast changes with different doses and elapsed times after irradiation. In comparison, at a single time point after irradiation (Figure 1(a)), the conductivity contrast was clearly distinguished at the 10 Gy dose from the other two lower doses. This indicates the reliability of electrical conductivity in that 10 Gy is an appropriate dose calculated considering the weight of the mouse. In addition, the conductivity contrast of 10 Gy showed a different pattern with the elapsed time (Figure 1(b) and (c)). Unlike the other two doses, the conductivity of 10 Gy showed a more sustained tissue response and residual conductivity even 10 days after irradiation.

Our quantitative results in Figure 7 represent the sensitivity of MR-based electrical conductivity imaging. The relative conductivity changes of the 10 Gy dose was highest at 31.3% 2 days after irradiation, the 5 Gy dose was at 10.2% 1 day after irradiation, and the 1 Gy dose was 4.0% on the day. This demonstrates two advantages derived from the measurement and quantification of electrical conductivity. First, conductivity changes can provide a dose-dependent response in irradiation and the time point of maximum response. Second, the staging of tissue damage caused by irradiation can be possible by measuring absolute values. Therefore, conductivity contrast can be an imaging marker for the irradiation effects by the different irradiation conditions.

This study has several limitations. First, there is a lack of evidence for a correlation between the imaging results and histological data. The correlation can better differentiate between RT-induced tissue damage by providing detailed information about the threshold dose for tissue response to RT. Second, the conductivity changes in this study focused on the acute brain response. Conductivity imaging of early and late delayed brain responses should be performed to determine reversible or irreversible tissue responses for clinical significance. Third, a conductivity image-based evaluation should be performed on various tissues or organs. Tissue injury varies from one tissue to another depending on the cellular composition, proliferation rate, and response mechanisms to radiation. Finally, together with the imaging data from a large sample size, statistical analysis between conductivity changes and tissue response is required at more time points for clinical applications

5. Conclusions

Tissue response to irradiation progresses slowly over time; sensitivity is one of the crucial factors in the image-based evaluation of irradiation effects. Ionizing radiation generally produces ions or charged particles within the cells; measuring absolute conductivity in tissues can provide highly sensitive information on the response following RT. This study focused on evaluating MR-based electrical conductivity imaging from the designed phantom and in vivo mouse brain by irradiation doses and the elapsed time of irradiation. A linear increase in conductivity with different doses in the phantom images can be evidence of ionizing radiation. From the *in-vivo* mouse brain, the change in conductivity at different doses can provide a way to quantify the response of the tissue to irradiation, and the variation in conductivity with the elapsed time shows potential as a tool to monitor the therapeutic effect of radiation. Future studies will focus on conductivity imaging of tumor patients following sufficient validation, including long-term time points that cover early and late delayed response and irradiation effects on various tissue types.

Acknowledgments

This research was funded by the National Research Foundation of Korea (NRF) grants funded by the Korea government (No. 2019R1A2C2088573, 2020R1I1A3065215, 2020R1A2C200790611, 2020R1I1A1A01073871, 2021R1A2C2004299).

References

Voges J, Treuer H, Sturm V, Büchner C, Lehrke R, Kocher M, Staar S, Kuchta J and Müller R P 1996 Risk analysis of linear accelerator radiosurgery *Int. J. Radiat. Oncol. Biol. Phys.* **36** 1055–1063

Baskar R, Dai J, Wenlong N, Yeo R and Yeoh K W 2014 Biological response of cancer cells to radiation treatment *Front. Mol. Biosci.* **1** 24

Park J A, Kang K J, Ko I O, Lee K C, Choi B K, Katoch N, Kim J W, Kim H J, Kwon O I and Woo E J 2019 In vivo measurement of brain tissue response after irradiation: Comparison of T2 relaxation, apparent diffusion coefficient, and electrical conductivity *IEEE Trans. Med. Imaging* **38** 2779–2784

Seo Y S, Ko I O, Park H, Jeong Y J, Park J A, Kim K S, Park M J and Lee H J 2019 Radiation-induced changes in tumor vessels and microenvironment contribute to therapeutic resistance in glioblastoma *Front. Oncol.* **9** 1259

Katoch N, Choi B K, Sajib S Z K, Lee E A, Kim H J, Kwon O I and Woo E J 2019 Conductivity tensor imaging of in vivo human brain and experimental validation using giant vesicle suspension *IEEE Trans. Med. Imaging* **38** 1569–1577

Proceedings of the International Conference of Bioelectromagnetism, Electrical Bioimpedance,
and Electrical Impedance Tomography June 29 – July 1, 2022 / Kyung Hee University, Seoul, Korea

Characteristics of High and Low Frequency Conductivities in Patients with Alzheimer's Disease

Geon-Ho Jahng[1], Mun Bae Lee[2], Soonchan Park[1], Sue Min Jung[3], Hak Young Rhee[4],
Chang-Woo Ryu[1], and Oh In Kwon[2]

[1]Department of Radiology, Kyung Hee University Hospital at Gangdong, College of Medicine, Kyung Hee University, Seoul, Korea
[2]Department of Mathematics, College of Basic Science, Konkuk University, Seoul, Korea
[3]Department of Biomedical Engineering, College of Electronics and Information, Kyung Hee University, Yongin-si, Korea
[4]Department of Neurology, Kyung Hee University Hospital at Gangdong, College of Medicine, Kyung Hee University, Seoul, Korea

Correspondence : Geon-Ho Jahng, e-mail : ghjahng@gmail.com ; Oh In Kwon, e-mail : oikwon@konkuk.ac.kr

Abstract–Previous studies reported increased concentrations of metallic ions and imbalanced Na+ and K+ ions in patients with Alzheimer's disease (AD) and the increased mobility of protons by microstructural disruptions in AD. The objective of this study was to evaluate characteristics of a high- and low-frequency conductivities in the participants with AD, amnestic mild cognitive impairment (MCI), and cognitively normal (CN) elderly people. This prospective study included 74 participants (23 AD patients, 27 amnestic MCI patients, and 24 CN elderly people) to explore the clinical application of high-frequncy conductivity (HFC). In addition, a independent prospective study included 34 participants (11 AD patients, 10 amnestic MCI patients, and 13 CN elderly people) to explore the clinical application of low-frequncy conductivity (LFC). The HFC value was higher in the AD group than in the CN and MCI groups. The high frequency conductivity (HFC) and low frequency conductivity of extra-neurite conductivity (EC) and intra-neurite conductivity (IC) were higher in the patients with AD than those with CN elderly people and patients with amnestic MCI. HFC values of the insula along with the GMV of the hippocampus can be used as an imaging biomarker to improve the differentiation of AD from CN.

Keywords: brain, Alzheimer's disease, MRI, high-frequency conductivity; low-frequency conductivity, diffusivity.

1. Introduction

The neuropathology of Alzheimer's disease (AD) is generally characterized by the presence of two abnormal proteins in the aggregated state in the brain, intracellular neurofibrillary tangles, and extracellular amyloid-beta (Aβ) plaques. Previous studies showed increased metallic ions (Wang et al., 2020; Zatta et al., 2009) and imbalanced Na+ and K+ ions in AD (Korol' et al., 2008; Vitvitsky et al., 2012). Changes in the ion concentrations can be caused by homeostasis alterations in AD patients. Furthermore, several previous studies showed increased diffusivity caused by demyelination and neurodegeneration in AD patients (Amlien and Fjell, 2014; Jahng et al., 2011; Zhang et al., 2007), indicating the increased mobility of protons by microstructural disruptions in AD compared to cognitively normal elderly controls.

The conductivity (σ) mapping of human brain tissue could be used as an imaging biomarker for diagnosing diseases and predicting treatment effects. Magnetic resonance electrical property tomography (MREPT) is a technique to derive *in vivo* internal electrical conductivity using a standard MRI system without applying externally mounted electrodes or currents (Katscher et al., 2009; Voigt et al., 2011). Conductivity by MREPT is called high-frequency conductivity (HFC) and is a non-invasive method. As the electrical conductivity is affected by cell membranes depending on the frequency, a two-compartment model based on the intra- cellular and extracellular separations is considered to investigate the low-frequency conductivity (LFC) properties. The multi-compartment spherical mean technique (MC-SMT) model (Kaden et al., 2016) represents the diffusion signal as a weighted sum of contributions of restricted and hindered compartments, and estimates the separated micro-structural parameters.

Conductivity values may provide clinically useful information for neuronal degeneration. Therefore, the purposes of this study were to compare the HFC values in the brain of participants with AD, amnestic mild cognitive impairment (MCI), and CN elderly people and evaluate the relationship between HFC values and cognitive decline. In addition, we developed a technique to map the low frequency conductivity using combination both MREPT and diffusivity data.

Furthermore, we applied this method to investigate conductivity changes in the patient with Alzheimer' disease (AD) compared with cognitively normal (CN) elderly people and in the patient with amnestic mild cognitive impairment (MCI) because previous studies demonstrated increased concentrations of metallic ions and imbalanced Na+ and K+ ions in AD.

2. Methods

2.1 Participants: Our Institutional Review Board (IRB) approved this cross-sectional prospective study and informed consent was obtained from the participants who were recruited in the neurological center of our institution. Participants provided a detailed medical history and underwent a neurologic examination, standard neuropsychological testing, and MRI scan. For HFC study, 74 participants were grouped as 24 CN, 27 MCI, and 23 AD. For LFC study, 34 participants were grouped as 13 CN, 10 MCI, and 11 AD.

2.2 **MRI acqusition:** MRI was performed using a 3.0 Tesla MRI system equipped with a 32-channel sensitivity encoding head coil (Ingenia, Philips Medical System, Best, The Netherlands). For the brain MREPT images, a multi-echo turbo spin-echo pulse sequence was used (Ahn et al., 2010). For MC-SMT, the diffusion of water molecules was measured using the single-shot spin-echo echo-planner imaging (SS-SE-EPI) pulse sequence. Diffusion-tensor weighting was achieved with two b-shells of nominally 800 and 2000 s/mm^2 with 16 and 32 gradient directions, respectively. For image registration and brain tissue segmentation, a sagittal structural three-dimensional (3D) T1-weighted (T1W) image was acquired with the fast field-echo (FFE) sequence, which is similar to the magnetization-prepared rapid acquisition of the gradient echo (MPRAGE) sequence.

2.3 **Post-processing:** A home-made software was used to map the HFC at the Larmor frequency of 128 MHz at 3T (Katscher et al., 2009). The MREPT formula based on a convection reaction equation was derived by adding the regularization coefficient (Gurler and Ider, 2017). To solve the convection reaction partial differential equation, we used the 2-dimensional finite-difference method. First, to obtain HFC, we used the following double derivative of the B1 field equation. Second, to obtain a low frequency conductivity and ion concentration information, the recovered HFC $\boldsymbol{\sigma_H}$ was decomposed into the intraneurite and extraneurite compartments. To map the intraneurite conductivity (IC), the extraneurite conductivity (EC), the intraneurite volume fraction (IVF), the intraneurite ion concentration (IIC), the extraneurite ion concentration (EIC), the intraneurite diffusivity (ID), and the extraneurite diffusivity (ED), we used the multi-compartment spherical mean technique (MC-SMT) (Kaden et al., 2016). More detailed theories and algorithms are described in our previous paper (Jahng et al., 2021).

2.4 **Statistical analyses:** The following pre-processing steps were performed to process the reconstructed maps of each participant using Statistical Parametric Mapping version 12 (SPM12) software (http://www.fil.ion.ucl.ac.uk/spm/software/spm12/). Statistical analyses of all maps were performed using voxel-based methods. First, all maps were compared between the three participant groups using the voxel-wised full factorial design of one-way analysis of covariance (ANCOVA) with age as a covariate. Second, all maps from all participants were evaluated to identify the association of ages or Mini-Mental State Examination (MMSE) scores with age as a covariate using voxel-based multiple regression analysis. A significance level of $\alpha = 0.05$ was applied with correction for multiple comparisons using the false-discovery rate (FDR) method and clusters with at least 100 contiguous voxels.

3. Results

3.1 HFC result

We obtained a good high-frequency conductivity (HFC) map noninvasively. **Figure 1** shows the results of the voxel-based ANCOVA analysis of the HFC among the three participant groups. The HFC values were lower in the CN

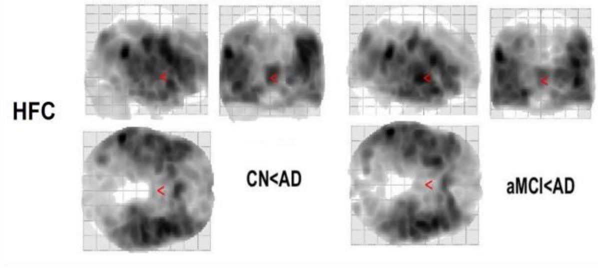

Figure 1. Results of the voxel-based ANCOVA analysis of the HFC.

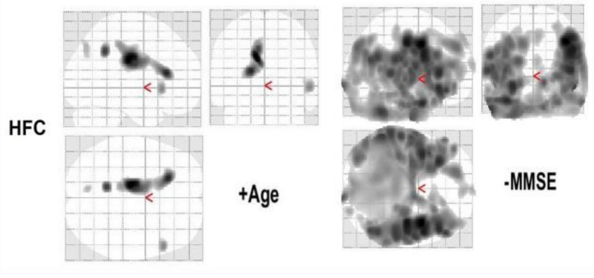

Figure 2. Results of the voxel-based multiple regression analysis of the HFC or brain tissue maps with age or MMSE scores. (+) and (-) symbols are indicated to positive and negative association, respectively.

and MCI groups compared to the AD group at most of brain areas including in the frontal lobe, the parietal lobe, the temporal lobe, the insula, and precuneus areas.

Figure 2 shows the results of the voxel-based multiple regression analysis of the HFC with age or MMSE scores using all participant data. Age was positively associated with HFC values. MMSE scores were negatively associated with HFC.

3.2 LFC result

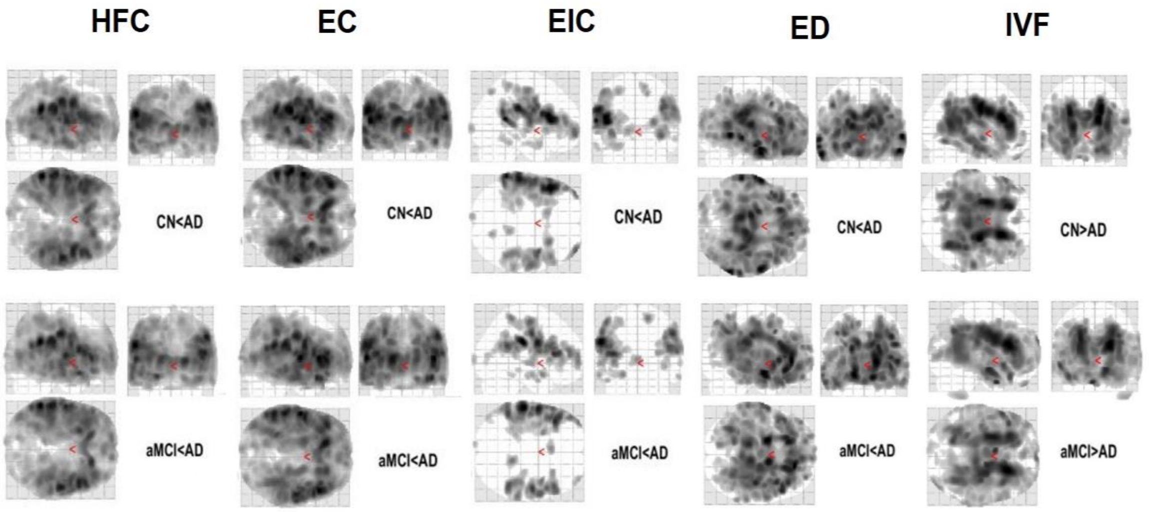

Figure 3. Results of the voxel-based group comparison of each map among the three participant groups

We developed a low frequency conductivity imaging technique from extra-neurite and intra-neurite areas in the brain without injecting external current. Results of the voxel-based group comparison of each map among the three participant groups were shown in **Figure 3**. Compared with the CN group and MCI group, the CSF volume, HFC, EC, EIC, and ED were increased in the AD group, but IVF was lower in the AD group. The two conductivities of HFC and EC were increased in the AD group at the large brain areas, including in the frontal, parietal, and temporal areas. IC and ID were not significantly different between the two groups.

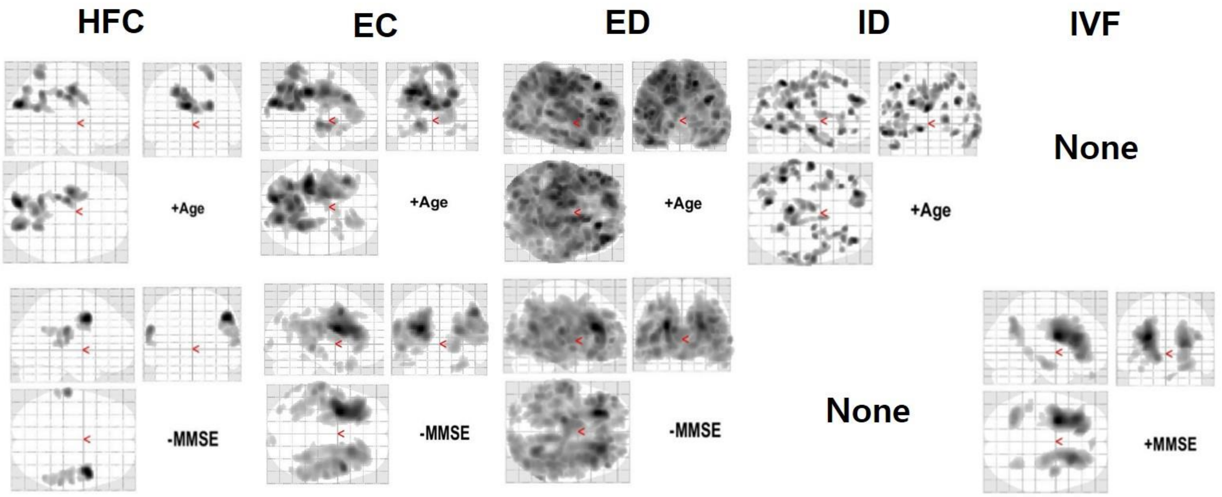

Figure 4. Results of voxel-based multiple regression analysis of each map with ages or MMSE scores. (+) and (-) symbols are indicated to positive and negative association, respectively.

Results of voxel-based multiple regression analysis of each map with ages or MMSE scores were shown in **Figure 4**. Age was positively associated with HFC, EC, ED, and ID, but was not associated with the CSF volume, IC, EIC, and IVF. The MMSE score was negatively associated with HFC, EC, and ED, but was positively associated with IVF. However, we did not find any association between ID, the CSF volume, IC, or EIC and the MMSE scores.

4. Conclusions

HFC values in the brain are significantly increased in AD patients compared to CN elderly people, are negatively associated with MMSE scores. Furthermore, we also developed a low frequency conductivity imaging technique in the brain without injecting external current and found the increased extra-neurite conductivity and intra-neurite conductivity in AD patients compared to CN elderly people and amnestic MCI patients. Therefore, conductivity information can be used as an imaging biomarker to improve the differentiation of AD from CN. Further studies should be conducted to evaluate the direct relationship between neuronal loss and conductivity changes in the brain of patients with AD.

Acknowledgments: The research was supported by the National Research Foundation of Korea (NRF) grants funded by Ministry of Science and ICT (2020R1A2C1004749, G.H.J.; 2019R1A2C1004660, O.I.K.; 2020R1F1A1A01074353, M.B.L.), Republic of Korea. The authors appreciate Miss Narae Lee (Kyung Hee Medical Science Research Institute, Seoul, Korea) for advice on the statistical analyses.

References

Ahn, H.J., Chin, J., Park, A., Lee, B.H., Suh, M.K., Seo, S.W., Na, D.L., 2010. Seoul Neuropsychological Screening Battery-dementia version (SNSB-D): a useful tool for assessing and monitoring cognitive impairments in dementia patients. J Korean Med Sci 25, 1071-1076.

Amlien, I.K., Fjell, A.M., 2014. Diffusion tensor imaging of white matter degeneration in Alzheimer's disease and mild cognitive impairment. Neuroscience 276, 206-215.

Gurler, N., Ider, Y.Z., 2017. Gradient-based electrical conductivity imaging using MR phase. Magn Reson Med 77, 137-150.

Jahng, G.H., Lee, M.B., Kim, H.J., Je Woo, E., Kwon, O.I., 2021. Low-frequency dominant electrical conductivity imaging of in vivo human brain using high-frequency conductivity at Larmor-frequency and spherical mean diffusivity without external injection current. Neuroimage 225, 117466.

Jahng, G.H., Xu, S., Weiner, M.W., Meyerhoff, D.J., Park, S., Schuff, N., 2011. DTI studies in patients with Alzheimer's disease, mild cognitive impairment, or normal cognition with evaluation of the intrinsic background gradients. Neuroradiology 53, 749-762.

Kaden, E., Kelm, N.D., Carson, R.P., Does, M.D., Alexander, D.C., 2016. Multi-compartment microscopic diffusion imaging. Neuroimage 139, 346-359.

Katscher, U., Voigt, T., Findeklee, C., Vernickel, P., Nehrke, K., Dossel, O., 2009. Determination of electric conductivity and local SAR via B1 mapping. IEEE Trans Med Imaging 28, 1365-1374.

Korol', T.Y., Korol', S.V., Kostyuk, E.P., Kostyuk, P.G., 2008. Disruption of Calcium Homeostasis in Alzheimer's Disease. Neurophysiology 40, 385-392.

Vitvitsky, V.M., Garg, S.K., Keep, R.F., Albin, R.L., Banerjee, R., 2012. Na+ and K+ ion imbalances in Alzheimer's disease. Biochim Biophys Acta 1822, 1671-1681.

Voigt, T., Katscher, U., Doessel, O., 2011. Quantitative conductivity and permittivity imaging of the human brain using electric properties tomography. Magn Reson Med 66, 456-466.

Wang, L., Yin, Y.L., Liu, X.Z., Shen, P., Zheng, Y.G., Lan, X.R., Lu, C.B., Wang, J.Z., 2020. Current understanding of metal ions in the pathogenesis of Alzheimer's disease. Transl Neurodegener 9, 10.

Zatta, P., Drago, D., Bolognin, S., Sensi, S.L., 2009. Alzheimer's disease, metal ions and metal homeostatic therapy. Trends Pharmacol Sci 30, 346-355.

Zhang, Y., Schuff, N., Jahng, G.H., Bayne, W., Mori, S., Schad, L., Mueller, S., Du, A.T., Kramer, J.H., Yaffe, K., Chui, H., Jagust, W.J., Miller, B.L., Weiner, M.W., 2007. Diffusion tensor imaging of cingulum fibers in mild cognitive impairment and Alzheimer disease. Neurology 68, 13-19.

DAY 2

Thursday, June 30, 2022

Invited Talk 04

Speaker Khin Khin Tha (Hokkaido University)

"Noninvasive Assessment of Tissue Electrical Conductivity: Potential Clinical Value"

ICBEM Bioelectromagnetism ICEBI Electrical Bioimpedance EIT Electrical Impedance Tomography

Proceedings of the International Conference of Bioelectromagnetism, Electrical Bioimpedance,
and Electrical Impedance Tomography June 29 – July 1, 2022 / Kyung Hee University, Seoul, Korea

Noninvasive Assessment of Tissue Electrical Conductivity: Potential Clinical Value

Khin Khin Tha
Global Center for Biomedical Science and Engineering, Hokkaido University Faculty of Medicine, Sapporo, Japan

e-mail : kktha@med.hokudai.ac.jp

Abstract– Electrical conductivity is an intrinsic property of tissue or material to conduct electric current. It varies among tissues and between physiological and pathological states. Before the era of computed tomography and magnetic resonance imaging, electrical properties of tissues measured by direct placement of electrodes on the brain surface were used to locate brain tumors during surgery. Nowadays, several imaging techniques allow non-invasive and in vivo assessment of tissue electrical conductivity. Of these, electric properties tomography calculates electrical conductivity from the phase of magnetic resonance imaging scans. This technique's validity and repeatability in measuring electrical conductivity have been documented. Preliminary studies have been conducted, which reveal the potential role of electrical conductivity extractable by this technique in distinguishing benign and malignant breast tumors, identifying HER2-overexpression in breast cancers, distinguishing diffuse gliomas by histological grades, distinguishing benign and malignant lung and mediastinal tumors, and distinguishing liver fibrosis from the normal liver. In addition, an increase in electrical conductivity with increasing cerebrospinal fluid albumin concentration or total cell count has also been observed, which may further extend the applicability of electric properties tomography to evaluate the cerebrospinal fluid biochemical composition.

Acknowledgments

The study was supported by the grants-in-aid for scientific research by Japan society for promotion of science (KAKENHI-26461817, 17K10390, 20K12590), global institution for collaborative research and education (GI-CoRE), Hokkaido University, and Philips.

References

Katscher U, Kim DH, Seo JK 2013 Recent progress and future challenges in MR electric properties tomography. *Comput Math Methods Med.* ***2013*** *546562*

Kim SY, Shin J, Kim DH, Kim MJ, Kim EK, Moon HJ, Yoon JH 2016 Correlation between conductivity and prognostic factors in invasive breast cancer using magnetic resonance electric properties tomography (MREPT) *Eur Radiol.* ***26*** *2317-26*

Mori N, Tsuchiya K, Sheth D, Mugikura S, Takase K, Katscher U, Abe H 2019 Diagnostic value of electric properties tomography (EPT) for differentiating benign from malignant breast lesions: comparison with standard dynamic contrast-enhanced MRI *Eur Radiol.* ***29*** *1778-86*

Tha K K, Katscher U, Yamaguchi S, Stehning C, Terasaka S, Fujima N, Kudo K, Kazumata K, Yamamoto T, Van Cauteren M, Shirato H 2018 Noninvasive electrical conductivity measurement by MRI: a test of its validity and the electrical conductivity characteristics of glioma *Eur. Radiol.* **28** 348-55

Tha KK, Kikuchi Y, Ishizaka K, Kamiyama T, Yoneyama M, Katscher U 2021 Higher Electrical Conductivity of Liver Parenchyma in Fibrotic Patients: Noninvasive Assessment by Electric Properties Tomography *J. Magn. Reson. Imag.* ***54*** *1689-91*

DAY 2

Thursday, June 30, 2022

Mini Symposium 02

Imaging Electrical Properties by MRI

Organizer Khin Khin Tha (Hokkaido University)
Moderator Nico van den Berg (University Medical Centre Utrecht)

M 02-01 **Imaging Electrical Properties by MRI: Principles and Technical Aspects**
Ulrich Katscher (Philips Research Laboratories)

M 02-02 **Tissue Electrical Properties: Findings of Animal Experiment on Tissue Response to Ionizing Radiation**
Jin Woong Kim (Chosun University Hospital)

M 02-03 **Measurements of Electrical Properties in humans in vivo using Magnetic Resonance Imaging**
Rosalind J. Sadleir (Arizona State University)

M 02-04 **Are we ready for the clinics?**
Stefano Mandija (University Medical Center Utrecht)

Proceedings of the International Conference of Bioelectromagnetism, Electrical Bioimpedance,
and Electrical Impedance Tomography June 29 – July 1, 2022 / Kyung Hee University, Seoul, Korea

Imaging Electrical Properties by MRI: Principles and Technical Aspects

Ulrich Katscher[1]
[1]Philips Research Laboratories, Hamburg, Germany

Correspondence : Ulrich Katscher, e-mail : ulrich.katscher@philips.com

Abstract–Mapping tissue electrical properties *in vivo* started with “Electrical Impedance Tomography” (EIT), injecting currents through electrodes mounted on the patient’s skin, allowing the reconstruction of a low-resolution impedance map. Electrode-based current injection can also be performed during Magnetic Resonance Imaging (MRI), if current injection intervals are suitably synchronized with the MR sequence applied. The injected currents produce specific alterations of the image phase, from which maps of current density (“MR Current Density Imaging”, MR-CDI) and conductivity (“MR Electrical Impedance Tomography”, MR-EIT) can be derived via numerical post-processing. Conductivity obtained via MR-EIT belongs to the timing of the current injection intervals, which is typically in the range of kHz.

However, MRI allows the mapping of conductivity also without the injection of external currents. Conductivity can be instead mapped by probing the currents induced by electric fields accompanying the standard RF pulses applied for spin excitation during conventional MRI (“MR Electrical Properties Tomography”, MR-EPT). MR-EPT allows mapping the electric conductivity (and also permittivity) in a spatial resolution of the order of standard MR images, i.e., in the range of mm. Conductivity and permittivity obtained via MR-EPT belongs to the Larmor frequency of the MR system used, which for standard clinical systems is typically 64 MHz or 128 MHz. In the roughly 10 years since its introduction, MR-EPT was evaluated by numerous phantom and *in vivo* volunteer measurements. Initial clinical studies were conducted mainly for investigation of tumors, consistently showing a relation between tumor conductivity and malignancy.

References

Haacke E M, Petropoulos L S, Nilges E W and Wu D H 1991 Extraction of conductivity and permittivity using MRI *Phys. Med. Biol.* **36** 723-34

Katscher U and van den Berg C A T 2017 Electrical Properties Tomography (EPT): Biochemical, physical and technical background, evaluation and clinical applications *NMR Biomed*. **30** 3729

Shin J, Kim M J, Lee J, Nam Y, Kim M O, Choi N, Kim S and Kim D H 2015 Initial study on in vivo conductivity mapping of breast cancer using MRI *J. Magn. Reson. Imag*. **42** 371-8

Tha K K, Katscher U, Yamaguchi S, Stehning C, Terasaka S, Fujima N, Kudo K, Kazumata K, Yamamoto T, Van Cauteren M, Shirato H 2018 Noninvasive electrical conductivity measurement by MRI: a test of its validity and the electrical conductivity characteristics of glioma *Eur. Radiol*. **28** 348-55

Woo E J and Seo J K 2008 Magnetic Resonance Electrical Impedance Tomography (MREIT) for high-resolution conductivity imaging *Physiol Meas*. **29** 1-26

M 02-02

Proceedings of the International Conference of Bioelectromagnetism, Electrical Bioimpedance,
and Electrical Impedance Tomography June 29 – July 1, 2022 / Kyung Hee University, Seoul, Korea

Tissue Electrical Properties: Findings of Animal Experiment on Tissue Response to Ionizing Radiation

Jin Woong Kim[1], Ji Ae Park[2], Young Hoe Hur[3], and Hyung Joong Kim[4]
[1]Department of Radiology, Chosun University Hospital and Chosun University College of Medicine, Gwangju, Korea.
[2]Division of Applied RI, Korea Institute of Radiological and Medical Science, Seoul, Korea.
[3]Department of Hepato-Biliary-Pancreas Surgery, Chonnam National University Hwasun Hospital and Chonnam National University Medical School, Gwangju, Korea
[4]Medical Science Research Institute, Kyung Hee University Hospital, Seoul, Korea.

Correspondence: Jin Woong Kim, e-mail: jw4249@gmail.com

Abstract– Radiation therapy (RT) has been widely used as a powerful treatment tool to address cancerous tissues because of its ability to control cell growth. Radiation-induced injury is damage to normal tissues caused by unintentional exposure to ionizing radiation during RT. Image-based evaluation of tissue damage by irradiation has an advantage for the early assessment of therapeutic effects by providing sensitive information on minute tissue responses *in situ*. Recent magnetic resonance (MR)-based electrical conductivity imaging has shown potential as an effective early imaging biomarker for treatment response and radiation-induced injury. However, to be a tool for evaluating therapeutic effects, validation of its reliability and sensitivity according to various irradiation conditions is required. We performed MR-based electrical conductivity imaging on designed phantoms to confirm the effect of ionizing radiation at different doses and on *in vivo* mouse brains to distinguish tissue response depending on different doses and the elapsed time after irradiation. To quantify the irradiation effects, we measured the absolute conductivity of brain tissues and calculated relative conductivity changes based on the value of pre-irradiation. The conductivity of the phantoms with the distilled water and saline solution increased linearly with the irradiation doses. The conductivity of *in vivo* mouse brains showed different time-course variations and residual contrast depending on the irradiation doses. Future studies will focus on validation at long-term time points, including early and late delayed response and evaluation of irradiation effects in various tissue types such as tumor.

Acknowledgments

This research was funded by the National Research Foundation of Korea (NRF) grants funded by the Korea government (No. 2019R1A2C2088573, 2020R1I1A3065215, 2020R1A2C200790611, 2021R1A2C2004299).

References

Park J A, Kang K J, Ko I O, Lee K C, Choi B K, Katoch N, Kim J W, Kim H J, Kwon O I and Woo E J 2019 In vivo measurement of brain tissue response after irradiation: comparison of T2 relaxation, apparent diffusion coefficient, and electrical conductivity *IEEE Trans. Med. Imaging* **38** 2779-2784.

Greene-Schloesser D, Robbins M E, Peiffer A M, Shaw E G, Wheeler K T and Chan M D 2012 Radiation-induced brain injury: a review *Front. Oncol.* **2** 73.

Kim J W, Park J A, Katoch N, Yang J U, Park S. Choi B K, Song S G, Kim T H and Kim H J 2021 Image-Based Evaluation of Irradiation Effects in Brain Tissues by Measuring Absolute Electrical Conductivity Using MRI *Cancers* **13** 5490.

Cuccurullo V, Stasio G D D, Cascini G L, Gatta G and Bianco C 2019 The molecular effects of ionizing radiations on brain cells: Radiation necrosis vs. tumor recurrence *Diagnostics* **9** 127.

ICBEM Bioelectromagnetism ICEBI Electrical Bioimpedance EIT Electrical Impedance Tomography

Proceedings of the International Conference of Bioelectromagnetism, Electrical Bioimpedance,
and Electrical Impedance Tomography June 29 – July 1, 2022 / Kyung Hee University, Seoul, Korea

Measurements of Electrical Properties in humans in vivo using Magnetic Resonance Imaging

R. Sadleir[1], S. Z. K. Sajib[1,2], E. Boakye[1], S. Sahu[1], and M. Chauhan[1,3]
[1]School of Biological and Health Systems Engineering, Arizona State University, Tempe, AZ, USA
[2]Canon Medical Research, Cleveland, OH, USA
[3]University of Kansas Medical Center, Kansas City, KS, USA

Correspondence : Rosalind J. Sadleir, e-mail : rsadleir@asu.edu

Abstract–Measurement of conductivity distributions at high (Larmor frequency) and low (<1 MHz) frequencies can be obtained using MRI image data obtained using Electric Properties Tomography (Voigt et al., 2011) (EPT), Magnetic Resonance Electrical Impedance Tomography (Seo et al., 2003) (MREIT), or Conductivity Tensor Imaging (Katoch et al., 2019) (CTI) strategies. In addition, electromagnetic fields in the brain resulting from transcranial or intracranial neuromodulation such as tDCS deep brain stimulation can be measured and used to inform electrode location methods or mechanism hypotheses. In the practical sense, measurement of these data on human subjects is relatively straightforward in CTI or EPT methods, where electrodes are not required, but more complex when the safety and artefactual implications of electrode and electrode wire locations and materials must be considered when using MREIT to measure field distributions. Subjects may also be affected by administration of MREIT currents. We will first review previous strategies to measure conductivity and field distributions in human subjects. We will then focus on methods for obtaining high quality and accurate images of the human brain using MREIT during neuromodulation (Chauhan et al., 2018), including practical details for ensuring that electrodes are applied safely, stable electrode contact is ensured, and wire tracks can be determined. Finally, because typical neuromodulation electrode locations may involve significant current flow out of the transverse plane, we will also demonstrate approaches that can improve reconstruction of full conductivity and electromagnetic field data in these cases.

Acknowledgments

The authors would like to thank Sharmeen Maze, Wendy Johnson and Chris Blais for their support in scanning and coordinating subjects imaged during our studies.

References

CHAUHAN, M., INDAHLASTARI, A., KASINADHUNI, A. K., SCHÄR, M., MARECI, T. H. & SADLEIR, R. J. 2018. Low-Frequency Conductivity Tensor Imaging of the Human Head in vivo using DT-MREIT: First Study. *IEEE Transactions on Medical Imaging,* 37**,** 966-976.

KATOCH, N., CHOI, B. K., SAJIB, S. Z. K., LEE, E., KIM, H. J., KWON, O. I. & WOO, E. J. 2019. Conductivity tensor imaging of in vivo human brain and experimental validation using giant vesicle suspension. *IEEE Transactions on Medical Imaging,* 38**,** 1569-1577.

SEO, J. K., YOON, J. R., WOO, E. J. & KWON, O. 2003. Reconstruction of conductivity and current density images using only one component of magnetic field measurements. *IEEE Transactions on Biomedical Engineering,* 50**,** 1121-1124.

VOIGT, T., KATSCHER, U. & DOESSEL, O. 2011. Quantative conductivity and permittivity imaging of the human brain using electric properties tomography. *Magnetic Resonance in Medicine,* 66**,** 456-466.

Proceedings of the International Conference of Bioelectromagnetism, Electrical Bioimpedance,
and Electrical Impedance Tomography June 29 – July 1, 2022 / Kyung Hee University, Seoul, Korea

Are we ready for the clinic?

Stefano Mandija[1,2]
[1]Department of Radiotherapy, University Medical Center Utrecht, Utrecht, The Netherlands
[2]Computational Imaging Group for MR Therapy and Diagnostics, University Medical Center Utrecht, Utrecht, The Netherlands

Correspondence : Stefano Mandija, e-mail : S.Mandija@umcutrecht.nl

Abstract-Tissue electrical properties represent an emerging MRI biomarker. At low frequencies (kHz), tissue conductivity information can be used for guidance of brain stimulation[1]. At high frequencies (hundreds of MHz), an increase in tissue conductivity has been observed in brain and breast tumours, correlating with tumour grade[2] and mitotic score[3]. Conductivity changes have also been observed in rat models after radiotherapy, opening a new window for conductivity imaging in radiotherapy where conductivity may provide additional information in evaluating the therapeutic effect of radiotherapy[4]. In this talk, we will review the value of MR-based conductivity imaging as clinical biomarker (in particular at high frequencies) with attention to these first in-vivo studies. However, while it is important to provide clinical evidences of the value of conductivity imaging, are we already ready for the clinic?

Several reconstruction methods have been developed in the past years, but these were tested on independent data. From the few reported in-vivo studies, differences in the reconstructed conductivity values are observed. Therefore, several steps will have to be undertaken to gain confidence in the reconstructed conductivity maps, necessary precursor before clinical translation. This will be one of the goals of the first reconstruction challenge[5], which will use a database of simulated and measured data that will be shared with the community. We will therefore conclude this talk presenting the upcoming initiatives (e.g. database and challenge) that we, as community, should undertake to turn conductivity imaging into a reliable biomarker.

Acknowledgments

The author would like to acknowledge Prof. C.A.T. van den Berg for his support to this work. This work is also supported by the Netherlands Organisation for Scientific Research (NWO), grant number:18078.

References

1) Sajib SZK, Lee MB, Kim HJ, Woo EJ and Kwon OI 2018 Extracellular Total Electrolyte Concentration Imaging for Electrical Brain Stimulation (EBS) *Scientific Reports* **8** 290
2) Tha KK, Katscher U, Yamaguchi S, Stehning C, Terasaka S, Fujima N, Kudo K, Kazumata K, Yamamoto T, Van Cauteren M and Shirato H 2018 Non-invasive electrical conductivity measurement by MRI: a test of its validity and the electrical conductivity characteristics of glioma *European Radiology* **28** 348-355
3) Kim SY, Shin J, Kim DH, Kim EK, Moon HJ and Yoon JH 2016 Correlation between conductivity and prognostic factors in invasive breast cancer using magnetic resonance electric properties tomography (MREPT) *European Radiology* **26** 2317-2326
4) Ko IO, Choi BK, Katoch N, Park JA, Kim JW, Kim, HJ, Kwon OI, Woo EJ 2018 In Vivo Conductivity Imaging of Tissue Response after Radiation Therapy *ISMRM* p547
5) Mandija S, van den Berg CAT 2022 The first MR Electrical Properties Tomography (MR-EPT) reconstruction challenge *ISMRM* p704

DAY 2

Thursday, June 30, 2022

Oral Session 07

Bio-impedance Measurement II

Chair Vincent Senez (University of Lille)

O 07-01 **Wearable Device for Blood Glucose Level Analysis Using Electrical Bioimpedance and Near-infrared: Preliminary ResultsS**
Pedro Bertemes Filho (State University of Santa Catarina)

O 07-02 **Total body water in Colombian older adults through bioelectrical impedance analysis**
Villada-Gómez Johan Sebastian (Universidad de Caldas)

O 07-03 **Skin impedance in a sensor-sock for diabetic foot assessment**
Christian Tronstad (Oslo University Hospital)

O 07-04 **The influence of isometric and isotonic muscle contraction on measured resistance and reactance during seated leg curls**
Alfred Hülkenberg (RWTH Aachen University)

O 07-05 **Neural Noise Module: Automated Error Modeling using Adversarial Neural Networks**
Benjamin Schindler (Universität Leipzig)

Proceedings of the International Conference of Bioelectromagnetism, Electrical Bioimpedance,
and Electrical Impedance Tomography June 29 – July 1, 2022 / Kyung Hee University, Seoul, Korea

WEARABLE DEVICE FOR BLOOD GLUCOSE LEVEL ANALYSIS USING ELECTRICAL BIOIMPEDANCE AND NEAR-INFRARED : PRELIMINARY RESULTS

Leonardo G Teixeira[1] and Pedro Bertemes-Filho[1]
[1]Department of Electrical Engineering, State University of Santa Catarina, Joinville, Brazil

Correspondence: Leonardo G Teixeira, e-mail: leonardo.teixeira@edu.udesc.br

Abstract– Diabetes is one of the most prominent diseases in the world, and self-monitoring of blood glucose is essential for effective treatment. Non-invasive techniques have been investigated, such as the skin's response to electrical and optical excitation signals. The objective of this work is to investigate the correlation between multifrequency electrical bioimpedance (EBIS) and near-infrared (NIR) spectroscopy with glucose level. A wearable prototype of the device composed of 3 LEDs and a 4-point bioimpedance was built. The volunteer was asked not to eat any food for at least 8 hours before measurements. After collecting the first data set, 75 grams of glucose were ingested and 8 data sets were recorded every 15 minutes. Data was collected in the frequency range of 0.1 to 100 kHz. A correlation greater than 0.9 was calculated for NIR, while >0.7 for EBIS when using the impedance module in the range of 1 to 10 kHz. Although no combination of NIR and EBIS data has been investigated, it is expected that both data may be used in a machine learning technique in order to improve correlation. However, more investigations are needed to increase the prototype's accuracy when dealing with a real, uncontrolled, day-to-day environment.

Keywords: glucose; bioimpedance; infra-red; wearable technology.

1. Introduction

Diabetes mellitus is a disease in which the body cannot produce enough insulin, which is important for maintaining the body's glucose level. It may be caused by lack of insulin secretion, defects in insulin action, or both (Alberi and Zimmet 1998). This disease is one of the main health problems in the world, also causing a great socioeconomic impact. For efficient management of diabetes mellitus, blood sugar level monitoring is highly necessary. Traditional monitoring devices on the market use invasive methods to determine blood glucose level. Home-use devices require a blood sample from the patient's fingertip, which is obtained using a needle, causing pain, discomfort, and possible infectious disease (Fouad, Mahmoud and Abd El Ghany 2018). However, optimal insulin dosing requires continuous glucose monitoring and currently available glucometers do not meet this requirement (Klonoff 2007). The current solution is continuous monitors, which need to be implanted under the skin, causing trauma during implantation, needing periodic replacement, in addition to using interstitial fluid measurements that have a delay of 5 to 10 minutes from the actual level of glucose in the blood (Cengiz and Tamborlane 2009, Klonoff 2007).

Many techniques have been researched and introduced as methods of measuring glucose non-invasively, under the assumption that glucose is the analyte in the blood that affects the physical parameters of tissues (Harman-Boehm *et al* 2009). Non-invasive methods can be divided into three groups: optical spectroscopes, non-optical and electrochemical spectroscopes. Optical techniques mainly depend on the fact that glucose molecules absorb, scatter and reflect light depending on their wavelength. Diffuse Reflectance (Yadav *et al* 2014), Raman Spectroscopy (Wrobel 2016), Polymetry (Malik and Cot 2010) and Near-Infrared (NIR) Spectroscopy (Yadav *et al* 2015) are some examples of recently used methods. Non-optical techniques include electrical methods such as Reverse Iontophoresis (Ching *et al* 2010), Microwave Resonators (Gelosi *et al* 2022) and Bioimpedance Spectroscopy (EBIS) (Amaral and Wolf 2007). Electrochemical sensors are based on glucose sensitive and selective enzymes (Chen *et al* 2017, Ghoreishizadeh *et al* 2018).

Methods using optical detection attract considerable attention (Huang, Zhang and Wu 2020), however all these methods have some deficiencies that may limit their sensitivity or estimation accuracy (Tian, Prestgard and Tiwari 2014). Non-optical techniques such as reverse iontophoresis have delayed measurements and can cause skin irritation (Huang, Zhang and Wu 2020). On the other hand, microwave resonators and bioimpedance spectroscopy are promising techniques, but with satisfactory results only in controlled environments (Amaral and Wolf 2007, Gelosi *et al* 2022).

For the use of electrochemical sensors, it has been tried to estimate the level of glucose in tears and sweat (Thulasi *et al* 2017), however a positive correlation with blood glucose has not yet been found.

A careful review of existing non-invasive blood glucose measurement methods shows that no single technique can provide accurate and reliable measurements on a regular basis (Nanayakkara, Munasingha and Ruwanpathirana 2018). Too many existing external dependencies are the cause of most errors. In Carduff et al. (2006), sensor signal quality reduces significantly when changing from a controlled to an uncontrolled environment. Combining several independent techniques results in better accuracy and reliability (Pathirage *et al* 2019). The NIR and EBIS methods are two widely used methods. NIR spectroscopy uses the wavelength frequency range from 700 nm to 2500 nm (Yadav *et al* 2015), with widespread use of 940 nm due to the glucose absorption peak at 939 nm (Yadav *et al* 2014) and of various wavelengths, improving the accuracy (Xiaoli and Chengwei 2015). The EBIS technique is used due to changes in cell membrane capacitance and intracellular fluid resistance caused by the ionic flow caused by the presence of glucose. These changes can be observed by injecting current (1 mA – 10 mA) at medium frequency (1 kHz – 1 MHz), measuring the response and calculating the impedance (Nanayakkara, Munasingha and Ruwanpathirana 2018).

The objective of this work is to develop a wearable prototype device to monitor the level of glucose in the blood using the techniques of near-infrared spectroscopy and electrical bioimpedance. The use of techniques as a tool to measure blood glucose in real time using different wavelengths and frequencies is investigated and then compared to the gold standard.

2. Materials and methods

The device consists of a module that measures the light reflection of three LEDs with different wavelengths (740, 810 and 850 nm) and a module that measures bioimpedance in the frequency range from 0.1 to 100 kHz. It uses 4 electrodes placed on the corner of a square (*a*=35 mm) having 3.2 mm in diameter and made of stainless steel (see Figure 1a). The three LEDs are equally space and the BPX61 photodiode is at the center of the device. Bioimpedance circuit is composed by a Howland current source (ADA4851 in Figure 1b), a voltage meter (AD620 in Figure 1c) and a processor (ATMega2560 from Arduino Mega 2560 kit). The source injects a DIBS (discrete interval binary sequences) current waveform of 1 mApp amplitude.

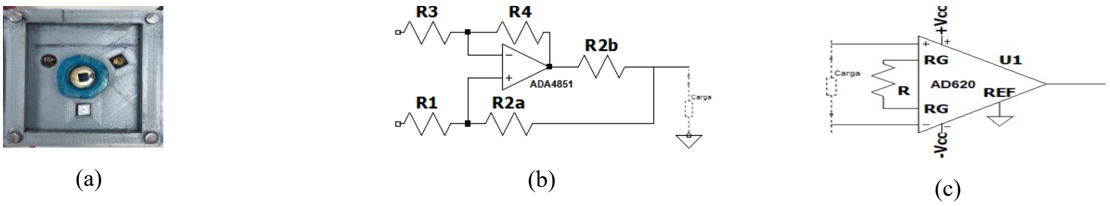

(a) (b) (c)

Figure 1. (a) Apparatus containing the electrodes, LEDs and the BPX61 photodiode; (b) Howland current source by ADA4851; (c) instrumentation amplifier AD620.

Measurements were taken in the back side of the forearm. The skin was sanded to partially remove the stratum corneum and hydrated with a 0.9% sodium chloride solution. The device was then fixed using a Velcro strap and connected by cable to the processor for data collection. Both bioimpedance by the prototype and a commercial impedance spectrometer (HF@S from Zurich instruments), as well as the blood output reading by a digital glucometer (Accu-check guide from Roche), were collected every 15 minutes for 2 hours. In the first measurement (=data at time zero), the volunteer was fasting for 8 hours. After that, the volunteer ingested a 75 grams of glucose and then more 8 data sets were collected.

3. Results and discussions

Figure 2 shows the variation in the glucose level measured by the digital glucometer and the measured LEDs outputs, including the respective linear regressions. The "*p*" correlation value was calculated using Pearson technique, such as: 0.0 stands for "no linear relationship"; 0.5 stands for "moderate linear relationship"; 1.0 stands for "perfect linear relationship".

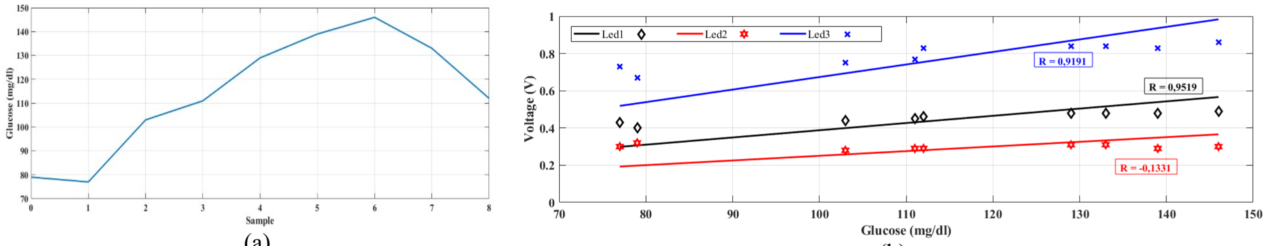

(a) (b)

Figure 2. Blood glucose data from Accu-check (a) and photodiode voltage output, where Led1=810 nm, Led2=740 nm and Led3=850 nm.

It was observed a strong data correlation using the LED of longer wavelength (Led3), as it was found by (Pathirage *et al* 2019) working at 939 nm. In contrast, the correlation of the 740 nm LED with the glucose level was weak. It must be bear in mind that these results may have water interferences. Seems that longer wavelengths may be necessary for increasing accuracy (Xiaoli and Chengwei 2015).

Bioimpedance modulus and phase of both HFI spectrometer and the proposed device were performed in the frequency range from 0.1 to 100 kHz. Table 1 shows eight discrete frequencies which presented the best Person correlation. It can be observed that the correlation is higher at lower frequencies for the impedance modulus. Even though, measurements below 1 kHz might have interferences caused by noise, movement artefacts and skin contact impedance. High frequencies (> 50 kHz) may include limitations from instrumentation processor and amplifiers, causing reading losses, measurement errors and signal deformation. Furthermore, capacitance of the dielectric membrane cause dispersions at higher frequencies (Pradhan, Mitra and Das 2012). On the other hand, impedance phase presented a low correlation, which may imply that this parameter is not useful for prediction for glucose level using non-invasive measurements.

Table 1. Pearson correlation of both prototype and spectrometer to the blood glucose level measured with the Accu-check device. Modulus (|Z|) and phase ($Ø_Z$) of the impedance are used for calculating the correlation.

Frequency (kHz)	**Prototype/Accu-check *p* correlation**		**HF/Accu-check *p* correlation**	
	|Z|	$Ø_Z$	|Z|	$Ø_Z$
1.25	-0.85	-0.28	-0.98	-0.65
2.50	-0.84	-0.59	-0.92	-0.54
3.75	-0.93	-0.24	-0.88	-0.42
5.00	-0.50	-0.46	-0.86	-0.31
7.50	-0.91	-0.62	-0.86	-0.17
37.50	-0.70	-0.51	-0.80	-0.21
50.00	-0.31	-0.45	-0.81	-0.23
75.00	-0.06	-0.43	-0.78	-0.20

Similar results were also found by other researches, as shown in table 2. It must be emphasized that each work used a different frequency range, different electrode setup and impedance measuring hardware. Furthermore, unique measuring systems vary from patient to patient which leads to interferes such as light absorption or tissue dielectric response (Huang, Zhang and Wu 2020).

Table 2. Comparison of correlation

Reference	Amaral and Wolf 2007	Fouad, Mahmoud and Abd El Ghany 2018	Jain, Maddila and Joshi 2019	This work
Technique	EBIS	NIR+EBIS	NIR	NIR+EBIS
Correlation	0,67	0,92	0,91	>0,90+>0,70

4. Conclusion

It can be concluded that the use of multifrequency electrical bioimpedance spectroscopy technology in conjunction with near-infrared spectroscopy can be used as a non-invasive glucose measuring device. Further studies are needed in order to increase the accuracy of this techniques in uncontrolled environments, then decreasing systemic errors for in a daily basis real time device.

Acknowledgments

The authors thank the State University of Santa Catarina (UDESC) and the Research Foundation of Santa Catarina (FAPESC) for the institutional and financial support, respectively.

References

Alberi K and Zimmet P 1998 Definition, diagnosis and classification of diabetes mellitus and its complications, part 1: diagnosis and classification of diabetes mellitus, provisional report *Diabet Med.*, **15**, 539-553.

Fouad M M, Mahmoud D Y and Abd El Ghany M A 2018 Joint NIR-BIS based non-invasive glucose monitoring system *30th International Conference on Microelectronics (ICM)* **2018** 88-91.

Klonoff D C 2007 The benefits of implanted glucose sensors *J. Diabetes Sci. Technol.*, **6**, 797–800.

Cengiz E and Tamborlane W 2009 A tale of two compartments: Interstitial versus blood glucose monitoring *Diabetes technology & therapeutics*, **11**, 11–16.

Harman-Boehm I, Gal A, Raykhman A M, Zahn J D, Naidis E and Mayzel Y 2009 Noninvasive glucose monitoring: a novel approach. *J. Diabetes Sci. Technol.*, **3**, 253–260.

Yadav J, Rani A, Singh V and Murari B 2014 Near-infrared LED based non-invasive blood glucose sensor *International Conference On Signal Processing And Integrated Networks (SPIN)* **2014** 591-594.

Wrobel M S 2016 Non-Invasive blood glucose monitoring with raman spectroscopy: prospects for device miniaturization *IOP Conference Series: Materials Science and Engineering* **104** 1-9.

Malik B and Cot G 2010 Real-time, closed-loop dual-wavelength optical polarimetry for glucose monitoring *J. Biomed. Opt.*, **15**, 1-6.

Yadav J, Rani A, Singh V and Murari B 2015 Prospects and limitations of non- invasive blood glucose monitoring using nearinfrared spectroscopy *Biomedical Signal Processing And Control*, **18**, 214-227.

Ching C, Sun T, Huang S, Shieh H and Chen C 2010 A mediated glucose biosensor incorporated with reverse iontophoresis function for noninvasive glucose monitoring *Annals Of Biomedical Engineering*, **38**, 1548-1555.

Gelosi I E, Avalos Ribas R, Uriz A J, Castiñeira Moreira J and Fuentes N 2022 Design and implementation of a non-invasive RF device to measure glucose in blood *IEEE Latin America Transactions*, **20**, 813–822.

Chen Y *et al*. 2017 Skin-like biosensor system via electrochemical channels for noninvasive blood glucose monitoring *Sci. Adv.*, **3**, 1-7.

Ghoreishizadeh S S, Zhang X, Sharma S and Georgiou P 2018 Study of electrochemical impedance of a continuous glucose monitoring sensor and its correlation with sensor performance *Ieee Sens. Lett.*, **2**, 1-4.

Huang J, Zhang Y and Wu J 2020 Review of non-invasive continuous glucose monitoring based on impedance spectroscopy *Sensors and Actuators A: Physical*, **311**, 103-112.

Tian K, Prestgard M and Tiwari A 2014 A review of recent advances in nonenzymatic glucose sensors *Materials Science and Engineering: C*, **41**, 100-118.

Thulasi A A, Bhatia D, Balsara P T and Prasad S 2017 Portable impedance measurement device for sweat based glucose detection 2017 *IEEE 14th International Conference on Wearable and Implantable Body Sensor Networks (BSN)* **2017** 63-66.

Nanayakkara N, Munasingha S and Ruwanpathirana P 2018 Non-invasive blood glucose monitoring using a hybrid technique *Moratuwa Engineering Research Conference,* **2018**, 7-12.

Caduff A, Dewarrat F, Talary M S, Stalder G, Heinemann L and Feldman Y 2006 Non-invasive glucose monitoring in patients with diabetes: a novel system based on impedance spectroscopy *Biosens Bioelectron.*, **22**, 598-604.

Pathirage K D, Roopasinghe P, Sooriyaarachchi J J, Weththasinghe R and Nanayakkara N D 2019 Removing subject dependencies on Non-Invasive Blood Glucose Measurement using Hybrid Techniques *Annu Int Conf IEEE Eng Med Biol Soc.* **2019** 7197-7200.

Xiaoli L and Chengwei L 2015 Research on glucose concentration sensing with single wavelength laser *IEEE 12th Int. Conf. Electron. Meas. Instruments (ICEMI)*, **3**, 1547–1551.

Pradhan R, Mitra A and Das S 2012 Impedimetric characterization of human blood using three-electrode based ECIS devices *J. Electr. Bioimpedance*, **3**, 12-19.

Amaral C E F and Wolf B 2007 Effects of glucose in blood and skin impedance spectroscopy *Africon* **2007** 1-7.

Jain P, Maddila R and Joshi A M 2019 A precise non-invasive blood glucose measurement system using NIR spectroscopy and Huber's regression model *Opt Quant Electron*, **51**, 1-15.

Proceedings of the International Conference of Bioelectromagnetism, Electrical Bioimpedance,
and Electrical Impedance Tomography June 29 – July 1, 2022 / Kyung Hee University, Seoul, Korea

Total body water in Colombian older adults through bioelectrical impedance analysis

Villada-Gómez Johan Sebastian [1,2], Pineda-Zuluaga Maria Camila [2] and González-Correa Clara Helena [2]
[1]Clinical Department, Universidad de Caldas, Manizales, Colombia
[2]Department of Basic Health Sciences, Research Group on Nutrition, Metabolism
and Food Security, Universidad de Caldas, Manizales, Colombia

Correspondence : González-Correa Clara Helena, e-mail : clara.gonzalez@ucaldas.edu.co

Abstract– Dehydration is the leading fluid disorder among older people. This condition is characterized by a reduction in total body water (TBW). For the estimation of the body's water volumes, bioelectrical impedance analysis has been defined as a good tool. However, it is necessary to have TBW healthy older adults reference values for an adequate assessment of their hydration status and, consequently, to optimize pharmacological and nutritional treatments as well as to implement preventive measures. Then, the present study aimed to estimate TBW by BIA and establish its relationship with gender, age, and body mass index in a population of healthy Colombian older adults. This was a descriptive cross-sectional quantitative study at the relational level. Anthropometric and bioelectrical measurements were evaluated in 147 older adults to estimate their body composition. As it was expected, TBW was higher in men. A relationship was found for % TBW with BMI, total % body fat, and lean mass index. Nevertheless, no relationship was found with age. As a conclusion, it could be said that the findings of this study would approach a first reference of body composition and TBW parameters that allow more precise diagnoses of conditions such as obesity, sarcopenia, and dehydration in healthy adults over 60 years of age with similar characteristics.

Keywords: Total Body Water, Elderly Adults, Bioelectrical Impedance Analysis, Colombia.

1. Introduction

Water is an essential element for the structural, metabolic, transport, and temperature control functions of the human body (Goldberg et al, 2014). Physiological changes and progressive biological deterioration present in aging influence water balance (Benelam y Wyness 2010). This alteration in fluid homeostasis is due to the diminished response of the renal neurohypothalamic-pituitary system. This is responsible for maintaining an adequate volume and composition of intracellular and extracellular fluid, which has an incomplete response to physiological stress, producing alterations in the body water balance and increasing the risk of dehydration (Núñez et al, 2012).

Dehydration is the leading fluid disorder among older people, and there are high rates of dehydration in older people (Botigué et al, 2021). This condition is characterized by a reduction in total body water (TBW) secondary to fluid loss (Begum y Johnson, 2010), lower lean body mass, and a higher percentage of body fat (Serra-Prat, 2019). The degree of dehydration in older adults must be carefully controlled, since failure to identify this risk in this population can cause considerable clinical consequences such as constipation, impaired cognitive functions, falls, orthostatic hypotension, salivary gland dysfunction, poor control of hyperglycemia in diabetes or hyperthermia (Manz, 2007), in addition, to an increase in mortality rates (Gille, 2010).

For the estimation of the body's water volumes, bioelectrical impedance analysis (BIA) has been defined as a good estimator of TBW, as it is a tool capable of identifying the changes caused by physiological degeneration in aging (Aristizábal, 2007). In this way, BIA is a non-invasive, portable, and inexpensive technique to quantitatively estimate body water compartments in healthy individuals and those affected by different pathologies (Quesada et al, 2016). This technique is based on the resistance of the cells to the passage of an alternating electric current. The lean mass contains most of the body's fluids and electrolytes and is, therefore, a good electrical conductor, while fat acts as an insulator (Woodrow et al, 2003).

Despite its great relevance in public health, the prevalence of dehydration due to a decrease in the volume of TBW has not been extensively investigated, especially in the population of healthy older adults living in the community (Stookey et al, 2005). Thus, is necessary to have TBW reference values from healthy older adults to rationally control fluids, optimize pharmacological and nutritional treatments that are normally dissolved and transported in body fluids, and implement preventive measures (Núñez et al, 2012).

It is for the above that the present study aimed to estimate TBW by BIA and establish its relationship with gender, age, and body mass index (BMI) in a population of older adults in Manizales, Colombia.

2. Materials and methods

2.1 Design of the study and subjects

This was a descriptive cross-sectional quantitative study at the relational level, with a sample of 147 older adults who attended the IPS of the University of Caldas. The patients were evaluated between March 2015 and March 2019. Patients older than 60 years, residents of Manizales, non-institutionalized, without known chronic disease, preserved health status and acceptance to voluntarily participate in the study were included.

People with exacerbated illnesses, decompensated mental illnesses, partial or total amputation of a limb, prosthesis, or orthosis, moderate or severe disability, edema, current use of diuretics and inability to move were excluded.

2.2 Measurements

Measurements were made in the morning hours by trained personnel. Patients had to be fasting and with an empty bladder. Body weight and height were measured with the Icob Detecto® brand digital scale with an accuracy of ± 0.1 Kg and the Seca® digital stadiometer with an accuracy of ± 0.1 cm, respectively. The body mass index (BMI) was calculated as body weight/height^2.

Bioelectrical measurements were estimated using Maltron Bio Scan 920-II® at a frequency of 50 kHz. The patients were placed in supine position according to the criteria of the European Society of Clinical Nutrition and Metabolism (Kyle, 2004). The standard tetrapolar technique was used, with the distal current measurement electrodes on the dorsal surfaces of the hand and foot near the metacarpophalangeal and metatarsophalangeal joints and the voltage sensing electrodes on the pisiform prominence of the wrist and between the medial and lateral malleolus of the ankle according to previously standardized protocols (González, 2012). Estimation of total body water was obtained directly from the BIA equipment in liters and percentage.

Patients included in the study were separated by sex (male and female) and age groups (60-69, 70- 79 y ≥80 years). With the BMI results, the participants were categorized as having low weight (<18,5 kg/m^2), normal weight (18,5-24,9 kg/m^2), obesity I (30-34.9 kg/m^2), obesity II (35-40 kg/m^2) and obesity III (≥40 kg/m^2).

2.3 Ethical aspects

The study protocol was evaluated by the ethics committee of the Faculty of Health of the University of Caldas. It was considered low risk and approved. All patients signed an informed consent. In addition, the international guidelines for research with human beings were followed (Declaration of Helsinki).

2.4 Statical Analysis

Qualitative variables were expressed as frequencies and quantitative variables as means with standard deviation. Chi^2 was used to compare frequencies between groups. The Kolmogorov-Smirnov or Shapiro-Wilk tests were used to establish the sample distribution, depending on the data to be analyzed.

Pearson's correlation coefficient (r) or Spearman's correlation coefficient were used to establish the level of relationship of numerical variables according to the sample distribution. Student's t-test or Mann Withney U test were used to compare means between two groups. To compare mean differences between decades, analysis of variance (ANOVA) was used. A post hoc analysis with Dumet's T3 was performed using the variable that showed differences between groups. A significance level of 5% (p= 0.05) was established. SPSS version 25.0 software licensed for the University of Caldas was used.

3. Results

A total of 147 volunteers between 61 and 86 years of age (mean 72.6 years) were evaluated, of whom 70.7 % (n=104) were women. The distribution by decade between 60-69 years (D1), 70-79 years (D2), and 80 years (D3) or more was 24.5 %, 67.3 % and 8.2 %, respectively. 49% (n= 72) of the population had normal weight. BMI as well as fat percentage were higher in women (p= 0.02 and p=0.00 respectively). TBW was higher in men (p= 0.00), however there were no differences in percentage of intracellular water (ICW) and extracellular water (ECW) ratio (ICW/ECW) (p= 0.99 and p= 0.882 respectively), between men and women (Table 1).

A relationship was found for % TBW with BMI (r= -0.713; p= 0.000), total % fat (r= -0.968; p= 0.000) and lean mass index (r= 0.227; p= 0.006) however, no relationship was found with age (p= 0.265). When the TBW was analyzed by decade, there were no differences by age group (p= 0.533), nevertheless, there was evidence of a statistically significant reduction in lean mass with increasing age (D1 (60-69 years): 16.4 kg/m^2; D2 (69-70 years): 15.6 kg/m^2 and D3 (80 years and older): 14.7 kg/m^2) (D1 vs D3 p= 0.001; D2 vs D3 p= 0.035).

Table 1. Body composition and bioelectrical measurements.

Variable	Total n= 147	Female n=104	Male n=43	p***
Age [years]*	72,7 (5,3)	72,1 (5,2)	74,1 (5,3)	0,65
BMI [kg/m^2] *	24,3 (4,3)	24,7 (4,7)	23,2 (3,2)	0,02
Fat mass [%] *#	33,7 (10,1)	37,4 (9,3)	24,6 (5)	0,00
Fat free mass index [kg/m^2] *	15,8 (1,7)	15,1 (1,4)	17,3 (1,5)	0,00
Total body Water [%] *#	49,9 (8,2)	47 (7,5)	57 (4,9)	0,00
Intracellular Water [%] *$	54,7 (1,9)	54,8 (2,1)	54,8 (1,5)	0,99
Low weight [%] **	13 (8,8)	12 (11,5)	1 (2,3)	0,074
Normal weight [%] **	72 (49 %)	42 (40,4)	30 (69,8)	0,001
Overweight [%] **	47 (32 %)	37 (35,6)	10 (23,3)	0,145
Obesity I [%] **	12 (8,2)	10 (9,6)	2 (4,7)	0,317
Obesity II [%] **	3 (2)	3 (2,9)	0	0,26

*Expressed as mean and Standard Deviation, (SD); # Body weight percentage; $ TBW percentage; *** Difference between sex

4. Discussion and conclusion

In this study, the TBW was higher in men than in women (vs ; p= 0,000), this finding can be explained by the lower amount of water in fatty tissue (10%) compared to lean mass (70-75%) (Lorenzo et al, 2019) and the difference in body composition between genders, where women have a greater amount of adipose tissue (Nuñez et al, 2012 & Malczyk et al, 2016) with less lean mass (Villada- Gómez et al, 2018). An interesting finding was the absence of statistically significant differences in the TBW when grouping the patients by decades of age (p=0,533). However, a reduction in lean mass index was found with increasing age (D1 (60-69 years): 16,4 kg/m^2; D2 (69-70 years): 15,6 kg/m^2 and, D3 (80 years and older: 14,7 kg/m^2), statistically significant (D1 Vs. D3 p= 0,001; D2 Vs. D3 p= 0,035). This is consistent with what has been reported in previous body composition studies that show how after 30 years of age, lean mass decreases, while fat mass increases, reaching a maximum at 60-70 years, the age from which begins to lose both lean mass and fat (Amarya et al, 2014). The lack of statistical significance in the TBW values could be associated with the small sample of people over 80 years of age, which reduces the statistical power to find statistically significant differences.

The inversely proportional relationship between BMI and TBW (r= -0.713; p= 0.000) is a relevant finding and provides evidence regarding the poor performance of BMI for diagnosing obesity in the elderly, due to the changes of aging that affect height (BMI denominator) (Nuñez et al, 2012) and lack of discrimination between lean and fat mass with BMI (Movsesyan, 2003). If there is loss of lean mass with gain of fat mass (change in body composition with aging), TBW decreases and BMI remains stable or tends to increase, causing total adiposity to be underestimated (Kalish, 2016). Likewise, the inverse relationship between TBW and fat mass (r= -0.968; p= 0.000), is explained by changes with age between lean and fat mass, since lean mass contains a high content of TBW (Bossingham et al, 2005).

No significant differences were found between the proportion of ICW and in the relationship between ICW/ECW, which does not agree with what has been reported by some authors, who propose that the hydration of lean mass remains relatively constant throughout life (Ritz, 2000). Although it has been said that an increase in the ICW/ECW ratio could be a marker of muscle aging (Serra-Prat et al, 2019; Taniguchi et al, 2021 & Yamada et al, 2017), the absence of differences between genders in the analyzed population could be associated with the fact that it is a healthy and functional non-sarcopenic population. and it was not compared with a population under 60 years of age or with osteoarticular pathology.

One limitation of the study has to do with the low number of patients over 80 years of age and the cross-sectional nature of the study, which does not allow associations with adverse outcomes. Its strength lies in being (to our knowledge) the first study to assess body composition in healthy people over 60 years of age in Colombia through BIA. In addition, the first study that evaluates its association with obesity and anthropometric parameters such as BMI.

In conclusion, in the investigated subjects, higher TBW was found in men than in women, in addition to finding a significant association between it and BMI, % total fat and lean mass index. This study could serve to establish parameters of body composition and TBW allowing more precise diagnoses of conditions such as obesity and sarcopenia in healthy adults over 60 years of age.

References

Amarya S, Singh K and Sabharwal M 2014 Health consequences of obesity in the elderly *J Clin Gerontol Geriatr* **5** 63–7

Aristizábal J C, Restrepo M T and Estrada A 2007 Evaluación de la composición corporal de adultos sanos por antropometría e impedancia bioeléctrica *Biomédica* **27** 216-24

Benelam B and Wyness L 2010 Hydration and health: a review *Nutrition Bulletin* **35** 3-25

Begum M N and Johnson C S 2010 A review of the literature on dehydration in the institutionalized elderly *e-SPEN* **5** e47-e53

Gille D 2010 Overview of the physiological changes and optimal diet in the golden age generation over 50 *EURAPA* **7** 27-36

Goldberg L R et al 2014 Hydration in older adults: The contribution of bioelectrical impedance analysis *Int J Speech Lang Pathol* **16** 273–8

González-Correa C H and Caicedo-Eraso J C 2012 Bioelectrical impedance analysis (BIA): A proposal for standardization of the classical method in adults. *J Phys Conf Ser*. 407 012018

Kyle U G et al 2004 Bioelectrical impedance analysis—part I: review of principles and methods *Clin Nutr* **23** 1226-43

Lorenzo I, Serra-Prat M and Yébenes J C 2019 The role of water homeostasis in muscle function and frailty: A review *Nutrients* **11** 1–15

Malczyk E, DzięGielewska-Gęsiak S, Fatyga E, Ziółko E, Kokot T and Muc-Wierzgoń M 2016 Body composition in healthy older persons: Role of the ratio of extracellular/total body water *J Biol Regul Homeost Agents* **30** 767–72

Manz F 2007 Hydration, and disease *J Am Coll Nutr* **26** 535S-41S

Movsesyan L, Tankó L B, Larsen P J, Christiansen C and Svendsen O L 2003 Variations in percentage of body fat within different BMI groups in young, middle-aged, and old women *Clin Physiol Funct Imaging* **23** 130–3

Núñez B, Rodríguez R Lara L A and Morales L R 2012 Estimación del agua corporal en adultos mayores que asistían a casas de abuelos en Santiago de Cuba *Panorama Cuba y Salud* **7** 2-8

Serra-Prat M, Lorenzo I, Palomera E, Ramírez S and Yébenes J C 2019 total body water and intracellular water relationships with muscle strength, frailty and functional performance in an elderly population *J Nutr Health Aging* **23** 96-101

Taniguchi M et al 2021 Enhanced echo intensity and a higher extracellular water-to-intracellular water ratio are helpful clinical signs for detecting muscle degeneration in patients with knee osteoarthritis *Clin Rheumatol* **40** 4207–15

Botigué T, Miranda J, Escobar-Bravo M A, Lavedán A, Roca J and Masot O 2021 Análisis de la deshidratación de adultos mayores en una residencia geriátrica de España: prevalencia y factores asociados *Nutr Hosp* **38** 252-59

Quesada-Leyva L, León-Ramentol CC, Betancourt-Bethencourt J and Nicolau-Pestana E 2016 Theoretical and practical facts about health electric bioimpedance *Rev Arch Médico* **20** 565–78

Stookey J D 2005 High prevalence of plasma hypertonicity among community-dwelling older adults: results from NHANES III *J Am Diet Assoc* **105** 1231-9

Villada-Gómez J S, González-Correa C H and Marulanda-Mejía F 2018 Puntos de corte provisionales para el diagnóstico de sarcopenia en ancianos de Caldas, Colombia *Biomedica* **38** 521–6

Woodrow G, Oldroyd B, Wright A, Coward W and Truscott J 2003 Comparison of anthropometric equations for estimation of total body *Nephrol Dial Transplant* **18** 384-89

Yamada Y et al 2017 The extracellular to intracellular water ratio in upper legs is negatively associated with skeletal muscle strength and gait speed in older people J Gerontol A Biol Sci Med Sci **72** 293–8

Proceedings of the International Conference of Bioelectromagnetism, Electrical Bioimpedance,
and Electrical Impedance Tomography June 29 – July 1, 2022 / Kyung Hee University, Seoul, Korea

Skin impedance in a sensor-sock for diabetic foot assessment

Christian Tronstad[1], Maryam Amini[1], Eline Olesen[2], Oliver Pabst[2], Tormod Martinsen[1], Sisay M. Abie[3], Ørjan G. Martinsen[2,1], Håvard Kalvøy[1], Jonny Hisdal[4,5], Trond G. Jenssen[6,5], Elisabeth Qvigstad[7,5]
[1]Department of Clinical and Biomedical Engineering, Oslo University Hospital, Oslo, Norway
[2]Department of Physics, University of Oslo, Oslo, Norway
[3]Faculty of Ecology and Natural Resource Management, Norwegian University of Life Sciences, Ås, Norway
[4]Department of Vascular Surgery, Oslo University Hospital, Oslo, Norway
[5]Institute of Clinical Medicine, University of Oslo, Oslo, Norway
[6]Department of Transplantation Medicine, Oslo University Hospital, Oslo, Norway
[7]Department of Endocrinology, Morbid Obesity and Preventive Medicine, Oslo University Hospital, Oslo, Norway

Correspondence : Christian Tronstad, e-mail : christian.tronstad@gmail.com

Abstract– Diabetic peripheral neuropathy (DPN) leads to several changes in the skin, and some of these may influence the skin impedance spectrum. In the present study we have developed a prototype solution for skin impedance spectroscopy at selected skin sites (big toe pulp, heel and toe ball) that was tested in a pilot study on five patients with DPN and five healthy controls. At the big toe, most of the controls had markedly lower impedance than the DPN group, especially in the range of 1-100 kHz. The separation between the groups seemed to be weaker at the heel and weakest at the toeball. The results may indicate that monitoring of the skin impedance spectrum may be a method for detection of skin changes associated with DPN, encouraging further studies with the big toe sensor in particular.

Keywords: Skin impedance, diabetes, diabetic foot, neuropathy

1 Introduction

Diabetic foot syndrome is an important cutaneous manifestation occurring in 15-25% of diabetic patients, in which diabetic peripheral neuropathy (DPN) and angiopathy play crucial roles in its development [Behm et al. 2012]. Diabetic peripheral neuropathy (DPN) is the most common acquired neuropathy and one of the main complications of diabetes due to high prevalence, hospitalizations, morbidities and mortalities [Fateh et al. 2016]. An early and accurate diagnosis is essential to reduce risk of complications [Yang et al. 2020, Yorek et al. 2018], but can be challenging given that almost half of DPNs are symptom-free [Pop-Busui al 2016]. A wide variety of screening tools are available for DPN [Brown et al. 2017, Bönhof et al. 2019], that test different properties related to nerve function such as nerve conduction, sensation to vibration and sudomotor function. There are also changes occurring in the skin that for some may even precede the diagnosis of diabetes [Bristow et al. 2008]. Long-standing diabetes may impair skin homeostasis resulting in skin manifestations in at least one third of all diabetics [Behm et al. 2012]. Bioimpedance is a non-invasive method for measuring the passive electrical properties of tissue and has been studied for several applications in dermatology such as skin cancer identification [Åberg et al. 2004], skin hydration [Morin et al. 2020] and transdermal drug delivery [Arpaia et al. 2017]. With respect to the diabetic foot and DPN there are several known skin changes that in theory may influence the skin impedance such as: dry skin, thinning of the epidermis, cracked skin and development of calluses. Dryness of skin is common in the diabetic foot, where autonomic neuropathy is considered a significant cause for anhidrosis, predisposing individuals to fissuring and cracking of the epidermis, which in turn can lead to secondary infections [Bristow et al. 2008]. The thickness of the epidermal layer of plantar skin has been found to be decreased in people with diabetic foot ulceration and neuropathy [Chao et at 2011]. Abnormal pressure on the foot may increase keratinization of skin cells developing into a callus, which predisposes to foot ulceration [Arosi et al. 2016]. In this paper, we present an early prototype for skin impedance measurement in a sensor-sock and data from the first tests in a pilot study on participants with DPN without ulcers and healthy controls. In addition to comparing skin impedance spectra between the two groups, we also aimed to compare the suitability of different skin sites.

2 Methods

2.1 Skin impedance electrode

A previous study compared different variants of three types of electrode geometries (concentric ring electrodes, row electrodes, interdigitated array electrodes and unipolar electrodes) with respect to sensitivity and repeatability of plantar skin impedance measurement, and found a bipolar ring electrode (as shown in figure 1) to be the best suited candidate for this purpose [Olesen 2020]. The small gap between the inner and outer electrodes (0.5mm) maintains focus of the impedance measurement to the skin (mainly the epidermis) up to high frequencies, and the circular design may average out anisotropic effects thus providing better repeatability of measurements.

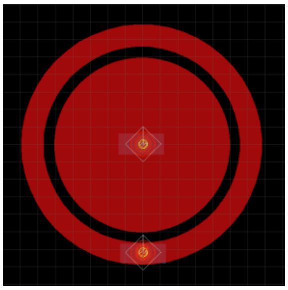

Figure 1. Screenshot from Eagle CAD design showing the electrode geometry (each grid unit is 1mm).

The electrode was drawn in Eagle (Autodesk Inc, CA, USA) and fabricated by printing of silver ink (Voltera Inc, ON, Canada) on FR4 boards using a Voltera V-One PCB printer (Voltera Inc, Canada) followed by curing and polishing of the surface. Electrode leads were soldered to via connectors at the backside of the PCB and sealed by epoxy.

2.2 Sensor sock prototype

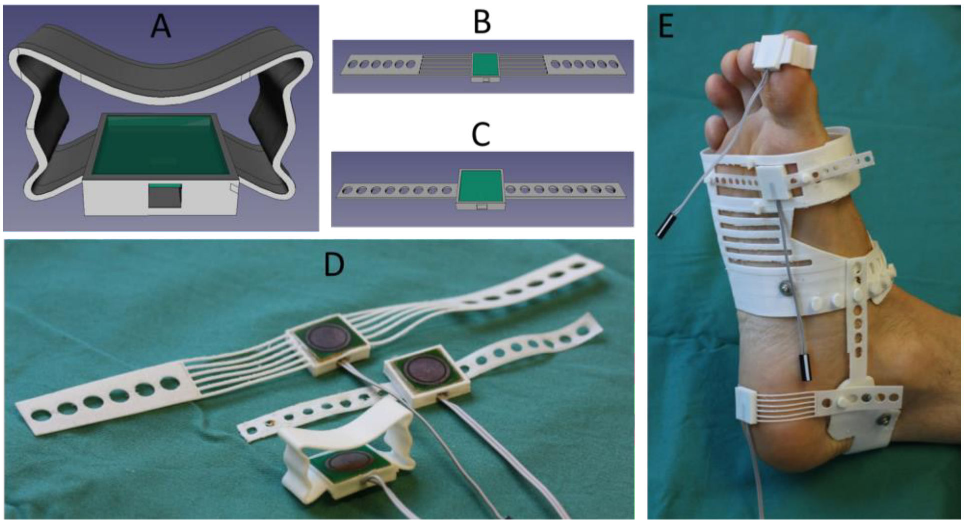

Figure 2. CAD design of sensor parts for skin impedance measurement at the big toe (A), toeball (B) and heel (C). The 3D printed parts for sensor housing are shown in D, and all parts connected to the foot are shown in E. s

The housing parts for attachment to different skin sites (big toe, toe ball and heel) shown in figure 2 A-C were designed in FreeCAD and 3D printed with a soft and elastic plastic material (thermoplastic polyurethane) with a Shore hardness of 85A (Ninjaflex, Ninjatek, PA, USA). The geometry and softness of the materials were selected in order to provide a gentle pressure on the skin with minimal variation between different feet. While the toe part (electrode + housing) could be attached separately around the toe, the toe ball and heel parts were made to be connected to a soft plastic sock with straps (figure 2 D) for soft but stable contact to the skin. The sock was also designed in FreeCAD and 3D printed with a soft and elastic plastic material using thermoplastic polyurethane with a Shore hardness of 95A (Cheetah, Ninjatek. PA, USA). With this prototype, we could measure the skin impedance spectra at these selected skin sites with stable contact for different foot sizes and shapes.

2.3 Pilot study

A pilot study was done at the Diabetes Laboratory, Oslo University Hospital, Aker, Norway. Five patients, diagnosed with DPN (4♂/1♀) but without ulcers and five healthy age-matched controls (2♂/3♀) were recruited for the study. The age distributions of the DPN group and the control group were 64.0±14.4 and 60.6±11.1 respectively. The study was approved by the regional ethics committee (REK#152845), and the appointed committee at Oslo University Hospital evaluated and approved the measurement setup in accordance to Annex VIII, to be applicable with the European Medical Devices Directive— 93/42/EEC with 2007/47/EC. Glycosylated haemoglobin (HbA1c), currently the main diagnostic test for diabetes, was initially measured in order to exclude potentially undiagnosed diabetes among the control participants. This was followed by the monofilament test [Dros et al. 2009] done by an experienced diabetes nurse at the laboratory. The right foot of the participant was then measured using selected non-invasive sensors including the presented skin impedance measurement. The skin impedance measurement was done immediately after electrode attachment – first at the toe pulp, then at the toe ball and finally at the heel. The skin was cleaned with an alcohol-based sanitizer just over an hour prior to the impedance measurement. During measurements, participants relaxed in a comfortable chair with legs resting horizontally on a foot rest, and were free to chat. This was part of a study using different types of non-invasive methods to assess DPN. Skin impedance frequency sweeps from 10 Hz to 5 MHz was done using a Zurich Instruments MFIA (Zurich Instruments AG, Switzerland) connected to the electrodes with a two-electrode configuration. Shielded cables with a length of 1.4m were used between the MFIA device and the sock. The electrodes were cleaned with peracetic acid, water and ethanol between each participant.

3. Results

Figure 4 summarizes the skin impedance spectra for all skin sites for both groups of participants, represented as the impedance modulus, resistance and reactance.

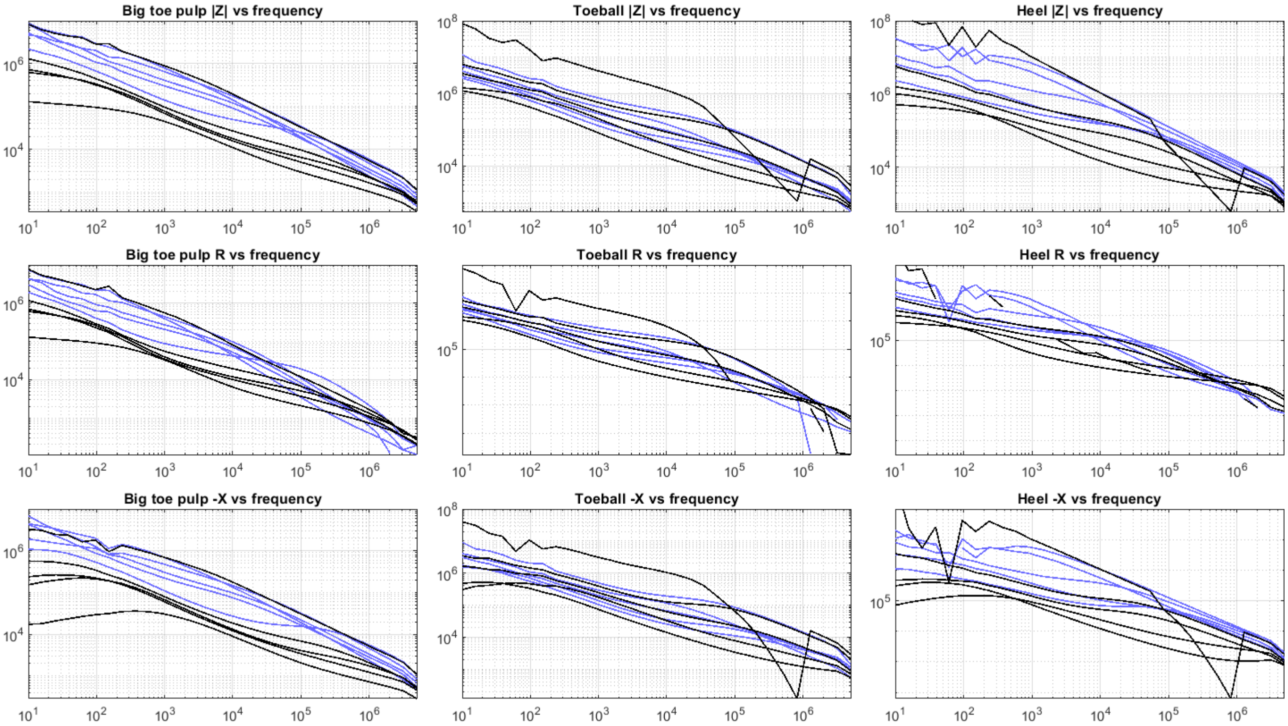

Figure 4. Impedance spectra presented as the impedance modulus (|Z|), resistance (R) and reactance (X) for all participants from the control (black) and DPN group (blue). The bumpy curves with the highest impedance in the toeball and heel plots curves are affected by measurement error due to the high impedance levels and do not represent a true frequency-dependency of the skin impedance.

4. Discussion

In most of the cases, the skin impedance spectra from the big toe and the heel were markedly different between the groups, while at the toeball, the distribution in skin impedance had a large overlap. The strongest separation between the groups was seen for the mid-range frequencies (10^3-10^5 Hz) at the big toe skin site. For the big toe pulp measurement, all but one control subject had a lower skin impedance over all frequencies compared to the DPN group. Due to the limitation of this pilot study, we cannot say for certain whether this one case was due to different skin properties or a technical cause such as electrode contact. In some cases, the skin impedance was reaching the GOhm range for the lowest frequencies, which was higher than expected from preliminary testing before the study. The differences between the groups are most likely mainly caused by decreased humidity of the plantar skin in the DPN group, which is a known effect of DPN [Nikoleishvili et al 2006]. For skin impedance measurement using dry electrodes, it is essential to maintain a soft but stable contact with the skin in order to reduce errors from pressure variations or poor electrical contact. In this study, we considered a measurement directly after electrode attachment to provide the most inert skin impedance measurement (without the electrode effects) compared to measuring some time after electrode attachment or after the electrode effects have completely stabilized. We do not know whether a measurement before or after electrode stabilization would provide the best measurement with respect to diabetic foot skin assessment, but a quick test (not requiring much time for stabilization) is desired with a clinical application in mind. One measurement (10 Hz to 5 MHz impedance sweep) takes just a few seconds to complete, and electrode effects during the measurement after electrode attachment would be small. We also gathered the following experiences from the pilot study: 1. Impedance levels of dry plantar skin could be much higher than anticipated based on preliminary testing of the electrode. 2. The geometry of the toe ball made it more difficult to position the electrode at a distinct place, compared to the big toe and heel skin sites. 3. The sock was not uncomfortable for any of the participants. It would have been of interest to also include lower frequencies than 10 Hz in the measurement in order to provide more information and possibly cover the alpha dispersion in the frequency spectrum. However, lower frequencies demand relatively high measurement time during which electrode effects may occur. At this point based on the results from this small study, it is yet unclear whether skin impedance spectroscopy may be useful in DPN detection, DPN grading in the skin, or ulceration risk estimation compared to other simple tests. However, the results from the present study indicate a potential to detect relevant skin changes associated with DPN, and with methodological improvements, the toe sensor in particular can be included in further studies. The toe site may also be the most relevant site to detect early changes, as DPN is known to begin distally and progress proximally [Dobretsov et al. 2007, Iqbal et al. 2018]. In a larger study, this sensor can be compared with the performance of other sensors and tests, and the potential of sensor combinations for improved DPN assessment can be evaluated. If this measurement is found to be clinically useful, the system can be further developed with miniaturized impedance spectroscopy electronics integrated in the sock, with a semi-automated analysis and wireless transfer of test results.

5. Conclusions

We present a prototype solution for impedance spectroscopy in diabetic foot assessment and early results comparing people with DPN and healthy controls. These early results indicate a potential to detect relevant skin changes associated with DPN, encouraging further studies with the big toe sensor in particular.

References

Arpaia, P, Cesaro, U, Moccaldi, N. Noninvasive measurement of transdermal drug delivery by impedance spectroscopy. Sci Rep 7, 44647 (2017). https://doi.org/10.1038/srep44647

Arosi I, Hiner G, Rajbhandari S. Pathogenesis and Treatment of Callus in the Diabetic Foot. Curr Diabetes Rev. 2016;12(3):179-83. doi: 10.2174/1573399811666150609160219.

Behm B, Schreml S, Landthaler M, Babilas P. Skin signs in diabetes mellitus. J Eur Acad Dermatol Venereol. 2012 Oct;26(10):1203-11. doi: 10.1111/j.1468-3083.2012.04475.x.

Bönhof GJ, Herder C, Strom A, Papanas N, Roden M, Ziegler D, Emerging Biomarkers, Tools, and Treatments for Diabetic Polyneuropathy, Endocrine Reviews, 2019, 40:153–192, https://doi.org/10.1210/er.2018-00107

Bristow I Non-ulcerative skin pathologies of the diabetic foot. Diabetes Metabolism Research and Reviews 2008, 24: 84-89

Brown JJ, Pribesh SL, Baskette KG, Vinik AI, Colberg SR, A Comparison of Screening Tools for the Early Detection of Peripheral Neuropathy in Adults with and without Type 2 Diabetes, Journal of Diabetes Research, vol. 2017, Article ID 1467213, 11 pages, 2017.

Chao CY, Zheng YP, Cheing GL. Epidermal thickness and biomechanical properties of plantar tissues in diabetic foot. Ultrasound Med Biol. 2011 Jul;37(7):1029-38. doi: 10.1016/j.ultrasmedbio.2011.04.004. Epub 2011 Jun 2.

Dobretsov M, Romanovsky D, Stimers JR. Early diabetic neuropathy: triggers and mechanisms. World J Gastroenterol. 2007;13(2):175-191

Dros J, Wewerinke A, Bindels PJ, van Weert HC. Accuracy of monofilament testing to diagnose peripheral neuropathy: a systematic review. Ann Fam Med. 2009;7(6):555-558. doi:10.1370/afm.1016

Fateh, HR, Madani, SP, Heshmat, R, Larijani B. Correlation of Michigan neuropathy screening instrument, United Kingdom screening test and electrodiagnosis for early detection of diabetic peripheral neuropathy. J Diabetes Metab Disord 15, 8 (2015). https://doi.org/10.1186/s40200-016-0229-7

Iqbal Z, Azmi S, Yadav R, Ferdousi M, Kumar M, Cuthbertson DJ, Lim J, Malik RA, Alam U. Diabetic Peripheral Neuropathy: Epidemiology, Diagnosis, and Pharmacotherapy. Clin Ther. 2018 Jun;40(6):828-849.

Morin, M., Ruzgas, T., Svedenhag, P. et al. Skin hydration dynamics investigated by electrical impedance techniques in vivo and in vitro. Sci Rep 10, 17218 (2020). https://doi.org/10.1038/s41598-020-73684-y

Nikoleishvili LR, Kurashvili RB, Virsaladze DK, Khachapuridze NG, Kurashvili LR. Characteristic changes of skin and its accessories in type 2 diabetes mellitus. Georgian Med News. 2006 Feb;(131):43-6. Russian.

Olesen E Development and Assessment of Electrodes and Instrumentation for Plantar Skin Impedance Measurements. Master Thesis 2020. http://urn.nb.no/URN:NBN:no-87615

Pop-Busui R, Boulton AJM, Feldman EL, Bril V, Freeman R, Malik RA, Sosenko JM, Ziegler D; Diabetic Neuropathy: A Position Statement by the American Diabetes Association. Diabetes Care 1 January 2017; 40 (1): 136–154. https://doi.org/10.2337/dc16-2042

Yang H, Sloan G, Ye Y, Wang S, Duan B, Tesfaye S, Gao L. New Perspective in Diabetic Neuropathy: From the Periphery to the Brain, a Call for Early Detection, and Precision Medicine. Front Endocrinol (Lausanne). 2020 Jan 17;10:929

Yorek M, Malik RA, Calcutt NA, Vinik A, Yagihashi S, Diabetic Neuropathy: New Insights to Early Diagnosis and Treatments, Journal of Diabetes Research, vol. 2018, Article ID 5378439, 3 pages, 2018. https://doi.org/10.1155/2018/5378439

Åberg P, Nicander I, Hansson J, Geladi P, Holmgren U and Ollmar S, Skin cancer identification using multifrequency electrical impedance-a potential screening tool. IEEE Transactions on Biomedical Engineering, vol. 51, no. 12, pp. 2097-2102, Dec. 2004, doi: 10.1109/TBME.2004.836523.

Proceedings of the International Conference of Bioelectromagnetism, Electrical Bioimpedance,
and Electrical Impedance Tomography June 29 – July 1, 2022 / Kyung Hee University, Seoul, Korea

The influence of isometric and isotonic muscle contraction on measured resistance and reactance during seated leg curls

Alfred Hülkenberg[a], Steffen Leonhardt[a], Chuong Ngo[a]
aChair for Medical Information Technology, RWTH Aachen University, Aachen, Germany

Correspondence : Alfred Hülkenberg, Chair for Medical Information Technology, RWTH Aachen University
e-mail : huelkenberg@hia.rwth-aachen.de Postal address : Pauwelsstr. 20, 52074 Aachen, Germany

Abstract:
Electrical Impedance Myography (EIM) is a painless and non-invasive approach for quantitative assessment of muscle-condition of the limbs, which is based on consideration of dielectric tissue properties. The purpose of this work is to analyse the impact of isometric (constant muscle length) and isotonic (constant muscle force) contraction on the respective frequency dependent resistance and reactance. Here while measuring the activity of the rectus femoris muscle under assumption of seated leg curls as target movement. It has been found that in *Bioimpedance Spectroscopy* (BIS) of such movements, the resistance mainly varies due to changes in angle and, thus, muscle length. Besides, reactance mainly dependents on the amount of effort or contraction required to lift a weight. A possible explanation for such is the concept of the *electromotive chain*, depicted here as the origin of physiological and morphological variations resulting from the muscle's contraction mechanism.

Keywords: Electrical Impedance Myography (EIM); muscle contraction; seated leg curls; electromotive chain

1 Introduction

Electrical Impedance Myography (EIM) is a non-invasive approach for assessment of muscle condition, based on the four electrode approach aligned over a specific muscle (sub-)group of interest [Sanchez et al., 2016]. Its specific *bioimpedance* $\underline{Z}(j\omega)$ is either determined as the quotient of *voltage* $\underline{u}(j\omega)$ and *current* $\underline{i}(j\omega)$, the sum of *resistance* R and complex *reactance* X, or as product of *magnitude* $\Omega(\omega)$ and a complex exponential function with *phase shift* $\Theta(\omega)$ as its argument

$$\underline{Z}(j\omega) = \underline{u}(j\omega) \div \underline{i}(j\omega) = R + jX = \Omega(\omega) \cdot e^{-j\Theta(\omega)} \,. \tag{1}$$

An interesting question is the contribution of physiological and morphological variations during muscle activity to these values. For the biceps muscle of the upper limbs Li et al., 2016, analyzed the impact of isometric contraction and Freeborn and Fu, 2018 effects of fatigue. Besides, for the lower limbs Shiffman et al., 2003 considered isometric contraction and Ngo et al., 2022 motions as weight lifting and sit-to-stand test. During this article, we analyzed the influence of isometric and isotonic contraction of the rectus femoris muscle onto the measured resistance and reactance values of a *Bioimpedance Spectroscopy* (BIS) trail. As target movement, we selected seated leg curl (rotation of the lower leg along the knee joint).

2 Methods

From physiology, it is known that an extension of the leg during a curl is performed by the quadriceps femoris muscle, subdivided into rectus femoris, vastus lateralis, vastus medialis and vastus intermedius [see Marieb et al., 2019, tab. 11.14]. During such, the muscle may vary its length to reach a *rotation angle* α and builds up a *torque* Γ by contraction to lift a *weight* we as shown in Figure 1a. In order to distinguish these effects and their impact on bioimpedance we developed a fitting electrode placement and a suitable mechanical test-bench.

2.1 Measuring device and electrode placement

All measurements of bioimpedance were performed using near-current electrode placement along the musculus rectus femoris. This setting provides effective control of directional current flow and precise measurements relative to muscle fibre direction, but is also sensitive to the condition of skin-fat layer [Jafarpoor et al., 2013; Rutkove et al., 2008]. The impact of the latter has been reduced by selecting an equidistant *inter-electrode distance* δ of 3 cm. The middle point of the electrode array was selected according to the SENIAM recommendation for *Electromyogram* (EMG) measurements, defined as half the distance between the spina iliaca anterior superior and the upper line of the patella [SENIAM, 2020, sensor array was selected according to the SENIAM recommendation for *Electromyogram* (EMG) measurements, defined as half the distance between the spina iliaca anterior superior and the upper line of the patella [SENIAM, 2020, sensor locations]. Note that the current application has been performed using the electrode pair IH-IL and voltage measurement by the pair VH-VL. For illustration of the applied electrode placement, see Figure 1b.

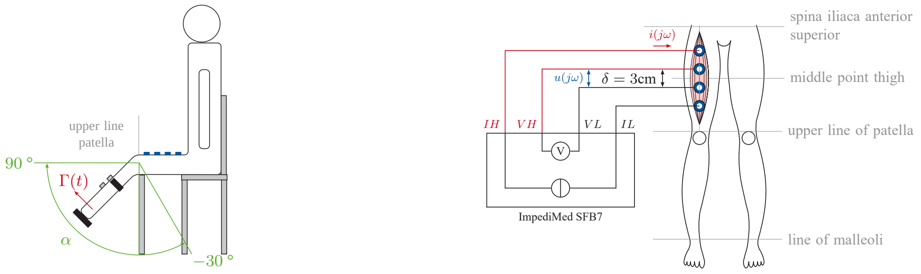

(a) Performed leg curl by angle α

(b) Near current electrode placement

Figure 1: Performed movement and applied electrode placement to measure Bioimpedance of the rectus femoris muscle.

During BIS we applied a SFB7 research device (ImpediMed Inc., Carlsbad, United States of America) operating at a current of $i_{RMS} = 200\ \mu$A and in a frequency range of 3 kHz $\leq f \leq 1$ MHz. Besides, due to their superior adherence and durability, electrodes applied in *Functional electrical stimulation* (FES) have been used. During this attempt circular electrodes with a diameter of 25 mm (ECM25, TensCare LTD, Epsom, United Kingdom) and prior to the placement a contact and cleaning spray (20083, axion GmbH, Leonberg, Germany) has been used to improve their contact to the skin.

2.2 Development of a test-bench to monitor the lower extremities

To capture the *rotation angle* α and the applied *torque* Γ shown in Figure 1a a test-bench similar to the leg curl exercise was constructed, see Figure 2a. The foot-attachment (2) enables a feasible fixation of the lower leg using belts (1) in order to minimize interference of other muscle groups, for instance due to a rotation of the leg. To modify the required effort during lifting, the movement can be done using different counterweights attached to a lever arm (4). As reference signals the test-bench enables monitoring of α using an angle encoder (MHAD 50-HDmag, Baumer GmbH, Friedberg, Germany) and -200 Nm $\leq \Gamma \leq 200$ Nm using a rotating torque sensor (DR-2477-p, Lorenz Messtechnik GmbH, Alfdorf, Germany).

To analyse the process of force development during a movement, it is fitting to distinguish different kinds of muscle contractions, as depicted in [Silbernagl et al., 2007, tab. 2.14]. Firstly, isometric contraction with a constant *muscle length* l_{mu} and varying *muscle force* F_{mu}, approximated by lifting the leg up to a certain angle α_i and fixation at this position. During this state, the subject was asked to relax his or her leg, see Figure 2b. Secondly, isotonic contraction implying a constant F_{mu} and varying l_{mu} during activity is performed by pressing against a foam padding to lift a counter-weight from a stopping-position to a minimal deflection $\alpha_m \approx 5°$. During this state, the subject was asked to keep the angle as constant as possible, see Figure 2c. Accordingly, the condition of passive lifting represents minimal muscle contraction and the weight exposure a minimal variation in muscle length. It was assumed that a motion kept within these stats establishes a stationary condition for the muscle, here captured by ten successive applications of BIS.

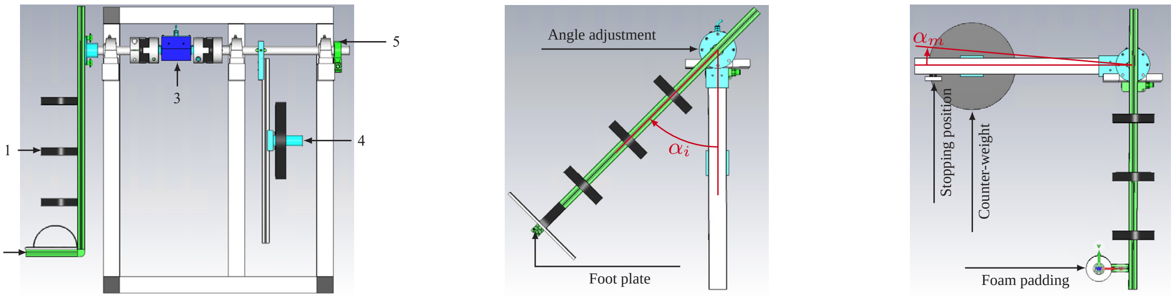

(a) Test-bench

(b) Passive lifting (minimal contraction)

(c) Weight exposure (min. length variation)

Figure 2: Applied testing bench (a) and foot-attachments to perform passive lifting (b) and weight exposure (c). Nomenclature: 1 fixation belt, 2.foot attachment 3. torque sensor 4. counterweight 5. angle sensor

3 Results

In case of passive lifting, a variation of the rotation angle was considered in-between the range of $-30° \leq \alpha_i \leq 89°$, see Figure 3. Interestingly, *resistance* R decreases with an increase in α_i forming decidable clusters over the measured frequency range. Contrary, *reactance* X increases with α_i, probably resulting from an increase in the acting weight force of the combined foot attachment and leg. Nevertheless, the clustering is not as clear as in the case of R and is not systematic over the whole frequency range.

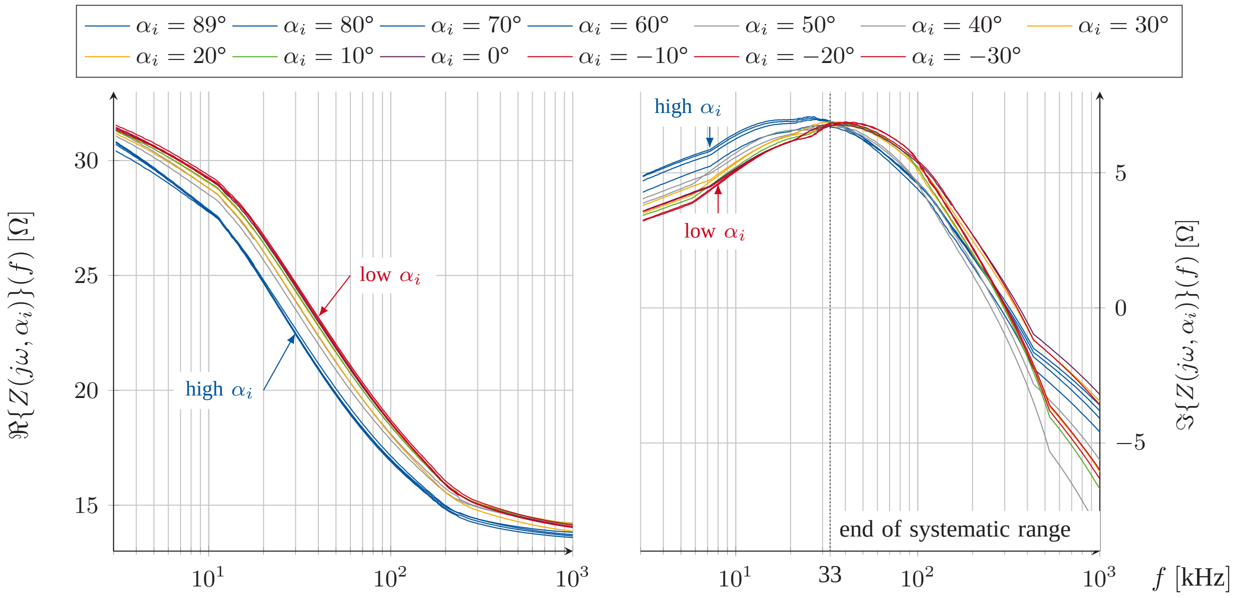

Figure 3: Bioimpedance measured under the condition of passive lifting. Note the connection between angle α_i and resistance R and reactance X and weight force. The respective torque has been observed as decreasing due to a loss in weight force $\Gamma \in (-43, -38, -31, -32, -26, -20, -18, -12, -3, +5, +12, +27, +30)$ Nm.

In case of weight exposure, a variation of the applied counter-weight was performed in-between the range of $0 \text{ kg} \leq we \leq 15$ kg, see Figure 4. Here, R mainly remains constant staying within the range similar to the reference position of $\alpha = 0°$, starting from a frequency of $f \geq 12$ kHz. Besides, reactance X increases with application of additional weight. However, a clear separation is only observable up to a frequency of $f \leq 50$kHz.

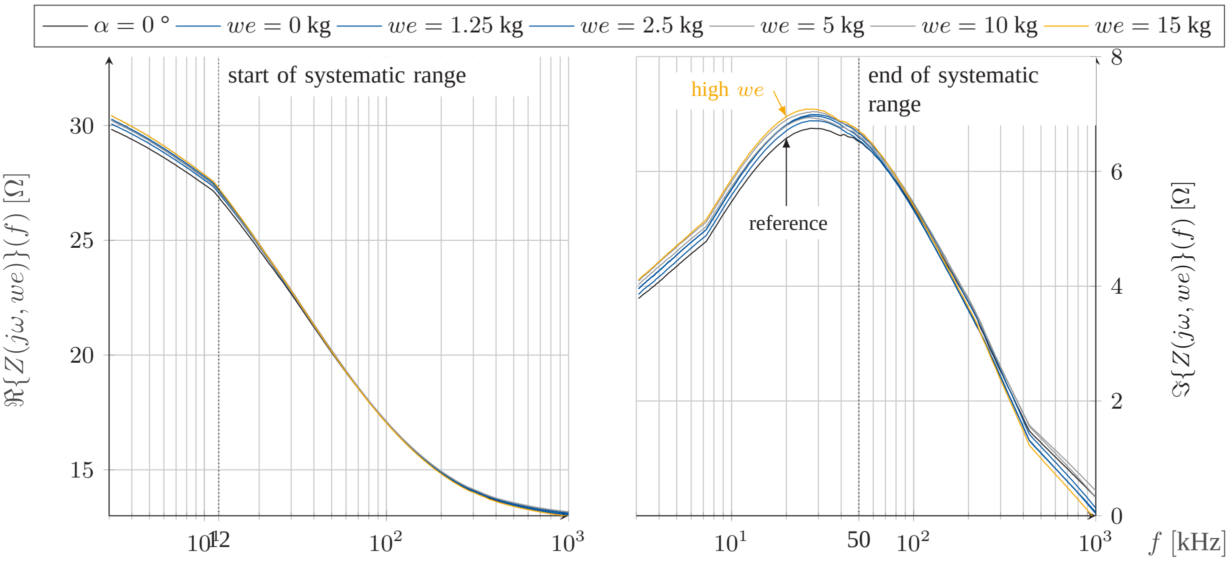

Figure 4: Bioimpedance measured under the condition of weight exposure. Note that resistance R remains nearly constant after $f = 12$ kHz and reactance X increases with the applied counterweight we.

4 Discussion

From the electrical point of view, this process of muscle contraction can be assigned to two general mechanisms, establishing the process of the so-called *electromotive chain*. Firstly, the *physiological process* of impulse conduction transmits a command of contraction from the motor cortex to the targeted muscle using the nervous system, basically by triggering action impulses due to the application of sodium and potassium pumps. After reaching the target muscles motor end plate and a couple of other processes such results in an inflow of calcium into the sarcomeres. Thus, enabling the start of a buckling movement of the Myosin caterpillar along with the Actin globular chalices [Silbernagl et al., 2007, chap. 2]. Secondly, *morphological variations* within the muscle's internal structure as a consequence of the movement of the filaments within multiple sarcomeres during contraction and thus, a variation of their corresponding myofibrils. These changes are affecting two kinds of electrical properties measured by bioimpedance, firstly the shape of the current path (affects *resistance* R) and secondly the state of charge separation due to a variation of charge carriers as calcium shifted during the process of muscle contraction (affects *reactance* X). For illustration, see Figure 5. Such behaviour is supported by the observation that R is mainly influenced by variations in *rotation angle* α thus, changes in the muscle's internal structure. During passive lifting, higher α_i (compressed muscle) show a decrease and lower α_i (stretched muscle) an increase of R value measured along rectus femoris muscle. Besides, the observed increase of X with *weight* we (heavier load) suggests that muscle contraction results in a rearrangement of charges, possibly due to movements of ions, dielectric variations in surrounding tissue layers as the fat layer or boundary movements of the electrodes.

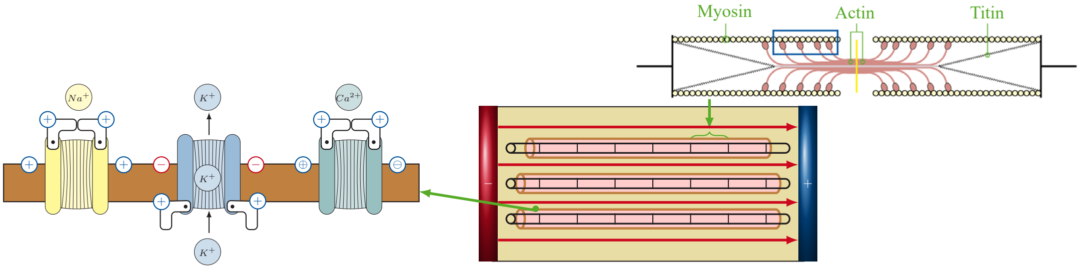

physiological changes (ion movement) **morphological changes (changes in structure)**

Figure 5: Principle of the electromotive chain as model for muscle contraction, based on physiological and morphologic variations.

5 Conclusions

During this work, we proposed an electrode setup for the assessment of muscle contraction performed by the rectus femoris muscle. Besides, we proposed a mechanical test-bench to perform leg curls under condition of isometric and isotonic contraction, using a feasible fixation to prevent influences of other muscle subgroups. Our results suggest that *resistance* R is mainly influenced by variations of angle α (muscle length) and *reactance* X mainly depends on muscle contraction (heavier weight). Finally, we proposed a possible explanation for these variations based on the concept of the electromotive chain. Nevertheless, the results require further testing to establish a solid fundamental base for further research.

Acknowledgements

The reported study was funded by German research foundation (DFG) according to the research project LE 817/41-1.

References

Freeborn, T. J., & Fu, B. (2018). Fatigue-Induced Cole Electrical Impedance Model Changes of Biceps Tissue Bioimpedance. *Fractal and Fractional*, *2*(4), 27. https://doi.org/10.3390/fractalfract2040027

Jafarpoor, M., Jia Li, White, J. K., & Rutkove, S. B. (2013). Optimizing Electrode Configuration for Electrical Impedance Measurements of Muscle via the Finite Element Method. *IEEE Transactions on Biomedical Engineering*, *60*(5), 1446–1452. https://doi.org/10.1109/TBME.2012.2237030

Li, L., Shin, H., Li, X., Li, S., & Zhou, P. (2016). Localized Electrical Impedance Myography of the Biceps Brachii Muscle during Different Levels of Isometric Contraction and Fatigue. *Sensors*, *16*(4), 581. https://doi.org/10.3390/s16040581

Marieb, E. N., Brady, P. M., & Mallatt, J. B. (2019). *Human Anatomy, Global Edition*. Pearson Education Canada.

Ngo, C., Munoz, C., Lüken, M., Hülkenberg, A., Bollheimer, C., Briko, A., Kobelev, A., Shchukin, S., & Leonhardt, S. (2022). A Wearable, Multi-Frequency Device to Measure Muscle Activity Combining Simultaneous Electromyography and Electrical Impedance Myography. *Sensors*, *22*. https://doi.org/10.3390/s22051941

Rutkove, S. B., Fogerson, P. M., Garmirian, L. P., & Tarulli, A. W. (2008). Reference values for 50-kHZ electrical impedance myography. *Muscle & Nerve*, *38*(3), 1128–1132. https://doi.org/10.1002/mus.21075

Sanchez, B., Pacheck, A., & Rutkove, S. B. (2016). Guidelines to electrode positioning for human and animal electrical impedance myography research. *Scientific Reports*, *6*(1), 32615. https://doi.org/10.1038/srep32615

SENIAM, S. E. f. t. N.-I. A. o. M. (2020). The SENIAM project (Surface ElectroMyoGraphy for the Non-Invasive Assessment of Muscles). http://seniam.org/

Shiffman, C. A., Aaron, R., & Rutkove, S. B. (2003). Electrical impedance of muscle during isometric contraction. *Physiological Measurement*, *24*(1), 213–234. https://doi.org/10.1088/0967-3334/24/1/316

Silbernagl, S., Despopoulos, A., Gay, R., & Rothenburger, A. (2007). *Taschenatlas Physiologie* (7th ed.). Thieme.

Proceedings of the International Conference of Bioelectromagnetism, Electrical Bioimpedance,
and Electrical Impedance Tomography June 29 – July 1, 2022 / Kyung Hee University, Seoul, Korea

Neural Noise Module : Automated Error Modeling using Adversarial Neural Networks

Benjamin Schindler[1], Dorothee Günzel[2] and Thomas Schmid[1,3,4]
[1]Machine Learning Group, Universität Leipzig, Leipzig, Germany
[2]Clinical Physiology/Nutritional Medicine, Charité - Universitätsmedizin Berlin, Berlin, Germany
[3]Martin-Luther-Universität Halle-Wittenberg, Halle (Saale), Germany
[4]Lancaster University in Leipzig, Leipzig, Germany

Correspondence : Benjamin Schindler, e-mail : bschindler@informatik.uni-leipzig.de

Abstract–In the field of impedance analysis, machine learning methods have become well established in recent years. However, as the complexity of the models increases, so does the risk of overfitting, which may lead to poor performance in real-world scenarios. In order to obtain more reliable and robust machine learning models, random noise is often added to the training data. However, in the field of bioimpedance, new ways of accurate automated error modeling are urgently needed to accelerate the analysis procedures. Here, we propose a new flexible error model with variable distribution parameters based on Adversarial Neural Networks, a generalization of the now popular Generative Adversarial Networks. Applied to published synthetic measurements on the epithelial cell line IPEC-J2, error magnitudes could be determined with a mean absolute error of 0.09 $\Omega \cdot cm^2$, giving a mean average percentage error of 13.0%. Compared to Maximum Likelihood Estimates that yielded a mean absolute error of 0.48 $\Omega \cdot cm^2$ and a mean average percentage error of 87.6%, this represents a significant improvement. Furthermore, this work demonstrates the versatility of Adversarial Neural Networks and shows their great potential in modeling measurement data.

Keywords: Impedance Spectroscopy; Error Modeling; Adversarial Neural Networks; Generative Adversarial Networks

1. Introduction

Recently, machine learning (ML) has achieved remarkable success in the medical analysis of impedance measurements and led to a variety of new diagnostic methods (McDermott et al 2020, Rahman et al 2020 and Młyńczak et al 2019). Although popular deep-learning systems are capable of representing even highly complex relationships (LeCun et al 2015), the increase in model parameters (i.e. neuron weights) leads not only to higher computational costs, but also to an increased risk of overfitting. Overfitted models exhibit poor generalization, as indicated by good results on the training data, but significantly worse performance on external datasets and in real-world scenarios. However, reliable and robust methods are indispensable, especially in the field of medical applications. A common way to obtain more robust ML models is to augment the training data, e.g. by modeling and adding noise (An 1996). It has been shown that manual noise modeling can lead to good ML-based analyses of bioimpedance measurements, but is also a complex and time-consuming approach (Schmid et al 2013). At this stage, a new flexible automatic error modeling would greatly improve the ML-based analysis of bioimpedance measurements by accelerating the procedure.

When performing impedance analysis on biological systems, we often face one or more of the following difficulties: First, domain-specific expertise is usually required to make preliminary assumptions. Second, biological systems are highly dynamic: biological processes (such as regulation, growth, and adaption) may alter the state of the investigated object, as a consequence pre-assumptions made may lose their validity, as described e.g. in (Schmid et al 2013). Third, the ground truth values of sought properties are subject of the investigation and accordingly not known. Furthermore, not all internal cause-effect relationships are known at the time of analysis. Therefore, the following requirements arise for automated error modeling of impedance measurements on biological systems:

1. To obtain flexible error modeling, the method should be designed with as few assumptions as possible about the distribution of the data and the dispersion of errors.
2. To accommodate various probes and conditions, no assumptions should be made about underlying circuit models.
3. Estimated error distribution parameters are not fixed, but may depend on unknown quantities that can be derived from the measurement.

In this paper, we present a novel method called Neural Noise Module (NNM), which satisfies all the above requirements based on Adversarial Neural Networks (ANN), a generalization of commonly known Generative Adversarial Networks (GAN).

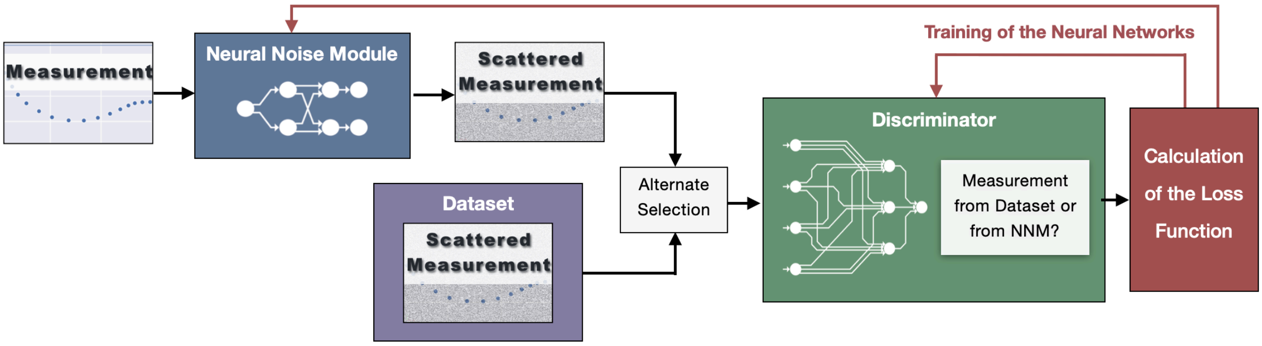

Figure 1. Training setup of an Adversarial Neural Network (ANN) as an automated impedance measurement error model. The ANN consists of two opposing neural networks, namely the Neural Noise Module (blue) and the Discriminator (green). While the Discriminator learns to distinguish scattered measurements of a given dataset (purple) and the ones synthesized by the NNM, it forces the NNM to accurately mimic underlying error magnitudes. Both Neural Networks are trained using ADAM by optimizing the two-player minimax game adopted from Equation 1.

2. Adversarial Neural Networks

As the most prominent example of ANNs, Generative Adversarial Networks (GAN) were first formulated in 2014 (Goodfellow et al 2014) and have since made amazing contributions, especially in image data generation (e.g. Karras et al 2018). As a generative model, a GAN learns implicit distributions in order to represent a given dataset. Therefore, a generator network G_θ generates synthetic data $X_{synth} = G_\theta(z)$ based on latent noise $z \sim p_z$ drawn from a chosen prior distribution p_z. The discriminator D_ϕ learns to discriminate between synthetic data $X_{synth} = G_\theta(z)$ and real samples $X_{data} \sim p_{data}$. As the discriminator becomes more accurate at distinguishing synthetic and real data, it forces the trainable generator to produce successively more realistic samples. Based on expectation maximization, training of D_ϕ and G_θ can be formalized as a two-player minimax game in which the trainable neuron weights θ, ϕ are gradually adjusted according to the following loss function:

$$\min_{\theta} \max_{\phi} V(G_\theta, D_\phi) = \mathbb{E}_{X_{data} \sim p_{data}}[\log D_\phi(X_{data})] + \mathbb{E}_{z \sim p_z}[log(1 - D_\phi(G_\theta(z)))] \tag{1}$$

We view adversarial neural networks (ANNs) as a generalization of GANs that leverages the concept of adversarial training to address a much broader range of problems, such as sleep stage classification (Zhao et al 2017) and fake news detection (Wang et al 2018). In the following chapter, we demonstrate how ANNs can also be used for automatic error modeling of spectral impedance measurements.

3. Methods

3.1 Neural Noise Module

The central algorithmic innovation of our approach is the introduction of the so-called Neural Noise Module (NNM) that is able to learn underlying error distributions in an automated fashion. Therefore, a GAN-inspired training setup was realized using *Pytorch,* in which two artificial neural networks compete against each other (see Figure 1). For this work, the generator of a GAN was replaced with the proposed NNM. Instead of learning inherent feature distributions of a dataset, NNM learns error distributions as a function of observed measurements with m features $X = (x_1, \ldots, x_m)^T$. In this proof-of-concept work, known measurements without scattering X_{clean} served as input to the NNM. Then the NNM synthesizes scattered Measurements $X_{scattered}$ by adding random errors $\epsilon_i \in N(0,\sigma_i^2)$ which are drawn based on predicted standard deviations $\sigma_1, \ldots, \sigma_m$. The NNM augmented data $X_{scattered}$ (label=0) and scattered data from the dataset X_{data} (label=1) serve alternately as input to a classifying discriminator, which attempts to distinguish the two sets of data. If successfully trained, the NNM mimics the error distribution X_{data} accurately, indicated by the fact that the discriminator is not able to detect any difference.

The re-parameterization trick has been used to determine distribution parameters by back-propagating networks, a technique that has become widely popular with Variational Autoencoders (An and Cho 2015). Discriminating between clean and scattered samples has been drastically improved by extracting finite forward differences for real and imaginary parts along the frequency axis, as described in (Schmid et al 2014). Additionally, second and third order differences and their absolute values were computed, resulting in an input vector of 564 features for the discriminator. After multiple grid-searches and subsequent selection of network architectures and model hyper-parameters, Discriminator and NNM were implemented as Multi Layer Perceptrons (MLP) with *tanh*-activation and network architectures $l_D = [564{,}900{,}1]$ and $l_{NNM} = [84{,}6{,}6{,}6{,}84]$. Both Networks were trained for 20 epochs using ADAM optimizer with a batch size of 8, an initial learning rate of $lr = 0.0001$ and momentum terms $\beta_1 = 0.5$ and $\beta_2 = 0.999$.

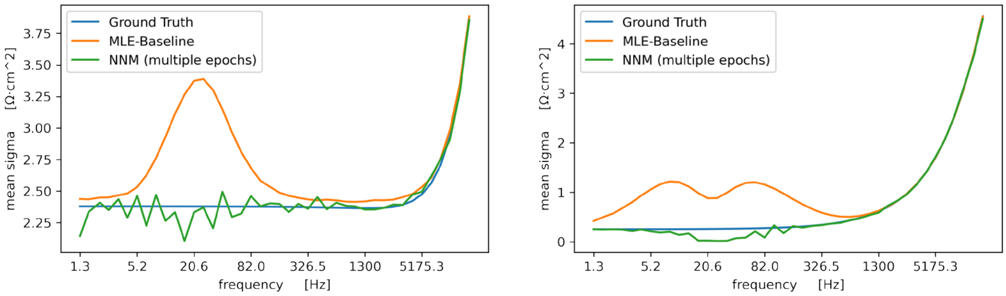

Figure 2. Standard deviations of impedance measurement errors for the IPEC-J2 cell line, measured at 42 frequencies between 1.3 Hz and 16.35 kHz, averaged over 50,000 validation samples, separated into real (left) and imaginary (right) parts. Each plot contains curves derived from the ground truth standard deviations of the synthesized dataset (blue), the baseline Maximum Likelihood Estimates MLE (orange), and multi-epoch averaged estimates of the Neural Noise Module NNM (green). Clearly, the NNM represents the error distribution parameters much more accurately than the MLE baseline.

3.2 Baseline Error Model

As a Baseline, Maximum Likelihood Estimates (MLE) of normal distributions $\hat{\sigma}_1, \dots, \hat{\sigma}_m$ (i.e. the sample standard deviations) were computed for each feature x_i. In accordance with (Schmid et al 2013), estimates were used to draw additive normally distributed errors $\hat{\epsilon}_i \in N(0,\hat{\sigma}_i{}^2)$. Note that real $\sigma_1, \dots, \sigma_m$ are not identical for each probe, as they depend on tissue properties, e.g. the transepithelial resistance (i.e. the larger the total resistance of the cell tissue, the larger the scatter of the measurement points). In reality, further non-linear relationships between tissue properties and the scatter of measurement points are expected.

3.3 Dataset

In order to compare our approach to the baseline method, we employ a dataset of artificial impedance spectra (Schindler et al 2021), modeled after the epithelial cell line IPEC-J2 (Berschneider 1989 and Schierack et al 2006), available at DSMZ-German Collection of Microorganisms and Cell Cultures (ACC 701). It consists of 150,000 impedance spectra measured at 42 frequencies between 1.3 Hz and 16.35 kHz. Considering real and imaginary parts separately, one obtains $m = 84$ features per measurement. All features were complemented by experimentally derived error modeling from (Schmid et al 2013). Note, that in contrast to real measurements, the underlying tissue model parameters and error magnitudes are known in this synthetic approach. Using the specified tissue properties, the corresponding impedance measurements were synthesized without measurement errors. Thus, for each probe, one measurement with measurement error and one without measurement error are obtained. For all subsequent steps, the data was standardized and split into training and validation sets according to 3-fold cross-validation.

4. Results

After the first six training epochs (i.e. individual runs with all training data) a rough equilibrium is reached, with a discriminator accuracy of ~50%. Nevertheless, improvements can still be observed from this point until the 15th epoch. Note, that even in the later course of training, the NNM predictions still vary slightly over time. With a training duration of about one minute per epoch on a 4-core CPU with 2.1 GHz, the computation time is short enough to train longer if needed. Particularly good results were obtained when the NNM model state was saved after each epoch and the predictions of the NNM were averaged over several epochs.

For the evaluation, the true standard deviations from (Schmid et al 2013) were compared to standard deviations estimates of MLE and NNM. From this, two metrics were calculated, namely the mean average percentage error (MAPE) and the mean absolute error (MAE). The baseline MLE resulted in a MAPE of 87.6% and a MAE of $0.48\ \Omega \cdot cm^2$. The prediction of the NNM after the 15th epoch obtains a MAPE of 22.3% and a MAE of $0.17\ \Omega \cdot cm^2$. When the predictions are averaged over epochs 5-20, a MAPE of 13.0% and a MAE of $0.09\ \Omega \cdot cm^2$ are obtained. At high frequencies, both estimates of the NNM and MLE are significantly more accurate than below 1300 Hz.

A simplified view is obtained when true and predicted standard deviations are averaged over all samples, as shown in Figure 2. From a good error estimate, one expects that averaged estimated standard deviations should match the averaged ground truth. In fact, this is not the case for the MLE baseline (for more on this see the discussion). The averaged NNM predictions, on the other hand, show a good approximation of the error magnitudes, as can be seen by the good alignment of the curves in Figure 2.

5. Discussion

Compared to the MLE baseline, the NNM shows more accurate estimates, especially for frequency channels where the measurement error strongly deviates from a normal distribution, which is the case for channels around 20.6 Hz. The MLE possibly compensates for the varying standard deviations present in the dataset by increasing the overall estimate. In contrast, the NNM is able to reflect the dependence of the measurement error on the total resistance, as evidenced by the fact that this relationship was also found in the data generated by the NNM.

The network architectures and hyper-parameters found here may be used to adapt the NNM to custom error modeling in the future. It is remarkable that a small MLP containing only 18 hidden neurons is able to determine 84 target values after training. This is contrasted by a discriminator with additional feature extraction and significantly more hidden neurons. Instead of MLPs, more elaborated neural networks could be used, as we have investigated one-dimensional convolutional neural networks as discriminators, which also performed well, but have been omitted here.

A significant challenge of this approach is the momentary given need for large training data, which currently limits this method to simulated measurements that can be synthesized in sufficient quantity. However, this may be resolved in the future, as many extensions of GANs have been proposed in recent years which significantly improve their training behavior and modeling capacity, e.g. (Salimans et al 2016) and (Arjovsky et al 2017).

6. Conclusions

In this work, the Neural Noise Module (NNM), a novel automated error model for impedance measurements, was presented and evaluated computationally that employs Adversarial Neural Networks to meet all the requirements described in the introduction. To the best of our knowledge, the NNM is the first attempt of estimate measurement errors by combining GAN-style training and the re-parametrization trick of Variational Autoencoders. The derived estimation is found to be very accurate, as evidenced by a low MAE of less than $0.1\ \Omega \cdot cm^2$. Consequently, the integration of NNM into existing ML models represents a promising application. By providing an automated and flexible data augmentation method, the NNM could greatly help to improve the generalization ability of ML-based impedance analysis by preventing overfitted models. As an adaptive error model with backpropagatable gradients, the NNM could easily be integrated into neural network based approaches. This would be a further step in improving the reliability and robustness we expect from ML methods, especially in the field of medical diagnostics.

Acknowledgments

Our research was supported by the Neuromorphic Information Processing group at Universität Leipzig. In particular, we would like to thank Martin Bogdan and Ferney Beltran for helpful discussion and advice.

References

An J and Cho S 2015 Variational autoencoder based anomaly detection using reconstruction probability *Special Lecture on IE* **2**(1) 1-18

An G 1996 The Effects of Adding Noise During Backpropagation Training on a Generalization Performance *Neural Computation* **8**(3) 643-674

Arjovsky M, Chintala S and Bottou L 2017 Wasserstein generative adversarial networks *International conference on machine learning* **2017** 214-223

Berschneider H M 1989 Development of normal cultured small intestinal epithelial cell lines which transport Na and Cl. *Gastroenterology* **96**(Suppl. Pt 2)

Goodfellow I, et al. 2014 Generative adversarial nets *Advances in neural information processing systems* **27**

Karras T, Laine S and Aila T 2019 A style-based generator architecture for generative adversarial networks. *Proceedings of the IEEE/ CVF conference on computer vision and pattern recognition* ***2019*** 4401-4410

LeCun Y, Bengio Y and Hinton G 2015 Deep learning *nature*, **521**(7553) 436–444

McDermott B, Elahi A, Santorelli A, O'Halloran M, Avery J and Porter E 2020 Multi-frequency symmetry difference electrical impedance tomography with machine learning for human stroke diagnosis *Physiological Measurement* **41**(7)

Młyńczak M, Borycka-Kiciak K, Uchman-Musielak M and Dziki A 2019 Impedance Spectroscopy Method to Detect Pelvic Floor Muscle Damage—A Feasibility Study *World Congress on Medical Physics and Biomedical Engineering* **2018** 875-878

Rahman S M, Ali M A, Altwijri O, Alqahtani M, Ahmed N, and Ahamed N U 2020 Ensemble-Based Machine Learning Algorithms for Classifying Breast Tissue Based on Electrical Impedance Spectroscopy *Advances in Artificial Intelligence, Software and Systems Engineering* ***965*** 260-266

Salimans T, Goodfellow I, Zaremba W, Cheung V, Radford A and Chen X 2016 Improved techniques for training gans *Advances in neural information processing systems* **29**

Schindler B, Günzel D and Schmid T 2021 Transcending Two-Path Impedance Spectroscopy with Machine Learning: A Computational Study on Modeling and Quantifying Electric Bipolarity of Epithelia *International Journal on Advances in Life Sciences* **13**(3-4) 134-148

Schierack P et al. 2006 Characterization of a porcine intestinal epithelial cell line for in vitro studies of microbial pathogenesis in swine *Histochemistry and cell biology* 125(3) 293-305

Schmid T, Bogdan M, and Günzel D 2013 Discerning apical and basolateral properties of HT-29/B6 and IPEC-J2 cell layers by impedance spectroscopy, mathematical modeling and machine learning. *PloS one*, **8**(7)

Schmid T, Günzel D, and Bogdan M 2014 Automated Quantification of the Relation between Resistor-capacitor Subcircuits from an Impedance Spectrum *BIOSIGNALS* 141-148

Wang Y et al. 2018. EANN: Event adversarial neural networks for multi-modal fake news detection. *Proceedings of the 24th acm sigkdd international conference on knowledge discovery & data mining* **2018** 849-857

Zhao M, Yue S, Katabi D, Jaakkola T S and Bianchi M T 2017 Learning sleep stages from radio signals: A conditional adversarial architecture *International Conference on Machine Learning* **2017** 4100-4109

DAY 2

Thursday, June 30, 2022

Oral Session 08

Bioelectromagnetic Instrumentation

Chair Orjan Grottem Martinsen (University of Oslo)
Ryan Halter (Dartmouth College)

O 08-01 **A Hybrid FE-EFG Method for 2D MIT Forward Problem Computation**
Hassan Yazdanian (K. N. Toosi University of Technology)

O 08-02 **Contactless magnetic induction phase shift measurement for assessment of cerebrovascular autoregulation on cerebral ischemic rabbits**
Xu Jia (Army Medical University)

O 08-03 **Reduced effective sensitivity of Acoustoelectric Tomography**
Ben Keeshan (Carleton University)

O 08-04 **A Modified Howland Current Source Design for Simultaneous EIT/ECG Data Acquisition**
Ahmed Abdelwahab (State University of New York)

O 08-05 **EIT-based Surgical Margin Probe Development**
Shannon Kossmann, Sophie Lloyd (Dartmouth College)

Proceedings of the International Conference of Bioelectromagnetism, Electrical Bioimpedance,
and Electrical Impedance Tomography June 29 – July 1, 2022 / Kyung Hee University, Seoul, Korea

A Hybrid FE-EFG Method for 2D MIT Forward Problem Computation

Hassan Yazdanian[1], Maedeh Hadinia[2]
[1]Department of Biomedical Engineering, K. N. Toosi University of Technology, Tehran, Iran
[2]Department of Electrical Engineering, College of Electrical Engineering, Langarud Branch, Islamic Azad University, Langarud, Iran

Correspondence : Maedeh Hadinia, e-mail : maedeh.hadinia@iau.ac.ir

Abstract– Magnetic induction tomography (MIT) is a modality for imaging the electrical conductivity of biological tissues. This paper presents a hybrid finite element-element free Galerkin (FE-EFG) method for solving 2D MIT forward problem. The numerical implementation of the hybrid method is validated by an analytical problem. A 16-coil 2D MIT system is modeled and the hybrid method is employed to solve the forward problem using a head phantom. The results hold promise for alternatively employing of the hybrid FE-EFG method in situations with meshing task problem.

Keywords: Element-free Galerkin method, finite element method, forward problem, magnetic induction tomography.

1. Introduction

Magnetic induction tomography (MIT) is a relatively emerging modality that attempts to image the electrical conductivity distribution inside an object (Korjenevsky *et al* 2000). MIT features non-contact, non-invasive, non-radiative, and low-cost which make it attractive for biomedical applications. Recently, several studies have focused on imaging of intracranial haemorrhage using MIT (Zolgharni *et al* 2010, Xiao *et al* 2018, Chen *et al* 2021). The forward problem in MIT is a boundary value problem which has mostly been solved by mash-based methods such as finite element (FE) method (Xiao *et al* 2018) or finite difference method (Zolgharni *et al* 2010). Using these methods in problems with complex geometries, like the human head in which generation of a mesh is a challenging task, may be problematic (Von Ellenrieder *et al* 2005). Furthermore, in some applications like imaging of lung ventilation, the shape and size of regions of the object under study are subject to frequent deformations. It can cause some difficulties for mesh-based methods.

There is another group of numerical techniques called mesh-free methods. They approximate an unknown function based on a set of nodes distributed in the problem domain, and do not need usual connection between nodes to construct discrete equations. Numerous mesh-free methods have been presented to solve boundary value problems, such as the element-free Galerkin (EFG) method (Hadinia *et al* 2016) and wavelet Galerkin method (Yousefi *et al* 2013). To the best of the authors' knowledge, mesh-free methods have not been employed to solve the biomedical MIT forward problem. In this paper, for the first time, we use the EFG method for solving 2D MIT forward problem. This method has been employed to solve the EIT forward problem in several studies (Cutrupi *et al* 2007, Hadinia *et al* 2016). EFG has also been used for the computation of static and quasi-static electromagnetic fields (Xuan *et al* 2004).

The EFG basis functions do not satisfy the Kronecker delta criterion (Hadinia *et al* 2016). This property makes the imposition of essential boundary conditions difficult compared to for instance the FE method. It is possibly the main drawback of the EFG method. The most efficient and accurate method to address the difficulty is coupling with FE method (Dolbow and Belytschko 1998). In this paper, we apply this method which results in the hybrid FE-EFG method for solving the MIT forward problem.

2. Methods

2.1 MIT forward problem

The forward problem in MIT includes a classical eddy current problem. By considering the magneto-quasi-static approximation, the 2D MIT forward problem in the frequency domain is governed by (Yazdanian *et al* 2020):

$$\begin{cases} (1/\mu_0)\nabla^2 A_z = -J & \text{in} \quad \Omega_N \\ (1/\mu_0)\nabla^2 A_z - \mathrm{j}\omega\sigma A_z = 0 & \text{in} \quad \Omega_C \end{cases} \tag{1}$$

where A_z and J are the z-component of the magnetic vector potential (MVP) and the applied current density to an excitation coil, respectively, and $\mathrm{j}=\sqrt{-1}$. Domains Ω_N and Ω_C are the non-conducting and conducting (or eddy current) regions, respectively, and μ_0, σ, and ω are the free space magnetic permeability, electrical conductivity, and angular frequency, respectively. The region Ω_C is the imaging region and Ω_N includes the MIT coils and air. Boundary conditions are required to obtain a unique solution for Equation (1). At the outer boundary of the problem, the far-field boundary condition is applied. In addition, at the interface of two different material, the continuity of normal component of magnetic flux density and tangential component of magnetic field intensity should be satisfied (Turner and Han 1987).

The output of the forward problem is the induced voltage in the sensing coils obtained by (Yazdanian *et al* 2020):

$$V = \mathrm{j}\omega \oint_C A_z\, \vec{a}_z \cdot \mathrm{d}\vec{\ell} \tag{2}$$

where C is a closed contour bounding the internal area of the sensing coil. The induced voltage is a complex value. In the low-conductivity applications of MIT, including biomedical applications, the real-part of V is proportional to the conductivity distribution in the imaging region (Yazdanian *et al* 2020). Equation (2) shows that the real-part of V is proportional to the imaginary-part of A_z. Therefore, we consider the real-part of V and imaginary-part of A_z in Section 3.

2.2 Numerical implementation

In the proposed hybrid FE-EFG method, regions Ω_N and Ω_C are formulated by FE and EFG methods and donated by Ω^{FE} and Ω^{EFG}, respectively. Then, the computational domain will be $\Omega = \Omega^{\mathrm{FE}} \cup \Omega^{\mathrm{EFG}}$. Formulating Ω_N by the FE method resolves the problem of imposing of essential boundary conditions for EFG method (Hadinia *et al* 2016) while formulating Ω_C by the EFG method handles the region with meshing task problem and/or moving objects.

Discretization with FE and EFG methods

The region Ω^{FE} is discretised by M triangular elements and includes N^{FE} nodes. The MVP A^{FE} at each point $\mathbf{x}$ inside Ω^{FE} is given by a linear interpolation of nodal value $\hat{A}_i^{FE}$ (Hadinia *et al* 2016):

$$A^{\mathrm{FE}}(\mathbf{x}) = \sum_{i=1}^{N^{\mathrm{FE}}} \phi_i^{\mathrm{FE}}(\mathbf{x})\hat{A}_i^{\mathrm{FE}} \qquad \forall\, \mathbf{x} \in \Omega^{\mathrm{FE}} \tag{3}$$

where $\phi_i^{\mathrm{FE}}(\mathbf{x})$ $(i = 1{:}\,N^{\mathrm{FE}})$ are linear nodal shape functions.

The region Ω^{EFG} is discretised by N^{EFG} nodes. The shape functions in the EFG method are constructed by moving least square approximation. Then, the MVP A^{EFG} at each point $\mathbf{x}$ inside Ω^{EFG} is approximated by (Hadinia *et al* 2016):

$$A^{\mathrm{EFG}}(\mathbf{x}) = \sum_{i=1}^{N^{\mathrm{EFG}}} \phi_i^{\mathrm{EFG}}(\mathbf{x})\hat{A}_i^{\mathrm{EFG}} \qquad \forall\, \mathbf{x} \in \Omega^{\mathrm{EFG}} \tag{4}$$

where the nodal parameter $\hat{A}_i^{\mathrm{EFG}}$ is the approximation to $A^{\mathrm{EFG}}(\mathbf{x})$ at the node $\mathbf{x}_i$ and $\phi_i^{\mathrm{EFG}}(\mathbf{x})$ is EFG shape function.

FE-EFG method

By discretization of Equation (1), a system of equations will be obtained for each region as follows:

$$\boldsymbol{\mathcal{K}}^{\mathrm{FE}}\ \ \boldsymbol{\mathcal{A}}^{\mathrm{FE}}\ \ = \boldsymbol{\mathcal{F}} \quad \text{in } \Omega^{\mathrm{FE}} \tag{5}$$

$$\boldsymbol{\mathcal{K}}^{\mathrm{EFG}}\,\hat{\boldsymbol{\mathcal{A}}}^{\mathrm{EFG}} = \mathbf{0} \quad \text{in } \Omega^{\mathrm{EFG}} \tag{6}$$

where $\boldsymbol{\mathcal{K}}^{\mathrm{FE}}$ and $\boldsymbol{\mathcal{K}}^{\mathrm{EFG}}$ were defined in (Wang *et al* 2007) and (Hadinia *et al* 2016), respectively, $\boldsymbol{\mathcal{A}}^{\mathrm{FE}}$ and $\hat{\boldsymbol{\mathcal{A}}}^{\mathrm{EFG}}$ contain node potentials in Ω^{FE} and the nodal parameters in Ω^{EFG}, respectively, and $\boldsymbol{\mathcal{F}}$ contain current density of an exaction coil. To couple FE and EFG methods, the following continuity conditions have to be enforced on the interface boundary Γ^{int} between two regions Ω^{FE} and Ω^{EFG} (Hadinia *et al* 2016):

$$A_z^{\mathrm{FE}}(\mathbf{x}) = A_z^{\mathrm{EFG}}(\mathbf{x}) \qquad \mathbf{x} \in \Gamma^{int} \tag{7}$$

$$\frac{1}{\mu_{\mathrm{FE}}} \nabla A_z^{\mathrm{FE}}(\mathbf{x}) \cdot \vec{\mathrm{n}}\Big|_{\Gamma^{int}} = \frac{1}{\mu_{\mathrm{EFG}}} \nabla A_z^{\mathrm{EFG}}(\mathbf{x}) \cdot \vec{\mathrm{n}}\Big|_{\Gamma^{int}} \tag{8}$$

where $\vec{\mathrm{n}} = \vec{\mathrm{n}}^{FE} = -\vec{\mathrm{n}}^{EFG}$ is outward unit vector which is normal to the Γ^{int}, and μ_{FE} and μ_{EFG} are the permeability in FE and EFG regions, respectively. To couple (5) and (6) and impose (7) and (8) as well, the Lagrange multiplier method is employed. Therefore, one can find the following system of equations (Hadinia *et al* 2016):

$$\begin{bmatrix} \boldsymbol{\mathcal{K}}^{\mathrm{FE}} & \mathbf{0} & \boldsymbol{\mathcal{H}}^{\mathrm{FE}} \\ \mathbf{0} & \boldsymbol{\mathcal{K}}^{\mathrm{EFG}} & \boldsymbol{\mathcal{H}}^{\mathrm{EFG}} \\ (\boldsymbol{\mathcal{H}}^{\mathrm{FE}})^T & (\boldsymbol{\mathcal{H}}^{\mathrm{EFG}})^T & \mathbf{0} \end{bmatrix} \begin{bmatrix} \boldsymbol{\mathcal{A}}^{\mathrm{FE}} \\ \hat{\boldsymbol{\mathcal{A}}}^{\mathrm{EFG}} \\ \boldsymbol{\eta} \end{bmatrix} = \begin{bmatrix} \boldsymbol{\mathcal{F}} \\ \mathbf{0} \\ \mathbf{0} \end{bmatrix} \tag{9}$$

where $\boldsymbol{\mathcal{H}}^{\mathrm{FE}}$ and $\boldsymbol{\mathcal{H}}^{\mathrm{EFG}}$ are explained in (Hadinia *et al* 2016).

3. Numerical experiments

3.1 Benchmark test

In order to validate the hybrid FE-EFG numerical techniques, a benchmark test was first attempted. The benchmark test was designed by inspiration of the one presented in (Peyton *et al* 1996). The problem region consists of seven concentric circle as shown in Figure 1. One may picture the region as the inside of an infinitely long cylinder whose outside extends to infinity. The conductivity and radii for each layer are similar to values given in (Dekdouk *et al* 2008). They are chosen to simulate a slice of head model. The excitation field is generated by a current density distribution of $J = J_0 \sin\varphi$ (A/m) at $r_7 = 100$ mm. The general solution for the test problem in the polar coordinate will be as follows:

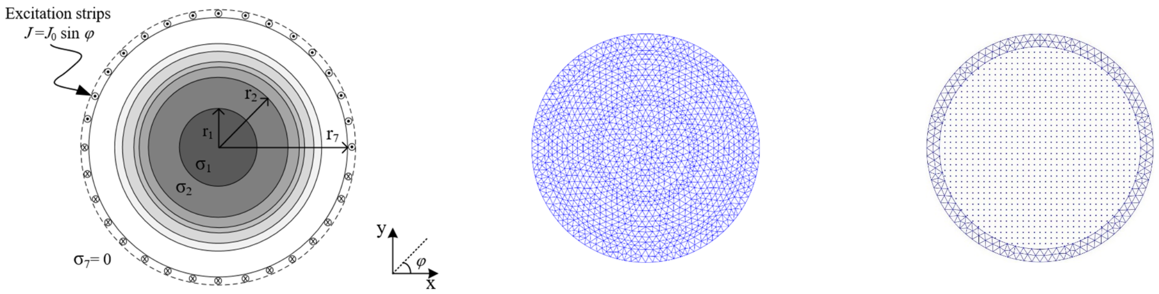

(a) (b) (c)

Figure 1. (a) 2D benchmark test assembly containing six conductive layers (σ_1 to σ_6) in a parallel magnetic field. The condictivity and radius of each laye are similar to values given in (Dekdouk *et al* 2008). Domain discretization for (b) the FE method and (c) the hybrid FE-EFG method.

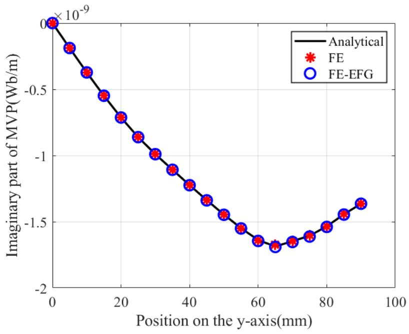

Figure 2. Imaginary part of MVPs calculated by (black line) analytical solution, (red stars) FE method, and (blue circles) FE-EFG method for points located on y-axis, from (0, 0) to (0, 90) mm (step by 5 mm).

$$A_z(r,\varphi) = \sum_{n=1}^{\infty} [a_n\, I_n(\alpha_k r) + b_n\, K_n(\alpha_k r)] \sin(n\varphi) \tag{10}$$

where I_n and K_n are modified Bessel functions of the first and second kinds, respectively, a_n and b_n are constant coefficients to be determined from the boundary conditions, and $\alpha_k = \sqrt{\omega\sigma_k\mu_0}$. Since the excitation filed is generated by $\sin\varphi$, (10) exists only for $n = 1$.

The test problem was then solved numerically by FE and FE-EFG methods. In the analytical problem, the excitation filed is unrealistically generated by surface current densities. Therefore, instead of using excitation strips as shown in Figure 1(a), we calculated MVPs by the analytical solution at $r = 90$ mm and then imposed them to numerical methods as the Dirichlet boundary conditions. FE mesh, as shown in Figure 1(b), has 1360 nodes and 2618 elements. In the hybrid method, as shown in Figure 2(c), the EFG domain has a uniform distribution of 1136 nodes and FE domain has 265 nodes and 366 elements. There are 76 common nodes on the interface boundary Γ^{int}. Figure 2 compares MVPs obtained from numerical solutions to those of obtained by the analytical solution. We calculated the percentage of the relative error for FE and FE-EFG methods for points located on y-axis, from (0, 0) to (0, 90) mm (step by 5 mm). The relative error for the imaginary part of MVPs obtained by FE and FE-EFG method was 0.26% and 0.24%, respectively. The runtime for FE and FE-EFG method was 0.17 s and 0.29 s, respectively.

3.2 Head model

Figure 3(a) shows the cross-sectional view of the 2D MIT system, which has 16 air-core coils used for both excitation and sensing. The imaging region has a radius of R_1=110 mm, which models by the EFG method in the hybrid numerical method. The homogeneous Dirichlet boundary condition was imposed at a radius of 250 mm. The space outside of the imaging region, including coils, is modelled by the FE method in the hybrid method. Sequential activation of coils using a sinusoidal alternating current of 10 A amplitude and frequency of 10 MHz excites the imaging region. Only independent measurements are gathered. They are labelled from 1 to 120.

As shown in Figure 3(b), an axial cross-section of a realistic head model (available in simnibs.org) is embedded in the MIT setup. Similar 2D model has been used in (Xiao *et al* 2018). The head model contained five tissue types, as shown in Figure 3(c). The conductivity of brain tissues were chosen similar to values given in (Dekdouk *et al* 2008).We solved the forward problem using both FE and hybrid FE-EFG methods and calculated the induced voltages using Equation (2). In addition, we have used an extremely fine mesh to solve the forward problem by the FE method as a ground truth. The FE mesh in the pure FE method has 5997 nodes and 11932 elements. In the FE-EFG method, the discretized FE domain includes 2263 nodes and 4382 elements. The discretized EFG domain has a uniform distribution and includes 3804 nodes. The ground truth solution is obtained with a FE with a mesh including 23447 nodes and 46576 elements. Figure 4(a) shows the real part of induced voltages for all independent measurements calculated by FE method, FE-EFG method, and ground truth. Figure 4(b) depicts the absolute error (AE) of induced voltages for each numerical method compared to the ground truth. We also calculated the relative error for each numerical method in comparison with the ground truth. The percentage of relative error of the FE and FE-EFG methods was 1.83% and 1.49%, respectively. The run-time for the FE and FE-EFG methods was 4.80 s and 3.67 s, respectively.

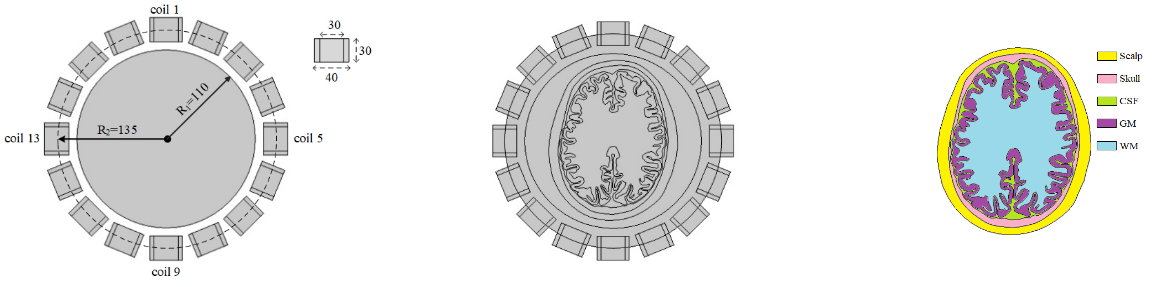

(a) (b) (c)

Figure 3. (a) 2D MIT system setup. Dimensions are in mm. (b) Head model inside MIT setup. (c) Different part of head model.

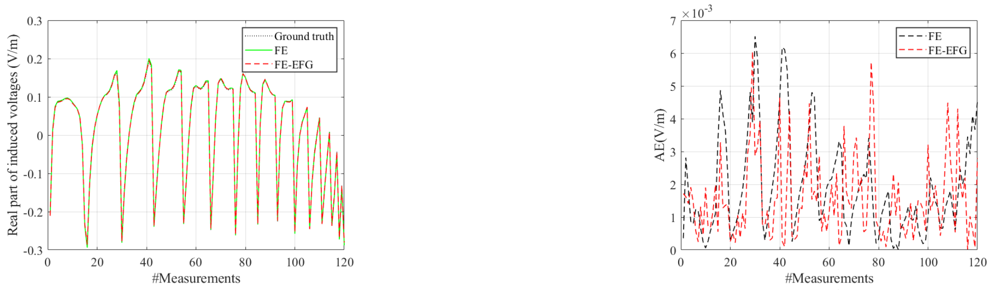

(a) (b)

Figure 4. (a) Real part of induced voltages calculated by the FE method, FE-EFG method, and ground truth. (b) Absolute error of the FE and FE-EFG methods compared to the ground truth.

4. Conclusions

In this paper, for the first time, a hybrid FE-EFG numerical method was developed to solve the 2D MIT forward problem. In the proposed numerical method, the EFG method was employed to solve the problem in the imaging region, and the FE method was used to solve the problem in coil and air around imaging region. In this way, we benefited from the advantages of both methods. Comparison of FE and FE-EFG methods through the numerical experiment revealed the superiority of the hybrid method. Results of this paper manifested that the hybrid FE-EFG method holds promise for solving MIT forward problem in domains with mesh difficulty task.

References

Chen Y, Tan C and Dong F 2021 Combined planar magnetic induction tomography for local detection of intracranial hemorrhage *IEEE Trans. Instrum. Meas.* **70**, 1-11

Cutrupi V, Ferraioli F, Formisano A and Martone R 2007 An approach to the electrical resistance tomography based on meshless methods *IEEE Trans. Magn.* **43**, 1717 - 1720

Dekdouk B, Pham M H, Armitage D W, Ktistis C, Zolgharni M and Peyton A J 2008 A feasibility study on the delectability of edema using magnetic induction tomography using an analytical model *IFMBE Proceedings*

Dolbow J and Belytschko T 1998 An introduction to programming the meshless element free Galerkin method *Arch. Comput. Methods Eng.* **5**, 207–241

Von Ellenrieder N, Muravchik C H and Nehorai A 2005 A meshless method for solving the EEG forward problem *IEEE Trans. Biomed. Eng.* **52**, 249-57

Hadinia M, Jafari R and Soleimani M 2016 EIT image reconstruction based on a hybrid FE-EFG forward method and the complete-electrode model *Physiol. Meas.* **37**, 863–78

Korjenevsky A, Cherepenin V and Sapetsky S 2000 Magnetic induction tomography: Experimental realization *Physiol. Meas.* **21**, 89-94

Peyton A J, Yu Z Z, Lyon G, Al-Zeibak S, Ferreira J, Velez J, Linhares F, Borges A R, Xiong H L, Saunders N H and Beck M S 1996 An overview of electromagnetic inductance tomography: Description of three different systems *Meas. Sci. Technol.* **7**, 261–71

Turner L and Han H C 1987 The Calculation of Transient Eddy-Current Fields Using Null-Field Integral Techniques *IEEE Trans. Magn.*

Wang C, Liu R, Fu F, You F, Shi X and Dong X 2007 Image reconstruction for magnetic induction tomography and preliminary simulations on a simple head model *IEMBS Proceedings* pp 4406–9

Xiao Z, Tan C and Dong F 2018 Multi-frequency difference method for intracranial hemorrhage detection by magnetic induction tomography *Physiol. Meas.* **39**, 055006

Xuan L, Zeng Z, Shanker B and Udpa L 2004 Element-free Galerkin method for static and quasi-static electromagnetic field computation *IEEE Trans. Magn.* **40**, 12 - 20

Yazdanian H, Jafari R and Moghaddam H 2020 Solution of 2D MIT forward problem by considering skin and proximity effects in coils *IEEE Trans. Comput. Imaging* **7**, 22 - 31

Yousefi M R, Jafari R and Moghaddam H A 2013 A combined wavelet-based mesh-free method for solving the forward problem in electrical impedance tomography *IEEE Trans. Instrum. Meas.* **62**, 2629 - 2638

Zolgharni M, Griffiths H and Ledger P D 2010 Frequency-difference MIT imaging of cerebral haemorrhage with a hemispherical coil array: Numerical modelling *Physiol. Meas.* **31**, S111

Proceedings of the International Conference of Bioelectromagnetism, Electrical Bioimpedance,
and Electrical Impedance Tomography June 29 – July 1, 2022 / Kyung Hee University, Seoul, Korea

Contactless magnetic induction phase shift measurement for assessment of cerebrovascular autoregulation on cerebral ischemic rabbits

Xu Jia[1,2], Li Haocheng[1,3], Jin Gui[1,2], Zhuang Wei[1,2], Bai Zelin[1,2], Sun Jian[1,2],
Chen Mingsheng[1,2] and Qin Mingxin[1,2]
[1]College of Biomedical Engineering, Army Medical University, China
[2]Institute of Brain and Intelligence, Army Medical University, China
[3]Department of Medical Engineering, General Hospital of Central Theater Command, China
Xu Jia and Li Haocheng contributed equally to this work

Corresponding author : Qin Mingxin, e-mail : qmingxin@tmmu.edu.cn

Abstract– Cerebrovascular autoregulation can maintain constant cerebral blood flow by adjusting cerebral vessels resistance. It is important to have an effective noncontact tool for assessment and monitoring of cerebrovascular autoregulation in patients with acute ischemic stroke. The adjustment of intracranial arteriole caliber leads to changes in the conductivity of entire brain by relative changes in cerebral blood volume. The electrical properties measurement of entire brain by magnetic induction phase shift is a valuable alternative to assess the function. Based on magnetic induction phase shift, we proposed a new index called conductivity reactivity index for the assessment of the function and investigated its feasibility in cerebral ischemic rabbits. Our experimental results show that there is a significant difference in the new index between cerebral ischemic group and control group and there is a significant correlation between the mean values of the new index using contactless coils and the mean values of the pressure reactivity index using invasive intracranial pressure for each rabbit. Comparing with the traditional methods, the novel index with magnetic induction phase shift has the potential to be used for noncontact, global, bedside and real-time assessment of cerebrovascular autoregulation of patients with cerebral ischemic stroke.

Keywords: Cerebrovascular Autoregulation, Magnetic Induction Phase Shift, Pressure Reactivity Index, Conductivity Reactivity Index, Cerebral Ischemia

1. Introduction

Cerebrovascular autoregulation (CVAR) is a brain protective mechanism maintaining the constant cerebral blood flow (CBF) by quickly adjusting the caliber of cerebral vessels when arterial pressure (ABP) or intracranial pressure (ICP) fluctuates. The dysfunction of CVAR has been reported in patients with acute ischemic stroke(Castro *et al.*, 2018) and may influence the outcomes and secondary complications(Hecht *et al.*, 2021). CVAR assessment and monitoring can be used to prevent complications and predict prognosis (Xiong *et al.*, 2017; Nogueira *et al.*, 2021).

CVAR assessment requires to detect the changes in CBF or cerebral blood volume (CBV).At present, there is no gold standard indicator for CVAR monitoring. For bedside real-time monitoring, ICP monitor has been used as surrogate physical quantitie for CBV(Zeiler *et al.*, 2020). Pressure reactivity index (PRx), a correlation coefficient between slow spontaneous oscillations (SSO) in ABP and corresponding SSO in ICP, has been established in clinical studies for CVAR assessment(Zeiler *et al.*, 2020). However, ICP monitoring requires surgical operations which may cause complications such as dislocation, bleeding and infection(Fabrice *et al.*, 2017; Chodobski *et al.*, 2011). Also, autoregulation is, unfortunately, rarely monitored in clinical practice because invasive ICP probes are not routinely implanted in patients with cerebrovascular pathologies.

Contactless magnetic induction phase shift (MIPS) measurement is a method that could realize noninvasive, non-contact, whole-brain, deep part, and real-time continuous monitoring(Zhuang *et al.*, 2020; Zhao *et al.*, 2020). It is based on MIPS being proportional to the conductivity of measured brain tissues(Jin *et al.*, 2014). The MIPS caused by change of CBV conductivity of the global brain can be used as a surrogate for CVAR assessment and monitoring. In this study, the CVAR in cerebral ischemia rabbits were detected by the conductivity reactivity index-CRx, established by the correlation coefficient between SSO in ABP and MIPS. This study preliminary investigated the feasibility of contactless MIPS measurement for assessment of CVAR on cerebral ischemic rabbit model.

2. Methods and Materials

2.1 Magnetic induction phase shift captures changes of CBV

For MIPS detection, the tissue to be tested is placed between the excitation coil and the detection coil. An alternating current in the excitation coil generates a sinusoidal alternating primary magnetic field (B). This primary magnetic field generates an induction current in the measured tissue and then generates an induced magnetic field (ΔB). Both the primary magnetic field and the induced magnetic field received by the detection coil are converted into induced voltage. If a sinusoidal signal with an angular frequency of ω is used for excitation, the magnetic vector potential(Griffiths, 2001):

$$\frac{\Delta B}{B} = Q\mu_0\omega\left(\omega\varepsilon_0\varepsilon_r - \mathrm{j}\sigma\right) \quad (1)$$

Here, σ represents the conductivity of the measured tissue, μ_0 and ε_0 represent the vacuum permeability and the vacuum permittivity respectively, ε_r represents the relative permittivity of the measured tissue, and Q represents geometric constants, which relating to the location, structure and size of the measured tissue.

For biological tissues, the ΔB produced by the measured tissue is much smaller than B, so $\Delta\theta$ can be approximated as imaginary part of $\Delta B/B$; that is, the induced magnetic field received by the detection coil lags behind the primary magnetic field by a phase shift $\Delta\theta$.The MIPS is influenced by the conductivity σ of the measured tissue:

$$MIPS = \Delta\theta \approx Q\omega\mu_0\Delta\sigma \quad (2)$$

Since the conductivity of brain tissue, blood and cerebrospinal fluid are different, the bulk conductivity σ of the brain altered by the changes of the relative volume of those types tissues reflects the MIPS value.

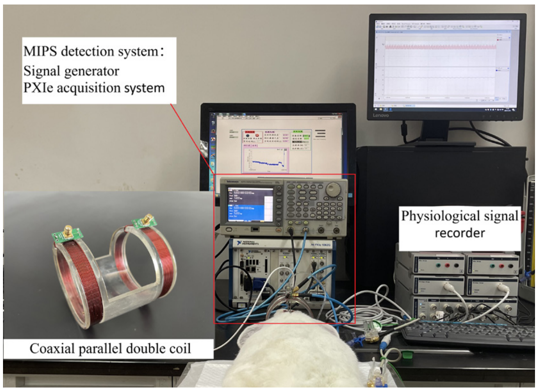

Figure 1. The experimental system of cerebrovascular autoregulation monitoring.

2.2 Experimental system

The experimental system of CVAR monitoring used in the experiment is shown in Figure 1. The experimental system of CVAR monitoring consists of a MIPS detection system with a signal generator (AFG3252 Tektronix Inc, Beaverton, Oregon, US) and a PXIe acquisition system (National Instruments Inc, Austin, Texas, US) and a physiological signal recorder (Power Lab 8/35, AD Instruments Inc, Sydney, New South Wales, Australia) for ICP and ABP monitoring.

A coaxial parallel double coil was used for MIPS measurement in this experiment. An excitation coil and a detection coil were wound with 32 AWG copper wire (diameter of 1 mm) on both ends of the plexiglass pipe, which have same turns (10 turns) and same radius (5.2 cm). The sinusoidal signal(6MHz) was used to generate the alternating primary magnetic field (B). The magnetic field changes (ΔB) are detected by the MIPS sensor and sent to the acquisition system. The MIPS was collected with 10Hz sampling frequency system, and synchronous ICP and ABP were monitored by the physiological signal recorder with 20 Hz sampling frequency.

2.3 The rabbit experiment model

Fifteen rabbits (2.2±0.3 kg) were obtained from the Animal Experimental Center of Army Medical University and were randomly divided into a cerebral ischemia group (n=10) and a control group (n=5). The animal experiments involved in this study were approved by the Animal Experiment Ethics Committee of the Army Medical University and were conducted in accordance with the Declaration of Helsinki and the guidelines issued by the International Pain Research Association. This study used bilateral common carotid artery ligation to establish a rabbit cerebral ischemia model. The control group operated the same except for the ligation. After the operation, the rabbit head was placed in the centre of the MIPS sensor. The MIPS, ABP and ICP measurements were simultaneously started.

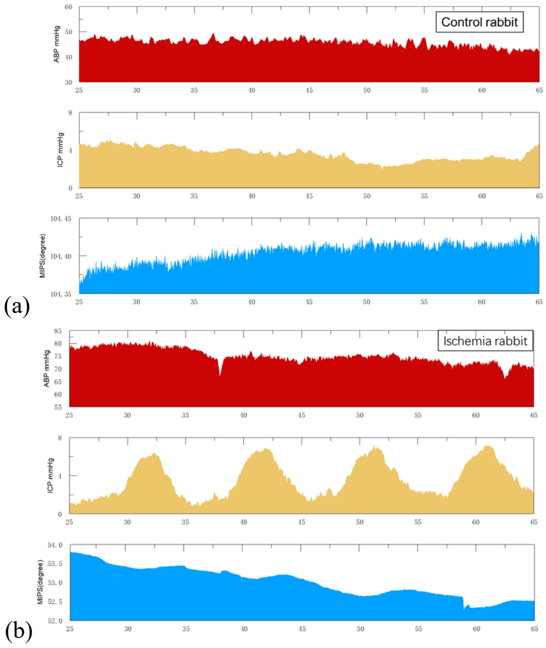

Figure 2. Time domain analysis of ABP, ICP, MIPS, (a) control rabbit (No. 1), (b) cerebral ischemia rabbit (No. 3).

2.4 Data collection and analysis

The monitoring time of each ischemic rabbit was 40 minutes. The control group were monitored for 80 minutes, each data averagely divided into 2 segments. The 20 samples of data were processed offline with MATLAB software (MathWorks, Inc., Natick, Massachusetts, US). The ABP, ICP, and MIPS signals were down-sampled to 1 Hz. SSO components (0.001-0.1Hz) were extracted by a 4 order lowpass filter and a 3 order high pass filter. In order to estimate the CVAR, we calculated the autoregulation index - CRx. Both ABP and MIPS signals are averaged over a 3 second period to get the mean ABP and the mean MIPS value to eliminate the influence of artifact and respiratory. Then, the Pearson correlation between the mean ABP and the mean MIPS is calculated using a 2-minute time window. This calculation process is repeated with a moving window every 3 seconds. ICP pressure reactivity index-PRx is calculated between ABP and the ICP in the same way. The CRx and PRx of each rabbit were averaged. The independent sample t test was done to analyze the difference of two indexes between the two groups with SPSS 25 software (IBM Corp., Armonk, New York, US).

3. Result

3.1 Original signals (ABP, ICP, MIPS) for CRx and PRx

ABP, ICP and MIPS were simultaneously monitored for CVAR evaluation from the experiment rabbits. Figure 2 shows the original signals of two group. The ICP and MIPS of the ischemic rabbits slowly oscillated with inverting regularity (Figure2(b)), which were different from the control rabbits. The frequencies of slowly oscillated is lower than frequencies of respiration and heartbeat. Also, the respiration, heartbeat, baseline drift has an influence on all signals. The frequency changes in the MIPS and ICP signals are consistent in the frequency spectrum, and the frequencies are concentrated below 0.01 Hz. Ischemia rabbits had more frequency components in low frequency SSO than control rabbits (Figure 3).

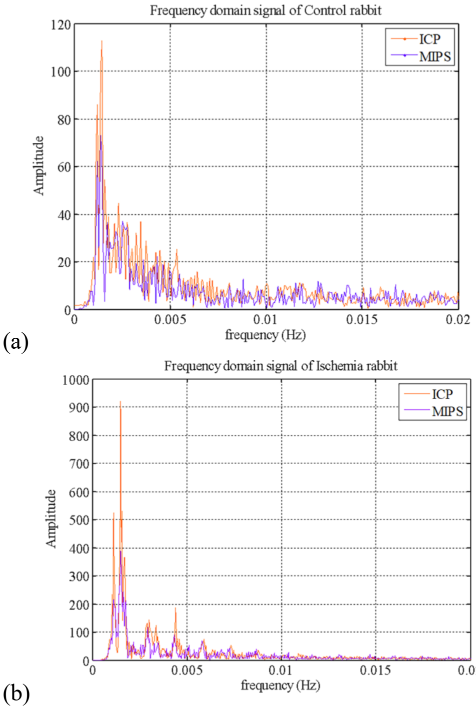

Figure 3. Frequency spectrum diagram of SSO in ICP and MIPS, (a) control rabbit (No. 1), (b) cerebral ischemic rabbit (No. 3).

3.2 The comparison of PRx and CRx between the cerebral ischemic group and control group

For CVAR assessment, the mean values of PRx and CRx were calculated with SSO in ABP, ICP and MIPS to compare CVAR of the two groups. As show in figure 4, the mean PRx was -0.126(SD=0.124) in the control group which means the ICP is not directly driven by ABP and hence the CVAR is intact, and the average PRx was 0.167(SD=0.086) in the cerebral ischemia group which indicates impaired CVAR due to a passive relationship between ABP and ICP. On the other hand, the mean CRx decreased from -0.002(SD=0.164) to -0.153(SD=0.117). There were significant differences in the CRx and PRx between the two groups (Table 1). The correlation analysis shows the CRx and PRx were significantly negatively correlated, with a correlation coefficient $r=-0.633$(95%CI, $p=0.003<0.05$).

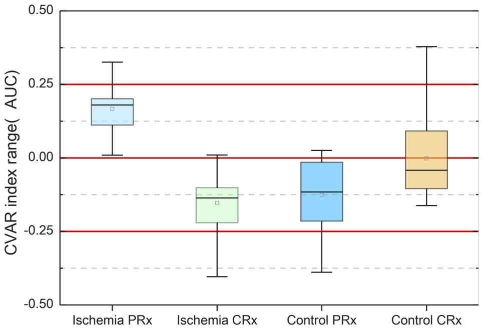

Figure 4. PRx and CRx statistics for the cerebral ischemia group and control group comparison.

Table 1. Independent sample t test results with the PRx and CRx between the cerebral ischemia group and the control group

Test Result Variable(s)	t	Std. Error Difference	Significance (2-tailed)	95% Confidence Interval	
				Lower Bound	Upper Bound
PRx	-6.118	0.048	0.000	-0.394	0.191
CRx	2.385	0.064	0.030	0.017	0.287

4. Discussion

In this study, we used a noncontact MIPS method to monitor CVAR and preliminarily indicated the feasibility of this method for monitoring CVAR of cerebral ischemia through a rabbit model. The MIPS method uses the overall intracranial conductivity as a surrogate for CBV to monitor CVAR. Since traversing the entire brain without the skull barrier, the magnetic field of the MIPS method can well cover the small blood vessels of the whole brain. Intracranial small blood vessels are the main contributor to CVAR and are distributed throughout the brain(Popovic *et al.*, 2013). Changes of the conductivity or volume of cerebral blood in the small blood vessels in response to SSO in ABP stimulus, will express themselves as changes in the bulk conductivity of the brain. There was a significant difference in the CRx between cerebral ischemia rabbits and control rabbits ($p<0.05$), indicating that the CRx can distinguish CVAR after cerebral ischemia in rabbits from that of control rabbits.

As we know that when CVAR is intact, ABP slowly increases and causes vasoconstriction; then, ICP decreases, and the correlation coefficient (PRx) between ABP and ICP is negative. However, when CVAR is impaired, the increase in ABP in the vascular lumen leads to passive cerebral vasodilation, increasing CBV and ICP, resulting in a positive PRx.

In this study, the CVAR in the control group was intact, i.e., PRx ≤ 0, while the PRx of the cerebral ischemia group was positive, indicating that the CVAR was impaired, which is consistent with the theory. The results presented that the noninvasive CVAR index-CRx was significantly correlated with the PRx index. However, it is negative correlation. This is mainly because ICP and MIPS are two different physical parameters to describe the properties of the brain, although both of them are related to CBV. As a mechanical parameter ICP reflecting intracranial local pressure, and as an electromagnetic parameter MIPS reflecting global conductivity changes, there is a time delay between the slow wave oscillations in MIPS and ICP. During ischemia, the correlation coefficient (CRx) between ABP and MIPS decreased, that means the response of whole brain conductivity caused by the impaired CVAR is slower than that of intact CVAR.

Non-invasive technologies such as TCD and NIRS are also being investigated as alternatives to invasive PRx. However, the TCD uses the cerebral blood flow velocity in the large blood vessels of the brain, such as the middle cerebral artery, rather than the CVAR small blood vessels, to surrogate the CBF for the CVAR monitoring, and is limited by operator experience and probe shift. The NIRS method detects the local cerebral oxygenation index instead of CBF to monitor CVAR. But systemic factors will influence NIRS based oxy/deoxy-hemoglobin signals. Compared with other noninvasive methods, the MIPS method is a noncontact, global, covering small vessels, and simple operation, and with taking spontaneous slow oscillations in ABP as the excitation of CVAR system it will not cause discomfort to patients.

This preliminary study was a small animal model of diffuse cerebral ischemia. In further study, the experimental model needs to be closer to the clinical practice of local cerebral ischemic stroke with a bigger sample size. At the same time, the relationship between CRx and the severity of CVAR injury was studied by contrast imaging experiments.

5. Conclusions

In this study, we explored the feasibility of a noncontact MIPS method to monitor CVAR based on an ischemic animal model with a conductivity reactivity index-CRx. The experimental results preliminarily prove that the conductivity reactivity index can be used to monitor CVAR and distinguish the impairment of CVAR under ischemic conditions. The contactless MIPS method has the potential to be bedside monitoring CVAR for patients with ischemic stroke.

Acknowledgments

We acknowledge the financial support of the National Natural Science Foundation of China (No. 51977214), Natural Science Foundation of Chongqing, China (No. cstc2018jcyjAX0671). This work was also supported by the brain science collaborative innovation centre of Army Military Medical University.

References

Castro P, Azevedo E and Sorond F 2018 Cerebral Autoregulation in Stroke *CURR ATHEROSCLER REP* **20** 37

Chodobski A, Zink B J and Szmydynger-Chodobska J 2011 Blood-brain barrier pathophysiology in traumatic brain injury *TRANSL STROKE RES* **2** 492-516

Fabrice, Giraudet, Franois, Longeras, Aurélien, Mulliez, Aurélie, Thalamy, Bruno and Pereira 2017 Noninvasive detection of alarming intracranial pressure changes by auditory monitoring in early management of brain injury: a prospective invasive versus noninvasive study *CRIT CARE* **21**

Griffiths H 2001 Magnetic induction tomography *Journal of Communications Technology & Electronics* **12** 1126

Hecht N, Schrammel M, Neumann K, Müller M M, Dreier J P, Vajkoczy P and Woitzik J 2021 Perfusion ‐ Dependent Cerebral Autoregulation Impairment in Hemispheric Stroke *ANN NEUROL* **89** 358-68

Jin G, Sun J, Qin M, Tang Q, Xu L, Ning X, Xu J, Pu X and Chen M 2014 A new method for detecting cerebral hemorrhage in rabbits by magnetic inductive phase shift *BIOSENS BIOELECTRON* **52** 374-8

Nai-Fang, Chi, Han-Hwa, Cheng-Yen, Wang, Lung, Chan, Chung-Kang, Peng and Vera 2018 Dynamic Cerebral Autoregulation Is an Independent Functional Outcome Predictor of Mild Acute Ischemic Stroke. *STROKE*

Nogueira R C, Beishon L, Bor-Seng-Shu E, Panerai R B and Robinson T G 2021 Cerebral Autoregulation in Ischemic Stroke: From Pathophysiology to Clinical Concepts *Brain Sciences* **11** 511

Popovic D, Bodo M, Pearce F, van Albert S, Garcia A, Settle T and Armonda R 2013 Assessment of cerebral blood flow autoregulation (CBF AR) with rheoencephalography (REG): studies in animals *Journal of physics. Conference series* **434** 12042

Smith M L, Bendek G, Dahlgren N, Rosén I, Wieloch T and Siesj B K 2010 Models for studying long-term recovery following forebrain ischemia in the rat. 2. A 2-vessel occlusion model. *ACTA NEUROL SCAND* **69** 385-401

Xiong L, Liu X, Shang T, Smielewski P, Donnelly J, Guo Z, Yang Y, Leung T, Czosnyka M, Zhang R, Liu J and Wong K S 2017 Impaired cerebral autoregulation: measurement and application to stroke *Journal of Neurology, Neurosurgery & Psychiatry* **88** 520-31

Zeiler F A, Aries M, Cabeleira M, van Essen T A, Stocchetti N, Menon D K, Timofeev I, Czosnyka M, Smielewski P, Hutchinson P and Ercole A 2020 Statistical Cerebrovascular Reactivity Signal Properties after Secondary Decompressive Craniectomy in Traumatic Brain Injury: A CENTER-TBI Pilot Analysis *J Neurotrauma* **37** 1306-14

Zeiler F A, Ercole A, Czosnyka M, Smielewski P and Aries M 2020 Continuous cerebrovascular reactivity monitoring in moderate/severe traumatic brain injury: a narrative review of advances in neurocritical care *BJA British Journal of Anaesthesia* **124**

Zhao S, Jin G, Bai Z, Chen J, Li M, Li G, Zhuang W, Liu Y and Qin M 2020 Twenty-four-hour real-time continuous monitoring of acute focal cerebral ischemia in rabbits based on magnetic inductive phase shift *BIOMED ENG ONLINE* **19** 1-83

Zhuang W, Qin M, Pan W, Xu L and Sun J 2020 A preliminary study on the feasibility of detecting global acute cerebral ischemia by the MIPS method *IEEE ACCESS* **PP** 1

ICBEM Bioelectromagnetism ICEBI Electrical Bioimpedance EIT Electrical Impedance Tomography

Proceedings of the International Conference of Bioelectromagnetism, Electrical Bioimpedance,
and Electrical Impedance Tomography June 29 – July 1, 2022 / Kyung Hee University, Seoul, Korea

Reduced effective sensitivity of Acoustoelectric Tomography

Ben Keeshan[1], Andy Adler[1], Carlos Rossa[1]
[1]Systems and Computer Engeering, Carleton University, Ottawa, Canada

Correspondence : Ben Keeshan, e-mail : benkeeshan@cmail.carleton.ca

Abstract- Acoustoelectric tomography is a promising hybrid imaging technique that exploits the coupled physical effect of electrical impedance tomography and ultrasound excitation. It reconstructs the interior conductivity distribution of the tissue using measurements of the voltage resulting from perturbations in the conductivity induced by the US wave. The acoustoelectric effect has been modelled as a linear coupling between the ultrasound coupling field and the conductivity distribution. The linear conductivity dependence of the acoustoelectric effect competes with the inverse dependence of the electrical impedance tomography sensitivity resulting in a suppression of the expected signal. This paper quantifies this effect using numerical simulations and shows that the conductivity contribution to the forward problem is dominated by the physics of electrical impedance tomography, resulting in a non-linear relationship between the signal and changes to the conductivity.

Keywords: Electrical Impedance tomography; Acoustoelectric tomography; Acoustoelectric Effect

1. Introduction

Electrical impedance tomography (EIT) is an inexpensive, portable, and non-invasive imaging technique with many interesting applications in medical imaging which involves an inherently inverse problem inverse problem. A hybrid imaging technique which combines ultrasound (US) and EIT is Acoustoelectric Tomography (AET). AET relies on the acoustic electric effect (AEE), which provides additional information about the interior regions of the body and can thus help stabilize the EIT inverse problem. AET pulsates an US wave through the body to perturb a classic EIT measurement, where there are some number of surface electrodes injecting a current and measuring the resultant surface voltages with no interior current sources. The time dependent AEE perturbations in the potential is measured by surface electrodes and can be used to calculate the interior power density, a non-linear function of σ, which is sensitive to the entire interior region. The conductivity can then be reconstructed with higher resolution from the measurements of the power density.

The EIT problem is to use some number of boundary voltage and current measurements and the generalized Laplace equation (which determines the potential, u, given no internal sources of current, if either Dirichlet i.e. specify the potential; or Neumann, i.e. specify the current, boundary conditions are specified) to reconstruct the conductivity $\sigma(x)$.

When the medium is perturbed with a ultrasound pulse, the change to the local conductivity is typically modelled by a linear relation:

$$\sigma_p(\boldsymbol{x}) = \sigma(\boldsymbol{x}) + \delta\sigma(\boldsymbol{x}, t) = (1 + kp(\boldsymbol{x}, t))\,\sigma(\boldsymbol{x}). \tag{1}$$

Here k is a coupling constant $k = O(10^{-8}, 10^{-9})\text{Pa}^{-1}$ while $p(\boldsymbol{x}, t)$ is the pressure at position $\boldsymbol{x}$ and time t. The perturbed potential, u_p, obeys its own generalized Laplace equation. Maintaining the non-perturbed boundary conditions results in a perturbation in the dissipated power given by:

$$P_d(t) = -\int_\Omega \delta\sigma \nabla u(\sigma) \nabla u_p(\sigma_p) dV = k \int_\Omega p(\boldsymbol{x}, t)\sigma \nabla u \nabla u_p dV. \tag{2}$$

Neglecting higher order contributions gives:

$$P_d(t) = -k \int_\Omega p(\boldsymbol{x}, t)\sigma|\nabla u|^2 dV = k \int_\Omega p(\boldsymbol{x}, t)M(\sigma)dV, \tag{3}$$

where $M(\sigma)$ is the power density. Equation 3 is a Fredholm equation of the first kind. The vast majority of the AET literature focuses on the last step of the AET process, reconstructing the conductivity from an assumed known power density (Ammari *et al* 2008; Kuchment P and Kunyansky 2010; Adesokan *et al* 2019). Recently, a more comprehensive method to solve the AET problem has tackled the initial step of solving for the power density (Li *et al* 2020). These methods rely on reconstructing the surface potential, which requires many surface electrodes. Thus, the possibility of a system involving very few electrodes makes an accurate estimation of the boundary surface very difficult. In this case, feasibility of an AET reconstruction depends on the strength of the AEE signal. With this in mind, this paper explores the competition between EIT and AEE effects in a single AET measurement.

2. Methods

Consider a quasi-minimal EIT setup with a single EIT measurement made with two drive electrodes and two measurement electrodes. After discretizing space, the measured voltage of a given electrode of the AEE is given by the matrix equation:

$$\delta V_i^{AEE}(t) = J^{EIT}\delta\sigma = kJ_{ij}^{EIT}p(t)_j\sigma_j, \tag{4}$$

where δV_{AEE} is the i^{th} voltage measurement, σ and $p(t)$ are a N dimensional vectors containing the conductivity and pressure for each element in the mesh as a function of time, and $j = 1, 2, ..., N$.

The time dependence of 4 is discretizing into T time points which yields for a single measurement i:

$$\delta V = kJ_{i,j}^{EIT}\sigma_j P_{j,t} = kP\hat{M}, \tag{5}$$

where $\delta V \in \mathcal{R}^{1\times T}$, $\delta\sigma \in \mathcal{R}^{N\times T}$, and $P_{j,t} = p_j(t)$, $t = 1, 2, ..., T$ and $\hat{M}$ is a N dimensional vector with j^{th} elements $J_{i,j}^{EIT}\sigma_j$.

A measurement's linear dependence on σ in 5 would naively and mistakenly suggest that the measurement should have a linear dependence on changes to σ. But this linear dependence on σ will compete with the implicit σ dependence of the Jacobian. For a given voxel, the current density is $j = \sigma E$, where E is the electric field. Assuming the current density is locally constant, $E \approx \frac{j}{\sigma}$, this gives:

$$J^{EIT} = \sigma|E|^2 \approx \frac{|j|^2}{\sigma}. \tag{6}$$

Plugging this in turn into Equation (4) with the (unrealistic) assumption of constant current flow gives:

$$\delta V_i \approx kp(t)_j\frac{1}{\sigma_j}\sigma_j. \tag{7}$$

This suggests that while the form of 4 seems to imply a strong proportionality between the local conductivity peturbed by the US and the AEE signal, the dependence of σ on the AEE signal competes with its dependence on EIT. In fact the naive expectation is the exact cancellation of the AEE dependence on the local conductivity. This exact cancellation will not occur as 6 is only a rough approximation resulting in a non-trivial σ dependence.

2.1. Simulation

The simulated phantom is a cylindrical with a height and radius of 1 cm with 4 electrodes attached. The simulated experimental setup is shown in Figure 1. Three different configurations are used to highlight the signal's dependence on the EIT sensitivity, where the electrodes are placed at a height of 2 mm, 5 mm, and 8 mm respectively. The AET forward problem is solved using the finite element method, employing a mesh of 310413 tetrahedral elements. The conductivity is discretized with a less fine mesh of 53398 tetrahedral elements using the Matlab software package EIDORS. We consider 4 different conductivity cases. A homogeneous case, and 3 heterogeneous cases with a background conductivity of 1 and a central cylinder (with a radius of 3 mm and height of 10 mm), central sphere (with a radius of 3mm), and a slightly off-center (centered at (0,0,4) mm) cube (with side length of 6 mm) inclusion respectively. Using 4 attached electrodes, electrodes 1 and 3 are driven with a 1 Amp current while the resultant voltage is measured between 2 and 4. The US wave is simulated using Field-ii (Jensen and Svendsen 1992; Jensen 1996). Field ii is a C-program with a Matlab interface

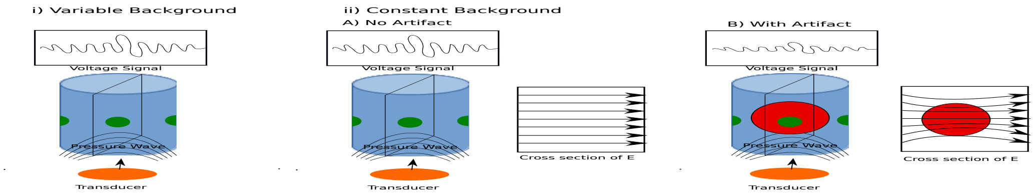

Figure 1: Pictorial representation of the numerical experiments. Two setups are considered: a phantom with an uniform background conductivity simulated with variable conductivity, and a phantom with a constant background conductivity of 1 S/m and a variable inclusion of various shapes which alters the electric field and the internal current flow as illustrated. In each setup an US pressure wave travels through the phantom, generating the AEE signal.

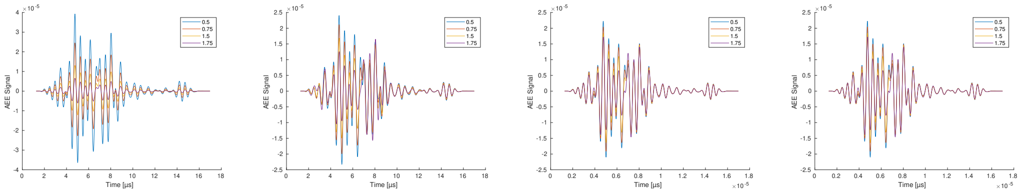

Figure 2: Simulated AEE signal for various conductivity distributions. Left: AEE signal for homogeneous conductivity. Middle left: AEE signal for conductivity with constant background of 1 and a cylindrical inclusion with a variable conductivity. Middle right: AEE signal for conductivity with constant background of 1 and a spherical inclusion with a variable conductivity. Right: AEE signal for conductivity with constant background of 1 and a cubic inclusion with a variable conductivity.

which can easily be interfaced with EIDORS. It does not require an internal spatial mesh in its simulation (instead relying on linear spatial impulse responses). For simplicity the same mesh for the pressure wave and the conductivity are used. It is assumed that the conductivity and the pressure are both constants on each mesh element. A single element concave transducer is simulated with a diameter of 19 mm, a focal length of 300 m with an element size of 1 mm. The excitation consisted of a single period of a 1.6 MHz sinusoid with a Hanning weighting. The excitation was scaled to produce a peak pressure of 2.6 MHz. Our simulated setup is shown in Figure 1. The acoustoelectric coupling constant is set to $k = 10^{-9}$. As EIDORS calculates the EIT Jacobian for a given conductivity mesh, the simulated measured signal can be calculated directly from Equation (5).

3. Results

To investigate the interplay between the EIT sensitivity, the local conductivity, and the AEE signal, the AEE signals are simulated for a variety of different conductivity distributions. Figure 2 shows the effect on the AEE signal from varying the background conductivity with no inclusion, and from varying the conductivity of the inclusion while maintaining a constant background conductivity of $1S/m$.

To highlight the competing effects of EIT in the AEE measurement, Figure 3 shows ratio of the sum of the absolute value of the expected signal (which computes the Aee signal using the homogeneous EIT Jacobian and the true conductivity distribution) to the actual signal (heterogeneous EIT Jacobian and the true conductivity distribution) as well as the ratio of the peak AEE signal per pulse and the EIT measurement as a function of the conductivity.

4. Discussion

The model of the AEE signal given by 4 to 5 has two main implications. Firstly, since the signal is proportional to the EIT Jacobian, areas of a body with zero sensitivity for EIT should still have zero sensitivity in AET. Secondly, and more importantly, the effect of the EIT Jacobian competes with the AEE effect, washing out the naively expected σ dependence. Equation (7) reveals, to first order, an exact cancellation between the conductivity dependence of the AEE and the EIT sensitivity under the assumption of constant current flow. If this held to higher orders, the signal would be determined by the geometry of the target and the form of the pressure wave. In turn the reconstruction of the interior conductivity distribution based solely on a small number of direct AEE measurements (as opposed to using a larger number of measurements to reconstruct the boundary potential is in (Li *et al* 2020)) would be extremely difficult. Fortunately,

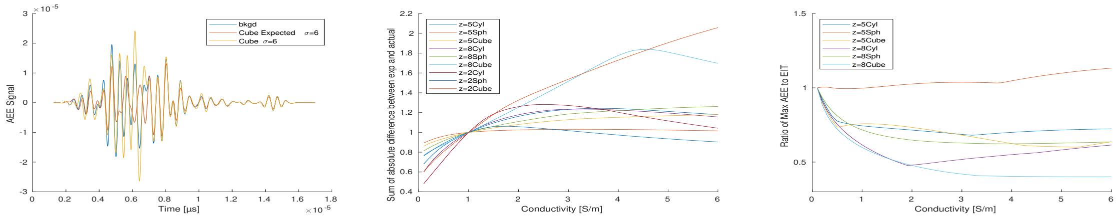

Figure 3: Left: An example of the differences between the expected (homogeneous Jacobian) and simulated (heterogeneous Jacobian) AEE signals. Middle: The ratio of the sum of the absolute value of the expected to actual AEE signals. Right: The ratio of the peak AEE signal to the EIT measurement as a function of changes in conductivity. The EIT in the denominator has been shifted up by 10 V to avoid a sign change which obscures the trend.

Figure 2 shows that while this washout effect does occur, it is hardly close to an exact cancellation. It is indeed the case that the EIT σ dependence overpowers the explicit σ dependence in the AEE coupling as can be clearly seen by the effect on the AEE signal in Figures 2. The signal is suppressed as the background conductivity increases but the rate of this suppression has a strong dependence on the EIT sensitivity (as the comparison between the different electrode placements and the different inclusions clearly demonstrate). The AEE sensitivity to the inclusion conductivity is not completely washed out though there is a suppression in signal when the pressure wave is maximally sensitive to the inclusion. As can be seen in Figure 3 there can be an enhancement relative to the naive expectation on the edge of the inclusion, which for some electrode placements can lead to an increase in the peak signal. The competition between suppression as the wave passes through the center of the inclusion and enhancement as it moves past the edge of the inclusion result in the different shapes seen for the cube ratio curves as edge effects are most significant for the cube. When we normalize the AEE signal to the unperturbed EIT signal, it can be seen that there is still a significant difference between the EIT and AEE signal's sensitivity to conductivity changes. This suggests that while the competition between EIT and AEE signals increases the difficulty of AET reconstructions using a small number of electrodes, a reconstruction relying on a minimal system with as few as two electrodes is achievable.

5. Conclusions

AET is a promising hybrid imaging method with the potential to overcome some of the limitations of EIT. To a good approximation, at a given point in space, th coupling between EIT and the US pressure wave has a linear dependence on the local pressure and the local conductivity and its effect can be modelled as a time dependent perturbation in the local conductivity. Given this linear dependence on σ, one would naively assume that the AEE signal is strongly dependent on the local values of the conductivity making it potentially feasible to reconstruct the conductivity using a small number surface of electrodes. However, the AEE's dependence on the conductivity is roughly cancelled by the measurement sensitivity of EIT, resulting in a partial suppression of the AEE signal as the local conductivity increases. While this cancellation is exact at first order and the EIT effects dominate the measurement's dependence on the conductivity, the AEE measurement is still sensitive to changes of the interior conductivity distribution, and as such conductivity reconstruction with minimal electrodes is still possible.

References

Adesokan B J, Jensen B, Jin B and Knudsen K 2019 Acousto-electric tomography with total variation regularization *Inverse Problems* **35** 035008

Ammari H, Bonnetier E, Capdeboscq Y, Tanter M and Fink M 2008 Electrical impedance tomography by elastic deformation *SIAM Journal on Applied Mathematics* **68**

Jensen J and Svendsen N 1992 Calculation of pressure fields from arbitrarily shaped, apodized, and excited ultrasound transducers *IEEE Transactions on Ultrasonics, Ferroelectrics, and Frequency Control* **39** 262–267

Jensen J 1996 Field: A program for simulating ultrasound systems *Medical and Biological Engineering and Computing* **34** 351–352

Kuchment P and Kunyansky L 2010 Kunyansky, l.: 2d and 3d reconstructions in acousto-electric tomography. inverse probl. 27, 055013 *Inverse Problems* **27**

Li C, An K, Zheng K and Lesselier D 2020 A complete framework for acousto-electric tomography with numerical examples *IEEE Access* **8** 98508–98517

Proceedings of the International Conference of Bioelectromagnetism, Electrical Bioimpedance,
and Electrical Impedance Tomography June 29 – July 1, 2022 / Kyung Hee University, Seoul, Korea

A Modified Howland Current Source Design for Simultaneous EIT/ECG Data Acquisition

Ahmed Abdelwahab, Omid Rajabi Shishvan, Gary J. Saulnier
Electrical and Computer Engineering Department, University at Albany - State University of New York, Albany, NY, USA

Correspondence : Ahmed Abdelwahab, e-mail : aabdelwahab@albany.edu

Abstract– The current source is one of the most critical circuits in electrical impedance tomography (EIT) hardware systems. The simplicity and excellent performance of the Howland current source makes it a prime candidate for this role in EIT systems. Although the Howland source and its family may be the best option for the high-frequency EIT operation, its low frequency noise may also limit the implementation of a system to simultaneously collect electrocardiogram (ECG) and EIT signals from the electrodes. This paper proposes modifications to the conventional Howland source to make is suitable for simultaneous EIT and ECG. The preliminary experimental results of this modified Howland show significant improvement in the collected ECG signal quality in the presence of the EIT signal.

Keywords: EIT, ECG, Howland source.

1 Introduction

A large set of important physiological parameters and vital signs can be measured from the chest. For example, chronic heart diseases can be diagnosed via ECG measurements (Bashi *et al.* 2017). Some other studies showed the ability to assess relevant vital signs of asthma or cystic fibrosis using EIT images (Frerichs *et al.* 2016). So, combining and relating the synchronized EIT and the ECG measurements may provide even a more profound insight into the relationship between lung ventilation events and cardiac activities. A robust, simultaneous EIT/ECG signal acquisition system is required for these applications. This system should be able to provide an acceptable resolution for both signals to be used for diagnostic purposes.

In this paper, we will be continuing and building upon the simultaneous EIT/ECG acquisition approach presented in (Abdelwahab *et al.* 2021). The approach integrates the combined EIT/ECG signal over an integral number of cycles of the EIT excitation frequency to produce the nearly complete suppression of the EIT signal. The experimental results shown in that paper validated the ability of the proposed approach to isolate synthesized ECG signals in the presence of EIT signals. Further investigation, however, showed that performance degraded significantly when the source of the ECG signal had a high output impedance, which is the case with actual ECG signals. Specifically, the recovered ECG signals became unacceptably noisy as the source impedance for the ECG signal was increased. This degradation was traced to the Howland current source (Franco 2003) that is used to supply the EIT excitation, leading to further exploration of the current source behaviour in the ECG band near DC. The scope of this paper will mainly focus on improving the Howland circuit design used for EIT imaging to enhance the recovered ECG waveforms. The proposed modification of the Howland circuit includes adding a series feedback capacitor in the positive feedback path of the Howland to reduce the injection of low frequency noise and the use of a series capacitor on the output to reduce the loading of the ECG signal. The sections below detail the modifications and show the performance improvement that they provide.

2 System Requirements

For excellent EIT performance, it is required that the current source maintain a very high output impedance over the EIT operation bandwidth. For a simultaneous EIT/ECG system, this high output impedance range must be expanded to cover the ECG bandwidth, which is from 100 mHz – 150 Hz (Bashi *et al.* 2017), orders of magnitude below the typical EIT excitation range of 10 kHz to 1 MHz, to avoid loading the ECG signal. Obtaining a high output impedance at low frequencies is not difficult with a Howland source; in fact, it is easier than at higher frequencies where output capacitance degrades performance. However, the output current noise of the Howland source, which is higher near DC due to the $1/f$ noise introduced by the op amp, will flow through the high low-frequency output impedance to produce a significant voltage noise. Given the small amplitude of the ECG signal, generally on the order of 1 mV or less, this noise voltage can severely degrade the recovered ECG signal. The challenge, then, is to modify the current source to provide high output impedance over the EIT and ECG frequency range while also maintaining low noise near DC.

3 Modifications to Howland circuit

The standard Howland current source, shown at the left in Figure 1, ideally can achieve an infinite output impedance by balancing its resistor bridge network (Franco 2003). The modified version of the Howland is shown at the right in the figure. The first modification introduced is moving the voltage source driving the Howland from R_1 to R_3, which makes the circuit perform as an inverting voltage-to-current converter. This change provides an extra degree of patient protection by electrically isolating the voltage source driving the Howland circuit from the Howland source output attached to the patient.

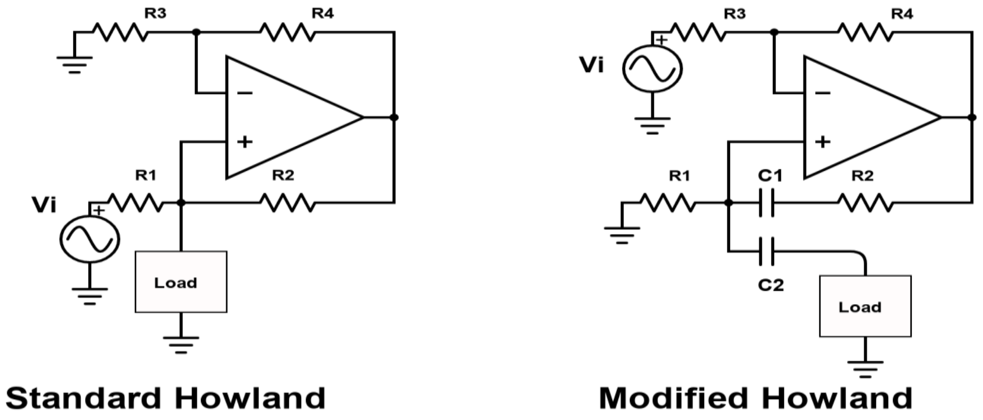

Figure 1. The Standard textbook version of the Howland source (Franco 2003) is shown vs the proposed modified Howland version.

The second modification to the standard Howland circuit is adding the capacitor C_1 into the positive feedback path. The insertion of this capacitor has double benefits. First, it blocks any path for a DC signal to propagate to the Howland output attached to the patient. Second, it reduces the noise generated by the Howland in the ECG bandwidth by unbalancing the resistor bridge at low frequencies, reducing the source output impedance. The value of C_1 is large enough that, at high frequencies in range of the EIT excitation, it presents a very low impedance relative R_2 and has little effect on the resistor balance. At low frequencies, however, the impedance presented by C_1 becomes large and, acting in series with R_2, makes the circuit unbalanced and reduces the output impedance. A lower output impedance for the source results in the output noise current producing a smaller noise voltage.

The output impedance results shown in Figure 2 were obtained from LTSpice (Analog Devices) simulation of the Howland circuit implemented using the low noise Analog Devices AD8033 op amp, 2 kΩ resistors for R_1 and R_3, and 0.5 kΩ resistors for R_2 and R_4. The load is a 100 kΩ resistor and this load resistance is considered to be part of the output impedance since it will contribute to the conversion of the output current noise into a voltage noise. The results on the left do not include C_1 while those on the right use a 10 µF capacitor for C_1. Each figure shows the output resistance and output capacitance when the output impedance is modelled as a parallel RC network. The capacitor C_1 is nearly an open circuit at low frequencies, and the results show that it greatly reduces the both the output resistance and capacitance at frequencies below 1 kHz while having little effect at higher frequencies.

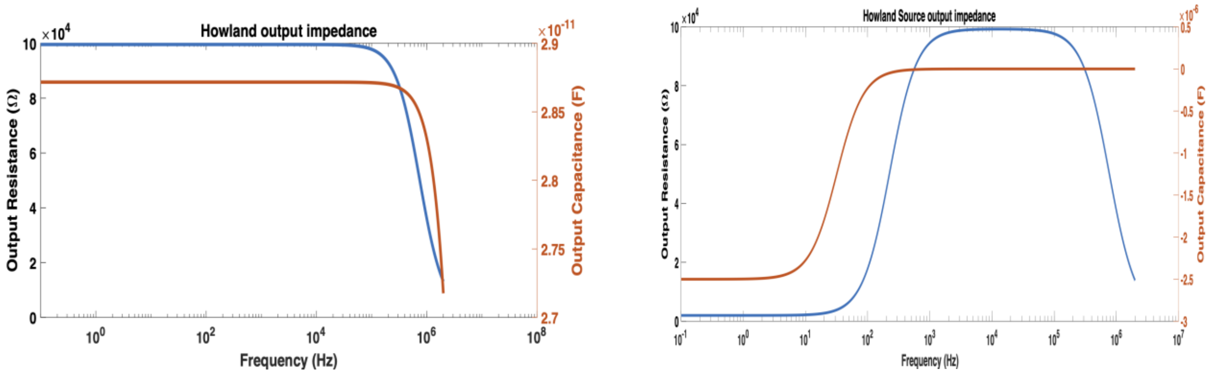

Figure 2. The figure shows a simulation results of the Howland output impedance, without C_1 (Left), with C_1 (Right).

Although the reduction in output impedance at low frequencies obtained adding the capacitor C_1 is beneficial for reducing noise in the ECG band, this same low output impedance will make the Howland output load down the ECG signal. The IEC-60601 medical standards for ECG recording indicates that the input impedance of the ECG buffer should not be less than 10 MΩ to provide a diagnostic ECG recording (Young & Schmid 2021). This high value of input impedance would be very difficult to achieve in a practical implementation of simultaneous EIT/ECG, but a reasonably high value is needed to recover an acceptable ECG waveform.

The addition of C_2 as shown in the diagram on the right in Figure 1 is one solution to the problem. If C_2 is a sufficiently small capacitor, it will introduce a reasonably high series impedance at the ECG frequencies, helping to isolate the Howland output from the ECG signal. In our experiments we have used $C_2 = 10$ nF. With this configuration, the overall output impedance Z_{out} seen from the load side, i.e. looking back from the electrode, is given by

$$\mathrm{Z_{out}} = \left(\frac{1}{j2\pi \mathrm{f} C_2} + Z_{Howland}\right) \parallel Z_{Load} \tag{1}$$

Where $Z_{Howland}$ is the intrinsic Howland output impedance, Z_{Load} is the load impedance shown on the right in Figure 1, and ‖ indicates that the impedances are in parallel.

From Equation (1), the Howland output impedance $Z_{Howland}$ with capacitor C_1 in the ECG range is low (as shown in Figure 2 Right), which results in a smaller noise voltage. While the overall impedance seen from the load side Z_{out} has a much larger magnitude of about 108 kΩ at 150 Hz due to the 10 nF capacitor C_2. So, this configuration has provided a lower voltage noise while reducing the ECG signal loading.

4 Experiments and Results

A combination of simulation and experimental setups were used to verify the validity of the proposed modification to the Howland design. The aim is to prove how these modifications enhanced quality of the recovered ECG signal with the simultaneous system in terms of noise reduction and reducing the loading effect caused by the DC blocking capacitor C_1.

4.1 Noise analysis

The Howland configuration described in the previous section was simulated in LTspice to evaluate its noise performance with and without the DC blocking capacitor C_1 of 10 µF. The resistor values remain the same with 2 kΩ for R_1 and R_3, and 0.5 kΩ for R_2 and R_4. For these simulations, the AD8033 op amp has been replaced with a lower noise device, the ADA4896. The new op amp provides about one-fourth of the voltage noise density compared with the AD8033 used earlier, with $2.4\ nV/\sqrt{Hz}$ compared with $11\ nV/\sqrt{Hz}$ at 100 kHz. The total RMS noise at the Howland output for the ECG bandwidth [100 mHz – 150 Hz] was $15.536\ \mu V$ without C_1, and dropped to $681.78\ nV$ with the presence of C_1. These results make perfect sense, as the capacitor C_1 is nearly an open circuit at simulated range and this configuration provides a low Howland output impedance and hence a smaller noise voltage with the same load connected.

4.2 Recovered ECG signal

The same ECG separation approach discussed in (Abdelwahab *et al.* 2021), along with the EIT system described in (Saulnier *et al.* 2020), was used to experimentally validate the enhancement of the ECG recording with an active EIT signal. A diagram of the experimental setup is shown in Figure 3. A lab-generated ECG waveform with a repetition rate of 1.5 Hz and amplitude of 1 mV_{pp} is fed into the system through a 100 kΩ series resistor. On the system side of the 100 kΩ, the signal sees the impedance denoted by Z due to the Howland current source as well as an AC-coupled voltage buffer. The RC high-pass filter that precedes the voltage buffer input has a cut-off (-3 dB) frequency of 159 mHz. The impedance Z presented by the Howland can be either Z_{out} from equation (1) when the capacitor C_2 is present or simply $Z_{Howland} \parallel Z_{Load}$ when the capacitor is replaced by a short. In the experimental setup, $Z_{Load} = 100$ kΩ. The output of the buffer is processed as described in (Abdelwahab *et al.* 2021) to produce one ECG sample per burst of the EIT signal, resulting in a final sampling rate of approximately 1 kHz. The digital signal at a 1 kHz sampling rate is processed by a second-order Butterworth 150 Hz low-pass filter to set the ECG bandwidth and a line frequency notch filter.

Figure 4 shows the impact of including the 10 nF C_2 capacitor. The waveforms show the digital signals after the filtering mentioned above. The waveform on the left is obtained when C_2 is replaced by a short. The signal is very small due to the low output impedance of the Howland source created by the presence of C_1 in its positive feedback path and dominated by noise. In contrast, the waveform on the right shows the improvement caused by using $C_2 = 10$ nF. The results confirmed that this capacitor had done its job of reducing the ECG signal loading and maintaining the low noise performance needed. The reconstructed ECG signal is less noisy with the proposed configuration of the Howland compared to the standard circuit and the results presented in (Abdelwahab *et al.* 2021).

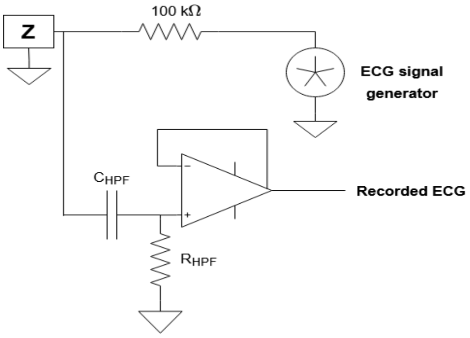

Figure 3. Experimental setup for ECG recording.

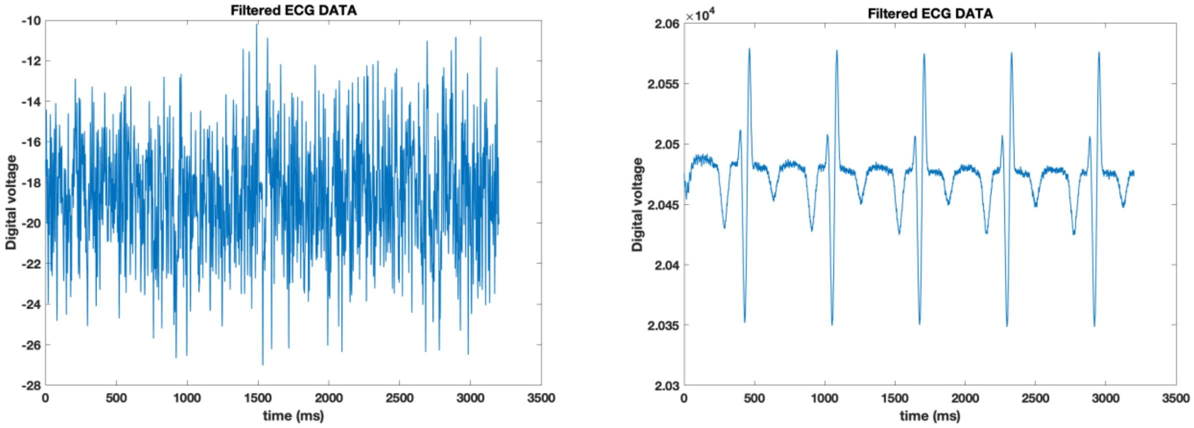

Figure 4. The reconstruced ECG waveform with the 100 kΩ in seres without capacitor C_2 (left), with C_2 (right).

5 Conclusions

In this paper, three modifications to the standard Howland circuit design were discussed. These modifications aim to enhance the simultaneous EIT/ECG data acquisition system to improve the ECG data recording. The initial experimental results were promising showing a clean reconstructed ECG signal which can be used for timing alignment with the collected EIT data. The added capacitor C_1 has provided a less noisy current source as it reduced the output impedance and hence, the total RMS voltage noise by about 96% for the same load. Also, it added an extra degree of patient protection by blocking DC from propagating to the patient side. Additionally, the capacitor C_2 has reduced the ECG loading while maintaining the noise performance improvement. In all, the two capacitors have introduced the DC blocking feature and the lower noise performance while reducing the ECG signal loading.

Acknowledgments

Research reported in this paper was supported by the National Institute of Biomedical Imaging and Bioengineering of the National Institutes of Health under award number 1R01EB026710-01A1. The content is solely the responsibility of the authors and does not necessarily represent the official views of the National Institutes of Health.

References

Abdelwahab, A., Rajabi Shishvan, O. & Saulnier, G. J. 2021, 'A new method for simultaneous EIT/ECG data acquisition', *Proceedings of 21st International Conference on Biomedical Applications of Electrical Impedance Tomography (EIT 2021).*

Bashi, N., Karunanithi, M., Fatehi, F., Ding, H. & Walters, D. (2017), 'Remote monitoring of patients with heart failure: An overview of systematic reviews', *Journal of Medical Internet Research* **19**, e18.

Franco, S. (2003), *Design with Operational Amplifiers and Analog Integrated Circuits*, 3rd edn, McGraw-Hill, Inc., New York, NY, USA.

Frerichs, I., Zhao, Z., Becher, T., Zabel, P., Weiler, N. & Vogt, B. (2016), 'Regional lung function determined by electrical impedance tomography during bronchodilator reversibility testing in patients with asthma', *Physiological Measurement* **37**(6), 698–712.

Saulnier, G. J., Abdelwahab, A. & Rajabi Shishvan, O. (2020), 'DSP-based current source for electrical impedance tomography', *Physiological Measurement* **41**(6), 064002.

Young, B. & Schmid, J.-J. (2021), 'The new ISO/IEC standard for automated ECG interpretation', *Hearts* **2**(3), 410–418.

Proceedings of the International Conference of Bioelectromagnetism, Electrical Bioimpedance,
and Electrical Impedance Tomography June 29 – July 1, 2022 / Kyung Hee University, Seoul, Korea

EIT-based Surgical Margin Probe Development

Shannon Kossmann[1], Sophie Lloyd[1], Ethan Murphy[1] and Ryan Halter[1,2]
[1]Thayer School of Engineering, Dartmouth College, Hanover, NH, USA
[2]Geisel School of Medicine, Dartmouth College, Hanover, NH, USA

Correspondence : Shannon Kossmann, e-mail : shannon.e.kossmann.th@dartmouth.edu

Abstract–The presence of positive surgical margins following prostate cancer surgery carry a risk of biochemical recurrence for patients undergoing these procedures. Our group is designing an impedance sensing probe with 8 current drive electrodes and 25 interior voltage pickup electrodes to provide intraoperative surgical margin assessment based on the electrical property contrast present between benign prostate, malignant prostate, and peri-prostatic tissues. Previously presented work has demonstrated successful localization of a 2mm inclusion in simulation. Here experimental validation of localizing small metal inclusions in saline using this small form-factor probe geometry is presented.

Keywords: prostate cancer; surgical margin assessment; EIT imaging

1. Introduction

Prostate cancer has the highest incidence rate of all cancers in men. In 2022, a total of 268,490 new diagnoses are expected and 34,500 men are projected to die as a result of their cancer (Siegel *et al* 2022). Robot-assisted radical prostatectomy is a common surgical procedure used to remove the prostate for men with localized prostate cancer. There is no efficient, reliable technology clinically available to assess the surgical margins while the patient is still in surgery, ensuring the cancerous tissue has been entirely removed (Eissa *et al* 2020). The length of the positive surgical margin is clinically relevant, with larger positive margins resulting in increased risk of recurrence and disease progression (Hollemans *et al* 2020). Our group has been developing a probe compatible with surgical robot systems that utilizes bioimpedance to detect and localize positive surgical margins during surgery. For a device to be compatible with the surgical robot, the device must be less than 12 mm in diameter requiring a small electrode array. A previous *ex vivo* study of 19 prostates has established our ability to distinguish benign and cancerous prostatic tissue with good predictive power (area-under the curve (AUC) values of 0.85) (Murphy *et al* 2017).

A redesign of the probe configuration to increase the signal to noise ratio has led to the introduction of dedicated current source/sink electrodes and smaller, internal voltage pickup electrodes. The increased size of the current drive/sink electrodes reduces the contact impedance while smaller voltage pickup electrodes allow for more accurate localization of an inclusion. This electrode array has already been demonstrated to localize a 2 mm inclusion at 10% conductivity contrast in simulation (Kossmann *et al* 2021). Here, initial saline experiments to validate simulated results are presented.

2. Methods

Prior work focused on developing a representative and accurate 3D finite element method (FEM) mesh with approximately 250 thousand nodes and 1.45 million elements. The mesh incorporates electrode boundaries and was designed to optimize sensitivity within the imaging region of the electrode array being deployed for laparoscopic tumor detection. The optimized mesh was then used to simulate absolute voltage differences measured at the inner electrodes when current is driven

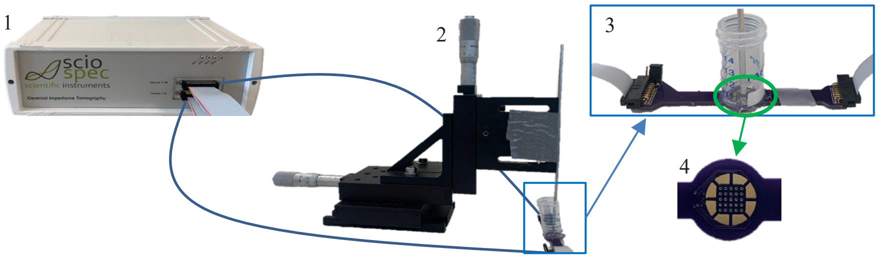

Figure 1. Experimental setup showing Sciospec EIT system (1) connecting to an optical stage with the metal inclusion (2) going into the electrode array with a tank attached for saline tests (3), with a zoomed in image of the electrode configuration (4).

through a series of patterns between the eight outer electrodes. Initial experimental validation tested localization of small metal inclusions based off simulated reconstructions of tumors in benign tissue and metal in saline solution (Fig 2a). To validate simulated predictions, a plastic tank was fixed around the printed circuit board electrode array and filled with 0.2 S/m saline. Drive patterns injecting current between the outer eight electrodes were performed using a Sciospec 32 channel EIT system while voltages were simultaneously measured on 24 of the 25 inner electrodes (the central interior electrode was not used due to the limit of 32 channels available). Voltage measurements initially recorded with only saline solution in the tank served as a background reference data set. Subsequent sets of voltages were recorded with a 2.4 mm diameter metal rod positioned 0.8 mm above the surface of the electrode array using an optical stage to control positioning. Difference EIT reconstructions were computed between the reference blank saline tank and the metal inclusion configurations. The metal inclusion was positioned at various locations within the imaging domain to evaluate the spatial sensitivity to localizing small inclusions.

3. Results and Conclusion

Our EIT reconstructions successfully localize and track a small, 2.4 mm inclusion around the electrode array (Figure 2c,d). Tracking was performed with the metal rod above the surface of the electrode array, demonstrating sensitivity to conductivity changes at depth. While the sensitivity decreases as depth is increased due to the drop off in the current density field, the application of surgical margin assessment is primarily concerned with inclusions located *at* the surface of the imaging domain. It should be noted that inclusions appeared closer to the center of the electrode array in experimental data which may be due to increased distance from the electrode surfaces. Future work includes using a phantom model with materials of approximately 10% contrast to mirror expected *in vivo* benign and cancerous prostate tissue admittivity. These preliminary experimental results help to validate previous simulation fiundings indicating the potential of this probe geometry for use in identifying and localizing positive surgical margins during prostatectomies.

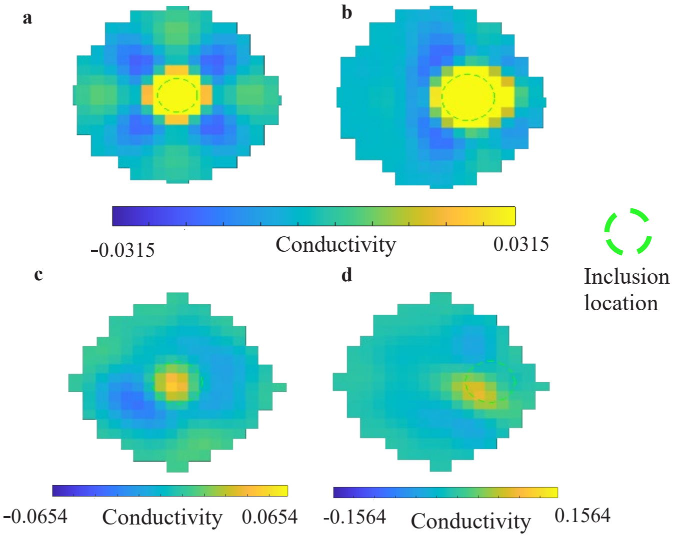

Figure 2. EIT reconstructions from simulations and experimental data. (**a**) Simulated 1.5 mm metal inclusion. (**b**) Simulated 2 mm metal inclusion near right-side current drive electrodes. (**c,d**) Experimental 2.4 mm metal inclusion in center and near right-side current drive electrodes.

Acknowledgments

This work was supported by NIH grants 1R01CA237654 and STTR R41CA235994.

References

Eissa A, Zoeir A, Sighinolfi M C, Puliatti S, Bevilacqua L, Del Prete C, Bertoni L, Azzoni P, Bonetti L R, Micali S, Bianchi G and Rocco B 2020 “Real-time” Assessment of Surgical Margins During Radical Prostatectomy: State-of-the-Art - ClinicalKey *Clin. Genitourin. Cancer* **18** 95–104

Hollemans E, Verhoef E I, Bangma C H, Rietbergen J, Helleman J, Roobol M J and van Leenders G J L H 2020 Prostate Carcinoma Grade and Length But Not Cribriform Architecture at Positive Surgical Margins Are Predictive for Biochemical Recurrence After Radical Prostatectomy *Am. J. Surg. Pathol.* **44** 191–7

Kossmann S, Murphy E K, Doussan A and Halter R J 2021 Simulation Study of a New EIT-based Surgical Margin Probe *Proceedings of the 21st International Conference on Biomedical Applications of Electrical Impedance Tomography* International Conference on Biomedical Applications of Electrical Impedance Tomography (Galway, Ireland) p 46

Murphy E K, Mahara A, Khan S, Hyams E S, Schned A R, Pettus J and Halter R J 2017 Comparative Study of Separation between Ex-Vivo Prostatic Malignant and Benign Tissue using Electrical Impedance Spectroscopy and Electrical Impedance Tomography *Physiol. Meas.* **38** 1242–61

Siegel R L, Miller K D, Fuchs H E and Jemal A 2022 Cancer statistics, 2022 *CA. Cancer J. Clin.* **72** 7–33

DAY 2

Thursday, June 30, 2022

Plenary Talk 02

Speaker Seon Jeong Kim (Hanyang University)

"Harvesting electrical energy from twisted carbon nanotube yarns and biomedical applications"

Proceedings of the International Conference of Bioelectromagnetism, Electrical Bioimpedance,
and Electrical Impedance Tomography June 29 – July 1, 2022 / Kyung Hee University, Seoul, Korea

Harvesting electrical energy from twisted carbon nanotube yarns and biomedical applications

Seon Jeong Kim
Center for Self-Powered Actuation, Department of Biomedical Engineering, Hanyang University, Seoul 04763, Korea

Correspondence : Seon Jeong Kim, e-mail : sjk@hanyang.ac.kr

Abstract– Mechanical energy harvesters such as piezoelectric, ferroelectric, or triboelectric nanogenerators are rising for supplying continuous electrical energy without batteries to biomedical systems from wearable health monitoring to implantable medical devices. Here, reported a novel carbon nanotube (CNT) yarn type energy harvester, which electrochemically converts mechanical energy into electrical energy. A highly twisted and coiled yarn has produced 250 W/kg of peak power with 30 Hz of stretching cycles. When the yarn was stretched, the twist-induced pressure decreases the intrabundle void space of the CNT bundles, and the resultant capacitance decrease produces a voltage change. This energy harvester was sewn into textiles for use as a self-powered respiration sensor and used in the ocean to harvest from wave energy. Also, when applied to an *in vitro* artificial gastric system, the coiled CNT yarn could sense the volumetric changes of stomach. To increase energy harvesting performance in biofluids, biomolecule was implemented to the CNT yarn. Further studies on increasing the output power and the energy conversion efficiency will make this high gravimetric power density twisted CNT yarn harvesters to assist or replace the batteries used in biomedical devices.

References

Kim S H, Haines C S, Li N, Kim K J, Mun T J, Choi C, Di J, Oh Y J, Oviedo J P, Bykova J, Fang S, Jiang N, Liu Z, Wang R, Kumar P, Qiao R, Priya S, Cho K, Kim M, Lucas M S, Drummy L F, Maruyama B, Lee D Y, Lepro X, Gao E, Albarq D, Ovalle-Robles R, Kim S J and Baughman R H 2017 Harvesting electrical energy from carbon nanotube yarn twist *Science* **357** 773-778

Jang Y, Kim S M, Kim K J, Sim H J, Kim B -J, Park J W, Baughman R H, Ruhparwar A and Kim S J 2019 Self-powered coiled carbon-nanotube yarn sensor for gastric electronics *ACS Sens.* **4** (11) 2893-2899

Kim H, Park J W, Hyeon J S, Sim H J, Jang Y, Shim Y, Huynh C, Baughman R H and Kim S J 2020 Electrical energy harvesting from ferritini biscrolled carbon nanotube yarn *Biosens. Bioelectron.* **164** 112318

DAY 2

Thursday, June 30, 2022

Mini Symposium 03

Stroke Volume and Lung Perfusion Measurements using Electrical Impedance Tomography : State of the Art

Organizer Zhanqi Zhao (Fourth Military Medical University)
Yun Long (Peking Union Medical College Hospital)

M 03-01 **Electrical Impedance Tomography Use for the Assessment of Regional Lung Perfusion**
Inéz Frerichs (University Medical Centre Schleswig-Holstein)

M 03-02 **Estimation of Stroke Volume using Lead forming for Continuous Monitoring without image reconstruction**
Kyounghun Lee (Kyung Hee University Hospital)

M 03-03 **Saline bolus-based EIT method of lung perfusion in the diagnosis of pulmonary embolism**
Siyi Yuan (Peking Union Medical College Hospital)

M 03-04 **Lung perfusion by EIT in COVID-19**
Tommaso Mauri (University of Milan)

M 03-05 **Regional Ventilation/Perfusion match by Electrical Impedance Tomography: where are we now?**
João Batista Borges (Charles University)

ICBEM Bioelectromagnetism ICBEI Electrical Bioimpedance EIT Electrical Impedance Tomography

Proceedings of the International Conference of Bioelectromagnetism, Electrical Bioimpedance,
and Electrical Impedance Tomography June 29 – July 1, 2022 / Kyung Hee University, Seoul, Korea

Electrical Impedance Tomography Use for the Assessment of Regional Lung Perfusion

Inéz Frerichs[1]

[1]Department of Anaesthesiology and Intensive Care Medicine, University Medical Centre Schleswig-Holstein, Campus Kiel, Kiel, Germany

Correspondence : I. Frerichs, e-mail : frerichs@anaesthesie.uni-kiel.de

Abstract–Chest electrical impedance tomography is the most frequent application of this functional imaging method both in research and clinical use. The focus lies primarily on the assessment of regional lung ventilation, i.e., of those changes of pulmonary electrical bioimpedance that are associated with the changes of air volume in the lungs during spontaneous or mechanically assisted ventilation. Equally important, however, is the assessment of regional lung perfusion, i.e., of the electrical bioimpedance variation related to the regional blood flow in pulmonary vessels. Both of these physiological processes of ventilation and perfusion are needed to secure adequate respiratory gas exchange in the lungs. The knowledge of their regional distribution allows an evaluation of ventilation-perfusion matching. Three different approaches to the measurement of regional lung perfusion have been described. They are based on the analysis of 1) the quasiperiodic heart beat-related impedance changes [e.g., 1], 2) the impedance fall caused by continuous oxygen uptake during a breath-hold after preceding preoxygenation [2] and 3) the impedance fall induced by a central venous administration of a hypertonic saline bolus which serves as a contrast agent [e.g., 3]. The latter method has been validated with reference imaging methods [e.g., 3, 4] and it enables a reliable estimation of regional pulmonary blood flow. It is also increasingly being applied in a clinical setting, for instance to determine the effects of mechanical ventilator settings on the degree of ventilation-perfusion mismatch in critically ill patients [e.g., 5] or in detection of pulmonary embolism.

Acknowledgments

The author acknowledges the current funding by the European Commission within the EU Research and Innovation Programme Horizon 2020 (project WELMO, grant 825572).

References

1. Frerichs I, Pulletz S, Elke G, Reifferscheid F, Schadler D, Scholz J, Weiler N 2009 Assessment of changes in distribution of lung perfusion by electrical impedance tomography. *Respiration* **77** 282-91.
2. Elke G, Pulletz S, Schadler D, Zick G, Gawelczyk B, Frerichs I, Weiler N 2011 Measurement of regional pulmonary oxygen uptake-a novel approach using electrical impedance tomography. *Physiol. Meas.* **32** 877-86.
3. Frerichs I, Hinz J, Herrmann P, Weisser G, Hahn G, Quintel M, Hellige G 2002 Regional lung perfusion as determined by electrical impedance tomography in comparison with electron beam CT imaging. *IEEE Trans. Med. Imaging* **21** 646-52.
4. Kircher M, Elke G, Stender B, Hernandez Mesa M, Schuderer F, Dossel O, Fuld MK, Halaweish AF, Hoffman EA, Weiler N, Frerichs I 2021 Regional lung perfusion analysis in experimental ARDS by electrical impedance and computed tomography. *IEEE Trans. Med. Imaging* **40** 251-261.
5. He H, Chi Y, Long Y, Yuan S, Frerichs I, Moller K, Fu F, Zhao Z 2020 Influence of overdistension/recruitment induced by high positive end-expiratory pressure on ventilation-perfusion matching assessed by electrical impedance tomography with saline bolus. *Crit. Care* **24** 586.

Proceedings of the International Conference of Bioelectromagnetism, Electrical Bioimpedance,
and Electrical Impedance Tomography June 29 – July 1, 2022 / Kyung Hee University, Seoul, Korea

Estimation of Stroke Volume using Lead forming for Continuous Monitoring without image reconstruction

Kyounghun Lee[1]
[1]Medical Science Research Institute, Kyung Hee University Hospital, Seoul, Korea

Correspondence : Kyounghun Lee, e-mail : imlkh84@gmail.com

Abstract–We first review conventional methods of estimating stroke volume (SV). Then, we propose leadforming method for beat-to-beat stroke volume measurement without image reconstruction, and assess its feasibility on an existing in vivo animal dataset. A deterministic leadforming algorithm was developed to extract a cardiac volume signal (CVS) from 208-channel trans-impedance data acquired every 20 ms by an electrical impedance tomography (EIT) device. SV_{EIT} value was computed as a valley-to-peak value in the CVS. The method was validated using the existing dataset from five mechanically-ventilated pigs undergoing ten mini-fluid challenges. An invasive hemodynamic monitor was used in the arterial pressure-based cardiac output (APCO) mode to simultaneously measure SV_{APCO} values. The leadforming method could reliably extract the CVS from the 208-channel trans-impedance data measured with the EIT device, from which SV_{EIT} was computed. The SV_{EIT} value was comparable to those from the invasive hemodynamic monitor.

References

Lee K, Jang G Y, Kim Y and Woo E J 2021 Multi-channel Trans-impedance Leadforming for Cardiopulmonary Monitoring: Algorithm Development and Feasibility Assessment using In Vivo Animal Data *IEEE Trans. Biomed. Eng.,* Early Access

Jang G Y, Jeong Y J, Zhang T, Oh T I, Ko R E, Chung C R, Suh G Y and Woo E J 2020 Noninvasive, simultaneous, and continuous measurements of stroke volume and tidal volume using EIT: feasibility study of animal experiments *Sci. Rep.* **10***,* 11242

Proceedings of the International Conference of Bioelectromagnetism, Electrical Bioimpedance,
and Electrical Impedance Tomography June 29 – July 1, 2022 / Kyung Hee University, Seoul, Korea

Saline bolus-based EIT method of lung perfusion in the diagnosis of pulmonary embolism

Siyi Yuan, Mengru Xu
Department of Critical Care Medicine, State Key Laboratory of Complex Severe and Rare Diseases, Peking Union Medical College Hospital, Peking Union Medical College, Chinese Academy of Medical Sciences, Beijing, China

Correspondence :Huaiwu He, e-mail : hehuaiwu@pumch.cn, Yun Long, e-mail : iculong_yun@163.com

Abstract

Introduction EIT was proposed to quantitatively assess regional lung perfusion with saline bolus injection, which has been gained attention in the diagnosis of pulmonary embolism. **Purpose** This lecture seeks to provide an overview of experimental and clinical studies with the aim of clarifying the clinical relevance of using saline bolus EIT method to identify pulmonary embolism(PE). **Main methods** systematic review and clinical practice experiences of our medical center. **Findings** Several experimental studies had shown that regional lung perfusion after pulmonary-embolism-like events could be effectively detected by EIT and bolus saline. The normal ventilation distribution with massive perfusion defects in the affected regions as determined by EIT imaging showed strong diagnostic efficiency. A prospective observational study found patients with PE had significantly higher dead space% and lower V/Q match% than patients without PE. A cutoff value of 30.37% for dead space% resulted in a sensitivity of 90.9% and a specificity of 98.6% for PE diagnoses. Moreover, it was demonstrated that EIT perfusion imaging was useful in diagnosing and monitoring the therapeutic response of PE at the bedside in our experiences. **Conclusion** Further study is required to validate the impact of the described saline bolus EIT method on decision-making, therapeutic management, and outcomes in critically ill patients with suspected pulmonary embolism.

Acknowledgments

N/A

References (3 to 5 recommended)[1-3]

1. Xu M, He H, Long Y: **Lung Perfusion Assessment by Bedside Electrical Impedance Tomography in Critically Ill Patients**. *Frontiers in physiology* 2021, **12**:748724.
2. He H, Chi Y, Long Y, Yuan S, Zhang R, Frerichs I, Moller K, Fu F, Zhao Z: **Bedside Evaluation of Pulmonary Embolism by Saline Contrast Electrical Impedance Tomography Method A Prospective Observational Study**. *American journal of respiratory and critical care medicine* 2020.
3. He H, Long Y, Frerichs I, Zhao Z: **Detection of Acute Pulmonary Embolism by Electrical Impedance Tomography and Saline Bolus Injection**. *American journal of respiratory and critical care medicine* 2020.

Proceedings of the International Conference of Bioelectromagnetism, Electrical Bioimpedance,
and Electrical Impedance Tomography June 29 – July 1, 2022 / Kyung Hee University, Seoul, Korea

Lung perfusion by EIT in COVID-19

Tommaso Mauri[1,2]
[1]Department of Anesthesia and Critical Care, Policlinico Hospital, Milan, Italy
[2]Department of Pathophysiology and Transplants, University of Milan, Italy

Correspondence : tommaso.mauri@unimi.it

Abstract

Introduction. COVID 19 may lead to bilateral lung injury requiring intubation and mechanical ventilation. Ventilation-perfusion mismatch is a specific feature of this condition and may be correlated with the patient physiological phenotype, the severity of the disease and the outcome of strategies like PEEP setting and the prone position. Electrical impedance tomography is a bedside imaging tool that allows quantification of pulmonary ventilation-perfusion mismatch.

Purpose. We conducted a series of studies investigating ventilation-perfusion mismatch ion intubated COVID 19 patients and the potential of PEEP and prone position in improving it.

Main methods. Intubated patients with moderate-severe ARDS due to COVID 19 were monitored by EIT and ventilation-perfusion matching was assessed in different regions of the lungs in various conditions (baseline, low-high PEEP, supine-prone position). Perfusion was assessed with the bolus of 5% NaCl solution during end inspiratory occlusion.

Findings. Ventilation-perfusion mismatch is a hallmark of COVID 19 ARDS, with high VQ and dead space as most represented alterations. Higher PEEP applied to recruitable patients and prone position appears to decrease dead space in the non-dependent regions of the lungs and to improve shunt in the dependent regions.

Conclusion. Bedside assessment of ventilation-perfusion matching may help characterize the physiological characteristics of COVID 19 ARDS to correctly stratify patients severity and guide personalised treatment.

Acknowledgments

The authors would like to express their gratitude to all the nurses and staff who cared for COVID 19 patients in Milan in years 2020 and 2021.

References

Grasselli G, Tonetti T, Protti A, Langer T, Girardis M, Bellani G, Laffey J, Carrafiello G, Carsana L, Rizzuto C, Zanella A, Scaravilli V, Pizzilli G, Grieco DL, Di Meglio L, de Pascale G, Lanza E, Monteduro F, Zompatori M, Filippini C, Locatelli F, Cecconi M, Fumagalli R, Nava S, Vincent JL, Antonelli M, Slutsky AS, Pesenti A, Ranieri VM; collaborators. Pathophysiology of COVID-19-associated acute respiratory distress syndrome: a multicentre prospective observational study. Lancet Respir Med. 2020 Dec;8(12):1201-1208. doi: 10.1016/S2213-2600(20)30370-2. Epub 2020 Aug 27. PMID: 32861276; PMCID: PMC7834127.

Spinelli E, Kircher M, Stender B, Ottaviani I, Basile MC, Marongiu I, Colussi G, Grasselli G, Pesenti A, Mauri T. Unmatched ventilation and perfusion measured by electrical impedance tomography predicts the outcome of ARDS. Crit Care. 2021 Jun 3;25(1):192. doi: 10.1186/s13054-021-03615-4. PMID: 34082795; PMCID: PMC8173510.

Mauri T, Spinelli E, Scotti E, Colussi G, Basile MC, Crotti S, Tubiolo D, Tagliabue P, Zanella A, Grasselli G, Pesenti A. Potential for Lung Recruitment and Ventilation-Perfusion Mismatch in Patients With the Acute Respiratory Distress Syndrome From Coronavirus Disease 2019. Crit Care Med. 2020 Aug;48(8):1129-1134. doi: 10.1097/CCM.0000000000004386. PMID: 32697482; PMCID: PMC7188034.

Fossali T, Pavlovsky B, Ottolina D, Colombo R, Basile MC, Castelli A, Rech R, Borghi B, Ianniello A, Flor N, Spinelli E, Catena E, Mauri T. Effects of Prone Position on Lung Recruitment and Ventilation-Perfusion Matching in Patients With COVID-19 Acute Respiratory Distress Syndrome: A Combined CT Scan/Electrical Impedance Tomography Study. Crit Care Med. 2022 Feb 11. doi: 10.1097/CCM.0000000000005450. Epub ahead of print. PMID: 35200194.

Proceedings of the International Conference of Bioelectromagnetism, Electrical Bioimpedance,
and Electrical Impedance Tomography June 29 – July 1, 2022 / Kyung Hee University, Seoul, Korea

Regional Ventilation/Perfusion match by Electrical Impedance Tomography : where are we now?

João Batista Borges M.D., Ph.D.[1]
[1]Institute of Physiology, First Faculty of Medicine, Charles University, Prague, Czech Republic

Correspondence : João Batista Borges, e-mail : joaobatistaborges8@gmail.com

Cyclic variations in pulmonary air and blood content are the major determinants for the changes in thoracic impedance. The high temporal resolution is a crucial aspect of electrical impedance tomography that allows for the study not only of ventilation but also of faster physiological phenomena, such as pulmonary perfusion and the pulsatility of the lung during the cardiac cycle. Lung pulsatility, however, cannot reliably estimate pulmonary perfusion because the cyclic perturbations in local impedance caused by the passage of the stroke volume through the lung can be influenced by changes in parenchyma architecture, distensibility of the small pulmonary vessels, and size and patency of the pulmonary microvascular bed. Notwithstanding, it is possible to estimate regional Ventilation/Perfusion for each pixel in an electrical impedance tomography functional image. The ventilatory component can be calculated as alveolar minute ventilation multiplied by the fraction of tidal volume directed to each pixel, after discounting the anatomical dead-space. Fractional perfusion can be estimated as the sum of maximum-slopes (negative slopes of impedance decay after the bolus of hypertonic solution) for pixels composing a region-of-interest, divided by the sum of maximum-slopes for all pixels within the lung, multiplied by the estimated cardiac output. Importantly, a full computation of Ventilation/Perfusion depends on the cardiac output, which can be calculated from the same saline bolus curve measured by electrical impedance tomography, using a modified Stewart-Hamilton approach. Real-time and timely monitoring of regional Ventilation/Perfusion matching during ongoing ventilation will be an invaluable tool for most causes of respiratory dysfunction.

DAY 2

Thursday, June 30, 2022

Workshop 02

Draeger Korea

W 02 **Image-Guided Lung Protection – Introducing the concept and clinical application examples**
Eckhard Teschner (Draegerwerk AG & Co. KGaA)

Proceedings of the International Conference of Bioelectromagnetism, Electrical Bioimpedance,
and Electrical Impedance Tomography June 29 – July 1, 2022 / Kyung Hee University, Seoul, Korea

Image-Guided Lung Protection – Introducing the concept and clinical application examples

Eckhard Teschner[1]
[1]Draegerwerk AG & Co. KGaA, Luebeck, Germany

Correspondence : Eckhard Teschner, e-mail : eckhard.teschner@draeger.com

Abstract–Various approaches for recruiting the lung of patients with acute respiratory distress syndrome (ARDS) and identifying best positive end-expiratory pressure (PEEP) have been intensively studied over the past decades. However, randomized controlled trials (RCT) have failed so far to demonstrate outcome improvements[1,2] if lung recruitability and regional ventilation distribution was not taken into consideration. The response to attempts of reopening the non-ventilated lung depends largely on the underlying lung conditions, which might be atelectasis, lung consolidation, pleural effusion, or a combination of various conditions. Electrical impedance tomography (EIT) provides non-invasively regional information on the lung continuously at the bedside, is capable of estimating the extent of non-ventilated areas and discriminating the lung conditions. With these capabilities, EIT might provide clinically useful information for optimizing respiratory therapy. First smaller studies investigating the benefits of EIT for titrating PEEP have recently shown promising results[3,4]. This lecture provides an introduction into the challenges of assessing lung recruitability and finding best PEEP, describes the most commonly used EIT-based images and parameters, and how they are used to support these clinical tasks. Clinical application examples are presented to illustrate the patient's heterogenous responses to the same maneuver and to discuss why these responses are so different. Finally, the results of RCTs with EIT-guided PEEP titration are discussed.

Acknowledgments

None

References

1 Cavalcanti AB, Suzumura EA, Laranjeira LN, et al. 2017 Effect of lung recruitment and titrated positive end-expiratory pressure (PEEP) vs low PEEP on mortality in patients with acute respiratory distress syndrome: a randomized clinical trial. *JAMA* 2017 Oct 10;318(14):1335-1345

2 Beitler JR, Sarge T, Banner-Goodspeed VM, et al. 2019 Effect of Titrating Positive End-Expiratory Pressure (PEEP) With an Esophageal Pressure-Guided Strategy vs an Empirical High PEEP-Fio2 Strategy on Death and Days Free From Mechanical Ventilation Among Patients With Acute Respiratory Distress Syndrome: A Randomized Clinical Trial. *JAMA* 2019 Mar 5;321(9):846-857

3 Hsu HJ, Chang HT, Zhao Z et al. 2021 Positive end-expiratory pressure titration with electrical impedance tomography and pressure–volume curve: a randomized trial in moderate to severe ARDS *Physiol. Meas.* 2021 Feb 6;42(1):014002

4 He H, Yang Y, Yuan S et al. 2021 Early individualized positive end-expiratory pressure guided by electrical impedance tomography in acute respiratory distress syndrome: a randomized controlled clinical trial *Critical Care* 2021 Jun 30;25(1):230

DAY 3

Friday, July 1, 2022

Invited Talk 05

Speaker Steffen Leonhardt (RWTH Aachen University)

“The EIT Experience at MedIT Aachen – history and perspectives”

Proceedings of the International Conference of Bioelectromagnetism, Electrical Bioimpedance,
and Electrical Impedance Tomography June 29 – July 1, 2022 / Kyung Hee University, Seoul, Korea

The EIT Experience at MedIT Aachen – history and perspectives

Steffen Leonhardt
Chair for Medical Information Technology, Helmholtz-Institute for Biomedical Engineering, RWTH Aachen University, Aachen, Germany

e-mail : leonhardt@hia.rwth-aachen.de

Abstract – After a short introduction to EIT and its history, the talk will focus on the development of EIT during the last 20 years and connect this to work performed by the presenter and his group. Starting with lung monitoring during artificial ventilation and the development of the Dräger PV500, we will then turn to the rationale for multi-frequency EIT, possible multi-frequency EIT algorithms and the new AixTOM research plattform developed at RWTH Aachen University. The talk will continue by highlighting other medical applications of EIT, like ventilation during contusio, electrical phrenicus stimulation and EIT monitoring during high G experiments, lung perfusion monitoring, and bladder volume monitoring. The talk will end with conclusions and an outlook.

Acknowledgments

The author would like to express his gratitude to all involved students and employees who participated in the presented projects. Without them, most of the results would not have materialized ...

References

Meier T, Luepschen H, Karsten J, Leibecke T, Großherr M, Gehring H and Leonhardt S 2008 Assessment of regional lung recruitment and derecruitment during a PEEP trial based on electrical impedance tomography. *Intensive care medicine* 34 (3) 543-550.

Leonhardt S, Lachmann B 2012 Electrical impedance tomography: the holy grail of ventilation and perfusion monitoring? *Intensive care medicine* 38 (12) 1917-1929.

Leonhardt S, Cordes A, Plewa H, Pikkemaat R, Soljanik I, Moehring K, Gerner HJ, Rupp R 2011 Electric impedance tomography for monitoring volume and size of the urinary bladder. *Biomed Tech* 56 (6) 301–307.

Menden T, Orschulik J, Dambrun S, Matuszczyk J, Santos SA, Leonhardt S, Walter M 2019 Reconstruction algorithm for frequency-differential EIT using absolute values. *Physiological Measurement* 40 (3), 034008.

Menden T, Alcaín GB, Stevenson AT, Pollock RD, Tank H, Hodkinson P, Jolley C, Smith TG, Leonhardt S, Walter M 2021 Dynamic lung behavior under high G acceleration monitored with electrical impedance tomography. *Physiological Measurement* 42 (9), 094001.

DAY 3

Friday, July 1, 2022

Special Session 02

Food Quality Control and Assessment by Impedance Spectroscopy

Organizer Pedro Bertemes Filho (State University of Santa Catarina)

S 02-01 **Bioimpedance spectroscopy as tool for bovine milk rastreability**
Pedro Bertemes Filho (State University of Santa Catarina)

S 02-02 **Measuring perishable seafood using bioimpedance spectroscopy**
Keith Cox (Certified Quality Foods)

S 02-03 **Electrical impedance for fast and simple assessment of sugar beet quality**
Chris Gansauge (Institut für Bioprozessund Analysenmesstechnik)

S 02-04 **Detection of PSE-like meat quality: How does subjective quality ranking compare with bioimpedance testing?**
Sisay Mebre Abie (Norwegian University of Life Sciences)

ICBEM Bioelectromagnetism ICEBI Electrical Bioimpedance EIT Electrical Impedance Tomography

Proceedings of the International Conference of Bioelectromagnetism, Electrical Bioimpedance,
and Electrical Impedance Tomography June 29 – July 1, 2022 / Kyung Hee University, Seoul, Korea

Bioimpedance spectroscopy as tool for bovine milk rastreability

Pedro Bertemes Filho[1], Kaue Felipe Morcelles[1]
[1]State University of Santa Catarina, Dept. Electrical Engineering, Joinville, Brazil

Correspondence: Pedro Bertemes-Filho, e-mail: pedro.bertemes@udesc.br

Abstract

Bovine milk is one of the most consumed foods in the world. However, it is also one of the most illegally adulterated with by biochemical processes. During the production, transport and storage process, many litters of milk end up suffering the addition of chemical adulterants, such as hydrogen peroxide and caustic soda. Like all mammals, the cow suffers from mastitis and whose treatment is carried out with some types of antibiotics. Cow's milk also contains somatic cells that are unsuitable for consumption according to the local standards (400,000 cells/ml, according to MAPA-Brazil). Therefore, there is an immediate need for an accurate and standardized method for detecting CCS, antibiotics and likely adulterants. In addition, the measurement of food parameters, such as fat level, somatic cell concentration and degradation level, are important for milk control and screening. Milk rastreability must also takes into account much more than the production and storage process itself, since adulteration may occur at any stage from farmers to industry. It is necessary to measure the biochemical properties in order to obtain accurate milk parameters. There is no tool for measuring the milk quality in local farmers in a daily basis, including somatic cells and antibiotics data. For this, a measuring device equipped with sensors and artificial intelligence should be developed and distributed by service providers and inspectors, so that the quality of any sample can be measured in loco. Bioimpedance spectroscopy (BIS) has been used over the last decades as robust, accurate, portable and low cost technique for measuring food quality, including bovine milk. It is expected to create a standardized classification of milk, as level "A" (premium), "B" (standard), "C" (regular) and "D" (disapproved). Santa Catarina (Brazil) is one of the largest producers of bovine milk in the country, occupying the fifth place in the national ranking, producing more than 3 billion litters (IBGE, 2021). Therefore, it is highly recommended the adoption of control measures to guarantee the quality of milk, in terms of adulterants, fat level and degradation. The creation of a BIS system for milk rastreability will provide greater reliability for the consumer, in addition to encouraging the adoption of more rigorous production, transport and storage processes.

Acknowledgments

Institutional support by UDESC and financially supported by FAPESC (Nr. 2021TR911).

References (examples)

Pliquett, U. Bioimpedance, (2010): A Review for Food Processing. Food Eng. Rev. 2, 74–94.

Ashoorirad, M., Baghbani, R., Ghalamboran, M. R. Bioimpedance sensor to detect water content in milk based on van Der Pauw method. IET Nanobiotechnol, 15(7):611–618, 2021. doi: 10.1049/nbt2.12056

Bertemes-Filho, P., Valicheski, R., Pereira, R. M., Paterno, A. S. Bioelectrical impedance analysis for bovine milk: Preliminary results. Journal of Physics: Conference Series, (224):012133, 2010. doi:10.1088/1742-6596/224/1/012133

Bertemes-Filho, P., Veiga, E. A. M. The Santa Catarina Mark 1 Bioimpedance System: Preliminary Results. International Journal of Engineering Research and Applications, 3(4):2399-, 2013. Available at http://www.ijera.com/pages/v3no4.html

Proceedings of the International Conference of Bioelectromagnetism, Electrical Bioimpedance,
and Electrical Impedance Tomography June 29 – July 1, 2022 / Kyung Hee University, Seoul, Korea

Measuring perishable seafood using bioimpedance spectroscopy

Keith Cox[1], Pedro Bertemes-Filho[2], and James Lincoln[3]
[1]CQ Foods in Juneau, Alaska, USA
[2]Department of Electrical Engineering in the State University of Santa Catarina, Brazil
[3]CQ Foods in Dallas, Texas, USA

Correspondence : Keith Cox, e-mail : mkcox@certifiedqualityfoods.com

Abstract

Seafood is one of the most expensive and perishable food items in the marketplace. Characterizing the quality or degradation of the tissue is problematic as most tests are either subjective or involve lengthy expensive laboratory techniques. What is clearly needed is a quick non-invasive objective test of seafood tissue quality. Bioelectrical impedance analysis (BIA) has provided some relief but most devices and research have focused on a single frequency of 50 kHz which represents striated skeletal muscle in mammals. Although fish muscle is also striated, its morphological characteristics are different and its characteristics may be better represented with different frequencies. The common practice of freezing seafood also changes the cellular membrane continuity attributing to the poor relationships between electrical measures taken at 50 kHz and quality. Bioimpedance spectroscopy (BIS) can be used to measure electrical properties within a broad range of frequencies thus extending the applicability of bioimpedance into other foodstuffs or improving existing models. The objective of this paper is to use BIS see what frequencies are best predictors of quality (degradation) in both fresh and frozen seafood products. Results indicated that 50 kHz was sensitive to daily tissue changes in fresh fish, but frequencies lower than 20 kHz were best for predicting tissue changes in frozen fish. Lower frequencies are more sensitive to change in connective tissue than at higher frequencies and higher frequencies are more sensitive to cellular membrane changes.

Acknowledgments

The authors would like to express their gratitude for their Institutional support.

References

COURTNEY,, K., J. A. FALKE, M. COX and J. NICHOLS. 2020 Energetic Status of Alaskan Chinook Salmon: Interpopulation Comparisons and Predictive Modeling Using Bioelectrical Impedance Analysis. North American Journal of Fisheries Management

TEIXEIRA, L G ; Bertemes-Filho, P ; KEITH COX, M. . Fish quality investigations using electrical impedance spectroscopy: preliminary results. JOURNAL OF PHYSICS. CONFERENCE SERIES (PRINT), v. 2008, p. 012008, 2021. doi: 10.1088/1742-6596/2008/1/012008

Proceedings of the International Conference of Bioelectromagnetism, Electrical Bioimpedance,
and Electrical Impedance Tomography June 29 – July 1, 2022 / Kyung Hee University, Seoul, Korea

Electrical impedance for fast and simple assessment of sugar beet quality

Chris Gansauge[1], Christa Hoffmann[2], Gunnar Kleuker[2], Uwe Pliquett1 and Thomas Nacke[1]
[1]Institut für Bioprozess- und Analysenmesstechnik Heilbad Heiligenstadt, Germany
[2]Universität Göttingen, Institut für Zuckerrübenforschung, Göttingen, Germany

Correspondence : Chris Gansauge, e-mail : chris.gansauge@iba-heiligenstadt.de

Abstract – Low sugarbeet firmness increases harvesting and storage losses for farmers. Furthermore, the efficiency of processes during handling is influenced by firmness. The aim of the research project was to determine the relationship between firmness parameters, storage losses, beet varieties, quality parameters and beet impedance. To this end, field trials were conducted over three years with up to ten different sugarbeet varieties at four different locations (environmental conditions). This involved extensive chemical laboratory analyses and firmness tests on thousands of beets. Electrical properties were measured using electrical impedance spectroscopy. Modelling of the impedance spectrum provided the parameters for further data processing. Measurements were made on stampings as well as external measurements on complete beets using penetration electrodes. The results of the easy-to-handle external measurement were comparable to those of the more demanding stamping. One important finding was that the influence of beet size on impedance was negligible. Further, it was shown that not only storage losses are significantly reflected in impedance, but also individual electrical parameters differ clearly between beets. The electrical intracellular resistance correlates well with the tissue strength and the penetration resistance - two decisive variables for the storability of sugar beets. Furthermore, a high correlation between quality parameters (such as dry matter content and sugar content) and electrical parameters was found. The results are an important step towards the establishment of impedance measurement in sugar beet quality testing. However, further investigations are necessary to prospectively derive quality parameters from results of particular impedance measurements.

Acknowledgments

Supported by IGF research project ‘Textur Zuckerrübe’ (Nr. 19836 BG)

References

Anderson F A 1988 Impedance plethysmography *Encyclopedia of medical devices and instrumentation* (New York, NY: John Wiley & Sons)

Castiglioni P, Parati G, Civijian A, Quintin L and Di Rienzo M 2009 Local scale exponents of blood pressure and heart rate variability by detrended fluctuation analysis: effects of posture, exercise, and aging *IEEE Trans. Biomed. Eng.* **56** 675–84

Malmivuo J, Honkonen J and Wendel K 2013 Did Jan Swammerdam do the first electric stimulation over 100 years before Luigi Galvani? *Proceedings of the XIII Mediterranean Conference on Medical and Biological Engineering and Computing* **2013** 13-16

Malmivuo J and Plonsey R 1995 *Bioelectromagnetism - Principles and applications of bioelectric and biomagnetic fields* (New York, NY: Oxford University Press)

Proceedings of the International Conference of Bioelectromagnetism, Electrical Bioimpedance,
and Electrical Impedance Tomography June 29 – July 1, 2022 / Kyung Hee University, Seoul, Korea

Detection of PSE-like meat quality : How does subjective quality ranking compare with bioimpedance testing?

Sisay Mebre Abie[1], Pawel Suliga[1], Bjørg Egelandsdal[2] and Daniel Munch[1]
[1]Faculty of Environmental Sciences and Natural Resource Management, University of Life Science, 1432 Ås, Norway
[2]Faculty of Chemistry, Biotechnology and Food Science, Norwegian University of Life Sciences, 1432 Ås, Norway.

Correspondence : Pedro Bertemes-Filho, e-mail : Sisay.Mebre.abie@nmbu.no

Abstract– Bioimpedance spectroscopy is inexpensive, easy, and well-established instrument which has been already used for medical and food quality assessment applications such as to detect meat defects. Defective meat has broader definition, but it has a limited functionality that will lead to unacceptable appearance (color), taste, texture (tenderness and juiciness), and processing ability or a combination of these. Furthermore, meat defects are also often characterized by an interrelated decline across different quality features, e.g., PSE-like meat is linked to a concomitant decline in pH, and increased paleness and drip loss and structural degradation. The majority of the consumers use organoleptic evaluation (smells and looks for discoloration) to identify the quality of the meat product. By incorporating French scoring and Japanese color scale, we established four label grade visual meat evaluation scaling methods. It is known that bioimpedance is one of the very sensitive tools that has been shown a direct correlation with micro-structural damage in meat [1]. Furthermore, the Py has been shown to correlate well with the common meat quality parameters like color, drip loss or pH [2]. Therefore, bioimpedance and other meat quality parameters including pH, color, were measured and visual quality evaluation was made by two different persons. To this end Pearson correlation analysis was made for 136 animals' data to investigate the relationship or correlation between the common meat quality parameters, bioimpedance and the visual evaluation method. To show how it helps to reveal the visual scoring profile of structurally defected pork meat samples in the markets.

Acknowledgments

The authors would like to express their gratitude to their Institutional support.

References

1. Egelandsdal, B., Abie, S.M., Bjarnadottir, S., Zhu, H., Kolstad, H., Bjerke, F., Martinsen, Ø.G., Mason, A. and Münch, D., 2019. Detectability of the degree of freeze damage in meat depends on analytic-tool selection. Meat science, 152, pp.8-19.
2. Pliquett, U., Altmann, M., Pliquett, F. and Schöberlein, L., 2003. Py—a parameter for meat quality. Mea t science, 65(4), pp.1429-1437.

DAY 3

Friday, July 1, 2022

Oral Session 09

Electrical Impedance Imaging Algorithm II

Chair Kiwan Jeon (National Institute for Mathematical Sciences)

O 09-01 **The Degree of Lung Collapse Estimation Method Using Convolutional Autoencoder and Neural Regression in Electrical Impedance Tomography**
Won-Doo Seo (Yonsei University Graduate School)

O 09-02 **The calculation of Flow Index by electrical impedance tomography**
Pu Wang (Fourth Military Medical University)

O 09-03 **Predicting outcomes of high flow nasal cannula based on EIT indexes using machine learning**
Zhe Li (Renji Hospital, Shanghai Jiao Tong University)

O 09-04 **A Physical Model of the Rat Thorax for EIT Measurements**
Silke Borgmann (University of Freiburg)

O 09-05 **Detection of a False Prior in Discrete Cosine Transformation based EIT Algorithm**
Rongqing Chen (University of Freiburg)

ICBEM Bioelectromagnetism ICEBI Electrical Bioimpedance EIT Electrical Impedance Tomography

Proceedings of the International Conference of Bioelectromagnetism, Electrical Bioimpedance,
and Electrical Impedance Tomography June 29 – July 1, 2022 / Kyung Hee University, Seoul, Korea

The Degree of Lung Collapse Estimation Method Using Convolutional Autoencoder and Neural Regression in Electrical Impedance Tomography

Won-Doo Seo[1], Hyeuknam Kwon[2]
[1]Department of Computer Science, Yonsei University Graduate School, Wonju, Korea
[2]Division of Software, Yonsei University, Wonju, Korea

Correspondence : Won-Doo Seo and Hyeuknam Kwon, e-mail : {wdseo, hyeuknamkwon}@yonsei.ac.kr

Abstract–To improve the development of ventilation strategies for patients under mechanical ventilation, evaluating the degree of lung collapse(DoLC) is crucial. We suggest AI-based model to measure DoLC by concatenating convolutional autoencoder and neural regression. This model predicts the DoLC with a single EIT image without any intervention of human's manipulation, and the resulting error is less than 5%.

Keywords: eletrical impedance tomography; degree of lung collapse; deep learning; convolutional autoencoder; neural regression

1. Introduction

The inhomogeneity of the tidal volume in the lungs can often be found from the patients under mechanical ventilation(Gattinoni et al. 1993). Ventilation strategies of patients based on integrated information on the entire lung may not provide optimal treatment unless lung inhomogeneity is included(Putensen et al. 2007). In order to develop improved ventilation strategies, it has been proposed to consider the degree of lung collapse(DoLC)(Rouby et al. 2002). One of the method to calculate DoLC, Global Inhomogeneity index(GI index) is widely used (Zhao et al. 2009). GI index shows the dispersion of pixel values within lung region set on EIT image. The lung area is determined as a value greater than the value obtained by multiplying the largest pixel value of the image by a user-defined threshold value. However, the GI index may be inaccurate because of manual selection of threshold value for lung region.

To overcome this problem, we introduce a novel method which does not have user-defined value such as threshold for lung area. To avoid using human intervention parameter, we adopt AI-based model which is a combination of encoder from convolutional autoencoder and neural regression. This AI-based model needs a single EIT image data as input and returns DoLC. We trained model with 7 datasets composed of various lung collapse situations, and test with 2 datasets. The error of the experimental results for the two datasets is about 0-5%.

2. GI index for evaluate degree of lung collapse

GI index is well-known interpretation method of the tidal volume distribution within the lung EIT image which shows how much lungs are collapsed(Zhao et al. 2009). The GI index is calculated as Equation (1):

$$GI = \frac{\sum_{xy\in lung}\left|\sigma_{xy} - Med(\sigma_{lung})\right|}{\sum_{xy\in lung}\sigma_{xy}} \tag{1}$$

where σ_{xy} is a pixel value of EIT image in the estimated lung area and σ_{lung} is all pixel values in the identified lung area. GI index is said to decrease to zero when the DoLC is low, and GI index goes up when the DoLC is high. To calculate GI index, we need to adjust threshold to confirm the appropriate lung area σ_{lung}. However, GI index has a problem from changing the threshold by manual. The result of GI index is differed from every threshold value we set. GI index goes down to zero if we choose high threshold, and vice versa. Thus, calculating GI index with choosing appropriate threshold is very tricky.

3. Suggested method for evaluate degree of lung collapse

3.1 Convolutional autoncoder & Neural regression model

In this section, we introduce CAENR(Convolutional AutoEncoder & Neural Regression), which is a very different way to approach raised problem(Martinesz-Murcia et al. 2019). CAENR is designed to predict the degree of lung collapse with EIT image as shown in Figure 1. To reduce the dimension of image, we train convolutional autoencoder(CAE). Also, we use neural regression(NR) to get a DoLC from reduced dimension of image. We generate 171,000 custom-made EIT image data and corresponding DoLC for training and testing. CAENR is made of Keras library with several custom modification on NVIDIA GTX 1660Ti 6GB GPU environment. Our CAENR model codes are publicly able to access through GitHub(Won-Doo S 2022).

3.2 Convolutional autoncoder

When the dimension of data is too high, we need too much information to explain it which costs a lot. Therefore, representing high dimensional data with a less information is important, and reducing the dimension helps to resolve this problem. CAE is appropriate method to reduce the dimension of image to a low dimension because of the existence of latent vector z between encoder and decoder. The role of CAE in this paper is training latent vector z to represent features of lung EIT images including collapsed cases. First, we train CAE with 128×128×1 sized EIT images. Each convolution layer has ReLU activation. At the encoder, every set of convolution stage has two convolution layers. And there are transposed convolution layer and convolution layer in every set of convolution stage at the decoder. To prevent overfitting, we use the batch normalization at every convolution layer(Garbin et al. 2020). Also we attach global average pooling layer at the end of encoder with same reason(Lin et al. 2013). We pool and upsample the size of convolution with stride instead of pooling or upsampling layer since both of methods give similar results, but stride method loses less information(Ayachi et al. 2020). We set the dimension of latent vector z in CAE as 10. We trained CAE using Adam optimizer and Mean Squared Error(MSE) loss function.

3.3 Neural regression

To achieve our goal predicting a degree of lung collapse, we use NR with a latent vector as input and the degree of lung collapse value as output. After training CAE, we train additional fully connected layer based NR with 2 hidden layers composed of 64 neurons with ReLU activation. Since fully connected layer prone to overfitting, we used batch normalization and dropout with $\sigma = 0.5$(Garbin et al. 2020). The output layer has one neuron with sigmoid activation to predict the percentage of collapse degree. We train NR model using Adam optimizer and MSE loss function.

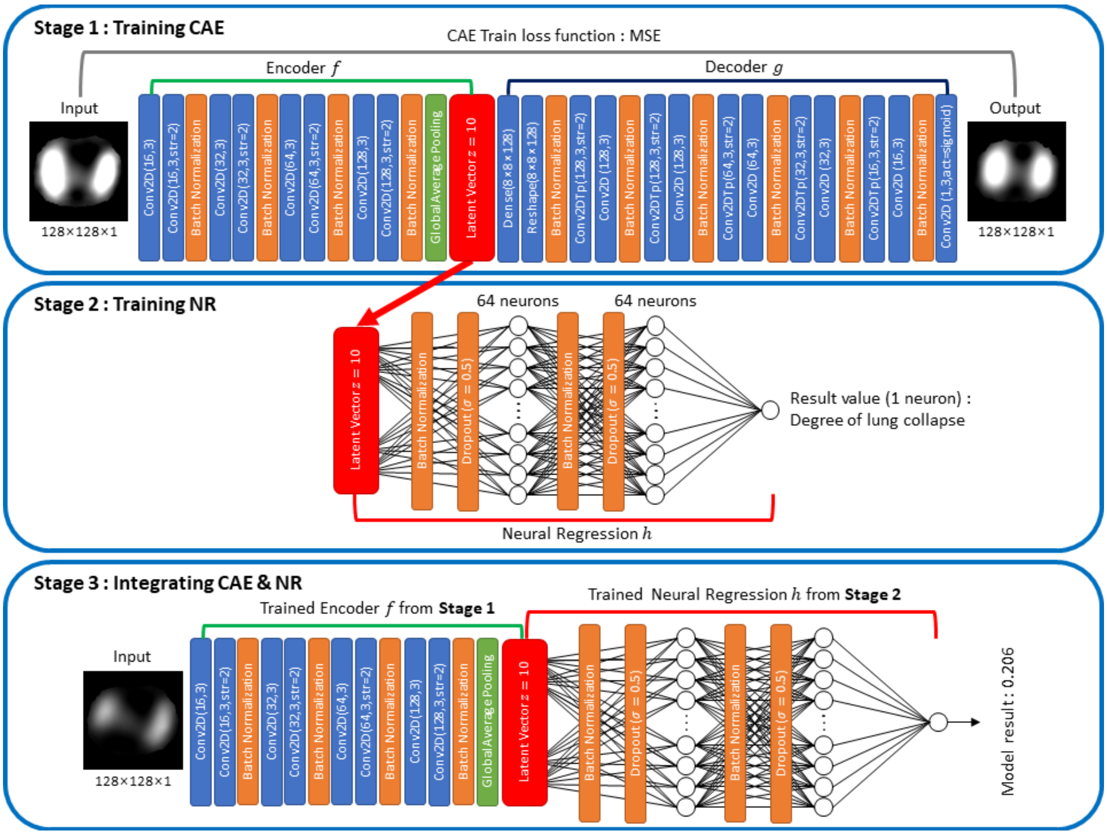

Figure 1. Schema of CAENR model. In stage 1, we train CAE to obtain encoder f and latent vector z from EIT images. The latent vector z will learn the features of lung EIT images with collapse. In stage 2, we use NR to derive DoLC from latent vector z. In stage 3, we concatnate decoder from CAE and NR.

4. Datasets

We use numerically generated EIT images for training and test. To obtain EIT images, we make 9 thorax models; 1 from EIDORS and 8 from CT images(Adler et al. 2006). For each model, we make 19 collapse cases as Figure 2; normal(0% collapse), 5 ~ 25% collapse on right/left lung with 5% increment, 5 ~ 40% equally collapse on both lung with 5% increment, which range of GI index is around 0 ~ 0.7(Trenk et al. 2016). The equation of degree of lung collapse is written as Equation (2):

$$Ground\ turth\ of\ DoLC = \frac{number\ of\ collasped\ element}{number\ of\ lung\ element} \tag{2}$$

where DoLC×100 is DoLC(%). We set artificial tidal volume as changing lung sensitivity so that all cases make 1,000 images. We use GREIT as a reconstruction method since it makes a quite big difference between each collapse cases(Adler et al. 2009). With 9 datasets, we use 7 datasets as train set and 2 datasets as test set. All of making dataset codes are run on MATLAB R2021b (The Mathworks, Natick, MA, USA) with EIDORS(Adler et al. 2006). Making dataset codes with reconstructed EIT data files are avail to access publicly on GitHub(Won-Doo S 2022).

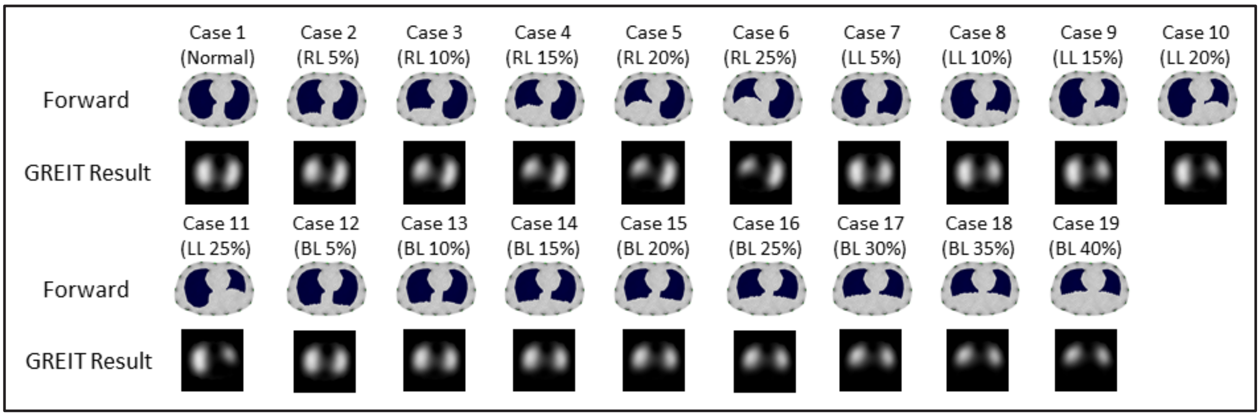

Figure 2. Forward data of thorax lung simulations and its corresponding GREIT results. In order to generate the lung EIT images for calcultaing DoLC, we make several collapsed lung cased using EIDORS with GREIT as reconstruction method. Lung collapse cases are composed of normal(0% collapse), 5-25% collapse on right/left lung(RL/LL) with 5% increment and 5-40% equally collapse on both lung(BL) with 5% increment.

5. Results

The results of trained CAENR with two test datasets outcome as Table 1. Each test dataset has 19 cases of lung collapse; normal(0% collapse), 5-25% collapse on right/left lung(RL/LL) with 5% increment and 5-40% equally collapse on both lung(BL) with 5% increment. Total test error mean and standard deviation between ground truths and model results are 0.030 and 0.021.

Table 1. Results of test datasets. Case 1 is normal(no collaspe), case 2-6 are 5-25% collapse at right lung(RL) with 5% increment, case 7-11 are 5-25% collapse at left lung(LL) with 5% increment, and case 12-19 are 5-40% collapse at both lung(BL) with 5% increment. There is an example of how the lungs are collapsed in Figure 2. Mean and standard derivation of error are 0.030 and 0.021.

Test dataset #1

Case #	1	2	3	4	5	6	7	8	9	10	11	12	13	14	15	16	17	18	19
Ground truth	0	0.051	0.103	0.154	0.205	0.250	0.050	0.099	0.152	0.199	0.251	0.053	0.099	0.153	0.203	0.248	0.298	0.355	0.404
Model result	0.049	0.079	0.108	0.172	0.207	0.246	0.083	0.115	0.145	0.202	0.235	0.078	0.126	0.170	0.207	0.236	0.327	0.380	0.425

Test dataset #2

Case #	1	2	3	4	5	6	7	8	9	10	11	12	13	14	15	16	17	18	19
Ground truth	0	0.051	0.099	0.149	0.199	0.249	0.050	0.102	0.149	0.199	0.252	0.049	0.101	0.150	0.201	0.250	0.302	0.351	0.399
Model result	0.022	0.050	0.107	0.141	0.181	0.207	0.060	0.096	0.127	0.162	0.223	0.061	0.097	0.136	0.186	0.229	0.275	0.321	0.380

Total test error mean : 0.030 Total test error STD : 0.021

6. Discussion

In this paper, the dimension of latent vector z in CAE is 10. To decide the dimensions of z, we experiment several dimensions from 8 to 20. Among these numbers, we decide to use $\dim(z) = 10$. Larger dimension has more noises from decoder and lower dimension may fail to have image structure.

The training datasets in this model are 7 custom generated datasets with 19 collapse cases, which means only 7 thorax models are used and it does not represent various human chests. When we get more datasets of thorax models with enough collapse cases, it will upgrade the accuracy of CAENR with high versatility on diverse collapse cases.

7. Conclusions

We introduced an AI-based DoLC prediction model using concatenation of CAE and NR, and the result of the experiment shows the possibility to suggest CAENR as a novel method to evaluate DoLC. Our future work is sharpening the model to increase accuracy of DoLC.

Acknowledgments

Seo and Kwon are supported by the National Research Foundation of Korea(NRF) grant funded by the Korea government(MSIT) (No. 2020R1F1A1A0107244511).

References

Adler A and Lionheart W R B 2006 Uses and abuses of EIDORS: an extensible software base for EIT *Physiol. Meas.* **27(5)** S25

Adler A et al. 2009 GREIT: a unified approach to 2D linear EIT reconstruction of lung images *Physiol. Meas.* **30(6)** S35

Ayachi R, Afif M, Said Y and Atri M 2020 Strided convolution instead of max pooling for memory efficiency of convolution neural networks *Proceddings of the 8th International Conference on Science of Electronics, Technologies of Information and Telecommunications* **2020** 234-243

Garbin C, Zhu X and Marques O 2020 Dropout vs. batch normalization: and empirical study of their impact to deep learning *Multimed. Tools Appl.* **79(19)** 12777-12815

Gattinoni L et al. 1993 Regional effects and mechanism of positive end-expiratory pressure in early adult respiratory distress syndrome *JAMA* **269** 2122-2127

Lin M, Chen Q and Yan S 2013 Network in network *arXiv preprint* **arXiv:1312.4400**

Martinez-Murcia F J, Ortiz A, Gorriz J-M, Ramirez J and Castillo-Barnes D 2019 Studying the manifold sturcture of Alzheimer's disease: a deep learning approach using convolutional autoencoders *IEEE J. Biomed. Health* **24(1)** 17-26

Putensen C, Wrigge H and Zinserling J 2007 Electrical impedance tomography guided ventilation therapy *Curr. Opin. Crit. Care* **13** 344-350

Rouby J J, Lu Q and Goldstein I 2002 Selecting the right level of positive end-expiratory pressure in patients with acute respiratory distress syndrome *Am. J. Respir. Crit. Care Med.* **165(8)** 1182-1186

Trenk F et al. 2016 Evaluation of lung ventilation distribution in chronic obstructive pulmonary disease patients using the global inhomogeneity index *38th Annual International Conference of the IEEE Engineering in Medicine and Biology Society* **2016** 5286-5289

Won-Doo S 2022 https://github.com/WondooSeo/Convolutional_AutoEncoder_Neural_Regression

Won-Doo S 2022 https://github.com/WondooSeo/Making_EIT_Data_with_EIDORS

Zhao Z, Möller K, Steubnabb D, Frerichs I and Guttmann J 2009 Evalutation of an electrical impedance tomography-based global inhomogeneity index for pulmonary ventilation distribution *Intensive Care Med.* **35(11)** 1900-1906

Proceedings of the International Conference of Bioelectromagnetism, Electrical Bioimpedance,
and Electrical Impedance Tomography June 29 – July 1, 2022 / Kyung Hee University, Seoul, Korea

The calculation of Flow Index by electrical impedance tomography

Pu Wang[1], Danqiong Wang[2], Zhanqi Zhao[1,3] and Feng Fu[1]
[1]Department of Biomedical Engineering, Fourth Military Medical University, Xi'an, China
[2]Quzhou People's Hospital, Quzhou, Zhejiang
[3]Institute of Technical Medicine, Furtwangen University, Villingen-Schwenningen, Germany

Correspondence : Feng Fu, fengfu@fmmu.edu.cn

Abstract–We aim to explore a new parameter for evaluating regional inspiratory effort in patients under mechanical ventilation. Electrical impedance tomography (EIT) measurement was performed in five patients under pressure support (PS). Compared to a previous study where global flow index was proposed, the global values calculated with EIT were reasonable. Besides, the EIT-based regional flow index suggested that inspiratory effort generated by respiratory muscles was heterogeneously distributed within the lungs. In conclusion, the regional flow index may be used to assess the inspiratory effort of the patient in clinical practice.

Keywords: *Flow Index, Electrical impedance tomography, Inspiratory effort, Pressure support*

1. Introduction

During mechanical ventilation, under-assistance may cause excessive diaphragmatic load and muscle injury, whereas over-assistance may lead to pulmonary hyperinflation and diaphragmatic atrophy and dysfunction. Therefore, assessing patient inspiratory effort is necessary. Various parameters inferred from patient efforts are used to assess the inspiratory effort, such as P0.1 (inspiratory pressure at 0.1 seconds) or Edi (electrical activity of the diaphragm). Recently a so-called flow index was proposed to deliver similar information (Albani, et al. 2021b). However, all these parameters are measured only by global information. As respiratory diseases may influence the regional lung tissue and function variously, regional information about inspiratory efforts might reveal new insight into the patient's status.

Electric Impedance Tomography (EIT) is a non-invasive imaging technique that can be used to monitor lung volume distribution (Frerichs, et al. 2017). In this study, we evaluated the feasibility of calculating the EIT-based regional flow index and the necessity to assess regional inspiratory effort.

2. Materials and methods

2.1 Protocol and EIT measurements

Five patients were analyzed retrospectively. Patients were ventilated under pressure support (PS) mode. EIT measurements were continuously performed (PulmoVista 500 Dräger Medical, Lübeck, Germany).

2.2 The Flow Index of EIT

The portion of the inspiratory flow-time waveform included between the end of the ramp and before the expiratory trigger was used to calculate the Flow Index (Albani, et al. 2021a) (Figure 1). The mathematical model for calculating flow index is shown in Equation (1).

$$\dot{V} = a + b \cdot \Delta time^{c} \tag{1}$$

where $\dot{V}$= the inspiratory flow $[L\cdot sec^{-1}]$
time = time [s]

In this model, $\dot{V}$ the inspiratory flow is a function of time. a, b and c are the three parameters fitted according to the model. The parameter c is Flow Index.

The Global Flow Index of EIT

Corresponding to the flow-time waveform obtained with the ventilator, the global flow index value of EIT was calculated by using the derivative of impedance Z' -time waveform (Figure 2).

The Functional EIT image of Flow Index

To begin with, the lung region was determined using 20% of the maximum value of the tidal image as the threshold (Figure 3). And the fEIT image of Flow Index was calculated by fitting the Z' -time waveform of every pixel in the lung region.

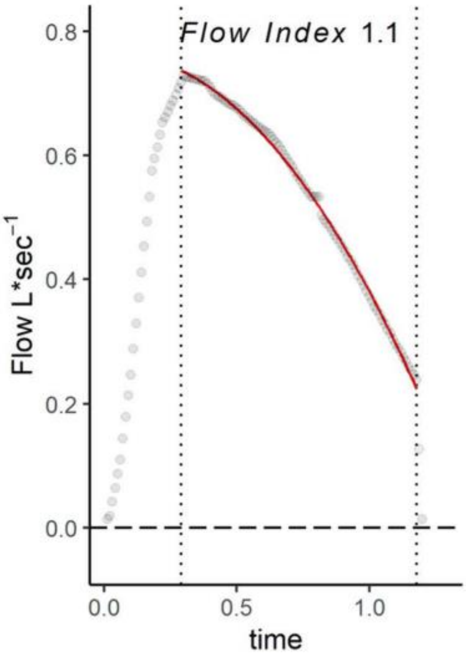

Figure 1. The red line is the portion for calculating the flow index(Albani, et al. 2021a)

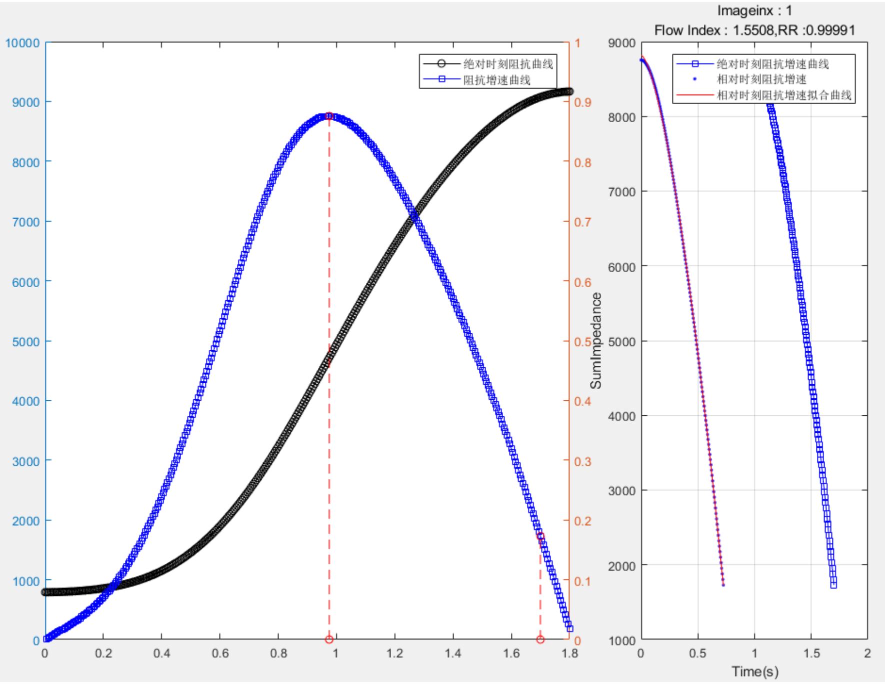

Figure 2. The portion of the blue line between two red points is the portion for calculating the flow index of EIT

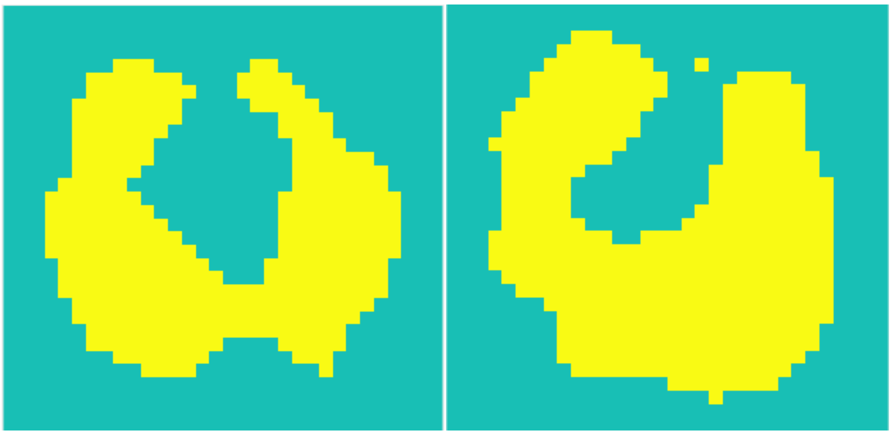

Figure 3. The example of lung region of EIT image

3. Results

Table 1 shows results for the performance of the EIT Global Flow Index of patients during PS. Figure 4 shows the image of two patients demonstrating a variation in patient efforts distribution.

Table 1. EIT Flow Index of patients

Patients	Global Flow Index	Standard Deviation
1	1.20	0.73
2	2.25	0.11
3	1.74	0.30
4	1.99	0.10
5	1.94	0.05

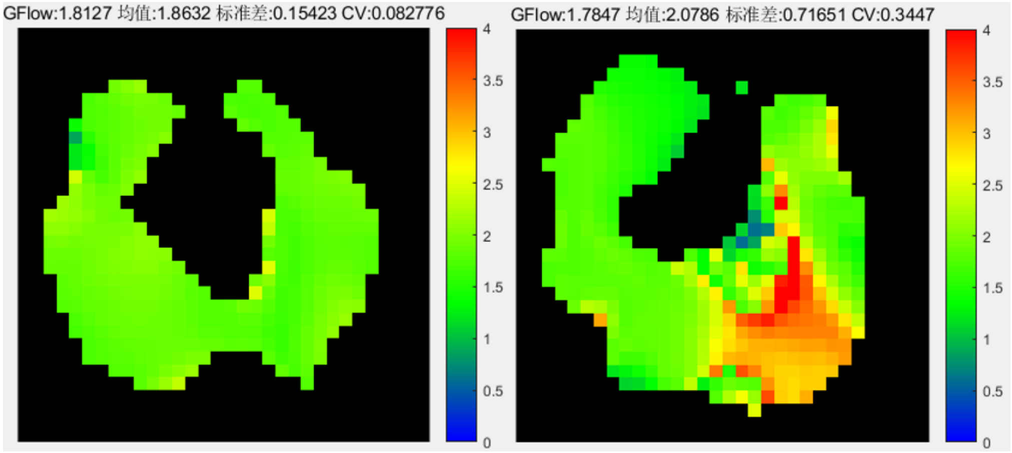

Figure 4. The functional EIT image

4. Discussion

This study proposed a new EIT-based parameter to assess the inspiratory effort of patients during PS. In the original study, Flow Index was able to detect high and low spontaneous inspiratory effort during PS (Albani, et al. 2021b). In the present study, we did not have a reference value to prove the EIT-based flow index but the values were in the same range as proposed in the previous studies. Furthermore, our study patients showed large variation in regional flow index suggesting the inspiratory efforts varied significantly among different lung regions.

Figure 4 shows that the global Flow Index values of the two patients at the same mode of PS were similar, but the distribution of inspiratory force different significantly. This indicates that the Functional EIT image of the Flow Index can provide more information for clinical practice.

5. Conclusions

In conclusion, the EIT-based calculation of the Flow Index is meaningful if its feasibility was developed successfully. And the fEIT image can give more regional information about the patient effort of inspiratory for clinical practice.

References

Albani, F., et al.
2021a Flow Index: a novel, non-invasive, continuous, quantitative method to evaluate patient inspiratory effort during pressure support ventilation. Critical Care 25(1).

Albani, Filippo, et al.
2021b Flow Index accurately identifies breaths with low or high inspiratory effort during pressure support ventilation. Critical Care 25(1).

Frerichs, I., et al.
2017 Chest electrical impedance tomography examination, data analysis, terminology, clinical use, and recommendations: consensus statement of the TRanslational EIT developmeNt stuDy group. Thorax 72(1):83-93.

Proceedings of the International Conference of Bioelectromagnetism, Electrical Bioimpedance,
and Electrical Impedance Tomography June 29 – July 1, 2022 / Kyung Hee University, Seoul, Korea

Predicting outcomes of high flow nasal cannula based on EIT indexes using machine learning

Zhe Li[1], Lin Yang[2], Meng Dai[3], Ri Tang[1], ZhangJun Tan[1], Yuan Gao[1*], Zhanqi Zhao[3,4]
[1] Department of Critical Care Medicine, Renji Hospital, School of Medicine, Shanghai Jiao Tong University, Shanghai, China
[2] Department of Aerospace Medicine, Fourth Military Medical University, Xi'an, China
[3] Department of Biomedical Engineering, Fourth Military Medical University, Xi'an, China
[4] Institute of Technical Medicine, Furtwangen University, Villingen-Schwenningen, Germany

*Correspondence: Yuan Gao, e-mail: rj_gaoyuan@163.com

Abstract– High flow nasal cannula (HFNC) is widely used to prevent or minimize the duration of invasive mechanical ventilation. However, a subset of patients with HFNC failure may also suffer worsened outcomes from delayed intubation. Therefore, this retrospect study investigates a proper machine-learning model for predicting HFNC outcomes using electrical impedance tomography (EIT) based indexes. Forty-six patients with acute respiratory failure (age: 66 ± 13 years; male: female was 35: 11) were included. HFNC and EIT were performed simultaneously. Afterward, we reorganized the EIT-based indexes into three groups, each containing 6 EIT indexes as the features. We perform eight common supervised learning for each feature group to establish the prediction models. Results demonstrated that the support vector machine (SVM) and the artificial neural network (ANN) had a higher prediction accuracy (92.31% for SVM; 84.62% for ANN) than other supervised learning models. However, they would also give a certain degree of false-positive rate (7.69% for Group 1; 15.38% for Group 2), which might lead to delayed intubation. In conclusion, using EIT temporal and spatial indexes, the SVM and ANN in supervised machine learning showed good promise in predicting the outcomes of HFNC. Future work focuses on increasing sample size and further optimizing the model.

Keywords: high flow nasal cannula; electrical impedance tomography; machine learning.

1. Introduction

High flow nasal cannula (HFNC) is a non-invasive oxygen therapy and respiratory support method. Unlike conventional oxygen therapy, in HFNC, a mixture of air-oxygen gas is warmed and humidified to a temperature and humidity close to the human body and then delivered to the patient through a nasal cannula (Ricard, 2012). At present, HFNC is widely used to prevent or minimize the duration of invasive mechanical ventilation(Alhazzani et al., 2020), and recent studies have shown that it improves respiratory drive and lung mechanics, enhances CO_2 removal and reduces 90-day mortality(Braunlich et al., 2013; Mauri et al., 2017; Frat et al., 2015). However, a subset of patients with HFNC failure may also suffer worsened outcomes from delayed intubation(Kang et al., 2015; Roca et al., 2019). Early warning of HFNC failure is thus helpful for doctors to promptly decide the timing of intubation. The best-known respiratory rate-oxygenation (ROX) ratio may predict HFNC failure, but it does not directly reflect lung ventilation status and thus requires a longer period (around 12 h).

Electrical impedance tomography (EIT) is a non-invasive, radiation-free imaging method capable of monitoring lung ventilation changes due to various lung conditions at the bedside, including oxygen therapy or respiratory support in patients with acute respiratory distress syndrome, chronic obstructive pulmonary disease, etc. (Franchineau et al., 2017; Scaramuzzo et al., 2020; Milne et al., 2019). In addition, several EIT-based parameters have also been successfully used to assess the effect of HFNC on regional ventilation (Zhang et al., 2020).

Using EIT, our previous study observed changes in spatial and temporal ventilation distributions in 46 patients with acute respiratory failure (ARF) during the first hour of HFNC (Li et al., 2021). Unfortunately, the EIT spatial and temporal indexes of ventilation distribution within the first hours did not individually show significant differences between the HFNC success and failure groups. Therefore, for the first time, this study aims to investigate a proper machine-learning model for predicting HFNC outcomes using those EIT indexes.

2. Methods and materials

Data were obtained from our previous study, which was approved by the local ethics committees (KY2021-057-B) (Li et al., 2021). Written informed consent was obtained from all the subjects before the study. Forty-six patients with acute respiratory failure (age: 66±13 years; male: female was 35: 11) were included. HFNC (Fisher and Paykel Healthcare, East Tamaki, New Zealand; Dräger Medical, Lübeck, Germany) and EIT (PulmoVista 500, Dräger Medical, Lübeck, Germany) were performed simultaneously. In addition, the ROX index was also obtained 1 h after HFNC for comparison. At last, 11 patients had failed HFNC, which meant that they underwent intubation within 48 h.

In the retrospective analysis, we mainly focused on EIT measurements at three time points (before HFNC, T1; 30 min after HFNC started, T2; 1 h after, T3). Three clinical EIT-based indexes, including the global inhomogeneity (*GI*) (Zhao et al., 2009), the center of ventilation (*CoV*) (Frerichs et al., 1998), and the inspiration time (T_{insp}), were calculated at T1, T2 and T3, respectively. Namely, we established a total of 9 EIT-based indexes (or features) for further machine learning. We choose those indexes because *GI* characterizes the ventilation heterogeneity, and *CoV* indicates the ventilation distribution influenced by lung diseases; While *GI* and *CoV* reflect the spatial ventilation distributions, T_{insp} denotes the temporal ventilation distributions. In machine learning, the median value was calculated for those nine features. The HFNC success patients were labeled as "1", the failure patients as "0". The ratio between the number of training samples and testing samples was 7:3. However, since only 46 samples were included, we had to reduce the feature dimensions and reselect six features from those nine EIT-based indexes and regroup them (as Table 1 shown) to guarantee a reasonable machine learning model.

Table 1 Combination of EIT-based indexes at three time points for machine learning

	Feature combination
Group 1	Median *GI* at T1, Median *GI* at T2, Median *GI* at T3; Median *CoV* at T1, Median *CoV* at T2, Median *CoV* at T3;
Group 2	Median *GI* at T1, Median *GI* at T2, Median *GI* at T3; Median T_{insp} at T1, Median T_{insp} at T2, Median T_{insp} at T3;
Group 3	Median *CoV* at T1, Median *CoV* at T2, Median *CoV* at T3; Median T_{insp} at T1, Median T_{insp} at T2, Median T_{insp} at T3;

In order to compare the performances of different machine learning models for predicting outcomes of HFNC, we included the eight common models for supervised learning as follows: k-nearest neighboring (KNN), artificial neural network (ANN), support vector machine (SVM), adaptive boosting (AdaBoost), eXtreme gradient boosting (Xgboost), logistic regression (LR), random forest (RM), gradient boosting decision tree (GBDT).

3. Results

The previous study showed that the ROX index was insignificantly different (p=0.23) between HFNC success patients (8.3±2.7) and HFNC failure patients (6.2±1.8). After we analyzed the features from those three groups for each machine learning model respectively, Table 2 summarized the optimal results for each group. Group 1 has the greatest accuracy of 92.31% when using the SVM model compared to other models, Group 2 84.62% using the ANN model, Group 3 84.62% using the SVM model. Besides, when Group 1 was modeled using SVM, there was a false-positive rate of 7.69%; namely, there was a chance that the HFNC failure patients might be predicted to be the HFNC success patients and the intubation could thus be delayed. This result was similar to Group 3.

Table 2 The optimal machine learning model for those three feature groups

	Model	Parameters	Accuracy for training data	Accuracy for testing data	The false-negative rate for testing data	The false-positive rate for testing data	Precision for testing data	Recall for testing data
Group 1	SVM	kernal: Radial Basis Function mlp-sigma:0.6 method:Sequential Minimal Optimization	96.67%	92.31%	0.00%	7.69%	100.00%	90.91%
Group 2	ANN	feed forward net: 10 training function: DUD	80.00%	84.62%	15.38%	0.00%	80.00%	100.00%
Group 3	SVM	kernal: Radial Basis Function mlp-sigma:0.6 method:Sequential Minimal Optimization	100.00%	84.62%	0.00%	15.38%	100.00%	83.33%

4. Discussion

HFNC was widely reported to outperform conventional oxygen therapy or non-invasive ventilation with respect to ventilation distribution, end-expiratory lung volume, respiratory rate, etc., but the prediction of the HFNC outcomes and timely intubation for HFNC failure patients were also essential. The ROX index was previously proposed to forecast the outcomes, but its cutoff value depends on observation time points or diseases. In our previous study, in order to obtain the outcomes of HFNC as soon as possible, we analyzed the ROX at 1 h; however, the specificity of ROX at 1 h was not great enough to identify HFNC failure.

Machine learning was previously used to predict flow rate escalation for pediatric patients on HFNC (Krachman et al., 2021). This study also attempted to leverage machine learning for predicting HFNC outcomes with the unique EIT indexes for the first time. Results showed that using the changes in EIT temporal and spatial indexes of ventilation distribution within the first hour, SVM or ANN had a higher prediction accuracy than other supervised learning models. Nevertheless, they would also give a certain degree of false-positive rate, which might lead to delayed intubation.

The main limitation of the study was the insufficiency of samples. For machine learning, the more samples provided, the model would have a higher prediction accuracy and a greater ability to generalization. Therefore, we plan to collect more data on HFNC patients with EIT measurement. In a future study, with an adequent number of samples, we also could combine EIT indexes with other clinical indexes to make a prediction.

5. Conclusions

Using EIT temporal and spatial indexes, the SVM and ANN in supervised machine learning showed good promise in predicting the outcomes of HFNC. Future work focuses on increasing sample size and further optimizing the model.

Acknowledgments

The work was partially supported by National Natural Science Foundation of China (NSFC 61901478 and 81601636), Medical Program of FMMU (Grant No. 2018HKTS10 and 2019ZTC01), Key R & D Program of Shaanxi Province (2021SF-027) and The Science and technology Innovation Project of Jinshan District(2018-3-8).

References

Alhazzani W, Moller M H, Arabi Y M, Loeb M, Gong M N, Fan E, et al. 2020 Surviving Sepsis Campaign: Guidelines on the Management of Critically Ill Adults with Coronavirus Disease 2019 (COVID-19). Crit Care Med. 48(6):e440-e69

Braunlich J, Beyer D, Mai D, Hammerschmidt S, Seyfarth H J and Wirtz H 2013 Effects of nasal high flow on ventilation in volunteers, COPD and idiopathic pulmonary fibrosis patients. Respiration. 85(4):319-25

Franchineau G, Brechot N, Lebreton G, Hekimian G, Nieszkowska A, Trouillet J L, et al. 2017 Bedside Contribution of Electrical Impedance Tomography to Setting Positive End-Expiratory Pressure for Extracorporeal Membrane Oxygenation-treated Patients with Severe Acute Respiratory Distress Syndrome. Am J Resp Crit Care. 196(4):447-57

Frat J P, Thille A W, Mercat A, Girault C, Ragot S, Perbet S, et al. 2015 High-Flow Oxygen through Nasal Cannula in Acute Hypoxemic Respiratory Failure. New Engl J Med. 372(23):2185-96

Frerichs I, Hahn G, Golisch W, Kurpitz M, Burchardi H and Hellige G 1998 Monitoring perioperative changes in distribution of pulmonary ventilation by functional electrical impedance tomography. Acta Anaesthesiol Scand. 42(6):721-6

Kang B J, Koh Y, Lim C M, Huh J W, Baek S, Han M, et al. 2015 Failure of high-flow nasal cannula therapy may delay intubation and increase mortality. Intens Care Med. 41(4):623-32

Krachman J A, Patricoski J A, Le C T, Park J, Zhang R, Gong K D, et al. 2021 Predicting Flow Rate Escalation for Pediatric Patients on High Flow Nasal Cannula Using Machine Learning. Front Pediatr. 9:734753

Li Z, Zhang Z, Xia Q, Xu D, Qin S, Dai M, et al. 2021 First Attempt at Using Electrical Impedance Tomography to Predict High Flow Nasal Cannula Therapy Outcomes at an Early Phase. Front Med (Lausanne). 8:737810

Mauri T, Alban L, Turrini C, Cambiaghi B, Carlesso E, Taccone P, et al. 2017 Optimum support by high-flow nasal cannula in acute hypoxemic respiratory failure: effects of increasing flow rates. Intensive Care Med. 43(10):1453-63

Milne S, Huvanandana J, Nguyen C, Duncan J M, Chapman D G, Tonga K O, et al. 2019 Time-based pulmonary features from electrical impedance tomography demonstrate ventilation heterogeneity in chronic obstructive pulmonary disease. J Appl Physiol. 127(5):1441-52

Ricard J D 2012 High flow nasal oxygen in acute respiratory failure. Minerva Anestesiol. 78(7):836-41

Roca O, Caralt B, Messika J, Samper M, Sztrymf B, Hernandez G, et al. 2019 An Index Combining Respiratory Rate and Oxygenation to Predict Outcome of Nasal High-Flow Therapy. Am J Resp Crit Care. 199(11):1368-76

Scaramuzzo G, Spadaro S, Dalla Corte F, Waldmann A D, Bohm S H, Ragazzi R, et al. 2020 Personalized Positive End-Expiratory Pressure in Acute Respiratory Distress Syndrome: Comparison Between Optimal Distribution of Regional Ventilation and Positive Transpulmonary Pressure. Critical Care Medicine. 48(8):1148-56

Zhang R, He H W, Yun L, Zhou X, Wang X, Chi Y, et al. 2020 Effect of postextubation high-flow nasal cannula therapy on lung recruitment and overdistension in high-risk patient. Critical Care. 24(1):

Zhao Z, Moller K, Steinmann D, Frerichs I and Guttmann J 2009 Evaluation of an electrical impedance tomography-based Global Inhomogeneity Index for pulmonary ventilation distribution. Intensive Care Med. 35(11):1900-6

Proceedings of the International Conference of Bioelectromagnetism, Electrical Bioimpedance,
and Electrical Impedance Tomography June 29 – July 1, 2022 / Kyung Hee University, Seoul, Korea

A Physical Model of the Rat Thorax for EIT Measurements

Silke Borgmann[1,2], Patryk Dzierzawski[1,2], Bernd Flamm[1,2], Christin Wenzel[1,2],
Sashko Spassov[1,2] and Stefan Schumann[1,2]
[1]Department of Anesthesiology and Critical Care, Medical Center, University of Freiburg, Freiburg, Germany
[2]Faculty of Medicine, University of Freiburg, Freiburg, Germany

Correspondence : Silke Borgmann, e-mail : silke.borgmann@uniklinik-freiburg.de

Abstract–Electrical impedance tomography is predestined for functional monitoring of lung ventilation due to the achievable excellent temporal resolution. In order to optimize electrical impedance tomography for small animals, we developed a ventilatable physical model of the rat thorax and studied it with electrical impedance tomography. We could verify, that the physical model could be ventilated and that manual and mechanical ventilation of the physical model could be visualized with electrical impedance tomography. This physical model allows for studying hardware configurations such as number and spacing of electrodes, and current injection patterns, but also for software configurations such as different reconstruction approaches.

Keywords: Physical model, rats, mechanical ventilation, electrical impedance tomography.

1. Introduction

Electrical impedance tomography (EIT) is an excellent tool to monitor lung ventilation. Since it is radiation-free and portable, it can be used to record data at the bedside or in the operating theatre. Due to its excellent temporal resolution, it provides valuable insights into the mechanics of breathing. Hence, it is useful not only in clinical trials but also very much so at the preclinical stage, where small animals and especially rats are often used to study physiological as well as pathophysiological processes (Wenzel et al. 2021).

To optimize EIT for the application in small animals, we developed a physical model of the rat thorax. With this physical model it is possible to develop the most suitable peripheral hardware configuration for EIT such as the optimum number of electrodes and their spacing. In addition, different current injection patterns can be studied and reconstruction can be adapted to rat physiology. On top of that, it is also possible to test different ventilation settings and monitor their effects with EIT under controlled conditions.

2. Materials and Methods

The physical model of the rat thorax (Figure 1) consists of a latex balloon filled with agar-agar (Carl Roth GmbH+Co.KG, Karlsruhe, Germany). For the application of needle electrodes, we reinforced the latex balloon after filling using latex milk (natural rubber, kept liquid with ammonia). The agar-agar was cooked with saline solution (NaCl 0.9%, Braun, B. Braun Melsungen AG, Melsungen, Germany) to make it conductive. A urinary catheter with inflatable cuff was inserted into the physical model. The cuff can be inflated via the respective tube and can thus simulate a ventilated lung. The catheters main lumen was tightly blocked.

2.1 Simulating ventilation

In order to ventilate the physical model, we used a syringe to manually inflate and deflate the cuff. Thus, a variable volume and respiratory frequency was applied. Our intention here was to test the response of the EIT device under aperiodic conditions.

Further, we connected the physical model to a self-developed small animal ventilator. This device is capable of applying tidal volumes of up to 16 ml and ventilation frequencies of up to 120 breaths per minute. Thereby, the ventilation patterns are freely programmable. We chose a sine shaped ventilation pattern with a tidal volume of 2ml at a frequency of 100 breaths per minute to test the model.

2.2 Electrodes

To collect EIT images, we attached 16 subdermal hooked needle electrodes (GVB- geliMED GmbH, Bad Segeberg, Germany) that we placed circumferentially and equidistantly in our physical model.

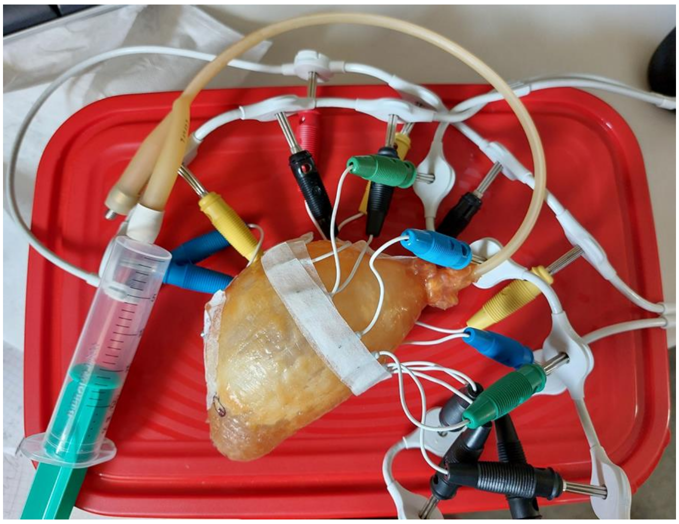

Figure 1. Physical model of the rat thorax. The model consists of a latex balloon filled with saline-cooked agar-agar in which a urinary catheter with inflatable cuff is inserted. The cuff is used to model a localized ventilated structure. 16 equidistant hook electrodes were placed circumferentially around the model and secured with self-adhesive tape. For manual ventilation the catheter's cuff was inflated with a syringe. The ends of the hook electrodes were connected to banana plugs. These were then connected to the cable of an EIT belt (size XS) of the Dräger Pulmo Vista 500 EIT device.

2.3 EIT

For the preliminary proof-of-concept EIT measurements we used a Dräger Pulmo Vista 500 (Dräger medical, Lübeck, Germany). In order to adapt it to the electrodes, we connected them to a cable of an electrode belt (size XS) via banana plugs.

With this setup, we collected EIT data of the physical model for both ventilation methods (manual and mechanical). For manual and for mechanical ventilation simulation, single recordings of five minute duration were taken. The frame rate was set to the maximum of 50 Hz. Reconstruction of the collected voltages was done using the EIT Data Analysis Tool 6.1 (Dräger medical, Lübeck, Germany). Further processing of the reconstructed images was done using custom code developed in Matlab (R2020b, The MathWorks, Natick, USA).

2.4 Data evaluation

To evaluate the data, we calculated the global impedance curves for both ventilation settings by summing the impedances for each recorded frame.

Additionally, for the data of mechanical ventilation we located the frames corresponding to the start and the stop of inspiration. These frames were than averaged and subtracted to get a functional tidal image. This image is a representation of the mean ventilation of the cuff.

To verify that the images generated by EIT originated genuinely from the ventilation of the cuff and not from bubbles of trapped air certainly present in the agar-agar as well, we collected sonograms (Vivid S5, GE healthcare, Boston, MA) as closely to the position of the electrode plane as possible. During the sonography, we applied manual inflation and deflation of the lung model via a syringe.

3. Results

The physical model proved to be practical in handling and manual as well as mechanical ventilation were applicable. The electrode contact was classified 'high' according to the EIT device. However, touching the physical model or the cables resulted in slight movements of the electrodes and consequently in artefacts in the EIT traces.

The global impedance curves represented accurately the ventilation of the physical model. The aperiodic conditions caused by manual ventilation (Figure 2, left panel) as well as the periodical conditions from mechanical ventilation in terms of frequency and curve form (sine curve, 100 breaths per minute) were well replicated in the global impedance curves. However, we observed a descending baseline in the global impedance curve in the latter case (Figure 2, right panel).

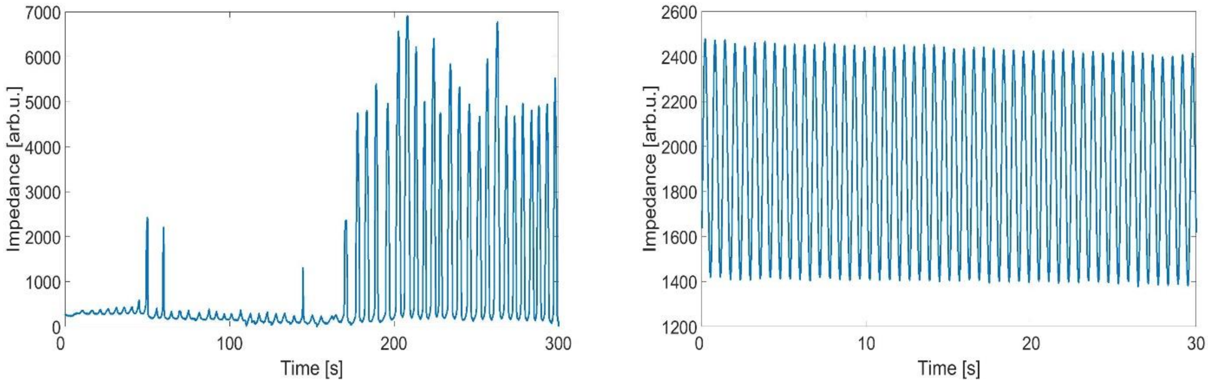

Figure 2. Global impedance curves when operating the physical model manually with a syringe (left) and with the dedicated small animal-ventilator (right). In the latter case, the baseline descended over the recording. Please note the different scales on both, the x and the y axis for both graphs.

The reconstructed images fairly accurately depicted the ventilated cuff (Figure 3, right panel). The ultrasonography showed that the cuff was placed directly beneath the electrode plane (Figure 3, left panel).

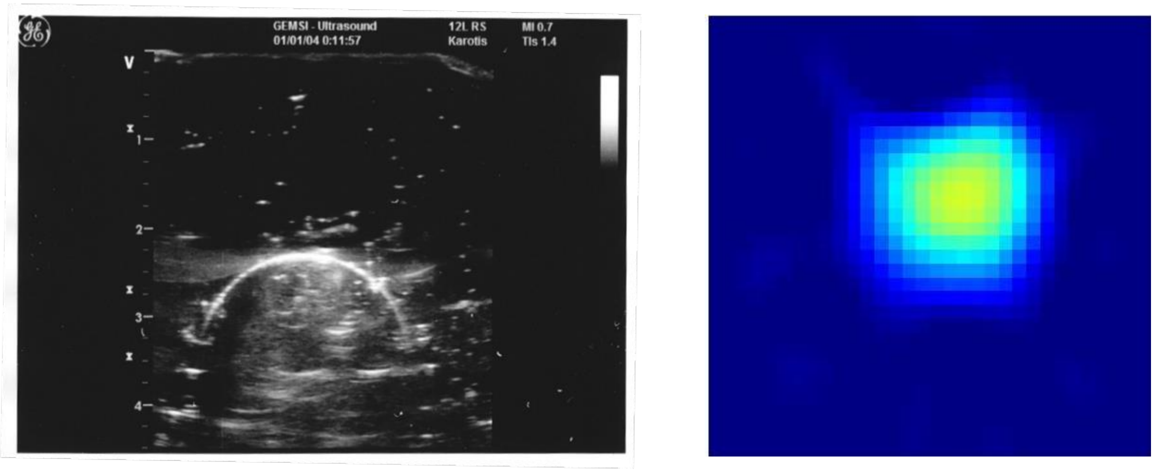

Figure 3. Sonogram (left) of fully inflated cuff and functional tidal EIT image (right).

4. Discussion

Our physical model of the rat thorax could be equipped with a commercial EIT device and worked well during both manual and mechanical ventilation. Ultrasonic imaging close to the electrode plane confirmed, that the images generated by EIT showed the cuff and not artefacts of trapped air inside the model.

Two major issues for adapting the EIT to rat physiology could be solved with the physical model. First, due to the rather small circumference of the rat thorax (approx. 15 cm), it was not clear, how closely spaced the electrodes can be placed and hence which number of electrodes was feasible. We were concerned that sixteen electrodes might result in too close spacing and thus in too small voltage between the electrodes. The second issue was which electrodes would be suitable and how they could be fixed in place. Rooney and colleagues as well as Dunster and colleagues (Rooney et al 2009, Dunster et al 2012) used 16 epicardial pacing wires and sutured them through the skin. Thus, we chose to try 16 electrodes as well. However, suturing the electrodes appears to be not feasible on a regular base since it would take too much time and thus would increase preparation and consequently ventilation time of the animal. This might not be accommodated easily within every study protocol. Hence, we decided for hook electrodes and fixed them using adhesive tape. Both, the number of electrodes as well as their attachment to the model worked well.

Accommodating the setup used for the physical model to a live rat may not be feasible without further precautions due to the amount of space the cabling takes up and the sensitivity to touch due to the resulting movement of the electrodes. However, artefacts do occur in measurements on patients as well, since moving of patients cannot be avoided. For our physical and live-animal model, occurrence of such artefacts could be reduced with a dedicated setup that leaves more space for the experimenter to handle the animal. Further, study protocols may include measurement times during which physical contact to the setup is avoided.

The descending baseline we observed in the global impedance curve, indicated that our system showed minor leakage over time. We could safely derive this, since applying additional pressure to the system to compensate for potential leakage stopped the descent of the baseline (not shown). In case of ventilation with positive end-expiratory pressure such drift would not occur.

One of the main advantages of this physical model certainly is that all of hard- and software adaptations to optimize application of EIT for small animals can be studied with it. Consequently, life animals need not be sacrificed to improve technical implementation.

5. Conclusions

We developed a working physical model representing biological impedance conditions of the rat lung. Preliminary EIT recordings were possible and showed the correct functioning of the physical model.

References

Dunster KR, Friese M, Fraser JF, Cowin GJ and Schibler A 2012 Ventilation distribution in rats: Part I – The effect of gas composition as measured with electrical impedance tomography BioMedical Engineering OnLine, **11**, 64

Rooney D, Friese M, Fraser JF, Dunster KR and Schibler A 2009 Gravity-dependent ventilation distribution in rats measured with electrical impedance tomography Physiol. Meas., **30**, 1075-1085

Wenzel C, Schmidt J, Urban G, Schumann S and Spassov SG 2021 Mechanical ventilation restores blood gas homeostasis and diaphragm muscle strength in ketamine/medetomidine-anaesthetized rats Exp. Phys., **106**, 396-400

ICBEM Bioelectromagnetism ICEBI Electrical Bioimpedance EIT Electrical Impedance Tomography

Proceedings of the International Conference of Bioelectromagnetism, Electrical Bioimpedance,
and Electrical Impedance Tomography June 29 – July 1, 2022 / Kyung Hee University, Seoul, Korea

Detection of a False Prior in Discrete Cosine Transformation based EIT Algorithm

Rongqing Chen[1,2], Stefan J. Rupitsch[2] and Knut Moeller[1,2]
[1]Institute of Technical Medical (ITeM), Hochschule Furtwangen, Villingen-Schwenningen, Germany
[2]Department of Microsystems Engineering (IMTEK), Faculty of Engineering, University of Freiburg, Freiburg, Germany

Correspondence: Rongqing Chen, e-mail: rongqing.chen@hs-furtwangen.de

Abstract–Structural priors incorporated with the discrete cosine transformation (DCT) based electrical impedance tomography (EIT) algorithm improves the interpretability of EIT results in a clinical setting. However, a false prior will produce a misleading result compromising clinical decisions. Detection of false priors is crucial. In our investigation, a redistribution index (RI) is proposed to quantify the potential error introduced by a false structural prior. Simulations in terms of different scales of atelectasis were conducted to evaluate the plausibility of the RI. The behaviour of RI makes it possible to detect a false prior with a defined threshold, which must be determined according to the requirements and tolerance of an application. The redistribution index depends also on the reconstruction method and different parameters like the regularization hyperparameter. Therefore, we investigated as well the sensitivity of the RI on the choice of the hyperparameter. From the evaluation, it seems plausible that the RI can be further developed into an indicator for false priors in EIT reconstruction.

Keywords: EIT algorithm; prior; discrete cosine transformation; redistribution index; morphological image

1. Introduction

Electrical Impedance Tomography (EIT) is capable of visualizing regional lung ventilation and aeration distribution from current induced voltage changes through the electrodes attached to the surface of the chest[1]. It was demonstrated to be practical in reducing ventilator induced lung injury (VILI) and instructing clinicians to set appropriate positive end-expiratory pressure (PEEP) levels for mechanically ventilated patients in the intensive care unit (ICU) [1]. However, low spatial resolution, blurred anatomical alignment, and reconstruction induced artefacts hinder the interpretation of EIT images in clinical settings. Introducing structural priors into EIT reconstructions will eventually help clinicians to gain a better understanding of EIT images and derive a more direct and comprehensive insight.

Structural priors can vary but are usually based on the tissue conductivities or the anatomical constraints or both. Assigning certain properties, e.g., conductivities, to a predefined area is the most common approach to include prior knowledge into the EIT reconstruction process. e.g., Glidewell et al. used the shape of the lungs to group FEM elements and to assign different values [2]. It is also practical to include the available prior in terms of basic constraint method, e.g., Vauhkonen et al. used basic functions represented by principal eigenvectors of a representative ensemble of expectable conductivity distributions [3]. Priors can as well be introduced by a subset of kernel functions, e.g., Gong et al. used a spectral graph wavelet transform for regularization [4].

The prior used in those algorithms can remain the same, but we propose to add personalized prior information to improve interpretability of EIT images. Schullcke et al. introduced an EIT algorithm with detailed information about the shape of lung derived from CT images. This algorithm also leads to decreased inverse problem dimensionality by representing the solution to the inverse problem with discrete cosine transformation (DCT) basic functions. Though this algorithm has shown an attractive result, it is accompanied by the same problem as all priors: results will be beneficial if the priors are accurate but may be misleading if not. A detailed lung shape as prior might be outdated and thus invalid, because the status of the patient has changed over time. An invalid prior might induce a risk of misinterpretation of images, which compromises diagnosis.

The objective of this contribution is to introduce a quantitative estimate to detect a false prior introduced into the DCT-based EIT algorithm. We propose a redistribution index (RI) to quantify the error introduced by a false structural prior and to develop a basic understanding of critical impact of a prior on the image. A first evaluation is conducted with simulated recordings in analogy to a clinical setting. Different scales of atelectasis were simulated. The simulation data were used for EIT reconstructions with different priors, as well as different regularization hyperparameters. Redistribution indices were calculated and compared to the reconstructions at every simulated clinical case.

2. Methods

2.1 DCT-based EIT algorithm

The reconstruction of conductivity variation $\hat{\mathbf{x}}$ in EIT is an ill-posed inverse problem. Conductivity distribution change $\mathbf{x} = \boldsymbol{\sigma}_2 - \boldsymbol{\sigma}_1$ is not linearly related to induced changes of the boundary voltages $\mathbf{y} = \mathbf{v}_2 - \mathbf{v}_1$. Under the assumption that the conductivity change $\mathbf{x}$ is very small in EIT, the reconstruction problem can be described in a linearized form:

$$\hat{\mathbf{x}} = (\mathbf{J}^T\mathbf{J} + \lambda^2\mathbf{R})^{-1}\mathbf{J}^T\mathbf{y} = \mathbf{B}\mathbf{y} \tag{1}$$

where $\mathbf{J}$ is the Jacobian matrix which maps the conductivity changes to the voltage variations. $\mathbf{R}$ is a regularization matrix. λ is a hyperparameter to control the regularization, and $\mathbf{B}$ is a reconstruction matrix.

Structural priors can be included in a subset $\mathbf{S}$ consisting of M kernel functions $s_1, s_2, \dots, s_M$. In addition, the Jacobian matrix can map the change of the kernel functions to the voltage variation, but $\mathbf{J}$ requires the modification in terms of $\mathbf{J}\cdot\mathbf{S}$, giving the perquisition that an image can be restored from the kernel functions. Basic function subset derived from image processing algorithms, e.g., discrete cosine transformation or wavelet transformation, can be used as appropriate choices of the kernel functions. In this investigation, the kernel function subset $\mathbf{S}$ is derived from a DCT subset of cosine coefficients. For a two-dimensional matrix $\mathbf{A}$ with M rows and N columns, we can define the DCT by:

$$\mathbf{V}_{p,q} = \sum_{m=0}^{M-1}\sum_{n=0}^{N-1} A_{m,n}\cdot\mathbf{D}(p,q)_{m,n} \tag{2}$$

where the $\mathbf{D}(p,q)$ is cosine function combinations in terms of $\mathbf{D}(p,q)_{m,n} = \alpha_\mathrm{p}\alpha_\mathrm{q}\cos\frac{(2m+1)p\pi}{2M}\cdot\cos\frac{(2n+1)q\pi}{2N}$. The parameters p and q are the frequencies of the cosine function at the x-axis and y-axis, respectively. The order of DCT is defined as $n_{DCT} = n_{xDCT}\cdot n_{yDCT}$. In our investigation, p and q are chosen as 15 frequencies at either axis ($n_{xDCT} = n_{yDCT} = 15$), that is $p, q \in (0,1,\dots,14)$. The multiplication of $\mathbf{D}(p,q)$ and an anatomical binary lung mask $\mathbf{P}$ from morphological image yields a matrix $\mathbf{C}(p,q) = \mathbf{P}\cdot\mathbf{D}(p,q)$. The columns of the basic function subset $\mathbf{S}$ are determined as $\mathbf{S}_j = T\big(\mathbf{C}(p,q)\big)$, where T is a mapping function assigning each pixel of $\mathbf{C}(p,q)$ to the FEM elements, which covers the corresponding pixel. The subset matrix $\mathbf{S}$ is then used to modify the Jacobian matrix in terms of $\mathbf{J}_{DCT} = \mathbf{J}^{n_{meas}\times n_{elem}}\mathbf{S}^{n_{elem}\times n_{subset}}$.

Substituting the modified $\mathbf{J}_{DCT}$ into Equation 1, the reconstructed change of DCT basic functions $\hat{\mathbf{x}}$ is calculated by:

$$\hat{\mathbf{X}}_{DCT} = \left(\mathbf{J}_{DCT}^T\mathbf{J}_{DCT} + \boldsymbol{\lambda}^2\mathbf{R}\right)^{-1}\mathbf{J}_{DCT}^T\mathbf{y} = \mathbf{B}_{DCT}\mathbf{y} \tag{3}$$

With the modified reconstruction matrix $\mathbf{B}_{DCT}$, the final EIT image is reconstructed in terms of inverse DCT: i.e., $\mathbf{C}(p,q)$ is multiplied with the corresponding values of $\hat{X}_{DCT,j}$, then summed element by element:

$$\mathbf{H} = \sum_{p=0}^{n_{xDCT}}\sum_{q=0}^{n_{yDCT}} \mathbf{C}(p,q)\cdot\hat{X}_{DCT,j} \tag{4}$$

2.2 Simulations

The simulations were carried out with MATLAB R2019a (Mathworks, Natick, MA, USA) using the EIDORS toolbox[6]. With the segmentation of a CT image, a lung shape $\mathbf{P}$ and a thorax shape were used to create a mesh for the simulation. In the simulation, elements belonging to lung area were assigned with conductivity $\sigma_{lung}^{initial} = 0.5$, while the remaining elements were set to $\sigma_{non-lung}^{initial} = 1$. Boundary voltage measurement $\mathbf{v}_{initial}$ was generated with this initial setting.

Different types of $\mathbf{P}$ can be derived from the same morphological tomography. For example, a binary lung contour can be derived from the CT image to constrain the reconstruction within the lung area. We can use more details from the images, e.g., extracting atelectasis areas where reconstruction is not allowed (atelectasis area in Figure 1). In this investigation, we include two categories of structural priors: the DCT contour prior using the external lung shape, and DCT detailed priors consisting of different atelectasis levels. Please note a detailed prior without atelectasis is identical to the contour prior in our research.

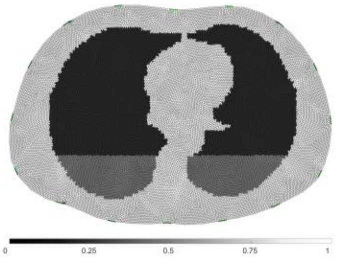

Figure 1. FEM model and electrodes layout used for simulation: exampled with 24% dorsal lung area atelectasis.

26 different scales of dorsal lung atelectasis area increasing from 0% to 50% (*AT0* to *AT50)* with equal step of 2% were simulated. It represents a simplified simulation of a patient initially suffering from 50% atelectasis but gradually recovering. One example of the simulation in terms of 24% dorsal lung atelectasis is depicted in Figure 1. Ventilated lung tissue was set to $\sigma_{lung}^{vent} = 0.25$, while the atelectasis area remained $\sigma_{lung}^{atelec} = 0.5$. For each simulation setting ATi, $\mathbf{v}_{atelec}^{i}$ was generated und used as boundary measurement for the EIT reconstructions.

Before reconstruction, 25% of Gaussian noise weighted by the standard deviation of $\mathbf{v}_{atelec}^{i} - \mathbf{v}_{initial}$ was superimposed to measurements $\mathbf{v}_{atelec}^{i}$.

2.3 Experimental Setup

For each patient status ATi ($\mathbf{v}_{atelec}^{i}$), we used the AT50 prior (increasingly false prior) for reconstruction. In addition, reconstruction was performed with the ATi prior, e.g., the correct one. Apart from different priors, three different hyperparameters, namely $\lambda_1 = 6e-2$, $\lambda_2 = 1e-2$, $\lambda_3 = 3e-3$, were evaluated in the reconstruction of each simulation setting. To prevent the 'inverse-crime', a different FEM mesh was implemented for reconstruction.

2.4 Redistribution index

The redistribution index is proposed to quantify the error induced by a detailed prior:

$$RI = \frac{\sum_{xy\in \text{cons}}\left(\mathbf{H}_{xy}^{cp} - \mathbf{H}_{xy}^{dp}\right)}{\sum_{xy\in \mathbf{H}^{dp}} \mathbf{H}_{xy}^{dp}} \tag{5}$$

$xy \in$ cons is the predefined constraining area in the detailed prior, e.g., atelectasis area; $\mathbf{H}^{dp}$ is the reconstruction using detailed prior, and $\mathbf{H}^{cp}$ is reconstruction using contour prior. The index is designed by quantifying the total reconstructed pixel redistribution from the non-constraining area to the constraining area, under the condition that predefined constraining area is removed. Equation 5 will yield an index value between 0 and 1. In this contribution, we simplified the calculation by setting the contour prior as AT0, and priors with atelectasis scales were considered as detailed priors.

3. Results

The redistribution index was calculated and depicted in Figure 2. The reconstructions, which use the fixed prior (AT50), constrained reconstruction within the 50% atelectasis area. Thus, when the atelectasis scales get reduced, the fixed AT50 prior will lose validity and produced misleading results. The quantified error is clearly shown in Figure 2. The RI from AT50 prior increased as the atelectasis scale decreases. In other words, when the difference between the real patient status and the fixed prior becomes larger, an increase will be expected in RI. When the priors are correct, the reconstructions will show less redistribution (yellow lines in Figure 2). When the atelectasis scale was less than 10%, the reconstructions with accurate priors would not exhibit no redistribution.

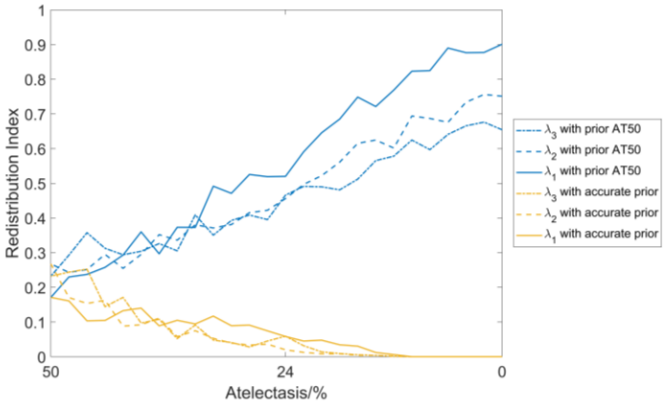

Figure 2. RI of EIT reconstructions using fixed prior and varying patient/ground truth with different λ. A simulated status ATi with AT50 prior is measured but is compared with different ground truth settings (AT50 down to AT0) (blue lines). As the AT50 prior loses validity, its RI increases independent of λ. The RI results when ground truth is used for the patient prior is shown in yellow lines. Solid lines: λ_1; dash-dot lines: λ_2; dashed lines: λ_3.

EIT reconstructions from two different simulation settings, namely 0% (AT0) and 24% (AT24) atelectasis, are shown in Figure 3. For each hyperparameter λ, the reconstructions using fixed prior and accurate prior are exampled. The choice of λ leads to different reconstructions, and the RI calculation is influenced (different types of lines in Figure 2). However, regardless of the choice of λ, RI results from AT50 prior all show the increasing tendency as atelectasis scale decreases.

4. Discussion

The redistribution index was proposed with the aim to gain hints about a false prior used in the DCT-based EIT reconstruction. It was demonstrated that there is a straightforward way to quantify the reconstruction error of a false prior. In Figure 2, an increasing trend of RI was obvious when the atelectasis scale decreased, or in other words, the increasing tendency of RI is caused by the error induced by false AT50 prior. This trend is observed in all the results from three different hyperparameter λ. In the meantime, the RI from accurate prior is rather small comparing with the RI from AT50 prior. The behaviour of RI suggests a potential to develop a RI threshold for the detection of a false prior in EIT. When the RI reached the threshold, it is assumed that the implemented prior is misleading. However, the RI threshold requires further research, and should be decided according to the requirements of different clinical applications.

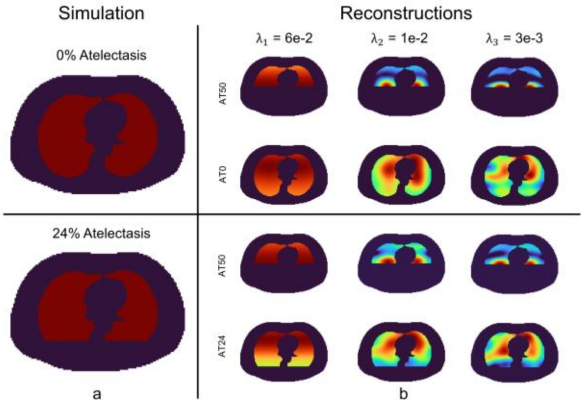

Figure 3. DCT-based EIT reconstructions from AT50 prior and accurate prior with three different regularization hyperparameter λ. a) simulation ground truth; b) reconstructions using different priors and regularization hyperparameters.

ATi prior implemented in the reconstruction are expected to be valid as it derives directly from the simulation ground truth, but a redistribution of pixel values was still observed in Figure 2. This can be explained by the nature of the solution to EIT inverse problem in terms of nonlinearity and artifacts. Nevertheless, the RI from an ATi prior is smaller and behaves differently comparing with the RI from a false prior.

It is worth noting that the behaviour of the RI is not very sensitive to the choice of regularization hyperparameter λ. The robustness of the RI might make it possible to detect a false prior even when an optimal λ is not guaranteed. However, selection of an optimal λ is still a key decision in regularization techniques of EIT[7]. Consequently, RI cannot be used as a figure of merit to characterize the performance of the EIT algorithm.

One of the limitations of this research is that a RI threshold cannot be defined by our simulation experiments. The RI threshold must be determined and changed based on the requirement and tolerance of the application, instead of remaining identical. It should be evaluated by further research with clinical data. Another limitation is that the conductivity distributions in simulations were based only on a simple physiological assumption. While in clinical settings, the patients are expected to have more complicated conductivity distribution.

Nevertheless, the behaviour of RI can be used to suggest the potential change of patient status. RI should be systematically developed to fulfil the ability as an indicator for false priors in EIT.

5. Conclusion

The redistribution index was proposed, and a preliminary evaluation was done in terms of simulations. The evaluation result reveals the potential of the RI to detect the false prior in DCT-based EIT algorithms. Considering the calculation of redistribution index, it should be possible to extend this definition to other EIT algorithms using priors.

References

[1] Frerichs I (TREND study group) 2017 Chest electrical impedance tomography examination, data analysis, terminology, clinical use and recommendations: Consensus statement of the TRanslational EIT developmeNt stuDy group Thorax 72 83–93

[2] Glidewell M and Ng K T 1995 Anatomically constrained electrical impedance tomography for anisotropic bodies via a two-step approach IEEE Transactions on Medical Imaging 14 498–503

[3] Vauhkonen M 1997 Electrical impedance tomography and prior information PhD Thesis (Kuopio, Finland: University of Kuopio)

[4] Gong B, Schullcke B, Krueger-Ziolek S, Vauhkonen M, Wolf G, Mueller-Lisse U and Moeller K 2017 EIT imaging regularization based on spectral graph wavelets IEEE transactions on medical imaging 36 1832–44

[5] Schullcke B, Gong B, Krueger-Ziolek S, Soleimani M, Mueller-Lisse U and Moeller K 2016 Structural-functional lung imaging using a combined CT-EIT and a Discrete Cosine Transformation reconstruction method Scientific reports 6 25951

[6] Adler A and Lionheart W R 2006 Uses and abuses of EIDORS: An extensible software base for EIT Physiological measurement 27 S25

[7] Braun F, Proenca M, Sola J, Thiran J-P and Adler A 2017 A Versatile Noise Performance Metric for Electrical Impedance Tomography Algorithms IEEE Trans Biomed Eng 64 2321–30

DAY 3

Friday, July 1, 2022

Invited Talk 06

Speaker Kirill Aristovich (University College London)

"Electrical Impedance Tomography to Aid Implantable Neural Interfaces"

Proceedings of the International Conference of Bioelectromagnetism, Electrical Bioimpedance,
and Electrical Impedance Tomography June 29 – July 1, 2022 / Kyung Hee University, Seoul, Korea

Electrical Impedance Tomography to Aid Implantable Neural Interfaces

Kirill Aristovich[1], Enrico Ravagli[1], Nicole Thompson[1], Svetlana Mastitskaya[1],
Anna Witkowska-Wrobel[1], Justin Perkins[2], and David Holder[1]
[1]University College London, London, UK
[2]Royal Veterinary College, London, UK

Correspondence : Kirill Aristovich, e-mail : k.aristovich@ucl.ac.uk

Abstract – Over the past several years there was a great success in the treatment of a wide range of intractable conditions such as epilepsy, chronic heart failure, chronic depression, chronic inflammation etc. using implantable electronic stimulators, which can be applied directly to the brain (Wu et al. 2021) or the peripheral nerve (Fitchett, Mastitskaya, and Aristovich 2021). Trial-and error open-loop stimulation, however, results in inefficient therapeutic outcomes and unwanted side effects. There is currently no technique however to visualise neural activity with the required prescision, which would allow imaging and mapping neural traffic to inform selective neuromodulation, and potentially serve as a feedback mechanism for closed-loop neurostimulation. Over the last several years there has been great progress in the development of fast neural EIT (fnEIT) to serve as such a tool. In the studies of rat and then porcine models of epilepsy, as well as preliminary studies in humans it was possible to image slow (~1s) and fast (~1ms) epileptiform activity in the brain with a ~1 cm (pig and human) or ~100 um (rat) resolution throughout the brain using penetrating depth electrodes (Witkowska-Wrobel et al. 2021; Hannan et al. 2020). In peripheral nerves, it was possible to image the spontaneous and evoked neural traffic in the crossection of the porcine vagus nerve with ~100um spatial (fascicular level) resolution (Thompson et al. 2022). Both advances can pave the way for a new generation of therapeutic devices, with fnEIT being currently the only tool capable of imaging real-time brain activity, or repetitive fast neural activity in the brain and peripheral nerves.

Acknowledgements

The authors would like to express their gratitude to the NIH SPARC initiative for the continuing funding under the award 3OT2OD026545.

References

Fitchett, Adam, Svetlana Mastitskaya, and Kirill Aristovich. 2021. “Selective Neuromodulation of the Vagus Nerve.” *Frontiers in Neuroscience* 15 (May): 600. https://doi.org/10.3389/FNINS.2021.685872/BIBTEX.

Hannan, Sana, Mayo Faulkner, Kirill Aristovich, James Avery, Matthew C. Walker, and David S. Holder. 2020. “In Vivo Imaging of Deep Neural Activity from the Cortical Surface during Hippocampal Epileptiform Events in the Rat Brain Using Electrical Impedance Tomography.” *NeuroImage* 209 (April): 116525. https://doi.org/10.1016/j.neuroimage.2020.116525.

Thompson, Nicole, Enrico Ravagli, Svetlana Mastitskaya, Francesco Iacoviello, Thaleia-Rengina Stathopoulou, Justin Perkins, Paul R. Shearing, Kirill Aristovich, and David Holder. 2022. “Organotopic Organization of the Cervical Vagus Nerve.” *BioRxiv*, February, 2022.02.24.481810. https://doi.org/10.1101/2022.02.24.481810.

Witkowska-Wrobel, Anna, Kirill Aristovich, Abbe Crawford, Justin D. Perkins, and David Holder. 2021. “Imaging of Focal Seizures with Electrical Impedance Tomography and Depth Electrodes in Real Time.” *NeuroImage* 234 (July): 117972. https://doi.org/10.1016/J.NEUROIMAGE.2021.117972.

Wu, Ying Chang, Ying Siou Liao, Wen Hsiu Yeh, Sheng Fu Liang, and Fu Zen Shaw. 2021. “Directions of Deep Brain Stimulation for Epilepsy and Parkinson’s Disease.” *Frontiers in Neuroscience* 15 (June): 671. https://doi.org/10.3389/FNINS.2021.680938/BIBTEX.)

DAY 3

Friday, July 1, 2022

Oral Session 10

Fast Neural Electrical Impedance Tomography

Chair Zhanqi Zhao (Fourth Military Medical University)

O 10-01 **Geometrical Optimisation of Depth Arrays for Fast Neural EIT**
Adam Fitchett (University College London)

O 10-02 **EIT imaging of rhythmic neural activity in the vagus nerve**
Enrico Ravagli (University College London)

O 10-03 **Characterising and imaging slow impedance responses to evoked somatosensory activity in the rat brain using EIT**
Karolina Kozeniauskaite (University College London)

O 10-04 **Imaging Conductvitiy Changes in a Saline Tank with Magnetic Detection Electrical Impedance Tomography with Optically Pumped Magnetometers**
Kai Mason (University College London)

Proceedings of the International Conference of Bioelectromagnetism, Electrical Bioimpedance,
and Electrical Impedance Tomography June 29 – July 1, 2022 / Kyung Hee University, Seoul, Korea

Geometrical Optimisation of Depth Arrays for Fast Neural EIT

Adam Fitchett[1], Anont Hewchaiyaphum[1], David S. Holder[1] and Kirill Aristovich[1]
[1]Medical Physics & Biomedical Engineering, University College London

Correspondence : Adam Fitchett, e-mail : adam.fitchett.16@ucl.ac.uk

Abstract–Fast neural EIT with penetrating depth electrode arrays offers promise as a technique to produce images of neural circuit activity with unparalleled spatiotemporal resolution. However, the geometry of these arrays must be optimised to ensure sufficient resolution and SNR while minimising neural tissue damage. A systematic examination of the performance of arrays with varying geometries was carried out via computational modelling, revealing the optimal electrode geometry to be 0.666 mm by 0.01 mm spaced 3 mm apart which results in 36 electrodes equally spread throughout the rat brain . In general, arrays with a small number of large electrodes and widely spaced shanks were more suitable for EIT than more compact geometries typical of the depth arrays that are currently used for single and multi-unit activity recording.

Keywords: brain, imaging, electrodes, probes, optimisation

1. Introduction

Fast neural EIT (fnEIT) is a novel brain imaging technique that offers superior spatial resolution to SEEG and LFP[1,2]. It works by injecting low amplitude alternating current through the tissue of interest and recording the voltage changes that occur when ion channels open. These voltage changes can then be used to reconstruct 3D images of the impedance changes caused by neural activity. Ideally, it would be implemented using non-penetrating surface electrodes, however, this has limited depth of field: it offers a spatial resolution of ~100μm in the cortex to a depth of 1.7mm, and so is unable to resolve deeper structures such as the thalamus or hippocampus[3].

fnEIT with penetrating depth probes has the potential to offer image reconstruction throughout the entire brain with sub 100 μm spatial resolution and sub 2 ms temporal resolution[4]. However, the depth probes currently employed for recording single and multi-unit neural activity are not optimised for fnEIT as they have small (<0.1mm^2) electrodes which severely limit EIT's SNR and current injection amplitude. **The purpose** of this study was to optimise the geometry of depth electrodes for EIT in computer simulations performed using realistic finite element modelling. This optimal geometry should maximise image resolution and localisation accuracy while minimising damage to neural tissue upon insertion.

2. Methods

2.1 Iterative Generation of Candidate Geometries

Candidates with systematically varying geometries were generated with MATLAB and COMSOL Multiphysics. The key geometrical parameters that varied were shank width (0.01 to 1 mm), electrode height (0.031 mm to 2.624 mm), inter-shank spacing (0.3 to 4 mm) and inter-electrode spacing along each shank (0.377 mm to 3.752 mm). Factors kept constant were the shank length (9 mm) and the shank thickness (0.05 mm).

Of the 1000 geometries delineated by this parameter set, 180 were physically impossible and so were excluded. The remaining candidates were used to produce a tetrahedral finite element mesh using COMSOL's default physics-controlled mesh-generation feature. Of these 820, 54 returned an error due to overlapping domains. This left a total of 766 candidates for final consideration.

2.2 Evaluation of Candidate Performance

Candidates were evaluated by simulating the EIT forward problem in COMSOL Multiphysics. To simulate the forward problem, the current was injected, and conductivity was perturbed in a known location by a set amount (0.4% compared to a uniform background conductivity of 0.3 Sm^{-1}); the resultant voltage changes were then recorded on every electrode.

The perturbations were either 0.2 or 0.05 mm in diameter and were placed halfway between two of the shanks at a depth of 5 mm below the tops of the shanks. The number of elements in each mesh was approximately 3 million.

Sinusoidal current was injected through the linearly independent set of injection pairs if there were 36 or fewer electrodes or through 36 equally spaced electrodes if there were more than 36. The amplitude was determined based on the area of the electrodes to ensure the maximum possible without exceeding the safe current density limit of 250 Am^{-2}. Noise on the electrodes was calculated according to an estimated electrode resistivity of 1 kΩmm.

2.3 Determination of Optimal Geometry

An objective function was formulated to determine the optimal geometry. This objective function attempted to maximise the average SNR and number of electrodes recording a voltage above the noise floor while minimising the shank width and the number of shanks per unit area. The negative parameters were designed to minimise damage to neural tissue. The objective function was computed for a range of different noise floors to assess the robustness of candidates to noise. The best candidate was selected on the basis of consistent performance across noise levels.

2.4 Image Reconstruction

Image reconstruction was performed with the best and worst candidates. The forward problem was solved with the bespoke software parallel EIT solver (PEITS)[5] to produce the Jacobian (sensitivity matrix). Perturbations of 0.4% conductivity change and radii varying from 0.05 to 1 mm were placed in the same location as in section 2.2. The Jacobian matrix was inverted, multiplied by the voltage changes, and projected onto a hexahedral mesh to produce the reconstructed images. Ill-conditioning was addressed by noise-based processing and zeroth-order Tikonov regularisation, with the regularisation parameter chosen by generalised cross-validation.

3. Results

3.1 Objective Function & Optimal Candidate

The objective function showed a general upward trend with candidate number. Roughly, lower numbers corresponded to more compact arrays with many small electrodes whereas larger numbers corresponded to larger arrays with a small number of large electrodes. Increasing the noise floor skewed the objective function towards these higher number candidates suggesting they were more robust to noise.

Candidate 555 displayed robustness across noise floors and also scored the highest of all candidates at a typical EIT noise floor of 1.1 µV[3]. For these reasons, it was chosen as the preferred candidate. This candidate's geometrical parameters were as follows: 36 electrodes, electrode height 0.666 mm, inter-electrode spacing 2.11 mm, shank width 0.01 mm, and shank spacing 3.00 mm.

Candidate 152 displayed the worst performance at a typical EIT noise floor. Its geometrical parameters were as follows: 153 electrodes, electrode height 0.0565 mm, inter-electrode spacing 0.502 mm, shank width 0.215 mm, and shank spacing 0.3 mm.

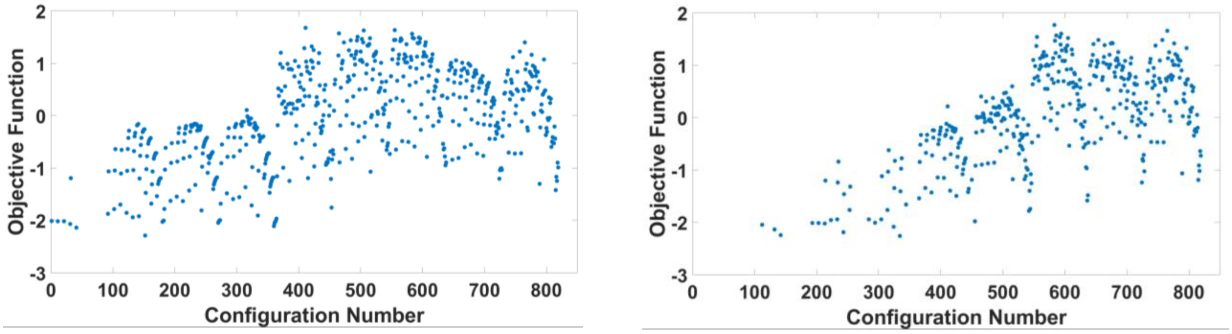

Figure 1: Objective function for all candidates when noise floor is 1.1 µV (left) or 10 µV (right). Raising the noise floor skews towards higher scores for higher candidate numbers

3.2 Image Reconstruction

With the optimal candidate, perturbations of all explored radii reconstructed as a sphere with the exception of the 0.05 mm perturbation. This perturbation did not reconstruct at all, suggesting it was completely below the threshold for detection. Localisation of the perturbations was highly accurate, with position error for all radii below $2*10^{-4}$%.

However, reconstruction of perturbation volume was considerably less accurate. The smallest volume error was 38% for a radius of 0.95 mm, while the largest volume error was 4220% for a radius of 0.1 mm. In general, perturbation radius and volume error were inversely correlated.

With the worst candidate, none of the explored perturbations reconstructed as a sphere. Unlike with the optimal candidate however, the 0.05 mm perturbation was detected and reconstructed, albeit with a high total error (1578%). Position error was much higher than the optimal candidate for all radii (minimum 7.5%). Volume error followed the opposite pattern from the optimal candidate, increasing with original volume. The lowest volume error was 13% for a radius of 0.15 mm, while the highest was 26000% for a radius of 0.65 mm.

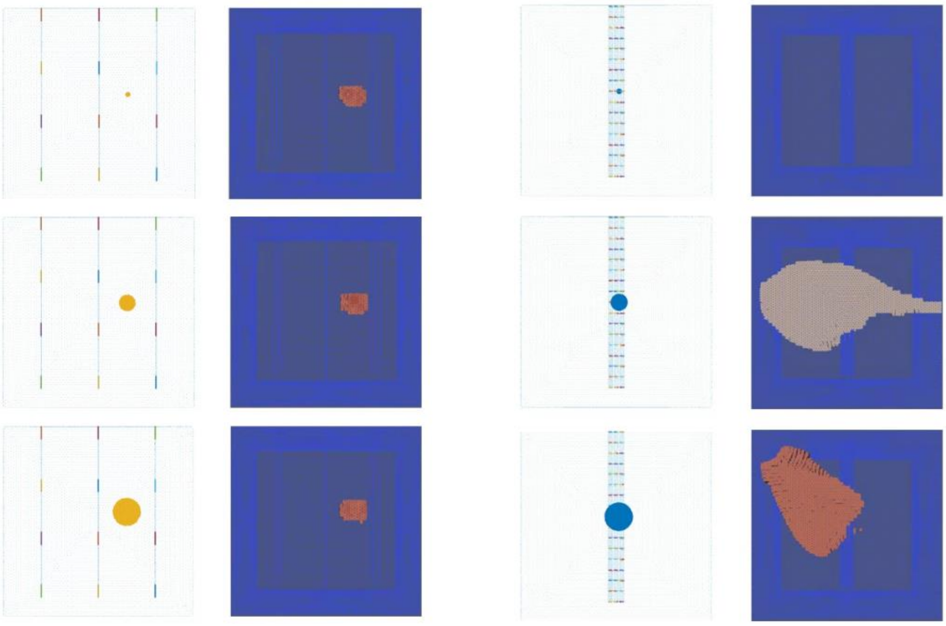

Figure 2: Reconstruction of perturbations with optimal candidate (left) and worst candidate (right). Perturbation radius: top 0.1 mm , middle 0.4 mm, bottom 0.7 mm.

4. Discussion

Geometrical optimisation of arrays for neural imaging is a vital but rarely performed task[6]. This study has provided valuable insights into the design of arrays for neural imaging. Clear trends emerged between key geometrical parameters of depth arrays and their performance in EIT imaging. This allowed an optimal candidate to be chosen and explained the variation in performance between different candidates. It also substantiated prior evidence that the most common depth array geometries would not be suitable for fnEIT[7].

Image reconstruction confirmed that the optimal candidate was far superior at EIT imaging than the worst candidate. However, while the optimal candidate provided much better localisation accuracy (maximum localisation error 0.000173% vs. 150%), the volume error was high, and the low correlation seen between real and reconstructed volume raised concern. Future optimisation studies could incorporate image reconstruction into the optimisation process itself, to ensure the chosen candidate is the best for image reconstruction. This however would be very time consuming.

Now that an optimal candidate has been chosen, it is necessary to manufacture this candidate and test its performance *in vivo*. This will both corroborate the results of modelling and allow for the development of better fnEIT techniques. Iterative adjustments to the geometry will be required during manufacturing and testing to ensure the array is easy to fabricate and insert. In particular, the optimal geometry chosen here has very narrow shanks which would likely break on insertion. The wide shank spacing will also test the limits of wire-bonding machinery. Design of depth arrays will always require a cyclic process informed by both modelling and practical use.

5. Conclusion

For fnEIT, a widely spaced array with a small number of large electrodes is preferable to more traditional depth array geometries with a large number of small electrodes and closely packed shanks. Future work will focus on manufacturing and testing the array, and performing proof of concept *in-vivo* imaging of thalamocortical interactions during somatosensory evoked activity in the anaesthetised rat brain.

References

1. Witkowska-Wrobel, A., Aristovich, K., Crawford, A., Perkins, J. D. & Holder, D. Imaging of focal seizures with Electrical Impedance Tomography and depth electrodes in real time. *Neuroimage* **234**, 117972 (2021).
2. Faulkner, M. Imaging of evoked neural activity in the rat brain using Electrical Impedance Tomography. (2019).
3. Faulkner, M., Hannan, S., Aristovich, K., Avery, J. & Holder, D. Feasibility of imaging evoked activity throughout the rat brain using electrical impedance tomography. *Neuroimage* **178**, 1–10 (2018).
4. Hannan, S. *et al.* In vivo imaging of deep neural activity from the cortical surface during hippocampal epileptiform events in the rat brain using electrical impedance tomography. *Neuroimage* **209**, 116525 (2020).
5. Jehl, M. *et al.* A fast parallel solver for the forward problem in electrical impedance tomography. *IEEE Trans. Biomed. Eng.* **62**, 126–137 (2015).
6. Fitchett, A., Mastitskaya, S. & Aristovich, K. Selective Neuromodulation of the Vagus Nerve. *Front. Neurosci.* **15**, 600 (2021).
7. Fitchett, A., Holder, D. S. & Aristovich, K. Feasibility of EIT in the Brain with an Extremely Compact Intracortical Array. in *Proceedings of the 21st International Conference on Biomediical Applications of EIT* (2021). 26.

Proceedings of the International Conference of Bioelectromagnetism, Electrical Bioimpedance,
and Electrical Impedance Tomography June 29 – July 1, 2022 / Kyung Hee University, Seoul, Korea

EIT imaging of rhythmic neural activity in the vagus nerve

Enrico Ravagli[1], Svetlana Mastitskaya[1], Nicole Thompson[1], Francesco Iacoviello[2], Thaleia-Rengina Stathopoulou[3], Justin Perkins[3], Paul R. Shearing[2], Kirill Aristovich[1], David Holder[1]
[1]Department of Medical Physics and Biomedical Engineering, University College London, United Kingdom
[2]Department of Chemical Engineering, University College London, United Kingdom
[3]Department of Clinical Science and Services, The Royal Veterinary College, United Kingdom

Correspondence : Enrico Ravagli, e-mail: e.ravagli@ucl.ac.uk

Abstract– *Background:* Effectiveness of vagus nerve stimulation as a therapeutic option is currently hampered by its lack of specificity. Spatially-selective stimulation allows for the targeting of individual groups of fibers but in addition to currently operating as trial-and-error, the functional anatomy of the vagus nerve is currently not known. *Purpose:* to enable functional imaging of organ-specific neural traffic over the cross-section of the vagus nerve using Fast Neural Electrical Impedance Tomography, for both neurophysiological research and targeted spatially-selective vagus nerve stimulation. *Methods:* Fast Neural EIT of evoked (larynx) and spontaneous (heart rate, respiration) cyclical activity was recorded in N=4 anaesthetized pigs together with selective stimulation. Coherent averaging over physiological triggers was performed to identify pulmonary- and cardiac-related functional activity. *Findings:* Distinct regions were seen in EIT images with activity from larynx, lungs and heart. Reconstructed EIT images correlated to microCT reference data with a center-of-mass error of 755±372µm, i.e. ≈25% of the nerve's diameter, and similarly to selective stimulation (704±323µm). *Conclusion:* Fast Neural EIT has, for the first time, demonstrated organotopic representation of larynx, hear and lung function in the vagus. This opens a path to improved selective vagus nerve stimulation with reduction of unwanted side effects.

Keywords: EIT; Fast Neural; Nerve; Fascicles; Neuromodulation.

1. Introduction

The cervical vagus nerve is currently one of the most common targets for neuromodulation [1], as it innervates multiple organs of the body and is relatively accessible for device implantation. However, vagus nerve stimulation (VNS) is currently carried out with bipolar stimulation of the entire nerve and thus hampered by the lack of specificity. Full-nerve stimulation may result in significant side effects to off-target organs such as the larynx and gastrointestinal system, which may cause hoarseness, dyspnoea, nausea, pain, anxiety, and cough [1]. More so, vagus nerve functional anatomy, while being under investigation by several research groups, is currently not known in detail. The technology for selective stimulation of the vagus nerve [2] is currently limited by operating on a trial-and-error basis as organization of individual fascicles inside the nerve is not known a priori.

The main purpose of this study was to enable functional imaging of organ-specific neural traffic over the cross-section of the vagus nerve, for both neurophysiological research and targeted, spatially-selective VNS, using Fast Neural Electrical Impedance Tomography (FN-EIT). This allows imaging of neuronal activity by detecting small variations in electrical impedance produced by the opening of ion channels during firing and leading to a decrease in membrane resistivity. In rat sciatic nerve, it produced images of electrical evoked compound action potential fascicle activity with a millisecond timescale and accuracy of ~10% of the nerve diameter [3,4]. In this study, an innovative version of FN-EIT triggered by physiological, rather than electrically-evoked, activity was performed to image respiratory- and cardiac-related neural traffic. We additionally imaged activity from the recurrent laryngeal branch for reference using the electrically-evoked version of the technique, and performed selective stimulation and post-mortem microCT scanning and tracing for validation of our results. By performing this study, we addressed the following questions:

1) Can FN-EIT be used to localize sources of spontaneous cyclical neural traffic in the vagus nerve? If so, is the accuracy sufficient to drive targeted VNS?

2) Can FN-EIT provide information about the functional organization of fascicles in the pig vagus nerve? How does this information compare to reference microCT data and prior findings? Are fascicles in the cervical vagus nerve organised organotopically?

2. Methods

2.1 Experimental Design

Spontaneous FN-EIT of pulmonary and cardiac activity in the left cervical vagus nerve was recorded together with electrically-evoked laryngeal FN-EIT in N=4 anaesthetized pigs. *In vivo* selective stimulation and *ex vivo* nerve microCT scans were also performed for co-registration purposes.

1. Pigs underwent surgery for exposure of the left vagus nerve in the cervical area. Multi-electrode cuffs for selective stimulation and EIT were applied proximally and distally, respectively. The recurrent laryngeal branch of the left vagus nerve was exposed and a bipolar stimulation cuff was implanted.
2. Rounds of selective stimulation were performed with the animal under spontaneous ventilation and stimulation parameters targeted at evoking pulmonary response. Following pulmonary selective stimulation rounds, pigs were restored to mechanically-assisted ventilation and further selective stimulation rounds were performed with larynx- and cardiac-targeted parameters.
3. Evoked-activity FN-EIT was performed to identify the position of the recurrent laryngeal branch over the cross section of the cervical vagus.
4. Spontaneous EIT recordings (i.e., with no electrical stimulation of the nerve) were performed while simultaneously recording physiological readout for the purpose of coherent averaging during post-processing.
5. Animals were sacrificed and dissection was performed to isolate and extract the left vagus nerve from the cervical level down to cardiac, laryngeal, and pulmonary branches. Nerves were then subject to microCT scanning.

All evoked and spontaneous EIT recordings were performed using a modified version of the ScouseTom EIT system [5] at 50kSamples/s and 24bit resolution. Modifications to the EIT system performed to improve performance in a surgery room setting included the use of a battery-powered EIT current source to reduce electrical noise and electrical shielding of the recording system and system-to-cuff cabling. All EIT traces underwent image reconstruction with noise-corrected 0-th order Tikhonov regularization [3,4].

2.2 Fast Neural Electrical Impedance Tomography

Electrically-evoked FN-EIT

FN-EIT of electrically evoked activity [3,4] was performed to image recurrent laryngeal location at the cervical vagus level due to its lack of spontaneous rhythmic activity. A nerve cuff embedding a ring-like array of 14 electrodes, 1.5 x 0.35 mm each, was used for this purpose. A bipolar cuff for stimulation (CorTec GmbH, Freiburg im Breisgau, Germany) was applied over the recurrent laryngeal branch of the left vagus nerve, approximately 40cm from the EIT cuff located on the cervical vagus common section. EIT was recorded at 6KHz carrier frequency and 200µA current amplitude in a skip-5 configuration while stimulating the bipolar laryngeal cuff with biphasic current pulses at 20Hz frequency, 50µs pulse width and 1.2mA pulse amplitude. Recordings were performed with a duration of 60s for each of the 14 injection pairs, for a total of 14min.

Spontaneous FN-EIT

Spontaneous EIT was performed at 6KHz carrier frequency and 200µA current amplitude in a skip-5 configuration on the same EIT cuff as for evoked laryngeal activity in the left cervical vagus nerve, with a duration of 480s for each of the 14 injection pairs, for a total of 112min. Recorded voltage traces were band-pass filtered with a ±2KHz bandwidth around carrier frequency and were subject to Hilbert demodulation. Demodulated voltage traces (δV) were high-pass filtered with a cut-off frequency of Fc=250 Hz, converted to root-mean-square (RMS) signals (δV-RMS) with moving average windows of 0.1s and 2s for pulmonary and cardiac traces, respectively, and subject to coherent averaging over cardiac- or pulmonary-gated cycles. δV-RMS traces were then subject to baseline subtraction. For cardiac-averaged traces, baseline time point was identified at the onset of QRS complex in the recorded ECG signals, i.e. immediately pre-contraction. For pulmonary-averaged traces, baseline time point was identified at the peak of ETCO2 signal, corresponding to the middle of expiration.

2.3 Selective neuromodulation

Spatially-selective stimulation was undertaken with consecutive stimulation of a pair of electrodes in the same radial positions in two rings of 14 electrodes spaced 4mm apart around the nerve and recording of changes in physiological parameters such as heart rate, breathing frequency, or laryngeal EMG) as an index of evoked end organ activity. Pulse width and frequency were 20Hz, 50µs for stimulation of laryngeal and pulmonary branches and 20Hz, 1ms for cardiac branch. Pulse amplitude was adjusted for each animal/organ to reach maximum selectivity and was in the range of 0.4-0.8/1-2/0.1-0.2mA for pulmonary, cardiac and laryngeal stimulation, respectively. Successful selective stimulation of pulmonary branch was assessed by identifying electrode pairs inducing partial or complete respiratory block, assessed by measurement and recording of ETCO2. Stimulation of cardiac branch was identified by pair-selective changes in heart rate (HR) measured from systemic blood pressure. Activation of fibers from the recurrent laryngeal branch was assessed by recording needle-based electromyograms (EMGs) from the larynx and identifying increase from baseline in RMS signal.

2.4 MicroCT imaging

Sections of the vagus nerve starting from the cervical level down to individual branching points were explanted post-mortem. Nerves were iodine-stained and imaged by X-ray microCT [6]. Branches leading to the heart, lungs and larynx were segmented from the rest of the nerve and traced back to the cervical level using Neurolucida 360 (Version 2021.1.3, MBF Bioscience LLC, Williston, VT USA).

2.5 Data analysis and image co-registration

SNR was computed as the ratio between average δV (for laryngeal branch EIT) or δV-RMS (for pulmonary/cardiac branches) signal at peak variation and baseline/pre-stimulus average noise. Precision of selective stimulation and EIT imaging were assessed by comparing center-of-mass (CoM) locations from the two techniques with CoMs identified from microCT imaging at cuff level. For EIT images, coordinates of peak spontaneous or evoked neural traffic were identified by computing the CoM of the highest-intensity 16 voxels (4x4 area) over the cross-section of the nerve at the time of signal peak. For selective stimulation, CoM was computed from angular coordinates of all electrode pairs inducing clearly observable neuromodulation and assuming peak stimulation at 2/3 of the average 1.5mm nerve radius. MicroCT images underwent rigid deformation to generate circular images and were rotated in accordance to the cuff opening location to have the same orientation as EIT/ selective stimulation data. All data reported as mean ± 1 standard deviation.

3. Results

Fast neural EIT allowed to image functional activity using flexible nerve cuffs in vivo and matched reference microCT data as well as trial-and-error selective electrical stimulation. For electrically-evoked laryngeal EIT, an SNR of 4.1±1.47 was achieved and 120±32 δV traces (≈83% of available) were used on average for reconstruction. For spontaneous EIT of cardiac and pulmonary activity, an SNR of 3.03±0.65 and 3.06±0.16 was achieved, respectively and 126±22 δV-RMS traces (87% of available) were used on average for reconstruction. CoM error computed in cartesian distance was 755±372µm and 704±323µm for EIT and selective stimulation in comparison to CoMs from microCT data, respectively. Angular component of CoM error was 43±28° for EIT, with a bias of 13°, and 37±27° for selective stimulation, with a 6° bias. Radial component of CoM error was 366±254 µm for EIT, with a bias of 195µm. Selective stimulation rounds with pulmonary and cardiac stimulation parameters achieved visible effects of 38.6±13.7% and -10.1±4.4% from baseline values over 3.5±2.4 and 3.5±0.6 electrode pairs, respectively. Both effects were statistically significant (T-test, $P<0.05$). Selective stimulation rounds with laryngeal parameters achieved strong laryngeal EMG activation (>10x baseline value). Angular separation with respect to the laryngeal fascicles was 118±37° and 114±77° for EIT, 125±42° and 128±36° for selective stimulation, 102±28° for cranial cuff level microCT, and 146±22° and 92±27° for caudal cuff level microCT for pulmonary and cardiac, respectively ($p<0.05$ except 0.06 for cardiac laryngeal FN-EIT).

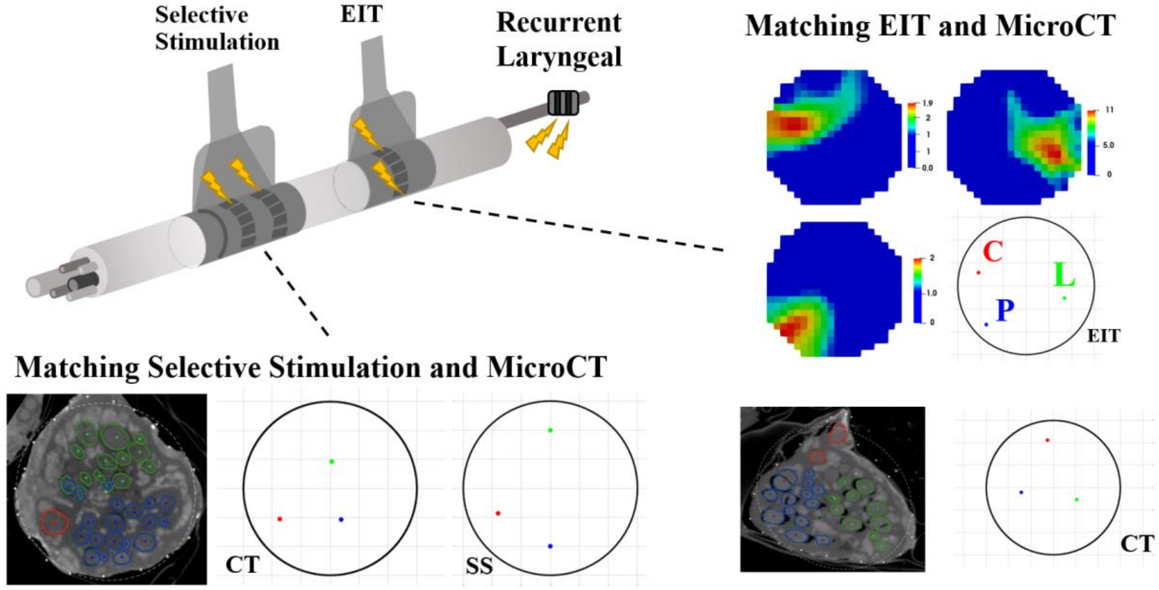

Figure 1. Selective stimulation and EIT performed with neural cuffs on the left vagus nerve in pig. Both techniques are matched to reference microCT images with segmented branches corresponding to pulmonary, cardiac and laryngeal innervation.

4. Discussion

The main technical novelty of this work is the methodology developed to detect and image fascicular neural traffic without any support from electrical stimulation, i.e. the transition from evoked to “spontaneous” EIT imaging. The physiological basis for spontaneous nerve EIT is the presence, in some particular branches or fascicles of the vagus nerve, of repeated firing of action potentials (Aps) in response to cyclical physiological activity; examples relevant for this specific study are stretch receptors firing APs along afferent nerve fibers in response to the mechanical expansion of the ventricles and lungs during the cardiac and respiratory cycles, respectively. The existence of neural traffic connected to cyclical and easily measurable physiological parameters provides, for fascicles related to such organs, the means to perform coherent averaging and reach adequate SNR levels without the repeated stimulation pulses required for evoked-activity EIT. However, the need to perform coherent averaging over physiological signals significantly extends recording time to ≈1.5h and restricts use to organ-related activity with a cyclical nature. This limitation could be overcome using an implanted ASIC-based device with SS, FN-EIT and telemetry capabilities, which would be able record and transmit data for several hours or days. More so, even identifying only sources of organ-related cyclical activity would prove very effective in avoiding multiple off-target effects in VNS.

Future work, already in progress, is to investigate the nature of the imaged spontaneous neural traffic (i.e., afferent/efferent fibers), expand to the right vagus nerve, and target more organs with spontaneous cyclical activity like the gastric system. Additionally, we plan to test our novel technique in a clinical setting by performing imaging of spontaneous vagus activity during a time window provided by surgical implantation of VNS devices.

5. Conclusions

1) Can FN-EIT be used to localize sources of spontaneous cyclical neural traffic in the vagus nerve? If so, is the accuracy sufficient to drive targeted VNS?

Yes. FN-EIT can image sources of spontaneous cyclical activity in the vagus nerve with an accuracy of ≈25% the nerve diameter, as proven by imaging pulmonary- and cardiac-related neural traffic. The angular accuracy of ≈12% is sufficient to drive targeted VNS by selective stimulation.

2) Can FN-EIT provide information about the functional organization of fascicles in the pig vagus nerve? How does this information compare to reference microCT data and prior findings?

Yes. FN-EIT was able to identify distinct areas of activity for laryngeal, pulmonary and cardiac activity in different regions of the nerve's cross-section which were consistent among animals. Functional organization also correlated with previous findings reporting organotopic organization and the microCT data from fascicular groups within the vagus nerve.

Acknowledgments

Funded by Medical Research Council UK grant MR/R01213X/1 and National Institutes of Health grant 1OT2OD026545-01 (NT, ER, SM, JP, KA, DH).

References

[1] Ben-Menachem E 2001 Vagus nerve stimulation, side effects, and long-term safety. *Journal of clinical neurophysiology : official publication of the American Electroencephalographic Society* **18** 415–8

[2] Aristovich K, Donega M, Fjordbakk C, Tarotin I, Chapman C A R, Viscasillas J, Stathopoulou T R, Crawford A, Chew D, Perkins J and Holder D 2021 Model-based geometrical optimisation and in vivo validation of a spatially selective multielectrode cuff array for vagus nerve neuromodulation *Journal of Neuroscience Methods* **352** 109079

[3] Ravagli E, Mastitskaya S, Thompson N, Iacoviello F, Shearing P R, Perkins J, Gourine A v., Aristovich K and Holder D 2020 Imaging fascicular organization of rat sciatic nerves with fast neural electrical impedance tomography *Nature Communications* **11** 1–10

[4] Aristovich K, Donegá M, Blochet C, Avery J, Hannan S, Chew D J and Holder D 2018 Imaging fast neural traffic at fascicular level with electrical impedance tomography: proof of principle in rat sciatic nerve *Journal of Neural Engineering* **15** 056025

[5] Avery J, Dowrick T, Faulkner M, Goren N, Holder D, Avery J, Dowrick T, Faulkner M, Goren N and Holder D 2017 A Versatile and Reproducible Multi-Frequency Electrical Impedance Tomography System *Sensors* **17** 280

[6] Thompson N, Ravagli E, Mastitskaya S, Iacoviello F, Aristovich K, Perkins J, Shearing P R and Holder D 2020 MicroCT optimisation for imaging fascicular anatomy in peripheral nerves *Journal of Neuroscience Methods* **338** 108652

Proceedings of the International Conference of Bioelectromagnetism, Electrical Bioimpedance,
and Electrical Impedance Tomography June 29 – July 1, 2022 / Kyung Hee University, Seoul, Korea

Characterising and imaging slow impedance responses to evoked somatosensory activity in the rat brain using EIT

Karolina Kozeniauskaite[1], Adam Fitchett[1], Kai Mason[1], Kirill Aristovich[1] and David S. Holder[1]
[1]Department of Medical Physics & Biomedical Engineering, University College London

Correspondence : Karolina Kozeniauskaite, e-mail : karolina.kozeniauskaite.20@ucl.ac.uk

Abstract– EIT can be used to image slow brain activity in response to physiological stimuli but the precise origin of those changes is unclear. The aim of this study was to charactarise and image the evoked slow impedance changes using an optimal EIT carrier frequency. Both positive and negative, slow impedance changes of 0.09 ± 0.01% (mean ± S. E.) and -0.10 ± 0.01 % respectively, were recorded around the active area in response to forelimb somatosensory stimulation across frequencies. EIT images showed consistent increases and decreases in conductivity around the active region of somatosensory cortex. Work is ongoing to investigate the spatiotemporal evolution of these changes throughout the rat brain with 3D-EIT.

Keywords: EIT, brain, rat, somatosensory activity.

1. Introduction

1.1 Background

Electrical impedance tomography (EIT) is capable of imaging fast (over milliseconds) and slow (over seconds) changes in brain tissue impedance associated with both, physiological and pathological, brain activity (Aristovich et al 2016, Hannan et al 2021). 'Fast' EIT images neural activity in real time whereas 'slow' EIT tracks impedance changes produced by the secondary processes coupled to neuronal activity (Holder, 2022). This is principally an increase in local cerebral blood volume which causes a slow local decrease in brain impedance which can be measured using EIT. It has been possible to image slow changes with EIT in rabbits with a ring of 16 electrodes placed on exposed cerebral cortex. Reproducible changes of ~2-4 % were observed in visual or somatosensory areas but there were changes of both increases and decreases (Holder et al. 1996). In humans, impedance decreases of ~ -0.5% were observed during sensory stimulation but it was not possible to reconstruct these into reproducible EIT images (Tidswell et al. 2001). EIT might be able to provide a chronic imaging device similar to fMRI but initial attempts in our group in rats with scalp electrodes showed no detectable slow impedance changes. The previous successful study in rabbits used an open craniotomy and just 16 circumferential electrodes where the imaged changes may have been due to transient brain swelling or temperature change. In this study, we aimed to characterise and image slow impedance responses to somatosensory stimulation in anesthetised rats using a planar epicortical array of 56 or 57 evenly spaced electrodes placed on exposed brain following a craniotomy. If successful, this could lead to a chronic fMRI-like portable low-cost imaging system if the skull and scalp were replaced.

The optimal SNR of the evoked slow changes was selected by recording the carrier frequency which yielded the largest signal amplitude. The expectation was that the largest SNR lay at the lower end of the frequency spectrum where the difference between the brain and blood impedance is maximal (Gabriel et al. 2009). However, noise and electrode impedance are larger at low frequencies, therefore, we set out empirically to ascertain if there was a "sweet-spot" likely to yield the clearest EIT images. The optimal frequency was then selected for EIT imaging to examine the spatiotemporal propagation of the slow neural changes following evoked somatosensory activity.

The purpose of this study was to image slow neural changes in rats with EIT and an epicortical electrode mat. Questions to be answered were: 1) What are the characteristics of single channel slow impedance changes in response to evoked somatosensory activity in rats? 2) What is the optimal carrier frequency yielding the best SNR for recording slow changes? 3) Can slow neural changes be reliably and reproducibly imaged using EIT and epicortical electrodes?

1.2 Experimental Design

Experiments were conducted in four anaesthetized rats. Three rats were used in frequency sweep experiments and one rat was used for imaging with EIT. To characterise the evoked slow impedance responses and to perform EIT, a 56 or 57-electrode epicortical array was placed on the exposed right cerebral hemisphere. Single channel impedance changes were recorded at five EIT carrier frequencies spanning from 200Hz to 10kHz. The lower frequency bound was chosen such that the majority of EEG and mains noise was eliminated during filtering. The upper frequency bound was limited by the specifications of the amplifier. The somatosensory stimulation was delivered at 11Hz in a boxcar paradigm (5s OFF - 2s ON - 13s OFF). A combination of high stimulation frequency and short duration was chosen to maximise the hemodynamic response. Slow neural changes were imaged using a parallel EIT system comprising 20 simultaneous injection pairs centred around 5kHz. The latter carrier frequency was chosen due to high SNR and consistent amplitude of recorded impedance changes. Injection protocol was optimised for maximal current density in the region of interest, that is, the forelimb area of somatosensory cortex.

2. Methods

2.1 Animal preparation

Adult Sprague-Dawley rats weighing between 300 – 400g were used in all experiments. Anaesthesia was induced and maintained by isoflurane in an oxygen/nitrous oxide vehicle. A craniotomy was performed on one hemisphere to allow implantation of a 15x9 mm^2 epicortical array manufactured from stainless steel and silicone rubber. Throughout the duration of the experiment, the core body temperature, ECG, invasive blood pressure, heart rate, respiratory rate, end-tidal and inspired CO_2 were monitored and maintained within physiological range.

2.2 Data collection and processing

Single-channel slow impedance recordings and EIT recordings were performed whilst delivering somatosensory stimulation into the contralateral forepaw at 11 Hz. A boxcar experimental design was used to quantify the change in impedance during somatosensory stimulation with respect to the baseline. Repeated periods of 2s stimulation were interleaved with periods of rest (5s OFF - 2s ON - 13s OFF). The frequency response of slow impedance changes was determined by injecting AC at 200Hz, 500Hz, 1kHz, 5kHz and 10kHz. In each recording, constant current was delivered via a single pair of injection electrodes located either side of the active area defined by the maximum amplitude of somatosensory evoked potentials (SEPs).

For EIT recordings, data was collected using a parallel EIT system of 20 current sources at 4.35-5.8kHz, spaced by approximately 50Hz, which injected 50 µA AC through a selection of injection pairs. Boundary impedance measurements were recorded simultaneously on 56 channels.

To extract slow impedance changes, the signal from each recording electrode was filtered ±20Hz around the carrier frequency using a 3rd and a 4th order Butterworth filter for single-channel recordings and EIT recordings, respectively. The filtered signal was then demodulated using the Hilbert transform. Epochs of alternating stimulation and rest were averaged together to yield a slow impedance change. To establish the relationship between the injection frequency and the magnitude or the SNR of the slow impedance responses, the top 5-7% positive and/or negative impedance changes from each recording were considered. To reconstruct EIT images of slow neural activity with a temporal resolution of 0.1s, a change in impedance with respect to baseline on all channels was calculated in 100ms intervals across the whole epoch. Images were then reconstructed using 3M forward and 80k inverse FEMs and Tikhonov regularisation.

3. Results

3.1 Characteristics of single-channel slow impedance responses across frequencies

Initial single-channel impedance measurements showed both positive and negative, impedance changes on neighbouring channels in the forelimb area of the somatosensory cortex in three rats. One rat showed only positive impedance responses (n = 1), one rat showed only negative impedance responses (n = 1), and one rat showed a mixture of positive and negative changes (n = 1). Regardless of the direction, the observed changes could be characterised by the rapid onset which coincided with the start of the somatosensory stimulation, a sharp peak at the end of the 2s stimulation and a gradual return to baseline within 8-10s after the cessation of stimulus.

The average magnitude of positive and negative impedance changes across frequencies was 0.09 ± 0.01% (mean ± S. E.) and -0.10 ± 0.01 %, respectively. There was no significant difference in the amplitude or the SNR of both positive and negative, changes across frequencies ($p > 0.05$, one-way ANOVA, Fig. 1 and 2). However, several atypically large SNR values for positive impedance changes were obtained at 5kHz (Fig. 2).

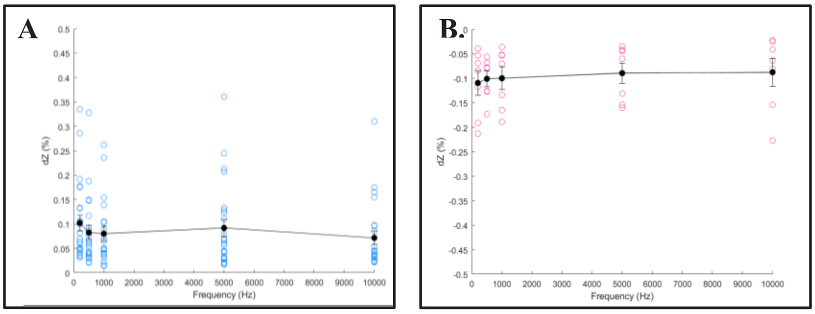

Figure 1. Magnitude of positive (A) and negative (B) impedance change dZ (%) with carrier frequency (Hz). (A) Blue dots represent top 7% of positive impedance changes from each recording in two rats (n = 2). (B) Pink dots represent top 5 % of negative impedance changes from each recording in two rats (n = 2). Black dots represent the mean impedance change at each frequency ± standard error represented by error bars. Maximum positive and negative impedance changes were not significantly different across injection frequencies ($p > 0.05$, one-way ANOVA).

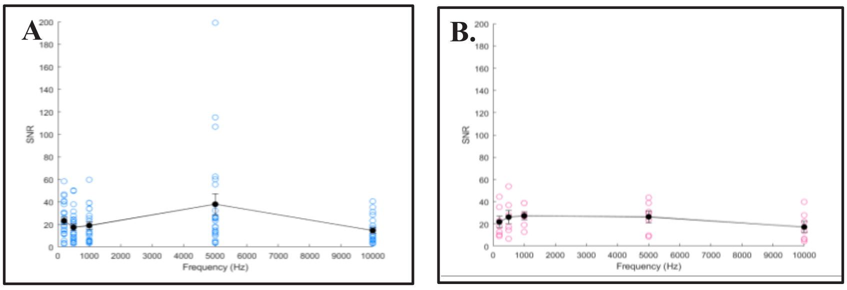

Figure 2. SNR of positive (A) and negative (B) impedance changes with carrier frequency. (A) Blue dots represent the individual SNR values for top 7% positive impedance changes from each recording in two rats (n = 2). (B) Pink dots represent the individual SNR values for top 5 % of negative impedance changes from each recording in two rats (n = 2). Black dots represent the mean SNR at each frequency ± standard error represented by error bars. SNR of positive and negative impedance changes were not significantly different across injection frequencies ($p > 0.05$, one-way ANOVA).

Preliminary data from the reconstructed EIT images indicated distinct sources of positive and negative slow impedance changes developing in parallel during the forepaw somatosensory stimulation (n = 1; Fig. 3). Qualitative visual analysis confirmed that the observed changes were localised around the area of the primary somatosensory cortex. EIT images revealed that the peak positive impedance responses had a faster onset and decline than the peak negative impedance responses. The observed slow impedance pattern was reliably reproduced 4 times within one rat (N = 4).

4. Discussion and Conclusion

4.1 Summary of the results

Somatosensory stimulation of the rat's forepaw evoked consistent positive and negative slow impedance responses in the forelimb region of the somatosensory cortex. These changes and their SNRs were not significantly different across frequencies between 200Hz – 10kHz. Consistent with the single channel data, the EIT images showed temporally aligned negative and positive slow impedance changes in the neighbouring areas of the somatosensory cortex.

4.2 Answers to questions

1) *What are the characteristics of slow impedance changes in response to evoked somatosensory activity in rats?*

The finding of bidirectional slow impedance changes in response to physiological brain stimulation is unexpected. However, it is consistent with the results from the previous studies. There are several possible explanations to these results. The sharp onset, slow decline and prolonged duration of the impedance change corresponds to the shape and the time course of both, neurovascular and neuromorphological, responses to the somatosensory stimulation in rats (Jung et al 2021, Nunes et al 2021). Recent high-field fMRI studies by Jung et al (2021) and Nunes et al (2021) investigating the spatiotemporal characteristics of hemodynamic response and transient cell swelling, respectively, demonstrate the fast onset (within <1s) and rapid propagation of slow neural responses along the thalamocortical signalling pathway. Our findings echo the results of these studies and suggest a role of distinct coupling pathways in simultaneously responding to localized neuronal activation. Alternatively, the impedance increase occurring nearby to the impedance decrease might indicate the 'blood-steal' effect (Harel et al., 2002). Future work is needed to further investigate the nature of the observed slow impedance responses.

2) What is the optimal carrier frequency yielding the best SNR for recording slow changes?

There was no significant difference in impedance responses at 200Hz – 10kHz in this study. It is unclear if this was due to experimental noise or an underlying lack of change over frequency. The carrier frequency of 5kHz was chosen on qualitative grounds for conducting the EIT recordings.

3) Can slow neural changes be reliably and reproducibly imaged using EIT and epicortical electrodes?

EIT images were obtained and reproduced within one rat. Therefore, work is in progress to collect a statistically significant dataset confirming the preliminary EIT images in a larger sample size, to improve the SNR of the images in order to evaluate their accuracy and to examine the origin and the development of evoked slow impedance changes temporally and spatially. This information would enable the functional assessment of the contribution of different coupling mechanisms towards the slow changes observed during the physiological activity in the brain.

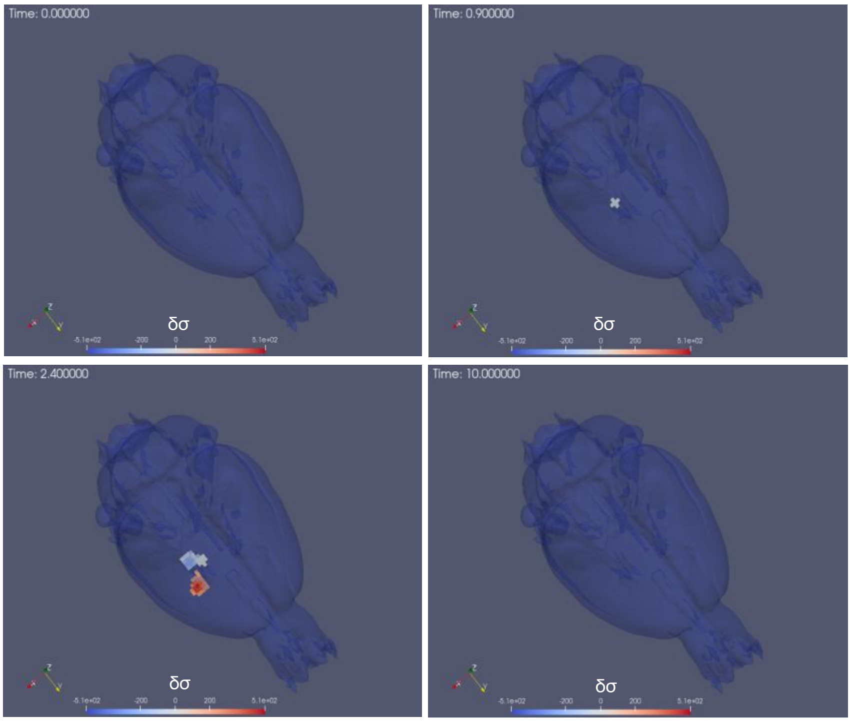

Figure 3. EIT images of slow impedance changes evoked by electrical stimulation of rat's forepaw (n = 1, N = 1). Time (top left corner) is indicated in seconds with 0 corresponding to the start of somatosensory stimulation. δσ represents the z-score of conductivity changes. Impedance increases are depicted by the blue end of the colour spectrum whereas impedance decreases are depicted by the red end of the colour spectrum.

References

Aristovich K Y, Packham B C, Koo H, Dos Santos G S, McEvoy A and Holder D S 2016 Imaging fast electrical activity in the brain with electrical impedance tomography *NeuroImage*, **124,** 204-213

Gabriel C, Peyman A, and Grant E H 2009. Electrical conductivity of tissue at frequencies below 1 MHz. *Physics in medicine & biology*, **54**(16), 4863

Hannan S, Aristovich K, Faulkner M, Avery J, Walker M C and Holder D S 2021 Imaging slow brain activity during neocortical and hippocampal epileptiform events with electrical impedance tomography *Physiological Measurement*, **42**(1), 014001

Harel N, Lee S P, Nagaoka T, Kim D S and Kim, S G 2002 Origin of negative blood oxygenation level—dependent fMRI signals *Journal of cerebral blood flow & metabolism*, **22**(8), 908-917

Holder, D 2022 EIT Imaging of Brain and Nerves. *Electrical Impedance Tomography | Methods, History Applications* **2022** (Boca Raton: CRC Press), 231-260

Holder D S, Rao A, Hanquan, Y 1996 Imaging of physiologically evoked responses by electrical impedance tomography with cortical electrodes in the anaesthetized rabbit. *Physiological measurement*, **17**(4A), A179

Jung W B, Im G H, Jiang H and Kim S G 2021 Early fMRI responses to somatosensory and optogenetic stimulation reflect neural information flow *Proceedings of the National Academy of Sciences*, **118**(11)

Nunes D, Gil R and Shemesh N 2021 A rapid-onset diffusion functional MRI signal reflects neuromorphological coupling dynamics *Neuroimage*, **231**, 117862

Tidswell T, Gibson A, Bayford R H, and Holder, D S (2001). Three-dimensional electrical impedance tomography of human brain activity. *NeuroImage*, **13**(2), 283-294

Proceedings of the International Conference of Bioelectromagnetism, Electrical Bioimpedance,
and Electrical Impedance Tomography June 29 – July 1, 2022 / Kyung Hee University, Seoul, Korea

Imaging Conductvitiy Changes in a Saline Tank with Magnetic Detection Electrical Impedance Tomography with Optically Pumped Magnetometerse

Kai Mason[1], Kirill Aristovich[1], and David Holder[1]
[1]Department of Medical Physics and Biomedical Engineering, University College London, London, UK
Correspondence : Kai Mason, e-mail : kai.mason@ucl.ac.uk

Abstract– Magnetic detection electrical impedance tomography (MDEIT) is a time difference imaging technique combining current injection with boundary electrodes and external magnetic field sensing in order to reconstruct the conductivity distribution in a conductive body. The purpose of this study was to demonstrate the functionality of the technique for conductivity distribution reconstruction in a saline tank with a resistive perturbation. Images were reconstructed using MDEIT with one ring of 16 electrodes and 25 magnetic field sensor positions using one optically pumped magnetometer (OPM). The technique successfully reconstructed images of the perturbations. NOSER and 0th order Tikhonov regularisation with simulated noise-based correction were the best performing reconstruction algorithms with position errors (mean ± SE) of 8.1% ± 0.7% and 6.7% ± 1.1% and reconstructed perturbation radius error (mean ± SE) of 5.1% ± 0.9% and 5.8% ± 0.9% respectively. This work demonstrates the functionality of MDEIT with OPMs for time-difference conductivity imaging and highlights the future potential of MDEIT for imaging fast neural activity in the human brain.

Keywords: EIT; image reconstruction; inverse problems; biomagnetism; optically pumped magnetometer

1. Introduction

Imaging fast neural activity using EIT with scalp electrodes typically involves long averaging times due to the low SNR partially caused by the resistive skull in between the point of current injection and the region of interest (Gilad & Holder, 2009). Because magnetic fields are equally attenuated by biological matter and free space, we propose that the SNR can be increased by injecting current with boundary electrodes and measuring the change in the magnetic field with external magnetic field sensors, which is called magnetic detection electrical impedance tomography. This is supported by previous computational modelling which indicated that we can expect an increase in SNR of up to 150% in the human brain by using MDEIT instead of EIT (Mason, et al., 2021). The purpose of this work was to undertake a series of experiments using MDEIT with a saline-filled tank and resistive perturbation to determine: (1) Does MDEIT with OPMs reconstruct accurate images of conductivity perturbations? (2) Which reconstruction algorithm reconstructs the best image?

2. Materials and Methods

2.1 Experimental setup

A tank of 80mm in diameter and 70mm in height was 3D printed out of a glass resin using an SLA printer (Formlabs, 2022). The tank contained recesses in the interior wall for 16 AgCl electrodes (9mm in diameter) to be equally spaced in one ring. One Quspin QZFM Gen 2.0 OPM (Quspin , 2022) was used as the magnetic field sensor and was set to measure the vertical component of the magnetic field. The OPM was held at a radial distance of 71mm from the centre of the tank in the same plane as the electrodes. The OPM's position was controlled by a system of custom-made gears and a stepper motor, allowing the OPM could be rotated in a plane around the tank. A plastic cylinder of 25mm in diameter was used as the conductivity perturbation and was placed 20mm from the centre of the tank. All experiments took place inside a 3-layer magnetically shielded chamber (Figure 1).

2.2 Experimental Procedure

The experimental procedure was as follows:

1. Start with the tank containing saline with no perturbation.
2. Position the OPM in position 1 (radially behind electrode 1).
3. Perform the entire injection protocol whilst measuring the magnetic field.
4. Move the OPM to the next position and repeat step 3.
5. Repeat step 4 for all OPM positions.
6. Repeat steps 2-5 with the perturbation in the tank.

The current was injected in a ‘skip 3’ protocol at 90Hz for 1s per injection pair. Three different peak-to-peak current amplitudes were used: 0.264mA, 0.8mA and 2.4mA, which were paired with amplifier gains of 3X, 1X and 0.33X respectively. Magnetic field data was output from the amplifier as a voltage which was sampled by an analogue to digital converter at a sampling frequency of 5kHz. 18 datasets were collected in total.

2.3 Data Processing and Analysis

Raw Data Processing

The raw magnetic field data was filtered with a 3rd order Butterworth bandpass filter with a bandpass of ±5Hz the carrier frequency, the data was then demodulated using the Hilbert Transform and filtered with a 3rd order Butterworth lowpass filter with a cut-off frequency of 5Hz. An average value of the magnetic field for the middle 20% of the injection time was then taken to obtain a value for the magnetic field. A magnetic field change due to the perturbation was then calculated.

Finite Element Mesh

All images were reconstructed on a circular, two-dimensional finite element mesh (FEM) consisting of 2014 triangular elements generated using EIDORS (Polydorides & Lionheart, 2002).

Jacobian

The Jacobian (sensitivity matrix) relating the change in magnetic field at the sensor locations to the change in conductivity of each element of the FEM was calculated using a brute-force method. The conductivity of each element was changed one by one and the response in the magnetic field at each sensor location was calculated. The code used for all forward and inverse modelling was a combination of the EIDORS software package (Polydorides & Lionheart, 2002) and custom-written code in MATLAB.

Inverse Solution and Image Reconstruction

For the image reconstruction, five different reconstruction methods were used to reconstruct images: NOSER (Cheney, et al., 1990), 0th Order Tikhonov regularisation (TR), 1st order TR (Vauhkonen, et al., 1998), 0th order TR with real noise-based correction (NBC) and 0th order TR with simulated NBC. The regularisation parameter was found using cross-validation for each method. The reconstructed images were quantitatively assessed based on the perturbation position error as a percentage of the diameter of the tank and the error in the radius of the reconstructed image assessed as the reconstructed perturbation radius as a percentage of the measured radius of the object.

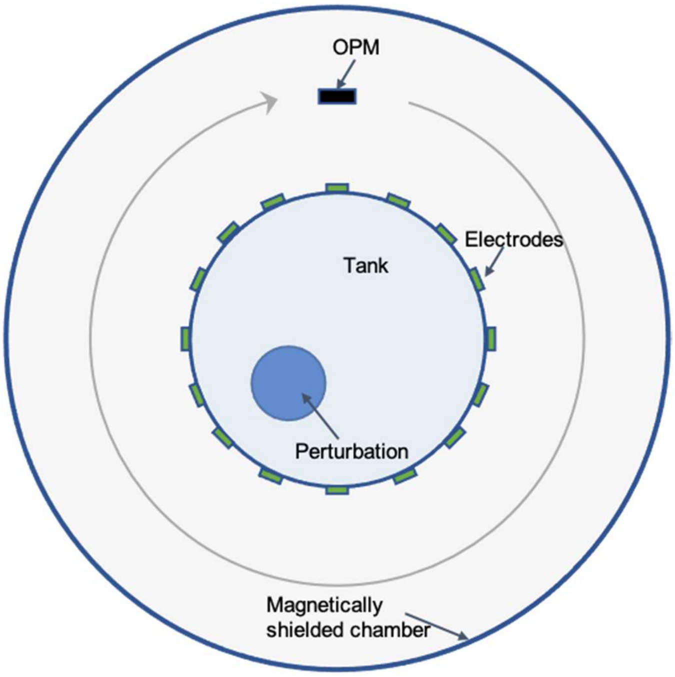

Figure 1: The setup used for the experiments showing the movement of the OPM.

3. Results

The mean of the top 10% of magnetic changes was 15% ± 4% (mean ± SD) and was reproducible across repeats. Faithful images could be consistently reconstructed in which the reconstructed perturbation's position correlated with the true location of the perturbation (Figure 3).

The NOSER and 0th Order TR with Random NBC algorithms are the best performers, and have a significantly lower position error than all other algorithms ($P < 0.009$, paired t-test). The mean position errors (mean ± SE) are 8.1% ± 0.7% and 6.7% ± 1.1% respectively (**Error! Reference source not found.**). There is no statistically significant difference in position error between NOSER and 0th Order TR with Random NBC ($P = 0.39$, paired t-test). The same two algorithms have significantly lower radius errors (mean ± SE) than all other algorithms ($P < 0.02$, paired t-test) with mean radius errors of 5.1% ± 0.9% and 5.8% ± 0.9% respectively. There is no statistically significant difference in radius error between NOSER and 0th Order TR with Random NBC ($P = 0.52$, paired t-test).

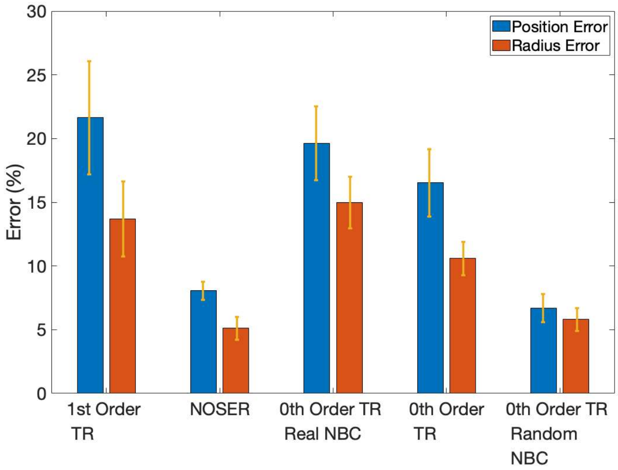

Figure 2: The mean error in position and radius of the reconstructed perturbation for each reconstruction algorithm.

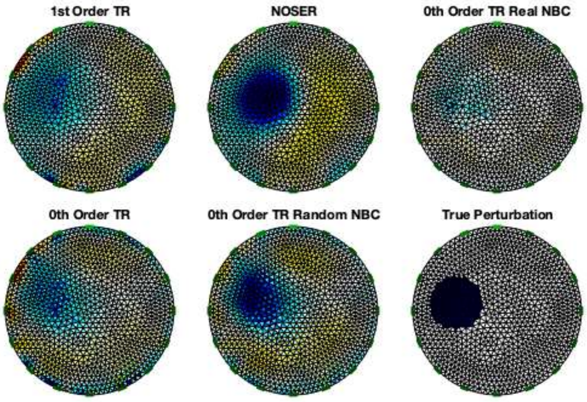

Figure 3: One example of the reconstructed images for each reconstruction algorithm considered alongside a representation of the true location and radius of the perturbation. Blue indicates an impedance increase (scales with intensity) and red indicates an impedance decrease (scales with intensity).

4. Conclusions

Following the analysis of the results the concluded answers to the previously stated questions are:

(1) MDEIT with OPMs does successfully reconstruct images of a resistive perturbation in a saline tank.

(2) The NOSER algorithm and 0th order TR with random NBC performed the best of the reconstruction algorithms that were considered based on reconstruction position and radius error. No conclusions could be drawn between these two algorithms and further testing is required to distinguish their performances.

5. Discussion

Implications of this study

The novelty of this work is in demonstrating that time-difference MDEIT with OPMs does successfully reconstruct conductivity images of a resistive perturbation in a saline-filled tank and completion of a comparison of reconstruction algorithms for MDEIT which yielded significant results. The implications of this are encouraging for the future applications of the technology for imaging fast neural activity in the brain. The fact that 0th order TR with real NBC does not perform as well as 0th order TR with random NBC indicates that the noise measured by the sensors does not accurately represent the noise from the tank. This is likely due to external noise such as vibration of the sensor and electronic noise from sources outside the magnetically shielded chamber which distort the true noise distribution from the tank and cause the output for certain pixels to be over or under suppressed, this can be seen in Figure 3 (top right) where a few, concentrated pixels show a large impedance increase.

Limitations

For this study, the perturbation was deliberately chosen to be a simple shape (a circle in 2D) and high conductivity contrast for the purpose of demonstrating the functionality of MDEIT, the limitations of this are that we cannot draw any conclusions about the ability of the technique to reconstruct more intricate geometries, or perturbations with a small conductivity contrast. The work was also limited by using one OPM in different positions rather than an array of OPMs, this could introduce sources of error such as inaccurate positioning of the sensor and/or external noise which could affect the quality of the reconstruction, particularly in the case of reconstruction with real NBC.

Future work

Future studies to build on the foundation of this work will include Imaging smaller conductivity contrasts, imaging different shaped perturbations and recording impedance changes with MDEIT in rats and humans.

References

Adler A. & Guardo R 1996 Electrical impedance tomography: regularized imaging and contrast detection. *IEEE transactions on medical imaging.* 170-179.

Cheney M. et al. 1990 NOSER: An Algorithm for Solving the Inverse Conductivity Problem. *International Journal of Imaging systems and technology.* 66-75.

Formlabs, 2022. *Rigid 10K Resin 1L.* [Online]
Available at: https://formlabs.com/eu/store/rigid-10k-resin/

Mason K, Aristovich K. & Holder D 2021. Feasibility of Imaging Fast Neural Activity Using Magnetic Detection Electrical Impedance Tomography. *21st International Conference on Biomedical Applications of Electrical Impedance Tomography (EIT2021)* **2021** 30.

Polydorides N & Lionheart W. R 2002. A Matlab toolkit for three-dimensional electrical impedance tomography: a contribution to the Electrical Impedance and Diffuse Optical Reconstruction Software project. *Measurement Science and Technology.* 1871.

Quspin , 2022. *QZFM Gen-2 (Update).* [Online]
Available at: https://quspin.com/qzfm-gen-2-update/

Vauhkonen M. et al. 1998 Tikhonov regularization and prior information in electrical impedance tomography. *IEEE transactions on medical imaging.* 285-293.

DAY 3

Friday, July 1, 2022

Oral Session 11

Clinical Application of Bio-impedance I

Chair Igor Serša (Jožef Stefan Institute)
Benjamin Sanchez (University of Utah)

O 11-01 **Screening of Cervical Intraepithelial Neoplasia based on Multiple Features Extraction of Bioimpedance Spectroscopy**
Tingting Zhang (Kyung Hee University Hospital)

O 11-02 **Bioelectrical impedance method to determine postoperative swelling of the knee joint**
Lucas Lindeboom (Stichting imec Nederland/Holst Centre)

O 11-03 **Estimation of skeletal muscle specific force in diseased muscle using needle electrical impedance myography**
Benjamin Sanchez (University of Utah)

O 11-04 **Assessment of the Diagnostic Value of Body Impedance in Pre-eclampsia Screening**
Svetlana Pavlovna Shchelykalina (Pirogov Russian National Research Medical University)

O 11-05 **Electrical Impedance Spectroscopy of Ex-Vivo Human Lung Tissue**
Harshavardhan Devaraj (Dartmouth College)

O 11-01

Proceedings of the International Conference of Bioelectromagnetism, Electrical Bioimpedance,
and Electrical Impedance Tomography June 29 – July 1, 2022 / Kyung Hee University, Seoul, Korea

Screening of Cervical Intraepithelial Neoplasia based on Multiple Features Extraction of Bioimpedance Spectroscopy

Tingting Zhang[1,2], Jin Won Mok[1,2,3], Jun Beom Heo[1,3], Dong Choon Park[4], and Tong In Oh[1,2,3]
[1]Medical Science Research Institute, Kyung Hee University Hospital, Seoul, Korea
[2]Department of Biomedical Engineering, School of Medicine, Kyung Hee University, Seoul, Korea
[3]Department of Medical Engineering, Graduate School, Kyung Hee University, Seoul, Kore
[4]Department of Obstetrics and Gynecology, Saint Vincent's Hospital, The Catholic University of Korea, Korea.

Correspondence : Tong In Oh, e-mail : tioh@khu.ac.kr

Abstract The screening of cervical intraepithelial neoplasia (CIN) aims to provide a chance for early detection and treatment of the pathological behavior of cervical tissues before it progresses to cervical cancer. In this study, a bioimpedance spectroscopy-based multi-electrode probe has been developed to measure the complex impedance of the cervix and adopted for the screening of CIN. In addition, the classical Cole-Cole model has been adopted to extract electrical parameters and thereby generate geometrical parameters with respect to cervical tissues, which were afterward exploited for CIN identification. Results show that the proposed features demonstrate a significant difference among different groups of CIN and thus provide a real-time, non-invasive, and cost-effective technique for screening CIN with high sensitivity and specificity.

Keywords: cervical intraepithelial neoplasia; multi-electrode probe; Cole-Cole model; geometrical features

1. Introduction

There have been continuously attempted to diagnose cancer using the electrical properties of in-vivo tissues since they vary with respect to the pathological status of tissues. In particular, cervical tissue is an excellent candidate in that it can easily contact electrodes for measuring impedance spectra compared to other tissues. For these reasons, a bioimpedance spectrum-based classification algorithm and system have been proposed for CIN screening of cervical tissues [Zhang2021, Oh2021, Abdul2006, Brown2000]. In this study, we characterized the electrical properties of cervical tissue based on the classical Cole-Cole model and the magnitude of the impedance spectrum corresponding to intra/extra-cellular resistivity [ColeCole1941]. Additionally, we extracted geometrical features from the Cole-Cole plot. All the extracted parameters are then employed to identify the pathological condition of the cervix: normal, low-grade squamous intraepithelial lesion (LSIL), and high-grade squamous intraepithelial lesion (HSIL).

2. Methods

The multi-electrode screening probe with 16 miniaturized electrodes was used to collect the frequency-dependent complex impedance of the cervical tissue in-vitro [Zhang2021, Oh2021] and let $Z_j = Z_j^r + iZ_j^i$ be the complex data at a frequency range of $f_j, j = 1,2, \dots ,6$. After that, the magnitude of $|Z_j|$ can be fitted by a least-square deviation method to a Cole-equation where the extracellular resistivity R, intracellular resistivity S, and the ratio R/S can be extracted [Brown2000]. Analogously, the real (Z_j^r) and imaginary part (Z_j^i) can be modeled by the Cole-Cole plot [ColeCole1941], which gives the extracted parameters like the geometrical center of the arc (X0, Y0), Radius, θ, maximum of the spectrum (MAXIP), the distance between spectral ends (DA) $|Z_1 - Z_6|$, projected distance DR $|Z_1^r - Z_6^r|$, the phase angle at 50kHz and 500kHz (P50, P500), the length of spectra P, and the derived parameters. Thereafter, all the above parameters with larger difference among groups will be used to classify the pathological condition of the cervix.

3. Results

To determine the feasibility of classification of cervical tissues with different pathological condition, the distribution of the features of each group has been studied. As shown in Fig. 1, we illustrated the statistical characteristics of all the extracted features studied in this work among the non-CIN, LSIL and HSIL groups. The data is represented as mean ± standard error. Except for the intracellular resistivity S, a reduction in the magnitude of all the other features can observe as the CIN increases, which provides new insights into the separation strategies of the pathological cervix. Additionally, more significant discrepancies can be observed between the normal cervix and HSIL. For better explanation, we have illustrated in Fig. 2 one example of the Cole-Cole plot of the normal cervix and HSIL cervix.

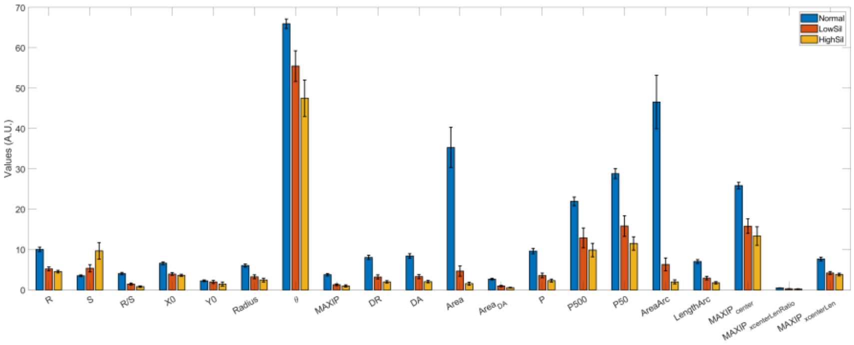

Figure 1. Bar graph of the mean and standard error (SE) for the extracted features with respect to the pathological conditions of cervix: normal, LSIL, and HSIL.

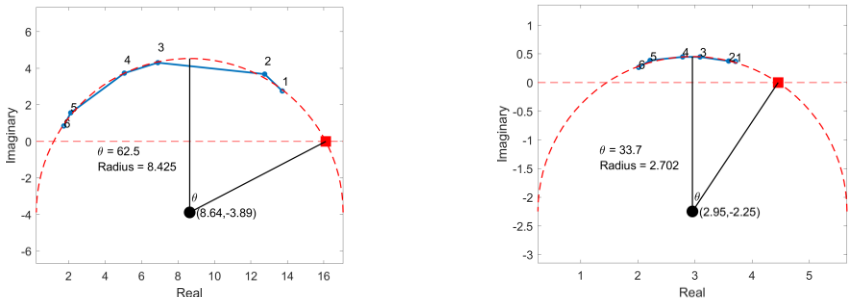

(a) (b)

Figure 2. One example of Cole-Cole plot of (a) normal cervix and (b) HSIL.

4. Conculusion

We proposed the classification method for screening CIN using multiple features extracted from the complex bioimpedance spectrum, including geometrical features from the Cole-Cole plot. The proposed technique could better characterize the properties of the cervix and thus improve the capability of CIN screening. Further research efforts should be focused on selecting the classifier and combining features for better performance in the separation of the cervix.

Acknowledgments

This research was supported by Basic Science Research Program through the National Research Foundation of Korea (NRF) funded by the Ministry of Education (NRF-2020R1I1A1A01066649), and the National Research Foundation of Korea (NRF) grant funded by the Korea government (NRF-2020R1A2C1008975 and NRF 2019R1A2C1086807).

References

Abdul S, Brown B H, Milnes P and Tidy J A 2006 The use of electrical impedance spectroscopy in the detection of cervical intraepithelial neoplasia *International Journal of Gynecologic Cancer* **16** 5

Brown B H, Tidy J A, Boston K, Blackett A D, Smallwood R H and Sharp F 2000 Relation between tissue structure and imposed electrical current flow in cervical neoplasia *The Lancet* **355** 892-895

Zhang T, Jeong Y, Park D and Oh T 2021 Performance evaluation of multiple electrodes based electrical impedance spectroscopic probe for screening of cervical intraepithelial neoplasia *Electronics* **10** 1933

Oh T I, Kang M J, Jeong Y J, Zhang T, Yeo S G and Park D C 2021 Tissue characterization using an electrical bioimpedance spectroscopy-based multi-electrode probe to screen for cervical intraepithelial neoplasia *Diagnostics* **11** 2354

Cole K S and Cole R H 1941 Dispersion and absorption in dielectrics I. Alternating current characteristics *The Journal of chemical physics* **9** 341-351

ICBEM Bioelectromagnetism ICEBI Electrical Bioimpedance EIT Electrical Impedance Tomography

Proceedings of the International Conference of Bioelectromagnetism, Electrical Bioimpedance,
and Electrical Impedance Tomography June 29 – July 1, 2022 / Kyung Hee University, Seoul, Korea

Bioelectrical impedance method to determine postoperative swelling of the knee joint

Heleen Boers[1], Wael Hamada[1], Lucas Lindeboom[1] and Walter van der Weegen[2]
[1] Stichting imec Nederland/Holst Centre, Eindhoven, The Netherlands
[2]Sports & Orthopedics Research Centre, Anna Hospital, Geldrop, The Netherlands.

Correspondence : Heleen Boers, e-mail : heleen.boers@imec.nl

Abstract– Postoperative swelling of the knee joint is part of an inflammatory response. However, if swelling is excessive it is an indicator of overload during rehabilitation. To date, there is no objective method to monitor knee swelling. Bioelectrical impedance analysis (BIA) has been used to measure body fluid balances and to indicate inflammation. Therefore, the aim of this study was to determine whether BIA can be used to quantify postoperative knee swelling. To relate the BIA parameters to the amount of fluid, an ex vivo experiment was performed using a porcine hindlimb with intact skin. NaCl 0.9% was injected in steps of 2mL and BIA was done after every step at 3 frequencies (5, 50 and 200 kHz). Subsequently, a clinical pilot was done with 10 patients with postoperative knee swelling. BIA was done on both the injured and the healthy leg. In addition to conventional gel electrodes, a brace with silver-plated nylon as dry electrodes was used. The results show a lower resistance, lower phase angle and higher impedane ratio for the injured knee vs. the healthy knee. Taken together, this exploratory study shows that BIA with a brace is a promising method to monitor postoperative swelling at home.

Keywords: *Bioelectrical impedance analysis; knee; brace; inflammatory response; swelling*

1. Introduction

Swelling of the knee joint is normal and expected in patients after surgery such as anterior cruciate ligament (ACL) reconstruction or total knee replacement (Loyd *et al.*, 2020). As these procedures are highly invasive, the associated tissue damage causes a major inflammatory response (Chovatiya and Medzhitov, 2014). The concomitant postoperative swelling restricts range of motion and can have a negative influence on perception of recovery and pain if it is excessive. Currently, the clinical assessment of knee swelling is done by trained physiotherapists. This is achieved by comparing the circumference of the knee (Jakobsen *et al.*, 2010), or by dynamically sensing the movement of the fluid across the knee with special techniques like the Bulge sign, Patellar tap, and sweep tests (Maricar *et al.*, 2016; Wang *et al.*, 2020). However, these methods have been shown to be imprecise and subjective (Hidding *et al.*, 2016).

Recently, bioelectrical impedance analysis (BIA) has been used as an objective method for quantification of swelling (Loyd *et al.*, 2021). To date, the method focuses on using single frequency (SF) at 50 kHz, where the main resistance is offered by the extracellular water (ECW). In other studies, focusing on inflammation, multi-frequency (MF) BIA is used to differentiate between intracellular (ICW) and extracellular fluids (Pichonnaz *et al.*, 2015; Cederholm *et al.*, 2017). In addition, BIA parameters such as phase angle and impedance ratio add information about the cell membrane function (da Silva *et al.*, 2022). As swelling is caused by an inflammatory response, it is hypothesized that the inclusion of MF BIA parameters might be beneficial for the quantification of postoperative swelling.

Therefore, the aim of this study was to develop an objective method to quantify postoperative swelling using MF BIA to assess ECW, ICW and cell membrane function. To evaluate the relation between the volume inside the joint and the MF BIA parameters, an ex vivo experiment was performed on a porcine hindlimb. Subsequently, a clinical pilot was performed on patients with postoperative swelling after ACL reconstruction. In addition, a novel electrode setup with conductive textile integrated into a brace was compared to the adhesive electrodes used in clinical practice. The application of the brace allows for easy adaption in clinics and at home measurements.

2. Materials & method

2.1 Ex vivo experiment

To mimic swelling in the knee joint, NaCl 0.9% was injected into the ankle joint of a fresh porcine hindlimb with intact skin (see figure 1). The fluid was injected in steps of 2 mL, up to a total of 80 mL. MF BIA was measured after each step using the Maltron Bioscan 920-II at 5, 50 and 200 kHz and Ag/AgCl adhesive gel electrodes. The electrodes were secured using duct tape, to avoid their detachment during the experiment.

2.2 Clinical pilot

At the physiotherapy center TopSupport in Eindhoven, 10 patients with ACL reconstruction were enrolled for a clinical pilot. The medical ethical committee of the MMC Veldhoven granted exemption for this study (N21.048). Both the healthy and the injured knee of each patient were measured using the Maltron Bioscan 920-II at 5, 50, and 200 kHz. All patients were measured with the adhesive gel electrodes first, followed by the brace (see figure 1). Adhesive electrodes were placed using a template to ensure that they were located at the same distance as in the brace. Patients were asked to lay supine for 5 minutes before the measurement. Knee circumference of both legs was then measured at the superior pole of the patella using a standard medical tape measure.

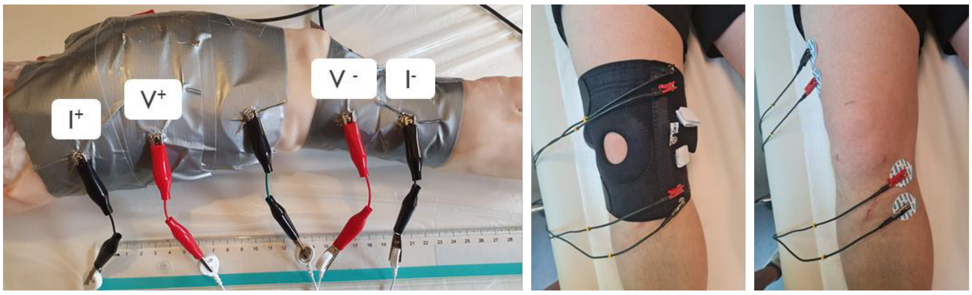

Figure 1. LEFT: photo of ex vivo experiment with porcine hindlimb, (I) location of current injecting. (V) location of voltage sensing electrodes.. RIGHT: photo of the clinical pilot with the brace and the gel electrodes. The current injection is on the outer electrodes (black lead), the voltage sensing on the inner electrodes (red leads).

2.3 Brace

The brace was made by integrating silver-plated nylon, with a resistance of less than 1Ω per 30 cm over the length, in the inside of a Velcro brace (see figure 2). The width of the nylon strips in the brace was 1 cm. The nylon serves as a dry electrode. The design of the electrodes was chosen such that the MF BIA measurement would cover the whole circumference of the knee joint. Push button connectors were added to allow the MF BIA device to connect to the conductive textile from the outside of the brace.

Figure 2. Custom-made brace. LEFT: inside of the brace. (I) shows the outer silver-plated nylon electrodes used for current injecting. (V) are the inner voltage sensing electrodes. Nylon is 1 cm in width. RIGHT: outside of the brace with push buttons to connect the MF BIA device.

2.4 Analysis

The relative resistance (relR) at 5 kHz was calculated using equation (1) (Loyd *et al.*, 2021):

$$relR = 1 - \left(\frac{R_{injured}}{R_{healthy}}\right) * 100 \tag{1}$$

where $relR$ = relative resistance (%)
$R_{injured}$ = resistance (Ω) of the injured leg
$R_{healthy}$ = resistance (Ω) of the healthy leg

In the ex vivo experiment, $R_{healthy}$ was replaced by the R_0 of the baseline measurement (before fluid injection). $R_{injured}$ was replaced by the R_{fluid} following each step of fluid injection. The $relR$ of the ex vivo experiment was used to fit a 2nd order regression model with $relR$ as regressor and the injected volume (in mL) as the predicted variable.

The phase angle at 50kHz of the clinical pilot was used for analysis of the cell membrane function. The impedance ratio (IR) was calculated using equation (2) (Rinninella *et al.*, 2018):

$$IR = (Z\ at\ 200kHz)/(Z\ at\ 5kHz) \tag{2}$$

Normality was assessed using histograms and the Anderson-Darling test for normality. To assess whether the injured knee was significantly different from the healthy knee, and depending on the outcome of the normality test, a paired t-test or a Wilcoxon signed rank test was used. Boxplots were visually inspected to assess the difference between the gel

electrodes and the brace. The correlation between the relative resistance and the knee circumference was determined using Pearson's R. A p-value of <0.05 was considered statistically significant.
All statistical analyses were performed in MATLAB R2018.

3. Results

3.1 Ex vivo experiment

The resistance at 5kHz decreased after every injection of 2mL NaCL 0.9% (from 198Ω at baseline to 105Ω after 80 mL). To relate the ex vivo experiment to the clinical pilot, the relative resistance was calculated as described with equation (1). The *relR* was related to the injected volume (*V)* (see figure 3) with the 2nd order polynomial equation shown in equation (3).

$$V = 0.017 * relR^2 + 0.87 * relR + 0.80 \qquad (3)$$

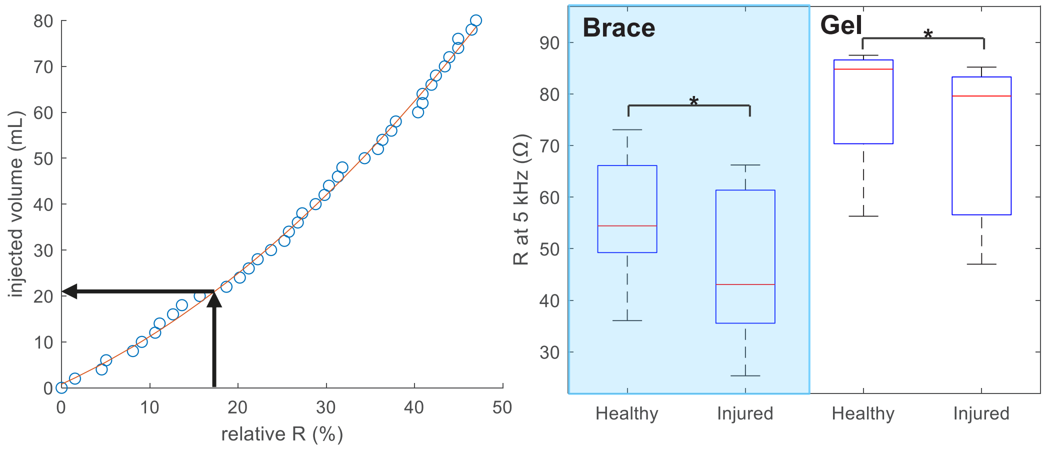

Figure 3. LEFT: graph of second order polynomial fit with arrows indicating the relative R of the brace. RIGHT: boxplots of the resistance at 5kHz for both healthy and injured leg, measured with both the brace and the gel electrodes.

3.2 Clinical pilot

Of the 10 subjects, 1 had excessive hair which interfered with the MF BIA measurement. As shaving was too invasive for the pilot, the data from this subject was excluded from the analysis. The subjects' demographics are shown in table 1. The mean difference in knee circumference was 1.23 cm, which was significantly different from zero ($p<0.01$).
The resistance at 5 kHz of the healthy knee was significantly higher compared to the injured knee for both the gel and the brace (see table 1). The phase angle at 50kHz of the healthy knee was higher compared to the injured knee. This difference was significant for both electrode types. Lastly, the IR of the healthy knee was lower compared to the injured knee. The difference was significant for both the brace and the gel electrodes. There was no significant correlation between the knee circumference and the resistance, for neither brace nor gel electrodes.

Table 1 - Subject Demographics

Characteristic	Mean (SD)
Age	28.9 (13.4)
Gender	Female (2) / Male (7)
BMI (kg/m^2)	25.1 (6.2)
Δ Knee circumference (cm)	1.23 (1.0)

To compare the results of the clinical pilot to the ex vivo experiment the relative resistance was calculated. For the brace the relR was 17.3% and significantly different from 0 ($p<0.05$), referring to a decrease of the resistance of the injured knee relative to the healthy knee. For the gel electrodes the relR was lower (11.4%), but also significant.
Using the polynomial equation in (3) from the ex vivo experiment to estimate the amount of fluid inside the knee, a volume of 20.9 mL for the mean relR of the brace (17.3%) was estimated.

Table 2 - MF BIA metrics: Mean (SD). * Difference injured vs. healthy significant $p<0.05$

MF BIA metric	Healthy (gel)	Injured (gel)	Healthy (brace)	Injured (brace)
R at 5 kHz (Ω)	78.5 (11.1)	70.0 (15.6)*	56.7 (12.4)	47.6 (14.5)*
relR (%)	-	11.4 (11.0)*	-	17.3 (9.9)*
PhA at 50 kHz	12.2 (3.4)	11.1 (3.5)*	8.4 (1.6)	7.3 (2.1)*
IR (200/5 kHz)	0.649 (0.085)	0.678 (0.088)*	0.714 (0.047)	0.751 (0.058)*

4. Discussion

It is known that the inflammatory response after ACL reconstruction leads to swelling of the knee joint. Due to the increase of fluid inside the joint the tissue resistance will decrease [7]. This was illustrated by an ex vivo experiment on the ankle joint of a fresh porcine hindlimb, in which the relation between fluid injection and the relative change in resistance at 5 kHz was determined. It was found that the relationship between the resistance and the injection of fluid was inverse of 2nd order, and not explainable with a first order regression model. This observation might be explained by morphological changes in the joint, in accordance with the Hanai mixture theory (i.e. change in length versus cross sectional area) (Hanai, 1962).

The findings from the ex vivo experiment were further strengthened in the clinical pilot study. In this study the BIA from the injured knee was compared to the healthy knee of patients after ACL reconstruction. The results show that it is possible to discriminate the healthy from the injured knee with all the three different metrics (R at 5 kHz, phase angle at 50 kHz and impedance ratio of 200/5kHz). The change in R at 5 kHz was in line with the ex vivo experiments and can be explained by an increase in fluid accumulation in the injured knee compared to the healthy knee. Both the phase angle and the impedance ratio are thought to reflect cellular health [11]. In former studies the phase angle has been correlated to inflammation [10], which might explain the results found in this study. The lower phase angle and higher IR can either be due to a change in cellular capacitance or a change in the ratio of ECW vs. ICW.

5. Conclusion

In this work, it was shown that BIA can be used to assess postoperative swelling of the knee joint in patient that underwent ACL reconstruction. With BIA it was possible to discriminate between the injured and the healthy knee, based on either the resistance at low frequency, the phase angle or the impedance ratio. Furthermore, it was shown that a custom-build brace with silver-plated nylon serving as a dry electrode gives superior results over commonly used gel electrodes. The BIA method holds the promise to be used as an objective method to assess swelling of the knee joint, next to or as a replacement of the assessment used in clinical practice, which might be subjective. Further development of this brace along with a wearable BIA device will allow for an objective and portable solution to monitor postoperative knee swelling.

References

Cederholm, T. *et al.* (2017) ‘ESPEN guidelines on definitions and terminology of clinical nutrition’, *Clinical Nutrition*, 36(1). doi: 10.1016/j.clnu.2016.09.004.

Chovatiya, R. and Medzhitov, R. (2014) ‘Stress, inflammation, and defense of homeostasis’, *Molecular Cell*. Elsevier Inc., 54(2), pp. 281–288. doi: 10.1016/j.molcel.2014.03.030.

Hanai, T. (1962) ‘Dielectric Theory on the Interfacial Polarization for Two-Phase Mixtures’, *Bulletin of the Institute for Chemical Research, Kyoto University*, 39(6).

Hidding, J. T. *et al.* (2016) ‘Measurement properties of instruments for measuring of lymphedema: Systematic review’, *Physical Therapy*. doi: 10.2522/ptj.20150412.

Jakobsen, T. L. *et al.* (2010) ‘Reliability of knee joint range of motion and circumference measurements after total knee arthroplasty: Does tester experience matter?’, *Physiotherapy Research International*, 15(3). doi: 10.1002/pri.450.

Loyd, B. J. *et al.* (2020) ‘Development of a reference chart to monitor postoperative swelling following total knee arthroplasty’, *Disability and Rehabilitation*, 42(12), pp. 1767–1774. doi: 10.1080/09638288.2018.1534005.

Loyd, B. J. *et al.* (2021) ‘Reliability and precision of single frequency bioelectrical impedance assessment of lower extremity swelling following total knee arthroplasty’, *Physiotherapy Theory and Practice*. Taylor & Francis, 37(1), pp. 197–203. doi: 10.1080/09593985.2019.1619886.

Maricar, N. *et al.* (2016) ‘Clinical assessment of effusion in knee osteoarthritis-A systematic review’, *Seminars in Arthritis and Rheumatism*. Elsevier, 45(5), pp. 556–563. doi: 10.1016/j.semarthrit.2015.10.004.

Pichonnaz, C. *et al.* (2015) ‘Bioimpedance spectroscopy for swelling evaluation following total knee arthroplasty: A validation study Orthopedics and biomechanics’, *BMC Musculoskeletal Disorders*. ???, 16(1), pp. 1–8. doi: 10.1186/s12891-015-0559-5.

Rinninella, E. *et al.* (2018) ‘Phase angle and impedance ratio: Two specular ways to analyze body composition’, *Annals of Clinical Nutrition*, 1(1), pp. 1–5. doi: 10.33582/2638-1370/1003.

da Silva, B. R. *et al.* (2022) ‘Exploring the potential role of phase angle as a marker of oxidative stress: A narrative review’, *Nutrition*. doi: 10.1016/j.nut.2021.111493.

Wang, Y. *et al.* (2020) ‘The bulge sign-a simple physical examination for identifying progressive knee osteoarthritis: Data from the Osteoarthritis Initiative’, *Rheumatology (United Kingdom)*, 59(6). doi: 10.1093/rheumatology/kez443.

Proceedings of the International Conference of Bioelectromagnetism, Electrical Bioimpedance,
and Electrical Impedance Tomography June 29 – July 1, 2022 / Kyung Hee University, Seoul, Korea

Estimation of skeletal muscle specific force in diseased muscle using needle electrical impedance myography

Benjamin Sanchez[1] and Seward B. Rutkove[2]
[1]Department of Electrical and Computer Engineering, University of Utah, Salt Lake City, UT, USA
[2]Department of Neurology, Beth Israel Deaconess Medical Center, Boston, MA, USA

Correspondence : Benjamin Sanchez, e-mail : benjamin.sanchez@utah.edu
and Seward Rutkove, e-mail : srutkove@bidmc.harvard.edu

Abstract– *Background*: Specific force (maximal muscle force normalized to muscle size) is the single most valuable measure of the intrinsic health of a muscle. However, obtaining this measure accurately in humans is challenging since it requires painful high frequency nerve stimulation and time-consuming muscle imaging. *Methods*: Here, we evaluated the potential for predicting muscle specific force with needle electrical impedance myography (EIM) in healthy and muscular dystrophy mice. *Results*: Similar to the force-stimuli relationship, our results show the impedance increases with isometric contraction and that the magnitude of change depends on muscle activation. This impedance-force relationship was found to be different in healthy and diseased muscle supporting the idea that EIM can provide additional functional information currently unavailable with standard electrodiagnostic techniques. *Conclusions*: Needle EIM could greatly simplify the approach for obtaining an accurate measure of muscle specific force, leading to its wide application in future clinical neuromuscular disease research and care.

Keywords: Specific force, electrical impedance myography, neuromuscular disorders.

1. Introduction

The assessment of function in neuromuscular disorders (NMDs) remains a major challenge to studying progression and the effect of therapy. Indeed, therapeutic clinical trials have incorporated a variety of approaches to assess disease progression, including outcome measures, questionnaires, and various types of force measurements to gauge disease progression or remission. These include the 6-minute walk test, used in Duchenne muscular dystrophy assessments and the ALS Functional Rate Scale-Revised in ALS. In addition to such questionnaires, measures of muscle force are used including, manual muscle testing in which strength is scored on a subjective 0-5 scale and quantitative muscle testing with a fixed-frame apparatus or via handheld dynamometry in which actual force values are produced.

While such outcomes are undeniably valuable, they are somewhat removed from the intrinsic muscle-related disease effects. They are also subject to considerable variability that are both patient and operator-generated, since outcomes are dependent on patient motivation, the presence of joint or limb pain, subjective fatigue, and full understanding of the testing request (which is especially limited in young children and those with intellectual disability). Moreover, they often require considerable skill on the examiner's part, leading to poor data quality. Finally, strength measurements are also incapable of providing actual quantification of the intrinsic force of the muscle. For all of these reasons, such clinical measures, while valuable and practical, have major limitations.

The term specific force (SF) implies measurement of the inherent force-generating capability of a muscle or muscle group. To muscle physiologists, it implies an understanding of not only the maximal force generated and the size of the muscles, but also the pennation angle of the muscle, since the greater the angle of pennation, the less intrinsic force generating capability. However, to practicing clinicians, a more practical meaning of SF is normalized force—that is maximal isometric force output simply divided by muscle size (measured as cross-sectional area or muscle volume with imaging if available). In pre-clinical studies, maximal isometric force can be normalized to muscle mass measured after animal euthanasia. In either case, rather than studying isometric force (that is maximal contraction of the muscle with no change in muscle length), maximal isokinetic force can also be used. An isokinetic muscle contraction occurs when the velocity of the muscle contraction remains constant while the length of the muscle changes. The terms muscle quality or muscle density are also used sometimes interchangeably with muscle SF, although they all have slightly different connotations.

Regardless, SF captures the intrinsic force producing capability of a muscle or muscle group and thus is an exceedingly powerful measure of function. Reductions in SF are a critical component of many causes of weakness and play a role in a variety of NMDs, ranging from primary diseases of muscle (muscular dystrophies, inflammatory myopathies, hospital acquired weakness, and metabolic muscle disease), to neurogenic disorders affecting muscles (amyotrophic lateral sclerosis, spinal muscular atrophy, nerve injury), to second conditions (e.g., aging impacted muscle –sarcopenia–, disuse related to major injury and prolonged hospitalization, and disease induced muscles wasting –cancer-related cachexia–). Critically, nearly all of these conditions, in addition to causing frank atrophy, also results in reductions in force-generating capability of muscle. Moreover, in seeking treatments for these diseases, it is clear that measurement of SF is critical as therapies associated with increased muscle size are often ineffective since the SF of the muscle ends up remaining unchanged. Indeed, a number of studies of myostatin pathway inhibitors in both Duchenne muscular dystrophy and inclusion body myositis have all failed to produce improvements in function, likely related to the fact that the therapies did not positively impact muscle SF, despite apparent increases in muscle size.

Thus, a convenient clinical tool capable of predicting SF without the need for painful high frequency stimulation or imaging would be extraordinarily valuable both for individual patient care as well as in the assessment of therapies in human clinical trials; it could serve a valuable role in preclinical research as well. One approach that could achieve this is via the simultaneous measurement of electrical impedance myography (EIM) outcomes from a muscle during voluntary contraction. Here, we extend our previous pre- and clinical studies to study the EIM-force relationship in healthy and myopathic muscle using mice.

2. Materials

2.1 Animals

Institutional Animal Care and Use Committee approval was obtained for all experiments. Male WT (DBA/2J; strain #000671) and D2-mdx mice (D2. B10-Dmdmdx/J; strain #013141) were obtained from Jackson Labs (Bar Harbor, Maine), and fed *ad libitum* and studied at approximately 6 months of age. Animals will underwent all procedural testing with inhaled isoflurane anesthesia, with temperature being maintained by a heated platform.

2.2 Specific force measurements

Force exerted by gastrocnemius with maximal contraction was obtained use a high-speed servomotor system (model 305C Aurora Scientific, Aurora, Ontario, Canada). The output force-length signals was interfaced with a PXIe-8135 quad-core processor based embedded controller and acquired using a 2-channel acquisition board PXI-4461 (National Instruments, Austin, Texas, USA). A program written in LabVIEW (National Instruments) controls the lever arm movement and the output of a biphasic pulses current muscle stimulator (model 701, Aurora Scientific).

2.3 Electrical impedance myography measurements

Muscle impedance was measured using the custom system reported in (1). The impedance measurement system was implemented on the same PXI (platform from National Instruments used to record force.

3. Methods

3.1 Animal experimentation

While still anesthetized, the animal underwent a non-survival surgery in which the gastrocnemius muscle was exposed. The calcaneal tendon was cut at its insertion point, dissected away from underlying fascia and soleus muscle, and connected to a force lever arm via silk thread. The leg was stabilized by inserting a needle through the knee joint. Twitch force was recorded a by a single stimulus using 200 µs square pulse delivered through insulated electrocardiogram needles (F-E2M-48, Grass Technologies) stimulating the sciatic nerve at the sciatic notch. Stimulation current and muscle length were adjusted to maximize tetanic force during a 200 ms duration stimulus train at 120 Hz. Before isometric force data collection, the optimal length was measured with digital calipers as the distance between the knee and the calcaneal tendon. All subsequent isometric data were collected at this pulse duration, stimulation current, and muscle length. At the conclusion of the study, the animals are sacrificed using carbon dioxide inhalation. The gastrocnemius was then be excised and weighed.

3.2 Specific force measurements

Force exerted by gastrocnemius with maximal contraction was obtained use a high-speed servomotor system (model 305C Aurora Scientific, Aurora, Ontario, Canada). The output force-length signals was interfaced with a PXIe-8135 quad-core processor based embedded controller and acquired using a 2-channel acquisition board PXI-4461 (National Instruments, Austin, Texas, USA). A program written in LabVIEW (National Instruments) controls the lever arm movement and the output of a biphasic pulses current muscle stimulator (model 701, Aurora Scientific).

4. Results

4.1 Impedance increases with isometric contraction

Figure 1 shows the impedance magnitude increases with force production and the peak magnitude occurs approximately 50 ms later than that of the force. Further, the magnitude during relaxation outlasts the force response by about 100 ms.

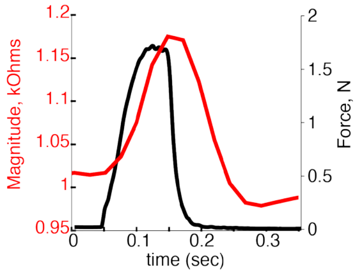

Figure 1. Force (black) and impedance magnitude (red) response during tetanic contraction in healthy muscle.

4.2 Impedance change depends on muscle activation

We studied the EIM-stimuli frequency relationship in healthy mice during isometric force experiments. EIM magnitude shown in Figure 2 B indicates that impedance changes parallel those shown in force production shown in Figure 2 A.

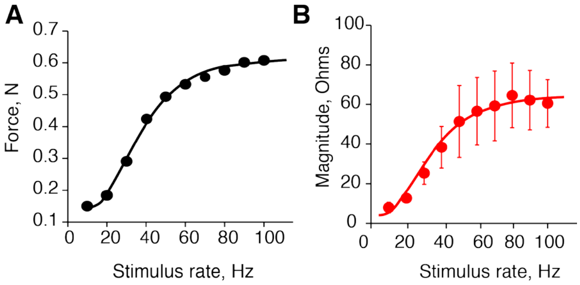

Figure 2. Impedance magnitude change at 50 kHz response in 14 mice recorded in vivo, mean and std represented (B). Note how closely this parallels the stimulus force curve shown in A.

4.3 Impedance is associated with peak power and maximal isometric force

Peak power shown in Figure 3 during isotonic experiments and maximal isometric force shown in Figure 3 were correlated to EIM phase angle at 50 kHz.

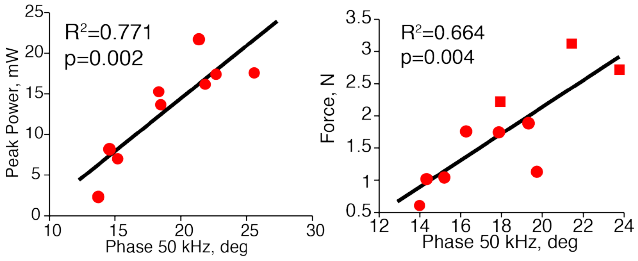

Figure 3. Peak power (A) and maximal isometric force (B) correlated with phase angle at 50 kHz.

4.4 Force-impedance curves follow different patterns in disease

Figure 4 shows force-impedance relationships from 8 mdx mice.

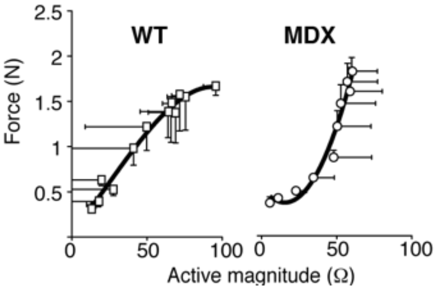

Figure 4. Relationships between force and impedance change in WT and mdx mice. Note the very different shape of the trajectories, supporting the need for different models based on disease type.

5. Discussion

The mechanisms of isometric muscle contraction were investigated experimentally in vitro in the abdominal (Hogben & Gordon, 1930) muscles in amphibians using impedance to obtain clues about the nature of the contraction process. Bozler and Cole were the first to describe an increase in impedance in actively contracting muscle (Bozler, 1935; Bozler & Cole, 1935). Later in 2003, Shiffman and Rutkove measured surface EIM at a single frequency during voluntary isometric contractions (Shiffman et al., 2003). The authors found distinctive temporal patterns in patients with different NMDs. However, it was not until (Sanchez et al., 2014) that a first multi-frequency approach was performed to disentangle the physiological phenomena causing such alterations measuring the impedance of muscle directly. Here, we extended our previous work and conduct an initial animal study to evaluate the impedance and force relationship in healthy muscle and a model of myopathic disease considering different contractile conditions. The impedance rises simultaneously with force, a finding that is consistent with previously reported in silico (Sekine et al., 2015), amphibian (Bozler, 1935; Bozler & Cole, 1935) and human (Nakamura et al., 2013) results. Our new results also show that the impedance magnitude follows a nonlinear dependence as a function of the stimulus similar to isometric force-frequency curves (Woledge et al., 1985). The 60% increase seen in the impedance magnitude at 40 Hz is in excellent agreement with 35-45% reported in (Bozler, 1935). Most notably, force-impedance relationships in diseased muscle are quite different from those observed in healthy animals, supporting the need to further study different basic pathologies to establish electromyographyc-impedance-force relationship models.

6. Conclusions

In the future, combining standard electrophysiology and needle EIM recordings has the potential to serve as a new clinical tool to predict function in health and disease.

References

Bozler, E. (1935). The change of alternating current impedance of muscle produced by contraction. Journal of Cellular and Comparative Physiology, 6(2), 217–228. https://doi.org/10.1002/jcp.1030060204

Bozler, E., & Cole, K. S. (1935). Electric impedance and phase angle of muscle in rigor. Journal of Cellular and Comparative Physiology, 6(2), 229–241. https://doi.org/10.1002/jcp.1030060205

Hogben, B. Y. L., & Gordon, C. (1930). Studies on the comparative physiology of contractile tissues. II. The relation of electrolytes to electrical conductivity. The Journal of Experimental Biology, 7(1), 269–285. https://doi.org/10.1007/BF01618834

Nakamura, T., Kusuhara, T., & Yamamoto, Y. (2013). Motion discrimination of throwing a baseball using forearm electrical impedance. Journal of Physics: Conference Series, 434(1), 012070. https://doi.org/10.1088/1742-6596/434/1/012070

Sanchez, B., Li, J., Geisbush, T., Bragos, R., & Rutkove, S. (2014). Impedance alterations in healthy and diseased mice during electrically-induced muscle contraction. IEEE Transactions on Biomedical Engineering, 63(8), 1602–1612. https://doi.org/10.1109/TBME.2014.2320132

Sekine, K., Yamada, A., Kageyama, H., Igarashi, T., Yamamoto, N., & Asami, K. (2015). Numerical calculations for effects of structure of skeletal muscle on frequency-dependence of its electrical admittance and impedance. Journal of Physics D: Applied Physics, 48(25), 255401. https://doi.org/10.1088/0022-3727/48/25/255401

Shiffman, C. A., Aaron, R., & Rutkove, S. B. (2003). Electrical impedance of muscle during isometric contraction. Physiological Measurement, 24(1), 213–234.

Woledge, R. C., Curtin, N. A., & Homsher, E. (1985). Energetic aspects of muscle contraction. Monographs of the Physiological Society, 41, 1–357.

Proceedings of the International Conference of Bioelectromagnetism, Electrical Bioimpedance,
and Electrical Impedance Tomography June 29 – July 1, 2022 / Kyung Hee University, Seoul, Korea

Assessment of the Diagnostic Value of Body Impedance in Pre-eclampsia Screening

Svetlana Pavlovna Shchelykalina[1,2,] Vera Sergeevna Romanova[2], Dmitry Viktorovich Nikolaev[2],
Igor Mikhailovich Matveev[3], Olga Valentinovna Trokhanova[3], Vladimir Alexandrovich Kolesnikov[2]
and Timur Salavatovich Tuikin [2]
[1]Biomedical faculty, Pirogov Russian National Research Medical University, Moscow, Russia
[2]Development Department, SRC Medas, Moscow, Russia
[3]Departments of Obstetrics and Gynecology, Yaroslavl State Medical University, Yaroslavl, Russia

Correspondence : Svetlana P. Shchelykalina, e-mail : snetlanath@gmail.com

Abstract– Pre-eclampsia occurs in 2–8% of pregnant women. Pre-eclampsia may develop to eclampsia followed by convulsions and eclamptic coma. The earliest possible diagnosis of pre-eclampsia during pregnancy is one of the main factors that influence the further management of pregnancy and its outcomes. The purpose of this study was to assess the diagnostic potential of routine body impedance in relation to the diagnosis of pre-eclampsia in pregnant women without obesity. 140 women without obesity at gestation periods from 28 to 34 weeks of pregnancy from four groups were included in the study: a normotensive pregnancy, the pregnancies were complicated by pre-eclampsia, by chronic hypertension, and by hypertension in pregnancy. All participants underwent a standard examination for pregnant women and body impedance measurement using the ABC-01 Medas analyzer. Statistical data analysis included intergroup comparison and ROC analysis. From the point of view of potential screening diagnosis, body impedance parameters that describe the sizes of body water sectors appeared out to be the most promising ones. The extracellular water and the total body water indices showed the best results for distinguishing patients with pre-eclampsia from the other groups - AUC ROC 0.90 (95% CI 0.83–0.97) and 0.89 (95% CI 0.82 – 0.97).

Keywords: bioimpedance analysis of human body composition, pre-eclampsia, pregnancy

1. Introduction

According to the World Health Organization, pre-eclampsia occurs in 2–8% of pregnant women (WHO 2014, Eiland *et al* 2012, Al-Jameil *et al* 2014). Pre-eclampsia (PE) is characterized by increased blood pressure after 20 weeks of gestation, significant proteinuria, and multiple organ failure, including CNS symptoms (Al-Jameil *et al* 2014, Wagner 2004). Every year, hypertensive complications during pregnancy are at the top of the list of causes of maternal death (WHO 2014).

There is currently no consensus on the pathogenesis of pre-eclampsia. The most common point of view on pathophysiological processes includes trophoblastic invasion disorders followed by perfusion impairment; endothelial cellular toxin production; blood coagulation activation; vasodepressor function impairment; and alterations in endothelial permeability (Dong *et al* 2017).

Within a few days, pre-eclampsia may develop to eclampsia followed by convulsions and loss of consciousness with the development of eclamptic coma (WHO 2014, Zeeman 2009). Despite the fact that timely detected pre-eclampsia cannot be completely cured without delivery or termination of pregnancy, the patient's condition can be partially stabilized and delivery can be delayed for up to 14 days (Letter of the Ministry of Health of the Russian Federation, 07.06.2016).

The earliest possible diagnosis of pre-eclampsia during pregnancy with an adequate assessment of the pathological process severity is one of the main factors that influence the further management of pregnancy and its outcomes.

To date, a number of approaches to the screening diagnosis of pre-eclampsia are known, including biomarkers and genetic markers (Savaj and Vaziri 2012, Zhao *et al* 2017), photoplethysmography and heart rate variability (Euliano *et al* 2018), etc. There is evidence of a potential prognostic value of body impedance data, but the studies have been performed in a small number of patients with pre-eclampsia (Trindade *et al* 2021).

The purpose of this study was to assess the diagnostic potential of routine body impedance in relation to the diagnosis of pre-eclampsia in pregnant women without obesity.

2. Materials and methods

For this purpose, in 2018, 140 women without obesity at gestation periods from 28 to 34 weeks of pregnancy were included in the study.

Minutes of the meeting of the Federal State Budgetary Educational Institution of Higher Education "Yaroslavl State Medical University" Ethics Committee dated 10/26/2017 No. 19. Minutes of the meeting of the Federal State Budgetary Educational Institution of Higher Education "Yaroslavl State Medical University" Problem Committee dated 11/15/2017 No. 1/17-18.

All participants underwent a standard examination for pregnant women as per Order No. 572n of the Ministry of Health of the Russian Federation, dated November 1, 2012, including anthropometry (weight, height, waist and hip circumference measurement) and body impedance measurement using the ABC-01 Medas analyzer (SRC Medas, Moscow, Russia) by the standard method using foot and hand bioadhesive electrodes (Grimnes and Martinsen 2014). All pregnant women were followed-up until the end of Week 2 after delivery. The study includes observations of Follow-up Week 1.

The study did not include patients with overt and gestational diabetes mellitus, signs of obesity (BMI $\geq$ 30 kg/m^2) at registration for pregnancy and at the time of the study, with a built-in pacemaker, in the event of assisted reproductive technologies used, and in the cases of multiple pregnancies or perinatal complications (polyhydramnios, fetal macrosomia).

Among the examined pregnant women, 68 patients had a normotensive pregnancy (Control group), the pregnancies were complicated by pre-eclampsia in 35 patients (PE group), by chronic hypertension in 16 patients (CH group), and by hypertension in pregnancy in 21 patients (HP group). The main characteristics of the patients are given in Table 1.

The values of active resistance at a frequency of 5 and 50 kHz, reactive resistance at a frequency of 50 kHz, impedance indices, relative values of body impedance estimates of fat mass, fat-free mass, active cellular and skeletal muscle masses, volumes of total and extracellular water were analyzed. Relative values of body composition parameter scores were given as a percentage of total or fat-free masses and ratio to the square of height in meters.

Table 1. Body composition parameters in the groups of pregnant women with normotensive pregnancy, chronic hypertension, gestational hypertension, pre-eclampsia, and total examined patients. Me [LQ; UQ]

Parameter	Control group (normotensive pregnancy)	Chronic hypertension	Hypertension in pregnancy	Pre-eclampsia	All
N	68	16	21	35	140
Gestation period [weeks]	31 [28; 33]	32 [29; 34]	31 [29; 33]	30 [29; 33]	
Age [years]	29 [25; 31]	31.5 [26; 34]	28 [27; 30]	30 [26; 33]	29.5 [26; 33]
BMI [kg/m2]	26.4 [25; 29.4]	27.3 [26.5; 28.3]	24.4 [22.8; 27.3]	25.8 [23.7; 27.1]	26.3 [23.9; 27.9]
%FM [%]	26.6 [19.1; 30.6] +*	32.7 [31.2; 36.0]+*	29.5 [25.9; 37.5]	31.9 [28.7; 35.5]	30.7 [26.4; 34.6]
FFM [kg]	52.3 [48.7; 58.5]+*	48.0 [46.9; 49.8]+*	46.7 [45.5; 48.6]+*	46.9 [44.3; 47.8]	47.5 [45.3; 49.9]
%ACM [%]	50.8 [47.8; 53.1]+*	55.8 [55.0; 57.3]+*	54.9 [53; 56.8]+*	54.9 [53.6; 56.9]	54.4 [52.2; 56.5]
%SMM [%]	50.9 [48.4; 52.8]+*	48.2 [47.3; 48.9]+*	49 [46.7; 49.9]+*	48.0 [47.1; 48.6]	48.4 [47.3; 49.8]
ICW/EW	0.78 [0.77; 0.8]+*	0.76 [0.75; 0.77]+*	0.76 [0.76; 0.77]+*	0.76 [0.74; 0.77]	0.76 [0.75; 0.78]
ICW/TBW	0.44 [0.44; 0.45]+*	0.43 [0.43; 0.43]+*	0.43 [0.43; 0.43]+*	0.43 [0.43; 0.43]	0.43 [0.43; 0.44]
iECW [kg/m2]	6.5 [6.0; 7.1]+*	5.8 [5.6; 5.9]+*	5.4 [5.3; 5.8]+*	5.5 [5.1; 5.7]	5.6 [5.3; 6.0]
iICW [kg/m2]	8.3 [7.8; 9.0]+*	7.5 [7.3; 7.6]+*	7.2 [7.0; 7.4]+*	7.2 [6.8; 7.5]	7.4 [7.0; 7.8]
iTBW [kg/m2]	14.8 [13.9; 15.7]+*	13.3 [12.9; 13.5]+*	12.6 [12.2; 13.2]+*	12.7[11.9; 13.2]	13.0 [12.3; 14.0]
R50/height [Omh/m]	270 [231; 306]+*	318 [306; 344]+*	334 [319; 350]+*	340 [320; 362]	328 [303; 350]
R5/height [Omh/m]	304 [255; 341]+*	361 [346; 395]+*	373 [361; 393]+*	386 [362.2; 410]	367 [339; 395]
Xc50/height [Omh/m]	27.1 [20.4; 31.3]+*	36.8 [34.3; 42.7]+*	36.3 [32.2; 37.7]+*	38.0 [34.5; 41.6]	35.7 [30.6; 39.5]
FFM/height2 [kg/m2]	20.2 [18.9; 21.4]+*	18.1 [17.6; 18.4]+*	17.2 [16.7; 18.0]+*	17.3 [16.3; 18.0]	17.7 [16.8; 19.1]
FM/height2 [kg/m2]	6.8 [5.2; 8.9]*	9.16 [8.4; 9.9]*	7.2 [5.6; 9.9]	8.7 [6.8; 9.5]	8.0 [6.3; 9.5]
SMM/height2 [kg/m2]	10.4 [9.04; 11.3]+*	8.7 [8.2; 9]+*	8.5 [8.1; 8.9]+*	8.3 [7.7; 8.6]	8.6 [8.0; 9.1]
ACM/height2 [kg/m2]	9.9 [9.0; 10.9]	10.2 [9.9; 10.4]	9.4 [8.8; 10.1]	9.5 [9.0; 10.0]	9.6 [9.0; 10.3]

* - p<0.017, + - p< 0,008 vs the pre-eclampsia group using the Bonferroni correction

BMI – bodye mass index, R50 – 50 kHz resistance, Xc50 – 50 kHz reactance, FM – fat mass, SMM - skeletal muscle mass, TBW – total body water, ECW – extracellular water, ICW – intracellular water, ACM – active cell mass.

Statistical data analysis included intergroup comparison of quantitative parameters using the Kruskal-Wallis test and subsequent pairwise comparison vs the PE group using the Mann-Whitney test. The critical level of significance was taken to be 0.05 and 0.017 using the Bonferroni correction, respectively. ROC analysis was used to assess the diagnostic significance of the parameters. The area under the ROC curve (AUC ROC) was assessed to distinguish the PE group from the other three groups and the pooled group of patients without pre-eclampsia. All calculations were made using scripts in the R statistical programming language in the RStudio software.

3. Results

Comparison of the study groups of patients with PE group patients found significant differences in the majority of body composition parameters (Table 1). At the same time, there were no differences in the patients' ages, BMIs, and gestational ages.

Parameters that describe the amount of body water were the best ROC analysis parameters for the assessment of body impedance diagnostic potential (Table 2). It has been shown that active cell mass (ACM) cannot be used for pre-eclampsia diagnosis, since the AUC ROC for this parameter has no differences from 0.5 for all comparisons. When distinguishing the PE group patients from the pooled group patients, the extracellular water index showed the best results (iECW) - AUC ROC 0.90 (95% CI 0.83–0.97). The same parameter showed a good result for distinguishing each group of patients from the PE group patients.

Table 2. The area under the ROC curve: control, chronic hypertension, gestational hypertension, and the pooled group vs the pre-eclampsia group. AUC ROC (95% CI).

Parameter	Nonpre-eclampsia	Chronic hypertension	Hypertension in pregnancy	Control group (normotensive pregnancy)
%FM [%]	0.75 (0.65 - 0.85)*	0.81 (0.68 - 0.93)*	0.67 (0.52 - 0.81)*	0.76 (0.66 - 0.86)*
%ACM [%]	0.82 (0.73 - 0.91)*	0.88 (0.78 - 0.97)*	0.75 (0.61 - 0.89)	0.83 (0.73 - 0.93)*
%SMM [%]	0.80 (0.70 - 0.90)*	0.79 (0.67 - 0.91)*	0.76 (0.63 - 0.88)*	0.82 (0.72 - 0.92)*
ICW/EW	0.79 (0.69 - 0.90)*	0.79 (0.66 - 0.91)	0.79 (0.67 - 0.91)	0.79 (0.69 - 0.89)*
ICW/TBW	0.79 (0.68 - 0.89)*	0.79 (0.66 - 0.92)	0.79 (0.67 - 0.92)	0.79 (0.68 - 0.89)*
iECW [kg/m2]	0.90 (0.83 - 0.97)*	0.86 (0.75 - 0.96)*	0.89 (0.80 - 0.98)*	0.91 (0.84 - 0.98)*
iICW [kg/m2]	0.88 (0.81 - 0.95)*	0.84 (0.73 - 0.95)*	0.88 (0.79 - 0.97)*	0.89 (0.82 - 0.96)*
iTBW [kg/m2]	0.89 (0.82 - 0.97)*	0.85 (0.75 - 0.96)*	0.89 (0.80 - 0.97)*	0.91 (0.84 - 0.97)*
R50/height [Omh/m]	0.87 (0.78 - 0.95)*	0.82 (0.7 - 0.93)*	0.86 (0.76 - 0.96)*	0.88 (0.8 - 0.96)*
R5/height [Omh/m]	0.87 (0.78 - 0.95)*	0.83 (0.72 - 0.94)*	0.85 (0.75 - 0.95)*	0.88 (0.8 - 0.96)*
Xc50/height [Omh/m]	0.87 (0.78 - 0.95)*	0.87 (0.77 - 0.96)*	0.82 (0.71 - 0.93)*	0.88 (0.79 - 0.96)*
FFM/height2 [kg/m2]	0.89 (0.82 - 0.97)*	0.86 (0.75 - 0.96)*	0.89 (0.8 - 0.97)*	0.91 (0.84 - 0.97)*
FM/height2 [kg/m2]	0.65 (0.54 - 0.76)*	0.73 (0.58 - 0.87)*	0.59 (0.43 - 0.75)	0.65 (0.54 - 0.77)*
SMM/height2 [kg/m2]	0.89 (0.81 - 0.97)*	0.85 (0.75 - 0.96)*	0.88 (0.78 - 0.97)*	0.90 (0.83 - 0.98)*
ACM/height2 [kg/m2]	0.58 (0.46 - 0.71)*	0.44 (0.4 - 0.71)	0.62 (0.47 - 0.77)	0.60 (0.47 - 0.73)*

* - $p<0.05$

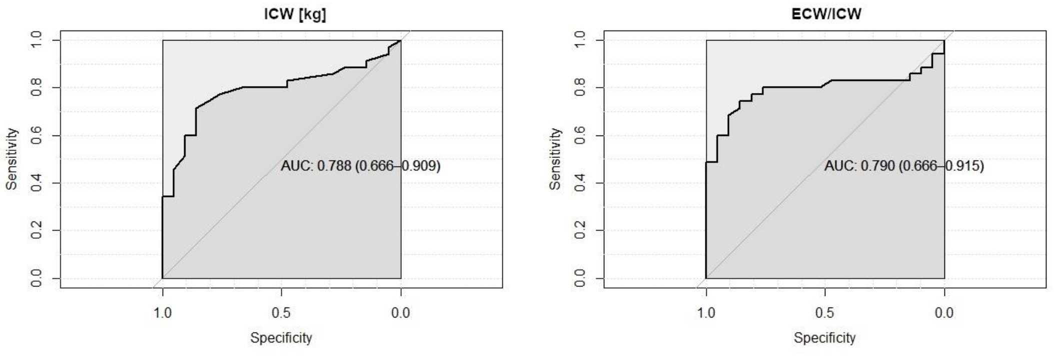

Figure 1. ROC curve for the ECW and ECW/ICW parameters with numerically the same AUC ROCs but different significance in the zero AUC ROC hypothesis testing.

4. Discussion

As diagnostic parameters, it is reasonable to use those that fairly well distinguish the PE group patients from patients of each of the other three groups. Maximizing all areas under the ROC curve may be an additional imposed requirement. Due to the relatively small groups of patients with pregnancy complicated by chronic hypertension (16 persons) and pregnancy complicated by hypertension in pregnancy (21 persons), in some cases the areas under the ROC curve had no statistically significant differences from 0.5. Such an effect was observed when the ROC curve crossed the reference diagonal (0.1)-(1.0) (Figure 1). We excluded such parameters from the list of potential diagnostic markers.

Interestingly, the parameters obtained in the paper by Trindade *et al* 2021 as predictive ones were not included in the list of potential markers in our study. Although the ECW/ICW parameter had statistically significant differences for all groups vs the PE group but showed no diagnostic value in the ROC analysis when distinguishing the PE group and the CP and HP group patients, and the PE group and the Control group patients, it was significantly inferior to the extracellular water (iECW), intracellular water (iICW), and total body water (iTBW) indices and the water volumes in liters. The fat mass percentage (%FM) had no statistically significant differences in the PE group vs the HP group and was significantly inferior for the AUC ROC to any parameter that describe water sectors. The skeletal muscle mass (SMM), the only of the parameters identified in the paper by Trindade *et al* 2021, could be included in the list of potential diagnostic markers, since it had statistically significant differences for all comparisons and had the AUC ROC significantly different from 0.5. However, AUC ROC values were lower than those of water parameters. The fat-free mass index (iFFM) has a fairly high AUC ROC value. This is due to the fact that the body impedance fat-free mass and total body water assessment equations are closely related.

Therefore, the iECW and iTBW indices are the most promising ones in terms of screening diagnosis from our point of view, the BIVA-R50/height and Xc50/height coordinates are also fairy good. The study power is not sufficient to make a clear choice in favor of one of these parameters. For a large amount of data, iECW can be indirectly considered a slightly more sensitive parameter than iTBW, but for practical purposes, iTBW can also be used if the available instruments do not distinguish ECW from the total TBW sample. BIVA coordinates are likely to be less sensitive than the iECW and iTBW indices for the assessment of larger studies.

5. Conclusions

From the point of view of potential screening diagnosis, body impedance parameters that describe the sizes of body water sectors appeared out to be the most promising ones. At the same time, the ECW/ICW ratio turned out to be less diagnostically valuable than the ratio of ECW to the square of height. The high diagnostic value of TBW and ECW and their derivatives is well explained by the symptoms and pathogenesis of pre-eclampsia as a condition followed by increased blood pressure and edema. The fact that iTBW and iECW showed equally high AUC ROC values make it possible to hope for the use of both fairly simple and widely applied body impedance instruments and professional multifrequency devices for pre-eclampsia screening.

References

WHO recommendations for prevention and treatment of pre-eclampsia and eclampsia. 2014. https://apps.who.int/iris/bitstream/handle/10665/44703/9789241548335_eng.pdf [Access 8 Mar 2022]

Eiland E, Nzerue C and Faulkner M 2012 Preeclampsia 2012 *Journal of Pregnancy* 586578

Al-Jameil N, Aziz Khan F, Fareed Khan M and Tabassum H 2014 A brief overview of preeclampsia *Journal of Clinical Medicine Research* **6 (5)** 1-7

Wagner L K 2004 Diagnosis and Management of Preeclampsia *Am Fam Physician* **70 (12)** 2317-2324

Dong X, Gou W, Li Ch, Wu M, Han Zh, Li X and Chen Q 2017 Proteinuria in preeclampsia: Not essential to diagnosis but related to disease severity and fetal outcomes *Pregnancy Hypertension: An International Journal of Women's Cardiovascular Health* **8** 60-64

Zeeman G G 2009 Neurologic Complications of Pre-eclampsia *Seminars in Perinatology* **33(3)** 166-172

Letter of the Ministry of Health of the Russian Federation dated 07.06.2016 N 15-4/10/2-3483 About clinical recommendations "Hypertensive disorders during pregnancy, childbirth and the postpartum period. Preeclampsia. Eclampsia" [in Russuian]

Savaj S and Vaziri N 2012 An overview of recent advances in pathogenesis and diagnosis of preeclampsia. *Iranian Journal of Kidney Disease* **6 (5)** 334-338

Litang Z, Hong W, Weimin Z, Xiaohui T and Qian S 2017 Serum NF-κBp65, TLR4 as biomarker for diagnosis of preeclampsia *Open Medicine* **12 (1)** 399-402

Euliano T Y, Michalopoulos K, Singh S, Gregg A R, Rio M D, Vasilopoulos T *et al* 2018 Photoplethysmography and Heart Rate Variability for the Diagnosis of Preeclampsia *Anesthesia and analgesia* **126(3)** 913–919

Trindade C R, Torloni M R, Mattar R and Sun S Y 2021 Good performance of bioimpedance in early pregnancy to predict preeclampsia *Pregnancy Hypertension* **26** 24-30

Grimnes S and Martinsen Ø 2014 *Bioimpedance and Bioelectricity Basics: Third Edition* (UK: Academic Press)

Proceedings of the International Conference of Bioelectromagnetism, Electrical Bioimpedance,
and Electrical Impedance Tomography June 29 – July 1, 2022 / Kyung Hee University, Seoul, Korea

Electrical Impedance Spectroscopy of Ex-Vivo Human Lung Tissue

Harshavardhan Devaraj[1], Ethan Murphy[1], Joseph Phillips[2,3], Jason Pettus[2,3] Kayla Fay[3] and Ryan Halter[1,2]
[1] Thayer School of Engineering, Dartmouth College, Hanover, NH, USA
[2] Geisel School of Medicine, Dartmouth College, Hanover, NH, USA
[3] Dartmouth Hitchcock Medical Center, Lebanon, NH, USA

Correspondence : Ryan Halter, e-mail : Ryan.J.Halter@dartmouth.edu

Correspondence: Ryan Halter, e-mail: Ryan.J.Halter@dartmouth.edu

Abstract–Defining the electrical property contrast between benign and malignant lung tissue plays an important role when designing surgical tools and imaging systems to differentiatiate these tissue types. Intraoperative procedures often involve tissue manipulation with instruments in which pressure is applied and tissue deformed. Embedding bioimpedance sensors within these instruments represents a potential mechanism for real-time intraoperative tissue assessment to ensure adqueate resection margins. We recorded impedance spectra (100 Hz – 10 MHz) under varied applied pressure from fresh ex vivo tissue specimens resected from 12 patients undergoing surgical treatment for lung nodules. Generally we see higher resistivities for normal lung tissue compared to lesions. With applied pressure, we see an increase in real part of resistivity while a decrease in the imaginary part. Finally, we observed significant differences ($p>0.05$) between normal and lesion tissue resisitivity at multiple frequencies. This electrical property contrast suggest electrical impedance spectroscopy could be implemented in intraoperative margin sensing devices in lung cancer surgeries.

Keywords: Electrical Impedance Spectroscopy; Lung Cancer; Margin Detection; Electrical Properties; Tissue Properties

1 Introduction

Lung cancer remains the leading cause of cancer-related mortality worldwide, with approximately 1.79 million deaths per year. It is the second most prevalent type of cancer and affects 2.2 million people worldwide. (World Health Organization 2020) At least microscopically positive margins are found in 5-15% of curative intent surgical cases and this negatively impacts cancer survival (Predina *et al* 2016). Electrical impedance spectroscopy (EIS) for intraoperative margin assessment has been previously suggested for prostate cancer (Mahara *et al* 2015, Murphy *et al* 2017). Establishing the available electrical property contrast between healthy and malignant tissues are important when developing new intraoperative margin sensing tools. Gao *et al* 2014, Baghbani *et al* 2019, Company-Se *et al* 2022 have previously reported on electrical impedance of lung tissues. However, there is a paucity of data on lung tissue impedances under compression like we would expect during intraoperative procedures. Here we examine the ex-vivo electrical properties of lung tissue using tetra-polar electrical impedance spectroscopy under different loads and present our initial findings.

2 Materials and Methods

2.1 Patients

Fresh tissue specimens were obtained from patients undergoing lung resection for suspected malignancy. Samples were sub-divided into sections for impedance analysis and standard-of-care frozen section analysis. A Certified surgical pathology physician-assistant sectioned the normal tissue and lesional tissue based on gross evaluation of the specimen. Samples were wrapped with physiological saline dipped low-lint paper to prevent drying. The patient population consisted of 12 patients, 7 female and 5 male, undergoing scheduled lung lobectomies, segmentectomy and wedge resection surgeries. They were aged between 58 and 79. Patient consent and study procedures were conducted under a Dartmouth-Hitchcock Medical Center Institutional Review Board (IRB) approved protocol.

2.2 Tissue Impedance Measurement System

EIS measurements were taken between 100 Hz and 10 MHz using Sciospec ISXv3 (Sciospec Scientific Instruments GmbH, Germany). Custom gold-plated concentric electrodes with a circular voltage sense inner electrode (1 mm diameter) and an annular outer current injection electrode (OD = 3.5 mm, ID = 2.5 mm) were fabricated on a printed circuit board (see Figure 1). Transimpedance measurements of a tissue was gauged by positioning the sample between two parallel sets of these electrodes. The electrode circuitry was mounted to the platforms shown in figure 1. The tissues were positioned on the stationary lower platform while the upper load platform translated vertically depending on the tissue thickness and served as a site for positioning loads of 50g to 200g. For case 1 and 2, the loads ranged from 100g to 700g. A digital caliper was rigidly mounted to the device to measure tissue thickness. A weighing scale attached to the bottom platform was used to ensure no additional pressure was applied by the measurement calipers.

The impedance spectra recorded by Sciospec system was processed using MATLAB (MathWorks, Natick, USA). A tissue-thickness dependent geometric factor was experimentally determined by testing saline of known conductivities for electrode gaps ranging from 1 to 10 mm. This geometric factor was applied to the resistance and reactance data recorded to transform these measurements into thickness-independent complex resistivities. Measurements exhibiting extremely high impedance values, due primarily to poor contact, were removed. Measurements from tissue thicknesses less than 1mm were removed since the geometric factor has high variability at such small distances.

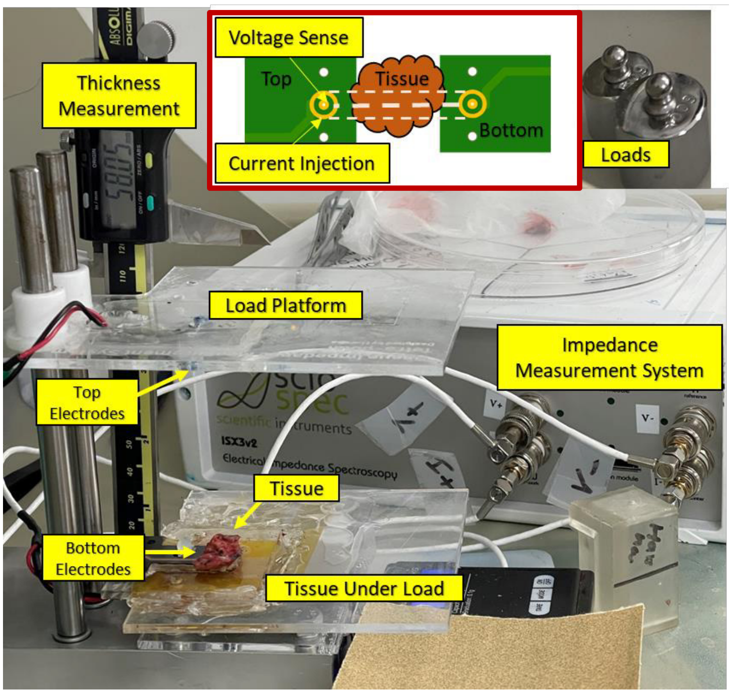

Figure 1. Tissue impedance measurement system with ex-vivo lung tissue placed on the bottom electode is shown. A schematic of electrode and tissue layout is also shown as an insert.

3 Results

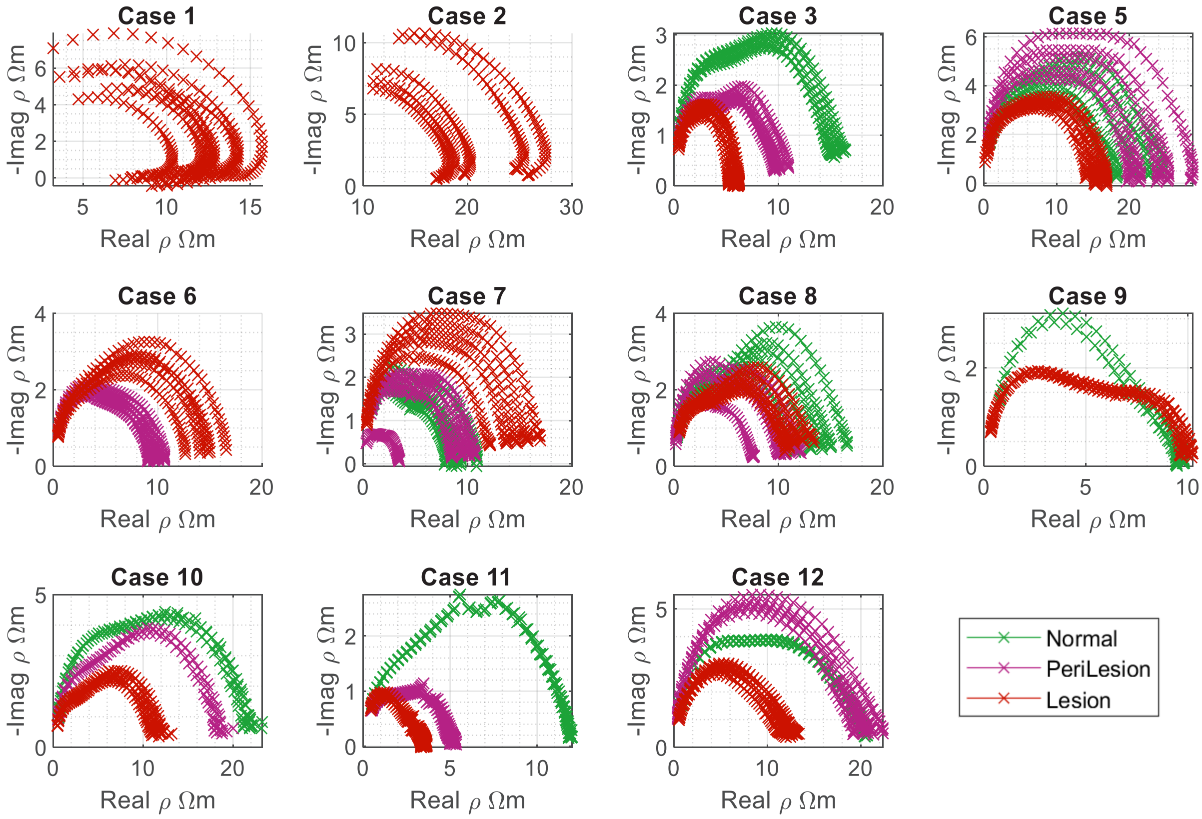

Figure 2. Cole-Cole resisitivity (ρ) plots of lesion, peri-lesion and normal tissues are shown. Each tissue type was tested under different loads between 100-10MHz frequency. With applied pressure, resistivity change is present but not significant. Some plots exhibiting double spectra can also be noted.

Cole-Cole plots of resistivities for each of the 12 patient cases at different pressures are shown in Figure 2. Some samples exhibit double dispersion in Cole-Cole plots. In most cases (7 of 8 in which both normal and malignant lesion tissue were probed), normal tissue resistivities are higher than lesion tissue. Variability is seen in peri-lesion tissue measurements. With applied pressure, real part of resistivity generally increases while imaginary resistivity generally decreases. This causes the shape of the spectra to remain consistent despite changes in magnitude. Table 1 presents case by case breakdown of differences between mean normal and mean lesion resistivities. The sign is positive except in case 7. Table 2 shows T-test results of real and imaginary resistivities at 5 different frequencies. At 1kHz and 100kHz, null hypothesis is rejected in both real and imaginary resistivities with significance level at 5%. At 100Hz, real resistivity shows the lowest p-value for null hypothesis. At higher frequencies, t-test fails to reject null hypothesis suggesting there might not be significant differences in normal and lesion tissue resistivities.

Table 1. Difference between mean resistivities of normal and lesion tissue at different frequencies

Case	*3*	*5*	*7*	*8*	*9*	*10*	*11*	*12*
1 kHz	8.881	4.695	-5.225	2.355	0.087	9.754	7.929	7.406
10 kHz	6.349	3.882	-3.998	1.8338	1.603	7.845	6.114	5.798
100 kHz	2.955	3.013	-1.676	0.575	2.546	4.937	2.437	3.273

Resistivities are in Ωm

Table 2. T-test results of normal vs lesion tissue. Null hypothesis tested at 5% significance level

Frequency (kHz)	*0.1*	*1*	*10*	*100*	*1000*
Real Resistivity	**R 3.526e-04**	**R 0.0040**	**R 0.0391**	FR 0.6699	FR 0.9789
Imag Resistivity	FR 0.0881	**R 0.0174**	**R 0.0302**	FR 0.5414	FR 0.3956

R-Reject. FR-Fail to reject.

4 Discussion

Identifying the differences in electrical impedance properties of normal and malignant human lung tissue is vital in designing intra-operative impedance-based margin sensors. In wedge resections, segmentectomies and lobectomies, the lung is deflated, and the lesion is removed. Our resistivity values of normal lung tissue are higher than the deflated lung in-vivo impedance values reported by C. Gabriel (Gabriel 1996) and in-vitro measurements by Baghbani *et al* 2019. This could be explained by the time and the tissue condition. While they measured data immediately after resection, our data was obtained 22 minutes to 3.5 hours after resection. Further, they measured directly on whole resection while we measured on slices to be used for surgical pathology frozen section assessment. However, similar to Baghbani *et al* 2019, we do see higher resistivity values in normal tissue compared to lesion tissue. Variabilities in peri-lesion tissue and outlier data could be explained by unclear histopathology of measured tissue.

With applied pressure, real part of resistivity generally increases while imaginary part decreases. This could be explained by intracellular contents of the tissue expelled with applied pressure and the membranes getting closer to each other to dominate measured impedance spectra. With case 1 and case 2, we were able to apply significantly higher loads (up to 700g) than other cases (up to 200g) as measurement loads were reduced per request from surgical pathology. It can be observed in Figure 2, these two spectra show higher negative change imaginary resistivities at lower frequencies with applied pressure than we observe in other cases. This reinforces the theory that cell membranes dominate as we apply pressure, and the tissue becomes more capacitive.

The significant ($p<0.05$) mean resistivity differences (see Table 2) suggests there is sufficient contrast for using impedance for tissue margin sensing. Further feature extraction and detailed analysis is necessary to demonstrate the best impedance parameters to distinguish these tissues (e.g. Cole parameters, discrete frequency resistivity magnitude or phase). Pathological slides of these tissues are being investigated and will provide more insight into how the peri-tumour tissue is assigned (i.e., normal, malignant, or mixed) and type of lesion studied.

5 Conclusions

Ex-vivo human lung tissue is studied using EIS and preliminary analysis is presented. Electrical property differences at different pressures of normal and malignant tissue are shown and compared between cases. Early results indicate significant differences exist between these tissue types at multiple frequencies. These contrasting properties could be taken advantage of to design future surgical instruments.

Acknowledgments

Funding for this work was provided through a Medtronic Research Grant.

References

Baghbani R, Moradi M H, Shadmehr M B and Sanat Z M 2019 A New Bio-Impedance Forceps Sensor for Measuring Electrical

Conductivity of the Biological Tissues *IEEE Sens. J.* **PP** 1–1

C. Gabriel. 1996 *Compilation of the Dielectric Properties of Body Tissues at RF and Microwave Frequencies, Report N.AL/OE-TR-1996-0037*

Company-Se G, Nescolarde L, Pajares V, Torrego A, Riu P J, Rosell J and Bragos R 2022 Minimally Invasive Lung Tissue Differentiation Using Electrical Impedance Spectroscopy: A Comparison of the 3- and 4-Electrode Methods *IEEE Access* **10** 7354–67

Gao J, Yue S, Chen J and Wang H 2014 Classification of normal and cancerous lung tissues by electrical impendence tomography *Biomed. Mater. Eng.* **24** 2229–41

Mahara A, Khan S, Murphy E K, Schned A R, Hyams E S and Halter R J 2015 3D Microendoscopic Electrical Impedance Tomography for Margin Assessment During Robot-Assisted Laparoscopic Prostatectomy *IEEE Trans. Med. Imaging* **34** 1590–601

Murphy E K, Mahara A, Khan S, Hyams E S, Schned A R, Pettus J and Halter R J 2017 Comparative study of separation between ex vivo prostatic malignant and benign tissue using electrical impedance spectroscopy and electrical impedance tomography *Physiol. Meas.* **38** 1242–61

Predina J D, Keating J, Patel N, Nims S and Singhal S 2016 Clinical implications of positive margins following non-small cell lung cancer surgery *J. Surg. Oncol.* **113** 264–9

World Health Organization 2020 Estimated number of incident cases and deaths worldwide, both sexes, all ages (excl. NMSC) *Int. Agency Res. Cancer* Online: https://gco.iarc.fr/

DAY 3

Friday, July 1, 2022

Oral Session 12

Clinical Application of Bio-impedance II

Chair Richard Bayford (Middlesex University)
Satoru Nebuya (Shimane University)

O 12-01 **Initial Results in a hdEEG/EIT Clinical Study on Strokes**
Haley Richards (Dartmouth College)

O 12-02 **Non-invasive Hemodynamic Monitoring during Hemodialysis using Electrical Impedance Images**
Jinwon Mok (Kyung Hee University)

O 12-03 **Neural Network-Based Cardiac-Related Image Denoising for Chest Electrical Impedance Tomography**
Ke Zhang (Tsinghua University)

O 12-04 **Quantitative Analysis of Severity in Obstructive Sleep Apnea Patients based on Tidal Volume Reduction and Event Duration for Sleep-related Breathing Disorders**
Taewook Chang (Kyung Hee University Hospital)

O 12-05 **Assessment of low back pain in helicopter pilots using electrical bio-impedance technique**
Hang Wang (Fourth Military Medical University)

ICBEM Bioelectromagnetism ICEBI Electrical Bioimpedance EIT Electrical Impedance Tomography

Proceedings of the International Conference of Bioelectromagnetism, Electrical Bioimpedance,
and Electrical Impedance Tomography June 29 – July 1, 2022 / Kyung Hee University, Seoul, Korea

Initial Results in a hdEEG/EIT Clinical Study on Strokes

Haley Richards[1], Alicia Everitt[1], Yinchen Song[2,3], Erik J. Kobylarz[1-3], Timothy G. Lukovits[2,3],
Diana M. Rojas-Soto[2,3], Ryan J. Halter[1,2], Ethan K. Murphy[1]
[1]Thayer School of Engineering, Hanover, NH, 03755, USA
[2]Geisel School of Medicine, Dartmouth College, Hanover, NH 03755, USA
[3]Dartmouth-Hitchcock Medical Center, Lebanon, NH, USA 03756

Correspondence : Ethan K. Murphy, e-mail : ethan.k.murphy@dartmouth.edu

Abstract–This paper summarizes our initial clinical results from an ongoing combined high-density Electroencephalogram (hdEEG) and Electrical Impedance Tomography (EIT) pilot study on stroke patients. Stroke is a major global problem affecting millions of people. Improvements in care can be made in earlier diagnosis of stroke type and in monitoring or predicting outcomes. We report on the first four stroke patients we have recruited, as well as prelminary results of our iPhone scanning/electrode registration technique of a 256-electrode hdEEG cap. Higher conductivity is found in 2 of 4 patients where the stroke is located, a third patient had a very mild stroke (NIHSS=0) and EIT was not able to detect it – *but otherwise is consistent with the initial two patients*, and the last case appeared to have artifact-filled reconstructions – *appearing to be related with too many poorly contacting electrodes*. The iPhone scanning results in roughly 3.4 mm electrode accuracy (compared to a commercial photogrammetry system) with on average 203 of the 256 electrodes labeled.

Keywords: Stroke, electrical impedance tomography, electroencephalogram, data fusion.

1. Introduction

Stroke is one of the global leading causes of premature death and disability. Every year 12.2 million people die of a stroke, and there are approximately 101 million people currently living with disability in the aftermath of a stroke (WSO 2022). The most vital step in treatment is fast diagnosis of ischemic or haemorrhagic stroke. Additionally, there are needs for prolonged monitoring after an acute stroke and in predicting outcomes. The technique under study is a system that combines high-density (256-electrode) electroencephalogram (hdEEG) and electrical impedance tomography (EIT) to potentially improve speed of diagnosis, yield an automatic monitoring system, and/or provide an improved metric for predicting patient outcomes. The novel combination of hdEEG and EIT technologies is exciting because these complementary technologies are: 1) inexpensive, portable, and use nonionizing radiation, 2) sensitive to stroke-related changes, and 3) measure fundamentally different entities (brain function vs. material properties). Here we show preliminary results of our clinical data collection and accuracies of our portable 3D scanning technique using an iPhone and custom Matlab-based GUI software for identifying and labelling electrodes.

2. Methods

This section details our clinical data collection and iPhone scanning processing. The IRB-approved clinical study, taking place at Dartmouth Hitchcock Medical Center, collects data on acute stroke patients with cerebral infarction, either ischemic or haemorrhagic pathologies and within < 4 days from onset. The EIT system has been designed to interface to the hdEEG cap which is a 256 electrode HydroCel sponge-based cap by EGI. Patient setup of the cap requires ~10 minutes to ensure all electrodes are in good contact as defined by the contact impedance mapping feedback from the hdEEG system. Once set, the data collection consists of 1) 10 minutes resting-state hdEEG recording (256 electrodes), 2) iPhone 3D scans of the head using an app called Heges, and 3) multi-frequency EIT data collection over 140 scalp electrodes and six additional electrodes place on the orbits and soft palate (at 800 Hz, 4, 8, 20, 40, 80, 400, 800 kHz). EIT is recorded on 20 electrode subsets using a custom-EIT system (Khan *et al* 2015). Additionally, we obtain CT or MRI scans collected through their standard-of-care treatment and diagnostic information (stroke type, NIH stroke score). There is a 2nd data collection planned for each patient (if available) at a follow-up appointment 4-6 weeks after the initial stroke.

The iPhone scanning is generally collected in 5-6 separate scans using the faceID sensor on a research-only iPhone 12 Pro (see Fig. 1A-B). Heges outputs, 50-100+ MB, coloured STL files. We developed a custom Matlab-based GUI to crop, identify, and label the electrodes from the scans. Identifying electrodes involves a sequence of zoomed-in views of the scan that allow for accurate electrode centres selection. The labelling involves two main steps: 1) manually labelling 3-6 electrodes, and 2) an automatic labelling approach that 'walks-out' from previously labels electrodes. To validate this process we have collected iPhone and photogrammetry data using a commercial system (Geodesic Photogrammetry System 3 Research (GPS)) on 8 subjects. We report on associated errors in the following section. In addition to scalp electrode labelling we record the nasion (NAS), left pre-auricular (LPA), and right pre-auricular (RPA) points in order to register the electrodes (iPhone scans) to the mesh or CT/MRI data.

The next step in the data processing is construction/modification of the finite element method (FEM) mesh, so that EIT reconstructions can be performed. This can be done by modifying a previously constructed mesh, or by constructing a fully-patient specific mesh after obtaining CT or MRI scans. We present results only from the former, where we use a NY head mesh (NYmesh) from the Parra Lab (Huang *et al* 2016), which has ~3 million nodes and 16.9 million elements. The same registration points are identified on this mesh (NAS, LPA, and RPA). Then a transformation (rotation, translation, and best x/y/z-scaling) is found between the merged iPhone scan and the NY mesh. Finally, the nearest outer surface point from the NYmesh to each iPhone electrode is found, so that electrodes can be incorporated into the FEM mesh. This allows us to reconstruct on a realistic mesh modelling the scalp, skull, cerebrospinal fluid (CSF), and grey and white matter. The alternative processing approach assumes knowledge of a CT or MRI of the patient. Ideally, the processing steps are 1) automatic segmentation using freesurfer (https://surfer.nmr.mgh.harvard.edu/), 2) exporting head, skull, and cortex surfaces using Brainstorm (https://neuroimage.usc.edu/brainstorm/Introduction, an EEG-focused Matlab-based software), and 3) construction of a FEM mesh using gmsh (https://gmsh.info/). The 3D tetrahedral mesh construction from surface triangulation is based on the approach described in (Murphy *et al* 2019). However, this process can be complicated by available MRI protocols that freesurfer cannot fully process. We discuss alternative approaches we have explored in Section 4. Finally, with a FEM mesh constructed we can perform EIT reconstructions using the collected impedance data. Currently, we are using a soft-prior absolute EIT reconstruction approach (Murphy *et al* 2017) that allows for jumps across the scalp, skull, CSF, and brain surfaces and forces voxels within tissues to have similar values. The method also uses the dual-mesh method, which relies on a coarse grid (hundreds or thousands of nodes) in each subdomain.

3. Results

An example iPhone collection on a mannequin (Fig. 1A) shows roughly how the data is collected and how it appears on the iPhone. Individual scans (Fig. 1B) when merged form the full head (Fig. 1D). The iPhone data is compared to photogrammetry data (Fig. 1C), qualitatively appearing to perform very well. In an ongoing study of 8 subjects, the average distance between iPhone and photogrammetry points is 3.4 mm with 203 electrodes (on average) being identified. When additionally labelling the remaining closest 256 electrodes, the average error rises to 4.1 mm with an average maximum error from each head being 10.2 mm.

The outer head and skull surfaces along with iPhone segmented electrodes (Fig. 2A) illustrates the modelled scenario. Results from absolute reconstructions from one slice of the full 3D reconstruction (Fig. 3B) reveal in two cases (S001 & S002) a significant increase in conductivity in the area affected by the stroke. The third case (S003) appears consistent, under the assumption that EIT was not sufficiently sensitive to detect the small deep stroke (NIHSS = 0). As it shows a relatively low conductivity in the entire brain region similar to the healthy regions in S001 & S002. The fourth patient's reconstruction appears inconsistent with the other subjects. We observed that S004 had significantly more noise than the other subjects. For instance, with our data checks S004 had 67% good electrodes whereas the other subjects had 86%, 89%, 92% good electrodes for S001, S002, and S003, respectively. When asymmetries are analysed as EIS (80 kHz) with the additional orbit electrodes, S001 S002 and S004 all see hemispherical changes in Z and Phase tracking with their respective infarct locations. S003 presented minimal asymmetry and displayed similar signals as the two healthy volunteers.

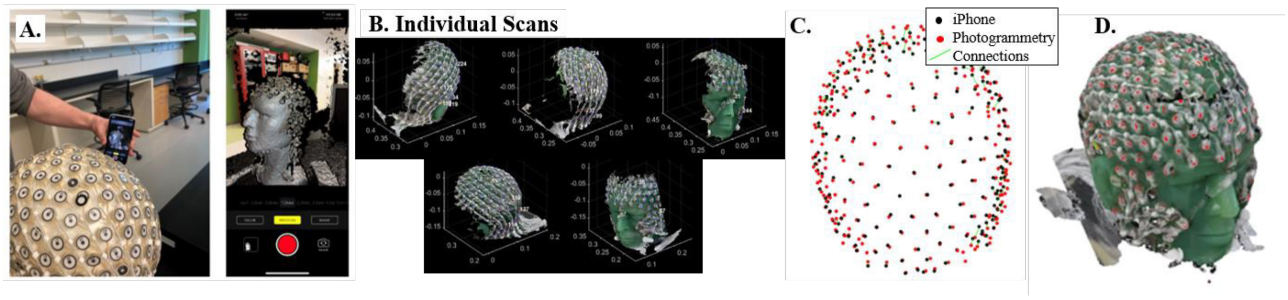

Figure 1. A. shows two views of the iPhone scanning of a mannequin (the scan and the corresponding iPhone screenshot). B. gives an example of 5 separate scans of a single gelatin head phantom, where C. shows the comparison between iPhone and photogrammetry results and D. shows the full merged head from all the iPhone scans.

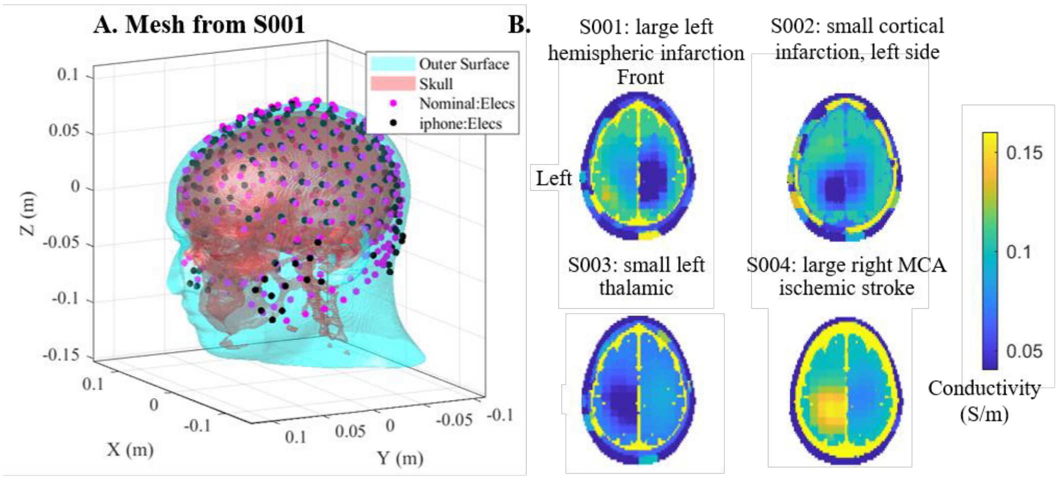

Figure 2. A. Presents the NYmesh best-fit to the electrodes found and labeled from the iPhone scans of Patient 1 (S001), and B. absolute EIT reconstructions of the first four stroke patients. S001 and S002 have a reduced conductivity in the cortex in the area related to their stroke, S003 appears to be relatively symmetric and had an initial NIHSS of 0, and lastly S004 shows inconsistent results (and also had the largest electrode noise).

4. Discussion

These preliminary results appear promising. The iPhone 3.4 mm error using a relatively inexpensive, portable scanner compared to the photogrammetry appears to be a very good result. However, ongoing studies are investigating how much this electrode position error affects source localization for hdEEG and EIT data and reconstruction accuracy. The preliminary absolute EIT reconstructions also appear promising in that we see consistent conductivity changes in 3 out of 4 cases. However, based on literature we would expect ischemic strokes to cause a decrease in conductivity as opposed to an increase. This could be due to oedema after the ischemic event, especially as recording time occurs more than a day after stroke onset.

There are significant approaches left to explore, such as 1) utilizing the CT or MRI data for patient-specific meshing and reconstruction, 2) exploring alternative EIT reconstruction algorithms such as multifrequency approaches (Malone *et al* 2014), and 3) exploring how hdEEG and or a combined hdEEG & EIT could be utilized for stroke applications. The processing steps may be the ideal processing steps noted in the methods section, or an ad hoc approach involving a combination of patient-specific and default/generic meshes or external and internal surfaces. Alternatively, other software approaches may be explored, e.g. a meshing toolbox called roast from Parralab, https://www.parralab.org/roast/, has been fund to be quite robust. Future work will analyse these combined approaches, including hdEEG and EIT data as a co-modality metric and multifrequency parameters, to potentially improve pathologic reconstructions and localization results. Additionally, as patient recruitment and mesh segmentation processing are both ongoing studies, additional data will provide further optimization opportunities and patient sub-analyses (e.g. patients with stroke <1 day instead of 4).

5. Conclusions

This study presents an iPhone scanning solution, which could be an inexpensive alternative approach applicable for general EIT and EEG electrode localization. Further the absolute EIT reconstructions appear promising.

Acknowledgments

This work was partially supported by a Hitchcock Foundation pilot grant and we would like to thank Joel Smith for significant help in debugging and processing the iPhone scans.

References

Huang Y, Parra L C and Haufe S 2016 The New York Head—A precise standardized volume conductor model for EEG source localization and tES targeting *Neuroimage* **140** 150–62 Online: http://dx.doi.org/10.1016/j.neuroimage.2015.12.019

Khan S, Manwaring P, Borsic A and Halter R 2015 FPGA-Based Voltage and Current Dual Drive System for High Frame Rate Electrical Impedance Tomography *IEEE Trans. Med. Imaging* **34** 888–901

Malone E, Sato Dos Santos G, Holder D and Arridge S 2014 Multifrequency Electrical Impedance Tomography using spectral constraints. *IEEE Trans. Med. Imaging* **33** 1–12 Online: http://www.ncbi.nlm.nih.gov/pubmed/24122550

Murphy E K, Amoh J, Arshad S H, Halter R J and Odame K 2019 Noise-robust bioimpedance approach for cardiac output measurement *Physiol. Meas.* **40** 074004 Online: https://iopscience.iop.org/article/10.1088/1361-6579/ab0d45

Murphy E K, Mahara A, Wu X and Halter R J 2017 Phantom Experiments using Soft-Prior Regularization EIT for Breast Cancer Imaging *Physiol. Meas.* **38** 1262–77 Online: https://doi.org/10.1088/1361-6579/aa691b

WSO 2022 *World Stroke Organizaion (WSO): Global Stroke Fact Sheet 2022* Online: https://www.world-stroke.org/assets/downloads/WSO_Global_Stroke_Fact_Sheet.pdf

O 12-02

Proceedings of the International Conference of Bioelectromagnetism, Electrical Bioimpedance,
and Electrical Impedance Tomography June 29 – July 1, 2022 / Kyung Hee University, Seoul, Korea

Non-invasive Hemodynamic Monitoring during Hemodialysis using Electrical Impedance Images

Jinwon Mok[2,3], Tingting Zhang[1,2], Jiwon Jung[2], A Rim Han[4], Joo Young Moon[4] and Tong In Oh[1,2]
[1]Medical Science Research Institute, Kyung Hee University Hospital, Seoul, Korea
[2]Department of Biomedical Engineering, School of Medicine, Kyung Hee University, Seoul, Korea
[3]Department of Medical Engineering, Graduate School, Kyung Hee University, Seoul, Korea
[4]Diviosn of Nephrology, Department Internal Medicine, College of Medicine, Kyung Hee University, Seoul, Korea

Correspondence : Tong In Oh, e-mail : tioh@khu.ac.kr

Abstract–Many patients rapidly develop hypotension during hemodialysis, causing great difficulties in continuing clinical treatments. When this intradialytic hypotension happens with some symptoms, clinicians prescribe therapeutic interventions like decreasing ultrafiltration rate (UF-) and injecting normal saline (S+) based on personal clinical experience. However, these kinds of interventions have a different response for each patient and could reduce the effectiveness of dialysis. This study attempted non-invasive real-time monitoring of hemodynamic parameters using electrical impedance tomography (EIT). We investigated the influence of prescribed interventions on hemodynamic changes during hemodialysis. Significant differences were observed in the EIT data before and after each intervention.

Keywords: Hemodialysis; Electrical Impedance Tomography; Intradialytic Hypotension; Stroke Volume; Intervention.

1. Introduction

Hemodialysis (HD) is a treatment to remove the waste products and excess fluid from patients with chronic renal failure [Himmelfarb2010]. Intradialytic hypotension (IDH) is the most common complication in 20-30% of patients during HD, leading to various discomforts such as severe pain. Also, dialysis efficiency is reduced by discontinuation of dialysis treatment [Kanbay2020]. To avoid the occurrence of IDH, several interventions are applied according to the patient's status and individual clinical experiences. Decreasing ultrafiltration rate or injecting normal saline are usually adopted to restore blood pressure and reduce the patient's pain when a high drop in systolic blood pressure with severe pain. Although blood pressure is intermittently monitored in a clinic, it is not sufficient to detect a patient's IDH in real-time due to the rapidly changing blood pressure of the patient. Recently, electrical impedance tomography (EIT) has been proposed to monitor pulmonary protective ventilation by imaging the air distribution in the lung area and hemodynamics by imaging the blood volume in the heart and lung regions of the chest [Frerichs2017]. This study collected hemodynamic parameters extracted from EIT measurements for patients who frequently suffered from IDH during HD. This study aims to quantify the degree and time of the patient's response according to the occurrence of IDH and the type of applied intervention from the hemodynamic parameters extracted from EIT images continuously in real-time.

2. Methods

At the starting time of a clinical trial, the patient's height and weight and body composition monitor (BCM) (Fresenius Medical Care, Germany) were collected to assess dry weight and determine fluid overload. During the four hours of HD using a hemodialysis machine (5008, Fresenius Medical Care, Germany), an E-pad including 16 electrodes was attached to the surface of the patient's thorax. EIT images were acquired at 100 frames/s using a high-speed EIT system (AirTom-R, BiLab, Korea). Additionally, blood pressure was periodically obtained every 15 minutes using non-invasive blood pressure (NIBP). To extract hemodynamic parameters like stroke volume (SV), heart rate (HR), and cardiac output (CO) from clinical data, cardiac volume signal (CVS) was firstly computed using the source-consistency EIT algorithm [Zhang 2020, Adler2021]. The motion artifact removal algorithm was implemented to reduce the influence of motion during the clinal trial. In addition, thoracic fluid content (TFC) could be derived from the impedance changes measured at the chest.

Since hemodynamic parameters have significantly different dynamic ranges depending on the patient and measurement, we calculated relative percentile change for each hemodynamic parameter. The recorded data for each category of events were rearranged based on the event time. The processed data was exploited to compare the changes of each hemodynamic parameter before and after the intervention point using the paired t-test. We consider it significantly different in this study when the p-value is less than 0.05.

3. Results

In advance, the type of applied intervention was determined according to the change in systolic blood pressure (SBP) with reference to the SBP measured 30 minutes after the start of HD. Among the interventions applied after the onset of IDH, the relative percentile changes in SV, HR, CO, and TFC for UF- and S+ events were reprocessed based on the time of application of the intervention and the value of each hemodynamic parameter. When we compared each hemodynamic parameter based on that obtained at 1 minute before applying intervention, 20-30% of SV was increased after 150 seconds in the UF- case. The p-value was less than 0.001, as shown in Figure 1(a). As the intervention of S+, about 50-60% increment has been observed after 180 seconds with $p < 0.001$ as described in Figure 1(b). We confirmed that the hemodynamic parameters measured in real-time changed differently according to different types of intervention and the occurrence of IDH.

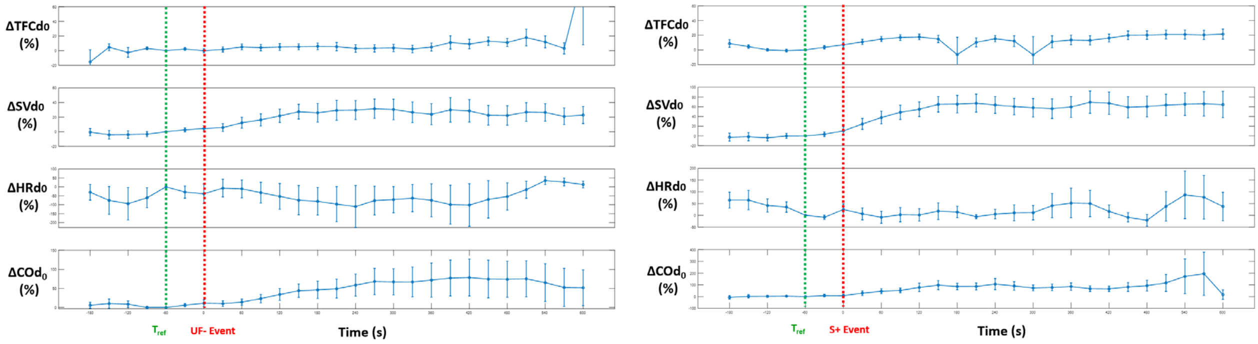

(a) (b)

Figure 1. Relative percentile changes of hemodynamic parameters (TFC, SV, HR, CO) with respect to the values measured at 1 minute before applying each intervention of (a) decreasing ultrafiltration rate (UF-) and (b) injecting normal saline (S+)

4. Conclusions

Real-time hemodynamic changes caused by IDH or various interventions during HD could be monitored using EIT images. In the future study, we will investigate the comparative analysis before and after various intervention events, and an algorithm will be developed to predict IDH concerning the patient-specific treatment interventions.

Acknowledgments

This work was supported by the Korea Medical Device Development Fund (NTIS, KMDF-RnD KMDF_PR_20200901_0207), NRF (NRF-2020R1I1A1A01066649, NRF-2020R1A2C1008975), and MOTIE (20006024) grants in Korea.

References

Adler A and Holder D 2021 Electrical impedance tomography: methods, history and applications. *CRC Press.*

Frerichs I, et al. 2017 Chest electrical impedance tomography examination, data analysis, terminology, clinical use and recommendations: consensus statement of the TRanslational EIT developmeNt stuDy group *Thorax* **72** 83-93

Himmelfarb J and Ikizler TA 2010 Hemodialysis *New England Journal of Medicine* **363** 1833-1845

Kanbay M, et al. 2020 An update review of intradialytic hypotension: concept, risk factors, clinical implications and management *Clinical Kidney Journal* **13** 981-993

Zhang T, Jang GY, Oh TI, Jeung KW, Wi H and Woo EJ 2020 Source consistency electrical impedance tomography *SIAM Journal on Applied Mathematics* **80** 499-520

Proceedings of the International Conference of Bioelectromagnetism, Electrical Bioimpedance,
and Electrical Impedance Tomography June 29 – July 1, 2022 / Kyung Hee University, Seoul, Korea

Neural Network-Based Cardiac-Related Image Denoising for Chest Electrical Impedance Tomography

Ke Zhang[1], Maokun Li[1], Fan Yang[1], Shenheng Xu[1] and Aria Abubakar[2]
[1]Beijing National Research Center for Information Science and Technology (BNRist),
Institute of Precision Medicine, Department of Electronic Engineering, Tsinghua University, Beijing 100084, China
[2]Schlumberger, Houston, TX 77056, USA

Correspondence : Maokun Li, e-mail : maokunli@tsinghua.edu.cn

Abstract−Cardiac-related signals contribute to the measurements of chest electrical impedance tomography. However, these signals are usually seriously interfered by ventilation-related signals while the subject is doing spontaneous breathing. Several methods have been developed for the separation of cardiac-related signals from spontaneous breathing signals. However, the separated cardiac-related signals may still be in low signal to noise ratio. As a result, the reconstructed cardiac-related images often show a distorted shape of the lung. To further improve the quality of cardiac-related images, we propose a neural network-based spatial denoising approach. This approach requires a reference ventilation-related image, which is usually in good image quality. Specifically, the cross-gradient constraint is applied to exert the boundary consistency of the cardiac- and ventilation-related images. The network is trained in an end-to-end fashion. The performance of the approach is tested using the data of two healthy subjects. Preliminary results show an improved image quality of the cardiac-related images in terms of the consistency of lung shape with the ventilation-related images.

Keywords: electrical impedance tomography; cardiac-related signal; image denoising; neural network

1. Introduction

Chest electrical impedance tomography (EIT) signals mainly contain two components: the ventilation-related component and the cardiac-related component. It is usually believed that the cardiac-related component originates from several sources (Adler A et al 2017), including the perfusion-related pulsatility of pulmonary vessels. The cardiac-related component may have potential value in pulmonary perfusion imaging and the related research is in progress. The first step toward the analysis of cardiac-related signals is to accurately separate it from the raw EIT signals. This is a challenging task because the cardiac-related component is seriously interfered by the ventilation-related component, which is one or two orders of magnitude stronger than the cardiac-related component. In the last decades, several methods have been developed for the separation of cardiac-related component, such as the ECG-gated method (Eyuboglu B M and Brown B H 1988), the frequency-domain filtering method (Frerichs I et al 2009) and the PCA-based method (Deibele J M et al 2008). However, the separated cardiac-related signals may still be in low signal to noise ratio. As a result, the reconstructed cardiac-related images are usually distorted, which makes it hard for the interpretation and quantification of these images. On the other hand, the separated ventilation-related component usually has a significantly better signal to noise ratio, and the reconstructed ventilation-related images are usually in good image quality. In view of this, we propose denoising the cardiac-related image with the guidance of the corresponding ventilation-related image. The proposed method is based on the neural network, the implementation detail of which is shown in Section 2. Section 3 presents some preliminary test results. Conclusions are drawn in Section 4.

2. Method

2.1 Network Architecture

The proposed network architecture is shown in Figure 1. Overall, the network contains three main building blocks: the denoising network, the image reconstruction network and the cross-gradient layer. Assume we have M frames of cardiac-related signal that are separated using an established separation method such as the frequency-domain filtering method or the PCA-based method. The input to the denoising network is a frame of cardiac-related signal $\mathbf{d}_C$ and the output is the denoised signal $\tilde{\mathbf{d}}_C$. The denoised signal $\tilde{\mathbf{d}}_C$ then goes through the image reconstruction network and the corresponding cardiac-related image $\mathbf{A}_C$ is reconstructed. Then the cross-gradient of the cardiac-related image $\mathbf{A}_C$ and the ventilation-related image $\mathbf{A}_V$ is calculated by the cross-gradient layer.

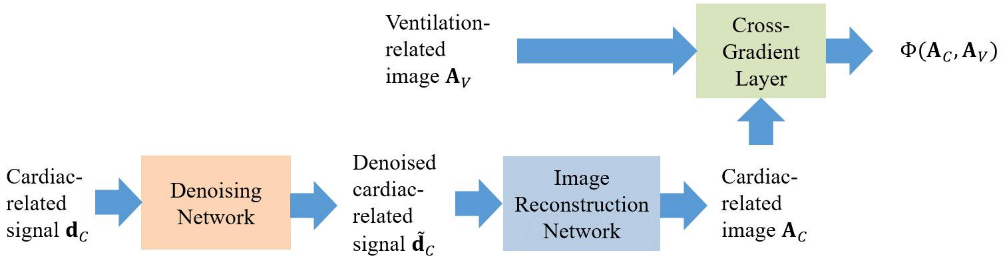

Figure 1. Network architecture.

The denoising network is implemented using a one-dimensional (1D) convolutional neural network (CNN). An encoder-decoder structure is adopted, as shown in Figure 2. The image reconstruction network is a neural network implementation of the linear EIT image reconstruction. Specifically, the linear EIT image reconstruction can be achieved simply by the following matrix-vector multiplication:

$$\mathbf{A} = \mathbf{R} \cdot \mathbf{d}, \tag{1}$$

where $\mathbf{R}$ is the reconstruction matrix. The above operation can be realized by a fully connected neural network with only one input layer and one output layer. Specifically, the weights of the neurons are set as the elements of $\mathbf{R}$; the biases of the neurons are set as zero; the activations of the neurons are set as linear.

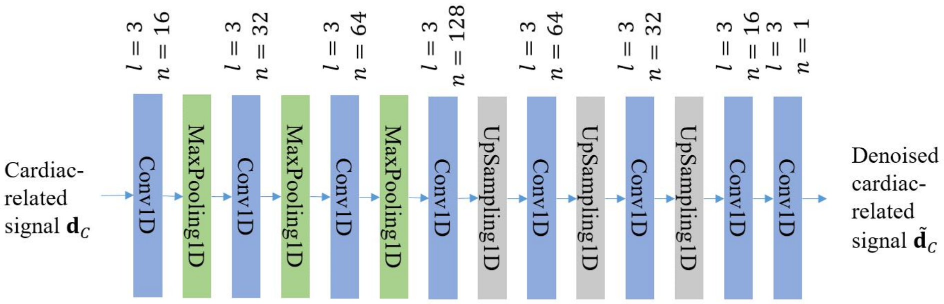

Figure 2. Detailed structure of the denoising network. The convolution layers are characterized by the kernel length l and the kernel number n.

Assume two images $\mathbf{A} = \{a_{i,j}\}$ and $\mathbf{B} = \{b_{i,j}\}$. The cross-gradient layer implements the cross-gradient function:

$$\Phi(\mathbf{A}, \mathbf{B}) = \nabla\mathbf{A} \times \nabla\mathbf{B}, \tag{2}$$

Where ∇ is the gradient operator and × is the cross product operator. The cross-gradient of image $\mathbf{A}$ and $\mathbf{B}$ in the (i, j) pixel can be calculated as

$$\Phi_{i,j} = \left[\left(a_{i,j+1} - a_{i,j}\right)\left(b_{i+1,j} - b_{i,j}\right) - \left(a_{i+1,j} - a_{i,j}\right)\left(b_{i,j+1} - b_{i,j}\right)\right]\hat{z}, \tag{3}$$

where $\hat{z}$ is the unit normal of the image plane.

2.2 Training of the Network

The weights of the image reconstruction network are set non-trainable, and there are no trainable parameters in the cross-gradient layer. Therefore, only the denoising network is trainable. During the training, a batch of N frames of cardiac-related signals is fed into the network each time for back propagation. The training loss for the network is defined as

$$loss = \frac{1}{N}\sum_{i=1}^{N}\left\|\mathbf{d}_C^i - \tilde{\mathbf{d}}_C^i\right\|^2 + \lambda\frac{1}{N}\sum_{i=1}^{N}\left\|\Phi\left(\mathbf{A}_C^i, \mathbf{A}_V^i\right)\right\|_1, \tag{4}$$

where λ is a hyper-parameter controlling the trade-off of the two terms in the right side of (4). The first term measures the fidelity of the denoised signal; the second term measures the boundary consistency of the cardiac- and ventilation-related images.

The training settings are as follows. The hyper-parameter λ is set as 10. Adam optimizer is used with a learning rate of 0.001. The batch size is set as $N = 32$. The total number of training epoch is set as 200.

3. Results

Human experiment was conducted to validate the proposed method. EIT data were collected from the chest of two healthy subjects. A 16-electrode EIT measurement system was used. The electrodes were attached at the level of the xiphoid process. Each subject took supine position and was measured for 2 minutes during spontaneous breathing. The measured EIT data are first processed using the PCA-based separation algorithm (Deibele J M et al 2008). In this way, we can obtain the cardiac- and ventilation-related signals. For the ventilation-related signal, we choose two frames of data, one at the end of inspiration and the other at the end of expiration. The difference of the two frames of data is then used for image reconstruction using the formula (1), and a ventilation image is obtained. This ventilation image is used as the reference (i.e., the $\mathbf{A}_V$ in Figure 1) for the denoising of cardiac-related images. On the other hand, the above separated cardiac-related signal is fed into the denoising network (see Figure 1).

The denoising results of the subjects are shown in Figure 3. The ventilation images are also shown for reference. Before denoising, the cardiac-related images show a somewhat distorted shape of the lung. This may be caused by 1) the low signal to noise ratio of the cardiac-related signal, and 2) the influence from the heart. After denoising, the matching of lung shape is significantly improved for the cardiac-related image and the ventilation image.

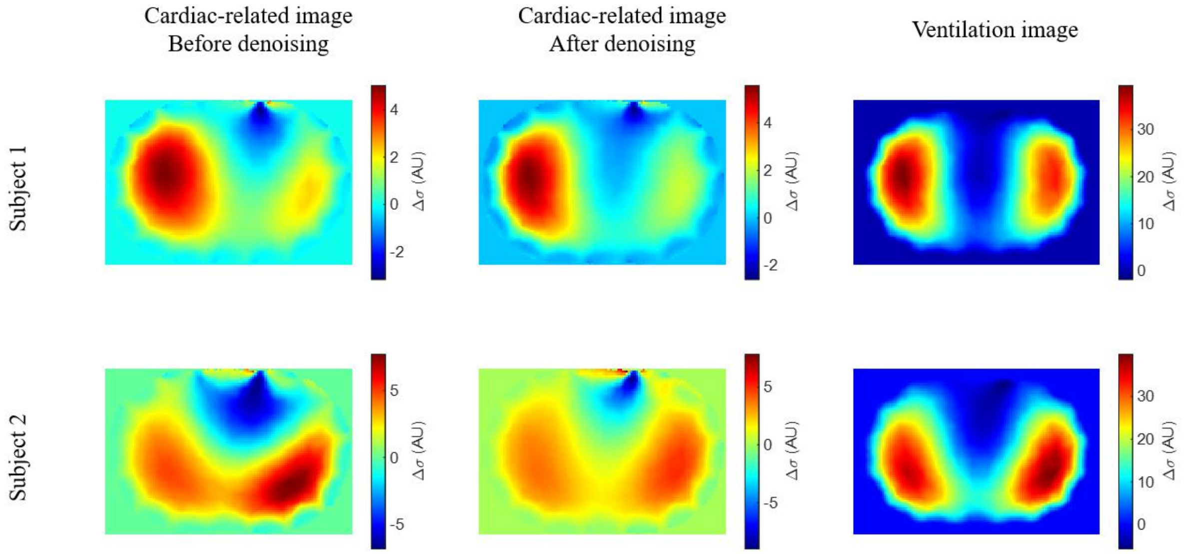

Figure 3. Denoising results for human subjects. (△ σ: conductivity change; AU: arbitrary unit)

4. Conclusions

This work proposes a neural network-based denoising method for EIT cardiac-related images. The denoising network is based on a 1D CNN, which is light weighted and can be trained efficiently. The cross-gradient constraint effectively guarantees the boundary consistency of cardiac- and ventilation-related images. Preliminary test results show that the proposed method is effective in correcting the distortion of the cardiac-related images, which may facilitate the interpretation of these images.

References

Adler A, Proença M, Braun F, et al 2017 Origins of cardiosynchronous signals in EIT *Proceedings of EIT 2017* 73

Deibele J M, Luepschen H, Leonhardt S 2008 Dynamic separation of pulmonary and cardiac changes in electrical impedance tomography *Physiological Measurement* **29** S1

Eyuboglu B M, Brown B H 1988 Methods of cardiac gating applied potential tomography *Clinical Physics and Physiological Measurement* **9** 43

Frerichs I, Pulletz S, Elke G, et al 2009 Assessment of changes in distribution of lung perfusion by electrical impedance tomography *Respiration* **77** 282-291

Proceedings of the International Conference of Bioelectromagnetism, Electrical Bioimpedance,
and Electrical Impedance Tomography June 29 – July 1, 2022 / Kyung Hee University, Seoul, Korea

Quantitative Analysis of Severity in Obstructive Sleep Apnea Patients based on Tidal Volume Reduction and Event Duration for Sleep-related Breathing Disorders

Taewook Chang[1,2,3], Tingting Zhang[1,2], Sung Wan Kim[4] and Tong In Oh[1,2]
[1]Medical Science Research Institute, Kyung Hee University Hospital, Seoul, Korea
[2]Department of Biomedical Engineering, Kyung Hee University, Seoul, Korea
[3]Department of Medical Engineering, Graduate School, Kyung Hee University, Seoul, Korea
[4]Department of Otorhinolaryngology, Head & Neck Surgery, School of Medicine, Kyung Hee University, Seoul, Korea

Correspondence : Tong In Oh, e-mail : tioh@khu.ac.kr

Abstract– The overnight polysomnography (PSG) is the gold standard to diagnose obstructive sleep apnea (OSA) using the apnea and hypopnea index (AHI), which is the average number of apnea and hypopnea per hour during sleep. Unfortunately, the single metric of AHI is not sufficient to quantify the severity of sleep disorder when patients with similar AHI have a significantly distinct amount of tidal volume. In this study, electrical impedance tomography (EIT) has been utilized to quantitatively evaluate the severity of OSA, which takes account of the tidal volume reduction and duration for sleep-related breathing disorders. We could present that the additional information obtained from EIT during overnight PSG describes a more accurate estimation of the OSA severity.

Keywords: Electrical impedance tomography; Obstructive sleep apnea; Tidal volume; Ventilation loss; Apnea-hypopnea index

1. Introduction

Obstructive sleep apnea (OSA) occurs when airflow is reduced or temporarily suspended due to the occlusion around the upper airway during sleep. Overnight polysomnography (PSG) is currently the gold standard diagnostic procedure for OSA [Durán2001]. In PSG, various sensors have been attached to the body surface, such as nasal pressure, thermistor, thoracic or abdominal belts, etc., to identify sleep-related breathing disordered events such as apnea and hypopnea, according to the AASM guidelines. Based on the PSG data obtained overnight, the average number of apnea and hypopnea events per hour is computed defined as an AHI index, indicating the severity of the OSA. Though the AHI index is commonly used in clinics, it does not consider the difference in tidal volume (TV) between apnea and hypopnea events and event duration. Thus, it would be helpful to describe the severity of OSA with the actual breathing amount during sleep, including AHI, quantitatively. Furthermore, the analytical studies of sleep-related breathing disordered events have not been actively investigated on how the TV changes according to the arousal [Sériès1999].

Recently, electrical impedance tomography (EIT) has been used in clinical applications for pulmonary protective mechanical ventilation due to being non-invasive and cost-effective [Adler2021]. In this study, EIT has been adopted to measure the tidal volume simultaneously during overnight PSG and further explore how the amount of tidal volume varies with respect to different types of sleep-related breathing disorders analyzed by PSG. We additionally proposed the various indexes to present the severity of OSA based on TV changes and event durations.

2. Method

The synchronized PSG and EIT data were collected from 13 subjects aged 19 to 75 years old in this study. They all suffered from sleep apnea symptoms with an AHI of 5 or higher, which a professional technician scored according to AASM guidelines [Durán2001, Berry2020]. Specifically, apnea is defined as a 90% reduction of thermistor signal with at least 10 seconds duration. Hypopnea is scored when the nasal pressure drops by more than 30% lasts for more than 10 seconds, with arousal occurring or desaturation decreasing by more than 3%. As to flow limitation (FL), it is the same as hypopnea without the occurrence of arousal and desaturation. Finally, respiratory effort-related arousal was defined with increased respiratory effort and flat nasal pressure signal with a duration of more than 10 seconds.

We determined the normal awake TV (TV_{NA}) for each patient as a mean TV value measured during the awake stage detected by EEG. We set the normal sleep TV as $TV_{NS}=0.8\times TV_{NA}$ [Krieger1990]. Based on TV from EIT measurements, we defined apnea when the average TV was below 70% of TV_{NS} during an event that lasted at least 10 seconds. Hypopnea was defined as a sustained 30% reduction of TV in more than 10 seconds. Analogous to AHI by PSG, we defined apnea and hypopnea count (AHC) as the sum of hypopnea and apnea events detected by TV reduction divided by total sleep time. To better quantify the TV reduction and event duration due to sleep-related breathing disorders, we proposed ventilation loss (VL) defined as the percentage of ventilation lost due to the detected apnea and hypopnea events throughout the total sleep time. Mathematically put,

$$VL = \left(1-\frac{\sum_{i\in[0,TST]} TV_i}{TV_{NS}\times\overline{RR}\times TST}\right)\times 100\ (\%) \tag{1}$$

where TST is total sleep time [min], $\overline{RR}$ is the mean reparation rate of all normal breaths during sleep [bpm], and TV_{NS} is the mean of normal tidal volume. It easily follows from formula (1) that VL reflects the influences of both durations and TV reduction from sleep-related breathing disordered events.

3. Results

Table 1 presents summarized results of sleep-related breathing disordered events scored by PSG and EIT for two subjects, P1 and P13. In the PSG result, the number of detected FL in P1 was 110, and that of P3 was 71. We found that the decrease in tidal volume was more in P1. It can be observed that there was no significant difference in AHC between the two subjects while AHI was quite different. For P1, the number of hypopnea events by EIT was increased due to the FL.

Table 1. Sleep-related breathing disordered events scored by PSG and EIT.

	PSG				EIT							
	Hypopnea	Apnea	AHI	FL	Hypopnea		Apnea		TV/TVns		AHC	VL (%)
	n	n			n	d (s)	n	d (s)	H	A		
P1	36	15	7.3	110	149	21.67 ±10.59	38	21.35 ±6.62	0.47	0.17	26.76	11.6
P13	114	5	19.4	71	130	40.62 ±21.65	31	33.59 ±12.59	0.47	0.19	26.24	18.3

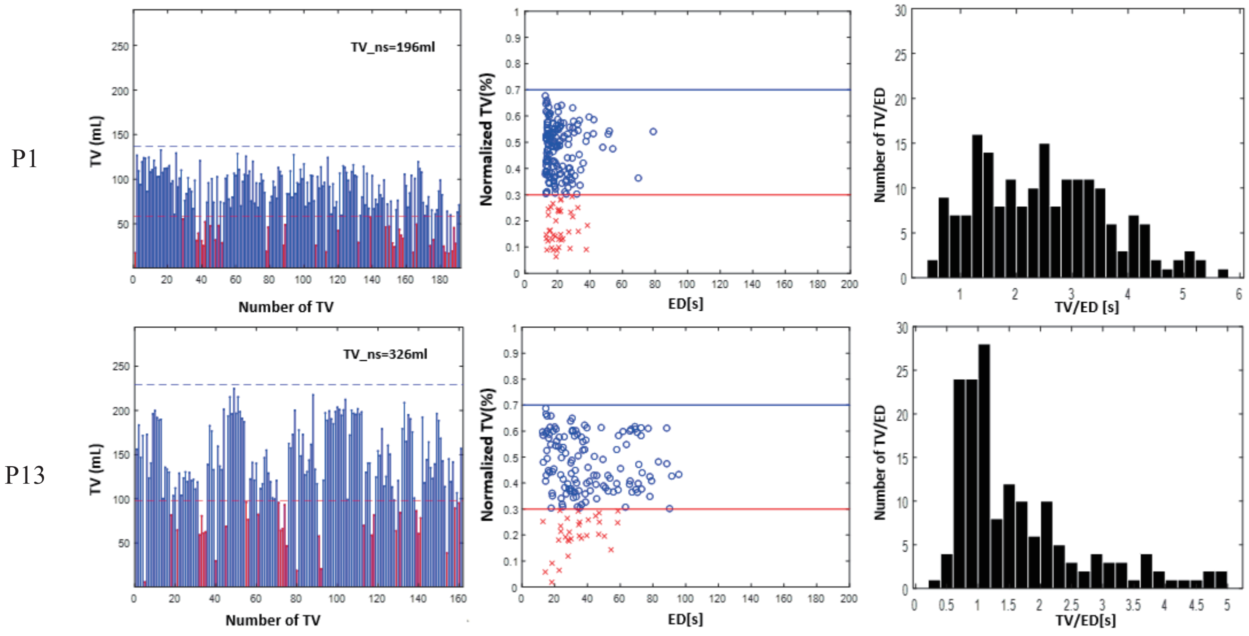

(a) (b) (c)

Figure 1. Overall view of TV during sleep. (a) TV distribution during respiratory events (b) Normalied TV w.r.t usual TV (c) Histogram distribution of TV/ED

The event duration of P13 was longer than that of P1. In detail, hypopnea was 87% longer, and apnea was 57% longer. These differences induced VL discrepancy even though two subjects possessed similar AHC. Therefore, VL in P13 was about 6.7% higher than P1. The resulting indexes presented different characteristics. Figure 1 presents different views with TV reduction and event duration (ED) based on tidal volume monitoring from EIT, where row 1 corresponds to P1 and row 2 to P13. Figure 1(a) shows the TV value for each disordered breathing event during total sleep time. Figure 1(b) illustrated with normalized TV and each event duration simultaneously. Finally, we provided a histogram in Figure 1(c) which the normalized TV is divided by the event duration. The lower value of TV/ED describes the lower TV or longer ED, which affects a higher loss of ventilation.

4. Discussion

Sleep-related breathing disordered event in PSG is detected by the flow reduction relative to a baseline value before the event using an oral-nasal thermistor and nasal pressure. They rely on short-term or local changes in the flow signal without considering the global reference values of all normal representative respirations throughout the TST. In this study, we described the disordered respiratory events using TV reduction regarding normal sleep TV, the global reference value of TV. In a conventional analysis from PSG, both long and short breathing disordered events contribute equally to AHI. However, the severity of each respiratory event may vary depending on the duration of the event and the amount of TV reduction. Therefore, we proposed the new ventilation loss parameter, which also described the sleep-related breathing disorder and how much ventilation was lacking during the entire sleep period.

5. Conclusions

In this study, EIT was proposed to detect the respiratory events of apnea and hypopnea based on TV reduction. In addition, newly proposed parameters of AHC and VL could supplement AHI in the sense that it separately expresses the frequency of respiratory events and ventilatory deficits. To further evaluate the clinical usefulness of AHC and VL in assessing the severity of OSA, more patients will be recruited and analyzed in future clinical studies.

Acknowledgments

This research was supported by Basic Science Research Program through the National Research Foundation of Korea (NRF) funded (NRF-2020R1I1A1A01066649, NRF-2020R1A2C1008975), and the Industrial Strategic Technology Development Program (20006024) funded by the Ministry of Trade, Industry & Energy (MOTIE) in Korea.

References

Durán J , et. al. 2001 Obstructive sleep apnea–hypopnea and related clinical features in a population-based sample of subjects aged 30 to 70 yr *American journal of respiratory and critical care medicine* **163(3)** 685-689

Sériès F and Marc I 1999 Nasal pressure recording in the diagnosis of sleep apnoea hypopnoea syndrome *Thorax* **54** 506-510

Berry RB, et. al 2020 The AASM manual for the scoring of sleep and associated events: rules, terminology, and technical specifications *American Academy of Sleep Medicine*

Adler A and Holder D 2021 Electrical impedance tomography: methods, history and applications *CRC Press*

Krieger J, et. al. 1990 Breathing during sleep in normal middle-aged subjects *Sleep* **13** 143–154

Proceedings of the International Conference of Bioelectromagnetism, Electrical Bioimpedance,
and Electrical Impedance Tomography June 29 – July 1, 2022 / Kyung Hee University, Seoul, Korea

Assessment of low back pain in helicopter pilots using electrical bio-impedance technique

Hang Wang[1], Meng Dai[2], Lin Yang[1] and Zhanqi Zhao[2,3]
[1] Department of Aerospace Medicine, Fourth Military Medical University, Xi'an, China
[2] Department of Biomedical Engineering, Fourth Military Medical University, Xi'an, China
[3] Institute of Technical Medicine, Furtwangen University, Villingen-Schwenningen, Germany

Correspondence : Zhanqi Zhao, e-mail : zhanqi.zhao@hs-furtwangen.de

Abstract– Low back pain (LBP) is known to pose a serious threat to helicopter pilots. This study aimed to explore the potential of electrical bio-impedance (EBI) technique to be used to assess LBP in primary aviation medical units. The LBP scales (severity) in 72 helicopter pilots were assessed using a pain questionnaire, while the impedance measurements of the lumbar muscle were carried out with a high precision EBI measurement system. Results showed that for different LBP scales, significant differences were found in the modulus of lumbar muscle impedance sum on both sides (Z_{sum}), as well as in the modulus and phase angle of lumbar muscle impedance difference between both sides (Z_{diff} and ϕ_{diff}), respectively ($P<0.05$). A strong correlation between Z_{sum} and LBP scale ($R=0.692$, $P<0.01$), an excellent correlation between Z_{diff} and LBP scale ($R=0.86$, $P<0.01$), and a desirable correlation between ϕ_{diff} and LBP scale ($R=-0.858$, $P<0.01$) were found. These findings demonstrated that EBI could sensitively and accurately detect the state of lumbar muscle associated with LBP.

Keywords: Low back pain; electrical bio-impedance; pilot; lumbar muscle.

1. Introduction

Low back pain (LBP) is a persistent disorder, which has been a common musculoskeletal disease worldwide (Krismer and van Tulder. 2007; Wu et al. 2020). For helicopter pilots, due to prolonged exposure to vibration of high-intensity and confined sitting posture, LBP occurs frequently (Posch et al. 2019; da Silva 2020). LBP poses a serious threat to pilots by causing flight safety issues, such as attention, motion control and postural stability (Gaydos 2012; Harrison et al. 2009). Studies showed that early detection of LBP and implementation of medical intervention could particularly be beneficial to the health and well-being of pilots (Marins et al. 2020). Therefore, early detection and evaluation of LBP is important to minimize the influences on pilots' health and flight performance.

Electrical bio-impedance (EBI) is a novel technique that provides information on physiological and pathological states of human tissues (Abe et al. 2021; Al-harosh et al. 2022). Up to date, several studies have explored the ability of EBI to detect LBP (Wang et al. 2019; Ching et al. 2013). These studies demonstrated the high sensitivity of EBI to lumbar muscle dysfunction caused by LBP. However, the results were insufficient to support direct use of EBI to detect LBP in pilots. The studied subjects were patients, not pilots. Besides, previous studies did not perform any quantitative pain rating so that no relationship between the severity of LBP and EBI was established.

In this study, the severity of LBP in 72 helicopter pilots was determined and EBI of the lumbar muscle were performed.

2. Methods and materials

This study was approved by local Ethics Committee (No.KY20163064-1). The Chinese version of Oswestry Disability Index (Chow and Chan, 2005) was used to evaluate the severity of LBP for each pilot. ODI consists of ten sections to and each section has 6 scales, corresponding to 0-5 points. The higher the score, the more severe the dysfunction. Total score was converted to an LBP scale, ranging from 1 to 5, corresponding to no pain, mild dysfunction, moderate dysfunction, severe dysfunction and complete dysfunction, respectively.

In vivo impedance measurement of lumbar muscle on both sides of the spine was performed. The bioimpedance measurement system consists of a Solartron 1260 impedance analyzer and a Solartron 1294 interface (Solartron Analytical, Farnborough, UK). In this study, the current of 1 mA at 50 kHz was applied. The four-electrode strategy was adopted and converted to four probes: two were used for excitation and the other two for measurement. The four probes were distributed at four corners of a square.

The participant was asked to maintain an upright sitting position. An experienced doctor determined the region over the L4-5 paraspinal skin and the impedance module was placed from the right side of the spine, and the impedance measurement was performed. Subsequently, the impedance measurement on the left side was carried out at the symmetrical position of the impedance module.

The impedance modulus and phase of the lumbar muscle on left and right sides were obtained and denoted as Z_L, ϕ_L, Z_R and ϕ_R, respectively. The sum of impedance on both sides (i.e. $Z_{sum} = Z_L + Z_R$ and $\phi_{sum} = \phi_L + \phi_R$) was compared between individuals with LBP (Scale 2-5) and those without LBP (Scale 1). Also, the sum of impedance on both sides for different LBP scales was respectively compared. Similarly, the impedance differences between the two sides (i.e. $Z_{diff} = |Z_L - Z_R|$ and $\phi_{diff} = |\phi_L - \phi_R|$) were compared between individuals with LBP (Scale 2-5) and those without LBP (Scale 1).

3. Results

Participants were aged from 22 to 48 (32.49 ± 6.56) years, with a weight range from 62 to 91(73.23 ± 6.78) kg and a height range from 167 to 185 (174.41 ± 3.90) cm. Fifty-one participants reported the presence of LBP, 14 individuals already had moderate and severe dysfunction, but no one had complete dysfunction.

There was a significant difference in impedance modulus Z_{sum} ($P<0.05$), whereas no significant difference was found in impedance phase angle ϕ_{sum} ($P=0.736$). The Z_{sum} increased whereas ϕ_{sum} the decreased along with the LBP severity. Significant differences in impedance modulus Z_{sum} were found between Scale 1 and 3 ($P <0.01$), Scale 1 and 4 ($P <0.01$), and Scale 2 and 4 ($P <0.05$), respectively. However, for impedance phase angle ϕ_{sum}, significant difference was only found between Scale 1 and 4 ($P <0.05$).

There were significant differences in both Z_{diff} ($P <0.01$) and ϕ_{diff} ($P <0.01$). Significant differences in Z_{diff} were found among four pain scales ($P <0.05$), except between Scale 3 and 4 ($P =0.465$). Similarly, significant differences were also found in ϕ_{diff} among four pain scales ($P <0.05$), except between Scale 3 and 4 ($P =0.402$).

A positive association between Z_{sum} and LBP scales ($R=0.692$, $P <0.01$) was found, as well as a weak negative association between ϕ_{sum} and LBP scales ($R=-0.281$, $P>0.05$). Also, the higher association was found between Z_{diff} and LBP scales ($R=0.860$, $P <0.01$), and between ϕ_{diff} and pain scales ($R=-0.858$, $P <0.01$).

4. Discussion

The modulus of lumbar muscle impedance increased and the phase angle decreased with the LBP severity. The present results were in accordance with the previous studies. Ching et al and Fujita et al observed that subjects with LBP had a higher impedance compared to the healthy ones (Ching et al. 2013; Fujita et al. 2001). Similar results were found in the study from Dibai-Filho et al 2018. Contrary to our present study, Yamamoto et al found a significant decrease in electrical impedance after pain provocation (Yamamoto et al 2006). This difference may be attributed to some practical factors, such as impedance measurement strategy. The impedance measurement was performed using three-electrode method with a low frequency current (10 Hz). Considering high the electrode-skin contact impedance at low frequencies (e.g. <1 kHz), their measurement results might include also the electrode-skin contact impedance (Yamamoto et al 2006). To minimize the influence of electrode-skin contact impedance, we adopted the four-electrode approach in the study.

The difference of lumbar muscle impedance for different LBP scales could be associated with the physiological structure of muscle tissue. Pilots are often exposed to the vibration and fixed sitting posture for a long time, which causes muscle fatigue. The accumulation of muscle fatigue could lead to chronic inflammation or microvascular damage in the internal muscle tissue. Inflammation could cause changes that have opposite effects on the lumbar muscle impedance.

5. Conclusions

EBI has the potential to be a daily detection tool in primary medical units to assess the state of the lumbar muscle associated with LBP. Future work will optimize the measurement parameters, extract the corresponding impedance features and develop a portable impedance measurement system to improve the practical application.

Acknowledgments

The work was partially supported by National Natural Science Foundation of China (NSFC 61901478 and 81601636), Medical Program of FMMU (Grant No. 2018HKTS10 and 2019ZTC01) and Key R & D Program of Shaanxi Province (2021SF-027).

References

Abe T, Yoshimura Y, Imai R, Yoneoka Y, Tsubaki A, Sato Y. 2021 Impact of Phase Angle on Physical Function in Patients with Acute Stroke. J Stroke Cerebrovasc Dis.30(9):105941.

Al-harosh M, Chernikov E, Shchukin S. 2022 Patient Specific Numerical Modeling for Renal Blood Monitoring Using Electrical Bio-Impedance. Sensors.22(2).

Ching CT, Chen YC, Lu LH, Hsieh PF, Hsiao CS, Sun TP, et al. 2013 Characterization of the muscle electrical properties in low back pain patients by electrical impedance myography. PLoS One.8(4):e61639.

Chow JHW, Chan CCH. 2005 Validation of the Chinese version of the Oswestry Disability Index. Work.25:307-14.

Dibai-Filho AV, Barros MA, de Oliveira AK, de Jesus Guirro RR. 2018 Electrical impedance of the torso is associated with the pressure pain threshold on myofascial trigger points in patients with chronic neck pain: A cross-sectional study. Journal of Back and Musculoskeletal Rehabilitation.31:275-84.

Fujita T, Fujii Y, Okada SF, Miyauchi A, Takagi Y. 2001 Fall of skin impedance and bone and joint pain. J Bone Miner Metab.19(3):175-9.

Gaydos SJ. 2012 Low back pain: considerations for rotary-wing aircrew. Aviat Space Environ Med.83(9):879-89.

Harrison MF, Neary JP, Albert WJ, Kuruganti U, Croll JC, Chancey VC, et al. 2009 Measuring neuromuscular fatigue in cervical spinal musculature of military helicopter aircrew. Mil Med.174(11):1183-9.

Krismer M, van Tulder M. 2007 Low back pain (non-specific). Best Practice & Research Clinical Rheumatology. 21(1):77-91.

Marins E, Caputo E, da Silva M, Dawes J, Orr R, Alberton CL. 2020 Conservative Interventions for Non-Specific Low Back Pain in Tactical Populations: A Systematic Review of Randomized Controlled Trials. Sustainability.12(19).

Posch M, Schranz A, Lener M, Senn W, Äng BO, Burtscher M, et al. 2019 Prevalence and potential risk factors of flight-related neck, shoulder and low back pain among helicopter pilots and crewmembers: a questionnaire-based study. BMC Musculoskeletal Disorders. 20(1):44.

da Silva GV. 2020 Low back pain prevalence in Brazilian helicopter pilots. Ergonomics international journal.4(3):e16000240-e.

Wang Y, Freedman L, Buck M, Bohorquez J, Rutkove SB, Keel J. 2019 Electrical Impedance Myography for Assessing Paraspinal Muscles of Patients with Low Back Pain. J Electr Bioimpedance.10(1):103-9.

Wu A, March L, Zheng X, Huang J, Wang X, Zhao J, et al. 2020 Global low back pain prevalence and years lived with disability from 1990 to 2017: estimates from the Global Burden of Disease Study 2017. Ann Transl Med.8(6):299.

DAY 3

Friday, July 1, 2022

Plenary Talk 03

Speaker Tobias Becher (University Medical Center Schleswig-Holstein, Campus Kiel)

“Electrical Impedance Tomography for advanced respiratory monitoring – perspectives beyond the Covid-19 pandemic”

Proceedings of the International Conference of Bioelectromagnetism, Electrical Bioimpedance,
and Electrical Impedance Tomography June 29 – July 1, 2022 / Kyung Hee University, Seoul, Korea

Electrical Impedance Tomography for advanced respiratory monitoring – perspectives beyond the Covid-19 pandemic

Tobias Becher[1]

[1]Department of Anesthesiology and Intensive Care Medicine, University Medical Center Schleswig-Holstein, Campus Kiel

Correspondence e-mail : tobias.becher@uksh.de

Abstract–This plenary talk will outline past, current and possible future clinical applications of Electrical Impedance Tomography (EIT) in the context of advanced respiratory monitoring. In particular, it will focus on the role of EIT in addressing the challenges clinicians face during the treatment of patients suffering from covid-19-associated respiratory failure, including monitoring of ventilation and perfusion, detection of pulmonary overdistension and alveolar cycling, individualized adjustment of positive end-expiratory pressure and detection of imminent patient self-inflicted lung injury. EIT's current capabilities and limitations in the context of respiratory monitoring will be adressed and potential barriers to a more widespread clinical application of EIT will be highlighted. In addition, conceivable future developments that could be helpful to improve the clinical applicability of EIT for daily patient care will be discussed.

DAY 3

Friday, July 1, 2022

Oral Session 13

Clinical Application of Bio-impedance III

Chair Inez Frerichs (University Medical Centre of Schleswig-Holstein)

O 13-01 **Using EIT to guide chest physiotherapy in patients with pneumonia**
Qing Li (Beijing Rehabilitation Hospital, Capital Medical University)

O 13-02 **Ventilation Volume of Mechanically Ventilated Patients from EIT Data on a Novel Electrode Solution: A Case Study**
Nilton Barbosa da Rosa Junior (Colorado State University)

O 13-03 **Impact of Patient Position on Neonatal Chest EIT**
Nima Seifnaraghi (Middlesex University)

O 13-04 **Electrical Impedance Tomography to Assess Pulmonary Function in Amyotrophic Lateral Sclerosis Patients**
Allaire Doussan (Dartmouth College)

Proceedings of the International Conference of Bioelectromagnetism, Electrical Bioimpedance,
and Electrical Impedance Tomography June 29 – July 1, 2022 / Kyung Hee University, Seoul, Korea

Using EIT to guide chest physiotherapy in patients with pneumonia

Qing Li[1#], Yi Li[1#], Hongying Jiang[1*], Zhanqi Zhao[2*]
[1]. Department of Pulmonary and Critical Care Medicine, Beijing Rehabilitation Hospital, Capital Medical University,
Xixiazhuang, Badachu Road, Shijingshan District, Beijing 100144, China
[2]. Department of Biomedical Engineering, Fourth Military Medical University, Xi'an 710000, China

Abstract– The study aimed to examine the feasibility and efficacy of chest physiotherapy (CPT) guided by electrical impedance tomography (EIT) compared to conventional CPT in patients with pneumonia. A total of 60 patients were randomized to the control and EIT-guided groups. Two sessions of CPT per day were conducted in both groups using a program determined prior to the randomization. In addition, the CPT was guided by the real-time ventilation distribution imaging in the EIT-guided group. The time required for symtom improvement reduced significantly in the EIT-guided group ($p<0.05$). Besides, the patients stayed shorter in the hospital ($p<0.001$). Furthermore, the patients who received EIT-guided CPT were more satisfied ($p<0.001$). EIT can be used to guide CPT in pneumonia patients, which resulted in better outcomes.

Keywords: Pneumonia; chest physiotherapy; electrical impedance tomography; visual feedback; ventilation distribution.

1. Introduction

Patients with community-acquired pneumonia (CAP) require hospitalization and some might end up in the ICU (Leeper, 1996). Hospital-acquired pneumonia (HAP) is one of the most common infections with significant clinical morbidity and mortality. Mechanical ventilation and ICU stay increases the incidence of HAP significantly (Rosenthal et al., 2014). Medical imaging is required for the diagnosis and follow-up for CAP and HAP. Bedside X-ray examination is even required daily for severe pneumonia, which exposes the patients to significant radiation.

Pulmonary rehabilitation has been developed to improve symptoms of pneumonia such as fever, cough, expectoration, chest pain, etc. Chest physiotherapy (CPT) has been used as an adjunctive treatment to facilitate airway clearance and promote an effective cough (Fahy and Dickey, 2010). Previous studies showed that lung function can be improved with CPT. Besides, the incidence of ventilator-associated pneumonia was also reduced (Longhini et al. 2020).

Electrical impedance tomography (EIT) has been proposed to evaluate the physiological changes introduced by CPT (Eimer et al. 2021; Yuan et al. 2021), The present study aimed to examine the feasibility and efficacy of EIT-guided CPT regarding patient outcomes.

2. Methods

The study was approved by local Ethical committee. Written informed consent was provided by all participants. The inclusion criteria were: age $\geq$ 18 years; presence of the diagnostic criteria for CAP or HAP; suitability for CPT. The exclusion criteria were: severe pneumonia; viral pneumonia; thoracic spinal deformity; any contraindications for the use of EIT; pregnant or lactating women; inability to cooperate with pulmonary rehabilitation; acute exacerbation of chronic obstructive pulmonary disease or acute attack of bronchial asthma.

A total of 182 patients with pneumonia were screened and 60 were randomized to control or EIT-guided group. In the control group, two sessions of CPT (morning and afternoon, 20 minutes each) were performed on each day. Each session consisted of various types of CPT according to our internal guidelines (e.g. modified postural drainage, assisted cough technique, positive expiratory pressure etc). Individualized program was formed according to the assessment, internal guidelines, the patient's tolerance, education level, and patient's preference prior to the randomization. In the EIT-guided group, EIT measurement was conducted during the CPT program and the images were used to guide the CPT treatments.

The primary outcome was the number of days until major symptoms improved after treatment started. The secondary outcomes were length of hospital stay, costs of hospitalization, and patients' satisfaction with the treatment.

3. Results

The days required for body temperature returning to normal was significantly longer in the control group (2 (2, 3) vs. 2 (1, 2) days, control vs. EIT-guided groups respectively; p=0.046). More days were needed until the absence of purulent sputum (5 (4, 6) vs. 3 (3, 4) days; p<0.001). The patients in the EIT-guided group spent one day less in the hospital (10 (9, 10) vs. 9 (8, 9) hospital days, p<0.001). The patients in the EIT-guided group were more satisfied with the CPT treatment (14 (13, 15) vs. 24 (23, 24) points, the higher the better, p<0.001).

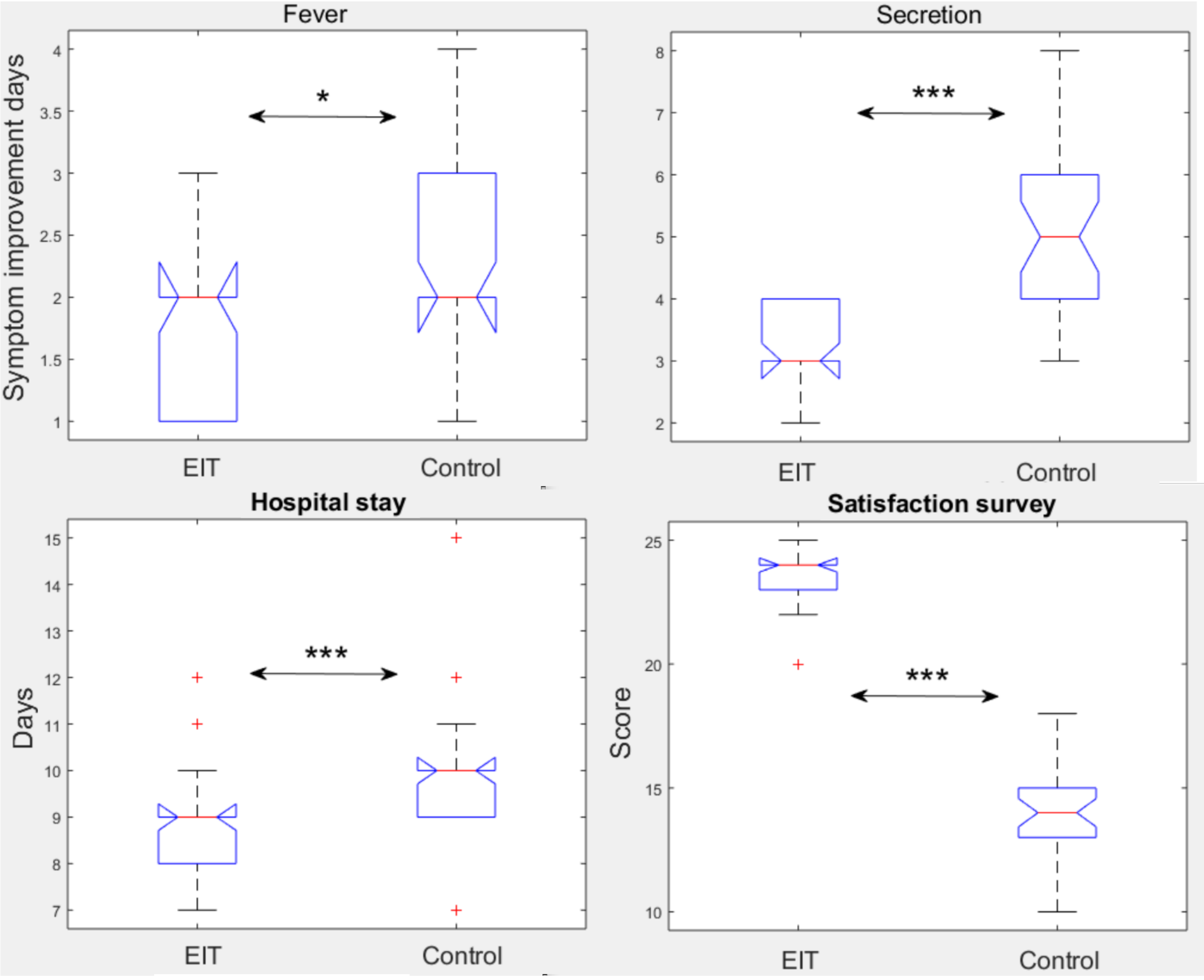

Figure 1. Endpoints comparison. * p<0.05; *** p<0.001

4. Conclusions

In the present pilot study, it was demonstrated that EIT-guided CPT was superior to to the conventional one in patients with pneumonia. The symptoms improved faster, and the patients were better motivated and satisfied with the treatment via the real-time visual feedback. Combining the conventional CPT, physiotherapist can develop individualized CPT plan with the real-time visual feedback provided by EIT.

References

Eimer C, Freier K, Weiler N, Frerichs I, Becher T. 2021 The Effect of Physical Therapy on Regional Lung Function in Critically Ill Patients. *Frontiers in physiology*. **12** 749542.

Fahy JV, Dickey BF. 2010 Airway mucus function and dysfunction. *N Engl J Med*. **363** 2233-47.

Leeper KV, Jr. 1996 Severe community-acquired pneumonia. *Semin Respir Infect.* **11** 96-108

Longhini F, Bruni A, Garofalo E, Ronco C, Gusmano A, Cammarota G, et al. 2020 Chest physiotherapy improves lung aeration in hypersecretive critically ill patients: a pilot randomized physiological study. *Critical Care*. **24** 479.

Rosenthal VD, Maki DG, Mehta Y, Leblebicioglu H, Memish ZA, Al-Mousa HH, et al. 2014 International Nosocomial Infection Control Consortium (INICC) report, data summary of 43 countries for 2007-2012. Device-associated module. *Am J Infect Control*. **42** 942-56.

Yuan S, Chi Y, Long Y, He H, Zhao Z. 2021 Effect of Position Change From the Bed to a Wheelchair on the Regional Ventilation Distribution Assessed by Electrical Impedance Tomography in Patients With Respiratory Failure. *Frontiers in Medicine*. **8** 744958.

Proceedings of the International Conference of Bioelectromagnetism, Electrical Bioimpedance,
and Electrical Impedance Tomography June 29 – July 1, 2022 / Kyung Hee University, Seoul, Korea

Ventilation Volume of Mechanically Ventilated Patients from EIT Data on a Novel Electrode Solution : A Case Study

Nilton Barbosa da Rosa Junior[1], Jennifer Mueller[1,2], Andre Vieira Pigatto[1], Tzu-Jen Kao[3],
Nancy Stoffel[3], Cheryl Bromirski[3], David Davenport[3], Patrick Offner[4] and Ellen Burnham[4]
[1]School of Biomedical Engineering, Colorado State University, Fort Collins, USA
[2]Department of Mathematics, Colorado State University, Fort Collins, USA
[3]GE Research, Niskayuna, USA
[4]Department of Medicine, University of Colorado Anschutz Medical Campus, Aurora, USA

Correspondence: Nilton Barbosa da Rosa Junior, e-mail: nilton@colostate.edu

Abstract–Monitoring patients receiving mechanical ventilation is a leading application of electrical impedance tomography. Electrical impedance tomography has been shown to be a viable imaging modality for bedside lung monitoring, which can provide visual information about regional ventilation and pulmonary perfusion. However, a significant challenge in its use for patients receiving mechanical ventilation is efficient and safe electrode placement. The purpose of this paper is to present results from a case study in which a novel electrode solution is being used in a larger study to image patients with acute respiratory distress syndrome. Data was collected during a spontaneous breathing trial using the General Electric simultaneous multiple current source prototype electrical impedance tomography system, and 3-D conductivity difference images were computed using a linearization-based reconstruction algorithm. Regional lung volume estimates were computed from the images. The images show good agreement with the chest x-ray that showed suspected pleural fluid accumulation and atelectesis, and the dynamic global lung volume estimate was in good agreement with the volume range provided by the ventilator.

Keywords: EIT; real-time lung monitoring; acute respiratory distress syndrome; lung volume estimates.

1. Introduction

Patients with ARDS (acute respiratory distress syndrome) are treated with mechanical ventilation, which reinflates the airways over time. Various methods have been used to monitor patients undergoing mechanical ventilation including monitoring blood gases and pressure-volume curves, but these quantities do not provide regional information about lung aeration, which is important because an aeration imbalance can lead to collapse of dependent lung zones and overdistension of non-dependent regions, potentially resulting in lung injury. Electrical impedance tomography has been shown to be a viable imaging modality for bedside lung monitoring, which can provide visual information about regional ventilation and pulmonary perfusion.

One challenge in the use of EIT for imaging mechanically ventilated patients is electrode placement. Patients are typically sedated, and rolling the patient to apply the electrodes comes with the risk of dislodging the endotracheal tube or tracheostomy and patient discomfort. Thus, it is important to have a fast and reliable method of electrode application. A novel textile electrode solution was developed to address this problem and is being used in an ongoing study of patients with acute respiratory distress syndrome at Anschutz Hospital in Aurora, CO. Here we present a case study of the results on one mechanically ventilated patient in the ICU undergoing a spontaneous breathing trial. The images are compared to a chest x-ray and reveal good agreement in the detection of fluid accumulation in the lung. Real-time regional lung volume estimates are computed from the EIT images and compared to the global ventilator values.

2. Materials and methods

2.1 EIT system and data collection

The study was conducted in accordance with the amended Declaration of Helsinki. Data were collected at Anschutz Hospital in Aurora, CO under the approval of the institutional review board (approval number 21-3315). Here we present preliminary results from data collected on one 73 year-old male patient with primary diagnoses of acute hypercapnic respiratory failure (AHRF) and pulmonary edema receiving mechanical ventilation. The WEAT was placed, and EIT data was collected with the patient in supine position. PEEP was set at 5 cm H20. The EIT data was collected using the GE SMS-EIT prototype system described in [Ashe et al, 2014] The system is a 32 channel real-time simultaneous multiple current source system, that collects data at 18 frames per second at 10 kHz. In this work, the 3-D trigonometric current patterns specified in [Kao et al, 2020] are applied with a maximum amplitude of 0.11 mA RMS.

2.2 Electrode placement solution: WEATs

An easy-to-apply array of electrodes is essential to efficient work flow in the hospital environment. The textile design, consisting of two independent halves, is shown in Figure 1. The wearable electrode applicator textile (WEAT) consists of two rows of 16 electrodes arranged in two C-shapes to enable 3-D imaging. The ends of the C-shape meet at the sternum and the spine, which has the advantages of not constricting the chest during breathing. The WEAT is made in a variety of sizes with the intent of maintaining a gap of approximately 3 to 4 cm between the electrodes at the sternum and spine. The leads come together in four groups of eight, and so two connectors under each arm connect the WEAT to the EIT system. A ground electrode is attached separately to the subject’s shoulder or abdomen.

Figure 1. Two views of the WEAT on a healthy volunteer.

2.3 ToDLeR algorithm and lung volume computation

The ToDLeR algorithm [Blue et al, 2000] with the real-time implementation described in [Kao et al, 2020] on a cylinder was modified to account for uneven electrode placement and varying height between the two rows of the electrodes, while keeping the cylindrical model in this work. A reference frame representing maximal expiration was chosen from a principal component analysis of the data, and 3-D difference images of the conductivity were computed relative to the reference frame on two vertically stacked 496-voxel Joshua tree meshes [Cheney et al, 1990] with height 7.5 cm. The reconstructions are displayed in DICOM format, and the cross-section through the lower row of electrodes is displayed in the bottom image of the figure and the cross-section through the upper row of electrodes is displayed as the upper image. Voxels of lower conductivity than the reference frame are blue, and those of higher conductivity are orange/red.

For each frame, the inspired volume of air in each voxel was estimated from the conductivity values in the EIT image using the method from [Muller et al, 2015] and [Pigatto et al, 2021]. We review the method here. For a given voxel p in the segmented lung region, let $\sigma_a(p,t)$ denote the conductivity in the *p*th voxel at time *t* corresponding to a given frame. The volume fraction $f_a(p,t)$, of air in the *p*th voxel at time t, is related to the conductivity in the *p*th voxel at time *t* by

$$\sigma_a(p,t) = \sigma_{aM}(1\text{-}f_a(p,t)) + \sigma_{am} f_a(p,t), \qquad (1)$$

where σ_{aM} and σ_{am} are the maximum and minimum values, respectively, of the conductivity over all voxels and over the entire data collection period of interest. The volume fraction of air can then be computed by

$$f_a(p,t) = \frac{\sigma_a(p,t)-\sigma_{aM}}{\sigma_{am}-\sigma_{aM}} \qquad (2)$$

The lung region was identified and segmented by a threshold method. Any voxel with a minimum relative conductivity value that remains larger than $0.5(\sigma_{aM} + \sigma_{am})$ over the entire data set was considered to be too conductive to be included as a lung voxel. Any voxel with maximum relative conductivity value over the entire data set exceeding 90% of σ_{aM} was also considered to be too conductive to be a lung voxel. Finally, voxels that have peak-to-peak conductivity smaller than 30% of the highest peak-to-peak voxel conductivity, which could represent voxels with small variations close to the electrodes (such as in the upper axilla), were excluded from the computations.

The images were divided into four quadrants to represent the upper left lung (ULL), upper right lung (URL), lower left lung (LLL) and lower right lung (LRL). To compute the volume of air in each quadrant at time t, the sum of $f_a(p,t)$ multiplied by the volume of the p^{th} voxel was taken over all of the voxels in the quadrant. In this work, the volume of a voxel was one half the distance between the upper and lower rows of electrodes multiplied by the cross-sectional area of the corresponding pixel in the Joshua tree mesh. The global lung volume was the sum of the volume in each quadrant.

3. Results

The patient received a chest x-ray as part of his standard care, which is shown in Figure 2. The radiology report stated, "… there is a new right basilar opacity suspected to reflect a combination of pleural fluid and underlying atelectesis, however pneumonia is not excluded." The EIT conductivity difference images for three frames in the data collection sequence are shown in Figure 3. The three frames correspond to a full inspiration, mid inspiration, and full expiration, with frame 2489 as reference. The total lung volumes computed by the method described in Section 2 are also plotted in Figure 2 for a portion of the sequence. The computed lung volume (Global Volume) ranged from 238 ml to 769 ml, which is in very good agreement with the range of exhaled tidal volume (VTE) provided by the ventilator of 200 to 1000 ml (See Figure 2).

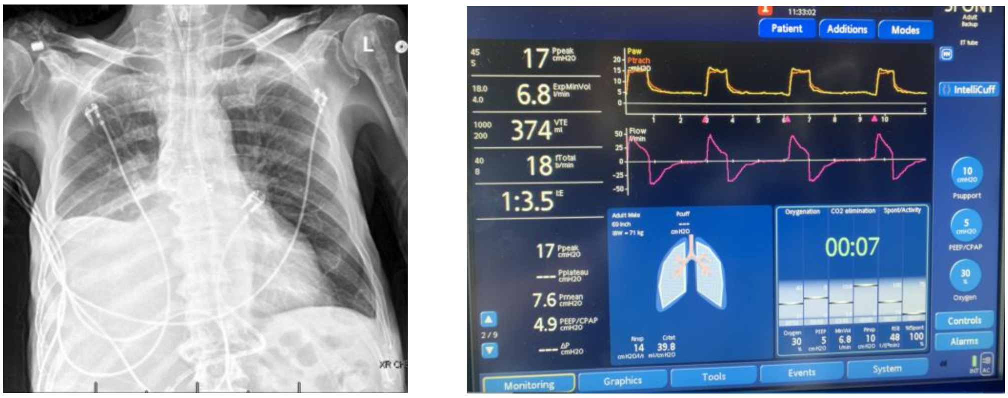

Figure 2. Chest x-ray taken two days after the EIT data collection. Radiology report indicates a right basilar opacity suspected to reflect a combination of pleural fluid and underlying atelectesis, but pneumonia is not excluded.

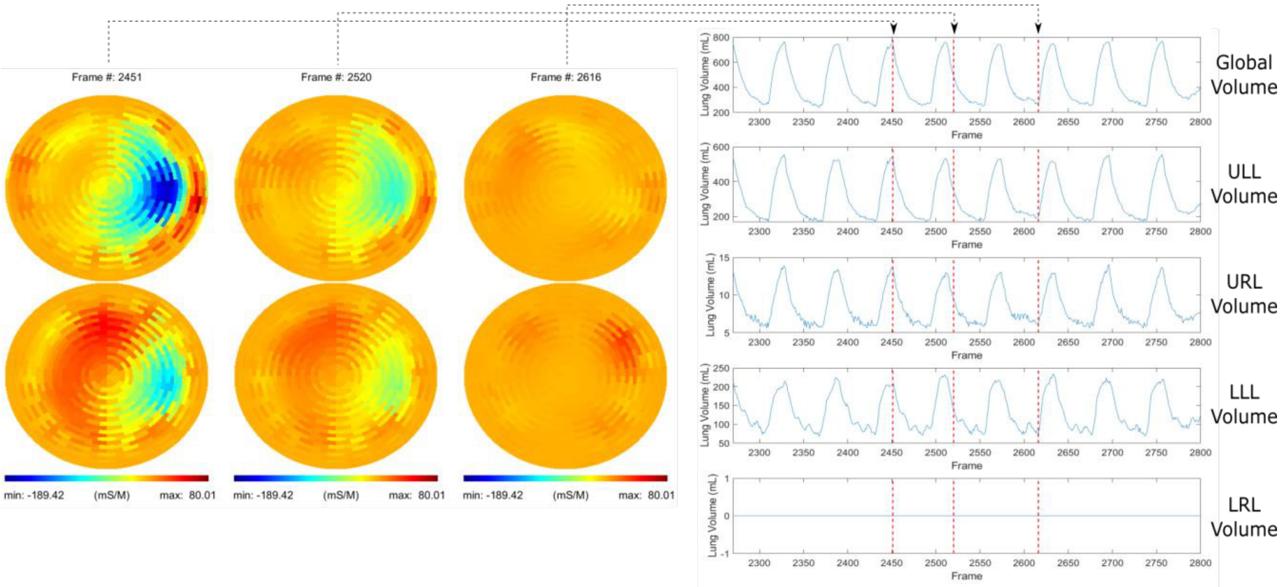

Figure 3. EIT conductivity difference images displayed in DICOM orientation for three frames in the data collection sequence. These frames are indicated by dashed red lines in the line plots below, which depict the lung volumes computed from the EIT images globally (Global Volume), in the upper left lung (ULL), upper right lung (URL), lower left lung (LLL), and lower right lung (LRL).

4. Discussion

One motivation for the design of the WEAT is to avoid restricting patient breathing by constricting the chest with elastic material. Recently, [Zhang et al, 2020] reported that an EIT electrode belt could reduce lung volumes in subjects with pre-existing lung diseases including respiratory muscle weakness patients and COPD patients. Therefore, a better electrode solution for fragile ICU patients is needed. While the WEAT does not constrict the chest, it does permit non-uniform electrode placement, which is then best accounted for in the reconstruction algorithm, and requires placement measurements by the attending clinician.

Regarding the images, at full inspiration (frame # 2451), the upper-left lung (ULL) and lower-left lung (LLL) show regions of ventilation represented by lower conductivity, while the upper-right lung (URL) only shows very few voxels that are being ventilated. The lower-right lung (LRL) shows highly conductive areas that are not being ventilated. This patient did not receive a CT scan as part of his care, and so comparisons can only be made with the chest x-ray in Figure 2. The regional ventilation in the EIT image is consistent with the chest x-ray and radiologist's report.

The method of computation of the lung volume estimates from the EIT images was also used in [Kao et al, 2020] to compute lung volume estimates in six healthy volunteers who performed a breathing maneuver with a volumetric incentive spirometer, and the volume of air inhaled was calculated from the EIT images. The relative errors between the total inhaled volume reported by the spirometer and the average calculated volume from the EIT images for each of the subjects were 6.5%, 1.5%, 9.2%, 47.2%, 4.4%, and 6.9%. In this study, we see that the global lung volume ranges from 238 ml to 769 ml, which is in very good agreement with the VTE on the ventilator, which ranged from 200 to 1000 ml. Further validation studies are needed to assess the accuracy of the computed lung volumes, both regionally and globally.

5. Conclusions

Preliminary results from this case study using the novel wearable electrode applicator textile (WEAT) demonstrate that the SMS-EIT system together with the WEAT provides 3-D conductivity difference images and regional lung volume estimates that detect ventilation deficiencies in real time and can quantify regional lung volumes. This is part of a larger study in which a statistical analysis will be performed to support quantitative results.

Acknowledgments

This project was supported by Award Number 3R01EB026710-02S1 from the National Institute Of Biomedical Imaging And Bioengineering. The content is solely the responsibility of the authors and does not necessarily represent the official view of the National Institute Of Biomedical Imaging And Bioengineering or the National Institutes of Health. We would also like to the staff in the medical ICU at the University of Colorado Hospital for their role in the data collection.

References

Ashe J, Shoudy D, Boverman G, Sabatini, Kao T J and Amm B 2014 A high precision parallel current drive experimental EIT system. *In 15th International Conference on Biomedical Applications of Electrical Impedance Tomography* **2014**

Blue R S, Isaacson D, and Newell J C 2000 Real-time three-dimensional electrical impedance imaging *Physiological Measurement,* **21,** 1-12

Cheney M, Isaacson D, Newell J C, Simske S and Goble J 1990 NOSER: An algorithm for solving the inverse conductivity problem *International Journal of Imaging systems and technology*, **2(2)**, 66-75

Kao T J, Amm B, Isaacson D, Newell J C, Saulnier G J and Mueller J L 2020 A 3D Reconstruction Algorithm for Real-time Simultaneous Multi-Source EIT Imaging for Lung Function Monitoring *bioRxiv*

Muller P A, Li T, Isaacson D, Newell J C, Saulnier G J, Kao T J, and Ashe J 2015 Estimating a regional ventilation-perfusion index. *Physiological measurement*, **36(6)**, 1283–1295

Pigatto A V, Kao T K, Mueller J L, Baker C D, DeBoer E M and Kupfer O 2021 Imaging ventilation before and after airway clearance therapy in spinal muscular atrophy using electrical impedance tomography *Respir Physiol Neurobiol*, **294**

Zhang N, Jiang H, Zhang C, Li Q, Li Y, Zhang B, Deng J, Niu G, Yang B, Frerichs I, Moeller K, Fu F and Zhao Z 2020 The influence of an electrical impedance tomography belt on lung function determined by spirometry in sitting position *Physiol Meas*, **41(4)**, 044002

ICBEM Bioelectromagnetism ICEBI Electrical Bioimpedance EIT Electrical Impedance Tomography

Proceedings of the International Conference of Bioelectromagnetism, Electrical Bioimpedance,
and Electrical Impedance Tomography June 29 – July 1, 2022 / Kyung Hee University, Seoul, Korea

Impact of Patient Position on Neonatal Chest EIT

Nima Seifnaraghi[1], Serena de Gelidi[1], Inéz Frerichs[2], Erich Sorantin[3],
Andreas Demosthenous[4] and Richard H. Bayford[1]
[1]Department of Natural Sciences, Middlesex University, London, United Kingdom
[2]Department of Anaesthesiology and Intensive Care Medicine, University Medical Centre Schleswig-Holstein, Kiel, Germany
[3]Department of Radiology, Medical University of Graz, Graz, Austria
[4]Department of Electronic and Electrical Engineering, University College London, London, United Kingdom

Correspondence : Nima Seifnaraghi, e-mail : n,seifnaraghi@mdx.ac.uk

Abstract– This paper investigates the possible effects of patient recumbency positions on one of the parameters used in clinical chest electrical impedance tomography (EIT) monitoring – the silent spaces. This parameter impacts medical decisions and interventions as it indicates how well each lung is being ventilated. Yet, it can be significantly affected by the assumed prior model including the alternations amid internal displacement and deformations caused by movement of heart, mediastinum and diaphragm based on their weight and abdominal cavity pressure when switching recumbency positions. To evaluate the effect of prior model adjustment in accordance to patient position, an 18-month old infant who was radiographed in supine and both decubitus lateral postures was used as a guide to create 3D compatible models and calculate corresponding silent spaces. These values were then compared with prior and post model updates according to recumbency positions for the patient. The results show average improvements of 7 and 15% in left and right lung silent spaces respectively when the updated models were applied.

Keywords: Chest EIT; Lateral decubitus; Modelling; Recumbency position; Silent spaces.

1. Introduction

Electrical impedance tomography (EIT) provides an electric conductivity image of a domain using electrodes attached to its boundary surface [1]. Small currents are injected through specific electrode pairs and the resulting potential differences on the remaining electrodes are measured and used to reconstruct a conductivity image. Despite the low spatial resolution of EIT relative to other imaging techniques like computed tomography (CT) and magnetic resonance imaging (MRI), the virtues such as non-invasiveness and high temporal resolution have made EIT desirable in the clinical field. Moreover, the inflation of lungs with air significantly changes the intrathoracic electrical conductivity, thus making EIT suitable for continuous bedside respiratory monitoring. EIT has been successfully used to image regional changes in pulmonary ventilation and perfusion in real time.

The application of lung EIT becomes vital when monitoring the neonatal patient age group amid the hazardous radiation effects of CT scan or complications of required sedation and time requirements of MRI for this age range. Yet, neither of these techniques provides dynamic images, for example, when the carer is interested to evaluate the impact of a certain clinical intervention performed on the patient earlier. Studies in new-born infants and children have demonstrated quantitatively identifiable changes in regional lung aeration and ventilation following alterations to respiratory support and interventions such as a recruitment manoeuvre, surfactant administration or nursing procedures [2].

One of the main challenges in EIT is solving the inverse problem to reconstruct the conductivity image since many different conductivity distributions may lead to the same measured electrode potential differences turning it to an ill-posed problem. Within the past decades many attempts have been made to improve the quality of reconstructions by implementing various inverse problem conditioning and solutions [3]. However, there have been very few attempts to improve the inverse solution by adapting the model to the situation of the individual patient. It has already been shown that, improving the model not only impacts the reconstructed images but has a direct impact on clinical parameters [4].

The prior models used in EIT reconstructions are typically based on averaged contours retrieved from CT scans of various patients, hence fall short of recognizing the differences of each patient amid their generic structure and possible contributing disorders. The situation worsens when dealing with neonatal age group as they preferably do not undergo CT scanning. Consequently, there are less data available corresponding to this age group and as a solution often the older models are scaled down to smaller body sizes and applied.

The patient specific modelling is a multi-fold problem and its beneficial to address these aspects individually. The first is the understanding of the exterior boundary of thoracic cross-section at the nipple line level of the patient where the EIT belt comprising the electrodes is placed. The second issue is to have an estimation of the organs internal distribution, meaning cross-sectional contours of lung and heart at the EIT belt level. Lastly is the issue of adapting the concluded model to the patient position both as external deformations and internally where the organs within the thoracic cavity may considerably displace or deform due to gravity dependent forces.

The first two issues have already been studied in our earlier works where in [5] the exterior contour are detected by embedded accelerometers in the belt and [6] has proposed a method based on Bayesian probability approach on how a proper internal model could be selected and assigned to the model. However, despite few studies have investigated the displacement of internal organs which is especially in lateral posture during surgery and under anaesthesia [7], to the authors' knowledge no attempt has been made to address this in neonatal age range and the effects on lung EIT.

In this work, we have investigated the impact of possible displacement of heart, mediastinum and diaphragm on deforming lungs and the corresponding outcome on the extracted clinical parameter namely, silent spaces [8]. This parameter shows the percentage of each lung area that is not being ventilated during breathing, i.e. it has remained silent and is considered one of the main clinical parameters for deciding on the required clinical intervention.

The rest of the paper is organized as follows. Section 2 describes the proposed method for estimating the changes occurring during recumbency position change from supine to either lateral positions. The results in Section 3 indicate the effect of consideration of adapting the prior model to body position by comparing the calculated silent spaces as a quantitative scale. Discussion of the results and concluding remarks are detailed in Section 4 and 5 respectively.

2. Method

There are limited situations, where a patient undergoes CT scan several times in different recumbency positions during each scan. However, there are occasions when chest X-ray radiography images are taken in decubitus lateral in addition to the typical supine/standing positions. This technique allows to avoid the undesired superimpositions of organs in the projected image via exploiting the movement of heart and mediastinum for better visualization of what is masked.

There are four possible major factors to consider regarding anatomical organ distribution in the thoracic cavity during recumbency changes. The deformation of rib cage, the displacement of the heart and mediastinum towards the gravity-dependent side, deformation/compression of the dependent lung due to its own weight and applied pressures from heart and lastly the change in diaphragm shape amid the pressure from abdominal cavity.

As the heart is connected to the posterior side of the sternum head via membranes in the cranial direction with non-uniform weight distribution (due to general cone shaped form along with major veins and arteries connections), in addition to transitional movement might experience a torque and consequently rotations. The uneven abdominal cavity pressure and diaphragm shape changes can intensify the rotation of the heart specifically in the coronal plane.

Fig. 1 shows the chest X-rays of an 18 months old male patient who was admitted to hospital following an acute onset respiratory distress while playing in the yard with a foreign body (radiodense stone) in his left bronchus. [9].

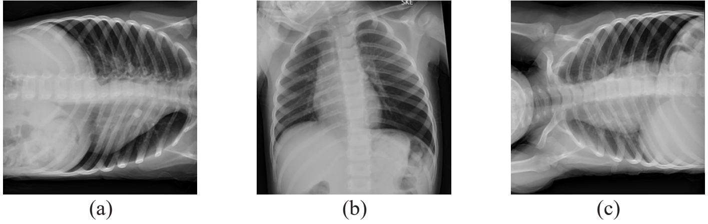

Figure 1. X-ray of the patient; (a) left lateral, (b) supine, (c) right lateral.

The studies of the thoracic outer deformation conducted previously, suggest an expansion in lateral directions with compression in ventral-dorsal direction during the supine and prone positions relative to the standing state. The opposite is true within lateral recumbency [10]. However, these studies were all based on adult cases, hence here a superimposition of laterals versus supine was performed to reveal if such deformation could be extended to this age range.

It should be noted that this evaluation would only provide an insight regarding lateral distance differences and ventral-dorsal could not be obtained from 2D projections. In order to compare the images in a consistent manner, the images should be normalised with respect to a unique scale and possible rotations relative to exposure source should be detected and compensated for.

2.1 Scaling

The X-rays images at the different positions should be normalised to the same scale. They should also be scaled to a realistic dimension corresponding to an individual of the same age as the X-rays do not carry any scale guide information. Therefore, the image in supine position was scaled to another CT scan of an 18 months and 7 days old patient in a manner that the corresponding width of the image matched the coronal 2D projection of the 3D CT-scan model. This image was then used for homogenizing the scale of the remaining lateral images using the 11th and 12th vertebras as a reference since they are invariant to rotation/deformation amid recumbency positions and position/angle of the head and neck.

A large rectangular pixel was created on the X-ray image such that it could cover the 11th and 12th vertebrae during supine position with its corners coinciding the centers of rib facets. The same rectangle was detected in lateral films and scaled to match the size and the position of the original pixel.

2.2 Adjusting exposure angle

It is not uncommon to have rotations in supine anterior-posterior (AP) chest radiography. This can be checked by comparing the lateral distance of each clavicle at the sternum side to the vertical line connecting the spinal process.

This rotation impacts the appearance of lung sizes and position of the heart on the film and hence should be adjusted. In frontal chest radiography the patient is considered to be correctly aligned when the clavicle heads at sternoclavicular joints on the film appear equally distant from the vertical line passing through spinous process of the vertebrae. Any spinous deviation from the mid-line towards clavicles indicates possible rotation of patient in the corresponding side from the aligned position.

These lines were detected for supine and in left and right lateral decubitus images where unlike the right lateral case the spinous process in the other two cases instead of middle was projected closer to the either clavicular head bones meaning the patient was rotated towards one side around the longitudinal axis.

To compensate for such rotations, the 3D model from CT scans used for scaling was applied again to recreate the situation that occurred during radiography process. The simulation revealed within the realistic model dimensions, a rotation of approximately 16.5 degrees could lead to such a situation in supine.

During right lateral because of cranial liver pressure, the diaphragm dome rises above the supine level and falls below this level in lateral left as liver starts shifting towards the center. The movement of diaphragm in the case study used here conforms with an earlier study where the diaphragm movement during various recumbency positioned was reported in adults [11].

Following the scale and rotations adjustments the realistic 3D model was adapted to mimic the internal movements revealed by the X-ray images creating three 3D models for supine, lateral left and right. These models were used to generate EIT signals from either of lateral positions and the silent spaces were calculated assuming the default supine prior model or the updated model according to patient real position.

3. Results

To simulate the EIT signals a 3D model of a patient at one of the lateral positions was used creating electric potentials on the 32 equally spaced electrodes around the patient's chest when the lungs were filled with air having electric conductivity of 0.3 S/m versus the homogeneous conductivity at 1 S/m. The signal was perturbed with a 10% noise repeated for 200 iterations.

The prior model used for reconstruction was a slice of the patient model at nipple line level with a thickness of 1 [cm]. All the applied models were meshed separately and the reconstructions were performed applying the GREIT [12] algorithm. The reconstruction parameters were kept constant among all the reconstructions.

The mean and standard deviation of silent spaces are reported in Table. 1. Only the values regarding the dependent lung (the lung closer to the mattress) at each position were recorded as the gravity prevented the non-dependent lung to be ventilated in the lateral positions during tidal breathing.

Table 1. Mean and standard deviations of the calculated silent spaces at dependent lung during lateral recumbency versus supine.

EIT Signal Generated at Patient Positioned	Silent Spaces Calculated Using Model	
	Default Forward Model Supine	Adjusted Forward Model to Recumbency
	Dependent Lung	Dependent Lung
Left Lateral	$\mu = 0.4115$ $\sigma = 0.0336$	$\mu = 0.3350$ $\sigma = 0.0175$
Right Lateral	$\mu = 0.4745$ $\sigma = 0.0271$	$\mu = 0.3288$ $\sigma = 0.0329$

4. Discussion

The evaluation of silent spaces is a twofold problem as it depends both directly and indirectly on the assumed prior model for reconstruction. The direct problem is where silent spaces are calculated as percentage of the total lung area making the size of the lung in prior model at the electrode plane crucial. The prior model used also affects the performance of reconstruction itself hence different images were reconstructed even before the silent spaces calculations.

Here, the GREIT algorithm was intentionally selected to reduce the indirect impact on the results as reconstruction method as this technique softens the effect of inaccurate forward model application through a training step in building the reconstruction matrix. In addition, due to availability of data, the references used to evaluate the movement of internal organs were based on a 2D X-rays which could have disguised certain rotations/displacements during projection on the film. Lastly, despite the low number of neonatal scans and rarity of radiographs of the same patient in different recumbency positions still more models should be studied for improved performance.

5. Conclusions

There is clear evidence that organ movements are present even in the early stages of life. The results show there is considerable potential to incorrectly calculate the lung's silent space parameter value by neglecting the effect of patient recumbency. This can be introduced either pre-stored or simulated as a calibration part before EIT recording.

Acknowledgments

This work was supported by the Engineering and Physical Sciences Research Council (EPSRC) under grant no. EP/T001259.

References

[1] B. Rigaud, J.-P. Morucci, and N. Chauveau, "Bioelectrical Impedance Techniques in Medicine Part I: Bioimpedance Measurement Second Section: Impedance Spectrometry," *Crit. Rev. Biomed. Eng.*, vol. 24, no. 4–6, pp. 257–351, 1996, doi: 10.1615/CritRevBiomedEng.v24.i4-6.20.

[2] I. Frerichs and T. Becher, "Chest electrical impedance tomography measures in neonatology and paediatrics - A survey on clinical usefulness," *Physiol. Meas.*, vol. 40, no. 5, Jun. 2019, doi: 10.1088/1361-6579/ab1946.

[3] N. Polydorides and W. R. B. Lionheart, "A Matlab toolkit for three-dimensional electrical impedance tomography: A contribution to the Electrical Impedance and Diffuse Optical Reconstruction Software project," *Meas. Sci. Technol.*, vol. 13, no. 12, pp. 1871–1883, Nov. 2002, doi: 10.1088/0957-0233/13/12/310.

[4] J.-F. P. J. Abascal *et al.*, "Use of anisotropic modelling in electrical impedance tomography; Description of method and preliminary assessment of utility in imaging brain function in the adult human head," *Neuroimage*, vol. 43, no. 2, pp. 258–268, 2008, doi: https://doi.org/10.1016/j.neuroimage.2008.07.023.

[5] S. de Gelidi *et al.*, "Torso shape detection to improve lung monitoring," *Physiol. Meas.*, vol. 39, no. 7, p. 74001, 2018, [Online]. Available: http://stacks.iop.org/0967-3334/39/i=7/a=074001.

[6] S. N *et al.*, "Model Selection Based Algorithm in Neonatal Chest EIT," *IEEE Trans. Biomed. Eng.*, vol. 68, no. 9, pp. 2752–2763, Sep. 2021, doi: 10.1109/TBME.2021.3053463.

[7] C. Klingstedt, G. Hedenstierna, H. Lundquist, A. Strandberg, L. Tgkics, and B. Brismar, "The influence of body position and differential ventilation on lung dimensions and atelectasis formation in anaesthetized man," *Acta Anaesthesiol. Scand.*, vol. 34, no. 4, pp. 315–322, May 1990, doi: 10.1111/J.1399-6576.1990.TB03094.X.

[8] I. Frerichs *et al.*, "Chest electrical impedance tomography examination, data analysis, terminology, clinical use and recommendations: consensus statement of the TRanslational EIT developmeNt stuDy group," *Thorax*, vol. 72, no. 1, pp. 83–93, Jan. 2017, doi: 10.1136/THORAXJNL-2016-208357.

[9] J. Jones, "Inhaled foreign body | Radiology Case | Radiopaedia.org," 2014. https://radiopaedia.org/cases/inhaled-foreign-body-2 (accessed Mar. 24, 2022).

[10] V. P. Vellody, M. Nassery, W. S. Druz, and J. T. Sharp, "Effects of body position change on thoracoabdominal motion," *https://doi.org/10.1152/jappl.1978.45.4.581*, vol. 45, no. 4, pp. 581–589, 1978, doi: 10.1152/JAPPL.1978.45.4.581.

[11] R. D. Adams and H. C. Pillsbury, "POSITION AND ACTIVITIES OF THE DIAPHRAGM AS AFFECTED BY CHANGES OF POSTURE," *Arch. Intern. Med.*, vol. 29, no. 2, pp. 245–252, Feb. 1922, doi: 10.1001/ARCHINTE.1922.00110020104005.

[12] A. Adler *et al.*, "{GREIT}: a unified approach to 2D linear {EIT} reconstruction of lung images," *Physiol. Meas.*, vol. 30, no. 6, pp. S35--S55, Jun. 2009, doi: 10.1088/0967-3334/30/6/s03.

Proceedings of the International Conference of Bioelectromagnetism, Electrical Bioimpedance,
and Electrical Impedance Tomography June 29 – July 1, 2022 / Kyung Hee University, Seoul, Korea

Electrical Impedance Tomography to Assess Pulmonary Function in Amyotrophic Lateral Sclerosis Patients

Allaire Doussan[1], Ethan Murphy[1], Courtney McIlduff[2], Chebet Yator[2], Sarah Verga[2],
Soleil Samaan[2], Hilda Gutierrez[2], Sophie Lloyd[1], Elijah Stommel[3], Christy Smith[2], Sean Levy[2],
Seward Rutkove[2], and Ryan Halter[1]
[1]Thayer School of Engineering, Dartmouth College, Hanover, NH, USA
[2]Department of Neurology, Beth Israel Deaconess Medical Center, Boston, MA, USA
[3]Department of Neurology, Dartmouth Hitchcock Medical Center, Lebanon, NH, USA

Correspondence: Allaire Doussan, e-mail: allaire.f.doussan.th@dartmouth.edu

Abstract–Respiratory function is a critical measure for monitoring the clinical status and planning interventions in amyotrophic lateral sclerosis patients as respiratory failure is the most common cause of death in this population. However, patients who develop orofacial weakness do not have a reliable method for monitoring lung function due to the inability to form a proper seal on existing spirometry devices. Use of a 32-electrode belt around the chest to capture electrical impedance data during pulmonary function tests shows promise as a relative measure of vital capacity in 16 amyotrophic lateral sclerosis patients and 9 healthy controls to date. There exists a moderate correlation between upright forced vital capacity percent of predicted normal and the proposed impedance metric captured from the electrical impedance data analysis ($r^2=0.51$, $p=0.00002$). Ongoing and future work focuses on characterizing the utility of electrical impedance data as a relative biomarker for pulmonary function tests in amyotrophic lateral sclerosis patients with and without bulbar dysfunction.

Keywords: Electrical impedance tomography; amyotrophic lateral sclerosis; orofacial weakness; bulbar dysfunction; pulmonary function.

1. Introduction

Amyotrophic Lateral Sclerosis (ALS) is the most common degenerative motor neuron disease in adults with an incidence of 2 to 3 people per 100,000 individuals (Hardiman *et al* 2017). Primary symptoms of ALS are progressive muscle weakness and spasticity. The onset of the disease tends to be quite heterogenous between patients with initial presentations separated into three main groups: bulbar-onset (facial muscle weakness, dysarthria, and dysphagia), spinal-onset (muscle weakness of the limbs), and respiratory-onset (weakness of the respiratory muscles). Regardless of the disease onset, respiratory failure accounts for 77% of deaths in the ALS population due to a lack of motor control of the inspiratory and expiratory muscles (Gil *et al* 2008). Failure of the inspiratory muscles leads to symptomatic respiratory fatigue, hypercapnia, and hypoxemia while failure of expiratory muscles lead to cough weakness and poor bronchial clearance, increasing the risk of respiratory infections (de Carvalho, Swash, and Pinto 2019). Therefore, one of the main clinical metrics for prognosis and planning interventions is pulmonary function testing (PFT) (Ackrivo *et al* 2019; Pirola *et al* 2019). However, patients with orofacial weakness have unreliable spirometry data due to the inability to form a seal around a mouthpiece to capture the complete airflow in and out of the lungs. While the use of a flanged mouthpiece with pressure on the lips to help form a complete seal was shown to improve the vital capacity for individuals with bulbar dysfunction, it is not a reliable solution (Pellegrino *et al* 2021). We propose to use electrical impedance data in the form of an impedance metric (Munir *et al* 2020) as a relative measure of the forced vital capacity (FVC) percent of predicted normal (PPN). The impedance data is captured by positioning a custom 32-electrode belt circumferentially around the patient's chest to record electrical impedance tomography (EIT) data during standard of care PFTs. Use of an impedance metric to quantify vital capacity has the potential to reliably monitor patients' respiratory function regardless of their bulbar involvement.

Methods

1.1 Data Collection

The circumference of the patient's chest was measured to determine the correct electrode belt size (small, medium, or large). A custom electrode belt was placed circumferentially around the patient's thorax just below the nipple (or below the pendulous breasts in women) to approximate the T5 level. The electrode belt consists of 32 equally spaced electrodes (OTC Patient's Choice® silver 0.8" round tan tricot electrodes) fixed to an elastic band with a clasp to secure the belt in place. Prior to placing the belt, the electrodes were prepared with a conductive gel (Spectra 360 electrode gel) to ensure good contact with the skin. EIT data was collected during 4 different PFTs: upright forced vital capacity (FVC), supine FVC, upright slow vital capacity (SVC), and supine SVC. PFTs were collected using an nSpire Classic Pulmonary Test Laboratory System (nSpire Health, Longmont, CO) or Pneumotrac 6800 (Vitalograph, Buckingham, UK). EIT data was collected during each of the PFTs using the SenTec EIT Pioneer System (SenTec AG, Landquart, Switzerland) with a 3 mA injection current at 195 kHz, 47.8 Hz frame rate, and 4-skip injection pattern. Two baseline EIT measurements of normal tidal breathing were recorded for 30 seconds, one at the beginning of the study and one at the end. Maximum inspiratory pressure (MIP) and maximum expiratory pressure (MEP) were also collected using a MicroRPM respiratory pressure meter (Micro Direct, Inc, Lewiston, ME). Additionally, a neurological examination was performed for the ALS patients on the day of the study to record ALS functional rating scale-revised score (ALSFRS-R) and presence of orofacial weakness (Cedarbaum *et al* 1999). Healthy controls were age and gender matched to the ALS population (±5 years). All procedures were approved by the Institutional Review Board of Dartmouth Hitchcock Medical Center and subjects provided written informed consent prior to participating. Data collection was performed at Dartmouth Hitchcock Medical Center and Beth Israel Deaconess Medical Center.

1.2 Preprocessing

Matlab 2021b (MathWorks, Natick, MA) was used to perform a manual preprocessing step to visualize the impedance data using a subset of the total IIVV patterns (cluster defined from simulation data centered at 3.5 Ω with 100 IIVV patterns). This cluster was chosen for the initial visualization because it gave the best correlation between the EIT data and PFT data in our previous study (Munir *et al* 2020). IIVV patterns containing electrodes with a contact impedance over 700 Ω were removed (default threshold from the Sentec EIT system). Additionally, any IIVV patterns with a standard deviation greater than 0.5 were removed. In the preprocessing step, each effort is displayed for the user to identify usable data. A usable interval of the 30 second baseline data was defined to include full breaths without any artifacts or significant trends (Figure 1a). Criteria for a usable vital capacity effort include a peak and valley corresponding to the max inhalation and exhalation, respectively (Figure 1b). The number and location of bad electrodes (if any) is also looked at for each effort and stored to find a common set of IIVV patterns to be used in the automatic processing across all efforts per patient per visit.

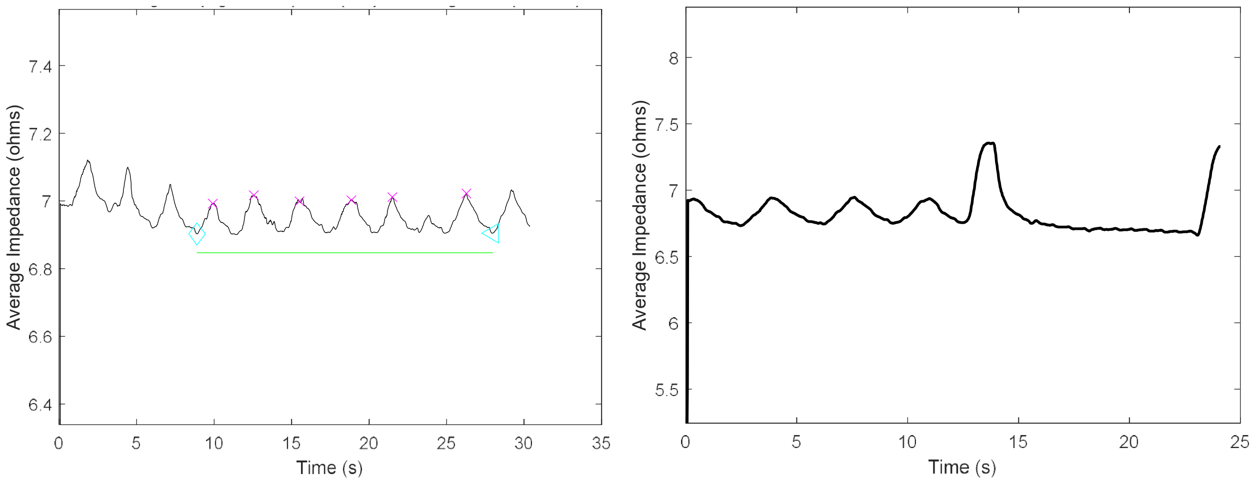

Figure 1. Average impedance data of an ALS patient for initial data visualization **(A)** 30 seconds of tidal breathing (baseline) with good interval manually defined (green line). **(B)** Upright FVC effort with 3 full tidal breaths prior.

1.3 Impedance Metric

The impedance metric as described in equation 1 looks at the difference in the global maximum and minimum over time of the average impedance across a set of IIVV patterns and is normalized by patient specific baseline measurements. This metric was developed as a relative measure of the impedance change between maximum inspiration and maximum expiration (Munir *et al* 2020). To evaluate the relationship between EIT and PFT, linear regressions between the maximum of the impedance metric for each test (3 efforts per test) and the PPN from the PFTs (based on the maximum of the 3 efforts) were performed.

$$\mathit{Impedance\ Metric} = \frac{Z_{max}-Z_{min}}{Z_{avg}} \times 100 \tag{1}$$

where Z_{max} = maximum average impedance over time during a PFT effort for selected IIVV patterns [Ω]
Z_{min} = minimum average impedance over time during a PFT effort for selected IIVV patterns [Ω]
Z_{avg} = average of the average impedance over time during normal tidal breathing for selected IIVV patterns [Ω]

The same clustering approach used in (Munir *et al* 2020) was adopted. In addition to using the complete set of 928 IIVV patterns, 51 clusters of IIVV patterns were identified using simulation data with centers ranging from 2 to 10 Ω in 0.5 Ω increments and cluster sizes of 50, 75, and 100 IIVV patterns. For each patient visit, a common set of IIVV patterns was determined. This set of IIVV patterns includes the selected cluster or set of IIVV patterns from simulations and removes any IIVV patterns that included an electrode with a contact impedance greater than 700 Ω or any IIVV patterns with a standard deviation greater than 0.5. The remaining IIVV patterns are used to identify the impedance metric.

2. Results and Conclusions

To date, 16 individuals (11 men, 5 women) with ALS and 9 healthy controls (5 males, 4 females) have been recruited. Of the 16 ALS patients, 6 have completed follow-up visits 3-4 months after the first visit. 3 of the 9 healthy controls have also completed a follow-up visit. The age range of ALS patients is 40-79 years (average 62) with an average total ALSFRS-R of 33. 50% of the ALS patients had bulbar dysfunction on their first visit and 60% had bulbar dysfunction on their second visit. Bulbar dysfunction was classified by an abnormal ALSFRS-R bulbar sub-score (≤ 11) or the presence of orofacial weakness as seen on the neurological exam. Moderate positive correlations between the maximum EIT metric among efforts and the upright FVC PPN have been identified in an initial analysis (r^2=0.51, p=0.00002) for the impedance cluster centered at 3 Ω with 50 IIVV patterns. This follows the trend reported in our previous study (Munir *et al* 2020), further suggesting that IIVV clusters centered in the range of 3 to 4 Ω are sensitive to changes in the lungs. Future work includes continuing the current study to reach our goal of 25 individuals per cohort, each with 2 visits along with an in-depth analysis on the use of impedance data as a relative measure of vital capacity in patients with and without bulbar dysfunction.

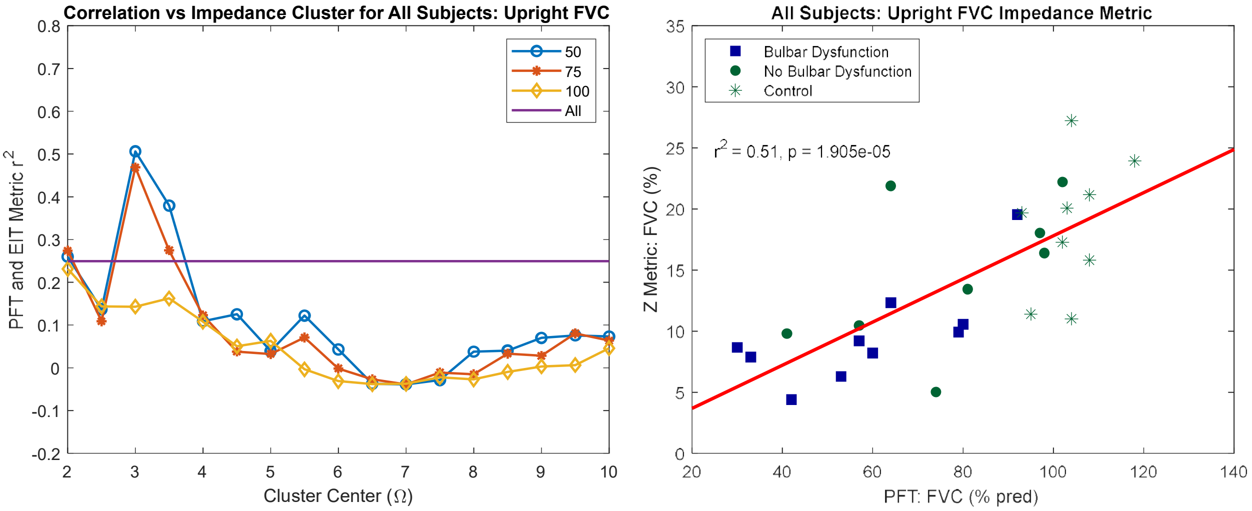

Figure 2. **(A)** Correlation between upright FVC PPN and the impedance metric for all subjects across 52 clusters of IIVV patterns **(B)** Linear regression for all ALS patients and controls with follow-ups when available for the IIVV cluster with the highest correlation (cluster centered at 3 Ω with 50 IIVV patterns).

Acknowledgments

The authors would like to gratefully acknowledge and thank the pulmonary function laboratory technicians and other clinical staff that made this work possible along with the organizing committee for the ICBEM-ICEBI-EIT 2022 conference. This work was supported by the National Institute of Health (1R21NS118434-01).

References

Ackrivo J, Hansen-Flaschen J, Jones B L, Wileyto E P, Schwab R J, Elman L, & Kawut S M 2019 Classifying Patients with Amyotrophic Lateral Sclerosis by Changes in FVC. A Group-based Trajectory Analysis. *American journal of respiratory and critical care medicine*, **200**(12), 1513–1521.

Cedarbaum J M, Stambler N, Malta E, Fuller C, Hilt D, Thurmond B, & Nakanishi A. 1999 The ALSFRS-R: a revised ALS functional rating scale that incorporates assessments of respiratory function. BDNF ALS Study Group (Phase III). *Journal of the neurological sciences*, **169**(1-2), 13–21.

de Carvalho M, Swash M, & Pinto S 2019 Diaphragmatic Neurophysiology and Respiratory Markers in ALS. *Frontiers in neurology*, ***10***, 143.

Gil J, Funalot B, Verschueren A, Danel-Brunaud V, Camu W, Vandenberghe N, Desnuelle C, Guy N, Camdessanche J P, Cintas P, Carluer L, Pittion S, Nicolas G, Corcia P, Fleury M C, Maugras C, Besson G, Le Masson G, & Couratier P 2008 Causes of death amongst French patients with amyotrophic lateral sclerosis: a prospective study. *European journal of neurology*, **15**(11), 1245–1251.

Hardiman O, Al-Chalabi A, Chio A, Corr E M, Logroscino G, Robberecht W, Shaw P J, Simmons Z, & van den Berg, L H 2017 Amyotrophic lateral sclerosis. *Nature reviews. Disease primers*, **3**, 17071.

Munir B, Murphy E K, Mallick A, Gutierrez H, Zhang F, Verga S, Smith C, Levy S, McIlduff C, Sarbesh P, Halter R J, & Rutkove S B 2020 A robust and novel electrical impedance metric of pulmonary function in ALS patients. *Physiological measurement*, **41**(4), 044005.

Pellegrino G M, Sferrazza Papa G F, Centanni S, Corbo M, Kvarnberg D, Tobin M J, & Laghi F 2021 Measuring vital capacity in amyotrophic lateral sclerosis: Effects of interfaces and reproducibility. *Respiratory medicine*, **176**, 106277.

Pirola A, De Mattia E, Lizio A, Sannicolò G, Carraro E, Rao F, Sansone V, & Lunetta C 2019 The prognostic value of spirometric tests in Amyotrophic Lateral Sclerosis patients. *Clinical neurology and neurosurgery*, **184**, 105456.

DAY 3

Friday, July 1, 2022

Invited Talk 07

Speaker Huaiwu He (Peking Union Medical College Hospital)

“Patterns of regional ventilation, perfusion and V/Q match images by EIT in acute respiratory failure”

Proceedings of the International Conference of Bioelectromagnetism, Electrical Bioimpedance,
and Electrical Impedance Tomography June 29 – July 1, 2022 / Kyung Hee University, Seoul, Korea

Patterns of regional ventilation, perfusion and V/Q match images by EIT in acute respiratory failure

Huaiwu He
Department of Critical Care Medicine, State Key Laboratory of Complex Severe and Rare Diseases, Peking Union Medical College Hospital, Peking Union Medical College, Chinese Academy of Medical Sciences, Beijing, China

Correspondence :Huaiwu He, e-mail : hehuaiwu@pumch.cn

Abstract–

Introduction Application EIT for regional lung ventilation, perfusion and V/Q match was relevant in the management of acute respiratory failure in ICU. **Purpose** This lecture seeks to provide a new patterns of regional ventilation, perfusion and V/Q match images by EIT in acute respiratory failure in ICU. **Main methods** Clinical researches and practice experiences of our hospital centre. **Findings** EIT provide lung ventilation, perfusion and V/Q information, which might be helpful for physicians to interpret the pathophysiology of ARF. Combined clinical issue with the patterns of regional ventilation, perfusion V/Q match imaging might be helpful for the three broad diagnosis of acute respiratory failure etiologies (pulmonary embolism related disease, diffuse lung involvement disease, focal lung involvement disease) and trigger further examination and treatment. **Conclusion** EIT could make a rapid differential diagnosis of related broad ventilation-issue or broad perfusion-issue for ARF at the bedside, but it could not determine a precise ARF etiology. Combined ultrasound with EIT is relevant in the difficult condition. ICU doctors should be confident with the indications and limitations of EIT lung imaging technique to improve patient care for acute respiratory failure. Further study is required to validate the impact of the EIT on decision-making, therapeutic management, and outcomes of the acute respiratory failure patients in ICU.

.

Acknowledgments

N/A

References (3 to 5 recommended)

1. He H, Chi Y, Yang Y, Yuan S, Long Y, Zhao P, Frerichs I, Fu F, Möller K, Zhao Z: **Early individualized positive end-expiratory pressure guided by electrical impedance tomography in acute respiratory distress syndrome: a randomized controlled clinical trial**. *Critical care* 2021, **25**(1).
2. He H, Chi Y, Long Y, Yuan S, Zhang R, Yang Y, Frerichs I, Möller K, Fu F, Zhao Z: **Three broad classifications of acute respiratory failure etiologies based on regional ventilation and perfusion by electrical impedance tomography: a hypothesis-generating study**. *Annals of intensive care* 2021, **11**(1).

Poster Presentation

P-01 **Using temporal electrical impedance spectroscopy measures to differentiate lung pathologies with the 3-electrode method**
Georgina Company-Se (Universitat Politècnica de Catalunya)

P-02 **Screening of Cervical Intraepithelial Neoplasia based on Electrical Bioimpedance Spectroscopy : Issues and Challenges**
Jun Beom Heo (Kyung Hee University Medical Center)

P-03 **Bioimpedance technologies use in dialysis patients: scoping review of clinical trials**
Lázaro Ibrain Cobiellas Carballo (Hospital General Universitario de Holguín)

P-04 **Normal Range of phase angle from bioelectrical impedance analysis for young adult and older adult in a Colombian population**
Maria Camila Pineda Zuluaga (Universidad de Caldas)

P-05 **A novel current source for multi-frequency Magnetic Resonance Electrical Impedance Tomography**
Zachary Colwell (Arizona State University)

P-06 **Feature-Based Model Compression Scheme for Electrical Impedance Tomography**
Zhichao Lin (Tsinghua University)

P-07 **EIDORS version 3.11**
Andy Adler (Carleton University)

P-08 **Projection-based Iterative Methods for Electrical Impedance Tomography**
Malena I. Espanol (Arizona State University)

Poster Presentation

P-09 **Algorithm for Detecting Motion Noise in Electrical Impedance Images during Hemodialysis**
Thi Hang Dang (Kyung Hee University Hospital)

P-10 **Identification of Collapse Pattern and Site of Upper Airway during Obstructive Apnea and Hypopnea using Double-layer Electrical Impedance Tomography and Polysomnography**
Tingting Zhang (Kyung Hee University Hospital)

P-11 **Wide-bandwidth FPGA-based EIT System with Multitone Implementation for Enhancing Medical Imaging in Space**
Kendall Farnham (Dartmouth College)

P-12 **Emerging Trends and Hot Spots of Electrical Impedance Tomography in Extrapulmonary Applications**
YuQing Xu (Shanghai Jiao Tong University)

P-13 **Emerging Trends and Hot Spots of Electrical Impedance Tomography in hardware**
YiRan Li (Fourth Military Medical University)

P-14 **A bibliometric analysis of the research on imaging algorithm of electrical impedance tomography**
ShaoJie Qin (Shanghai Jiao Tong University)

P-15 **Regulate the human artificial skin elasticity by weak electric field stimulation**
Se Jik Han (Kyung Hee University)

Proceedings of the International Conference of Bioelectromagnetism, Electrical Bioimpedance,
and Electrical Impedance Tomography June 29 – July 1, 2022 / Kyung Hee University, Seoul, Korea

Using temporal electrical impedance spectroscopy measures to differentiate lung pathologies with the 3-electrode method

Georgina Company-Se[1], Lexa Nescolarde[1], Javier Rosell[1], Pere J. Riu[1], Virginia Pajares[2],
Alfons Torrego[2] and Ramon Bragós[1]
[1]Department of electronic engineering, Universitat Politècnica de Catalunya, Barcelona, Spain
[2]Department of Respiratory Medicine, Hospital de la Santa Creu i Sant Pau, Barcelona, Spain

Correspondence: Georgina Company-Se, e-mail: georgina.company@upc.edu

This work was supported in part by the Spanish Ministry of Science and Innovation under Grant RTI2018-098116-B-C21/C22, and in part by the Secretariat of Universities and Research of the Generalitat de Catalunya and the European Social Fund.

Abstract– Minimally invasive lung bioimpedance measurements could serve in the future diagnosis of lung pathologies complementing biopsies and imaging techniques. Through the electrical impedance spectroscopy (EIS) technique using the 3-electrode method, distinction of lung pathologies could be possible depending on the state of the tissue. Since now, only averaged information has been used for the analysis of bioimpedance data in lungs. The aim of this study is to use temporal information to evaluate changes in the impedance signal due to the mechanism of ventilation and perfusion produced by the lungs. Preliminary results show: 1) correlation between ventilation and perfusion with the bioimpedance signal and 2) changes in the amplitude of the bioimpedance time signal depending on the pathology. As conclusion, together with cycled averaged data, temporal data could be useful for lung pathologies distinction.

Keywords: lung; electrical impedance spectroscopy (EIS); modulation; bronchoscopy.

1. Introduction

Lung pathologies present different histological results. Some pathologies lead to an increase of cell concentration and extracellular matrix in lung tissue while others lead to the destruction of the lung parenchyma. Moreover, other lung pathologies lead to the increase of mucous that hinders the passage of air in the respiratory tract. Electrical impedance spectroscopy (EIS) offers an opportunity to differentiate lung disorders based on the different patterns associated with each of them. Moreover, changes in the blood perfusion and changes in the ventilatory movement of the tissue (two phenomena present during the acquisition of lung bioimpedance measures) may help to differentiate these lung pathologies.

In previous studies, Sanchez *et al.* observed the effect of the ventilation and the perfusion of the blood present in the alveoli in the EIS measurements taken using the 4-electrode method [2]. However, the 4-electrode method, as discussed in Company-Se *et al.* [1] when measuring lung tissue is more difficult for the clinicians than the measurement of bioimpedance data with the 3-electrode method due to the difficulty of ensuring the contact of the 4 electrodes with the tissue target. Also, the capacity of tissue differentiation is the same on both methods. For this reason, EIS lung measurements using the 3-electrode method are being taken in the current project during a bronchoscopy process.

The aim of this study is to demonstrate the effect of the ventilation and the perfusion mechanisms in the bioimpedance signal in preliminary measurements.

2. Materials and methods

Participants

Minimally invasive EIS lung measurements are being taken in patients for whom a bronchoscopy is indicated at the "Hospital de la Santa Creu i Sant Pau" using the 3-electode method in bronchi, healthy lung tissue and in pathological tissue if applied (neoplasm, emphysema, pneumonia and fibrosis). Ethics approval has been obtained from the Ethics Committee of Hospital de la Santa Creu i Sant Pau (CEIC-73/2010) according to principles of the declaration of Helsinki. All patients participating in the study have provided signed informed consent.

Measurement system

To acquire the bioimpedance measures, a tetrapolar catheter, 115 cm long with a diameter of 1.65 mm (5 F) is being used (Medtronic 5F RF Marinr steerable catheter with electrode separation 2/5/2 mm). Also, two skin electrodes (Ambu BlueSensor VLC ref: VLC-00-s/10 and 3M Company ref: 9160F) placed on the right side of the patients at the level of the ribs are being used.

The measurement system consists of an optically insulated battery powered patient interface (including the impedance front end), a rugged PC platform based on a National Instruments PXI system and an analog-optical interface to connect the PXI with the insulated front end. An arbitrary waveform generator generates a multisine excitation signal which is a broadband signal composed of 26 frequencies between 1 kHz and 1 MHz.

To acquire the bioimpedance measurements, only the electrode located at the tip of the catheter is used to inject the current and to detect the potential while the low current and the low potential electrodes correspond to the two skin electrodes. A more detailed explanation of the measurement system is included in Company-Se *et al.* [1].

To acquire the ventilation and the ECG signals the polygraphy monitoring device Embletta MPR from Natus, with a thoracic inductive band, is used.

Measurement protocol

Records of 12 seconds of bioimpedance measurements (60 spectra/s) are obtained by inserting the catheter through the bronchoscope working channel. Patients are placed in a supine position during the process. Topical 2% lidocaine is used to anaesthetise the upper airway as well as intravenous sedation is provided through the procedure. Prior to bronchoscopy, computed tomography (CT) of the thorax was performed as part of the diagnostic process of respiratory diseases and to guide the bronchoscopy procedures.

Data extraction

To compare the effect of the ventilation and the perfusion on the bioimpedance signal a 30-points double-pass moving-average filter is applied to the signal to extract the ventilatory modulation. The difference between the original signal and the signal filtered is supposed to be the modulation corresponding to the perfusion.

3. Results

Efect of the ventilatory and perfusion modulations in the bioimpedance signal

Figure 1 shows the 12 seconds acquisition of the bioimpedance magnitude signal at 33 kHz, in blue, as well as the breathing, in black, and electrocardiographic (ECG), in red, signals.

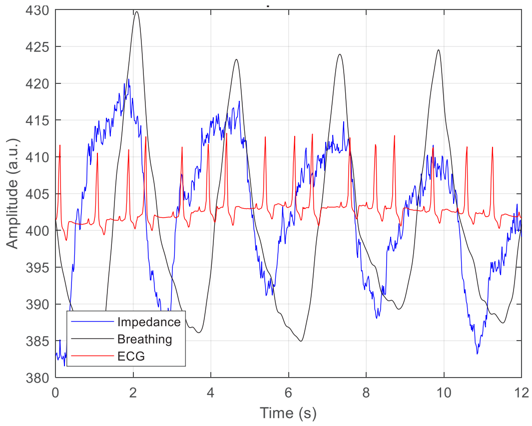

Figure 1. Superposition of the 12 seconds impedance signal at 33 kHz with the ventilation and ECG signals in a healthy lung tissue location

Figure 2 shows the power spectral density of the impedance signal (blue) after applying the 30-points double-pass moving-average filter and the ventilation signal (orange).

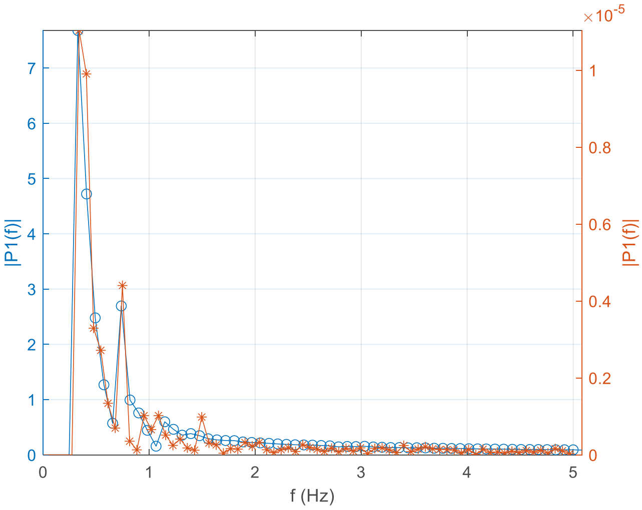

Figure 2. Power spectral density of the bioimpedance signal after applying a 30-points double-pass moving-average filter (blue, peak at 0.33 Hz) and power spectral density of the ventilation signal (orange, peak at 0.33 Hz).

Figure 3 shows the power spectral density of the signal after making the difference between the original signal and the signal resulting of the application of the 30-points double-pass moving-average filter (blue), considered to be the perfusion signal, and the power spectral density of the ECG signal (orange).

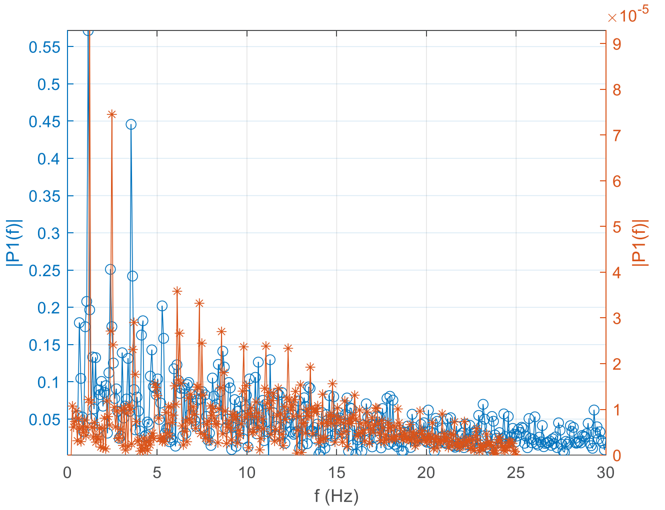

Figure 3. Power spectral density of the perfusion signal (blue, peak at 1.2 Hz) and ECG signal (orange, peak at 1.2 Hz).

Changes in amplitude of the bioimpedance signal based on different states of the tissue

Figure 4 shows amplitude changes due to ventilation depending on the state of the tissue measured at 33 kHz from 3 different cases (healthy tissue, pneumonia and neoplasic tissue). Healthy tissue shows a higher breathing modulation than neoplasic lung tissue which, in turn, shows higher breathing modulation than the area of lung with pneumonia. Also, different ventilatory frequencies and shapes are visible.

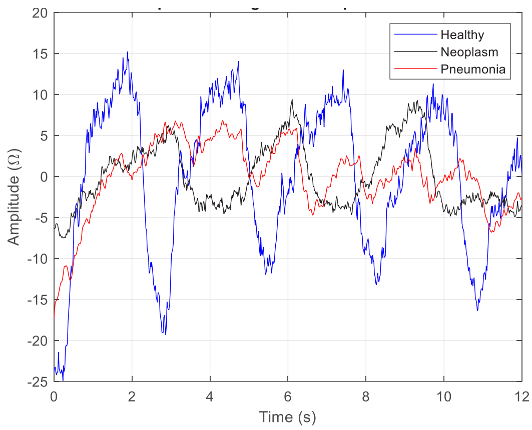

Figure 4. Amplitude changes in bioimpedance signals at 33 kHz from different patients and different tissue states.

4. Discussion

Electrical impedance spectroscopy can represent an opportunity to differentiate lung pathologies in order to complement the actual diagnostic processes. Together with averaged impedance results, temporal information could be useful to improve the tissue differentiation through changes in amplitude and shape of the signals acquired due to the effect of the ventilation and the perfusion.

The effect of the modulation is easily observable while the effect of the perfusion is not (Figure 1). The comparison between the spectrum of the signal considered to be the breathing modulation and the spectrum of the breathing signal (Figure 2) show a high frequency component at the same frequency (between 0.3 and 0.4 Hz) validating the existing modulation due to the inhalation and exhalation of the patients during the acquisition of the measure.

The effect of the perfusion is not so easily observable. This effect is demonstrated in the power spectrum of the two signals, the one representing the perfusion extracted from the bioimpedance signal and the ECG. In both cases there is a high frequency component in the 1.2 Hz corresponding to the cardiac rhythm.

The presence or absence of these two modulations could be used in the future to distinguish between different tissue states. An absence of breathing modulation could represent that the tissue measured is rigid while a high modulation of perfusion could represent the presence of neoplasic tissue, due to the nature of this pathology. These changes have also been demonstrated on Figure 4 in which the amplitude of the neoplasic tissue due to breathing is lower than the amplitude for healthy tissue. This phenomenon is due to the higher concentration of cells in the neoplasic tissue and, in consequence, the lower concentration of air. We have also seen that the amplitude of the signal related to breathing in lung with pneumonia is lower than the amplitude of the neoplasic tissue signal. This phenomenon could be due to the excessive concentration of mucous, which hinders the air flowing through the ventilatory ways.

5. Conclusions

Ventilatory and perfusion modulations are present in the bioimpedance signal and could be a tool to distinguish between different lung pathologies.

Acknowledgments

The authors would like to specially thank the patients without whom this study would not have been possible. In addition, the authors would like to thank Marta Navarro Colom, Laura Romero Roca and Margarita Castro Jiménez from the Interventional Pulmonology Unit, Respiratory Medicine Department, Hospital de la Santa Creu i Sant Pau for the invaluable support.

References

[1] Company-Se G, Nescolarde L, Pajares V, Torrego A, Riu P J, Rosell J and Bragós R 2022 Minimally Invasive Lung Tissue Differentiation Using Electrical Impedance Spectroscopy: A Comparison of the 3- and 4-Electrode Methods *IEEE Access* **10** 7354–67

[2] Sanchez B, Vandersteen G, Martin I, Castillo D, Torrego A, Riu P J, Schoukens J and Bragos R 2013 In vivo electrical bioimpedance characterization of human lung tissue during the bronchoscopy procedure. A feasibility study *Med. Eng. Phys.* **35** 949–57

ICBEM Bioelectromagnetism ICEBI Electrical Bioimpedance EIT Electrical Impedance Tomography

Proceedings of the International Conference of Bioelectromagnetism, Electrical Bioimpedance,
and Electrical Impedance Tomography June 29 – July 1, 2022 / Kyung Hee University, Seoul, Korea

Screening of Cervical Intraepithelial Neoplasia based on Electrical Bioimpedance Spectroscopy : Issues and Challenges

Jun Beom Heo[1,2,3], Tingting Zhang[1,2], Tong in Oh[1,2], and Dongchoon Park[4]
[1]Medical Science Research Institute, Kyung Hee University Medical Center, Seoul 02447, Korea
[2]Department of Biomedical Engineering, School of Medicine, Kyung Hee University, Seoul 02447, Korea
[3]Department of Medical Engineering, Graduate School, Kyung Hee University, Seoul, Korea
[4]Department of Obstetrics and Gynecology, Saint Vincent's Hospital, The Catholic University of Korea, Suwon 16247, Korea

Correspondence : Dongchoon Park, e-mail : dcpark@catholic.ac.kr

Abstract–Cervical intraepithelial neoplasia (CIN) is the precancerous stage of cervical cancer. Accurate and straightforward CIN screening and subsequent treatment and management of early detected CIN highly reduce the occurrence of cervical cancer, which is the 4th most common cancer among women. Bioimpedance spectroscopy (BIS) has been proposed as a CIN screening method since it is varied in the electrical characteristics depending on the progression of CIN. Before applying the BIS system, including a multi-electrode probe to in-vivo tissue, we wanted to evaluate it on the in-vitro cervical tissues obtained from loop electrosurgical excision procedure (LEEP). Unfortunately, the measurement accuracy of in-vitro cervical tissues is highly determined by the size, the presence or absence of mucus, and the condition of the surface of tissue samples. This study presents a brief investigation into the technical issues during the impedance measurements for tissue samples. A few methods, including model fitting, gain adjustment, and saline calibration, have been introduced to check measurement quality using our newly proposed multi-electrode probe.

Keywords: Cervical intraepithelial neoplasia; Bioimpedance spectroscopy; Multi-electrode probe; Model fitting

1. Introduction

CIN is the precancerous stage of cervical cancer, and screening and subsequent treatment of CIN highly reduce the occurrence of cervical cancer, which is the 4th most common cancer among women [Cohen2019]. Depending on the severity of the pathological condition of the cervix, CIN can be classified as a low-grade lesion of CIN 1 and high-grade lesions like CIN 2 and CIN 3. Conventionally, Pap (Papanicolaou) test is a screening method for cervical cancer. In addition, patients with cervical dysplasia will undergo a loop electrosurgical excision procedure (LEEP), which removes the abnormal tissues and prevents cervical cancer. BIS could be a candidate to screen the CIN since the cervix's electrical properties are also changed when the cervix's pathological status devolvement [Cohen2019]. In this study, we want to apply our proposed multi-electrode probe to in-vitro tissue samples excised from the cervix to evaluate the performance [Zhang2021, Oh2021]. Several technical issues exist when acquiring impedance spectroscopic complex numbers of data that influence measurements' accuracy. Before conducting impedance measurements of cervical tissue with the proposed BIS system, it is necessary to check the performance of the system, including the replaceable multi-electrode probe, and calibrate the measured impedance spectrum because it is adopted the sensitivity analysis used in electrical impedance tomography. Although unlikely to happen in in-vivo tissue measurements, bleeding that occurs during tissue excision from the cervix affects the measured data value. For this reason, the appropriate preprocessing steps of the tissue sample are very important. In the proposed method of deriving the impedance spectrum under the probe by using the impedance measurements between several pairs of electrodes, the distances between the electrodes are significantly different. To improve the accuracy of the measurement, we properly set the gain depending on the amplitude of measured voltages. Since the measured complex data may contain noise, and the quality of measurement of the imaginary component may be lower than that of the real component, it is also necessary to check whether the measured complex data is fitted to the Cole-Cole model well [Brown2000, Cole1941].

2. Methods

2.1 Subjects

The 100 women, 50 with suspected CIN who underwent LEEP and 50 without CIN expectation who underwent hysterectomy for benign disease, participated in this study's age from 20s to 60s.

2.2 Multi-electrode probe

A replaceable multi-electrode probe was developed for future in-vivo clinical trials. It has a long shaft to pass through the vergina to reach the cervix. It includes signal connections and a front-end circuit to enable current injection and voltage measurement between any pair of 16 electrodes established on the front of the probe, as shown in Fig. 1. In this study, we used it with the previously developed BIS system to measure the electrical properties of excised tissue.

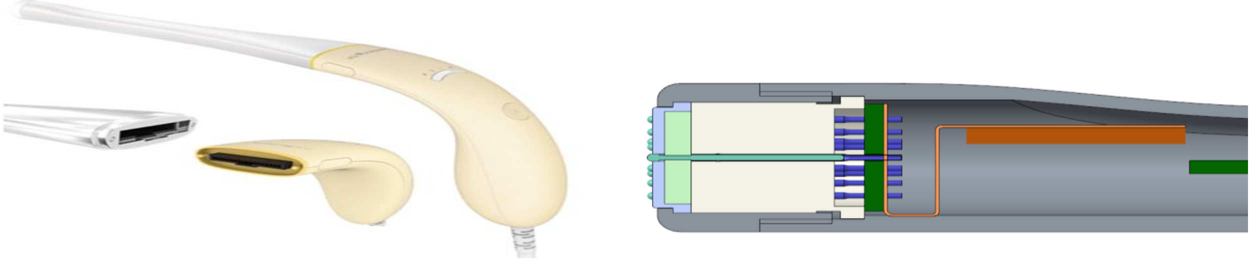

(a) (b)

Figure 1. (a) Schematic of multi-electrode probe (b) 16 electrodes established in the front face of the probe.

2.3 Calibration

Before measuring the impedance spectrum of tissue, we calibrated the measurements with saline of 0.34 S/m at all operating frequencies. Simultaneously, we checked the system quality using the same sample. We considered the system was ready to measure when all normalized 28 measured data were matched with the simulated data with over 70%.

2.4 Sample preparation and gain settings

The surface of an excised sample could bleed due to the preparing tissue. We removed the blood with a cotton ball soaked in saline. It was spread flat and wide so that the tissue could be in good contact with the front face of the probe. To use the system's maximum performance for each measurement of tissue, we adjusted the gain without occurring voltage saturation appropriately in the operating settings of Low (x5), Middle (x20), and High (x40).

2.5 Modeling with complex measurements

After measuring the complex number of data for each cervical tissue after surgery, the quality of the measured data was reconfirmed through the fitting of the Cole-Cole biological model using reconstructed complex resistivity data. In particular, if the gain setting was not optimized, or if there was a problem with the preparation of samples due to bleeding, etc., the Cole-Cole model could not be fitted well due to the reliability issue of the measured real or imaginary data. So we programmed Matlab software to reconfirm this more quickly.

3. Results

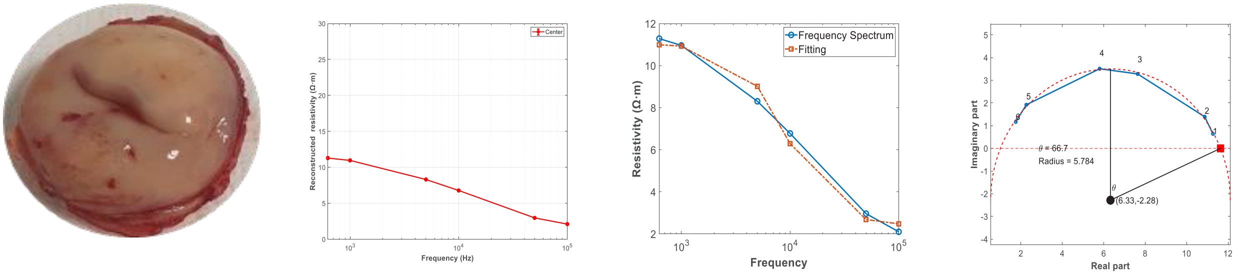

(a) (b) (c) (d)

Figure 2. (a) An excised cervical tissue sample, (b) reconstructed resistivity spectrum of the normal sample, (c) model with the magnitude of resistivity spectrum, and (d) model with complex impedance spectrum.

In order to screen CIN from the excised cervical tissue sample, we calibrated it with saline. We verified the performance of the system including the multi-electrode probe was performed in advance. After removing blood and mucus from the sample, we adjusted the system gain to Middle(x20) to measure the complex impedance spectrum. In Figure 2, we presented the reconstructed resistivity spectrum and fitted the magnitude of the resistivity spectrum to the simple model, and the complex impedance spectrum to the Cole-Cole model. Through this process, it was possible to acquire data stably from the extracted samples and accumulate data for developing an algorithm to classify the stages of CIN.

4. Discussion

Since there is a slight discrepancy between the frequency spectrum of the CIN group and the Non-CIN group, it requires an accurate and robust measurement technique. Additionally, other technical issues were generated because we verified our method on the excised tissues. For example, when the size of the excised cervical tissue was very small, there was a tissue with a scar, or there was mucus and blood from surgery, the bias in measuring the complex impedance occurs, leading to a measurement error. In this work, several technical methods have been proposed to improve the measurement performance of cervical tissues, including the validation through saline calibration and normalization, maximal gain setting depending on the tissue characteristics, and fitting of the mathematical model. Therefore, more insights into the spectral difference of bias according to the shape and surface condition of mucus, blood, and tissue should be pursued in-vivo experiments on cervical tissues.

5. Conclusions

Practical methods were proposed to improve the performance of the BIS system, including a multi-electrode probe and measuring the electrical properties of excised cervical tissue stably. We collected 100 samples following these methods. It may be utilized to develop an algorithm for classifying CIN using such complex impedance data.

Acknowledgments

This research was supported by Basic Science Research Program through the National Research Foundation of Korea (NRF) funded by the Ministry of Education(NRF-2020R1I1A1A01066649), and the National Research Foundation of Korea (NRF) grant funded by the Korea government (NRF-2020R1A2C1008975 and NRF 2019R1A2C1086807).

References

Cohen PA, Jhingran A, Oaknin A, and Denny L 2019 Cervical cancer *The Lancet* **393** 169-182

Zhang T, Jeong Y, Park D, and Oh T 2021 Performance Evaluation of Multiple Electrodes Based Electrical Impedance Spectroscopic Probe for Screening of Cervical Intraepithelial Neoplasia *Electronics* **10** 1933

Oh TI, Kang MJ, Jeong YJ, Zhang T, Yeo SG and Park DC 2021 Tissue Characterization Using an Electrical Bioimpedance Spectroscopy-Based Multi-Electrode Probe to Screen for Cervical Intraepithelial Neoplasia. *Diagnostics* **11** 2354

Brown BH, Tidy JA, Boston K, Blackett AD, Smallwood RH, and Sharp F 2000 Relation between tissue structure and imposed electrical current flow in cervical neoplasia *The Lancet* **355** 892-895

Cole KS and Cole RH 1941 Dispersion and absorption in dielectrics I. Alternating current characteristics *The Journal of chemical physics* **9** 341-351

ICBEM Bioelectromagnetism ICEBI Electrical Bioimpedance EIT Electrical Impedance Tomography

Proceedings of the International Conference of Bioelectromagnetism, Electrical Bioimpedance,
and Electrical Impedance Tomography June 29 – July 1, 2022 / Kyung Hee University, Seoul, Korea

Bioimpedance technologies use in dialysis patients : scoping review of clinical trials

Lázaro Ibrain Cobiellas Carballo[1,2], Miguel Enrique Sánchez Hechavarría[2,3], Gustavo Alejandro Muñoz Bustos[2,4], Mario Muñoz Bustos[2,5], Alcibiades Lara Lafargue[2], Pedro Bertemes Filho[6]
[1]Departamento de Nefrología. Hospital General Universitario de Holguín, Cuba
[2]División de Tecnología. Biohidrical Spa. Tomé, Chile
[3]Facultad de Medicina. Universidad Católica de la Santísima Concepción. Chile
[4]Escuela de Kinesiología. Universidad de las Américas, Metropolitana, Chile
[5]Departamento of Kinesiología. Universidad de Concepción, Chile.
[6]Department of Electrical Engineering. State University of Santa Catarina, Joinville, Brazil.

Correspondence : Lázaro Ibrain Cobiellas Carballo, e-mail : lcobiellasc@gmail.com

Abstract− Bioimpedance is largely used in dialysis patients instead, being a simple, precise, noninvasive and inexpensive method to assess fluid status and body composition. This scoping review aims to describe and synthesize scientific evidence on bioimpedance technologies use in dialysis patients. A literature search was done for peer-reviewed journal clinical trials using PubMed/Medline, Scopus and Web of Science databases. The initial search yielded 145 clinical trials; there were 24 duplicated and 90 title-abstract excluded articles. 31 studies were full-text assessed for eligibility for inclusion in the scoping review. There were 23 full-text articles excluded; finally, eight articles were included in the review. The mainly uses for bioimpedance technologies in dialysis patients founded were in fluid volume, dry weight assessment, post-dialysis target weight, and fluid overload management in peritoneal dialysis or hemodialysis patients. Most of the reported primary outcomes in the selected clinical trials were focused on all-cause mortality and hospitalization rate. All the included studies described a significant reduction in the overhydration status in the BIA group. Despite the fact that in many trials use of BIA was not superior to traditional clinical methods, its results have been shown to be similar and not inferior to expert clinical evaluation. Thus, bioimpedance technologies could be very useful when using it as a complement to traditional methods in peritoneal dialysis and hemodialysis patients. Moreover, BIA technologies could be even more useful in home dialysis settings or ambulatory dialysis centers, where expert clinical evaluation is not possible.

Keywords: bioimpedance; bioelectrical impedance analysis; dialysis; fluid overload; dry weight.

1. Introduction

Chronic kidney disease (CKD) is a long-term condition in which the kidneys do not function effectively (Scotland et al., 2018). It is estimated that there are approximately 9.7 million of patients with end-stage chronic kidney disease requiring kidney replacement therapy around the world, and to 2030, this number will rise to 14.5 million. (Bello et al., 2019)

Volume overload is the most common complication in dialysis patients, extremely associated with hypertension, left ventricular hypertrophy and cardiovascular mortality in the dialysis population. The assessment of fluid status in dialysis patients is of paramount importance. Due to the absence or reduction of renal function and the intermittency of the treatment, hemodialysis (HD) patients may experience wide variations between fluid overload and fluid depletion. (van der Sande et al., 2020) Overhydration (OH) is relatively common among patients receiving dialysis, with an incidence of 56.5% to 73.1%. (Y. Wang & Gu, 2021) Therefore, it is essential to objectively measure patients' hydration status to obtain a more clearly defined assessment of prognosis in patients on dialysis. Common clinical approaches, such as measuring weight changes and the isotope dilution method, have certain limitations, which have led to the development of bioimpedance analysis (BIA).

However, determining dry weight is a challenge for nephrologists because of the above-mentioned problems. Methods for determining dry weight have been suggested, including by reference to biochemical parameters, such as atrial or brain natriuretic peptide levels, inferior vena cava diameter on ultrasonography, and blood volume monitoring. However, dry weight estimates obtained using these methods are not accurate (Park et al., 2018).

Bioelectrical impedance analysis is a noninvasive portable tool that effectively assesses body composition and offers insights into nutritional and fluid status. BIA determines the electrical impedance, or the opposition to an electrical current flow, through body tissues and measures resistance, which is inversely proportional to total body water, and reactance, which is proportional to intracellular mass. (K. Wang et al., 2021). Moreover, multiple-frequency bioimpedance device measurement may be cost-effective way of improving fluid management in patients with CKD on dialysis. (Jacobsen et al., 2021)

Thus far, to the best of our knowledge, no scoping reviews have been conducted to describe the use of bioimpedance technologies use in dialysis patients. Therefore, there is a need to describe and synthesize scientific evidence on bioimpedance technologies use in dialysis patients, which is the purpose of this scoping review.

2. Methods

This scoping review aims to describe and synthesize scientific evidence on bioimpedance technologies use in dialysis patients.

2.1 Database and search strategy

The scoping review was conducted according to the PRISMA-ScR checklist (Tricco et al., 2018). Literature search was done between November and December 2021 for peer-reviewed journal articles published mainly in English using PubMed/Medline, Scopus and Web of Science databases. Fist an all; some journal articles were consulted to determine the best keywords, and its similar were located at the MeSH (https://www.ncbi.nlm.nih.gov/mesh/). The search strategy was designed from these keywords and some combinations ("bioimpedance", "dialysis", "hemodialysis", "clinical trials"). Additionally, a green literature search was conducted using articles' references and printed documents. No restrictions were made for the year of publication. All studies were manually reviewed to ensure applicability, and duplicated, uncompleted, and suspended studies were removed.

The initial search yielded 145 clinical trials; there were 24 duplicated and 90 title-abstract excluded articles. 31 studies were full-text assessed for eligibility for inclusion in the scoping review. There were 23 full-text articles excluded; finally, eight articles were included in the review. Figure 1 shows the flow chart of the studies' selection.

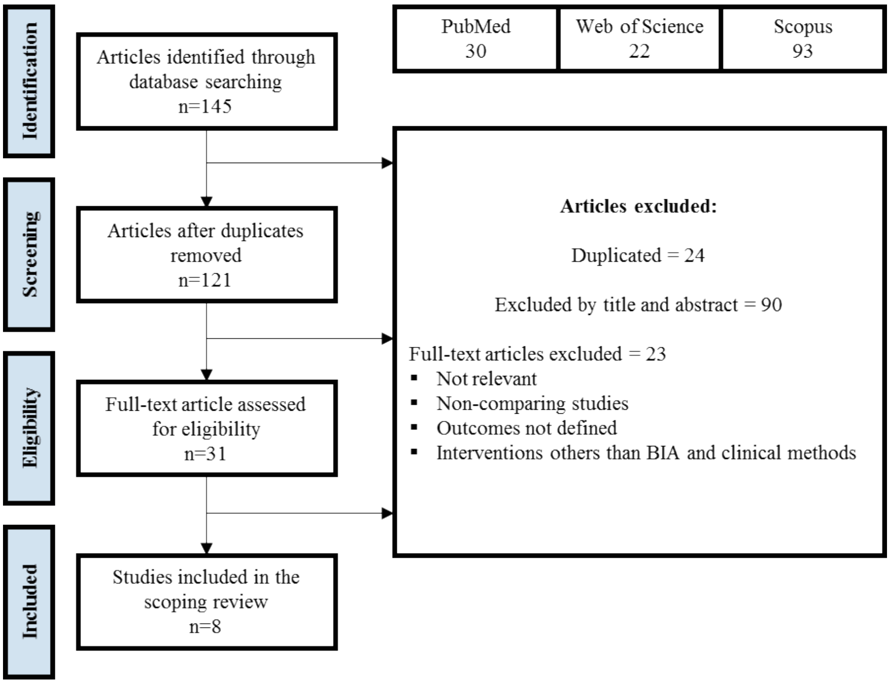

Figure 1: Flow chart of studies' selection. According to PRISMA model.

2.2 Inclusion and exclusion criteria

The inclusion criteria were: Peer-reviewed clinical trials on use of bioimpedance analysis in peritoneal dialysis and/or hemodialysis patients, to asses dry weight, inter-dialysis gain, overhydration, and fluid overload, compared with traditional methods. Accessible in English full text. Patients aged above 18 years, and currently in maintenance peritoneal dialysis or hemodialysis.

The exclusion criteria were: Any study other than clinical trial. Unpublished or uncompleted clinical trials. Clinical trials using methods other than traditional clinical assessment.

2.3 Study selection

Based on the initial titles retrieved, duplicates were removed. Abstracts identified from the literature searches were screened for potential inclusion by two authors and a third author when there was a disagreement between the first two.

2.4 Data extraction

Data were extracted by three reviewers using the prespecified data extraction forms. Extracted information included studies, objective, renal replacement modality (hemodialysis or peritoneal dialysis), sample size, participants' characteristics, countries, intervention, primary and secondary outcomes, results, and limitations. Data analysis was completed in Microsoft Excel.

3. Results

Eight clinical trials were fully reviewed and included in the current scoping review, conducted in six countries: China, Germany, Romania, South Korea, Taiwan, and Turkey; and published between 2013-2022 in high-impact journals (*American Journal of Kidney Disease*, *Clinical Journal of American Society of Nephrology*, *Hemodialysis International*, *International Urology and Nephrology*, *Nephrology*, *and Peritoneal Dialysis International*).

The included clinical trials summarizes information from 1 482 patients (967 hemodialysis and 515 peritoneal dialysis). The mainly uses for bioimpedance technologies in dialysis patients founded were in fluid volume, dry weight assessment, post-dialysis target weight, and fluid overload management in above mentioned patients. Table 1 summarizes the characteristics of clinical trials included in the scoping review.

3.1 Primary outcomes

Most of the reported primary outcomes in the clinical trials selected were focused on all-cause mortality and hospitalization rate.

All-cause mortality

Three trials (Onofriescu et al., 2014; Siriopol et al., 2017; Tian et al., 2020) reported all-cause mortality as the primary outcome. (Tian et al., 2020) tested whether BIA-guided fluid management could improve short-term outcomes in 240 peritoneal dialysis patients. After 1-year follow-up, three patients died in BIA group versus eight patients died in clinical group. Concluding that all-cause mortality was higher in clinical group than BIA group, and showing one potential benefit of bioimpedance analysis in peritoneal dialysis patients when combining it with clinical methods.

On the other hand, (Siriopol et al., 2017) included 250 chronic hemodialysis patients to explore whether combining lung ultrasound and bioimpedance, may provide complementary information to guide treatment. And, concluded that LUS-guided dry weight adjustment protocol, as compared with clinical evaluation, does not reduce all-cause mortality and/or cardiovascular events in hemodialysis patients. However, this study has several limitations; it was underpowered for the primary endpoint. Only studied patients from two dialysis units, excluding patients with severe cardiac failure or inappropriate vascular access, and as such the results cannot be inferred to other HD populations.

Finally, (Onofriescu et al., 2014) compared strict volume control based on bioimpedance versus clinical methods for guiding ultrafiltration prescription in 131 HD patients. The results were very encouraging, the lower all-cause mortality was found in bioimpedance analysis group. Even with these results, an echocardiography was not performed as cardiovascular assessment and the caregivers were not masked to the intervention, this is a limitation for the above study.

All-cause hospitalization

Only one trial (Huan-Sheng et al., 2016) reported all-causa hospitalization rate as the primary outcome. This trial evaluated whether BIA approach could improve clinical outcomes compared to patients who had post-dialysis target weight decided clinically in 298 chronic hemodialysis patients. The results show that the incidence rate for all-cause hospitalization and mortality was not significantly different in both groups.

Changes in residual kidney function

(Yoon et al., 2019) evaluated the effect of BIS-guided fluid management on residual kidney function, volume status, and cardiovascular events in 194 peritoneal dialysis patients. The results allow affirming that BIS-guided fluid management is as useful as clinical methods to preserve residual kidney function in peritoneal dialysis patients. However, this trial had a potential limitation, due to drop-out rate was higher in the intervention group than in the control group. This was mainly associated to the higher protocol violation rate in the intervention group. More and larger clinical trials are needed with the same objective.

Fluid status

Different ways of reporting this outcome were found: overhydration, ECW, ICW, E/I, relative fluid overload, percentage of patients overhydrated, etc. Using different methods to report changes in hydration status, all the included studies described a significant reduction in the overhydration status in the BIA group. Similar to the results obtained in a recent meta-analysis by (Covic et al., 2017).

Others

More recently, (Sommerer et al., 2021) compared hydration status measured by clinical assessment to BIA using a body composition monitor, and the primary outcome was the decline of cardiac biomarker NTproBNP. This trail concluded that BIA is not superior to clinical methods in assessing dry weight, due to the number of patients with severe overhydration (>2 L) were significantly higher in the BIA group (46.0% vs. 30.6%, p = 0.04). However, one limitation of this study is the lack of echocardiography, which would have provided additional information about cardiac function and structure. It would, for example, be interesting to have data on left ventricular mass, especially to monitor changes over a longer time. In addition, the study duration was not sufficient to provide information about mortality or long-term changes in cardiac function.

Results from (Hur et al., 2013) trial in 156 hemodialysis patients concluded that time-averaged fluid overload values significantly decreased in the BIA group, but not in the clinical group. Also, left ventricular mass index regressed in the BIA group, but not in the clinical group. Values for left atrial volume index, blood pressure, and arterial stiffness parameters decreased in the BIA group, but not in the control group. Demonstrating that BIA was superior to clinical methods in preventing cardiac adverse events in hemodialysis patients.

4. Discussion

Bioimpedance provides a quantification of extracellular water, which should be higher in fluid overloaded patients compared with a healthy population. The data emanating from bioimpedance measurements provides explicit quantitation of the deviation of the patient’s present status from his or her ideal body water content, thereby providing concrete guidance for the ultrafiltration prescription.(Beaubien-Souligny et al., 2019)

The introduction of tool-assisted fluid management led to a small reduction in systolic arterial blood. The use of bioimpedance to guide target weight was associated with a decreased rate of hospitalization, and all-cause mortality in dialysis patients.

Bioimpedance is largely used instead, being a simple, precise, noninvasive and inexpensive method. Despite all the advances made in bioimpedance for dialysis applications, there are still many challenges and open study fields for future research.

Some of the challenges are related to the device design. This circumstance poses the challenge of portability in bioimpedance systems, since the typical applications of bioimpedance measurement on the human body use electrodes on the skin.

Bioimpedance devices must be seamless to the user and caregivers. To that aim, important challenges are related to the miniaturization and contact-free and unobtrusive use of bioimpedance systems, which must also have processing and wireless communication capabilities for its integration into an e-Health system.

The use of high frequency signals generally requires a high energy consumption, so this new horizon involves a hardware optimization in size, robustness, and precision, but also in energy consumption, to maximize the autonomy of the devices, fundamental in the case of implants.

Regarding the patient, the anisotropic properties of the skin and tissues must be taken into account, since the flow of the electric current inside the human body is modified by the composition and orientation of the cells in the tissues.

Another important challenge in bioimpedance use is perceptions in patients and cares. One recent qualitative study published in 2018 (Stenberg et al., 2018) reveled that several users had been enthusiastic about bioimpedance initially, but expressed declining confidence in the method.

4.1 Limitations

To our knowledge, this is the first scoping review that assesses the use of bioimpedance technologies in dialysis patients. The main strengths of this review include the comprehensive searches of three great databases, application of PRISMA recommendations, and inclusion of completed and published clinical trials. However, this review has some limitations. Not all the selected studies used same BIA devices, and differences could affect final reports. Primary outcomes differ between studies and comparing it could introduce a bias. Also, the included studies did not standardize blood pressure measurements or echocardiography parameters. Some patients were anuric and other non-anuric, and the results could be not comparable. Finally, the included studies had small sample sizes with short follow-up and variability of follow-up period.

Table 1: Summary of clinical trials included in the scoping review. (BIA=bioimpedance analysis; BIS=bioimpedance spectroscopy; BP=blood pressure; CVD=cardiovascular disease; CV=cardiovascular; GFR=glomerular filtration rate; LUS=lung ultrasound; NTproBNP=biomarker N-terminal pro brain natriuretic peptide; RKF=residual kidney function)

Study/Country	*Objective*	*Participants*	*Intervention*	*Outcomes*	*Results*
(Sommerer et al., 2021) Germany	To compare hydration status measured by clinical assessment compared to BIA using a body composition monitor	132 chronic hemodialysis patients	**IG (65)**: BIA group. **CG (67)**: clinical group.	**Primary**: decline of cardiac biomarker NTproBNP. **Secondary**: reduction of OH, number of adverse.	No differences on NTproBNP between intervention and control group. The number of patients with severe overhydration were significantly higher in the BIA group
(Tian et al., 2020) China	To test whether BIA-guided fluid management could improve short-term outcomes in patients on peritoneal dialysis.	240 peritoneal dialysis patients	**IG (120)**: BIA plus clinical methods. **CG (120)**: only clinical methods.	**Primary**: all-cause mortality. **Secondary**: CVD mortality and technique survival.	After 1-year follow-up, 11 (5%) patients died (three in intervention group versus eight in control group). The technique survival rates were 91% and 83% in the intervention and control groups, respectively
(Yoon et al., 2019) South Korea	To evaluate the effect of BIS-guided fluid management on residual kidney function, volume status, and cardiovascular events in peritoneal dialysis patients.	144 peritoneal dialysis patients	**IG (66)**: BIA group. **CG (78)**: clinical methods group.	**Primary**: change in RKF. **Secondary**: change in volume status, echocardiographic variables, the rates of CV event	Control and intervention groups did not differ significantly in terms of change in RKF during the entire study period. The two groups did not differ in terms of echocardiographic variables
(Oh et al., 2018) South Korea	To investigate whether routine BIS-guided fluid management in peritoneal dialysis patients preserves RRF better than clinical information alone	131 peritoneal dialysis patients	**IG (65)**: BIA group. **CG (66)**: clinical group.	**Primary**: net change in the GFR. **Secondary**: GFR; time to anuria; CV events,	Routine BIS-guided fluid management in non-anuric peritoneal patients did not provide additional benefits in volume status control, RKF preservation, or CV parameters.
(Siriopol et al., 2017) Romania	To explore whether combining LUS and BIA may provide complementary information to guide treatment in HD patients.	250 chronic hemodialysis patients (for ≥3 months)	**IG (123)**: LUS plus BIA group. **CG (127)**: only clinical methods group.	**Primary**: all-cause mortality and first CV event. **Secondary**: all-cause hospitalization, dialysis-related adverse events.	LUS-guided dry weight adjustment protocol, as compared with clinical evaluation, does not reduce all-cause mortality and/or CV events in hemodialysis patients.
(Huan-Sheng et al., 2016) Taiwan	To evaluate whether BIA approach could improve clinical outcomes compared to patients who had post-dialysis target weight decided clinically.	298 chronic hemodialysis patients (for ≥3 months)	**IG (148)**: BIA group. **CG (150)**: clinical methods group.	**Primary**: all-cause hospitalization rate. **Secondary**: incidence of hypertension, CV events, incidence complications	The incidence rate for all-cause hospitalization and mortality was not significantly different in both groups. CV events was lower in intervention group.
(Onofriescu et al., 2014) Turkey	To compare strict volume control based on BIA versus clinical methods for guiding ultrafiltration in HD patients.	131 chronic hemodialysis patients (for ≥3 months)	**IG (62)**: BIA group. **CG (69)**: clinical methods group	**Primary**: all-cause mortality. **Secondary**: changes in fluid overload, and blood pressure.	Lower all-cause mortality in bioimpedance group. Greater decline in arterial stiffness, relative fluid overload, and systolic BP in the bioimpedance group than the clinical-methods group
(Hur et al., 2013) Turkey	To Investigate whether objective measurement of fluid overload with bioimpedance spectroscopy is helpful in optimizing fluid status.	156 chronic hemodialysis patients (for ≥3 months)	**IG (78)**: BIA group. **CG (78)**: clinical methods group.	**Primary**: regression of left ventricular mass index during. **Secondary**: improvement in blood pressure, left atrial volume, and changes in arterial stiffness parameters.	Time-averaged fluid overload values significantly decreased in the intervention group, but not in the control group. Left ventricular mass index regressed in the intervention group, but not in the control group. Values for left atrial volume index, blood pressure, and arterial stiffness parameters decreased in the intervention group, but not in the control group.

5. Conclusions

The use and applications of bioimpedance technologies in dialysis patients is still contradictory and more evidence is needed. Despite the fact that in many trials use of BIA was not superior to traditional clinical methods, its results have been shown to be similar and not inferior to expert nephrology evaluation. Thus, bioimpedance technologies could be very useful when using it as a complement to traditional methods to assess fluid volume management in peritoneal dialysis and hemodialysis patients. Moreover, BIA technologies could be even more useful in home dialysis settings or ambulatory dialysis centers, where expert clinical evaluation is not possible.

Disclosure of potential conflicts of interest

Nothing to disclosure.

References

Beaubien-Souligny, W., Kontar, L., Blum, D., Bouchard, J., Denault, A. Y., & Wald, R. (2019). Meta-Analysis of Randomized Controlled Trials Using Tool-Assisted Target Weight Adjustments in Chronic Dialysis Patients. *Kidney International Reports*, *4*(10), 1426-1434. https://doi.org/10.1016/j.ekir.2019.07.003

Bello, A., Levin, A., Lunney, M., Osman, M., Ashuntantang, G., Bellorin-Font, E., Benghanem Gharbi, M., Ghnaimat, M., Harden, P., & Jha, V. (2019). *Global Kidney Health Atlas: A report by the International Society of Nephrology on the Global Burden of End-stage Kidney Disease and Capacity for Kidney Replacement Therapy and Conservative Care across World Countries and Regions*. International Society of Nephrology.

Covic, A., Ciumanghel, A.-I., Siriopol, D., Kanbay, M., Dumea, R., Gavrilovici, C., & Nistor, I. (2017). Value of bioimpedance analysis estimated "dry weight" in maintenance dialysis patients: A systematic review and meta-analysis. *International Urology and Nephrology*, *49*(12), 2231-2245. Scopus. https://doi.org/10.1007/s11255-017-1698-4

Huan-Sheng, C., Yeong-Chang, C., Ming-Hsing, H., Fan-Lieh, T., Chu-Cheng, L., Tsai-Kun, W., Hung-Ping, C., Sze-Hung, H., Hsien-Chang, C., Chia-Chen, L., Chun-Cheng, H., Chun-Ting, C., Hung-Hsiang, L., Chun-Ju, L., & Paik-Seong, L. (2016). Application of bioimpedance spectroscopy in Asian dialysis patients (ABISAD-III): A randomized controlled trial for clinical outcomes. *International Urology and Nephrology*, *48*(11), 1897-1909. https://doi.org/10.1007/s11255-016-1415-8

Hur, E., Usta, M., Toz, H., Asci, G., Wabel, P., Kahvecioglu, S., Kayikcioglu, M., Demirci, M. S., Ozkahya, M., Duman, S., & Ok, E. (2013). Effect of fluid management guided by bioimpedance spectroscopy on cardiovascular parameters in hemodialysis patients: A randomized controlled trial. *American Journal of Kidney Diseases*, *61*(6), 957-965. https://doi.org/10.1053/j.ajkd.2012.12.017

Jacobsen, E., Cruickshank, M., Cooper, D., Marks, A., Brazzelli, M., & Scotland, G. (2021). Cost-effectiveness and value of information analysis of multiple frequency bioimpedance devices for fluid management in people with chronic kidney disease having dialysis. *Cost Effectiveness and Resource Allocation : C/E*, *19*, 24. https://doi.org/10.1186/s12962-021-00276-6

Oh, K.-H., Baek, S. H., Joo, K.-W., Kim, D. K., Kim, Y. S., Kim, S., Oh, Y. K., Han, B. G., Chang, J. H., Chung, W., & Na, K. Y. (2018). Does Routine Bioimpedance-Guided Fluid Management Provide Additional Benefit to Non-Anuric Peritoneal Dialysis Patients? Results from Compass Clinical Trial. *Peritoneal Dialysis Internationa*, *38*(2), 131-138. https://doi.org/10.3747/pdi.2016.00241

Onofriescu, M., Hogas, S., Voroneanu, L., Apetrii, M., Nistor, I., Kanbay, M., & Covic, A. C. (2014). Bioimpedance-guided fluid management in maintenance hemodialysis: A pilot randomized controlled trial. *American Journal of Kidney Diseases*, *64*(1), 111-118. https://doi.org/10.1053/j.ajkd.2014.01.420

Park, J. H., Jo, Y.-I., & Lee, J.-H. (2018). Clinical usefulness of bioimpedance analysis for assessing volume status in patients receiving maintenance dialysis. *The Korean Journal of Internal Medicine*, *33*(4), 660-669. https://doi.org/10.3904/kjim.2018.197

Scotland, G., Cruickshank, M., Jacobsen, E., Cooper, D., Fraser, C., Shimonovich, M., Marks, A., & Brazzelli, M. (2018). Multiple-frequency bioimpedance devices for fluid management in people with chronic kidney disease receiving dialysis: A systematic review and economic evaluation. *Health Technology Assessment*, *22*(1), 1-138. https://doi.org/10.3310/hta22010

Siriopol, D., Onofriescu, M., Voroneanu, L., Apetrii, M., Nistor, I., Hogas, S., Kanbay, M., Sascau, R., Scripcariu, D., & Covic, A. (2017). Dry weight assessment by combined ultrasound and bioimpedance monitoring in low cardiovascular risk hemodialysis patients: A randomized controlled trial. *International Urology and Nephrology*, *49*(1), 143-153. https://doi.org/10.1007/s11255-016-1471-0

Sommerer, C., Felten, P., Toernig, J., Zeier, M., & Dikow, R. (2021). Bioimpedance analysis is not superior to clinical assessment in determining hydration status: A prospective randomized-controlled trial in a Western dialysis population. *Hemodialysis International*, *25*(3), 380-390. https://doi.org/10.1111/hdi.12919

Stenberg, J., Henriksson, C., Lindberg, M., & Furuland, H. (2018). Perspectives on clinical use of bioimpedance in hemodialysis: Focus group interviews with renal care professionals. *BMC Nephrology*, *19*(1), 121. https://doi.org/10.1186/s12882-018-0907-4

Tian, N., Yang, X., Guo, Q., Zhou, Q., Yi, C., Lin, J., Cao, P., Ye, H., Chen, M., & Yu, X. (2020). Bioimpedance Guided Fluid Management in Peritoneal Dialysis: A Randomized Controlled Trial. *Clinical Journal of the American Society of Nephrology*, *15*(5), 685-694. https://doi.org/10.2215/CJN.06480619

Tricco, A. C., Lillie, E., Zarin, W., O'Brien, K. K., Colquhoun, H., Levac, D., Moher, D., Peters, M. D. J., Horsley, T., Weeks, L., Hempel, S., Akl, E. A., Chang, C., McGowan, J., Stewart, L., Hartling, L., Aldcroft, A., Wilson, M. G., Garritty, C., … Straus, S. E. (2018). PRISMA Extension for Scoping Reviews (PRISMA-ScR): Checklist and Explanation. *Annals of Internal Medicine*, *169*(7), 467-473. https://doi.org/10.7326/M18-0850

van der Sande, F. M., van de Wal-Visscher, E. R., Stuard, S., Moissl, U., & Kooman, J. P. (2020). Using Bioimpedance Spectroscopy to Assess Volume Status in Dialysis Patients. *Blood Purification*, *49*(1-2), 178-184. https://doi.org/10.1159/000504079

Wang, K., Zelnick, L. R., Chertow, G. M., Himmelfarb, J., & Bansal, N. (2021). Body Composition Changes Following Dialysis Initiation and Cardiovascular and Mortality Outcomes in CRIC (Chronic Renal Insufficiency Cohort): A Bioimpedance Analysis Substudy. *Kidney Medicine*, *3*(3), 327-334.e1. https://doi.org/10.1016/j.xkme.2020.12.008

Wang, Y., & Gu, Z. (2021). Effect of bioimpedance-defined overhydration parameters on mortality and cardiovascular events in patients undergoing dialysis: A systematic review and meta-analysis. *The Journal of International Medical Research*, *49*(9), 03000605211031063. https://doi.org/10.1177/03000605211031063

Yoon, H. E., Kwon, Y. J., Shin, S. J., Lee, S.-Y., Lee, S., Kim, S.-H., Lee, E. Y., Shin, S. K., & Kim, Y.-S. (2019). Bioimpedance spectroscopy-guided fluid management in peritoneal dialysis patients with residual kidney function: A randomized controlled trial. *Nephrology*, *24*(12), 1279-1289. https://doi.org/10.1111/nep.13571

Proceedings of the International Conference of Bioelectromagnetism, Electrical Bioimpedance,
and Electrical Impedance Tomography June 29 – July 1, 2022 / Kyung Hee University, Seoul, Korea

Normal Range of phase angle from bioelectrical impedance analysis for young adult and older adult in a Colombian population

González-Correa Clara Helena[1], Pineda-Zuluaga Maria Camila[1] and Marulanda-Mejía Felipe [2]
[1]Department of Basic Health Sciences, Research Group on Nutrition, Metabolism
and Food Security, Universidad de Caldas, Manizales, Colombia
[2]Clinical Department, Universidad de Caldas, Manizales, Colombia

Correspondence : González-Correa Clara Helena, e-mail : clara.gonzalez@ucaldas.edu.co

Abstract– The phase angle (PA), a bioelectrical impedance analysis parameter, is obtained from the resistance/reactance ratio produced by the passage of an electric current through biological tissues. Different studies reveal that there are important differences between the reference values of the PA in different populations and there is currently no universal reference value. Since proper values for our population do not exist, the objective of this study was to obtain provisional data of PA from a sample of young adult and old adults (without declared diseases) that can serve as a reference for the evaluation of patients. This was an observational, cross-sectional, analytical study. Anthropometric measurements (weight, height and body mass index) and bioelectrical measurements (AP and SMI) were taken from 145 young adults and 244 older adults using the Hydra 4200 bioimpedance meter by Xitron Technologies©. The young adult women had a middle PA of 8.04° (±1.3), and the elderly it was 5.87° (±0.87). For young adult men 9.73° (±1.37) and older adults of 6.41° (±0.66). In conclusion, the reference values presented in this study are different from those reported for other populations. They may provisionally serve to assess PA and so the state of health at the clinical level in the region.

Keywords: Phase angle, Young Adult, Older adult, Bioelectical impedance analysis, Colombia.

1. Introduction

Bioelectrical impedance analysis (BIA) has emerged in recent years as a low-cost, easy-to-handle tool for body composition assessment (Lyons-Reid, 2020). The phase angle (PA), a BIA parameter, is a fast-moving research area (Marroni et al, 2016). This variable is obtained from the resistance/reactance ratio produced by the passage of an electric current through biological tissues. Our cell membranes have a layer of lipids that act as insulators, so they do not conduct electricity well. This layer is trapped between two other layers of liquids that are highly conductive. This type of arrangement makes the cell membrane become a true capacitor that offer opposition to the passage of electric current but also impose a barrier to the passage of some substances which can be toxic (Mosgaard et al, 2015). This is how a healthy membrane performs these functions better than a weakened membrane and has been associated with the size, integrity, and function of cell membranes, as well as with inflammation, intra- and extracellular water distribution, nutritional status, and risk of sarcopenia and frailty (Barrea et al, 2021 & Tanaka et al, 2008). Therefore, this parameter can be low in pathological conditions such as HIV, sarcopenia and in malnourished people and can increase as they receive the appropriate treatments (Schwenk et al, 2000 & Silva et al, 2015). An advantage of this parameter is that weight and height are not required for its calculation.

Different studies reveal that there are important differences between the reference values of the PA in different populations and there is currently no universal reference value. The differences have been explained by age and body mass index (BMI) (Gonzalez et al, 2016). The reference values allow detecting changes in an individual in relation to the general average, however, the published values are discrepant between different populations and that is why it is recommended to carry out studies to have the own reference values (Matiello, 2020). Since proper values for our population do not exist, the objective of this study was to obtain provisional data from a sample of normal young adult and old adults (without declared diseases) that can serve as a reference for the evaluation of patients. This sample will be progressively expanded in order to make it more useful.

2. Materials and methodds

2.1 Desing of the study and subjects

This was an observational, cross-sectional, analytical study. 145 young adults (18-39 years) and 244 elders (> 60 years) were evaluated. The young adults were recruited mainly among the students at the University of Caldas. For the population of older adults, an invitation was made to the citizens of Manizales through different media.

Volunteers who were using medications that alter BIA such as diuretics, steroids, growth hormone, dihydropyridine calcium channel blockers, anorectics, high-dose gabapentin were excluded. The presence of edematous syndrome, history of decompensation of chronic disease in the last three months, presence of major neurocognitive disorder, presence of amputations or alterations in body geometry, skin lesions or abnormalities, presence of prostheses, pacemakers or other elements that affect BIA measurements, were also excluded. Therefore, this was a non-probabilistic sample.

2.2 Measurements

Measurements were made in the morning. Relative ambient humidity and temperature was controlled with electric heater (BFH416 by Bionaire TM) and dehumidifier (BMD100 by Bionaire TM). Relative humidity and ambient temperature were measured with a thermohygrometer (13307 by Delta Trak®, ± 0.1 ºC). The volunteers were asked to meet the standardized requirements before the test (fasting for at least 6 hours, empty bladder, not wearing items such as watches or bracelets that alter data collection, not having ingested diuretics). For height, a Heightronic-235 brand stadiometer by Seca®, ± 0.01 cm, and an electronic scale (PP2000 by Icob-Detecto®, ± 0.1 kg) were used for weight. Both measurements were done twice. A third measurement was taken when a difference greater than 0.5 cm or 0.1 kg was found, in height or weight, respectively.

All participants were measured with a bioimpedance meter on the dominant side of the body three times on a non-conductive surface with a Hydra 4200 by Xitron Technologies© equipment according to a rigorous protocol previously published (Gonzalez-Correa et al, 2013) and the PA at 50 kHz was recorded. This device displays the raw data as well as the calculations needed to obtain the PA. Skeletal muscle mass index (SMI) was obtained from muscle mass calculated using the Janssen formula (Janssen, 1985) and subsequently divided by squared height in order to rule out the presence of sarcopenia in the volunteers.

The study protocol was evaluated by ethics committee of the Faculty of Health of the University of Caldas. It was considered low risk and approved. All patients signed an informed consent. In addition, the international guidelines for research with human beings were followed (Declaration of Helsinki).

2.3 Statical Analysis

Data analysis was performed with the statistical package SPSS version 25.0, licensed to the University of Caldas. The Kolmogorov-Smirnov test was applied to the PA values of young adults and older adults to determine if there was a normal distribution of the data. When they presented normal distribution, they were presented as mean and standard deviation (SD) and when they presented non-normal distribution they were described as median and interquartile range (IR) and the respective non-parametric tests. The difference between the PA values between young and adult women and men was determined using the Mann-Whitney U. A significance level of 0.05 was adopted for all statistical analyses.

3. Results

According to the Kolmogorov-Smirnov test for normality, the PA data for both young and adults did not have a normal distribution. The characteristics of the subjects are shown in table 1. PA values established for both sexes in the two types of samples are shown in table 2, where they are also compared with those obtained in other countries. A linear tendency to reduce the PA with advancing age, in both sexes can be seen in figures 1 and 2.

Table 1. Characteristics of the subjects.

	n	Age [years] $\bar{X}$ ± SD	BMI [Kg/m^2] $\bar{X}$ ± SD	SMI [Kg/m^2] $\bar{X}$ ± SD
Young women	62	22.8 ± 3.2	24.8 ± 3.9	8.1 ± 0.9
Young men	83	23.3 ± 4.2	24.6 ± 3.3	10.8 ± 1.0
Total	**145**			
Old women	143	69.2 ± 4.9	26.5 ± 4.2	7.1 ± 0.9
Old men	101	68.0 ± 6.1	25.2 ± 3.7	10.0 ± 1.0
Total	**244**			

Expressed as mean ($\bar{X}$) and Standard Deviation, (SD); BMI, Body Mass Index; SMI, Skeletal Muscle Mass Index.

Table 2. PA for young and old adults from Colombia and other countries.

	PA [°]				
	Colombia (González et al, 2022)	Switzerland (Kyle et al, 2012)	Germany (Dittmar, 2003)	Germany (Bosy et al, 2006)	U.S.A (Barbosa et al, 2005)
Young women n= 62	8.04 ± 1.30	6.63 ± 0.83	5.71 ± 0.06	5.98 ± 0.05	6.96 ± 0.09
Young men n=83	9.73 ± 1.37	7.33 ± 0.83	6.37 ± 0.08	6.79 ± 0.35	7.98 ± 0.07
Old women n=143	6.00 ± 0.81	5.97 ± 0.55	5.33 ± 0.04	5.73 ± 0.23	6.48 ± 0.47
Old men n=101	6.42 ± 0.72	6.63 ± 0.90	5.82 ± 0.06	6.16 ± 0.35	7.34 ± 0.40

Expressed as mean ($\overline{X}$) and Standard Deviation, (SD); PA, Phase Angle.

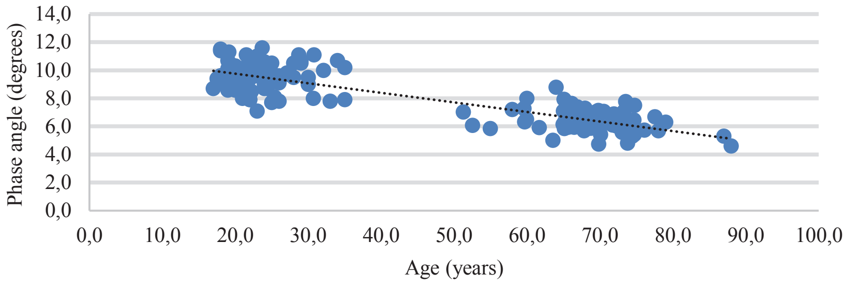

Figure 1. Phase angle for young and old men.

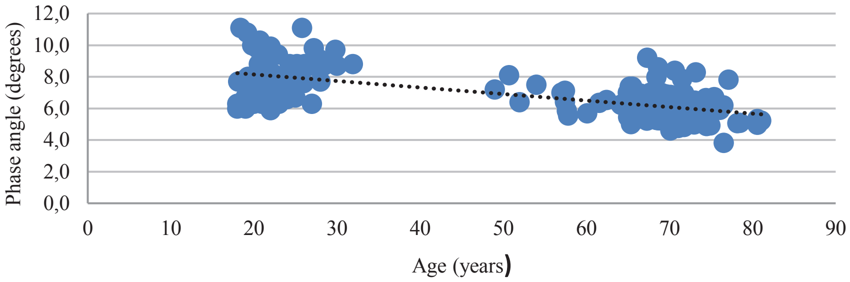

Figure 2. Phase angle for young and old women.

The median PA for adult old women was 6.02° with an IR of 1.13° and for older men it was 6.37° with an IR of 0.91°. When comparing these values between adult men and women, a statistically significant difference was found (p=0.000). On the other hand, the median PA for young men was 9.20° with IR of 4,20° and 6, 65 with IR of 3.68° for young women. When contrasting the PA values of young men with that of young women, a statistically significant difference was also found (p=0.000). Finally, when evaluating the PA in young and old men, there was also a significant difference (p=0.000, NC=95%). This did not happen when comparing PA between young and old women (p=0.174).

4. Discussion and conclusion

After many years of trying different equations to establish body composition with the parameters of BIA, we have advanced in the use of this technique, being able to interpret and use the raw data obtained from the direct measurements. The PA and resistance ratio at 200 kHz/5 kHz are now widely used (López-Gómez, 2011; Ballarin et al, 2021 & Lukaski et al, 2017). Given that it is recommended to have own values due to the ethnic and anthropometric differences of the different populations, this study was done to present preliminary data on normal PA values in young and older adults that can serve as a reference to establish abnormalities for local population but that can be expanded, with a larger sample, to national levels.

As expected, the PA was lower in older populations. This is probably due to a slower speed of the body to repair tissues and form new cells and the loss of them, especially muscle cells (Vincenzo et al, 2021). Moreover, the same can happen in the course of pathologies such as cancer of different organs. This is how this parameter obtained from BIA is currently used to establish the quality of the muscles as well as to determine the "biological age" of a person (Mohamed, 2021).

The PA obtained for young men and women were above those found in similar populations in Germany, the United States and Switzerland (Table 1). It is likely that these differences are not only due to ethnic, race, and anthropometric differences but also to the different years in which the various studies were carried out. Nowdays, young people are more willing to exercise and go to gyms in order to have higher muscle health (Söderström, 2021). Even so, there is still a task to be done and that is to have cut-off points to establish different degrees of affectation of PA in the different types of diseases. On the other hand, the values for older men and women were similar to those reported for these same countries.

On the other hand, the average SMI value for both young adult and older adult women and men were above the reference value for our population. These results, together with those found for AP, show us how there is an important relationship between these two parameters, since, as demonstrated in a study carried out in 2021, higher values of AP are significantly related to better strength and muscle mass (Matías et al, 2021).

These results in healthy individuals are of interest for clinical practice and research, since the use of the PA obtained from BIA can be very useful in the diagnosis and prognosis of health status, always considering differences by age and sexes.

Limitations of the study have to do with the sample size because the results cannot be extrapolated to other population groups. Even so, we believe that strength of the study is related to the rigor with which the measurement protocols were applied, and subjects were selected.

In conclusion, the reference values presented in this study are different from those reported for other populations. They may provisionally serve to assess the PA and so the state of health at the clinical level in the region.

References

Ballarin G, Scalfi L, Monfrecola F, Alicante P, Bianco A, Marra M and Sacco A M 2021 Body composition and bioelectricalimpedance-analysis-derived raw variables in pole dancers *Int. J. Environ. Res. Public Health* **18** 1-11

Barbosa-Silva M C, Barros A J, Wang J, Heymsfield S B and Pierson-Jr R N 2005 Bioelectrical impedance analysis: population reference values for phase angle by age and sex *Am J Clin Nutr* ***82*** 49-52

Barrea L, et al 2021 Phase angle as an easy diagnostic tool of meta-inflammation for the nutritionist *Nutrients* **13** 1446

Dittmar M 2003 Reliability and variability of bioimpedance measures in normal adults: effects of age, gender, and body mass *Am J Phys Anthropol* **122** 361-70

Bosy-Westphal A, Danielzik S, Dörhöfer R P, Later W, Wiese S and Müller MJ 2006 Phase angle from bioelectrical impedance analysis: population reference values by age, sex, and body mass index *JPEN J Parenter Enteral Nutr* **30** 309-16

Di Vincenzo O M, Marra A, Di Gregorio, et al 2021 Bioelectrical impedance analysis (BIA) -derived phase angle in sarcopenia: a systematic review C*lin Nutr* **40** 3052-61

Gonzalez-Correa C H and Caicedo-Eraso J C 2013 Bioelectrical impedance analysis (BIA): A proposal for standardization of the classical method in adults *Journal of Physics Conference Series*. **2013** 1-13

Gonzalez M C, Barbosa-Silva T G, Bielemann R M, Gallagher D and Heymsfield S B 2016 Phase angle and its determinants in healthy subjects: influence of body composition *Am J Clin Nutr.***103** 712–716

Janssen I, Heymsfield S, Baumgartner R and Ross R 1985 Estimation of skeletal muscle mass by electrical impedance analysis *J Appl Physiol* **89** 465-71

Kyle U G, Soundar E P, Genton L and Pichard C 2012 Can phase angle determined by bioelectrical impedance analysis assess nutritional risk? A comparison between healthy and hospitalized subjects *Clin Nutr.* **31** 875-81

López-Gómez J M 2011 Evolution and applications of bioimpedance in managing chronic kidney disease *Nefrología* **31** 537-44

Lukaski H C, Kyle U G and Kondrup J 2017 Assessment of adult malnutrition and prognosis with bioelectrical impedance analysis: phase angle and impedance ratio *Curr Opin Clin Nutr Metab Care* **20** 330-39

Lyons-Reid J, Ward L C, Kenealy T and Cutfield W 2020 Bioelectrical impedance analysis-an easy tool for quantifying body composition in infancy? *Nutrients* **12** 920

Matías C N, Campa F, Nunes C L et al 2021 Phase angle is a marker of muscle quantity and strength in overweight/obese former athletes Int. J. Environ. Res. Public Helath **18** 1-10

Marroni C A, Miranda D, Boemeke L and Fernandes S 2016 *Biomarkers in Liver Disease* Phase angle bioelectrical impedance analysis (bia) as a biomarker tool for liver disease (Alegre, Brazil: Springer Science+Business Media Dordrech)

Mattiello R, Azambuja A M, Mundstock E and Klarmann Z P 2020 Meta-analyses reference values for the phase angle of the electrical bioimpedance: Systematic review and meta-analysis involving more than 250,000 subjects *Clin Nutr.* **39** 1411-17

Mohamed S H 2021 Estimating biological age according to biomarkers, anthropometric and Bioelectrical Impedance measures, and its relationship to physical fitness age **42** 24-53

Mosgaard L, Zecchi K, Heimburg T and Budvytyte R 2015 The effect of the nonlinearity of the response of lipid membranes to voltage perturbations on the interpretation of their electrical properties. a new theoretical description *Membranes* **4** 495-512

Schwenk A, Beisenherz A, Römer K , Kremer G , Salzberger B and M Elia 2000 Phase angle from bioelectrical impedance analysis remains an independent predictive marker in HIV-infected patients in the era of highly active antiretroviral treatment *Am J Clin Nutr.* **72** 469-501

Silva R, Pinho C, Rodrigues I and Gildo J 2015 Phase angle as an indicator of nutritional status and prognosis in critically ill patients *Nutricion hospitalaria* **31** 1278-1285

Söderström T 2021 A 20-year analysis of motives and training patterns of Swedish gym-goers *Annals of Leisure Research* DOI: 10.1080/11745398.2021.2010223

Proceedings of the International Conference of Bioelectromagnetism, Electrical Bioimpedance,
and Electrical Impedance Tomography June 29 – July 1, 2022 / Kyung Hee University, Seoul, Korea

A novel current source for multi-frequency Magnetic Resonance Electrical Impedance Tomography

Z. Colwell[1], M. Manetta[1], S. Sohn[1] and R. J. Sadleir[1]
[1]School of Biological and Health Systems Engineering, Arizona State University, Tempe, AZ, USA

Correspondence : Rosalind J. Sadleir, e-mail : rsadleir@asu.edu

Abstract– Multifrequency Magnetic Resonance Electrical Impedance Tomography (MF-MREIT) may provide a method of investigating biological electrical properties below 1 MHz. We designed a waveform generator for MF-MREIT that can accurately deliver dual polarity rectified sine waves to recover higher frequency MREIT phase data. It was based on a synchronous balanced modulator/demodulator architecture (AD630, Analog Devices, Inc.) with switching and logic signals controlled by a microprocessor. The function generator source was based on an earlier Howland design constant current source (Tucker et al., 2012). An integrated waveform metric was used to evaluate the performance and phase accuracy of the new source. In future steps wireless control will be added to the source to enable remote operation from within the magnet bore.

References

TUCKER, A., FOX, R. M. & SADLEIR, R. J. 2012. Biocompatible, high precision, wideband, improved Howland current source with lead-lag compensation. *IEEE Transactions on Biomedical Circuits and Systems,* 7**,** 63-70.

ICBEM Bioelectromagnetism ICEBI Electrical Bioimpedance EIT Electrical Impedance Tomography

Proceedings of the International Conference of Bioelectromagnetism, Electrical Bioimpedance,
and Electrical Impedance Tomography June 29 – July 1, 2022 / Kyung Hee University, Seoul, Korea

Feature-Based Model Compression Scheme for Electrical Impedance Tomography

Zhichao Lin[1], Rui Guo[1], Ke Zhang[1], Maokun Li[1], Fan Yang[1], Shenheng Xu[1], and Aria Abubakar[2]
[1]Beijing National Research Center for Information Science and Technology,
Institute of Precision Medicine, Tsinghua University, Beijing, China
[2]Schlumberger, Houston, Texas, USA

Correspondence : Maokun Li, e-mail : maokunli@tsinghua.edu.cn

Abstract– Electrical impedance tomography (EIT) is a nonlinear ill-posed problem. To alleviate the ill-posedness of EIT, we present a feature-based model compression scheme based on deep learning. A set of EIT images are constructed based on the CT scans and prior information of the targets. A variational autoencoder (VAE) is trained to learn the features of targets from these images. After training the VAE, each EIT image can be parametrized by a latent code in a low-dimensional feature space. In the inversion, the latent code is taken as unknowns and inverted by the Gauss-Newton method. In this way, the number of unknowns is largely reduced and the inversion is conducted at the feature level. Both synthetic and experimental data inversion verify the effectiveness of the proposed method.

Keywords: absolute imaging; model compression; variational autoencoder; electrical impedance tomography

1. Introduction

Electrical impedance tomography (EIT) aims to reconstruct the conductivity distribution of the domain of investigation (DoI) according to the voltage measurements on the boundary. It has wide applications in biomedical imaging due to its radiation-free and non-invasive advantages (Khan *et al* 2019). EIT is a typical nonlinear ill-posed problem. The nonlinearity is caused by the inherent property of the current field, and the ill-posedness is mainly because the number of unknowns in EIT is usually much larger than that of equations. These two properties make EIT challenging.

To solve the EIT problem stably, we must combine prior information with inversion algorithms. A common strategy is to constrain the solution space with regularization methods, such as Tikhonov method (Vauhkonen *et al* 1998) and multiplicative regularization (Zhang *et al* 2019). Besides, many machine learning and deep learning methods are also applied to embed prior information in the inversion, such as supervised descent learning algorithm (Zhang *et al* 2020) and deep D-bar method (Hamilton *et al* 2019). The above methods describe the prior information at the pixel level, where the number of unknowns is often large and the inversion process may be computationally expensive. Another promising kind of way to fuse prior information is model-based inversion methods, where the DoI is parameterized based on the features of models. For example, shape-driven approaches assume the conductivities of inclusions in DoI to be piecewise constant and represent the inclusions with their boundaries (Babaeizadeh *et al* 2007). Level-set methods represent the inclusions implicitly by a set of manually designed functions (Liu *et al* 2017).

In this work, we propose a feature-based model compression scheme for absolute imaging in 2D EIT. First, a set of EIT images are constructed from CT scans, where the prior information of target structures and conductivity ranges are embedded in the EIT images during the processing. VAE learns the model features from these EIT images and parameterizes EIT images by latent codes in a low-dimensional feature space. The properties of VAE guarantee the compactness and continuity of the feature space. Then, the latent code in the feature space is employed as the unknowns of EIT inversion and is inverted under a deterministic framework. Finally, by decoding the latent code, we can obtain the reconstructed model.

2. Methods

2.1 Variation autoencoder

We apply the VAE (Zhang *et al* 2018) to learn the features of targets and parametrize the EIT images. A schematic diagram of the VAE structure is shown in Figure 1. It contains an encoder $E(\boldsymbol{x})$ and a decoder $D(\boldsymbol{x})$. During the training, the VAE encoder maps each EIT image $\boldsymbol{x}$ to a low-dimensional Gaussian distribution with mean of $\boldsymbol{\mu}_v$ and variance of $diag(\boldsymbol{\sigma}_v^2)$. The latent code $\boldsymbol{v}$ for the input $\boldsymbol{x}$ is randomly sampled from this distribution using the reparameterization trick,

$$\boldsymbol{v} = \boldsymbol{\mu}_v + \boldsymbol{\varepsilon} \otimes \boldsymbol{\sigma}_v, \quad \boldsymbol{\varepsilon} \sim \mathcal{N}(0, \boldsymbol{I}) \tag{1}$$

where $\otimes$ denotes the element-wise multiplication, and $\boldsymbol{\varepsilon}$ is randomly sampled from a standard normal distribution. Then, the latent code $\boldsymbol{v}$ is input to the VAE decoder to recover the EIT image. Besides, the Gaussian distributions from different EIT images are all set to approximate the standard normal distribution $\mathcal{N}(0, I)$, which guarantees the compactness and continuity of the feature space. The final loss function for training the VAE can be written as

$$\mathcal{L} = \alpha \sum_{k=1}^{N_v}\left(\mu_{(k)}^2(\boldsymbol{x}) + \sigma_{(k)}^2(\boldsymbol{x}) - \ln \sigma_{(k)}^2(\boldsymbol{x}) - 1\right) + \frac{1}{L}\sum_{l=1}^{L}(x_l - \hat{x}_l)^2 \tag{2}$$

where the first term is a regularization that tries to maximize the similarity between the Gaussian distribution $\mathcal{N}\left(\boldsymbol{\mu}_v, diag(\boldsymbol{\sigma}_v^2)\right)$ and the standard normal distribution $\mathcal{N}(0, \boldsymbol{I})$, and the second term is the reconstruction errors between the input and output of the VAE; N_v is the length of the latent code, L is the number of pixels of EIT image, and α is the regularization coefficient that controls the regularization strength.

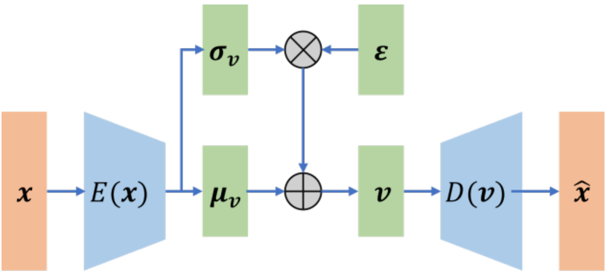

Figure 1. A schematic diagram of VAE structure.

After training, the decoder $D(\boldsymbol{x})$ can map a latent code that is sampled from the standard normal distribution to a reasonable EIT image. Then, the decoder is employed to conduct the EIT inversion in the latent space.

2.2 Inversion algorithm

We formulate the EIT inversion in the deterministic framework. The complete electrode model (CEM) is used to model the forward problem of EIT, and is numerically solved by the finite element method (FEM), denoted as $\boldsymbol{u} = F(\boldsymbol{m})$, where $\boldsymbol{m}$ is the EIT model represented by finite elements and $\boldsymbol{u}$ is the simulated data. It is noted that the pixel-based EIT image $\boldsymbol{x}$ is mapped onto a triangular mesh to generate the EIT model $\boldsymbol{m}$, as shown in Figure 2. The transformation is denoted as $\boldsymbol{m} = T(\boldsymbol{x})$. Then, the forward modeling w.r.t the latent code $\boldsymbol{v}$ can be simplified as

$$\boldsymbol{u} = F \circ T \circ D(\boldsymbol{v}) = S(\boldsymbol{v}). \tag{3}$$

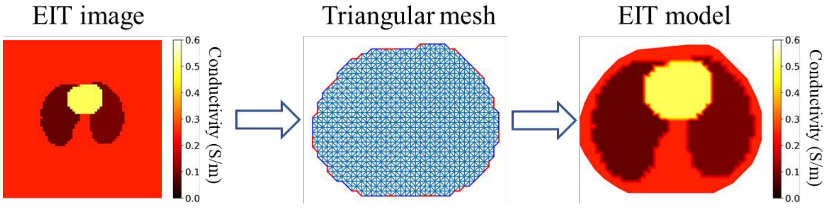

Figure 2. Illustration of the transformation that maps the EIT image onto a triangular mesh to generate the EIT model. The red lines in the triangular mesh denote the electrodes.

In the inversion, the cost function is defined as

$$\phi(\boldsymbol{v}) = \phi^d(\boldsymbol{v}) + \beta\phi^r(\boldsymbol{v}) = \frac{\|\boldsymbol{u}_* - S(\boldsymbol{v})\|^2}{2\,\|\boldsymbol{u}_*\|^2} + \frac{1}{2}\beta\|\boldsymbol{v}\|^2 \tag{4}$$

where $\phi^d(\boldsymbol{v})$ and $\phi^r(\boldsymbol{v})$ are the data misfit and regularization term, respectively; $\boldsymbol{u}_*$ is the measured data, $\|\cdot\|$ denotes the l^2-norm, and β is the regularization term.

To minimize the cost function (4), we apply the Gauss-Newton method. The descent direction at the n-th iteration, $\boldsymbol{p}_n$, is calculated by

$$\boldsymbol{H}_n \boldsymbol{p}_n = -\boldsymbol{g}_n \tag{5}$$

where $\boldsymbol{g}_n$ and $\boldsymbol{H}_n$ are the gradient and Hessian matrix of the cost function, respectively, given by

$$\boldsymbol{g}_n = -\frac{1}{\|\boldsymbol{u}_*\|^2}\boldsymbol{J}_n^T\big(\boldsymbol{u}_* - S(\boldsymbol{v})\big) + \beta_n\boldsymbol{v}_n \tag{6}$$

$$\boldsymbol{H}_n = \frac{1}{\|\boldsymbol{u}_*\|^2}\boldsymbol{J}_n^T\boldsymbol{J}_n + \beta_n\boldsymbol{I} \tag{7}$$

where $\boldsymbol{J_n}$ is the Jacobian matrix of the forward modeling $S(\cdot)$ computed at $\boldsymbol{v}_n$, and $\beta_n = \beta\phi_n^d$ is set to adaptively lower the regularization strength. It is noted that $\boldsymbol{J}$ is calculated by the chain rule,

$$\boldsymbol{J} = \boldsymbol{J}_F \cdot T(\boldsymbol{J}_D) \tag{8}$$

where $\boldsymbol{J}_F$ is the Jacobian matrix of $F(\cdot)$ that computed by the adjoint method, $\boldsymbol{J}_D$ is the Jacobian matrix of $D(\cdot)$ that is obtained by the automatic differentiation in the deep learning framework, and $T(\cdot)$ maps the derivation of pixels in EIT image w.r.t the latent code $\partial x_p/\partial v_q$ to the derivation of parameters of EIT model w.r.t the latent code $\partial m_j/\partial v_q$.

The latent code is updated by $\boldsymbol{v}_{n+1} = \boldsymbol{v}_n + \boldsymbol{p}_n$. The iteration stops when the preset maximum number of iterations is reached. The last latent code is input to the decoder to obtain the final inversion result.

3. Results

3.1 Numerical examples

We validate the proposed method with synthetic data inversions. First, we generate a total of 93040 EIT images based on the thorax CT scans that are collected from the cancer imaging archive (TCIA) (Clark *et al* 2013) for training the VAE. Each EIT image contains two lungs, one heart, and the background. The conductivity values of lungs, heart, and background are randomly sampled from 0.06 S/m to 0.16 S/m, 0.4 S/m to 0.6 S/m, and 0.2 S/m to 0.25 S/m, respectively. The shape of each EIT image is 64×64. The length of the latent code is 36, and the regularization coefficient α is 5×10^{-3}.

After training the VAE, we select 6 new EIT images that are beyond the training data to test the proposed method, and the chest meshes are also generated based on the corresponding CT scans. The conductivity values of lungs, heart, and background in 6 images are the same, i.e., the conductivity of the left lung is 0.1 S/m, the right lung is 0.08 S/m, the heart is 0.5 S/m, and the background is 0.25 S/m. The 6 images are mapped onto 6 different chest meshes to synthesize the EIT models. We set 16 electrodes evenly located on the boundary of the chests to simulate the measured data. All the simulated data for inversion are corrupted with 2% white Gaussian noise. The pixel-based Gauss-Newton method with Tikhonov regularization $\|\nabla\boldsymbol{m}\|^2$ is also performed to have a comparison with the proposed method.

The inversion results of the two methods are shown in Figure 3. As can be seen, the GN method can roughly reconstruct the lungs and heart with right positions and conductivities, but their edges are hard to tell apart. On the other hand, the feature-based method reconstructs the models at the feature level. Thus, the inverted lungs and hearts have clear edges that are basically consistent with the ground truths.

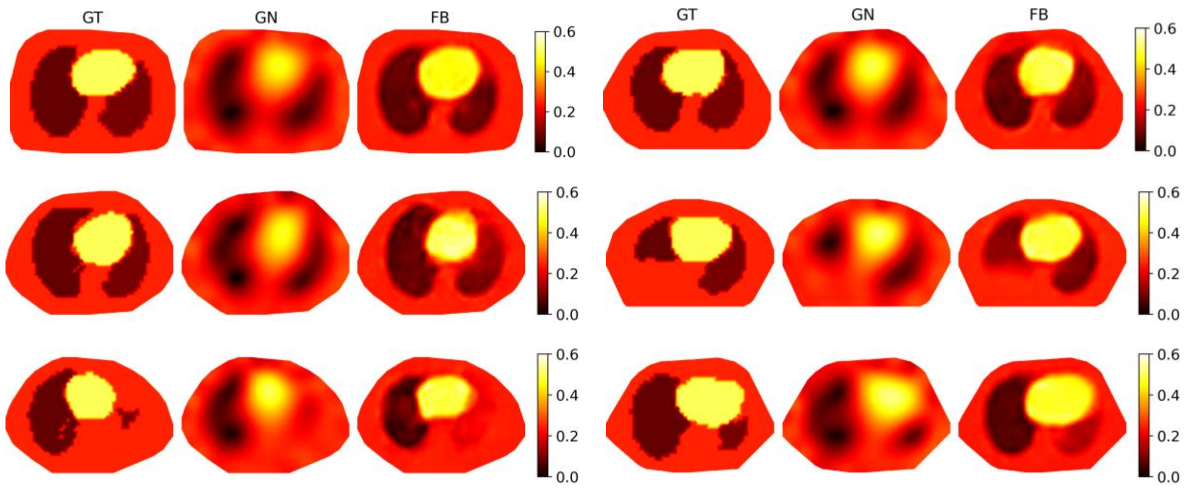

Figure 3. Inversion results of 6 EIT models. The GT columns are the ground truths, the GN columns are the results of pixel-based inversion, and the FB columns are the results of feature-based inversion. The conductivity unit is S/m.

3.2 Experimental example

We apply the widely used experimental data (Isaacson *et al* 2004) to verify the proposed method. The phantom chest is a cylindrical tank with a radius of 15 cm. It contains an agar heart with conductivity of 750 mS/m and two agar lungs with conductivity of 240 mS/m. The background is saline with conductivity of 424 mS/m. 32 electrodes of width 2.5 cm are evenly attached to the boundary of the tank. 31 trigonometric current patterns are applied with amplitude of 0.2 mS on all 32 electrodes, and the voltages are measured simultaneously, resulting in 992 data points. For convenience, we process the original data to synthesize the measured data of 16 electrodes with adjacent protocol for the inversion.

The trained VAE in the numerical examples is directly applied to invert the measured data. To make the conductivity values of the phantom meet the conductivity ranges of the training data, we amplify the measured data by 1.8. Then, the conductivities of the lungs, heart, and background become 0.13 S/m, 0.42 S/m, and 0.24 S/m, respectively. Besides, we also rotate the decoded image of VAE 180 degrees to fit the direction of the ground truth. The inversion results are shown in Figure 4. The GN method successfully reconstructs the gap between the heart and lungs. However, we cannot observe the gap in the result of feature-based method. This is mainly because the samples in the training data do not have gaps between the heart and lungs.

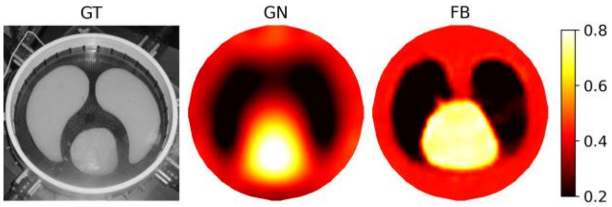

Figure 4. Inversion results of the phantom model. GT is the ground truth, GN is the result of pixel-based inversion, and FB is the result of feature-based inversion. The conductivity unit is S/m.

4. Conclusions

We present a feature-based model compression scheme based on deep learning for absolute imaging in 2D EIT. The EIT images generated from CT scans can flexibly embed the prior information of target structures and conductivity ranges. The VAE learns high-level features from these EIT images and constructs the mappings between EIT images and low-dimensional feature space. The latent code in the feature space is used as unknowns in the data inversion, thus alleviating the ill-posedness of the EIT problem. Both synthetic and experimental data inversions validate the effectiveness of the proposed method, and prove its superiority over the pixel-based Gauss-Newton method. Our future work will focus on extending the feature-based model compression scheme to 3D absolute imaging in EIT.

Acknowledgments

This work was supported in part by the National Natural Science Foundation of China (61971263), the National Key R&D Program of China (2018YFC0603604), Institute for Precision Medicine, Tsinghua University, and Beijing Innovation Center for Future Chip.

References

Babaeizaden S and Brooks D H 2007 Electrical impedance tomography for piecewise constant domains using boundary element shape-based inverse solutions *IEEE Transactions on Medical Imaging* **26** 637-647

Clark K, Vendt B, Smith K, Freymann J, Kirby J, Koppel P, *et al* The cancer imaging archive (TCIA): maintaining and operating a public information repository *Journal of Digital Imaging* **26** 1045-1057

Hamilton S J and Hauptmann A 2018 Deep D-bar: Real-time electrical impedance tomography imaging with deep neural networks *IEEE Transactions on Medical Imaging* **37** 2367-2377

Isaacson D, Mueller J L, Newell J C and Siltanen S 2004 Reconstructions of chest phantoms by the D-bar method for electrical impedance tomography *IEEE Transactions on Medical Imaging* **23** 821-828

Khan T A and Ling S H 2019 Review on electrical impedance tomography: artificial intelligence methods and its applications *Algorithms* **12** 88

Liu D, Khambampati A K and Du J 2017 A parametric level set method for electrical impedance tomography *IEEE Transactions on Medical Imaging* **37** 451-460

Vauhkonen M, Vadasz D, Karjalainen PA, Somersalo E and Kaipio JP 1998 Tikhonov regularization and prior information in electrical impedance tomography *IEEE Transactions on Medical Imaging* **17** 285-293

Zhang C, Butepage J, Kjellstrom H and Mandt S 2018 Advances in variational inference *IEEE Transactions on Pattern Analysis and Machine Intelligence* **41** 2008-2026

Zhang K, Guo R, Li, M, Yang F, Xu S and Abubakar A 2020 Supervised descent learning for thoracic electrical impedance tomography *IEEE Transactions on Biomedical Engineering* **68** 1360-1369

Zhang K, Li M, Yang F, Xu S and Abubakar A 2019 Three-dimensional electrical impedance tomography with multiplicative regularization *IEEE Transactions on Biomedical Engineering* **66** 2470-2480

Proceedings of the International Conference of Bioelectromagnetism, Electrical Bioimpedance,
and Electrical Impedance Tomography June 29 – July 1, 2022 / Kyung Hee University, Seoul, Korea

EIDORS version 3.11

Andy Adler[1], Bartek Grychtol[2]
[1]Systems and Computer Engineering, Carleton University, Ottawa, Canada
[2]Independent Researcher, the Hague, Netherlands

Correspondence : Andy Adler, e-mail : adler@sce.carleton.ca

Abstract−This paper announces the release of version 3.11 of the EIDORS software suite. We review its new features, and discuss its growth and use.

Keywords: Open source Software, EIDORS, Image Reconstruction

1. Introduction

We proudly announce the release of EIDORS version 3.11, for the 22th Int. Conf. on Biomedical Applications of EIT, in June 2022. The software is available at eidors.org and licensed under the GNU GPLv2 or GPLv3. Archived versions are now available on Zenodo [1–5].

EIDORS provides free software algorithms for forward modelling and inverse solutions of Electrical Impedance and (to some extent) Diffusion-based Optical Tomography, in medical, industrial and geophysical settings. EIDORS also aims to share data and promote collaboration amongst its users.

2. New Features

Release 3.11 of EIDORS builds upon a strong foundation in reconstruction algorithms, adding and improving several features.

- Expanded hardware support
- Cleaned-up the interface of some functions that accept many options.
- HDF5-Based file format
- Improved LQ4 support
- Forward models include linear circuits as "extra_nodes"
- Higher order system matrix speedups
- Improvement to system_mat_fields (stability & speed)
- Custom high-density regions in Netgen meshing functions (ng_write_opt)
- Caching on ng.opt file
- User-friendly presets for ng.opt file
- 2D meshing with gmsh
- Improved graphics functions incl. more intuitive slicing
- Improved mesh interpolation (speedups and new functionality)
- Use Matlab's Triangulation class for speed in several functions
- Improvements to print_convert: speedups, clipboard functionality, better control of size & resolution
- Draeger image format
- model of stimulation patterns from monopolar data (mono2stim)
- faster noise figure search
- distmesh improvements/bug fixes
- (As always) bug fixes

3. Impact

EIDORS continues to be a popular software suite. At above 200, the average number of monthly downloads of the latest release is very high. The continued use of v3.6 is both surprising and concerning. While EIDORS has been downloaded in over 100 countries, China, United States, Germany and the United Kingdom account for over half the downloads.

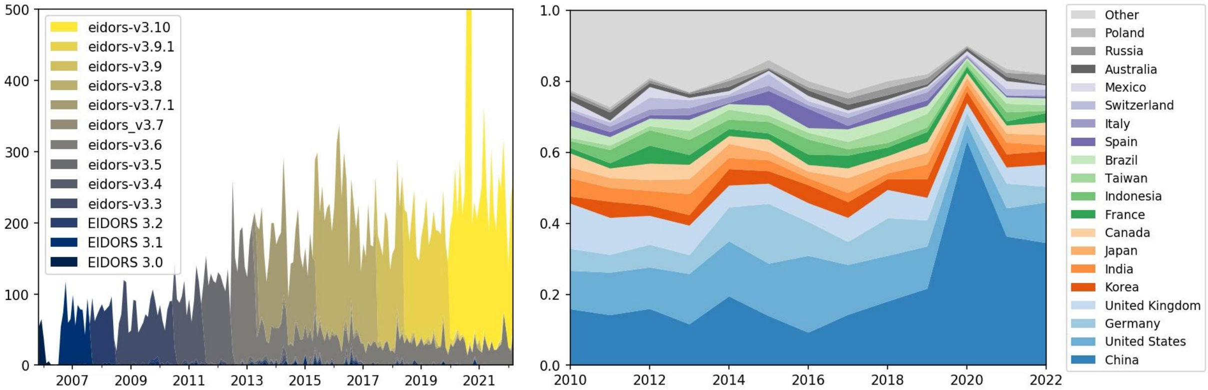

Figure 1. EIDORS download statistics. Left: monthly per release; right: yearly fraction per country.

4. Growth

EIDORS-related citations continue to grow. Current citation results are shown in table 1. The EIDORS code-base is growing with significant effort being applied to improving test coverage, refining performance and implementing new features (figure 2).

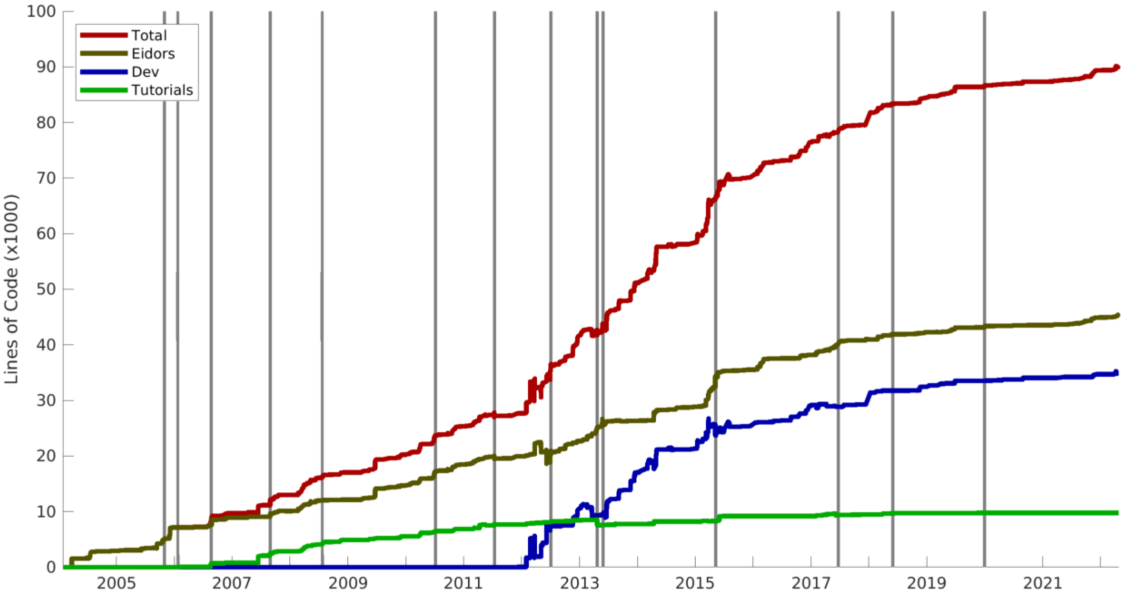

Figure 2. Lines of Code (LoC) in Matlab files in the EIDORS code-base vs. time; Total (red), EIDORS (i.e. release branch, brown), Tutorials (green), development code (blue). Releases are indicated by gray bars (The 3.11 release is at the right).

Table 1. EIDORS Citations (April 2022, scholar.google.com)..

Ref	Paper	Date	Citations
[6]	A MATLAB package for the EIDORS project to reconstruct two-dimensional EIT images	2001	311
[7]	Image Reconstruction Algorithms for Soft-Field Tomography	2002	180
[8]	A Matlab toolkit for three-dimensional electrical impedance tomography: a contribution to the Electrical Impedance and Diffuse Optical Reconstruction Software project	2002	511

[9]	EIDORS: Towards a community-based extensible software base for EIT	2005	30
[10]	Uses and abuses of EIDORS: an extensible software base for EIT	2006	784
[11]	Simple FEMs aren't as good as we thought: experiences developing EIDORS v3. 3	2008	25
[12]	EIDORS version 3.8	2015	2
[13]	EIDORS version 3.9	2017	29
[14]	EIDORS version 3.10	2022	2

5. Conclusion

The structure of EIDORS has been relatively stable due, in part, to some early design choices: a modular framework and data structure, cross-platform support, integration of meshing, tutorials, and the contributed data repository. These aspects, along with an open source code-base, have enabled EIDORS to maintain research relevance. Version 3.11 (hopefully) continues the tradition.

References

[1] Adler A, “EIDORS version 3.11”, DOI:10.5281/zenodo.6483956, 2022.
[2] Adler A, “EIDORS version 3.10”, DOI:10.5281/zenodo.3247168, 2019.
[3] Adler A et al, “EIDORS version 3.9.1”, DOI:10.5281/zenodo.1257670, 2018.
[4] Adler A et al, “EIDORS v3.9”, DOI:10.5281/zenodo.583266, 2017.
[5] Adler A et al, “EIDORS v3.8”, DOI:10.5281/zenodo.17559, 2015.
[6] Grychtol B et al https://iopscience.iop.org/article/10.1088/1361-6579/ab291d Physiol Meas, 2019.
[7] Vauhkonen M, Lionheart WRB et al, Physiol Meas, 22:107–111, 2001.
[8] Polydorides N, Ph.D. thesis, U Manchester, UK, 2002.
[9] Polydorides N, Lionheart WRB, Meas Sci Tech, 13:1871–1883, 2002.
[10] Adler A, Lionheart WRB, Proc EIT2005, London, UK, 2005.
[11] Adler A, Lionheart WRB, Physiol Meas 27:S25–S42, 2006.
[12] Adler A, Borsic A et al, Proc EIT2008, Hannover, NH, USA, 2008.
[13] Adler A et al, Proc EIT2015, p.19, Neuchâtel, Switzerland, 2015.
[14] Adler A et al, Proc EIT2017, p.63, Dartmouth, NH, USA, 2017.
[15] Adler A, Proc EIT2019, London, UK, 2018

Proceedings of the International Conference of Bioelectromagnetism, Electrical Bioimpedance,
and Electrical Impedance Tomography June 29 – July 1, 2022 / Kyung Hee University, Seoul, Korea

Projection-based Iterative Methods for Electrical Impedance Tomography

Mirjeta Pasha[1], Brian Aguilar[2], Lucia Ramirez[1], Jacob Roarty[1],
Rosalind Sadleir[2] and Malena I. Espanol[1]
[1]School of Mathematical and Statistical Sciences, Arizona State University, Tempe, USA
[2]School of Biological and Health Systems Engineering, Arizona State University, Tempe, USA

Correspondence : Malena I. Espanol, e-mail : malena.espanol@asu.edu

Abstract– Electrical Impedance Tomography (EIT) is a low-cost, portable, and noninvasive imaging system that does not use ionizing radiation. It has many potential applications including the continuous monitoring of patients with acute respiratory distress syndrome, which in particular is affecting many patients during the current Covid-19 pandemic. The mathematical formulation of the problem yields a severely ill-posed inverse problem. Therefore, regularization methods are needed to recover meaningful images representing internal conductivities. Many numerical methods exist to solve the EIT problem. Most recent results using sparsity and TV show very promising results. However, the computational cost of those approaches is still very high. Therefore, we combine a Gauss-Newton approach algorithm and a majorization-minimization (MM) Krylov Generalized Subspace (KGS) method that allows us to choose parameter automatically and efficiently. Furthermore, we explore different regularization operators defined on the grid. We demonstrate we can obtain more accurate reconstructions at faster convergence rates compared to other more traditional methods.

References

Huang, G., Lanza, A., Morigi, S., Reichel, L., & Sgallari, F. (2017). Majorization–minimization generalized Krylov subspace methods for ℓp–ℓq optimization applied to image restoration. BIT Numerical Mathematics, 57(2), 351-378.

Chambolle, A., & Pock, T. (2020). Crouzeix–Raviart approximation of the total variation on simplicial meshes. Journal of Mathematical Imaging and Vision, 62(6), 872-899.

Proceedings of the International Conference of Bioelectromagnetism, Electrical Bioimpedance,
and Electrical Impedance Tomography June 29 – July 1, 2022 / Kyung Hee University, Seoul, Korea

Algorithm for Detecting Motion Noise in Electrical Impedance Images during Hemodialysis

Thi Hang Dang[1,2,3], Jinwon Mok[1,2,3], Tingting Zhang[1,2], Joo Young Moon[4] and Tong In Oh[1,2]
[1]Medical Science Research Institute, Kyung Hee University Hospital, Seoul, Korea
[2]Department of Biomedical Engineering, School of Medicine, Kyung Hee University, Seoul, Korea
[3]Department of Medical Engineering, Graduate School, Kyung Hee University, Seoul, Korea
[4]Division of Nephrology, Department Internal Medicine, College of Medicine, Kyung Hee University, Seoul, Korea

Correspondence : Tong In Oh, e-mail : tioh@khu.ac.kr

Abstract– Electrical impedance tomography (EIT) could be used to monitor cardiopulmonary function for patients undergoing hemodialysis (HD), non-invasively. Cardiac-related volume signals (CVS) extracted from EIT measurements have limited performance in monitoring hemodynamic changes during HD because of their small size and high sensitivity to motion noise. These motion artifacts (MA) may cause misinterpretation of hemodynamic status monitored by EIT. In this study, a MA detection algorithm has been proposed for hemodynamic monitoring during HD using an electrocardiogram (ECG) signal acquired simultaneously. For the sake of performance evaluation, the heart rate (HR) extracted from CVS before and after MA is compared with that by ECG. The proposed method demonstrated a good performance to detect MA (Sensitivity = 0.74, Specificity = 0.9) and facilitates the correction of MA in the CVS signal.

Keywords: EIT; Motion artifact detection; Hemodialysis; Hemodynamic monitoring; Heart rate

1. Introduction

HD is the common treatment for patients with renal failure by removing the waste products from the body. Unfortunately, significant hemodynamic imbalances occur during HD, and the considerable stress on the heart and peripheral vasculature give rise to the changes in cardiac function [Germain2018]. Thereby, real-time monitoring of HD procedures is highly required to prevent the complications induced by the massive fluid reduction within a short time. EIT would be a candidate method for noninvasively real-time monitoring of cardiopulmonary function [Adler2021]. Real-time hemodynamic monitoring during HD could improve the patients' safety and performance standards of dialysis by guiding appropriate interventions, especially in the cases of hypertension and hypotension [Germain2018]. However, hemodynamic monitoring parameters extracted from EIT measurements are highly affected by motion since the CVS is of relatively small magnitude and very sensitive to the contact of electrodes. It may result in miscalculation of hemodynamic parameters extracted from CVS with high noise and artifacts and thus leads to a misunderstanding of hemodynamic status. To provide stable and robust outputs from noise, including motions, detecting MA and correcting the CVS data are highly required. Considering the similar frequency and phase between electrocardiogram (ECG) and CVS, ECG signal acquired simultaneously could be used to detect MA in CVS. We aim to develop a MA detection algorithm for real-time hemodynamic monitoring with the support of ECG signal and evaluate its usefulness in hemodynamic monitoring during HD.

2. Methods

Electrical impedance images were recorded with a single-lead ECG signal and inertia measurement unit (IMU) simultaneously and continuously during HD. IMU sensors include 3-axis accelerations and 3-axis gyroscopes. The CVS was extracted from EIT measurements using the source consistency EIT algorithm [Zhang2020, Jang2021]. Since both ECG and CVS signals were generated from the heartbeat and blood pumping, they have phase matching, and extracted heart rate (HR) from CVS should be the same as HR extracted from ECG. Furthermore, the CVS and ECG signals were obtained from two independent devices in our experiments and had different characteristics of artifacts. The MA gives rise to a significant change in amplitude, frequency, and phase of CVS. Therefore, the phase matching and HR similarity between CVS and ECG signals are no longer valid (excess setting thresholds). The abrupt changes appear in both HR and SV (stroke volume) extracted from CVS due to the motion artifacts. However, the physiological condition of cardiac function does not change discontinuously. SV and HR extracted from CVS follow a regular and stable pattern and are highly correlated with ECG signals. When at least one of the following conditions is fulfilled, the cardiac cycle is considered to be affected by MA and marked as 1 (positive). Otherwise, it is marked as 0 (negative).

$$(1)\ \#\text{Peak} \neq 1,\ \ (2)\ \text{Diff}\,(\text{HR}_{\text{ECG}-\text{CVS}}) > \text{th1},\ \ (3)\ \text{Diff}\,(\text{SV}_{\text{CVS}}) > \text{th2},\ \ (4)\ \text{SV}_{\text{CVS}} > \text{th3 or SV}_{\text{CVS}} < \text{th4}$$

where #Peak is the number of positive peaks in CVS between two adjacent R peaks in ECG, Diff $(\text{HR}_{\text{ECG}-\text{CVS}})$ is the relative difference between HR by ECG and CVS, Diff (SV_{CVS}) is the relative difference between two adjacent SV by CVS, and SV_{CVS} is the SV calculated from CVS. Thereby, the sensitivity and specificity are computed to confirm the performance of the proposed algorithm in terms of MA detection. In addition, HR by EIT (HR-EIT) before and after MA detection and correction was compared with HR by ECG (HR-ECG). Analysis results by Pearson's correlation and limit of agreement (LOA) are presented.

3. Results

MA detected by the proposed algorithm had a sensitivity of 0.74 and specificity of 0.9 with reference to the MA detected by the IMU. After data correction to remove MA, the correlation between HR-EIT and HR-ECG increases from 0.68 to 0.88. The limit of agreement (LOA) decreased from 2.3 (3.7%) to 0.65 (1.1%) beats, as described in Figure 1, which indicates the good performance of the proposed algorithm. The performance to detect MA of the new algorithm could reduce when the quality of ECG is low. In the future, we are planning to apply the proposed algorithm to more datasets, and real-time MA detection and correction will also be considered.

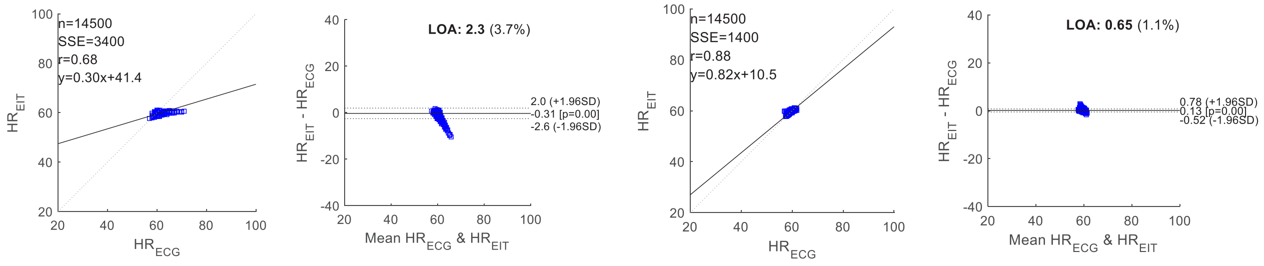

(a) HR-EIT-O vs HR-ECG

(b) HR-EIT-N vs HR-ECG

Figure 1. The comparison results of HR-EIT were extracted from CVS with HR-ECG from ECG: (a) HR-EIT-O before MA correction and (b) HR-EIT-N after MA correction.

4. Conclusion

The introduced MA detection algorithm using ECG acquired simultaneously from an independent device showed an excellent performance in detecting MAs in CVS and improved the correction of calculated HR.

Acknowledgments

This work was supported by the Korea Medical Device Development Fund (NTIS, KMDF-RnD KMDF_PR_20200901_0207), NRF (NRF-2020R1I1A1A01066649, NRF-2020R1A2C1008975), and MOTIE (20006024) grants in Korea.

References

Adler A and Holder D 2021 Electrical impedance tomography: methods, history and applications. *CRC Press.*

Germain MJ, Joubert J, O'Grady D, Nathanson BH, Chait Y, and Levin NW 2018 Comparison of stroke volume measurements during hemodialysis using bioimpedance cardiography and echocardiography. Hemodialysis International **22** 201-208

Jang GY, et al 2020 Non-invasive, simultaneous, and continuous measurements of stroke volume and tidal volume using EIT: feasibility study of animal experiments *Scientific Reports* **10** 1-12

Zhang T, Jang GY, Oh TI, Jeung KW, Wi H and Woo EJ 2020 Source consistency electrical impedance tomography *SIAM Journal on Applied Mathematics* **80** 499-520

Proceedings of the International Conference of Bioelectromagnetism, Electrical Bioimpedance,
and Electrical Impedance Tomography June 29 – July 1, 2022 / Kyung Hee University, Seoul, Korea

Identification of Collapse Pattern and Site of Upper Airway during Obstructive Apnea and Hypopnea using Double-layer Electrical Impedance Tomography and Polysomnography

Tingting Zhang[1,2], Jin Won Mok[1,2,3], Sang-Wook Kim[4], and Tong In Oh[1,2,3]
[1]Medical Science Research Institute, Kyung Hee University Hospital, Seoul, Korea
[2]Department of Biomedical Engineering, School of Medicine, Kyung Hee University, Seoul, Korea
[3]Department of Medical Engineering, Graduate School, Kyung Hee University, Seoul, Kore
[4]Department of Otorhinolaryngology, Gyeongsang National University College of Medicine and Gyeongsang National University Hospital, Jinju, Republic of Korea

Correspondence: Tong In Oh, e-mail: tioh@khu.ac.kr

Abstract–In the previous studies, single-layer electrical impedance tomography (EIT) combined with polysomnography (PSG) has been proposed to detect the upper airway narrowing or closure during sleep noninvasively. Unfortunately, by generating the cross-sectional EIT image at one level, single-layer EIT fails to identify the collapse site in terms of the retropalatal and retroglossal levels of the upper airway, which is of great importance in the clinical practice. In this study, double-layer EIT has been proposed to image the obstruction site of patients with obstructive sleep apnea (OSA). It could provide beneficial supplementary information to facilitate the personalized surgical procedure for OSA.

Keywords: double-layer EIT image; upper airway; obstructive sleep apnea

1. Introduction

Obstructive sleep apnea (OSA) is a sleep disorder featured with the narrowing or closure of the upper airway. The first-line treatment for patients with OSA is applying continuous positive airway pressure (CPAP). However, it is not satisfactory due to poor adherence, unfortunately [Berry2012]. Therefore, alternative treatment like surgery has gained attraction among patients. However, there is no additional information to predict the success rate of surgical treatment or to determine the surgical method. In this study, double-layer EIT has been applied to provide supplementary information on the obstruction site and direction of the upper airway occlusion during natural sleep noninvasively. Thereby it allows for more accurate obstruction site and direction-guided surgical therapy for OSA patients.

2. Methods

Enrolled subjects underwent in-laboratory PSG (Grael 4K PSG, Compumedics, Melbourne, Australia) to precisely diagnose sleep patterns or types of OSA. The participants were instrumented with standard PSG recording sensors: electroencephalography, left and right electrooculography, electrocardiogram, submental and limb electromyography, pulse oximetry probe, nasal pressure sensor, oronasal thermistor, and respiratory effort belts around the chest and abdomen. On the night of the second visit, computed tomography (CT) scans with EIT and PSG measurements were performed simultaneously in the CT room. For this experiment, a double-layer EIT system (AirTom$^{\mathrm{TM}}$-UA; BiLab. Seongnam-si, Gyeonggi-do, Korea) was developed to identify changes in the retropalatal and retroglossal levels. The surface landmarks for attaching electrodes reflecting each level were determined based on a series of mid-sagittal and volume-rendering magnetic resonance images of the head, obtained from dozens of middle-aged men and women, as described in our previous study [Kim2019, Lee2018, Ayoub2020]. When sleep-related breathing disorder events were detected, a series of CT scans were taken accordingly by an experienced sleep technologist [Berry2012]. At the beginning and end of each measurement, we recorded EIT and PSG data in several sessions of momentary maneuvers: normal breath, deep breath, breath-holding, and swallowing to evaluate the quality of EIT data and synchronize the measured data from three medical devices (EIT, PSG, and CT images). The cross-sectional area of the upper airway from acquired EIT images was calculated in the retropalatal and retroglossal levels, respectively, using source consistency EIT techniques [Zhang2020]. In parallel, we applied image segmentation algorithms to CT images to obtain the upper airway area. The correlation between the area changes in CT and conductivity change $\Delta\sigma$ in EIT was calculated by Pearson's correlation coefficient, and the coefficient of determination R^2 was also calculated to evaluate the degree of correlation between them.

3. Results

In order to show the conductivity intensities with respect to obstructive events as well as the collapse site, we illustrated them in Fig. 1: conductivity changes from two different layers, PSG data of nasal pressure, thermistor and thorax movements and oxygen saturation, and the corresponding CT images and EIT images at the moments of normal respiration (baseline), hypopnea, and apnea which were determined by PSG guidelines. We apparently observed greater conductivity changes from EIT images at the retropalatal level than those in the retroglossal level during apnea events, which was consistent with the airway change of CT scans. Analogously, a bigger conductivity change can be seen in apnea than that of hypopnea since the airway is fully collapsed during the apnea event, as shown in Fig 1.

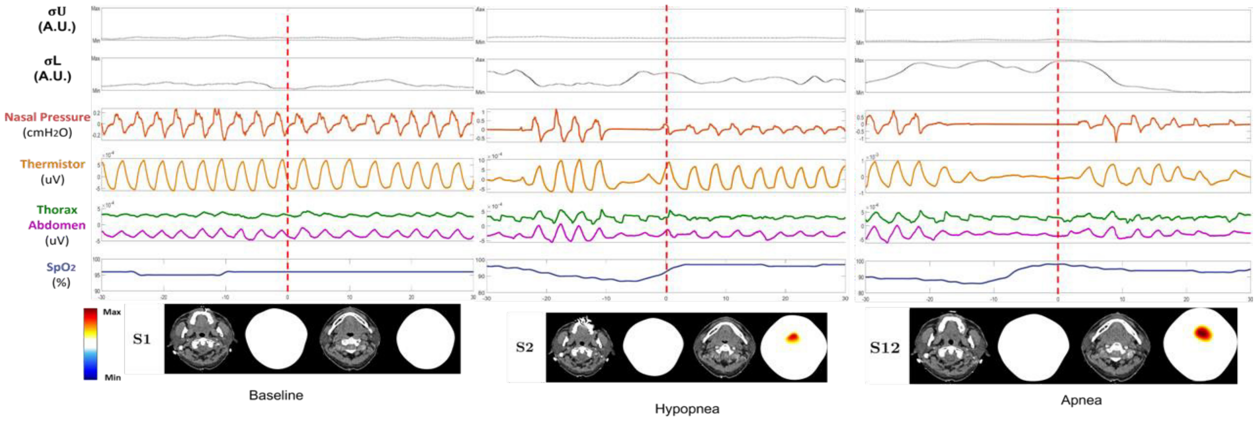

Figure 1. Conductivity changes from two different levels, PSG data, CT and EIT images during normal respiration, hypopnea and apnea

4. Conclusions

In this study, we demonstrated that double-layer EIT could be exploited to identify the collapse site of obstructive sleep apnea in terms of the retropalatal and retroglossal levels, which allows the individualization of surgery planning for OSA patients. Further research efforts will be allocated to the investigation of the structural direction of upper airway occlusion, which is additional information for OSA surgery.

Acknowledgments

This work was supported by a grant of the Korea Health Technology R&D Project through the Korea Health Industry Development Institute (KHIDI), funded by the Ministry of Health & Welfare, Republic of Korea (grant number: HI17C0984), the National Research Foundation (NRF-2017R1A2B2002169) in Republic of Korea, and Basic Science Research Program through the National Research Foundation of Korea (NRF) funded by the Ministry of Education (NRF-2020R1I1A1A01066649).

References

Zhang T, Jang GY, Oh TI, Jeung KW, Wi H and Woo EJ 2020 Source consistency electrical impedance tomography *SIAM Journal on Applied Mathematics* **80.1** 499-520

Kim YE, Woo EJ, Oh TI, Kim SW 2019 Real-time identification of upper airway occlusion using electrical impedance tomography *Journal of clinical sleep medicine : JCSM : official publication of the American Academy of Sleep Medicine* **15** 563-571

Berry RB, Budhiraja R, Gottlieb DJ, Gozal D, Iber C, Kapur VK, Marcus CL, Mehra R, Parthasarathy S, Quan SF, Redline S, Strohl KP, Davidson Ward SL, Tangredi MM 2012 Rules for scoring respiratory events in sleep: update of the 2007 AASM Manual for the Scoring of Sleep and Associated Events. Deliberations of the Sleep Apnea Definitions Task Force of the American Academy of Sleep Medicine *Journal of clinical sleep medicine : JCSM : official publication of the American Academy of Sleep Medicine* **8** 597-619

Lee MH, Jang GY, Kim YE, Yoo PJ, Wi H, Oh TI, and Woo EJ 2018 Portable multi-parameter electrical impedance tomography for and hypoventilation monitoring: Feasibility study *Physiological Measurement* **39** 124004

Ayoub G, Dang TH, Oh TI, Kim SW and Woo EJ 2020 Feature extraction of upper airway dynamics during sleep apnea using electrical impedance tomography *Scientific Reports* **10** 1-10

ICBEM Bioelectromagnetism ICEBI Electrical Bioimpedance EIT Electrical Impedance Tomography

Proceedings of the International Conference of Bioelectromagnetism, Electrical Bioimpedance,
and Electrical Impedance Tomography June 29 – July 1, 2022 / Kyung Hee University, Seoul, Korea

Wide-bandwidth FPGA-based EIT System with Multitone Implementation for Enhancing Medical Imaging in Space

Kendall Farnham[1] and Ryan J Halter[1,2]
[1]Thayer School of Engineering, [2]Geisel School of Medicine, Dartmouth College, Hanover, NH USA

Correspondence : Kendall Farnham, e-mail : kendall.farnham@dartmouth.edu

Abstract–We are developing a space-deployable FPGA-based EIT data acquisition system (DAQ) to integrate with ultrasound for a low-cost, low-resource imaging solution for deep space. The DAQ utilizes a multitone implementation to achieve high-speed spectroscopic impedance data acquisition, and the wide-bandwidth analog design provides versatility for imaging a range of conditions associated with deep space travel. Integrating the small form factor EIT DAQ with state-of-the-art ultrasound will provide high contrast, high resolution images, ultimately enabling crew members to monitor health without the need for telemedical support.

Keywords: FPGA; EIT hardware; ultrasound; dual-modality imaging; space medicine

1. Introduction

Ultrasound is the medical imaging system currently used on the International Space Station, but the greyscale images are difficult to acquire and interpret in the hands of a non-specialist, limiting its effectiveness for isolated deep space missions. Although there is ongoing research to advance ultrasound with the goal of reducing human error and eventually providing automated diagnosis, these technologies violate spacecraft restrictions (e.g. communication, mass, volume) and do not address ultrasound's limited sensitivity to injury type (e.g. detecting cancer in soft tissue, internal bleeding) (NASA HRP 2017). One technique to improve ultrasound image readability is to increase the contrast at injury sites with electrical impedance tomography (EIT), as impedance is sensitive to cellular content, blood flow, tissue type, and tissue injury, all of which are relevant for monitoring physiological effects of the space environment (e.g. tissue injury, muscle atrophy, thoracic function, cancer presence) (Paulsen *et al* 1999). Key design features of a space-deployable EIT system include small form factor, low power, multifunctional, compatible with spacecraft systems, and able to meet NASA EMI/EMC requirements and Technical Standards (NASA Technical Standards System). Additionally, the system should have high SNR (>80 dB) to ensure accurate EIT reconstruction and high-speed acquisition (>30 fps) to capture fast moving processes like blood flow. We are developing a FPGA-based multifrequency, wide bandwidth (100 Hz to 1 MHz) EIT data acquisition system (DAQ) to be integrated with ultrasound for high contrast imaging. The FPGA provides low-cost design flexibility and a low-power, high-speed platform for the EIT DAQ. The multitone implementation allows for high-speed spectroscopic acquisition, and the wide bandwidth provides sensitivity for a range of medical conditions applicable to space travel. This space-deployable EIT system integrated with ultrasound will provide a low cost, low-resource intuitive imaging solution that can accurately characterize deep internal injury (e.g. detect internal bleeding that needs immediate intervention) while meeting space travel constraints, enabling autonomous medical care for deep space missions.

2. Methods

A 64-channel FPGA-based semi-parallel DAQ with a multi-frequency voltage source and dual-channel voltage measurement scheme is being designed for the space-deployable EIT system. The DAQ consists of a medically compliant power supply (IEC 60601-1), Artix-7 FPGA (Xilinx, San Jose, CA, USA), and a custom analog front end (AFE). VHDL code is being developed in Vivado 2018.2.2 (Xilinx) for synchronous control of the DAQ modules, and high-performance Trenz Electronics TE0703 carrier and TE0711 (Artix-7) FPGA boards are used to implement the custom digital design and interface the AFE. Figure 1 outlines the detailed set of digital control modules and AFE components developed for the EIT DAQ. Signal paths through the FPGA and analog components are shown in black (digital) and red (analog). For the voltage source portion of the circuit, a multitone direct digital synthesis (DDS) signal is generated on the FPGA, converted to a voltage using a 14-bit, 125 MSPS digital-to-analog converter (DAC) (THS5671A) and custom differential-to-single-ended I-to-V circuit, and sent to the current sensing and patient isolation circuits. The sensed current on the voltage source PCB is amplified and buffered, then converted to the digital domain using a custom differential driver circuit interfacing a 16-bit, 15 MSPS analog-to-digital converter (ADC) (LTC2387-16). The 16-bit ADC digital output is sent to the FPGA for demodulation and gain control. A similar analog circuit is used for the dual-channel voltage pickup scheme. Multiplexers are used on the source and pickup to allow for any combination of IIVV patterns, and UART commands control frequency and channel selection through a MATLAB-based user interface.

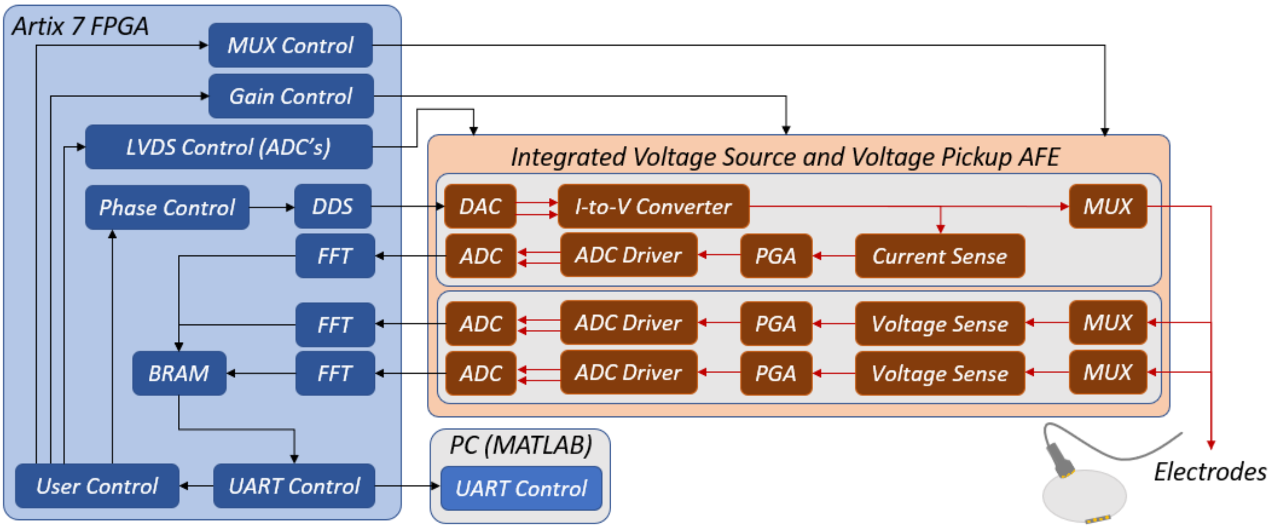

Figure 1. Block diagram of key functionality integrated on the 64-channel US-EIT DAQ. Digital blocks are shown in blue and analog circuits are in orange. Signal paths are denoted with arrows and represent digital (black) and analog (red) signals.

The 64-channel custom analog front end (AFE) has been fabricated onto a single PCB and stacks directly on top of the FPGA carrier for a full system size of 2x2.5x4 inches (Figure 2). An example dual-tone signal generated by the DAQ is shown in the oscilloscope screenshot in Figure 2 – this signal was generated using two DDS cores on the FPGA and converted to the analog domain on the AFE. Acquiring data from multiple frequencies simultaneously will allow for the high speeds needed for real-time ultrasound integration, and the 64 channels provide flexibility for a multi-probe interface with a range of inputs for imaging different conditions.

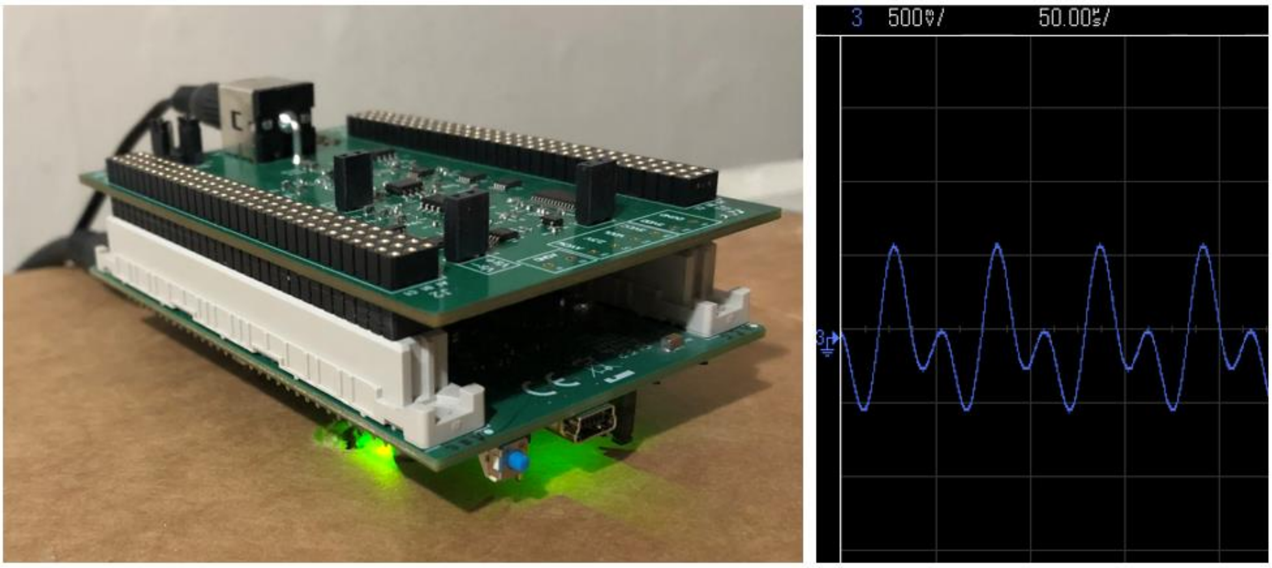

Figure 2. Left) Integrated FPGA-based space deployable EIT DAQ. The bottom board is the FPGA carrier (Trenz Electronics), and the custom voltage source and voltage pickup AFE is stacked on top via 96-pin connectors. Right) Oscilloscope screen capture of a dual-tone voltage source signal from the AFE, generated by two DDS cores on the FPGA.

3. Conclusions

A wideband FPGA-based EIT DAQ with a multitone source and 64-channel interface will provide a low-cost, low-resource solution for imaging a wide range of medical conditions associated with long-duration space travel. Integrating the DAQ with ultrasound will improve image readability and enable astronauts to self-monitor and diagnose injury when isolated in deep space.

Acknowledgments

This work was supported by a NASA Space Technology Graduate Research Fellowship.

References

NASA Human Research Program, Antonsen E *et al* 2017. *Evidence Report: Risk of Adverse Health Outcomes and Decrements in Performance due to In-Flight Medical Conditions* (Houston, Texas). https://ntrs.nasa.gov/archive/nasa/casi.ntrs.nasa.gov/20170004604.pdf

NASA Technical Standards System, Wright A, Gill P. *NASA Technical Standards*. https://standards.nasa.gov/nasa-technical-standards. Retrieved Oct 24 2018.

Paulsen K, Osterman K, Hoopes P 1999. In Vivo Electrical Impedance Spectroscopic Monitoring of the Tissue Injury Progression of Radiation-Induced Tissue Injury. *Radiation Research*, **152(1)**,41–50.

Proceedings of the International Conference of Bioelectromagnetism, Electrical Bioimpedance,
and Electrical Impedance Tomography June 29 – July 1, 2022 / Kyung Hee University, Seoul, Korea

Emerging Trends and Hot Spots of Electrical Impedance Tomography in Extrapulmonary Applications

YuQing Xu[1], Lin Yang[2], Meng Dai[3], Zhe Li[1], ShunPeng Xing[1],
YuXiao Deng[1*], Zhanqi Zhao[3,4]
[1]Department of Critical Care Medicine, Renji Hospital, School of Medicine, Shanghai Jiao Tong University, Shanghai, China,
[2] Department of Aerospace Medicine, Fourth Military Medical University, Xi'an, China
[3]Department of Biomedical Engineering, Fourth Military Medical University, Xi'an, China,
[4]Institute of Technical Medicine, Furtwangen University, Villingen-Schwenningen, Germany

*Correspondence: YuXiao Deng, e-mail: dengyuxiao@renji.com

Abstract- Electrical impedance tomography (EIT) applications have been progressed in technology and applications, and EIT began to be used in multiple clinical and experimental scenarios including pulmonary, brain,tissues monitoring etc. This study explores the emerging trends and hot topics concerning applications on EIT in extrapulmonary applications by bibliometrics analysis. 443 research articles, reviews, letters, and proceeding papers etc. published from 1987 to 2021 in English were analyzed from a global perspective, covering global publications, cooperation between countries, and clustering of keywords. The global annual publications on extrapulmonary applications gradually increased slowly in the last 30 years, and USA, UK and China ranked as the top three prolific contributors in keywords of EIT extrapulmonary applications. “cutaneous melanoma”,“breast cancer detection”,“brain” were research hotspots. Overall, EIT extrapulmonary applications bibliometrics analysis gives us a unique insight to identify scientific advances, hot spots, research trends, and provide future directions of EIT in extrapulmonary applications.

Keywords: EIT; application; extrapulmonary; hotspot; bibliometric analysis;

1. Introduction

Electrical impedance tomography (EIT) is a noninvasive , radiation-free monitory instrument. With the development of hardware and algorithm, the clinical and laboratory application of EIT is getting widespread, especially in regional lung ventilation monitoring(1). Meanwhile, progress has also been made in applications related to extrapulmonary fields such as brain, tissue and skin (2, 3). However, the emerging trends and hot spots of publications of EIT in extrapulmonary have not been evaluated.

Bibliometric analysis indicates the trend of time changes in a certain research field, and make qualitative and quantitative analysis of scientific journals and books, contributing greatly to disease treatment and the development of clinical guidelines. It is beneficial for researchers to identify scientific advances, research trends and cooperative relationships.

In this study, a bibliometric analysis was conducted on EIT extrapulmonary applications to highlight the significant and impactful hotspot of EIT in extrapulmonary applications.

2. Methods

In this study, all data were retrieved from the Web of Science Core Collection (WoSCC) database. The search strategy was TS=(electrical impedance tomography) AND TS=(Hemodynamic OR brain OR nerve OR Cancer OR Venous OR vessel OR Tumour OR Veterinary OR tissue OR cell OR Wearable OR application) NOT TS=(lung OR Ventilation OR respiratory OR pulmonary OR algorithm OR current OR voltage OR electrode)), Time window: January 1, 1987, to 2021.12.31, Publication type: “Article,” “Review,” “Letter,” and “Proceeding paper” ,“ Meeting abstract”, “Early access ” , “note”.Language: English. To avoid database update bias, all searches, including publications, author, title, abstract, keyword, source, language, and citation, were conducted by two investigators independently on 2022.03.23. Then the data were imported to Microsoft Excel 2019 (Microsoft Corporation, Redmond, WA, United States) for bibliometric analysis and VOS (VOS viewer 1.6.15, Leiden University, Leiden, the Netherlands) or CiteSpace 5.7R5 (Chen Meichao, Drexel University) for network analysis.

3.Result

3.1 Growth Trend of Global Publications

The literature counts between 1987 to 2021 illustrated the growth trend slowly increased, first exceeding 30 in 2018. This indicates that EIT in extrapulmonary applications has been a hotspot in the field of EIT research in recent years.

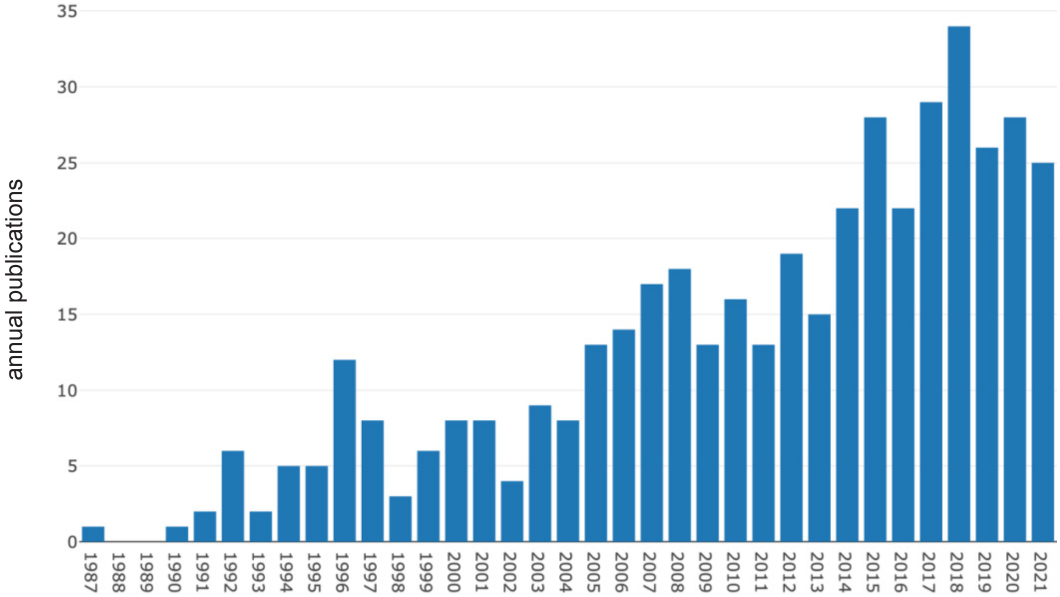

Figure1. Annual publications and growth trends of global electrical impedance tomography (EIT) extrapulmonary applications research from 1987 to December 31, 2021. The blue bars indicate annual publications.

3.2 Global Cooperation between Countries/Regions

The geographical distribution map of global productivity revealed that articles on EIT extrapulmonary applications had been mainly published in North America, European countries and Asia,. Among these, the United States of America (USA), United Kingdom and China ranked as the top three prolific contributors in keywords of EIT extrapulmonary applications. The cross-country collaboration map indicated that cooperation among countries/regions was relatively close (Figure 2). China collaborated most closely with the United Kingdom and Germany. The United States cooperated frequently with China and Israel.

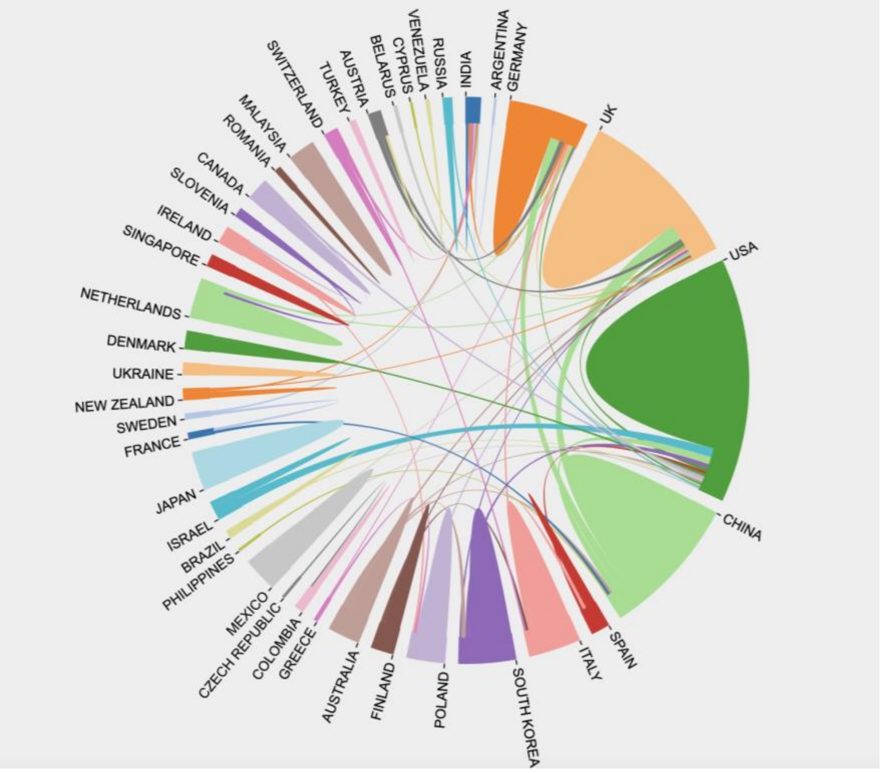

Figure2. Country coauthorship analysis on electrical impedance tomography (EIT) Extrapulmonary Applications research from 1987 to December 31, 2021. Color plate size indicates the number of publications, and the thickness of lines indicates linkage strength.

3.3Bibliometric Analysis of Keywords Co-occurrence

1949 keywords were identified from the included articles, keywords that occurred five or more times were enrolled to be co-occurrence network and overlay analysis. The keywords co-occurred in 18 clusters. “Electrical impedance tomography” (co-occurrences:216) takes the top. The next top four high-frequency keywords were “tissues” (co-occurrence: 61), “conductivity” (co-occurrence: 37), “model” (co-occurrence: 30) and “reconstruction” (co-occurrence: 29).(Figure 3) . The research hotspots of EIT extrapulmonary applications mainly distributed in “brain”, “breast cancer detection”, “hemorrhage” etc. The top ten highly frequent keywords are ranked in Table 1.

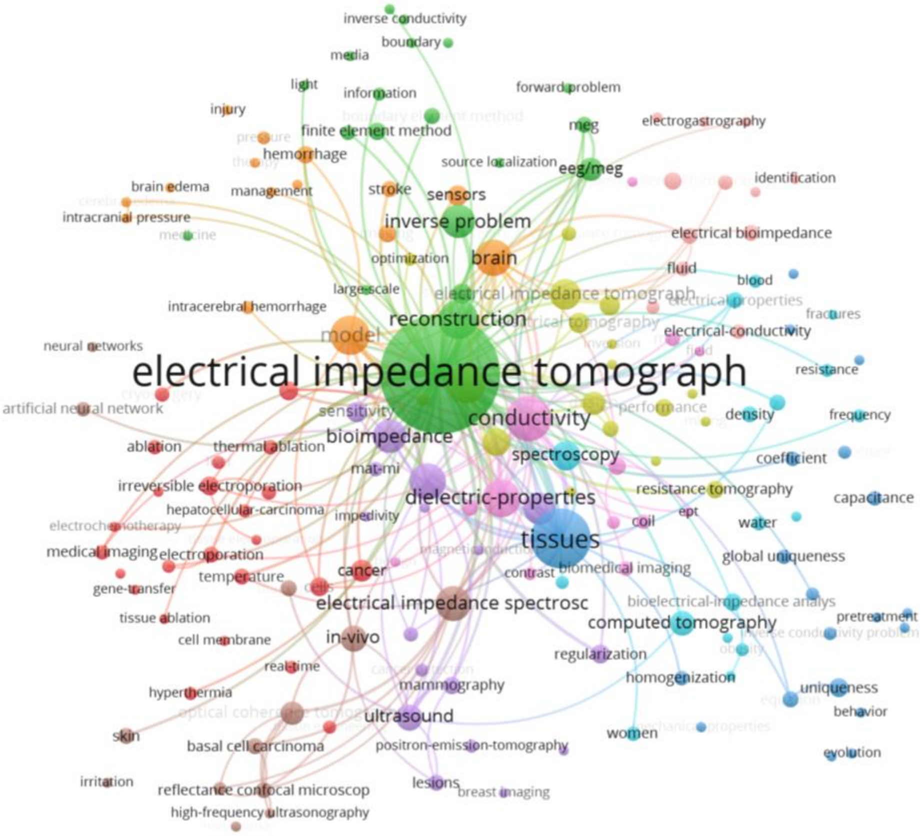

Figure3 Network visualization maps of the keyword co-occurrence. The color indicates clusters respectively. The circle size indicates the number of occurrences, the thickness of lines indicates linkage strength. The distance between circles indicated their relationship.

Table 1. Top 10 highly frequent keywords from the included publications on EIT in extrapulmonary applications

Rank	keyword	occurrences	link strength
1	electrical impedance tomography	216	456
2	tissues	61	224
3	conductivity	37	171
4	model	30	106
5	reconstruction	29	83
6	system	28	100
7	dielectric-properties	27	140
8	brain	25	98
9	breast	25	87
10	inverse problem	22	55

4 Discussion

Electrical impedance tomography is a noninvasive, radiation-free monitory instrument, EIT lung applications research is relatively mature, more focuses on optimal respiratory treatment strategies for ARDS, such as monitoring “regional mechanical ventilation distribution”, “PEEP titration” and “regional pulmonary perfusion”(4). Our study is the first bibliometric analysis to evaluate publications on EIT extrapulmonary applications.

Generally, since 1987 the annual number and cross-country collaboration of EIT extrapulmonary applications publications in the world is slowly increasing (Figure1,2), suggesting EIT extrapulmonary applications start relatively late but rather little. Keywords co-occurrence analysis indicates EIT extrapulmonary applications hotspots mainly distributed in “brain”, “breast cancer detection”, “hemorrhage”, etc. With the improvement of electrical impedance characteristics and algorithms, the brain EIT has become prehospital screening tool to identify intracranial hemorrhage(5), brain tumour, and epilepsy. In addition, EIT as an additional method examinate pregnant and women with high risk of carcinogenesis (BRCA1, BRCA2 genes)(6). Equally important, EIT as an adjunct to visual methods have increased the sensitivity and specificity of skin cancer detection up to 100% and 87%, respectively, thus demonstrating their potential to minimize unnecessary biopsies(7). (Figure 3 and Table 1). This study is likely to help improve the extrapulmonary application of EIT.

5. Conclusions

EIT extrapulmonary applications development is relatively slow compared to pulmonary application. USA contributed the largest number of research in this field. EIT application detection of brain hemorrhage, breast and skin cancer were research focus in the past two decades and will continue as research hot spots. More diversified function monitoring techniques, such as hemodynamics(8) and gastrointestinal tract(9) with EIT are potential emerging research trends on EIT extrapulmonary applications.

Acknowledgments

The work was supported by Shanghai Talent Development Fund (No：2020078)

References

1. Bayford R, Bertemes-Filho P, Frerichs I. Topical issues in electrical impedance tomography and bioimpedance application research. *Physiol Meas* 2020; 41: 120301.
2. Tarotin I, Aristovich K, Holder D. Model of Impedance Changes in Unmyelinated Nerve Fibers. *IEEE Trans Biomed Eng* 2019; 66: 471-484.
3. Murphy EK, Mahara A, Wu X, Halter RJ. Phantom experiments using soft-prior regularization EIT for breast cancer imaging. *Physiol Meas* 2017; 38: 1262-1277.
4. Pan Q, Jia M, Ge H, Zhao Z. Electrical impedance tomography captures heterogeneous lung ventilation that may be associated with ineffective inspiratory efforts. *Crit Care* 2021; 25: 303.
5. Tang T, Weiss MD, Borum P, Turovets S, Tucker D, Sadleir R. In vivo quantification of intraventricular hemorrhage in a neonatal piglet model using an EEG-layout based electrical impedance tomography array. *Physiol Meas* 2016; 37: 751-764.
6. Akhtari-Zavare M, Latiff LA. Electrical Impedance Tomography as a Primary Screening Technique for Breast Cancer Detection. *Asian Pac J Cancer Prev* 2015; 16: 5595-5597.
7. Anushree U, Shetty S, Kumar R, Bharati S. Adjunctive Diagnostic Methods for Skin Cancer Detection: A Review of Electrical Impedance-Based Techniques. *Bioelectromagnetics* 2022; 43: 193-210.
8. Braun F, Proenca M, Lemay M, Bertschi M, Adler A, Thiran JP, Sola J. Limitations and challenges of EIT-based monitoring of stroke volume and pulmonary artery pressure. *Physiol Meas* 2018; 39: 014003.
9. Podczeck F, Mitchell CL, Newton JM, Evans D, Short MB. The gastric emptying of food as measured by gamma-scintigraphy and electrical impedance tomography (EIT) and its influence on the gastric emptying of tablets of different dimensions. *J Pharm Pharmacol* 2007; 59: 1527-1536.

P-13

Proceedings of the International Conference of Bioelectromagnetism, Electrical Bioimpedance,
and Electrical Impedance Tomography June 29 – July 1, 2022 / Kyung Hee University, Seoul, Korea

Emerging Trends and Hot Spots of Electrical Impedance Tomography in hardware

YiRan Li[5] ,Meng Dai[1] ,YuQing Xu[2], ShaoJie Qin[2], Lin Yang[3] ,Zhen Q[i2], Zhe Li[2], Zhanqi Zhao[1,4]
[1]Department of Biomedical Engineering, Fourth Military Medical University, Xi'an, China,
[2]Department of Critical Care Medicine, Renji Hospital, School of Medicine, Shanghai Jiao Tong University, Shanghai, China,
[3] Department of Aerospace Medicine, Fourth Military Medical University, Xi'an, China
[4] Institute of Technical Medicine, Furtwangen University, Villingen-Schwenningen, Germany
[5] Department of Intensive Care Medicine, Eastern Hepatobiliary Surgery Hospital, The Third Affiliated Hospital of Naval Medical University, Shanghai, China.

Correspondence : Meng Dai, e-mail : daimeng@fmmu.edu.cn

Abstract−Electrical impedance tomography (EIT) is a technique to image the electrical properties of tissue based on measuring electrical impedance by body-surface electrodes. With the progress of clinical experience, the major components of EIT instruments becomes an active area of research to improve all aspects of performance, and huge among of studies regard to EIT hardware have been presented in prestigious journals. Therefore, in this study publications on EIT hardware from 1987 to 2021 were extracted from the Web of Science Core Collection (WoSCC) database for bibliometric analysis to trace the EIT developing trends. A total of 2698 publications were analyzed, showing that the annual publications have steadily increased, and the USA was the first prolific contributor in the field of EIT hardware. Among institutions, Kyung Hee University (publications: 164; citing frequency: 3,563) contributed the most publications. “Electrical impedance tomography”, “reconstruction”, and “conductivity” were the top three frequent keywords.

Keywords: bibliometric analysis; EIT, hardware; WoSCC; hotspot.

1. Introduction

Electrical impedance tomography (EIT) is a non-invasive and radiation-free functional imaging technology with the real-time application of monitoring integral and regional lung function and ventilation distribution at the bedside. Since the introduction of the first systems in the early 1980s, EIT instrumentation has continued to evolve in step with advances in analog and digital electronics. While early instruments were designed using primarily analog techniques, newer instruments shift much of the processing to the digital domain, making extensive use of digital signal processors, and programmable logic devices. Many of the most recent instruments use commercially-available computer-based instrumentation, minimizing the amount of custom hardware. Also, along with advances in technology have come advances in system performance, particularly in the areas of system bandwidth and precision. With the developing progress of equipment design and clinical application, topics regarding EIT hardware have been presented in different professional journals and scientific conferences. However, the studies that show the emerging trends and hot spots of publications in the field have not been reported.

Bibliometric analysis analyzes research publications based on big data and artificial intelligence (AI), which has an innate advantage in dealing with huge amounts of data. Therefore, bibliometric analysis is used to assess contributions to a research field, including those by countries, institutions, authors, and journals. In order to explore the current situation, new trends and hot spots of EIT in hardware research, we conducted a bibliometric analysis of this subject for nearly three decades. This study may help researchers identifying the most important and influential articles. Furthermore, the study may highlight the application characteristics of EIT in hardware research, provide valuable insights for the most noteworthy research areas, and predict future work.

2. Methods

In this study, we searched the data against the Web of Science Core Collection (WoSCC) database. Herein, two investigators conducted the search following the strategy of TS = (“electrical impedance tomography”) AND ((“current”) OR (“voltage”) OR (“electrode”) OR (“system”)); Time window: January 1, 1987, to 2021.12.31; Publication type: “Article,” “Proceeding paper,” “Review,” and “Letter,”; Language: English. The search results were imported to Microsoft Excel 2019(Microsoft Corporation, Redmond, WA, United States) for description of the publications, and imported to software VOS viewer 1.6.15 (Leiden University, Leiden, Netherlands) to visualize occurrence network analysis, mapping the scientific literature based on the data of countries, institutions, co-authorship, co-occurrence of keywords, and co-citation.

3. Results

3.1 Growth Trend of Global Publications

Literature from 1987 to 2021 illustrated the growth trend and geographic distribution of global productivity in this field. The sum number of global publications is shown in Figure 2, indicating that the number of annual global EIT publications is increasing generally. In addition, annual publications before 2006 were lower than 100, while the number of publications exploded since 2007, and has remained at a steady level since then. Bisides, Physiological Measurement (publications: 353; citing frequency: 8,378) and Woo, E J (publications: 62; citing frequency: 3,752) were the journal and author with the largest number of articles in the EIT hardware research field.

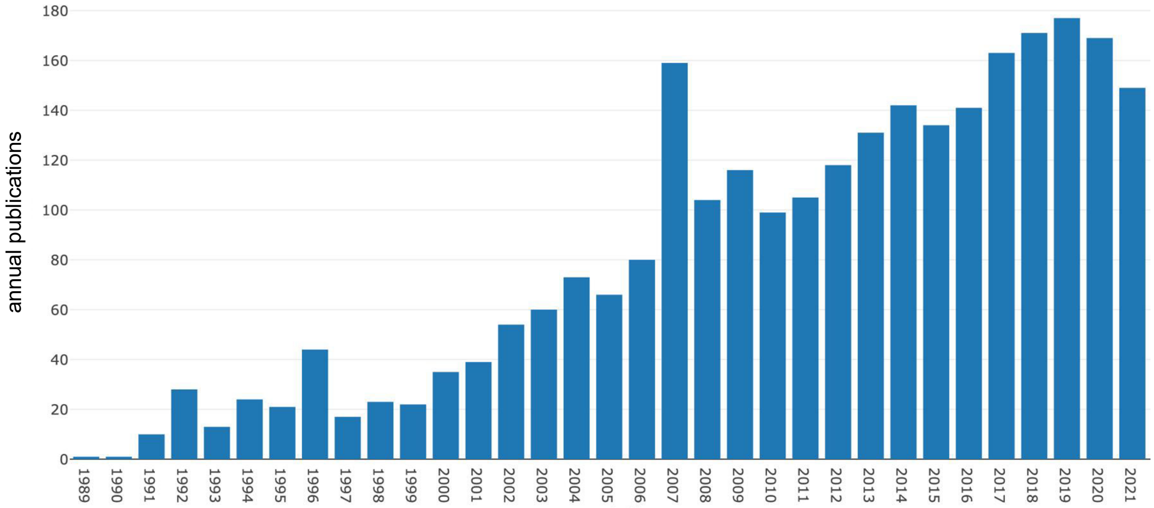

Figure 1. Annual publications and growth trends of global electrical impedance tomography (EIT) hardware research from 1987 to December 31, 2021. The blue bars indicate annual publications.

3.2 Global Cooperation between Countries/Regions

Up to now, 71 countries or regions have published literature on EIT hardware, mainly from North America, Europe, and Asia. Among these, the United States of America (USA), England, China, South Korea, and Germany ranked as the leading five prolific contributors in the field of EIT hardware. The global cooperation between countries in the EIT hardware research field is shown in Figure 2. Through our analysis, England (total link strength: 248), the United States of America (total link strength: 225), and Germany (total link strength: 210) hold the most active cooperation in EIT hardware studies with other countries. Close and active collaboration can be observed in the visualization map.

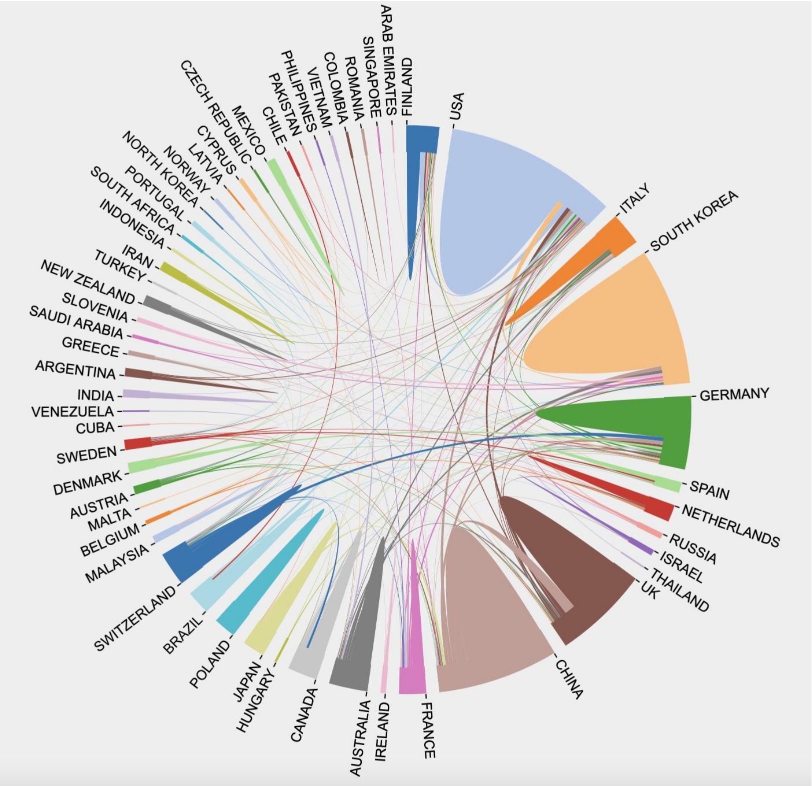

Figure2. Country co-authorship analysis on electrical impedance tomography (EIT) hardware research from 1987 to December 31, 2021. Color plate size indicates the number of publications, and the thickness of lines indicates linkage strength.

3.3 Bibliometric Analysis of Keywords Co-occurrence

6520 keywords were extracted from the collected 2,698 articles. A total of 236 keywords that met the threshold of appearing ten or more times, were classified as high-frequency keywords and added to the co-occurrence network for analysis. The keywords co-occurred in 6 clusters as shown in the network map. The prominent high-frequency keywords were “reconstruction” (co-occurrence:385), “conductivity” (co-occurrence:288), “algorithms” (co-occurrence:228), and “inverse problem” (co-occurrence:215) (Figure 3). The top ten highly frequent keywords are listed in Table 1. In addition, the keyword ″current computed tomography” (strength23.54) had the highest burst value.

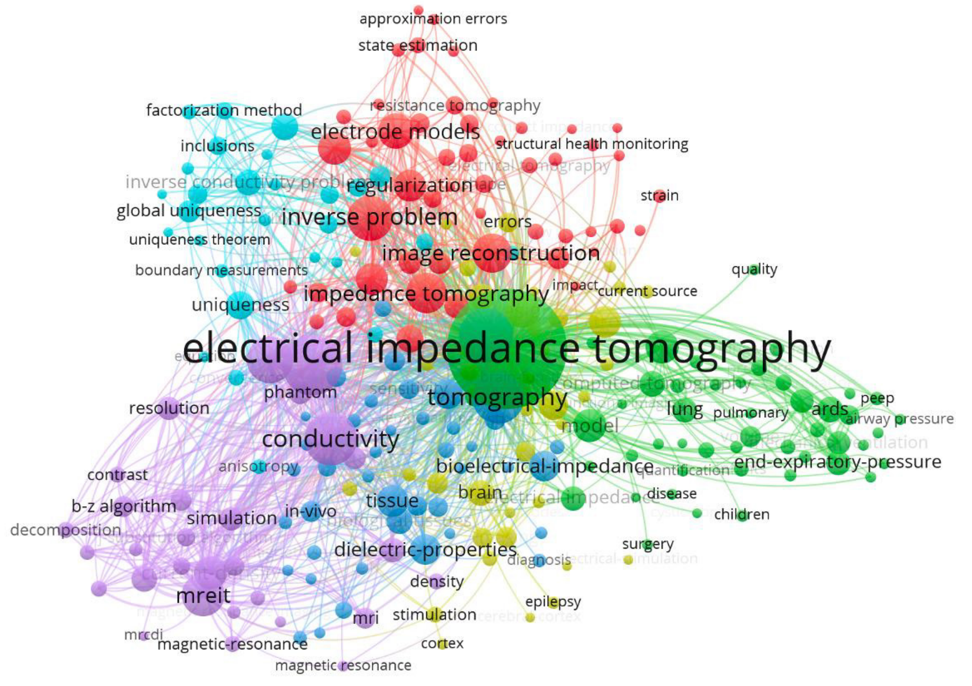

Figure3. Network visualization maps of the keyword co-occurrence. The color indicates clusters respectively. The circle size indicates the number of occurrences, and the thickness of lines indicates linkage strength. The distance between circles indicated their relationship.

Table 1. Top 10 Highly frequent keywords from the included publications on EIT hardware (n = 236).

Rank	keyword	occurrences	Total link strengths
1	electrical impedance tomography	1583	5810
2	reconstruction	385	1934
3	conductivity	288	1663
4	algorithms	228	1279
5	inverse problem	215	1023
6	mrEIT	184	1143
7	image reconstruction	162	700
8	electrode models	127	611
9	current-density	113	765
10	regularization	102	495

4. Discussion

Since the introduction of the first systems in the early 1980s, EIT instruments have evolved with advances in analog and digital electronics. EIT instruments are designed primarily using analog techniques and processing the digital domain, with extensive use of digital signal processors and programmable logic devices(1). Our analysis shows some of the components that are combined to produce EIT instruments in order to optimize the direction of a particular system, such as application drivers, algorithms, voltages, reconstructions, etc. Additionally, it is possible that novel imaging modalities by means of combining EIT and other imaging techniques will continue to be developed for improving the practicality of EIT(2).

5. Conclusions

To sum up, research related to EIT hardware remains to be explored. Based on current global trends, publications on EIT hardware research will increase significantly. The United States, South Korea, China, and England are leading in this field. Up to now, the existing literature mainly focuses on the discussion of “reconstruction”, and “conductivity”, “algorithms”. Furthermore, “Shape reconstruction” and “regularization” will become the next research focus.

Acknowledgments

N.A.

References

(1) Bayford R, Polydorides N. Focus on Recent Advances in Electrical Impedance Tomography. Physiol Meas. 2019;40(10):100401. Published 2019 Nov 4. doi:10.1088/1361-6579/ab42cd

(2) D. Goss, R. O. Mackin, E. Crescenzo, H. S. Tapp, and A. J. Peyton. Development of electromagnetic inductance tomography (emt) hardware for determining human body composition. In Proc. 3rd World Congress on Industrial Process Tomography, pages 377–383, 2003.

ICBEM Bioelectromagnetism ICEBI Electrical Bioimpedance EIT Electrical Impedance Tomography

Proceedings of the International Conference of Bioelectromagnetism, Electrical Bioimpedance,
and Electrical Impedance Tomography June 29 – July 1, 2022 / Kyung Hee University, Seoul, Korea

A bibliometric analysis of the research on imaging algorithm of electrical impedance tomography

ShaoJie Qin[1], Zhe Li[1], Meng Dai[2], RunZhi Chen[4,5], Lin Yang[3*], Zhanqi Zhao[2,6]
[1] Department of Critical Care Medicine, Renji Hospital, School of Medicine, Shanghai Jiao Tong University, Shanghai, China,
[2] Department of Biomedical Engineering, Fourth Military Medical University, Xi’an, China,
[3] Department of Aerospace Medicine, Fourth Military Medical University, Xi'an, China
[4] School of Medicine, Tongji University, Shanghai 200092, China.
[5] Department of Joint Surgery, Shanghai East Hospital, School of Medicine, Tongji University, Shanghai 200092, China
[6] Institute of Technical Medicine, Furtwangen University, Villingen-Schwenningen, Germany

[*]Correspondence: Lin Yang, e-mail: yanglin.0601@163.com

Abstract–Medical electrical impedance tomography (EIT) reconstruction algorithms are approximately forty years old and are now being used to treat patients. At the same time, many advanced concepts are still active research areas, and literature regarding EIT algorithms has been presented in different professional journals and scientific conferences. Bibliometrics analysis method is used to assess the 30 years of scientific output and activity regarding EIT algorithm research from a global perspective, covering global publications, cooperation between countries, and clustering of keywords. 2467 research articles, reviews, letters, and proceeding papers published from 1987 to 2021 in English on EIT reconstruction algorithm were analyzed. Literature statistics show that the worldwide growth trend is rising, and global geographic distribution of publications in this field indicates that USA, South Korea, and China ranked as the top three prolific contributors in terms of EIT algorithm. “inverse problem” “regularization” “electrode models” were research focus. Overall, EIT algorithms bibliometric research provides the current hotspots and future directions of algorithm research.

Keywords: bibliometric analysis; EIT, algorithm; WoSCC; hotspot

1. Introduction

Electrical Impedance Tomography (EIT) is a technique to create tomographic images of the electrical properties of tissue within a body based on electrical impedance measurements at body-surface electrodes. Algorithms run through the whole process of EIT imaging, including but not limited to tissue electrical properties analysis, EIT electronics, sensitivity matrix calculations, EIT image reconstruction, and image interpretation, and exciting current development in reconstruction algorithms has caught much more attention.

Bibliometrics analysis is a good choice to analyze the knowledge structure and the development trend of research activities in a scientific field over time. It is a feasible method for qualitative and quantitative evaluation of publications on a particular topic and has been widely used in various fields to estimate the productivity and international cooperation of countries, institutions and authors. However, a specific bibliometric analysis of EIT algorithms research has not yet been performed.

In the present study, we conducted bibliometric analysis to systematically evaluate EIT algorithm research from 1987 to 2021. We used this new technique to combine mathematical and statistical methods with data visualization to evaluate the publication patterns of research on EIT algorithm. Furthermore, we assessed the patterns of collaboration between countries and tried to make clear the research hotspot and future in this field.

2. Methods

In this study, all data were retrieved from the Web of Science Core Collection (WoSCC) database. The search strategy was TS = (“electrical impedance tomography”) AND ((“algorithm”) OR (“reconstruction”)), Time window: January 1, 1987, to 2021.12.31, Publication type: “Article,” “Review,” “Letter,” and “Proceeding paper,” Language: English. To avoid database update bias, all searches, including publications, author, title, abstract, keyword, source, language, and citation, were conducted by two investigators independently on 2022.01.23. Then the data were imported to Microsoft Excel 2019 (Microsoft Corporation, Redmond, WA, United States) for bibliometric analysis and VOS (VOS viewer

1.6.15, Leiden University, Leiden, the Netherlands) or CiteSpace 5.7R5 (Chen Meichao, Drexel University) for network analysis.

3. Results

3.1 Growth Trend of Global Publications

Literature statistics from 1987 to 2021 show the growth trend in the EIT algorithms research field. Overall, since the first publication by Cheney et al in 1987, the annual number of articles has steadily increased over the last decade, from one in 1987 to exceeding 140 in 2017. This indicates that image reconstruction algorithm has been a hotspot in the field of EIT research.

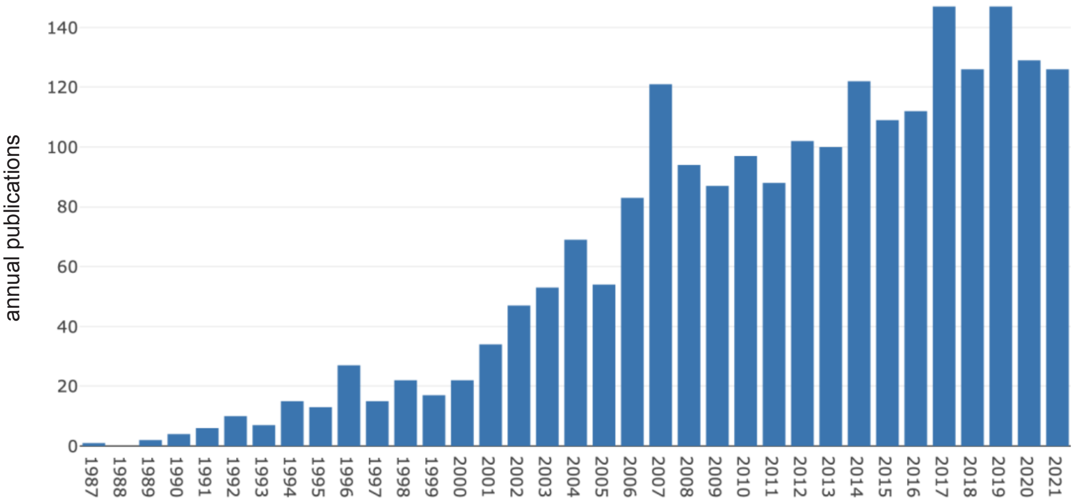

Figure 1. Annual publications and growth trends of global electrical impedance tomography (EIT) algorithms research from 1987 to December 31, 2021. The blue bars indicate annual publications.

3.2 Global Cooperation between Countries/Regions

The geographical distribution map of global productivity revealed that articles on EIT algorithms had been mainly published in Asia, North America, and European countries. Among these, the United States of America (USA), South Korea, and China ranked as the top three prolific contributors in terms of EIT and algorithm. The cross-country collaboration map indicated that cooperation among countries/regions was relatively close (Figure 2). China collaborated most closely with the United States and Austria. The United States also cooperated frequently with South Korea.

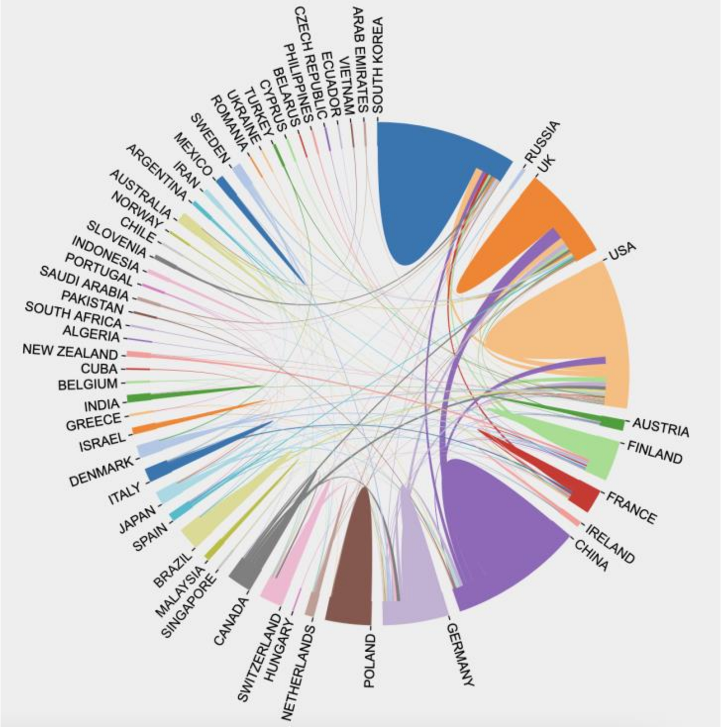

Figure 2. Country coauthorship analysis on electrical impedance tomography (EIT) algorithms research from 1987 to December 31, 2021. Color plate size indicates the number of publications, and the thickness of lines indicates linkage strength.

3.3 Bibliometric Analysis of Keywords Co-occurrence

4884 keywords were identified from the collected articles, and a total of 447 keywords that appeared five or more times were defined as high-frequency terms for co-occurrence network analysis. The terms co-occurred in 9 clusters. “Electrical impedance tomography” (co-occurrence:1410) takes the top. The next top four high-frequency keywords were “reconstruction” (co-occurrence: 598), “algorithm” (co-occurrence: 322), “inverse problem” (co-occurrence: 177), and “regularization” (co-occurrence: 165)(Figure 4). The researches mainly focused on typical theories of solving EIT inverse problems, such as “uniqueness theorem” and “boundary value problem”, etc. Besides, a trend were shown that researchers attempt to obtain more reliable EIT images by integrating some additional conditions, including boundary shape or impedance distribution (“prior information”) and magnetic resonance imaging (“MREIT”). The top ten highly frequent keywords are ranked in Table 1.

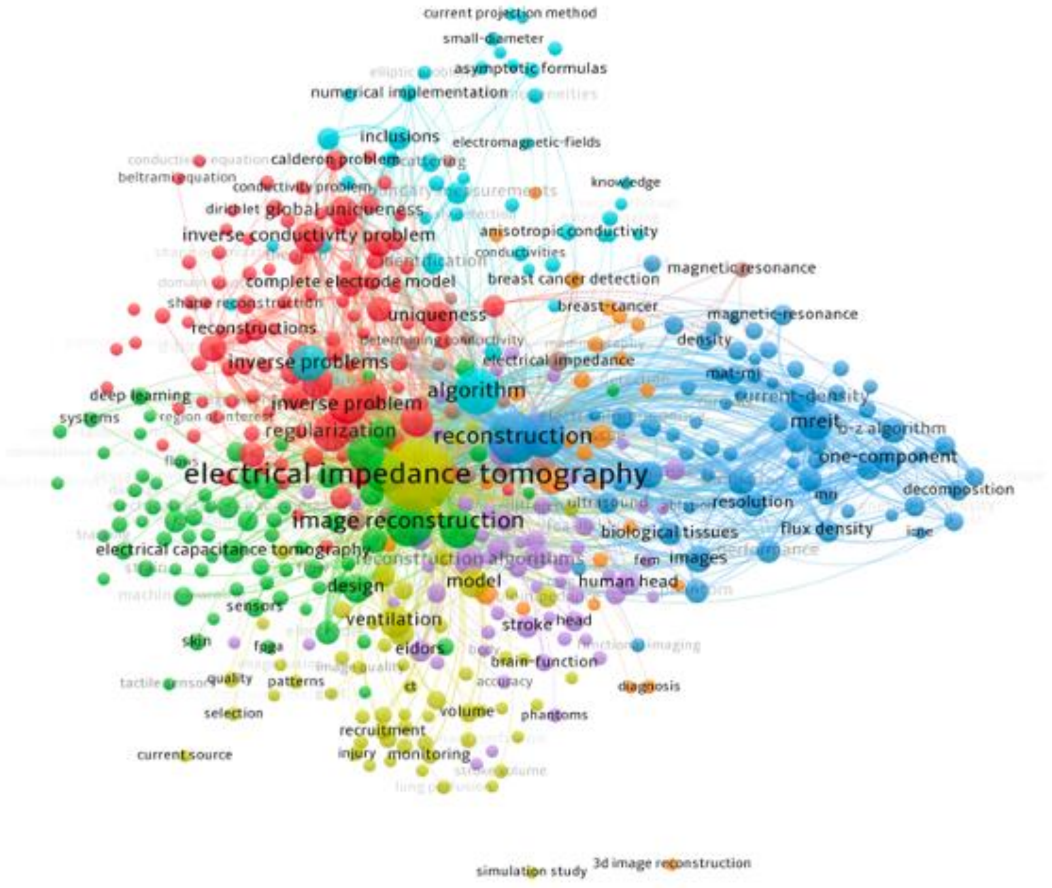

Figure 3. Network visualization maps of the term co-occurrence. The color indicates clusters respectively. The circle size indicates the number of occurrences, the thickness of lines indicates linkage strength. The distance between circles indicated their relationship.

Table 1. Top 10 highly frequent terms from the included publications on EIT in algorithms

Rank	term	occurrences	link strength
1	electrical impedance tomography	1410	6533
2	reconstruction	487	2562
3	algorithms	322	1965
4	inverse problem	177	885
5	regularization	165	936
6	impedance tomography	155	739
7	electrode models	104	623
8	uniqueness	98	695

9	ventilation	92	535
10	current-density	88	656

4. Discussion

EIT image reconstruction algorithm is one of the most important aspects regarding EIT research because it directly determines the quality of EIT reconstruction. In this study, we carried out a bibliometric analysis of publications on EIT image reconstruction algorithms to explore its development process, current situation, and emerging trends so as to provide an informative reference for future algorithm research. Generally, since 1987 the annual number of EIT algorithms publications in the world is increasing and exceeded one hundred for the first time in 2007(Figure 1). International cooperation facilitates technical exchange, thereby improving the research quality and promoting rapid research progress. The same goes for EIT research, where strong collaboration exists among different countries(Figure 2). For example, for lung EIT researchers from Canada, USA, UK, Netherlands and Germany developed a consensus linear reconstruction algorithm, called GREIT (Graz consensus Reconstruction algorithm for EIT)(1). In addition, researchers from China, Germany and Canada have proposed a new algorithm that uses anatomical information to modify the calculation of the global inhomogeneity index(2).

Beyond that, the emphasis of EIT algorithm studies coincides with the highly frequent keywords, such as ‘inverse problem’ and ‘regularization’ (Figure 3 and Table 1). Essentially, EIT image reconstruction is a process of solving the inverse problem, in which the measured boundary voltages are mapped to the impedance distribution. Thus, the purpose of developing EIT algorithm is to obtain a desirable solution to the inverse problem. In addition, it will do justice to the EIT hardware by giving the reconstruction algorithms the best chance of succeeding. For more advanced image reconstruction, there are many unsolved questions, and this study is likely to help improve the state of the art.

5. Conclusions

In conclusion, our analysis indicated that high-quality publications from research groups with deep accumulation in the professional field can provide the current state of algorithm research and the future directions of algorithm research. From 1987 to 2021, developed countries are the main pioneers in this field and have contributed to the development of EIT research. Professional macro and in-depth reviews and interdisciplinary literature can provide reliable references for EIT research, while collaboration can promote the development of the research field.

Acknowledgments

N.A.

References

(1) Grychtol, Bartłomiej et al. “3D EIT image reconstruction with GREIT.” Physiological measurement vol. 37,6 (2016): 785-800. doi:10.1088/0967-3334/37/6/785

(2) Zhao Z, Moller K, Steinmann D, Frerichs I and Guttmann J 2009 Evaluation of an electrical impedance tomography-based Global InhomogeneityIndex for pulmonary ventilation distribution. Intensive Care Med. 35(11):1900-6

ICBEM Bioelectromagnetism ICEBI Electrical Bioimpedance EIT Electrical Impedance Tomography

Proceedings of the International Conference of Bioelectromagnetism, Electrical Bioimpedance,
and Electrical Impedance Tomography June 29 – July 1, 2022 / Kyung Hee University, Seoul, Korea

Regulate the human artificial skin elasticity by weak electric field stimulation

Se Jik Han[1,2], Sangwoo Kwon[2*]

[1]Department of Biomedical Engineering, Graduate school, Kyung Hee University, Seoul, Korea
[2]Department of Biomedical Engineering, College of medicine, Kyung Hee University, Seoul, Korea

Correspondence : Sangwoo Kwon, e-mail : kwonsw@khu.ac.kr

Abstract– The elasticity of skin tissue can be used as an indicator of health and aging. Tissue elasticity is affected by changes in collagen. Therefore, research on regulating the condition of collagen by various external stimuli is in progress, and one of these regulate methods is electric field(EF) stimulation. Electric field stimulation is a classical stimulus that can change the biological processes of cells and tissues. In particular, when an electric field of a specific intensity is applied to the skin tissue, effects such as wound healing, regeneration, and pain suppression have been confirmed, and has been used for therapeutic and cosmetic purposes for a long time. However, the EF shows different results according to the intensity and time of stimulation, more research is needed in the future. In this study, we observed the effect of a weak EF (1 V/cm) stimulation on the artificial skin tissue and confirmed the change in collagen. When a weak EF stimulation was applied for about 600 seconds, the viscoelasticity of the skin tissue was increased compared to the control group. In contrast, the viscoelasticity decreased at stimulation for more than 600 seconds. These changes were also found in collagen. The density, amount, and fiber of collagen also increased at 600 seconds of stimulation and then decreased. This study suggested that stimulation of a weak electric field for a specific time could induce changes in the amount of collagen and fiber structure in artificial skin tissue to increase elasticity.

Keywords: Electric field; Collagen; Artificial skin tissue; Elasticity;

1. Introduction

The elasticity of the skin tissue refers to its ability to return to its original shape after stretching. So it is an indicator that can evaluate the health and age of the skin tissue. Skin tissue loses elasticity due to external stress (sun exposure, air pollution, poor nutrition, smoking) and aging.(Kohl *et al* 2011, Sibilla *et al* 2015) Conversely, specific external stimuli have the effect of improving or maintaining the elasticity of the skin tissue.

In general, stimulation such as lase and hormone therapy has been confirmed by several researchers to improve skin elasticity and is used in patients. For example, 100-200 V/cm EF stimulation can improve wound healing by modulating cell movement.(Robinson and Messerli 2003) Also, when an EF is applied to the dermal fibroblasts, the expression of various extracellular matrix(ECM) is changed.(Schoenbach *et al* 1997) EF stimulation induces various functional changes in skin tissue as well. When an EF stimulation is applied to the skin of a rat, morphological and functional changes in the skin tissue and blood vessels. In addition, quantitative changes in collagen are also observed.(Golberg *et al* 2015)

Collagen is an ECM component produced by dermal fibroblasts and is the most important factor in forming the structure of skin tissue.(Shoulders and Raines 2009) Collagen is abundantly present in the dermis layer of the skin tissue, and the amount, structure, and shape are different depending on the disease or age. In general, the amount and thickness of collagen increases until the age of 40-50, and then decreases after that. In the form of single collagen fibers, the number of broken fibers increases as aging progresses. Therefore, the elasticity of the skin tissue decreases with age.(Marcos-Garcés *et al* 2014, Lynch *et al* 2022)

In this study, we investigated the effect on elasticity after applying a weak EF stimulation to artificial skin that can replace skin tissue. EF stimulation was applied for various times, and the resulting elastic change was observed using a rheometer. Collagen in artificial skin was analyzed by staining method, SEM image, and collagen soluble assay. Finally, we can confirm the correlation between the elasticity of artificial skin and the change in collagen.

2. Materials and Method

2.1 Electric field stimulation

To apply an Electric field to the artificial skins, Platinum were immersed in 35-mm diameter cell culture dishes and connected to a DC power supply. A DC EF of 1.0 V/cm was applied through the electrodes.(Figure. 1)

2.2 Artificial skin

Neoderm®-ED human skin equivalent was purchased from TEGO Science. Neoderm®-ED is a three-dimensional skin culture model that can be used instead of experimental animals. The models included are epidermis, dermis, and epidermis-dermis. All artificial skins were used 24 hours after EF stimulation.

2.3 Sirius red staining

The artificial skin was stained with Sirius red stain following standard procedures for histological analysis. The tissue was deparaffinized and rehydrated in ethanol. Nuclei were stained with Weigert's hematoxylin for 10 minutes, and the slides were washed for 10 minutes in tap water. Next, the tissues were stained for 1 hour using Picro-Sirius Red and washed with two changes of acidified water. Most of the water was removed physically and then dehydrated with three changes of 100% ethanol. The stained images were edited using an iScan HT digital pathology image scanner (Ventana Medical Systems, USA).

2.4 Scanning electron microscopy

A platinum coating was applied around the sliced artificial skin according to the standard procedure for preparing biomaterial for electron microscopy. The collagen fibers was visualized using scanning electron microscopy(SEM, Hitachi S-4700, Japan). Collagen fiber thickness was analyzed by image J software(Version 1.52a, USA).

2.5 Collagen content

The total collagen concentration was assayed using QuickZyme Total collagen assay(QuickZyme Bioscience, Neterlands) according to the manufacturer's protocol. Artificial skin was mixed with 6M HCl and hydrolysis was performed for 20 h at 95 ℃, and then was centrifuged. Samples and dilution assay buffer was added to well in plates. The plate is covered with an enclosed and incubated for 20 min at room temperature. Detection reagent was added to each well of the plate, and samples were incubated for 60 min at 60℃ while shaking. Absorbance was recorded by a microplate reader(Synergy H1, BioTek, USA)with a 570 nm.

2.6 Viscoelasticity measurements

The viscoelasticity of the artificial skin was measured using a discovery HR-2 rheometer(TA Instruments, USA). Samples were loaded onto the stage, and the spacing between the stage and the probe disk was constantly adjusted for all measurements. The viscoelastic storage modulus (G′) and loss modulus (G″) were determined as a function of strain and frequency. Strain was swept from 0.01% to 1000.0% at and angular frequency of 10.0 rad/s, and frequency was increased from 0.1 to 100 rad/s. All experiments were carried out at a constant temperature of 23℃.

3. Results

An EF of 1.0 V/cm was applied to artificial skin for 1800 seconds. The skin structure did not collapse. The collagen density, epidermis and dermis thickness, collagen fiber, and quantitative changes related to expression of collagen levels in artificial skin were investigated by the stimulation condition. To investigate changes in collagen fiber density, the artificial skin was treated with an EF for up to 1800 seconds and analyzed by Sirius Red staining.(Figure. 2A) The collagen fibers were stained red, and their density was analyzed with Image J software. The density of collagen fibers slightly increased by about 5% at 600 seconds in response to EF stimulation, but there was no significant change in other conditions. The change in thickness of artificial skin (Epidermis + Dermis) was observed under a microscope using the dyed tissue. As a result, it increased slightly compared to the control group at 600 seconds and decreased at 1800 seconds. A similar increase/decrease was observed in both the dermis and epidermis layer. (Figure. 2B)

Change in the structure of the collagen fibers were investigated using SEM. Most of the collagen was visible as long fibers.(Figure. 3A) The thickness of the collagen fibers of the control group was 79 nm, which is similar to the normal thickness of collagen.(SHUSTER *et al* 1975) Collagen thickness increased slightly to 87 nm in response to EF stimulation of 300 and 600 seconds, respectively (Figure. 3B). The collagen partially formed a bundle, as indicated by the arrows, and the bundle was more frequently observed in the electrically stimulated groups.

Changes in collagen content due to EF stimulation were measured using a plate reader. As a result, the collagen content increased at 600 seconds of and decreased to the to control group content level at 1800 seconds.(Figure. 3C) That is, EF stimulation induces an increase in the amount of collagen and the thickness of collagen fiber in the artificial skin tissue.

The viscoelastic changes of artificial skin by EF stimulation were analyzed through dynamic strain and frequency(Figure 4A,B). An EF stimulated the artificial skin for up to t = 1,800 seconds. When the strain amplitude was small, the storage modulus (G′) and loss modulus (G″) curves of the artificial skin did not show changes and showed linear viscoelasticity. The G′ of the artificial skin decreased gradually with increasing strain amplitude and the sample(Figure. 4A). G″ increased significantly with increasing strain and decreased at higher strains(Figure. 4B). Both modulus are increased up to 600 seconds by EF stimulation. However, it decreased at the longer stimulus 1800 seconds. As a result of measuring the viscoelasticity when the frequency was increased, both modulus increased up to 600 sec and then decreased(Figure. 4C,D). These results indicate that the deformation resistance of artificial skin increases in response to stimulation for a specific time and decreases in response to excessive stimulation.

4. Discussion

Human skin cells and tissues respond to internal and external stimuli that cause changes in their characteristics or function. Cells lose their ability to metabolism with age, which disrupts the molecular balance and changes their shape.(Scoggin 1981, McHugh and Gil 2018) The blood vessels of the dermis are more easily destroyed(Gunin *et al* 2015), the number and size of melanocytes decreases(Kim *et al* 2017), and the skin becomes dry and uneven.(Sator 2006, Diridollou *et al* 2001) Cells change their appearance or function by the environment of external stimuli.(Lo *et al* 2000) The effects of EF stimulation on skin cells and tissues have been reported in many studies. EF has been used clinically for wound healing and regeneration of damaged and aged skin tissues.(Jaffe and Vanable 1984, Wang and Zhao 2010)

In this study, the effects of EF stimulation on the elastic property of artificial tissues were investigated. We analyzed the changes in collagen density, content, fiber thickness related to elasticity. The density of collagen did not change significantly, but the thickness and collagen content of the artificial skin increased. In addition, it was found that a single collagen fiber was thickened by electric field stimulation. It was shown that the aggregation of collagen was increased in the EF simulation sample. However, it is unclear whether formation of a collagen bundle was due to EF stimulation of artificial skin production. Interestingly, it was confirmed that these changes appeared for a specific time and decreased with excessive stimulation time. Viscoelastic changes in the human artificial skin induced by electrical stimulation were correlated with changes in collagen.

5. Conclusions

In conclusion, we demonstrated that weak EF-induced changes in human artificial skin elasticity and expression of the collagen protein. These changes were observed specific conditions. In addition, changes in elasticity and collagen showed a correlation.

6. Figure

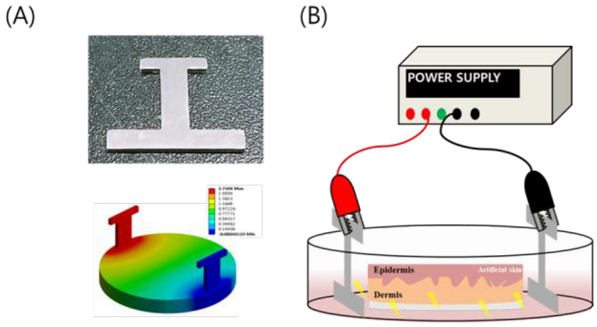

Figure 1. (A) Platinum electrodes used for electric field stimulation and the potential generated were simulated using FEM computer program, (B) Schematic diagram of the EF generation system.

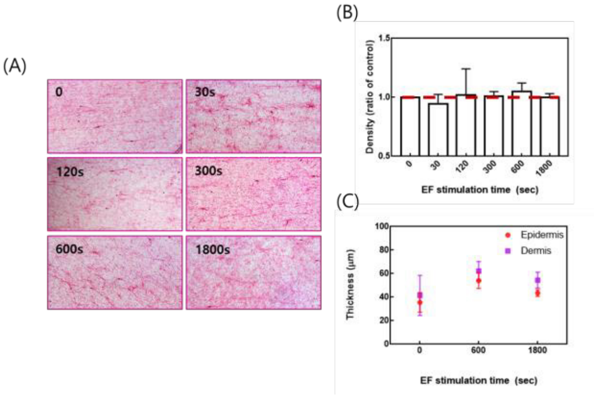

Figure 2. (A) Collagen in the human artificial skin stained with Sirius Red, (B) Collagen fiber density in the sample according to electrical stimulation time. (C) Change of epidermis and dermis thickness by electric field stimulation.

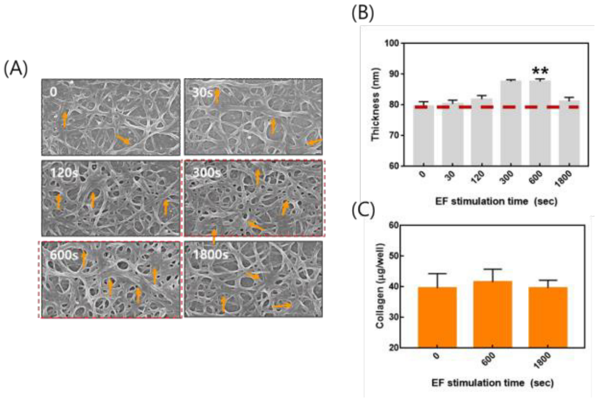

Figure 3. (A) Microstructure of the collagen fibers was visualized using scanning electron microscopy(SEM), (B) Collagen fiber thickness measured in SEM image, (C) Change in collagen concentration by electric field stimulation.

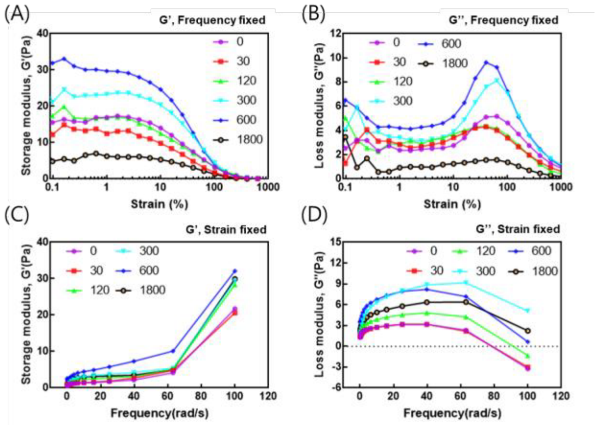

Figure 4. Log profile of strain-dependent (A) storage modulus(G′) and (B) loss modulus(G″) for the skin equivalent. Dependence of (C) G′ and (D) G″ curves on the frequency of different electrical stimulation conditions.

Acknowledgments

This research was supported by the National Research Foundation of Korea (NRF) (Grant number 2021R1I1A1A01055772) funded by the Korean government (MSIT).

References

Diridollou S, Vabre V, Berson M, Vaillant L, Black D, Lagarde J M, Grégoire J M, Gall Y and Patat F 2001 Skin ageing: Changes of physical properties of human skin in vivo *Int. J. Cosmet. Sci.*

Golberg A, Khan S, Belov V, Quinn K P, Albadawi H, Felix Broelsch G, Watkins M T, Georgakoudi I, Papisov M, Mihm M C, Austen W G and Yarmush M L 2015 Skin rejuvenation with non-invasive pulsed electric fields *Sci. Rep.*

Gunin A G, Petrov V V., Vasilieva O V. and Golubtsova N N 2015 Age-related changes of blood vessels in the human dermis *Adv. Gerontol.*

Jaffe L F and Vanable J W 1984 Electric fields and wound healing *Clin. Dermatol.*

Kim J, Cho S Y, Kim S H, Cho D, Kim S, Park C W, Shimizu T, Cho J Y, Seo D B and Shin S S 2017 Effects of Korean ginseng berry on skin antipigmentation and antiaging via FoxO3a activation *J. Ginseng Res.*

Kohl E, Steinbauer J, Landthaler M and Szeimies R M 2011 Skin ageing *J. Eur. Acad. Dermatology Venereol.*

Lo C M, Wang H B, Dembo M and Wang Y L 2000 Cell movement is guided by the rigidity of the substrate *Biophys. J.*

Lynch B, Pageon H, Le Blay H, Brizion S, Bastien P, Bornschlögl T and Domanov Y 2022 A mechanistic view on the aging human skin through ex vivo layer-by-layer analysis of mechanics and microstructure of facial and mammary dermis *Sci. Rep.* **12** 1–14 Online: https://doi.org/10.1038/s41598-022-04767-1

Marcos-Garcés V, Molina Aguilar P, Bea Serrano C, García Bustos V, Benavent Seguí J, Ferrández Izquierdo A and Ruiz-Saurí A 2014 Age-related dermal collagen changes during development, maturation and ageing - a morphometric and comparative study *J. Anat.* **225** 98–108

McHugh D and Gil J 2018 Senescence and aging: Causes, consequences, and therapeutic avenues *J. Cell Biol.*

Robinson K R and Messerli M A 2003 Left/right, up/down: The role of endogenous electrical fields as directional signals in development, repair and invasion *BioEssays*

Sator P G 2006 Skin treatments and dermatological procedures to promote youthful skin. *Clin. Interv. Aging*

Schoenbach K H, Peterkin F E, Alden R W and Beebe S J 1997 The effect of pulsed electric fields on biological cells: experiments and applications *IEEE Trans. Plasma Sci.* **25** 284–92

Scoggin C H 1981 The cellular basis of aging *West. J. Med.*

Shoulders M D and Raines R T 2009 Collagen structure and stability *Annu. Rev. Biochem.* **78** 929–58

SHUSTER S, BLACK M M and McVITIE E 1975 The influence of age and sex on skin thickness, skin collagen and density *Br. J. Dermatol.* **93** 639–43

Sibilla S, Godfrey M, Brewer S, Budh-Raja A and Genovese L 2015 An overview of the beneficial effects of hydrolysed collagen as a nutraceutical on skin properties: Scientific background and clinical studies *Open Nutraceuticals J.*

Wang E T and Zhao M 2010 Regulation of tissue repair and regeneration by electric fields *Chinese J. Traumatol. - English Ed.*

Author Index

Author Index

Author Index

Author Index


Thomas Goo
2021.07.14
1:32:10 PM
12
0.79
18
27
12
37
6.0
395
BiLab
AirTom

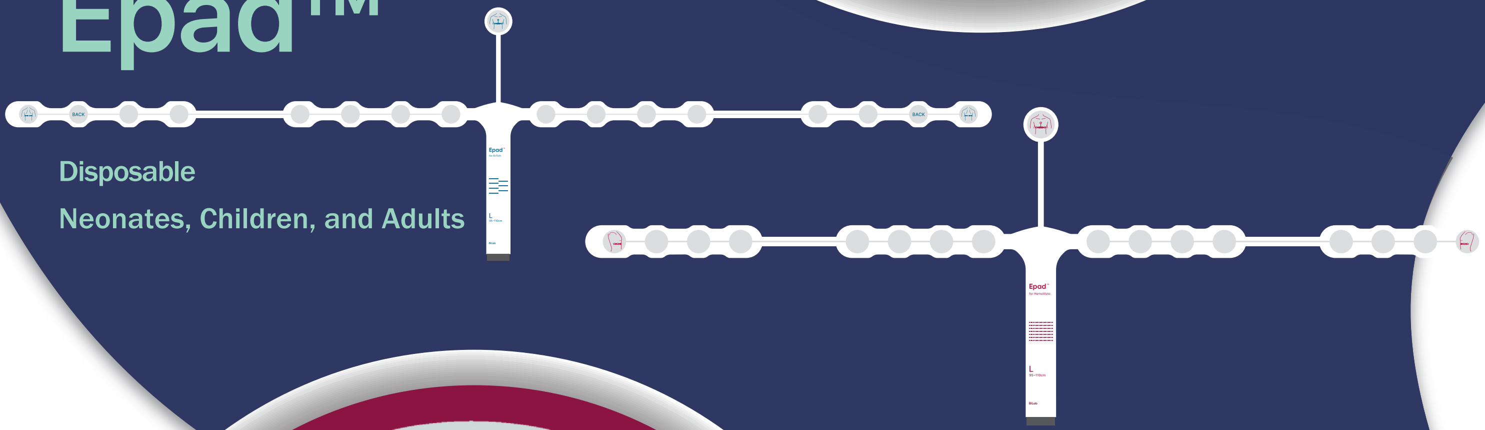
Epad


Thomas Goo
2021.07.14
7:48:28 PM
72
34
4.3
2.2
13
4.3
69
97
BiLab
HemoVista

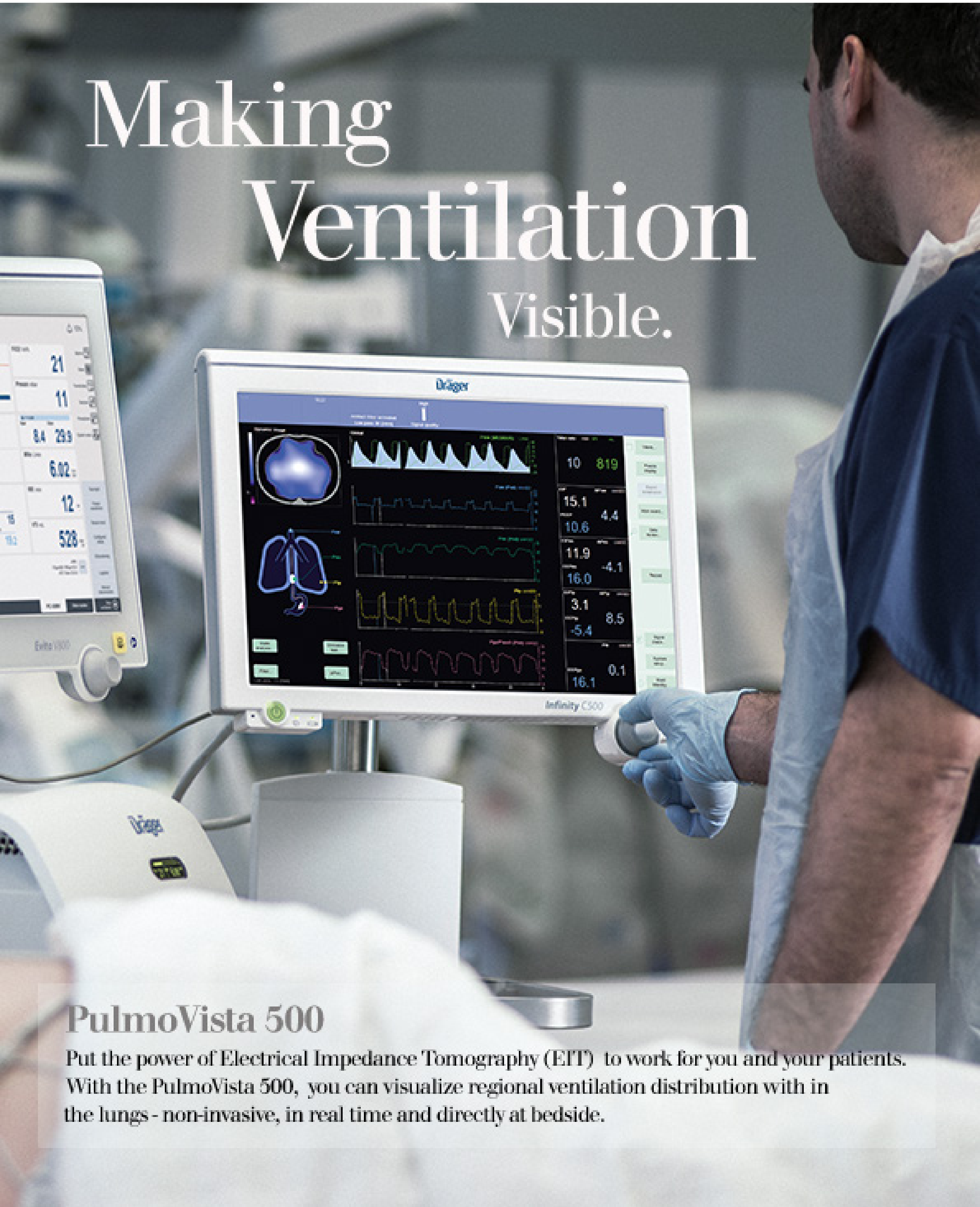
Making
Ventilation
Visible.

This document is the collection of papers accepted for presentation at the

International Conference on Bioelectromagnetism, Electrical Bioimpedance, and Electrical Impedance Tomography 2022

(ICBEM-ICEBI-EIT 2022), Seoul, South Korea.

Collected work : Eung Je Woo, Tong In Oh, Hyung Joong Kim, EunAh Lee

DOI : 10.5281/zenodo.6860841

Hosted by **ICBEM** Bioelectromagnetism **ICEBI** Electrical Bioimpedance **EIT** Electrical Impedance Tomography

Organized by **KYUNG HEE** UNIVERSITY **Impedance Imaging Research Center**

International Conference on Bioelectromagnetism,
Electrical Bioimpedance, and Electrical Impedance Tomography

ICBEM-ICEBI-EIT 2022